THE JOURNAL OF

PHYSICAL

CHEMISTRY

Keep pace with the new...

through these basic research journals of the American Chemical Society

The Journal of the American Chemical Society
The premier American chemistry journal publishing original research papers in every field. Biweekly.

*ACS members: U.S. $22.00	Canada, PUAS $26.50	Other nations $27.50
Nonmembers: U.S. $44.00	Canada, PUAS $48.50	Other nations $49.50

The Journal of Organic Chemistry
Embraces the field, from synthesis to structure to behavior. Biweekly publication.

*ACS members: U.S. $20.00	Canada, PUAS $24.50	Other nations $25.50
Nonmembers: U.S. $40.00	Canada, PUAS $44.50	Other nations $45.50

The Journal of Physical Chemistry
Maintains a balance between classical areas of chemistry and modern structural quantum oriented areas. Biweekly.

*ACS members: U.S. $20.00	Canada, PUAS $24.00	Other nations $25.00
Nonmembers: U.S. $40.00	Canada, PUAS $44.00	Other nations $45.00

Biochemistry
Covers enzymes, proteins, carbohydrates, lipids, nucleic acids and their metabolism, genetics, biosynthesis. Biweekly.

*ACS members: U.S. $20.00	Canada, PUAS $23.00	Other nations $23.50
Nonmembers: U.S. $40.00	Canada, PUAS $43.00	Other nations $43.50

The Journal of Agricultural and Food Chemistry
Places special emphasis on the chemical aspects of agricultural and food chemistry. Bimonthly.

*ACS members: U.S. $10.00	Canada, PUAS $13.00	Other nations $13.50
Nonmembers: U.S. $20.00	Canada, PUAS $23.00	Other nations $23.50

The Journal of Medicinal Chemistry
Emphasis is on synthesis, mode of action and pharmacology of medicinal agents. Monthly.

*ACS members: U.S. $15.00	Canada, PUAS $18.00	Other nations $18.50
Nonmembers: U.S. $30.00	Canada, PUAS $33.00	Other nations $33.50

The Journal of Chemical and Engineering Data
Quarterly journal presenting data on properties and behavior of both new and known chemical systems.

*ACS members: U.S. $15.00	Canada, PUAS $18.00	Other nations $18.50
Nonmembers: U.S. $30.00	Canada, PUAS $33.00	Other nations $33.50

Inorganic Chemistry
Publishes original research, both experimental and theoretical, in all phases of inorganic chemistry.

*ACS members: U.S. $18.00	Canada, PUAS $21.00	Other nations $21.50
Nonmembers: U.S. $36.00	Canada, PUAS $39.00	Other nations $39.50

Macromolecules
Presents original research on all fundamental aspects of polymer chemistry. Bimonthly publication.

*ACS members: U.S. $12.00	Canada, PUAS $15.00	Other nations $15.50
Nonmembers: U.S. $24.00	Canada, PUAS $27.00	Other nations $27.50

THE JOURNAL OF
PHYSICAL CHEMISTRY

NOTES

COMMUNICATIONS TO THE EDITOR

AUTHOR INDEX

In papers with more than one author the name of the author to whom inquiries about
the paper should be addressed is marked with an asterisk in the by-line

Loose and Tight Activated Complexes in the Ion Fragmentations

of a Dimethylthiocarbamate and a Phosphorothioate

by James C. Tou

Chemical Physics Research Laboratory, The Dow Chemical Company, Midland, Michigan 48640
(Received December 3, 1970)

The ion fragmentations involving rearrangement (r) and simple bond scission (s) of a dimethylthiocarbamate and a phosphorothioate are investigated.   The energy dependence of the relative intensity of the rearrangement ion to the ion generated from a simple bond scission is interpreted based on the quasiequilibrium theory of mass spectra.   The rate ratio, $k_r(E)/k_s(E)$, can be expressed as $W_r^{\ddagger}(E - \epsilon_{0,r})/W_s^{\ddagger}(E - \epsilon_{0,s})$, and its value decreases monotonically from $W_r^{\ddagger}(\epsilon_{0,s} - \epsilon_{0,r})$ and approaches zero asymptotically, as the ionizing energy increases.

Introduction

The principles of the quasiequilibrium theory have been used in the interpretation of comparable ion fragmentation reactions comprising rearrangements and simple bond scissions.[1,2]   This reasoning has also been applied to the investigation of aryl participation in the expulsion of a bromine atom from the molecular ion of β-phenylethyl bromide[3] which involves rearrangement mechanism.   The approach aids in understanding the fundamental differences between the spectra of complex molecules at 70 eV and at low voltages.

In this paper, the rearrangements occurring in the ion fragmentations of a dimethylthiocarbamate and a phosphorothioate are studied.   The thermal isomerization of O-aryl dimethylthiocarbamates to S-aryl dimethylthiocarbamates has been reported, which provides a new efficient way of converting phenols into thiophenols.[4]   Similar rearrangement involving S=YO— → O=YS— isomerization, where Y = C or P, have also been observed in both thermal reaction (ArOC(=S)-

OAr → ArOC(=O)SAr, Schönberg rearrangement) and ion fragmentation (ArOC(=S·⁺)OR → ArSC(=O·⁺)OR[6] and ROP(=S·⁺)= → RSP(=O⁺)=[7]).

Results

In our recent mass spectrometric study of a series of dimethylthiocarbamates,[8] two intense peaks were observed at m/e 88 and 72 with ion compositions C_3H_6NS

(1) D. H. Williams and R. G. Cooks, *Chem. Commun.*, 663 (1968).

(2) (a) R. G. Cooks, I. Howe, and D. H. Williams, *Org. Mass Spectrom.*, 2, 137 (1969); (b) A. N. H. Yeo and D. H. Williams, *J. Amer. Chem. Soc.*, 92, 3984 (1970).

(3) R. H. Shapiro and T. F. Jenkins, *Org. Mass Spectrom.*, 2, 771 (1969).

(4) M. S. Newman and H. A. Karnes, *J. Org. Chem.*, 31, 3980 (1966).

(5) H. R. Al-Kazimi, D. S. Tarbell, and D. Plant, *J. Amer. Chem. Soc.*, 77, 2479 (1955).

(6) J. B. Thomson, P. Brown, and C. Djerassi, *ibid.*, 88, 4049 (1966).

(7) F. J. Biros and R. T. Ross, Paper G3, Eighteenth Annual Conference on Mass Spectrometry and Allied Topics, June 1970, San Francisco, Calif.
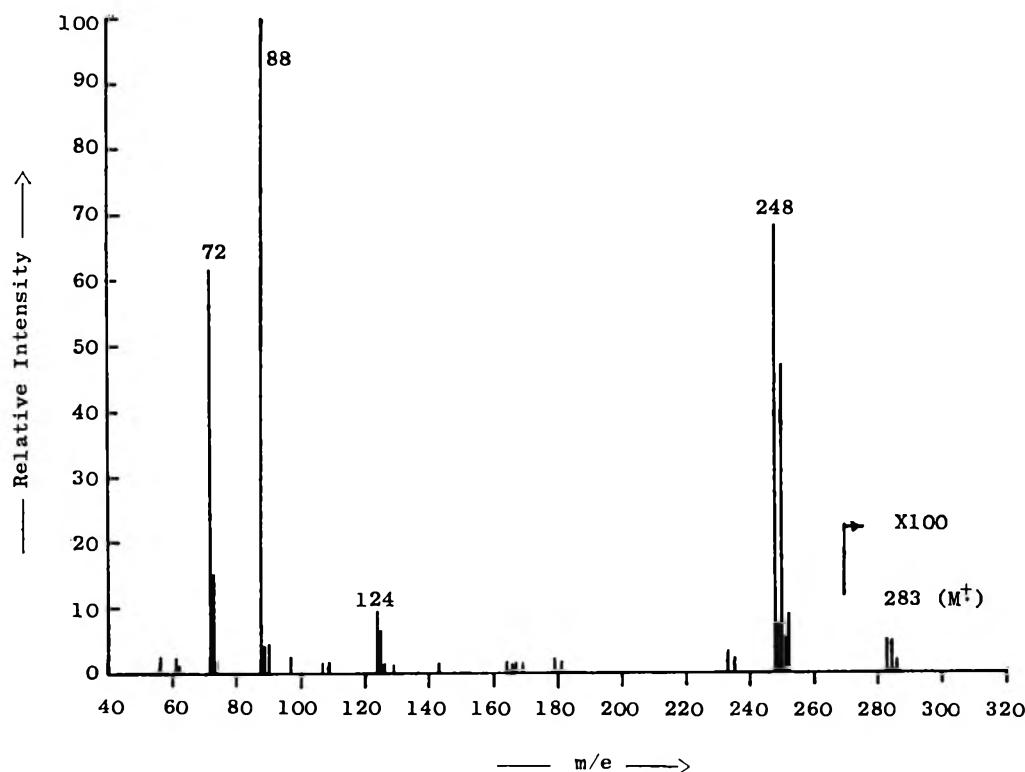
Figure 1. Mass spectrum of O-2,3,6-trichlorophenyl dimethylthiocarbamate (150°).

and C_3H_6NO, respectively. The mass spectrum of O-2,3,6-trichlorophenyl dimethylthiocarbamate at 150° is shown in Figure 1. The spectrum is simple. The molecular ion was detected with extremely weak intensity and shows a loss of Cl· in the generation of a fragment ion at m/e 248. No significant metastable ion transitions to the ions at m/e 88 and 72 were observed in the beam defocusing experiment. It would not be illogical, however, to assume the following reaction scheme

Scheme I
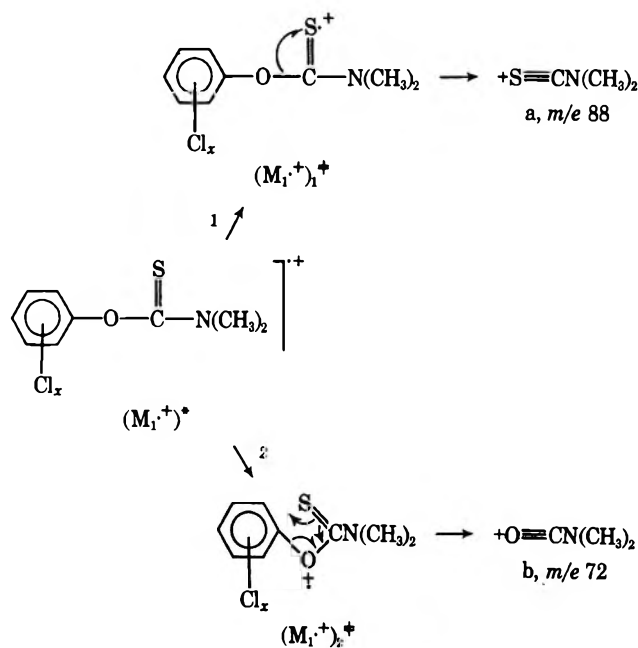
where $(M\cdot^+)^*$ represents the excited molecular ions, $(M_1\cdot^+)_1^{\ddagger}$ and $(M_1\cdot^+)_2^{\ddagger}$ the activated complexes for the reactions of the simple bond scission and the rearrangement leading to the formation of ions at m/e 88 and 72 respectively, and $x = 2$ and (or) 3. In order to determine the extent of thermal rearrangement of —OC(=S)— to —SC(=O)—[4] prior to ionization, the temperature effect on the ion fragmentation was investigated. The intensity ratio of the peaks at m/e 72 and 88, I_{72}/I_{88}, were recorded at the sample temperatures 150, 200, and 250° as a function of residence time in the inlet system. The results are shown in Figure 2. It is noted that a rapid isomerization, —OC(=S)— to —SC(=O)—, took place at 250° and reached equilibrium in about 25 min. However, the ratio shows only a very slight increase with residence time at 150°. Therefore, the ion at m/e 72 shown in Figure 1 (150°) is purely generated from the molecular ion, $(M_1\cdot^+)^*$, upon electron impact through rearrangement reaction 2. This presents another example of the similarity between two energetic processes, thermolysis and ion fragmentation.[9] Under the condition where the thermal effect upon ion fragmentation can be eliminated, i.e., at 150 and 100°, the ratio, I_{72}/I_{88} was studied as a function of ionizing energy. The results are shown in Figure 3. A drastic increase of the ratio near threshold was observed. This indicates that reaction 2 involving rearrangement over-

(8) J. C. Tou and R. M. Rodia, unpublished work.

(9) A. Maccoll in "Modern Aspects of Mass Spectrometry," R. I. Reed, Ed., Plenum Press, New York, N. Y., 1968, pp 143–168, and the references therein.
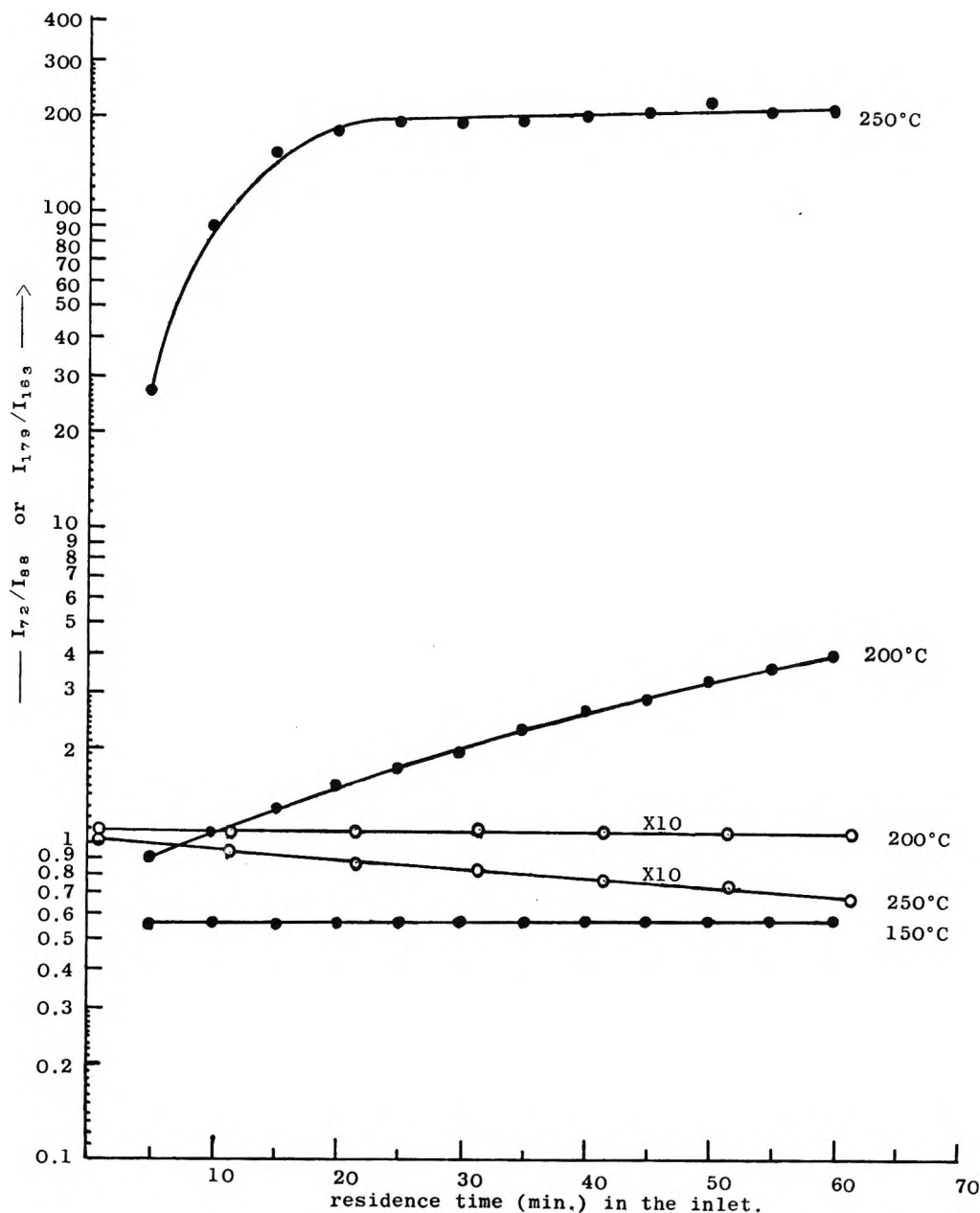
Figure 2.   Temperature dependence of I_{72}/I_{88} (●) in the mass spectrum of the dimethylthiocarbamate and I_{179}/I_{163} (O) in the mass spectrum of the phosphorothioate.

whelmingly overcomes reaction 1 involving simple bond scission in low-energy electron impact.

In contrast to the above case, two comparable rearrangement processes occurring in the ion fragmentation of O-(3,6-dichloro-2-pyridyl)-O,O-diethyl phosphorothioate were investigated. The mass spectrum is shown in Figure 4. The molecular ion shows stepwise losses of one chlorine atom and two ethylene molecules in the generation of fragment ions at m/e 280, 252, and 224 involving one hydrogen rearrangement in each of the last two steps. This is similar to the case of O,O-diethyl phthalimidophosphorothioates,[10] but different from that of triethyl phosphate where a double-hydrogen rearrangement[11] is involved. The ion at m/e 97 is

reasonably assumed to be formed from a simple O–P bond scission of the ion at m/e 224, and has a plausible structure $^+\mathrm{S}{=}\mathrm{P}{\Big\langle}_{\mathrm{OH}}^{\mathrm{OH}}$. The mechanism of the generation of the ion at m/e 174 is unknown. The empirical formula of this ion was determined, however, to be

(10) (a) G. J. Kallos and L. A. Shadoff, "Mass Spectral Studies of Organophosphorus Compounds," The Pittsburgh Conference on Analytical Chemistry and Applied Spectroscopy, 1967; (b) G. J. Kallos, unpublished data.

(11) H. Budzikiewicz, C. Djerassi, and D. H. Williams, "Mass Spectrometry of Organic Compounds," Holden-Day, San Francisco, Calif., 1967, p 651, and the references therein.
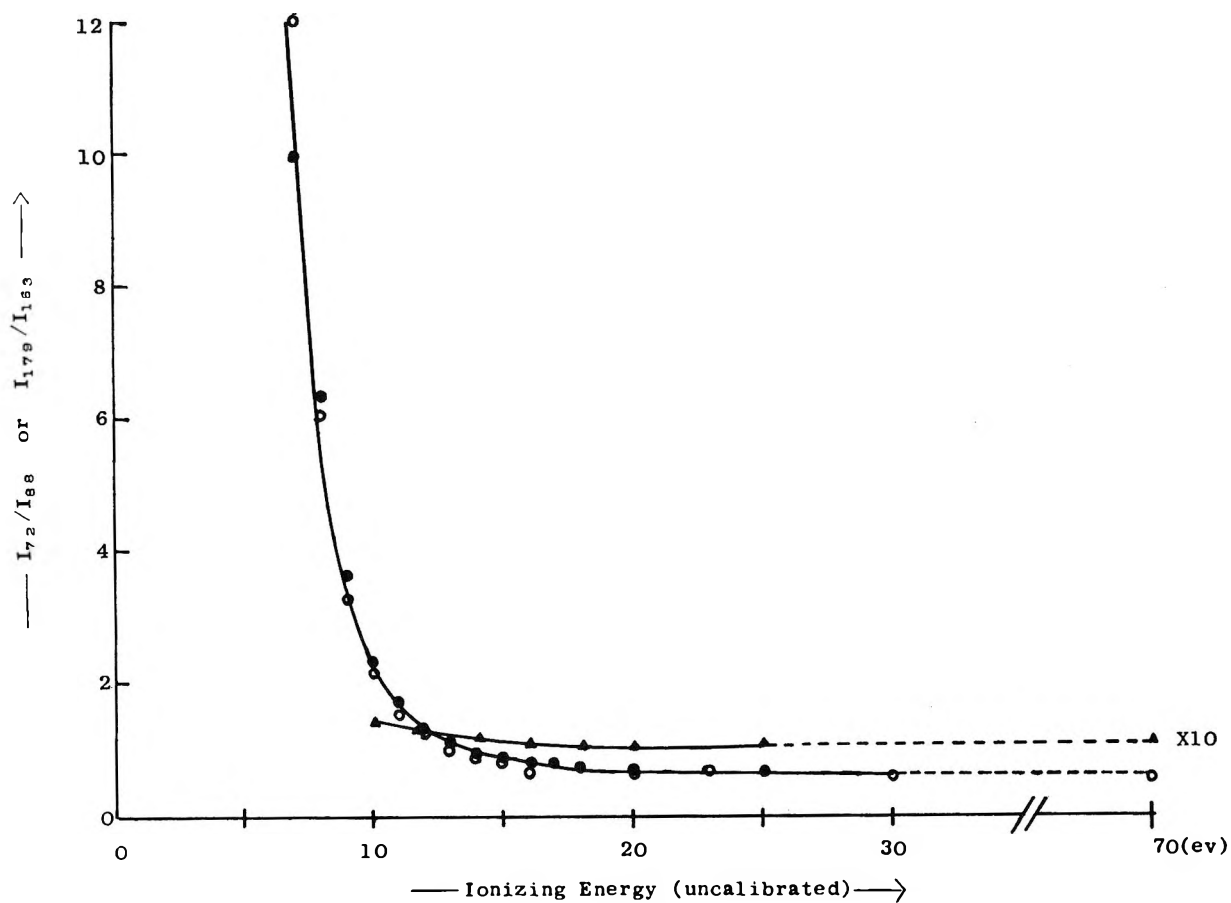
Figure 3. Energy dependence of I_{72}/I_{88} ($\bullet$, 150°; $\bigcirc$, 100°) in the mass spectrum of the dimethylthiocarbamate and I_{179}/I_{163} ($\blacktriangle$) in the mass spectrum of the phosphorothioate.
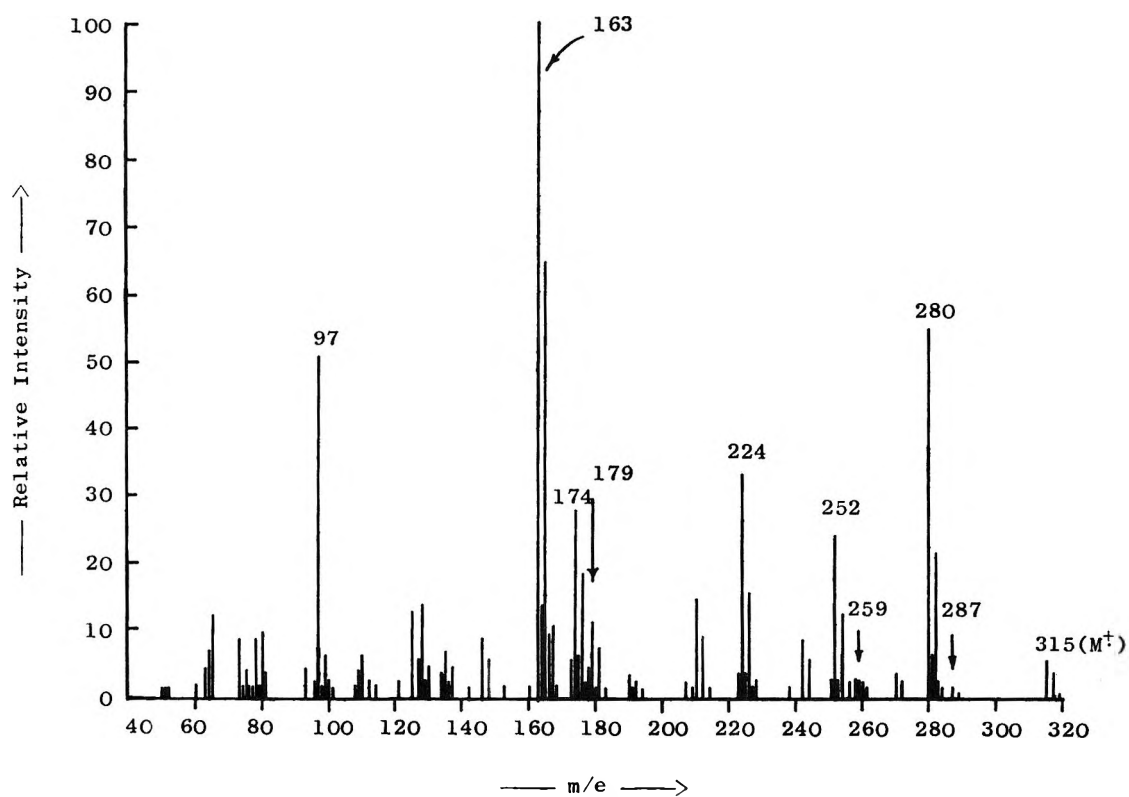
Figure 4. Mass spectrum of O-(3,6-dichloro-2-pyridyl)-O,O-diethylphosphorothioate.

$C_7H_6NCl_2$, which indicates the occurrence of a possible skeletal rearrangement involving one of the alkyl groups. The ions of most interest are the ions at m/e 163 and 179 with empirical formulas $C_5H_3ONCl_2$ and $C_5H_3NCl_2S$, respectively, determined by high-resolution mass spectrometry. No significant metastable ion transition was detected for the generation of these two ions in the beam defocusing experiment. Two possible schemes are assumed.

Scheme IIa
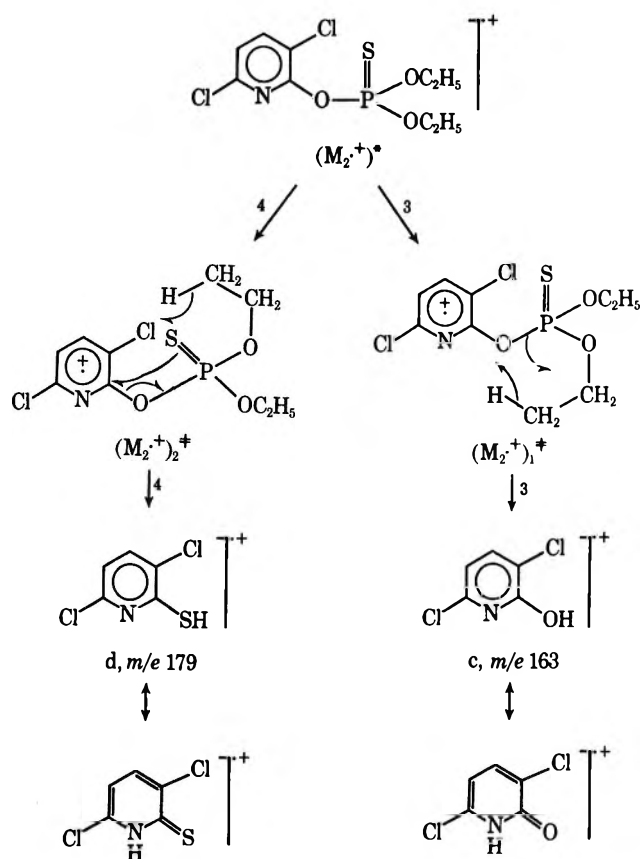
Scheme IIb
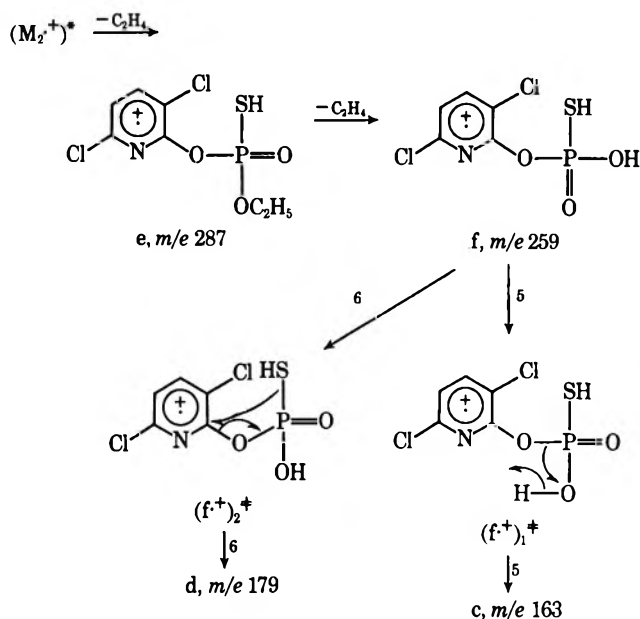
The notations are similar to the ones defined previously. These two comparable rearrangement reactions were studied in detail. The monoisotopic intensity ratio of these two ions, I_{179}/I_{163}, were investigated as a function of residence time at 250 and 200° as well as of ionizing energy at 200°. The results were plotted in Figures 2 and 3, respectively. The constancy of the ratios at 200° in Figure 2 demonstrates the negligible thermal effects upon the ratio-energy curve in Figure 3. The results show a slight increase of the curve as the ionizing energy decreases in contrast to the I_{72}/I_{88} curve in the case of the dimethylthiocarbamate.

Discussion

The data given above clearly show that the rearrangement reaction is increasingly important relative to the simple bond scission reaction as the ionizing energy decreases. However, the comparison of two rearrangement reactions indicates that one is not preferentially favored over another.

According to the quasiequilibrium theory of mass spectra, the rate of dissociation of an isolated excited ion with internal energy, E, can be expressed[12,13] as

$$k(E) = h^{-1}\frac{W^{\ddagger}(E - \epsilon_0)}{\mathrm{d}W(E)/\mathrm{d}E} \qquad (1)$$

where h is Planck's constant, W, the number of states of the ion with internal energy less than and equal to E, $W^{\ddagger}$ that of the activated complex leading to the reaction with activation energy ϵ_0. The rates for the rearrangement reaction $[k_r(E),\ \epsilon_{0,r}]$ and the simple bond scission reaction $[k_s(E),\ \epsilon_{0,s}]$ can then be written

$$k_r(E) = h^{-1}\frac{W_r^{\ddagger}(E - \epsilon_{0,r})}{\mathrm{d}W(E)/\mathrm{d}E} \qquad (2)$$

$$k_s(E) = h^{-1}\frac{W_s^{\ddagger}(E - \epsilon_{0,s})}{\mathrm{d}W(E)/\mathrm{d}E} \qquad (3)$$

The experimental data frequently show $\epsilon_{0,r} < \epsilon_{0,s}$ for two comparable reactions. The activated complex, like $(M_1 \cdot {}^+)_2^{\ddagger}$, $(M_2 \cdot {}^+)_1^{\ddagger}$, or $(M_2 \cdot {}^+)_2^{\ddagger}$, etc., of a rearrangement reaction involves new bond formation and hence certain vibrational frequencies will increase and internal rotation will be stopped. Therefore, the activated complex of this type is called a tight complex. The activated complex, like $(M_1 \cdot {}^+)_1^{\ddagger}$, of a simple bond scission reaction only involves stretching of a bond along the reaction coordinate. The electronic interactions between the atoms of two recoiling groups will be reduced and hence certain vibrational frequencies will decrease and certain torsional and skeletal vibrations in the ground state of the molecular ion might change to allow free internal rotation in the activated state. This

(12) H. M. Rosenstock, M. B. Wallenstein, A. L. Wahrhaftig, and H. Eyring, *Proc. Nat. Acad. Sci. U. S.*, **38**, 667 (1952).

(13) J. C. Tou, L. P. Hills, and A. L. Wahrhaftig, *J. Chem. Phys.*, **45**, 2129 (1966).
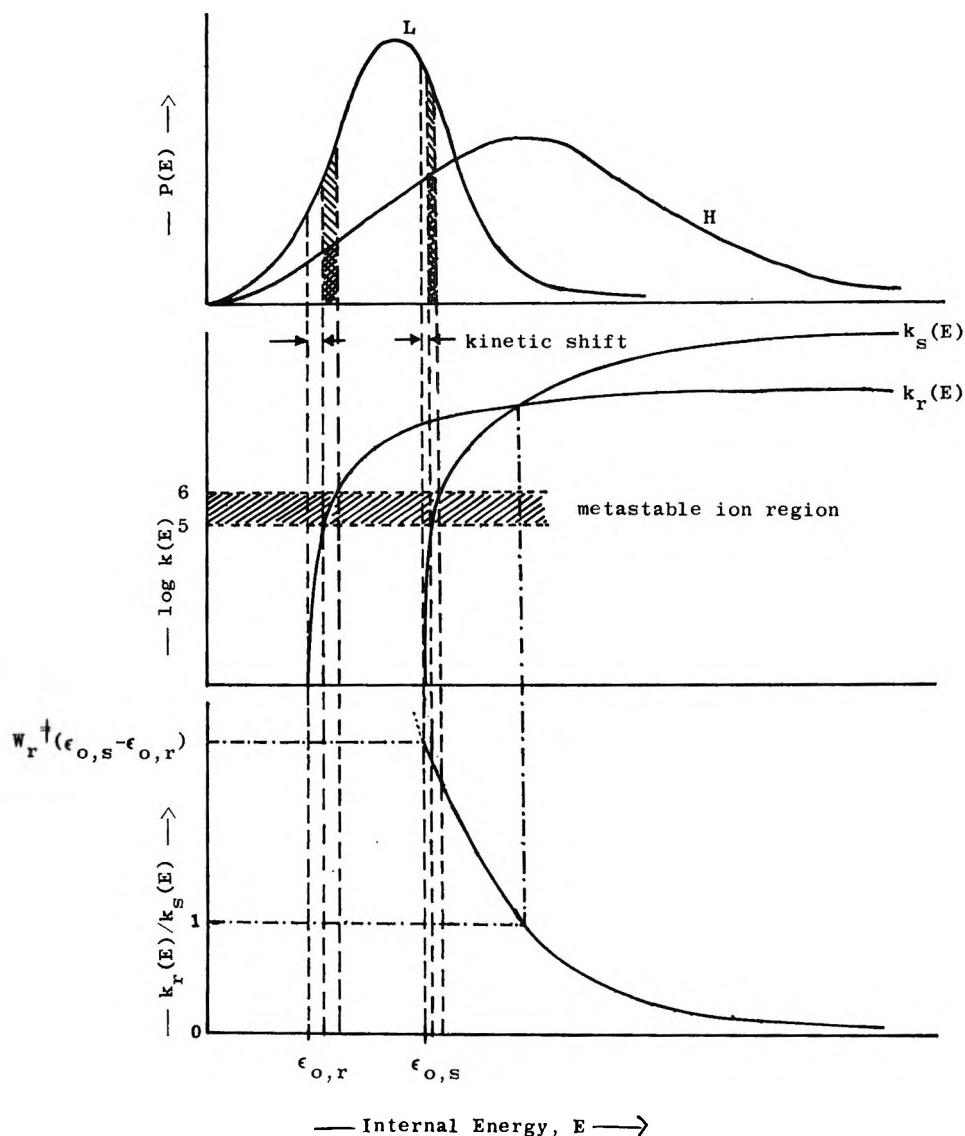
Figure 5. Rate curves for reactions involving rearrangement and simple bond scission.

type of activated complex is called a loose complex. Therefore, $W_s^{\pm}$ increases much faster than $W_r^{\pm}$ as a function of active internal energy, $E - \epsilon_0$.[14] By definition, the rate constants are then being affected.[15] The effect is shown in the quantitative calculations of the transitions $86 \cdot{}^+ \rightarrow 71^+ + \cdot CH_3$ (simple bond scission) and $86 \cdot{}^+ \rightarrow 70 \cdot{}^+ + CH_3$ (rearrangement reaction) in the case of 2-methylpentane.[13] It is clear that the rates involving simple bond scission increase faster than those involving rearrangement even though the former process has a higher activation energy than the latter. These typical curves are plotted in Figure 5. The ratio of the two rate constants can be expressed as a function of internal energy.

$$\frac{k_r(E)}{k_s(E)} = \frac{W_r^{\pm}(E - \epsilon_{0,r})}{W_s^{\pm}(E - \epsilon_{0,s})} \qquad (4)$$

For $E < \epsilon_{0,r} < \epsilon_{0,s}$, no reaction will occur. For $\epsilon_{0,r} \leqslant E < \epsilon^0{}_{,s}$, only rearrangement reaction will take place.

Taking the quantum mechanical tunneling effect into consideration, the ratios, $k_r(E)/k_s(E)$, still have finite values. For $E = \epsilon_{0,s}$, $W_s^{\pm}(0) = 1$ and hence

$$\frac{k_r(E)}{k_s(E)} = W_r^{\pm}(\epsilon_{0,s} - \epsilon_{0,r})$$

For $E \gg \epsilon_{0,r} > \epsilon_{0,s}$, then

$$0 < \frac{k_r(E)}{k_s(E)} \sim \frac{W_r^{\pm}(E)}{W_s^{\pm}(E)} < 1$$

because $W_r^{\pm}(E)$ is always less than $W_s^{\pm}(E)$. In other words, the tight complex has a lower frequency factor than the loose complex as derived from the classical rate expression of the quasiequilibrium theory.[1,2,12] Since both $W_r^{\pm}$ and $W_s^{\pm}$ are monotonically increasing

(14) J. C. Tou and S. H. Lin, *J. Chem. Phys.*, **49**, 4187 (1968).

(15) B. S. Rabinovitch and D. W. Setser, *Advan. Photochem.*, **3**, 1 (1964).

functions of energy,[14] the rate ratio, $k_r(E)/k_s(E)$, decreases monotonically from $W_r^{\ddagger}(c_{0,s} - c_{0,r})$ and approaches zero asymptotically, as the internal energy increases. This is shown in Figure 5.

For simplicity, the internal energy distribution functions, $P(E)$, of the molecular ions are assumed to have shapes as shown in Figure 5 for high ionizing energy (curve H) and low ionizing energy (curve L). It is obvious that when $P(E)$ shifts from high energy to low energy, as illustrated in Figure 5, the distribution of the rate ratios, $k_r(E)/k_s(E)$, shifts to the region of larger values. Therefore, the measured intensity ratio of the fragment ions produced by the rearrangement reaction and the simple bond scission reaction increases as the ionizing energy decreases. This is demonstrated in the experimental data for the case of O-2,3,6-trichlorophenyl dimethylthiocarbamate as shown in Figure 3.

For the two comparable rearrangement processes in the ion fragmentation of O-(3,6-dichloro-2-pyridyl)-O,O-diethyl phosphorothioate, the intensity ratio, I_{179}/I_{163} is expected to be insensitive to the ionizing energy if the assumed Scheme IIb is involved, for the reasons stated previously. However, in the Scheme IIa, the activated complex, $(M_2\cdot{}^+)_2{}^{\ddagger}$, involving a double rearrangement, appears tighter and is expected to have lower activation energy than the activated complex, $(M_2\cdot{}^+)_1{}^{\ddagger}$, involving single rearrangement. In order to explain the I_{179}/I_{163}–E curve, the double rearrangement might proceed as a two-step transition with the reaction rate of the rate-determining step comparable to that of reaction 3.

It is also noted in Figure 5 that $k_r(E)$ increases slower than $k_s(E)$. Therefore, the rearrangement reaction is expected to give more intense metastable ions and more kinetic shift than the reaction involving a simple bond scission. However, the directions of the changes of the relative intensities, $I_{m_r}*/I_{m_s}*$, of the metastable ions ob-

served in the above two processes are dependent upon the crossing of the two rate curves, below or above the metastable ion region. If the crossing is below the metastable ion region, a decrease of the ratio, $I_{m_r}*/I_{m_s}*$ is expected as the ionizing energy increases and *vice versa*.[16] While the theory does not indicate that the metastable ion can always be detected, as shown in the two cases studied, it does tell that the metastable ion of a rearrangement reaction is more readily detected than that of a simple bond scission.

Conclusions

The energy dependence of the relative intensity of the rearrangement ion to the ion generated from a simple bond scission is interpretable based on the quasiequilibrium theory of mass spectra. The rate ratio, $k_r(E)/k_s(E)$, can be expressed as $W_r^{\ddagger}(E - \epsilon_{0,r})/W_s^{\ddagger}(E - \epsilon_{0,s})$, and its value decreases monotonically from $W_r^{\ddagger}(\epsilon_{0,s} - \epsilon_{0,r})$ and approaches zero asymptotically, as the ionizing energy increases.

Experimental Section

The mass spectra were taken on a standard 90° magnetic sector mass spectrometer operating at an acceleration voltage of 450 V and equipped with a Faraday collector. The sample was introduced into the ion source from a 5-l. reservoir through a molecular leak. The accurate masses were measured with a Nier-type matching unit attached to a CEC 21-110B double focusing mass spectrometer. The accuracy of the measurement is within 10 ppm.

(16) P. Brown, *Org. Mass Spectrom.*, **3**, 1175 (1970).

Intermediates Produced in the Flash Photolysis of Acetone and Amides in Aqueous Solution

by M. Nakashima and E. Hayon*

Pioneering Research Laboratory, U. S. Army Natick Laboratories, Natick, Massachusetts 01760   (Received January 7, 1971)

Publication costs assisted by U. S. Army Natick Laboratories

The flash photolysis of air-free aqueous acetone solutions was shown to produce $\dot{C}H_2COCH_3$ and $(CH_3)_2\dot{C}OH$ radicals. The acetonyl $\dot{C}H_2COCH_3$ radical has an absorption maximum at 295 nm and an extinction coefficient $\epsilon_{295} = 800 \pm 150\ M^{-1}\ cm^{-1}$. No intermediates could be observed in the flash photolysis of air-free aqueous amide solutions. In presence of acetone, photosensitized decomposition of amides has been observed. Formamide (F), N,N-dimethylformamide (DMF), acetamide (A), N-methylacetamide (NMA), and N,N-dimethylacetamide (DMA) have been examined, and the transient species produced in the presence of acetone have been observed. These species are produced by H-atom abstraction by triplet excited acetone. With the N-methylated amides, abstraction takes place mainly from the N-methyl group producing $HCON\dot{C}H_2(CH_3)$, $CH_3CONH\dot{C}H_2$, and $CH_3CON\dot{C}H_2(CH_3)$ radicals. With F and A, the main radicals are $\dot{C}ONH_2$ and $\dot{C}H_2CONH_2$. It is interesting to note that the site of H-atom abstraction by triplet acetone is the same as that recently found for abstraction by OH radicals. This correlation is further discussed.

Introduction

Comprehensive spectroscopic studies of the optical absorption spectra of simple aliphatic amides in solution have recently been carried out.[1,2] The effect of substitution on the intensity of the strong (molar extinction coefficient $\sim 8000\ M^{-1}\ sec^{-1}$, oscillator strength ~ 0.25) π,π^* transition of the amide band at ~ 190 nm, and the location of the n,π^* transition, were determined.[1] The photochemistry which these molecules undergo, however, is far from understood.[3] Early work[4] on the photochemistry of acetamide in aqueous solution indicated the formation of ammonia and acetic acid at temperatures higher than 60°; at room temperature, these products were not observed. The photolysis of aliphatic amides in organic solvents was suggested[5] to occur by a molecular mechanism, not involving free radicals. In the gas phase,[6] acetamide produced CH_4, C_2H_6, CO, and NH_3.

To observe the primary intermediates produced on direct optical excitation of amides in aqueous solution, the flash photolysis and kinetic absorption spectrophotometry technique was used. On flash photolysis at $\lambda < 200$ nm of oxygen-free 10^{-4} to $1.0\ M$ aqueous solutions of acetamide, dimethylformamide, dimethylacetamide, and formamide at pH ~ 5.0–6.0, no transient species could be observed in the wavelength region 250–700 nm, time resolution $\sim 20\ \mu sec$. No intermediates were observed on flash photolysis of oxygen-free neat dimethylformamide or dimethylacetamide. In pulse radiolysis studies[7] of the same amides in aqueous solution, a number of radicals were observed and characterized as due to the rupture of C–H and N–H bonds.

Amides and amino acids are known[8] to decompose on exposure to sunlight in the presence of photosensitizers

(TiO$_2$ and ZnO). In an attempt to pursue the reactions which simple amides undergo, the intermediates produced in the photosensitized decomposition of amides were examined. Acetone was chosen as the sensitizer since it had previously been used[9] to produce esr spectra of amide radicals in solution.

Numerous investigations have been carried out on the photochemistry of acetone in the gas phase, but only a few in aqueous[10-12] or nonaqueous (see ref 3, 13–15, and references cited therein) solutions. This paper presents the results obtained on flash photolysis of acetone in aqueous solution, as well as the intermediates produced in the acetone-photosensitized decomposition

(1) E. B. Nielsen and J. A. Schellman, *J. Phys. Chem.*, **71**, 2297 (1967).

(2) D. B. Wetlaufer, *Advan. Protein Chem.*, **17**, 303 (1962); W. B. Gratzer, "Poly-α-amino Acids," G. Fasman, Ed., Marcel Dekker, New York, N. Y., 1969.

(3) J. G. Calvert and J. N. Pitts, Jr., "Photochemistry," Wiley, New York, N. Y., 1966, p 461.

(4) D. H. Volman, *J. Amer. Chem. Soc.*, **63**, 2000 (1941).

(5) G. H. Booth and R. G. W. Norrish, *J. Chem. Soc.*, 188 (1952).

(6) B. C. Spall and E. W. R. Steacie, *Proc. Roy. Soc., Ser. A*, **239**, 1 (1957).

(7) E. Hayon, T. Ibata, N. N. Lichtin, and M. Simic, *J. Amer. Chem. Soc.*, **92**, 3898 (1970).

(8) G. G. Rao and K. M. Pandalai, *J. Indian Chem. Soc.*, **11**, 623 (1934).

(9) R. Livingston and H. Zeldes, *J. Chem. Phys.*, **47**, 4173 (1967).

(10) D. H. Volman and L. W. Swanson, *J. Amer. Chem. Soc.*, **82**, 4141 (1960).

(11) H. Zeldes and R. Livingston, *J. Chem. Phys.*, **45**, 1946 (1966).

(12) I. A. I. Taha and R. R. Kuntz, *J. Phys. Chem.*, **73**, 4406 (1969).

(13) R. Doepker and G. J. Mains, *J. Amer. Chem. Soc.*, **83**, 294 (1961).

(14) R. F. Borkman and D. R. Kearns, *J. Chem. Phys.*, **44**, 945 (1966).

(15) Reference 3, p 393; P. Wagner and G. S. Hammond, *Advan. Photochem.*, **5**, 87 (1968).

of formamide (F), N,N-dimethylformamide (DMF), actamide (A), N-methylacetamide (NMA), and N,N-dimethylacetamide (DMA).

Experimental Section

The flash photolysis apparatus used has already been described.[16] In the aqueous acetone-amide solutions, to prevent photolysis by light below ~200 nm, the chamber of the apparatus was not pumped down. Flashes of energies of about 2000–3000 J were normally used.

Water which was purified by triple distillation followed by radiolysis and photolysis was employed. Solutions were thoroughly deoxygenated by bubbling prepurified nitrogen, and the concentration of acetone in the solution was determined spectrophotometrically after the bubbling. Acetone, DMF, and DMA were Eastman Spectrograde solvents, acetamide was Mallinckrodt reagent grade, and formamide was purified[7] by multiple distillation.

Pulse radiolysis work was carried out using a Febetron 705 (Field Emission Corp.) machine, and the details are described elsewhere.[17] Quartz cells of 2-cm optical path were used.

Results

To interpret the results obtained in the acetone-photosensitized decomposition of amides, it was necessary to study first the intermediates produced in the flash photolysis of acetone in aqueous solution.

Figure 1a shows the transient absorption spectrum observed on flash photolysis of ~30 mM acetone in water at pH ~5.5. Due to the absorption by acetone itself (quartz cells of 20-cm optical path were used) it was not possible to detect transient absorptions below ~310 nm. The decay kinetics of the transient absorption showed the presence of two intermediates, decaying at somewhat different rates. On addition of an excess concentration of an efficient hydrogen donor, isopropyl alcohol, an increased absorption is found (Figure 1b) the transient decays faster, and clean second-order kinetics, apparently due to only one species, are observed.

Since one of the intermediates expected to be formed in the photolysis of acetone is the acetonyl radical, $\cdot CH_2COCH_3$, this species was produced independently, by pulse radiolysis of aqueous solutions of acetone. From known[18] rate constants for OH, e_{aq}^-, and H radicals with acetone, under the conditions of the experiments and dose rate used (Figure 2) only $\cdot CH_2COCH_3$ radicals are considered to be formed by the reaction

$$OH + CH_3COCH_3 \longrightarrow \dot{C}H_2COCH_3 + H_2O$$
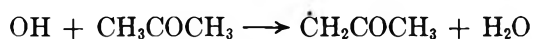
A transient with an absorption maximum at ~295 nm is observed, Figure 2, with an extinction coefficient $\epsilon_{295} = 800 \pm 150\ M^{-1}\ cm^{-1}$. The decay kinetics of the acetonyl radical were neither first nor second
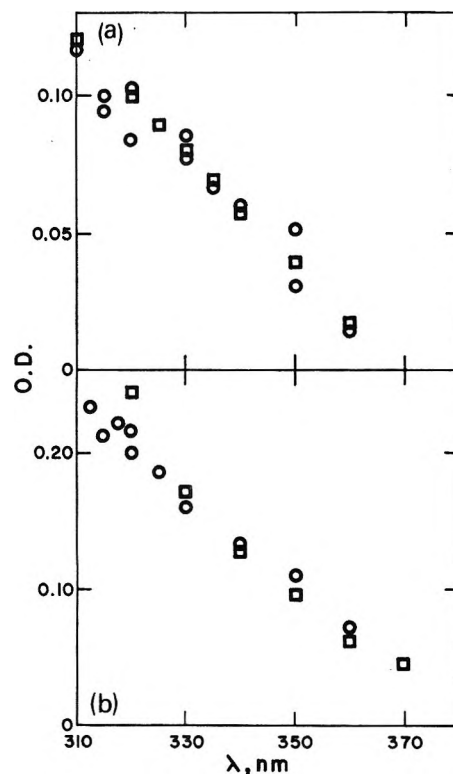
Figure 1. Flash photolysis of air-free aqueous solutions of 30 mM acetone (top curve) and 30 mM acetone in presence of 3 M isopropyl alcohol (bottom curve) at pH 5.5. Square symbols represent spectrum of $\dot{C}H_2COCH_3$ and of ($\dot{C}H_2COCH_3$ + $(CH_3)_2\dot{C}OH$) radicals, respectively.
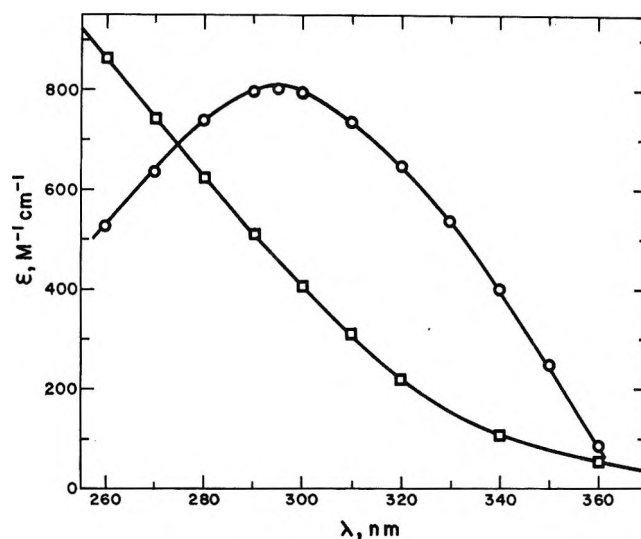
Figure 2. Absorption spectrum of $\dot{C}H_2COCH_3$ ($\odot$) (obtained from the pulse radiolysis of 2 × 10^{-2} M acetone, 0.2 M HClO$_4$) and CH$_3\dot{C}$(OH)CH$_3$ radicals ($\square$) (from pulse radiolysis of 0.1 M isopropyl alcohol, pH 6.0, 1 atm N$_2$O). Data ($\square$) reproduced from ref 17a.

(16) J. R. Huber and E. Hayon, J. Phys. Chem., 72, 3820 (1968).

(17) (a) M. Simic, P. Neta, and E. Hayon, ibid., 73, 3794 (1969); (b) E. Hayon, J. Chem. Phys., 51, 4881 (1969).

(18) M. Anbar and P. Neta, Int. J. Appl. Radiat. Isotopes, 18, 493 (1967).

Table I: Intermediates Observed in the Acetone-Sensitized Photochemical Decomposition of Amides in Aqueous Solution, at pH 5.5

System	λ_{max}, nm	$2k/\epsilon^a$	ϵ, M^{-1} cm$^{-1 b}$	$2k$, M^{-1} sec^{-1}	Suggested radical
20 mM CH$_3$COCH$_3$ + 3.2 M HCONH$_2$	320	5.1×10^6 (3.7×10^6)	350	1.9×10^9	$\dot{C}ONH_2$
30 mM CH$_3$COCH$_3$ + 1.0 M HCON(CH$_3$)$_2$	380	2.0×10^6 (1.4×10^6)	1600	3.2×10^9	HCONH$\dot{C}H_2$
20 mM CH$_3$COCH$_3$ + 5.0 M CH$_3$CONH$_2$	400	3.0×10^6 (2.0×10^6)	1050	3.1×10^9	$\dot{C}H_2CONH_2$
10 mM CH$_3$COCH$_3$ + 0.2 M CH$_2$CONHCH$_3$	340	9.0×10^5 (7.0×10^5)	2000	1.8×10^9	CH$_3$CONH$\dot{C}H_2$
30 mM CH$_3$COCH$_3$ + 0.5 M CH$_3$CON(CH$_3$)$_2$	350	7.5×10^5 (8.0×10^5)	2000	1.5×10^9	CH$_3$CON$\dot{C}H_2$(CH$_3$)

^{a} Figures given in brackets are the corresponding values for the same radicals produced from the reaction of OH radicals with amides by pulse radiolysis (ref 7). ^{b} Taken from ref 7.
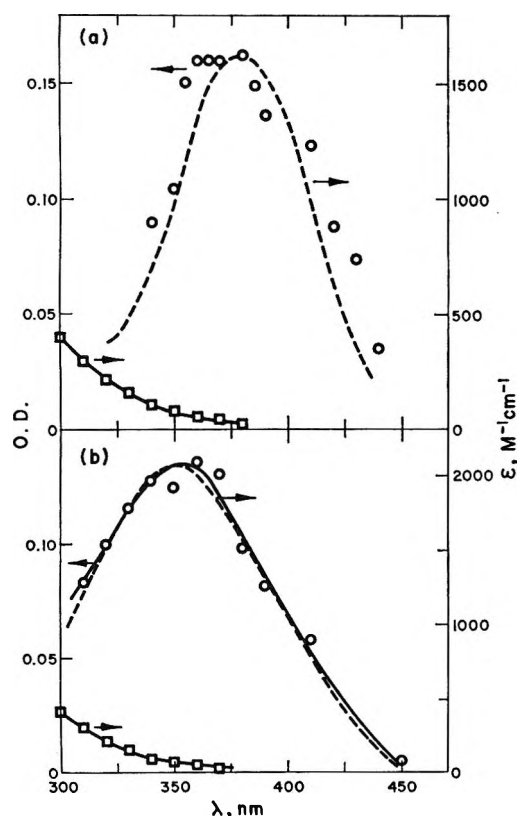
Figure 3. Flash photolysis of oxygen-free aqueous solutions of 30 mM acetone, pH $\sim$5.5, in presence of (a) 1.0 M DMF, OD read at 160 μsec, and (b) 0.5 M DMA, OD read at 200 μsec. Symbols ($\square$) represent the equimolar concentration of CH$_3\dot{C}$(OH)CH$_3$ radicals produced under stated conditions. Dotted line represent absorption spectra of HCON($\dot{C}H_2$)(CH$_3$) and CH$_3$CON($\dot{C}H_2$)(CH$_3$) radicals reproduced from ref 7.

order. At high [$\cdot$CH$_2$COCH$_3$] it approached second-order decay, indicating presumably competition between dimerization and unimolecular decomposition to produce ketene (CH$_2$=C=O) and CH$_3\cdot$ radicals. For comparison, the absorption spectrum of the (CH$_3$)$_2\dot{C}$-(OH) radical, previously obtained,[17a] is shown in Figure 2.

On addition of amides to aqueous solutions containing acetone, new transient absorptions are observed, and different decay kinetics are obtained. Figure 3 shows the transient spectra produced on flash photolysis of air-free 30 mM acetone in presence of 1.0 M dimethylformamide and 0.5 M dimethylacetamide.

On flash photolysis of air-free aqueous solutions of 20 mM acetone in presence of 3.2 M F, 5.0 M A, and 3.0 M NMA weaker transient absorptions were observed, with maximum at $\sim$320, 400, and 340 nm, respectively. All these intermediates decayed by second-order kinetics, and the values are given in Table I. From the decay kinetics, it is possible that R$_1$ + R$_1$ and R$_1$ + R$_2$ radical-radical reactions are occurring.

The flash photolysis of neat DMF in presence of $\sim$30 mM acetone produced the same radicals as found in aqueous DMF–acetone solutions.

Discussion

Flash Photolysis of Acetone. The absorption band of acetone ($\lambda_{max} \sim$280 nm, $\epsilon_{280} \simeq 18\ M^{-1}$ cm^{-1}) is related to a single–singlet ^{1}n–π transition involving the nonbonding electron of the oxygen atom. Borkman and Kearns[14] have found that the excited singlet state of acetone in liquid acetone at 23° has a $\tau \simeq 25$ nsec and a $\phi_F = 0.01$; it undergoes intersystem crossing to the triplet state ^{3}n–π with $\phi_{Ic} \simeq 1.0$ and $k_2 = 4 \times 10^7$ sec^{-1}. In pure acetone,[14] the triplet lifetime is >30 μsec (k_4 can be estimated to be $\geqslant 2 \times 10^5\ M^{-1}$ sec^{-1}), while in liquid hexane[19] it is $\sim$0.4 μsec. The following primary photodissociative processes are considered

$$CH_3COCH_3 \xrightarrow{h\nu} CH_3COCH_3{}^1 \tag{1}$$

$$CH_3COCH_3{}^1 \longrightarrow CH_3COCH_3{}^3 \tag{2}$$

$$CH_3COCH_3{}^3 \longrightarrow CH_3 + CH_3CO \tag{3}$$

$$CH_3COCH_3{}^3 + CH_3COCH_3 \longrightarrow$$
$$\dot{C}H_2COCH_3 + CH_3\dot{C}(OH)CH_3 \tag{4}$$
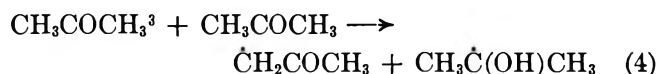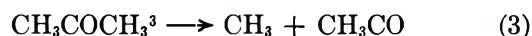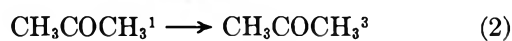
(19) F. Wilkinson and J. T. Dubois, *J. Chem. Phys.*, **39**, 377 (1963).

The methyl radical produced can abstract hydrogen, and all the radicals undergo combination and disproportionation reactions. In presence of an efficient hydrogen donor, e.g., isopropyl alcohol, reaction 5

$$CH_3COCH_3{}^3 + CH_3CH(OH)CH_3 \longrightarrow$$
$$2CH_3\dot{C}(OH)CH_3 \quad (5)$$
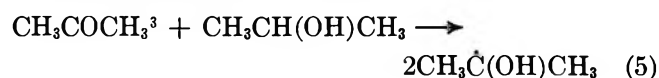
occurs and dissociation of triplet excited acetone via reaction 3 can be almost completely suppressed.[12]

The transient absorption observed in the flash photolysis of acetone in water, Figure 1a, is suggested to be due to the ·CH₂COCH₃ and (CH₃)₂Ċ(OH) radicals. The absorption spectra and extinction coefficients of these radicals are shown in Figure 2. Assuming the formation of equal concentrations of each radical, a transient absorption was reconstructed (based on the spectra in Figure 2) and is superimposed on Figure 1a. The agreement is satisfactory. Zeldes and Livingston[11] have observed the esr spectra of ĊH₂COCH₃, (CH₃)₂-ĊOH, and CH₃ radicals on photolysis of aqueous acetone in the cavity of the esr spectrometer. Diacetone alcohol and the pinacol are among the products recently observed[20] in the liquid phase photochemistry of acetone.

In presence of excess isopropyl alcohol, only (CH₃)₂-Ċ(OH) radicals are produced, Figure 1b, and agreement with the spectrum obtained independently from pulse radiolysis[17a] by the reaction OH radicals with isopropyl alcohol (OH + CH₃CH(OH)CH₃ → CH₃Ċ(OH)CH₃ + H₂O) is excellent. In 20 mM acetone and 3.0 M isopropyl alcohol, the decay at 320 nm is second order with $2k/\epsilon = 4.7 \times 10^6$, compared to $2k/\epsilon = 4.6 \times 10^6$ from pulse radiolysis work.[17a] Taking the extinction coefficient given in ref 17a, $2k = 1.1 \times 10^9\ M^{-1}\ \mathrm{sec}^{-1}$.

Flash Photolysis of Acetone and Amides. In the presence of amides, the triplet excited acetone can be expected to abstract H atoms at two sites, e.g.

In the flash photolysis of acetone containing A and DMA, the transient spectra observed and the decay kinetics are in accord with the formation of ·CH₂-CONH₂ and CH₃CONĊH₂(CH₃) radicals, via reactions 6 and 9, with the CH₃Ċ(OH)CH₃ radicals formed in all cases. It would appear that the extent of reaction 8 is quite small compared to 9, in agreement with esr observations.[9] The presence of CH₃COṄH could not be established since it absorbs below 310 nm and is masked by the absorption of ground state acetone.

In the photolysis of acetone plus formamide the amide radicals ·CONH₂ and HCOṄH could be formed. From pulse radiolysis work,[7] the ·CONH₂ radical has a $\lambda_{max} \sim 320$ nm and the HCOṄH was found to have a maximum below 245 nm. In the acetone-photosensitized decomposition of formamide, ĊONH₂ is the main radical observed in flash photolysis and by esr spectroscopy.[9] The products observed[21] in the steady-state photolysis of CH₃COCH₃ and HCONH₂ include (CONH₂)₂ and (CH₃)₂C(OH)(CONH₂), in good agreement with our conclusions.

With dimethylformamide, the main hydrogen abstraction by triplet CH₃COCH₃ appears to be at the N–CH₃ group, to produce HCONĊH₂(CH₃). This radical was found[7] to have two peaks at 380 and 248 nm, with extinction coefficients of 1600 and 6900 M^{-1} cm^{-1}, respectively.

It could be argued that the transient species observed are not produced by hydrogen abstraction by triplet excited acetone, but by methyl radicals. This is not considered to be the case since (a) the rate[22] of H-atom abstraction by CH₃ radicals is approximately four to five orders of magnitude lower than that of recombination of CH₃, and at the relatively high intensities produced in flash photolysis most of the CH₃ radicals would form[12] C₂H₆; (b) the CH₃Ċ(OH)CH₃ radical is observed in the photolysis of acetone–amide mixtures.

$$CH_3COCH_3{}^3 + CH_3CONH_2 \longrightarrow \begin{cases} \dot{C}H_2CONH_2 + CH_3\dot{C}(OH)CH_3 & (6) \\ CH_2CO\dot{N}H + CH_3\dot{C}(OH)CH_3 & (7) \end{cases}$$

$$CH_3COCH_3{}^3 + CH_3CON(CH_3)_2 \longrightarrow \begin{cases} \dot{C}H_2CON(CH_3)_2 + CH_3\dot{C}(OH)CH_3 & (8) \\ CH_3CON\dot{C}H_2(CH_3) + CH_3\dot{C}(OH)CH_3 & (9) \end{cases}$$

The transient absorption spectra of the four amide radicals in reactions 6–9 have been observed[7] by pulse radiolysis, and their decay rates and extinction coefficients have been determined. The ĊH₂CONH₂ radical has an absorption maximum at 400 nm and $\epsilon_{400} = 1050\ M^{-1}$ cm^{-1}, and the CH₃COṄH radical $\lambda_{max} <235$ nm and $\epsilon_{235} = 2000\ M^{-1}$ cm^{-1}. The CH₃-CONĊH₂(CH₃) radical has λ_{max} 350 and 245 nm with $\epsilon_{350} = 2000\ M^{-1}$ cm^{-1} and $\epsilon_{245} = 7000\ M^{-1}$ cm^{-1}; the ĊH₂CON(CH₃)₂ radical absorbs λ_{max} 490 nm and $\epsilon_{490} = 1000\ M^{-1}$ cm^{-1}.

Quenching of singlet excited acetone is not considered likely. Energy transfer from triplet acetone to the amides cannot be ruled out, since the triplet energy level of the amide group is not known. However, this possibility could be discarded since direct optical excitation of these amides did not produce any transients

(20) J. T. Przybytek, S. P. Singh, and J. Kagan, *Chem. Commun.*, 1224 (1969).

(21) H. Grossman, *Z. Naturforsch. B*, **20**, 209 (1965).

(22) J. K. Thomas, *Advan. Radiat. Chem.*, **1**, 150 (1970).

(of course the ϕ_{ISC} might be low) and, again, $CH_3\overset{.}{C}$-$(OH)CH_3$ radicals are formed.

Conclusions

These results can best be interpreted on the basis of hydrogen-atom abstraction from the amides by triplet excited acetone. It is interesting to note that the site of abstraction by triplet excited acetone, as observed by flash photolysis (this work) and by esr spectroscopy,[9] is the same as that which has been found[7] for OH radicals produced under pulse radiolysis conditions. Hydroxyl radicals are known to be electrophilic in their reaction with compounds. Furthermore, it would appear that, qualitatively, the rate of abstraction from different amides by triplet acetone follows the same order as the rate[7] of abstraction by OH radicals. Should these relationships be found to hold with other sensitizers and H-atom donors, it would be possible to predict the site of abstraction by triplet excited molecules based on the wealth of information available for OH radicals.

Ultraviolet Photochemistry of Acetatopentaamminecobalt(III)

in Aqueous Solution[1]

by Evan R. Kantrowitz, Morton Z. Hoffman,*

Department of Chemistry, Boston University, Boston, Massachusetts 02215

and John F. Endicott

Department of Chemistry, Wayne State University, Detroit, Michigan 48202   (Received February 1, 1971)

Publication costs borne completely by The Journal of Physical Chemistry

The 254-nm photolysis of $Co(NH_3)_5O_2CCH_3^{2+}$ in aqueous solution generates Co^{2+}, CO_2, C_2H_6, and CH_4 with $\phi_{Co^{2+}} \simeq \phi_{CO_2} \simeq (2\phi_{C_2H_6} + \phi_{CH_4}) = 0.19$. The stoichiometry and absence of any photoaquation products indicate that irradiation of the charge-transfer band of the complex results in electron transfer from the acetato ligand to the metal center. Isotopic substitution, radical scavenging, and light intensity studies demonstrate that CH_3 radicals are released into solution. At 366 nm, on the other hand, irradiation of the ligand-field band with slight charge-transfer overlap yields $(NH_3)_4Co(OH_2)O_2CCH_3^{2+}$ with very small amounts of Co^{2+}. There is no evidence of primary acetate aquation or the oxidation of an ammonia ligand.

Introduction

Irradiation of pentaammine complexes of Co(III) [of the general form $Co(NH_3)_5X^{2+}$] in their intense ligand-to-metal charge-transfer absorption band results in a number of possible processes, the most predominant of which is photoreduction with the formation of Co^{2+} and an oxidized ligand free radical from the one-electron transfer. Only in a limited number of cases has the radical been identified and characterized, either by direct flash photolytic observation or through the variation of final products in the presence of radical scavengers.[2] Penkett and Adamson[3] observed Br_2^- and I_2^- from the flash photolysis of $Co(NH_3)_5Br^{2+}$ and $Co(NH_3)_5I^{2+}$, respectively, and concluded that Br and I atoms were generated in the primary process. On the other hand, the flash photolysis of $Co(NH_3)_5Cl^{2+}$ gave no transient unless free Cl^- was present; under those conditions a transient species was detected that could not be identified as Cl_2^- but rather as NH_2Cl^- or NH_3Cl.[4] Product yields and scavenger studies are consistent with the formation of the N_3 radical from $Co(NH_3)_5N_3^{2+}$.[5] Kinetic and flash results show that a radical is implied in the photochemistry of oxalato-

(1) This work was supported by Grant GP 11213 from the National Science Foundation. Aspects of it were presented at the Second Northeast Regional Meeting of the American Chemical Society, Providence, R. I., Oct 1970.

(2) V. Balzani and V. Carassiti, "Photochemistry of Coordination Compounds," Academic Press, New York, N. Y., 1970.

(3) S. A. Penkett and A. W. Adamson, *J. Amer. Chem. Soc.*, **87**, 2514 (1965).

(4) G. Caspari, R. G. Hughes, J. F. Endicott, and M. Z. Hoffman, *ibid.*, **92**, 6801 (1970).

(5) J. F. Endicott, M. Z. Hoffman, and L. S. Beres, *J. Phys. Chem.*, **74**, 1021 (1970).

amine complexes.[6] Because of the generally high values of the extinction coefficients of these complexes in the 250-nm region, Co(III) complexes have potential value as a convenient source of selected radicals for their study in aqueous solution. This technique would be of particular interest if other methods of generation of the radicals involved vacuum ultraviolet photochemistry, radiation chemistry, or thermal reactions where complexities of the system have limited the study of the radicals in the past.

Spectral evidence has indicated that ammonia aquation is an accompanying process in $Co(NH_3)_5Cl^{2+}$;[7] kinetic evidence has demonstrated the same effect upon irradiation of the charge-transfer band of $Co(NH_3)_5$-N_3^{2+}.[8] On the other hand, irradiation in the ligand-field (d-d) bands results in ligand substitution, generally aquation, with a small amount of internal oxidation–reduction depending upon the overlap of the charge-transfer and d-d bands. The heterolytic bond fission leading to aquation would be expected to occur at the more weakly bonded ligand resulting in the formation of $Co(NH_3)_5OH_2^{3+}$ and release of the free ligand.[9]

In this study the ultraviolet photochemistry of Co-$(NH_3)_5O_2CCH_3^{2+}$ was examined for the identification and further reactions of the reaction intermediates and for the wavelength dependence of the quantum yields. In a preliminary review, Adamson[10] reported that the 366-nm photolysis of this complex leads to the formation of Co^{2+} and the "free acid." More recently,[11] the quantum yield for photoreduction in the 340–380-nm region was given as $<7 \times 10^{-4}$ with no indication of the occurrence of aquation processes, if any. No consideration was given to the fate of the free radicals formed in the primary process.

Experimental Section

Preparation of Complexes. $[Co(NH_3)_5O_2CCH_3](ClO_4)_2$. The method reported by Jackman, Scott, and Portman[12] was found to be the best method for the preparation of this complex. Almost quantitative yields were obtained by allowing $[Co(NH_3)_5OH_2](ClO_4)_3$ and acetic anhydride to react in aqueous solution with an excess of NH_3 for a few hours at 25°. The complex was recrystallized from distilled water at 50° (λ_{max} 505 nm; ϵ_{505} 74.4 M^{-1} cm^{-1}).

$[Co(NH_3)_5O_2CCD_3](ClO_4)_2$. Since the deuterium of the methyl group of CD_3COOD exchanges with water in basic solution,[13] a preparation had to be found which would produce the desired complex in good yield below pH 7. A modification of the method of Jones and Thomas[14] gave the best results. A sample of 2.5 g of $[Co(NH_3)_5CO_3](NO_3)$ was dissolved in a minimum volume of water at 50°. To this solution 1.5 ml of CD_3-$COOD$ was added. The mixture was heated at 45–55° for 3.5 hr, and the desired complex was precipitated by the addition of 60% $HClO_4$, then filtered and washed

with $HClO_4$, ethanol, and ether. The complex was recrystallized twice from distilled water which had been acidified slightly with $HClO_4$ (λ_{max} 504 nm; ϵ_{504} 73.6 M^{-1} cm^{-1}).

$[Co(NH_3)_5O_2CCH_2Cl](ClO_4)_2$. $[Co(NH_3)_5CO_3](NO_3)$ (2.5 g) and 4.0 g of $ClCH_2COOH$ were suspended in 10 ml of water. The suspension was heated on a steam bath for 2 hr after which the complex was precipitated by addition of 60% $HClO_4$. The precipitate was washed and recrystallized as above (λ_{max} 503 nm; ϵ_{503} 61.2 M^{-1} cm^{-1}).

$[Co(NH_3)_5O_2CCCl_3](ClO_4)_2$. The method of Gould and Taube[15] was used with the modification that no extraction with ether was carried out. The parent acid was soluble in water so that separation from the complex was accomplished by recrystallization (λ_{max} 503; ϵ_{503} 65.6 M^{-1} cm^{-1}).

The complexes were generally recrystallized two or three times before use. Absorption spectra agreed to within a few per cent of those given in the literature.[14] All solutions were prepared using distilled and/or de-ionized water and reagent grade chemicals.

Photolysis Apparatus. The Hanovia low-pressure mercury resonance lamp ($I_0 \sim 6.6 \times 10^{-3}$ einstein l.$^{-1}$ min^{-1}) and the mercury immersion lamp ($I_0 \sim 5.5 \times 10^{-4}$ einstein l.$^{-1}$ min^{-1}) have already been described[5] and were used for most of the experiments. For the low light intensity studies at 254 nm ($I_0 \sim 10^{-6}$ einstein l.$^{-1}$ min^{-1}) and photolyses at 366 nm, a Bausch and Lomb high-intensity monochromator with a super-pressure mercury lamp was used. The band pass was 15 nm. The photolysis techniques have already been described in detail.[4,5,16]

Uranyl oxalate[17] or potassium ferrioxalate[18] were used as standard chemical actinometers. Solutions of $Co(NH_3)_5Cl^{2+}$ in 0.1 M $HClO_4$ were used to check periodically the output of the photolysis units at 254 nm using $\phi_{Co^{2+}} = 0.17$ at 25°.[16]

(6) H. Way and N. Filipescu, *Inorg. Chem.*, **8**, 1609 (1969); A. F. Vaudo, M. Z. Hoffman, E. Papaconstantinou, and J. F. Endicott, unpublished work.

(7) L. Moggi, N. Sabbatini, and V. Balzani, *Gazz. Chim. Ital.*, **97**, 980 (1967).

(8) J. F. Endicott and M. Z. Hoffman, *J. Amer. Chem. Soc.*, **90**, 4740 (1968).

(9) A. W. Adamson, W. L. Waltz, E. Zinato, D. W. Watts, P. D. Fleischauer, and R. D. Lindholm, *Chem. Rev.*, **68**, 541 (1968).

(10) A. W. Adamson, *Coord. Chem. Rev.*, **3**, 169 (1968).

(11) A. W. Adamson, A. Vogler, and I. Lantzke, *J. Phys. Chem.*, **73**, 4183 (1969).

(12) L. M. Jackman, R. M. Scott, and R. H. Portman, *Chem. Commun.*, 1338 (1968).

(13) D. J. G. Ives, *J. Chem. Soc.*, 81 (1938).

(14) W. E. Jones and J. D. R. Thomas, *ibid.*, 1482 (1966).

(15) E. S. Gould and H. Taube, *J. Amer. Chem. Soc.*, **86**, 1318 (1964).

(16) J. F. Endicott and M. Z. Hoffman, *ibid.*, **87**, 3348 (1965).

(17) W. A. Noyes, Jr., and P. A. Leighton, "The Photochemistry of Gases," Reinhold, New York, N. Y., 1941.

(18) C. A. Parker and G. C. Hatchard, *Proc. Roy. Soc., Ser. A*, **235**, 518 (1956).

Flash photolysis was performed using a Xenon Corp. Model 720 unit in the manner already described.[4]

Analytical Procedures. Co^{2+} was determined using a modification of Kitson's method:[19] 4 ml of the solution containing Co^{2+} ($\leq 5 \times 10^{-3}$ M) and 8 ml of a 50% solution of NH_4SCN were diluted to 25 ml with acetone, and the absorbance at 620 nm was recorded (ϵ_{620} 1.86×10^3 M^{-1} cm^{-1}).

Gaseous products were detected and determined by gas chromatography and mass spectrometry from photolyses performed *in vacuo.*[20] The complex products of the reactions were separated on cation-exchange resins (Dowex 50W-4X, 200–400 mesh) and examined spectrophotometrically. Since the parent compound underwent a slow, acid-catalyzed thermal aquation on the column when eluted with $HClO_4$, all separations made use of Na^+ or H^+ columns using 0.1–2.0 M $Mg(ClO_4)_2$ for elution.

Results

Photolysis at 254 nm. Products. The major products from the irradiation of $Co(NH_3)_5O_2CCH_3^{2+}$ are Co^{2+}, CO_2, C_2H_6, and CH_4 with minor amounts of H_2. Table I summarizes our determinations of the quantum yields of product formation at high and low light intensity. The data presented here are slightly different than those reported previously[21] and are the result of more refined gas handling and analysis techniques. The quantum yields were not noticeably dependent on $[H^+]$ from pH 0 to 4 or on [complex] under conditions where I_a remained essentially constant during the exposure period (1–5 $\times$ 10^{-3} M). Results were not dependable at lower concentrations due to depletion of the substrate and the increasing error in the collection and analysis of small quantities of gas. Reactions were generally run to 10–20% of completion and in no case greater than 50%.

Table I: Quantum Yields of Products at 254 nm[a]

Product	ϕ (high I_a)[b]	ϕ (low I_a)[c]
Co^{2+}	0.192 ± 0.007[d]	0.22 ± 0.02[e]
CO_2	0.174 ± 0.003	0.184 ± 0.006
CH_4	0.005 ± 0.001	0.045 ± 0.003
C_2H_6	0.085 ± 0.002	0.063 ± 0.002
H_2	Trace	Trace
N_2	None detectable[f]	None detectable[f]

[a] $[Co(NH_3)_5O_2CCH_3^{2+}]$ = 5.0×10^{-3} M; $[HClO_4]$ = 0.1 M; 25°. Error limitations are average deviations. [b] $I_a \simeq 4.6 \times 10^{-3}$ einstein l.$^{-1}$ min^{-1}; four determinations. [c] $I_a \simeq 5.9 \times 10^{-6}$ einstein l.$^{-1}$ min^{-1}; two determinations. [d] $I_a \simeq 5.5 \times 10^{-4}$ einstein l.$^{-1}$ min^{-1}; six determinations. [e] $I_a \simeq 1.8$–2.9 $\times 10^{-6}$ einstein l.$^{-1}$ min^{-1}; two determinations. [f] All N_2 detected could be accounted for as leakage.

A variation in the product yield was observed at low light intensities as indicated in Table I. The increase

in $\phi_{Co^{2+}}$ and ϕ_{CO_2} may be significant; the effect on CH_4 and C_2H_6 is far beyond any experimental error.

A continuous purge of O_2 had no effect on $\phi_{Co^{2+}}$ and a pressure of 600 Torr of O_2 above the solution had no effect on ϕ_{CO_2}; the yield of C_2H_6 was reduced by 40% and the CH_4 yield became so small that it could not be determined. A positive chromotropic acid test for formaldehyde[22] was obtained for solutions irradiated in the presence of O_2.

Isotopic Substitution. A 1:1 mixture of $Co(NH_3)_5$-$O_2CCH_3^{2+}$ and $Co(NH_3)_5O_2CCD_3^{2+}$ was photolyzed at high intensity and the gaseous products were collected, analyzed mass spectrometrically, and compared with the results from the pure isotopic species. The intensities of the various peaks corresponding to CH_3CH_3, CD_3CH_3, and CD_3CD_3 and their daughter fragments were normalized to that of CO_2 (m/e 44) and are shown in Table II. The m/e 30 peak in the D-substituted cases cannot be used to obtain meaningful results because of the contribution from the fragmentation of CD_3CD_3 and CH_3CD_3. Similarly, a small contribution to the m/e 33 peak may arise from H-substituted impurity in the D complex or from spurious material.

Table II: Mass Spectrometry Data[a]

m/e	Relative intensities[b] $Co(NH_3)_5$-$O_2CCH_3^{2+}$	$Co(NH_3)_5$-$O_2CCD_3^{2+}$	1:1 H–D complex mixture
30 (CH_3CH_3)	3.9		
33 (CH_3CD_3)	0.0		1.9
36 (CD_3CD_3)	0.0	3.6	1.0

[a] [complex] = 5.0×10^{-3}; $[HClO_4]$ = 0.1 M; exposure time = 1 min. [b] Normalized to the value of m/e 44.

Examination of the methane peaks uncomplicated by the overlap of daughter fragments reveals the following: (1) over 90% of the methane from the pure D complex is CD_3H rather than CD_4; (2) the m/e 19 and 20 peaks are reduced by approximately a factor of 2 when the H–D complex mixture is used as compared with the pure D complex. Photolysis of the pure H complex in 83% D_2O produced a sixfold increase in m/e 17 as compared with a photolysis run in H_2O. Although this experiment was performed rapidly with total contact of the complex with D_2O restricted to 2.5 min, the possibility of H–D exchange with the acetate or ammonia hydrogens and the overlap of the methane

(19) R. E. Kitson, *Anal. Chem.,* **22**, 664 (1950).

(20) R. G. Hughes, J. F. Endicott, and M. Z. Hoffman, *Chem. Commun.,* 195 (1969).

(21) E. R. Kantrowitz, J. F. Endicott, and M. Z. Hoffman, *J. Amer. Chem. Soc.,* **92**, 1776 (1970).

(22) C. E. Bricker and H. R. Johnson, *Ind. Eng. Chem. Anal. Ed.,* **17**, 400 (1945).

daughter fragments renders this observation somewhat equivocal.

Presence of Alcohols. The values of $\phi_{Co^{2+}}$ and ϕ_{CO_2} were not measureably altered by the presence of up to 10 M CH$_3$OH. However, ϕ_{CH_4} increased and $\phi_{C_2H_6}$ decreased as [CH$_3$OH] was increased as has already been shown;[21] the value of $(2\phi_{C_2H_6} + \phi_{CH_4})$ remained constant and approximately equal to $\phi_{Co^{2+}}$ and ϕ_{CO_2}. Tests for formaldehyde[22] and ethylene glycol[23] were positive; quantitative data are given in Table III. Since H$_2$CO and (CH$_2$OH)$_2$ arise from the disproportionation and recombination of the CH$_2$OH radical which would be expected to be formed from CH$_3$OH upon H abstraction, the material balance should be H$_2$CO + 2 glycol = CH$_4$. The data show that this stoichiometry is followed.

Figure 1. Quantum yields of products at 254 nm in the presence of 2-propanol. [Co(NH$_3$)$_5$O$_2$CCH$_3$$^{2+}$] = 5.0 × 10^{-3} M; [HClO$_4$] = 0.1 M.

Table III: Material Balance in the Presence of CH$_3$OH[a]

Exposure time, min	[H$_2$CO], μM	[glycol], μM	[CH$_4$], μM[b]
0	0.0	0.0	0.0
2	39.8	5.9	52.1
4	87.0	18.0	141.1
6	180.0	23.0	214.0

[a] [Co(NH$_3$)$_5$O$_2$CCH$_3$$^{2+}$] = 5.0 × 10^{-3} M; [HClO$_4$] = 0.1 M; [CH$_3$OH] = 5.0 M. [b] The CH$_4$ yield was not measured in these experiments but calculated from the measured Co^{2+} yield since under these conditions, [CH$_4$] = 0.34[Co^{2+}]; see Figure 2 of ref 21.

The effect of the presence of 2-propanol is more complex. In addition to its role as scavenger of the radical precursor to CH$_4$ and C$_2$H$_6$ resulting in an increase in the CH$_4$ yield while the C$_2$H$_6$ yield decreases, the presence of 2-propanol also affects $\phi_{Co^{2+}}$. Figure 1 shows that the increase in $\phi_{Co^{2+}}$ parallels the change in the quantum yields of the gaseous products. For example, a plot of ϕ_{CH_4} vs. $\phi_{Co^{2+}}$ at various values of [2-propanol] results in a straight line with a slope of unity. The limiting value of $\phi_{Co^{2+}}$ is almost exactly twice the value in the absence of 2-propanol. At the same time, ϕ_{CO_2} is unchanged. It appears that the variation of $\phi_{Co^{2+}}$ as a function of [2-propanol] is independent of I_a over three orders of magnitude. However, in the presence of 1 atm of O$_2$ and 5 M 2-propanol, the value of $\phi_{Co^{2+}}$ is ≈0.2.

Flash Photolysis. No transients were observed from the flash photolysis (500 J) of deoxygenated solutions of Co(NH$_3$)$_5$O$_2$CCH$_3$$^{2+}$. When a 5 × 10^{-5} M solution at pH 3.1 was purged with air or pure O$_2$, a transient spectrum was observed at λ <320 nm with increasing o.d. at decreasing λ. Because of the strong absorption of the complex at λ <260 nm, λ_{max} of the transient spectrum could not be determined. The decay of the

transient followed at 285 nm was second order. Under the reasonable assumption that the transient is formed from the reaction of O$_2$ with a radical that arises from a primary process and is stoichiometric with Co^{2+}, the measurement of the Co^{2+} yield from a single flash would provide a value of the concentration of the transient species immediately after the flash. For [complex] = 1 × 10^{-4} M, [Co^{2+}] = 2.5 × 10^{-5} M from one flash (unfiltered). From this value and the extrapolation of the decay curve back to "zero time," a value of 120 M^{-1} cm^{-1} was calculated for ϵ_{285} giving a second-order rate constant of 7 × 10^7 M^{-1} sec^{-1}.

Chlorine-Substituted Complexes. A small but measureably significant increase in $\phi_{Co^{2+}}$ was observed when solutions of the monochloro or trichloroacetato complexes were photolyzed at high light intensities. For Co(NH$_3$)$_5$O$_2$CCH$_2$Cl^{2+}, $\phi_{Co^{2+}}$ = 0.22; for Co(NH$_3$)$_5$-O$_2$CCCl$_3$$^{2+}$, $\phi_{Co^{2+}}$ = 0.25. The only gaseous product noncondensible at −78° was CO$_2$ in slightly less than stoichiometric amounts; no attempt was made to extract the chlorine-containing products. No Cl$^-$ was released into solution. Neither complex exhibited any marked change in $\phi_{Co^{2+}}$ or ϕ_{CO_2} in the presence of up to 5 M 2-propanol.

Photolysis at 366 nm. Products. Upon photolysis at 366 nm, the color of the solution changed from its original red-orange color to red-purple, unlike the fading observed at 254 nm. Very small yields of Co^{2+}, CH$_4$, C$_2$H$_6$, and CO$_2$ were found. Separation of the dissolved material by ion-exchange chromatography gave three fractions, two with a 2+ charge and one with a 3+ charge. One of the 2+ fractions was identified as the starting material. The other 2+ fraction which had eluted with 0.3 M Mg(ClO$_4$)$_2$ was concentrated on a rotatory evaporator and allowed to precipitate; approximately 25 mg of product was isolated. Its visible–uv spectrum indicated that the product was a Co(III)

(23) F. E. Critchfield and J. B. Johnson, *Anal. Chem.*, **29**, 797 (1957).

complex very similar to the starting material, possibly $Co(NH_3)_4(OH_2)O_2CCH_3{}^{2+}$. This complex was prepared[24] although not isolated as the solid. A comparison of the behavior of the unknown 2+ fraction and the prepared complex showed that they both eluted before the substrate and had virtually identical spectra (λ_{max} 350, 509 nm). On the basis of the evidence, it appears that the observed 2+ product is the result of NH_3 aquation. The quantity of the 3+ species recovered was much smaller; in fact there was insufficient material from the 3+ fraction to characterize its spectrum. However, the photolysis of $Co(NH_3)_4(OH_2)O_2CCH_3{}^{2+}$ at the 366 nm gave a 3+ species as its predominant product leading to the speculation that the 3+ product from $Co(NH_3)_5O_2CCH_3{}^{2+}$ arises from secondary photolysis and can be identified as $Co(NH_3)_4(OH_2)_2{}^{3+}$.

The quantum yields shown in Table IV were based on these identifications.

Table IV: Quantum Yields of Products at 366 nm[a]

Product	ϕ
Co^{2+}	1×10^{-3}
CH_4	2×10^{-4} [b]
C_2H_6	2×10^{-5} [b]
CO_2	5×10^{-4} [b]
H_2	Trace
N_2	None detectable[c]
$Co(NH_3)_4(OH_2)-$ $O_2CCH_3{}^{2+}$	0.011
3+ product	$<5 \times 10^{-4}$

[a] $[Co(NH_3)_5O_2CCH_3{}^{2+}] = 1.0 \times 10^{-2} M;$ $[HClO_4] = 0.1 M;$ $I_a \simeq 1.2 \times 10^{-4}$ einstein l.$^{-1}$ min^{-1}; room temperature. [b] Large chromatograph errors due to the small quantities of gas involved. [c] All N_2 detected could be accounted for as leakage.

Discussion

Charge-Transfer Excitation. The stoichiometry of the photoreaction at 254 nm, given by $\phi_{Co^{2+}} \simeq \phi_{CO_2} \simeq (2\phi_{C_2H_6} + \phi_{CH_4})$, accounts for virtually all the electron equivalents in the charge-transfer process as has been noted before[21] and implies the primary process

$(NH_3)_5Co(O_2CCH_3)^{2+} \xrightarrow[H^+]{h\nu}$

$$Co^{2+} + 5NH_4{}^+ + CH_3CO_2 \quad (1)$$
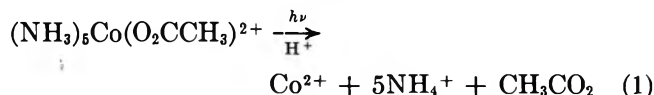
The lifetime of the CH_3CO_2 radical in solution is believed to be very short[25] and decarboxylation would be expected to occur before any significant bimolecular processes took place.

$$CH_3CO_2 \longrightarrow CH_3 + CO_2 \quad (2)$$

$$2CH_3CO_2 \longrightarrow CH_3CO_2CH_3 + CO_2 \quad (3)$$
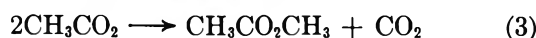
Reaction 3 could account for the slight deficiencies in the yields of CO_2 produced although small amounts of CO_2 are difficult to recover quantitatively, even from

highly acidic solution. Because there is no evidence that CH_3CO_2 ever exists as a free entity in our system (e.g., ϕ_{CO_2} is independent of [alcohol]), it is possible that CH_3 and CO_2 are released directly from the cttm excited state. At high light intensities the predominant fate of the CH_3 radicals is combination to yield C_2H_6

$$CH_3 + CH_3 \longrightarrow C_2H_6 \quad (4)$$
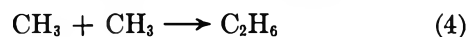
for which $k_4 = 2 \times 10^{10} M^{-1} \sec^{-1}$.[26]

There appears to be ample evidence that CH_3 radicals are generated free in solution by the photolysis of the complex. The ratio of the isotopically substituted ethanes from the photolysis of the H–D mixture is accounted for by the statistical combination of CH_3 and CD_3 radicals. Scavenging of CH_3 by the alcohols increases the CH_4 yield at the expense of C_2H_6.

$$CH_3 + CH_3OH \longrightarrow CH_4 + CH_2OH \quad (5)$$

$$CH_3 + (CH_3)_2CHOH \longrightarrow CH_4 + (CH_3)_2COH \quad (6)$$
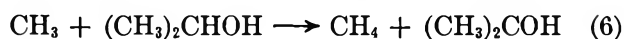
The use of 1 M allyl alcohol causes the C_2H_6 yield to be quenched while the CH_4 yield becomes 30% of $\phi_{Co^{2+}}$. With still nearly quantitative recovery of CO_2 and no apparent effect on $\phi_{Co^{2+}}$, $(2\phi_{C_2H_6} + \phi_{CH_4}) \neq \phi_{CO_2}$ indicating CH_3 radical insertion and H-abstraction reactions with the alcohol.

The reaction of O_2 with CH_3 is efficient with $k_7 = 4.7 \times 10^9 M^{-1} \sec^{-1}$ [27] and should have completely

$$CH_3 + O_2 \longrightarrow CH_3O_2 \quad (7)$$

quenched the C_2H_6 yield. However, the experimental conditions did not provide for the replacement of the reacted O_2 from the gas phase. The quantum yield of C_2H_6 observed in the presence of O_2 compares very favorably with that calculated for reaction of CH_3 with only that O_2 originally dissolved. There is apparently no reaction of O_2 with the excited state or radical precursor since $\phi_{Co^{2+}}$ and ϕ_{CO_2} are unaffected by O_2. Sleppy and Calvert[28] report that the CH_3O_2 radical undergoes disproportionation followed by the similar reaction of CH_3O

$$2CH_3O_2 \longrightarrow 2CH_3O + O_2 \quad (8)$$

$$2CH_3O \longrightarrow CH_3OH + H_2CO \quad (9)$$
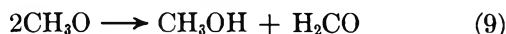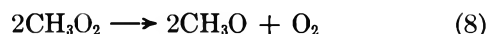
A positive test for H_2CO found in the presence of O_2 supports this mechanism. The CH_3O_2 radical has been observed spectrophotometrically from the reaction of O_2 with CH_3 radicals produced by pulse radiolysis through the reaction of $e_{aq}{}^-$ and CH_3I in aqueous solu-

(24) K. D. Kopple and R. R. Miller, *Inorg. Chem.*, **2**, 1204 (1963).

(25) L. Herk, M. Feld, and M. Szwarc, *J. Amer. Chem. Soc.*, **83**, 2998 (1961).

(26) W. A. Pryor, "Free Radicals," McGraw-Hill, New York, N. Y., 1966, p 161.

(27) J. K. Thomas, *J. Phys. Chem.*, **71**, 1919 (1967).

(28) W. C. Sleppy and J. C. Calvert, *J. Amer. Chem. Soc.*, **81**, 769 (1959).
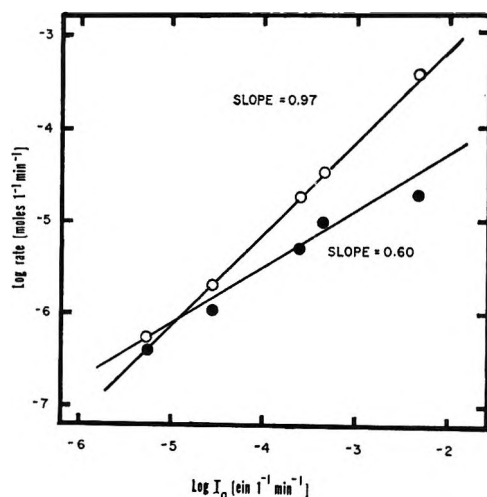
Figure 2. Light intensity dependence of CH_4 and C_2H_6 formation. $[Co(NH_3)_5O_2CCH_3{}^{2+}] = 5.0 \times 10^{-3} M;$ $[HClO_4] = 0.1 M;$ ●, CH_4; ○, C_2H_6.

tion.[27] There is no maximum in the spectrum; only a tail from 250–320 nm is shown.[27] The transient we observe can be identified as the CH_3O_2 radical although we realize the problems associated with the comparison of spectra having no defined λ_{max}. Our calculated rate constant for the second-order decay of the transient, presumably reaction 8, of $7 \times 10^7 M^{-1}$ sec^{-1} is to be compared with that for the cyclohexylperoxy radical $(2.8 \times 10^6 M^{-1}$ sec$^{-1})$ and the cyclohexanolperoxy radical $(1.8 \times 10^7 M^{-1}$ sec$^{-1})$.[29] It is to be expected that the activation energy and steric restrictions that cause these peroxy radical reactions to be so much slower than those which are diffusion controlled operates to a somewhat lesser extent in the case of CH_3O_2.

The CH_4 in the absence of any added scavenger must arise from some H-atom abstraction reaction

$$CH_3 + S \longrightarrow CH_4 + ? \qquad (10)$$
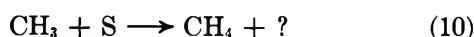
Regardless of the nature of S, consideration of reactions 1, 2, 4, and 10 and a steady-state treatment for the radicals (assuming that $k_{10}[S] \ll k_4[CH_3]$) leads to the prediction that $d[C_2H_6]/dt \propto I_a$ and $d[CH_4]/dt \propto I_a{}^{1/2}$. Thus, a plot of log rate $vs.$ log I_a should generate straight lines with slopes equal to the value of the exponent of I_a. Figure 2 shows this behavior over three orders of magnitude of I_a and lends further support to the proposed mechanism.

It is not completely clear what is the source of CH_4 and the nature of species S in reaction 10. If the complex is the scavenger, then the isotopic substitution data indicate that H abstraction does not primarily take place at the acetato ligand; the data are not sufficiently clear to demonstrate that attack is on the NH_3 ligands. However, the reaction of H atoms with $Co(NH_3)_6{}^{3+}$ produces Co^{2+},[30] either through the formation of a coordinated NH_2 ligand which then reduces the Co(III) or via direct H-atom attack on the metal center.[31] We

therefore propose that the source of CH_4 in the absence of added scavengers is through reaction with the complex at the NH_3 ligand with the formation of additional Co^{2+}.

$$CH_3 + Co(NH_3)_5O_2CCH_3{}^{2+} \xrightarrow[H^+]{}$$

$$CH_4 + Co^{2+} + 4NH_4{}^+ + NH_2{}^+ + CH_3CO_2H \qquad (11)$$
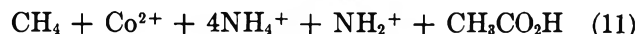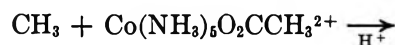
Unfortunately it was not possible to vary [complex] sufficiently to test this aspect of the mechanism due to considerations of light intensity, solubility, and the error in the analysis of small quantities of CH_4. The additional yield of Co^{2+} from reaction 11 would not be detectable in the presence of Co^{2+} from reaction 1. At low light intensities, on the other hand, where reaction 11 becomes more probable at the expense of reaction 4 a small increase in $\phi_{Co^{2+}}$ should be observed. As was pointed out in the Experimental Section, the observed apparent increase in $\phi_{Co^{2+}}$ at low intensities may be significant. The fate of the $NH_2{}^+$ radical is unclear but it does not appear to be the formation of measurable amounts of N_2. A search for other nitrogenous products, often an exercise in frustration,[20] was not attempted. The probability of CH_3 attack on the solvent appears to be very low due to the unfavorable energetics.

Considering reactions 4 and 10, it is easy to show that

$$\frac{k_{10}}{k_4{}^{1/2}} = \frac{(\text{rate of formation of } CH_4)}{[S] \,(\text{rate of formation of } C_2H_6)^{1/2}}$$

for any scavenger for CH_3 that serves as a H donor. Applying this relationship to the complex at a concentration of $5 \times 10^{-3} M$ over three orders of magnitude of light intensity, we obtain a value of $4 \pm 1 \times 10^3 M^{-1}$ sec^{-1} for the rate constant of reaction 11. No data appear to be available in the literature for CH_3 radical reactions with Co(III) complexes to use as a comparison. However, $k(H + Co(NH_3)_5O_2CCH_3{}^{2+}) < 1.3 \times 10^6 M^{-1}$ sec^{-1} [32] and H-atom rates are known[27] to be $\sim 10^3$ times as fast as CH_3 radical rates.

Using the scavenging data for the alcohols as shown in Figure 1 and ref 21, the rate constants for the CH_3–alcohol reactions can be evaluated in the same way. Only lower limits of these values can be obtained from our data; the gas yields were obtained under conditions whereby the extent of reaction was high and I_a, and thus the steady-state concentration of CH_3, was varying during the photolysis. We find $k_5 \geq 1 \times 10^2 M^{-1}$ sec^{-1} and $k_6 \geq 1.6 \pm 0.3 \times 10^3 M^{-1}$ sec^{-1} as compared with Thomas' values[27] of 2.2×10^2 and 3.4×10^3, respectively. Although our absolute values are a factor of 2 lower, the ratios are identical. By taking the appro-

(29) R. L. McCarthy and A. MacLachlan, *Trans. Faraday Soc.*, **57**, 1107 (1961); *J. Chem. Phys.*, **35**, 1625 (1961).

(30) G. Navon and G. Stein, *J. Phys. Chem.*, **69**, 1390 (1965).

(31) G. Navon and D. Meyerstein, *ibid.*, **74**, 4067 (1970).

(32) J. Halpern and J. Rabani, *J. Amer. Chem. Soc.*, **88**, 699 (1966).

priate precautions concerning variation of I_a, we have no doubt that reliable absolute values can be obtained.

In this regard we would like to point out that the 254-nm photolysis of $Co(NH_3)_5O_2CCH_3^{2+}$ may serve as a convenient source of CH_3 radicals in aqueous solution. Because of the relatively high absorptivity of the complex at 254 nm (ϵ_{254} 3440 M^{-1} cm^{-1}), the high quantum yield (0.2) of radical production, and the relatively low reactivity of the complex towards the radical, this technique has some obvious advantages for the study of CH_3 radical reactions in aqueous solution over other methods.[27]

In a previous communication,[21] we attributed the increase in $\phi_{Co^{2+}}$ with increasing [2-propanol] as due to chemically scavengable excited states of the complex. However, consideration must be given to the possibility that the $(CH_3)_2COH$ radical produced in reaction 6 may reduce the complex via H-atom transfer to form Co^{2+}, $(CH_3)_2CO$, and release of the ligands. Such a reaction would produce the results shown in Figure 1. Analysis for acetone in these systems did not produce useful results since the disproportionation of $(CH_3)_2$-COH also produces acetone; the difference in the stoichiometry could not be critically discerned. The effect of O_2 in reducing $\phi_{Co^{2+}}$ to its value in the absence of the alcohol is taken as strong indication that radical attack is the predominant source of the additional Co^{2+}. Under the conditions of the reaction, where O_2 is continuously bubbling through the photolysis solution at 1 atm and [2-propanol] = 5 M, reaction 7 would be much faster than reaction 6. It does not appear necessary to invoke chemically scavengable excited states in this system to any great extent at the present time.

In the same regard, the CH_2OH radical generated in reaction 5 may attack the complex. The yield of H_2CO is far in excess of that expected from the ratio of combination and disproportionation of CH_2OH to form $(CH_2OH)_2$ and H_2CO; such a ratio is known[33] to have a value of 6 in aqueous CH_3OH solutions. It appears from the material balance cited in Table III that CH_2-OH reacts with the complex to form H_2CO, presumably by H-atom transfer. If analogous to the 2-propanol case, Co^{2+} would be expected to be formed in such a process. We do not observe an increase in $\phi_{Co^{2+}}$ up to 5 M CH_3OH; the calculated increase of 0.02 quantum

yield units based on the stoichiometry is within the margin of error of $\phi_{Co^{2+}}$.

The chlorine-substituted complexes appear to behave in the same way as does the parent compound. The lack of a dependence of $\phi_{Co^{2+}}$ on [2-propanol] may reflect the low reactivity of CCl_3 for H abstraction as compared with CH_3.

Ligand-Field Excitation. This appears to be the first indication that NH_3 aquation occurs from ligand-field excitation; previous reports[9,34] have stressed the labilization of the X ligand. It appears that the secondary photolysis of $Co(NH_3)_4(OH_2)O_2CCH_3^{2+}$ results in the loss of the acetate ligand. This observation raises the question of the assignment of the aquation product in the *primary* photoprocess in the past; the low quantum yields for aquation and the possibility of secondary photolysis make a complete analysis very difficult. We wish to suggest that NH_3 aquation at this wavelength may be a much more common process than originally thought and may actually be the predominant mode of ligand aquation in many cases. However, because of the experimental difficulties involved in separation and analysis, the failure to discover such a process is not sufficient to rule it out absolutely. For example, in the $Co(NH_3)_5O_2CCH_3^{2+}$ case at 254 nm, a quantum yield for NH_3 aquation of 0.02 would not be detected under the conditions of the experiment; a higher quantum yield may still not allow buildup of product due to secondary photolysis. Thus, the observed absence of any photoaquation products here at 254 nm may not be unexpected. The previous reports[5,7,8] of such processes in the charge-transfer region have relied on somewhat indirect evidence.

The very low quantum yield for photoreduction observed at 366 nm can be attributed to slight spectral overlap of the charge-transfer band on the d-d band. Our values of $\phi_{Co^{2+}}$ are comparable to those observed by Adamson.[11]

It is clear that irradiation of different absorption bands produces different excited states which, because of their charge distributions, geometries, and energetics, lead to the observed variations in products and yields as a function of wavelength.

(33) U. Sokolov and G. Stein, *J. Chem. Phys.*, **44**, 3329 (1966).
(34) A. W. Adamson, *Discussions Faraday Soc.*, **29**, 163 (1960).

The External Heavy-Atom Effect on the Quantum Yield of Sensitized

Phosphorescence of Some Aromatic Molecules[1]

by S. E. Webber

Department of Chemistry, University of Texas at Austin, Austin, Texas 78712 (*Received November 23, 1970*)

Publication costs borne completely by The Journal of Physical Chemistry

The quantum yield of benzophenone-sensitized phosphorescence (q_A)[2b] has been obtained for the following acceptor molecules: naphthalene, phenanthrene, biphenyl, fluorene, m-terphenyl, and diphenylacetylene. It has been found that heavy-atom solvents increase q_A for all cases studied. The sphere of quenching[3] has been determined for the above acceptor molecules and diphenyldiacetylene. The sphere of quenching has not been found to be significantly dependent on solvent, nor to vary by more than a factor of 2 for all the acceptors studied.

I. Introduction

In this paper we will present data relating to the effect of heavy-atom solvents on the quantum yield of sensitized phosphorescence[2] of several planar aromatic molecules (biphenyl, fluorene, m-terphenyl, diphenyl-acetylene, naphthalene, and phenanthrene are the acceptor molecules with benzophenone as the donor in all cases) and study the efficiency of triplet–triplet transfer, measured by the "sphere of quenching,"[3] as a function of acceptor molecule and solvent. Our results demonstrate quite clearly that the external heavy-atom serves to enhance the radiative efficiency of all the molecules studied. A similar result for naphthalene has been obtained by Birks[4] in his analysis of the data of McGlynn, *et al.*[5] In view of our results it appears plausible that this enhancement will be found in most aromatic molecules. The fact that k_{PT} (the phosphorescence rate of the triplet) should be enhanced more than k_{GT} (the radiationless T $\rightsquigarrow$ G rate, where G is the ground state of the molecule) will be discussed in Section IV.

We have found more variation in our spheres of quenching for a benzophenone donor than in the previous work of Ermolaev[3] in which substituted naphthalenes were used as acceptors, yet the difference of the quenching volume of the most efficient quencher and the least efficient quencher was only about a factor of 2. When these values are translated into a radius of quenching the range is from about 11 to about 14 Å. This lack of variation is consistent with the theory of Dexter[6] and will be discussed in Section IIIb. As expected, no striking solvent effects were detected in $v_{\text{quenching}}$.

In the next section we will discuss the experimental procedures employed and discuss the analysis of data.

II. Experimental Section

a. Optical Arrangement. Excitation of a solution containing benzophenone (0.025 m) and an acceptor was

effected by a low-pressure mercury lamp, Pyrex lens system, and a 3650-Å interference filter (100-Å band-pass, Oriel Optical Co.). The solutions were contained in thin-walled precision bore 5 mm o.d. Pyrex tubes and were immersed in liquid nitrogen contained in a partially silvered Pyrex dewar. No mercury lines other than the 3650-Å group were detectable in the steady-state emission spectra (no choppers were used). The emission was observed at a 45° angle from the excitation axis with a McPherson Model 218 0.3 m monochromator and a EMI 9514 S photomultiplier. Typical slit widths were 200 μ. The sample tubes were held by means of a Teflon insert which could be accurately re-positioned. Such an arrangement is necessary to ensure reproducible intensities. Reproducibility with a fluorescent solution at room temperature (such as anthracene) was on the order of 1%.

The acceptor phosphorescence spectra could be separated from the benzophenone by use of a cylindrical phosphorimeter. All the acceptors studied have a lifetime considerably in excess of that of benzophenone $(\tau_P \sim 5 \text{ msec})$. When the phosphorimeter was used, reproducible intensities were not obtained, but only the distribution of the intensity of the acceptor phosphorescence was required in our analysis of data (*vide infra*).

The spectral response of our system was determined by recording the spectrum of NBS standardized tung-

(1) An account of this research was presented at the 160th National Meeting of the American Chemical Society, Chicago, Ill., Sept 1970.

(2) (a) A. Terenin and V. L. Ermolaev, *Dokl. Acad. Sci. USSR, Earth Sci. Sect.*, **85**, 547 (1952); *Trans. Faraday Soc.*, **52**, 1042 (1956); (b) for a review see V. L. Ermolaev, *Usp. Fiz. Nauk*, **80**, 3 (1963).

(3) V. L. Ermolaev, *Dokl. Akad. Nauk SSSR*, **139**, 348 (1961).

(4) J. B. Birks, "Photophysics of Aromatic Molecules," Wiley-Interscience, New York, N. Y., 1970, p 210 and Table 6.6.

(5) S. P. McGlynn, M. J. Reynolds, G. W. Daigre, and N. D. Christodouleas, *J. Phys. Chem.*, **66**, 2499 (1962).

(6) D. L. Dexter, *J. Chem. Phys.*, **21**, 836 (1953).

sten lamp. The lamp was positioned in such a way that its intensity had to pass through the same set of lens as the light due to a phosphorescent sample. A photomultiplier response curve was thereby derived and was used to correct the experimental phosphorescence spectra for the purpose of calculating quantum yield (*vide infra*).

b. Chemicals. All chemicals used were reagent grade. Reagent grade naphthalene, biphenyl, *m*-terphenyl, fluorene, and phenanthrene were obtained from the Aldrich Chemical Co. The diphenylacetylene and diphenyldiacetylene were obtained from the Farchan Chemical Co. The phenanthrene contained anthracene, which interferes with the present experiments. This impurity was removed following the procedure of Clar.[7] The anthracene reacts with maleic anhydride and the phenanthrene is removed from the reaction mixture by sublimation. No anthracene fluorescence could be detected in phenanthrene samples under the experimental conditions used for phosphorescence. The other chemicals were sufficiently pure for our experiments without further purification, although as a precaution recrystallization and/or zone refining was carried out. The benzophenone was chromatographic quality obtained from the Aldrich Chemical Co. The *n*-propyl halides were obtained from both the Eastman Chemical Co. and the J. T. Baker Co. Only the propyl iodide tended to show discoloration due to photodecomposition. The discoloration was removed by passing the liquid through a 3-ft column of activated alumina. The other propyl halides were similarly treated as a precautionary measure. The ethanol was reagent grade absolute alcohol, which was distilled before each set of experiments. Any water in the ethanol tends to enhance cracking of the glasses at 77°K. Consequently, the distillation was carried out from a magnesium ethoxide solution to ensure dryness. The propyl halide–ethanol glasses are generally less prone to crack than pure ethanol, but are very sensitive to the presence of water (especially in the case of propyl iodide).

c. Collection and Analysis of Data. The most serious problem in experiments of this type is the condition of the glass, especially since the concentration of the solute is quite high in some cases (0.5 m in the case of *m*-terphenyl is the highest concentration of donor used). The area of the phosphorescence spectrum of each sample was determined by an electronic integrator in two different orientations of the sample tube each time the sample tube was frozen. Each solution was run in three different tubes and frozen down two times in a given experiment, and the area of the twelve phosphorescence spectra averaged. Each experimental run consisted of measurements as above of the unquenched benzophenone (0.025 *m*) and the mixture of benzophenone (0.025 *m*) and some acceptor. The former spectrum will be denoted as the unquenched donor spectrum and the latter as the total spectrum. The average area

of the unquenched donor spectrum is denoted as A_{OD} and the area of the total spectrum as A_T. The standard deviation of these quantities (as well as related quantities, such as emission peak heights, etc.) was on the order of ±5% of the measured quantity. Each acceptor, solvent combination was studied in at least four independent runs by at least two different operators. The results always agreed for experienced operators. The only quantity that was required for the data analysis was the ratio A_T/A_{OD} $(\equiv R)$. For purposes of calculated error bars the maximum and minimum value of R was obtained by the following

$$\frac{A_T \pm \sigma_T}{A_{OD} \mp \sigma_{OD}} = \left(\begin{matrix} R_{max} \\ R_{min} \end{matrix}\right) \qquad (1)$$

The upper sign refers to R_{max} and the lower sign refers to R_{min}. The quantities σ_T and σ_{OD} are the values of the standard deviation of A_T and A_{OD}, respectively. In view of the good reproducibility between experiments we feel that we are overestimating the actual probable error of our results. When the resultant values of R_{max} and R_{min} are used in the calculation of the quantum yields (*vide infra*) the uncertainty in this quantity becomes ±15–20%. Thus determination of accurate quantum yields using glasses and the techniques employed here is problematical. However, the trends of the quantum yields are quite striking even with the rather large error bars we have calculated.

The quantum yields were determined as follows: the total spectra, donor spectra, and acceptor spectra (obtained by use of the cylindrical phosphorimeter) were digitized and read into a computer program. This program fits the total spectrum to a sum of donor and acceptor spectra by a trial and error method. The value of a in the function

$$F_T(\lambda)^{trial} = aF_D(\lambda) + (1 - a)F_A(\lambda) \qquad (2)$$

is determined so that

$$\sigma = \frac{1}{N} \sum_{i=1}^{N} |F_T(\lambda_i)^{trial} - F_T(\lambda_i)^{exp}|^2 \qquad (3)$$

is a minimum. $F_D(\lambda)$ and $F_A(\lambda)$ are the donor and acceptor spectrum for the given solvent, normalized to unit area. The experimental total spectrum $F_t(\lambda)^{exp}$ was likewise normalized to unit area. The value of a was quite accurately determined by this technique, as could be seen by plotting σ *vs.* a. The area of $F_T(\lambda)^{trial}$ was normalized to unity and the unquenched donor spectrum, $F_{OD}(\lambda)$, was related to $F_D(\lambda)$ by

$$F_{OD}(\lambda) = \frac{1}{R} F_D(\lambda) \qquad (4)$$

(recall that $R = A_T/A_{OD}$).

These experimental spectra were corrected for the

(7) E. Clar, *Chem. Ber.*, **65**, 846 (1932).

spectral response of the photomultiplier, and three new spectra (as a function of energy) were obtained: $\mathfrak{F}_{OD}(\omega)$, $\mathfrak{F}_D(\omega)$, and $\mathfrak{F}_A(\omega)$. The "quantum areas" of each spectrum were obtained by a numerical integration, i.e.

$$A_D' = a \int_0^\infty \mathfrak{F}_D(\omega) \, d\omega = aI_D$$

$$A_A' = (1 - a) \int_0^\infty \mathfrak{F}_A(\omega) \, d(\omega) = (1 - a)I_A \quad (5)$$

$$A_{OD}' = \frac{A_D'}{aR}$$

The quantum efficiency[8] of the acceptor is computed from the relation

$$q_A = \frac{A_A' q_D}{(A_{OD}' - A_D')}$$

$$= \frac{A_A' q_D}{A_D'} [(aR)^{-1} - 1]^{-1} \quad (6)$$

$$= \frac{I_A q_D}{I_D} \frac{1 - a}{a} \frac{aR}{1 - aR}$$

where in general q_D is the phosphorescence quantum yield of the donor. For the present case $\Phi_{fluorescence} = 0$ for the donor so that for our purposes the quantum yield of donor phosphorescence is equivalent to the donor quantum efficiency. The quantity q_A is an absolute quantum efficiency if the absolute value of q_D is known. We may see this as follows: the number of photons emitted under steady-state conditions is taken to be proportional to the area of the corrected spectrum, i.e., $N_P^{OD} = CA_{OD}'$, where C is a geometric factor. The quantum efficiency of phosphorescence is the number of photons emitted for a given number of molecules excited. The number of excited donor molecules in the absence of quenching is given by

$$N_{OD} = \frac{N_P^{OD}}{q_D}$$

$$= \frac{CA_{OD}'}{q_D} \quad (7)$$

It is assumed that in the mixed acceptor–donor solution the donors are either close enough to an acceptor to be quenched totally or are unaffected by the presence of the acceptor.[9] The decrease in the number of donor molecules is equated to the number of acceptor molecules excited, so that

$$N_A = N_{OD} - N_D$$

$$= \frac{C}{q_D} (A_{OD}' - A_D') \quad (8)$$

(where N_P^A is the number of photons emitted by the acceptor). Since $q_A = N_P^A / N_A$ and $N_P^A = CA_A'$, we obtain eq 6. Ermolaev usually presents his data as

γ_A, where

$$\gamma_A = q_A / q_D \quad (9)$$

From experience we feel that the ratio I_A/I_D and the constant a are accurate. Thus the main source of error in our calculation of q_A (other than the multiplicative factor q_D) is in the uncertainty in R. In calculating the "error bars" of q_A we have used the R_{max} and R_{min} value, respectively (which now contain about 10% variation, see eq 1). We denote the q_A derived from R_{max} as q_A^{max} and likewise q_A^{min} is derived from R_{min}. The greatest sensitivity to errors in R arises when $aR \sim 1$, which is the case for a weak quencher. Thus the greatest experimental accuracy is obtained when a sufficiently high concentration of acceptor can be used to significantly quench the donor, which implies $a <$ 0.75 as a rule. The resultant q_A^{max} and q_A^{min} show a variation of $\pm 20\%$ around the mean, which we regard as an upper limit of experimental error. The trends we report in the next section are quite striking even with the addition of these error bars. We stress the details of our calculation of experimental error because the reader must be warned against taking our reported values of q_A too literally. We should note that our quoted error is somewhat higher than that quoted by Ermolaev (10–15%) but as this latter worker presents no details of his data analysis or method of computing experimental error we regard our method of analysis as comparing favorably with Ermolaev's. We note that our value of γ_A for naphthalene (0.067) agrees with Ermolaev's value (0.07).[2b]

III. Results

a. *Effect of the External Heavy Atom on the Quantum Efficiency of Sensitized Phosphorescence.* We choose to present our data in terms of γ_A, where

$$\gamma_A = A_A'(A_{OD}' - A_D')^{-1}$$

$$= \frac{I_A}{I_D} \frac{1 - a}{a} \frac{aR}{1 - aR} \quad (10)$$

in order that a direct comparison to Ermolaev's results[2b,10] can be made by the interested reader (Table I). The quantum yield of phosphorescence for benzophenone in ethanol–ether glasses has been determined by Gilmore, *et al.*,[11] and Ermolaev[10] to be 0.84 and 0.74, respectively. We have measured the relative quantum

(8) We are using the nomenclature of Birks (ref 4), where

$$q_D = k_{PT}^D (k_{PT}^D + d_{GT}^D)^{-1}$$

(9) This assumption is apparently supported by the good fit of Perrin's law to the quenching data (see Section IIIb). However, this model would also imply that the benzophenone phosphorescence delay curve in mixed solutions would be exponential with τ_P^D (lifetime of donor phosphorescence) unchanged from that of the donor in the absence of an acceptor. Ermolaev (ref 3) has found that this is not the case. Thus one must interpret the quantum yields calculated by eq 6 with some care.

(10) V. L. Ermolaev, *Opt. Spektrosk.*, **13**, 90 (1962).

(11) E. Gilmore, G. Gibson, and D. McClure, *J. Chem. Phys.*, **20**, 829 (1952); *ibid.*, **23**, 399 (1955).

Table I: Quantum Yield of Sensitized Phosphorescence As a Function of Glass Composition

Acceptor[a]	γ_A (X)[b]							
	O		Cl		Br		I	
Naphthalene (0.25 m)	0.067	+0.017	0.054	+0.015	0.25	+0.02	0.53	+0.16
		−0.013		−0.011		−0.02		−0.12
Phenanthrene (0.10 m)	0.16	+0.04	0.12	+0.03	0.36	+0.09	0.62	+0.16
		−0.04		−0.03		−0.09		−0.16
Biphenyl (0.25 m)	0.24	+0.05	0.18	+0.04	0.41	+0.04	0.70	+0.08
		−0.04		−0.03		−0.04		−0.07
Fluorene (0.0625 m)	0.40	+0.12	0.33	+0.11	0.57	+0.14	0.89	+0.32
		−0.08		−0.07		−0.10		−0.20
m-Terphenyl (0.50 m)	0.38	+0.08	0.20	+0.05	0.55	+0.21	0.73	+0.25
		−0.06		−0.04		−0.13		−0.17
Diphenylacetylene (0.25 m)	0.14	+0.04	0.09	+0.02	0.09	+0.02	0.21	+0.05
		−0.03		−0.02		−0.02		−0.04

[a] The donor was benzophenone (0.025 m) in all cases. [b] The symbol X refers to the heavy atom present.   The following glasses were used: X = O, ethanol; X = Cl, 1:1 propyl chloride–ethanol; X = Br, 1:1 propyl bromide–ethanol; X = I, 1:1 propyl iodide–ethanol.   In all cases n-propyl halides were used.

yield of benzophenone in our various solvents and found the variation to be relatively small (Table II). We may convert our relative donor efficiencies into absolute efficiencies by assuming either of the above values (0.84 or 0.74) apply to our ethanol glasses and then multiplying by the relative quantum yields in Table II.

Table II: Relative Quantum Yield of Phosphorescence for Benzophenone As a Function of Glass Composition

O[a]	Cl	Br	I
1.00 ± 0.05[b]	1.25 ± 0.05	1.14 ± 0.03	1.17 ± 0.01

[a] See Table I for notation. [b] The intensity in ethanol is arbitrarily taken to be unity. Note that these results are uncorrected for optical effects such as reflectivity losses, etc. Consequently, these relative quantum yields represent the appropriate correction factor for the quantities in Table I, but the above ratios may not be exactly equal to the true quantum yield ratios.

In Figure 1 we have displayed values of γ_A for different solvents. This figure demonstrates the strong effect of heavy-atom solvents on γ_A. Only diphenylacetylene (tolan) fails to show a value of $\gamma_A \sim 0.5$ in the propyl iodide–ethanol glass. Note that none of the acceptors has a quantum efficiency equal to that of the donor (which would imply $\gamma_A \sim 1$), even in the propyl iodide–ethanol glass. The external heavy atom is undoubtedly increasing both k_{PT} and k_{GT}, but evidently the former is increased more than the latter. It would be interesting to estimate $k_{PT} + k_{GT}$ from the phosphorescence decay curves, but these curves are quite nonexponential such that a tabulation of τ_P values (phosphorescence lifetimes) is likely to be misleading.[5,12]

According to Ermolaev[2b,10] the value of γ_A is indepen-
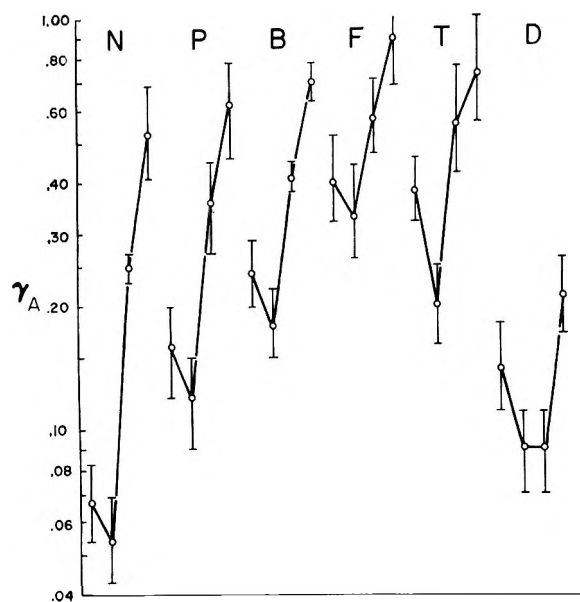
Figure 1.   Plot of γ_A for different acceptors in heavy-atom glasses (derived from Table I). The four points per plot from left to right are the following glasses; ethanol, 1:1 propyl chloride–ethanol, 1:1 propyl bromide–ethanol, and 1:1 propyl iodide–ethanol. The following letters identify the acceptors: N = naphthalene, P = phenanthrene, B = biphenyl, F = fluorene, T = m-terphenyl, and D = diphenylacetylene. In all cases n-propyl halides were used.

dent of donor–acceptor concentrations. While we have not extensively studied this point, the γ_A values obtained from different concentrations of acceptors show the trends present in Figure 1 very clearly, and agree numerically within experimental error.

One feature of Figure 1 that is surprising at first is the decrease in γ_A in going from an ethanol glass to an ethanol–propyl chloride glass. However this effect is seen

(12) S. E. Webber, *Chem. Phys. Lett.*, **5**, 466 (1970).

to be an "artifact" when the γ_A values are converted q_A values as described above.

b. Effect of the Solvent on the Sphere of Quenching. Ermolaev[10] has verified that Perrin's formula[13] correctly describes the dependence of donor quenching on acceptor concentration. Perrin's formula is

$$\frac{I_D(C)}{I_D(0)} = \exp(-vN_0C) \tag{11}$$

where $I_D(C)$ is the intensity of the donor phosphorescence in the presence of a concentration C (moles/liter) of acceptor, N_0 is 6.023×10^{20} (molecules/cm³ for a 1 mol/l. solution), and v is the volume of quenching. Perrin's formula is based on a "critical volume" model; if an acceptor is inside the critical volume surrounding a donor it is completely quenched (*i.e.*, does not phosphoresce), if the acceptor is outside the critical volume the donor is unaffected by the former's presence (*i.e.*, the donor phosphoresces with its normal quantum yield). This model is consistent with the predictions of theory concerning external heavy-atom effects and triplet transfer, both of which arise from overlap or exchange-like interactions.

In our experiments the ratio on the left-hand side of eq 11 was determined by measuring the peak height of the benzophenone phosphorescence at $\sim$24,250 cm⁻¹ in a variety of solutions with constant donor concentration (0.025 *m* at room temperature) and variable acceptor concentration. The concentrations were corrected for the solution contraction upon cooling to 77°K. The experimental fit to eq 11 is quite good except for the most concentrated solutions in some cases. The values of v obtained (Table III) were derived from a least-squares fit to eq 11.

Table III: Spheres of Quenching As a Function of Glass Composition

| Acceptor[a] | $v_{quenching}$[b] $\times 10^{21}$ cm³ | | |
	Cl[c]	Br[c]	I[c]
Fluorene	7.85	8.38	9.78
Biphenyl	6.16	5.42	5.56
m-Terphenyl	8.28	8.86	8.07
Diphenylacetylene	5.69	8.31	9.11
Phenanthrene	8.90	9.72	9.29
Naphthalene	8.97	9.13	8.36
Diphenyldiacetylene	11.20	10.87	11.32

[a] The donor was benzophenone (0.025 *m*) in all cases. [b] The experimental error of these quantities is on the order of $\pm 10\%$. [c] See Table I for notation.

Two observations may be made from the data in Table III. First, v does not seem to be particularly sensitive to solvent, with the possible exception of diphenylacetylene. As the glasses used for this study are very similar to each other, being composed of 1:1 propyl

halide–ethanol, the insensitivity to solvent presumably demonstrates the absence of any external heavy-atom effect on the $T_D \rightsquigarrow T_A$ process. This result is analogous to Ermolaev's work with halonaphthalenes,[10,14] in which v for 1-methyl, 1-chloro-, 1-bromo-, and 1-iodonaphthalene were essentially equal. Such a result is expected on the theoretical grounds that the transfer rate is dependent on an exchange integral[6] (*vide infra*) between orbitals located on the donor and acceptor molecules, which are nonvanishing for pure triplet states (stated differently, triplet–triplet transfer is a spin-allowed process). Thus the presence of a small component of singlet character in the donor or acceptor wave function is not expected to change the energy-transfer rate. Those variations with solvent which do exist probably result from differences in solvation due to different dipole moments associated with the solvent molecules.

The second observation that can be made from the data in Table III is that the values of v are not very different from each other. When the v data are converted into a radius of quenching ($R = (3v/4\pi)^{1/3}$), the differences are even less dramatic. The same can be said of Ermolaev's data,[10] which include fewer acceptors for a given donor than the present study, but do include a greater variety of donor–acceptor combinations. It is perhaps surprising that acceptor molecules differ so little in their quenching ability. The theoretical expression for the transfer rate[6,15] is given by the following proportionality

$$k_{T_D \rightsquigarrow T_A} \propto Z^2 \int_0^{\infty} P_D(\bar{\nu}) \epsilon_A(\bar{\nu}) \, d\bar{\nu} \tag{12}$$

where $P_D(\bar{\nu})$ is the normalized[16] donor phosphorescence spectrum and $\epsilon_A(\bar{\nu})$ is the normalized[16] acceptor $T_1 \leftarrow S_0$ absorption spectrum (both expressed on an energy scale). The integral in (12) is essentially an application of the Franck–Condon principle to the transfer process. The quantity Z is an exchange integral of the type

$$\langle \psi_D^*(1)\psi_A^{\circ}(1) | r_{12}^{-1} | \psi_D^{\circ}(2)\psi_A^*(2) \rangle \tag{13}$$

where ψ_D^* and ψ_A^* are excited molecular orbitals and ψ_D° and ψ_A° are valence molecular orbitals for the donor and acceptor molecule, respectively. The molecular orbitals in (13) are used to form the open shell configuration of the triplet states of the molecules in question, *i.e.*, $\psi_D^*(i)\psi_D^{\circ}(i')$ for the donor and $\psi_A^*(j)\psi_A^{\circ}(j')$ for the acceptor. As Dexter[6] discussed in his original for-

(13) F. Perrin, *C. R. Acad. Sci. Paris*, 178, 1978 (1924).

(14) V. L. Ermolaev, *Opt. Spektrosk.*, 5, 642 (1959).

(15) Reference 4, eq 11.47. Our notation essentially follows this author.

(16) Both $P_D(\bar{\nu})$ and $\epsilon_A(\bar{\nu})$ are normalized to unity, *i.e.*

$$\int_0^{\infty} P_D(\bar{\nu}) \, d\bar{\nu} = \int_0^{\infty} \epsilon_A(\bar{\nu}) \, d\bar{\nu} = 1$$

mulation of eq 12, this integral is expected to fall off approximately exponentially with R, the intermolecular separation (this is consistent with Perrin's law, as was mentioned above). One might expect the average value of this integral to be quite different for different acceptors due to the different "contact" geometries that may be realized and the variation in the amplitude of the molecular orbitals involved in (13) with position on the molecular frame. Also one might expect the overlap integral in (12) to contain considerable variation for different acceptor–donor pairs.

We have attempted to evaluate the overlap integral in (12) using a "mirror image" assumption to obtain $\epsilon_A(\bar{\nu})$ (that is, we assumed $\epsilon_A(\bar{\nu})$ to be the mirror image of the acceptor phosphorescence spectrum). It is well known that this condition is not satisfied particularly well for all the molecules studied,[17] but available $T_1 \rightarrow S_0$ spectra often overlap with the tail of the $S_1 \leftarrow S_0$ absorption, which makes the proper normalization of $\epsilon_A(\bar{\nu})$ impossible. There was a variation of about a factor of 2 in the overlap integral for our set of acceptors, but there was essentially no correlation with the quenching efficiency (i.e., diphenylacetylene has a larger overlap integral than diphenyldiacetylene but the latter molecule has nearly twice the quenching volume). While our calculation of the overlap integral is admittedly crude, we feel justified in concluding that the Z integral is a function of the particular donor–acceptor pair, such that one will not in general be able to estimate $k_{T_D \leadsto \cdot T_A}$ from an evaluation of the spectral overlap integral in eq 12 alone.[18]

IV. Discussion

We will take up the results of Section IIIa only, as the "sphere of quenching" data of Section IIIb do not require discussion.

The data of Section IIIa demonstrate that the quantum efficiency

$$q_A = \frac{k_{PT}^A}{k_{PT}^A + k_{GT}^A} \tag{14}$$

(k_{PT}^A phosphorescence rate of acceptor; k_{GT}^A radiationless rate $T_1 \leadsto S_0$ of acceptor) increases in the presence of external heavy-atom spin-orbit coupling. In view of the consistency of this result for all the molecules we studied (with the possible exception of diphenylacetylene), one must look for a rather general explanation. Our interpretation of this effect may be summarized as follows: (1) the external heavy atom mixes the T_1 state with a large number of zeroth-order singlet states[19]

$$\Psi_{T_1} = a\psi_{T_1}^0 + \sum_j b_j \psi_{S_j}^0 \tag{15}$$

The mixing with other triplet states makes no contribution to the rates in the present simplified scheme and will be ignored. We will neglect the mixing of the gound state with the triplet manifold in the interest of

algebraic simplicity so $\Psi_{S_0} \approx \psi_{S_0}^0$. Inclusion of some triplet character into our S_0 state does not change the present qualitative argument. The total Born–Oppenheimer wave function for the T_1 state is given by $\theta_t^{T_1} = \Psi_{T_1} \cdot \chi_v^{T_1}$ where $\chi_v^{T_1}$ is the vibrational wave function for the T_1 electronic state potential surface. (2) The radiative rate arises from the electromagnetic perturbation operator

$$H_{\text{radiative}} \equiv H_{PT}$$
$$\equiv -eE_0 \sum_i x_i z_i \tag{16}$$

where ez_i is the charge of the ith particle and the electric field vector is taken to be in the x direction. This operator connects states subject to rather stringent selection rules. Consequently only a limited number of states in a set of $\{\psi_{S_j}^0\}$ will be coupled radiatively to ψ_{S_0}. Usually one or two states are dominant. In the simplest case

$$|\langle \Psi_{T_1}|H_{PT}|\Psi_{S_0}\rangle|^2 \approx b_P^2|\langle \psi_{S_P}^0|H_{PT}|\psi_{S_0}^0\rangle|^2 \tag{17}$$

where $\psi_{S_P}^0$ has the largest oscillator strength in the set $\{\psi_{S_j}^0\}$. (3) The radiationless rate has recently been discussed assuming that the important coupling operator arises from Born–Oppenheimer terms,[20] i.e.

$$H_{\text{radiationless}} \equiv H_{GT}$$
$$\equiv \sum_i \frac{-\hbar^2}{2m_i}\left\{\frac{\partial^2}{\partial Q_i^2}\right\}_{\text{el}} - \frac{-\hbar^2}{m_i}\left\{\frac{\partial}{\partial Q_i}\right\}_{\text{el}}\frac{\partial}{\partial Q_i} \tag{18}$$

where $\{\ \}_{\text{el}}$ implies that the matrix element of the operator inside the brackets is computed with respect to the electronic part of the wave function, while the remainder of the operator operates on the vibrational wave function. The sum in (18) is over all the normal modes of the ground-state potential. The operator H_{GT} is not expected to be very selective in the states it couples. Thus we expect all the singlet states in Ψ_{T_1}

(17) A. P. Marchetti and D. R. Kearns, J. Amer. Chem. Soc., 89, 768 (1967).

(18) We should emphasize that it is not at all obvious that any simple relationship exists between $k_{T_D \leadsto \cdot T_A}$ and $v_{\text{quenching}}$. It would be useful to directly determine the triplet–triplet transfer rate. This could be effected by measuring the buildup of acceptor phorphorescence after a short duration flash excitation of the donor.

(19) We should note that there are two ways in which the external heavy atom can exert an influence on the spin-orbit coupling of molecular states: (1) direct coupling by means of penetration of atomic orbitals centered on the acceptor molecule into the region of the heavy-atom potential; and (2) indirect coupling due to the orthogonalization of the atomic orbitals centered on the molecule to the atomic orbitals centered on the heavy atom. In the former case the matrix element coupling two molecular states would be proportional to $\langle \phi_i^A|H_{so}^P|\phi_j^A\rangle$ where ϕ_i^A, ϕ_j^A are molecular orbitals centered on the acceptor (A) molecule and H_{so}^P is the spin-orbit coupling operator centered on the perturber (P) molecule. In the latter case the relevant matrix element will be $\langle \phi_i^A|\phi_k^P\rangle\langle \phi_l^P|\phi_j^A\rangle \cdot \langle \phi_k^P|H_{so}^P|\phi_l^P\rangle$. It has been found that the latter term is far more important than the former for atomic impurities in alkali halide lattices (E. Cavin, III, Ph.D. Thesis, University of Texas, 1970). It is expected that the same will be true for molecular systems.

(20) See, for example, M. Bixon and J. Jortner, J. Chem. Phys., 48, 715 (1968); R. Kubo, Phys. Rev., 86, 929 (1952).

to be coupled to Ψ_{S_0}, with the matrix squared given by

$$|\langle\Psi_{T_1}|H_{GT}|\Psi_{S_0}\rangle|^2 \approx$$

$$\sum_{i,j} b_i{}^*b_j\langle\Psi_{S_i}{}^0|H_{GT}|\Psi_{S_0}{}^0\rangle\cdot\langle\Psi_{S_0}{}^0|H_{GT}|\Psi_{S_j}{}^0\rangle \quad (19)$$

Equation 19 contains many cross terms which tend to cancel out as the relative signs of the set $\{b_j\}$ will be random.

It is our contention that a reasonable explanation for the relative efficiency of the external spin-orbit coupling in increasing k_{PT} relative to k_{GT} lies in the tendency for cancellation to occur in (19) which will be largely missing in (17).[21] The same argument would apply to the internal heavy-atom effect, which agrees with the increase of γ_A found by Ermolaev[2b,10] along the series naphthalene, 1-chloro-, 1-bromo-, and 1-iodonaphthalene.

We do not intend to imply that the above explanation is uniquely capable of rationalizing our observations. McGlynn, et al.,[22] have presented a treatment of the heavy-atom effect which presumes that a weak charge-transfer (CT) complex is formed between the heavy-atom perturber and the aromatic molecule. In this scheme the $T_1 \rightarrow S_0$ emission of the acceptor borrows intensity from the $^3P \rightarrow {}^1P$ transition of the perturber (P). In a recent paper Giachino and Kearns[22] have presented evidence that atomic-like states of the perturber mix with the aromatic triplet state and enhance the radiative rate of the latter preferentially. It is reasonable that the addition of CT states with the perturber would tend to enhance the radiative process *only*, due to the probable weak coupling of the perturber electronic states to the normal modes of the aromatic molecules.

Both the analysis of Birks[4] and a similar analysis of

our data[12] indicates that k_{GT} does increase due to heavy-atom solvents, albeit less than the increase of k_{PT}. Similar conclusions have been reached by Giachino and Kearns,[23] Siegal and Judeikas,[24] and El-Sayed and Eisenthal.[25] We take the view that: (1) external spin-orbit coupling increases the singlet character in T_1 (and S_0), with the result that

$$\Delta k_{PT} \geqslant \Delta k_{GT}$$

(the Δk standing for the change in rates due to heavy-atom solvent, both rates assumed to increase). This follows from our discussion of eq 17 and 19 (but see footnote 21). (2) CT states tend to increase k_{PT} exclusively with the final result that

$$\Delta k_{PT} > \Delta k_{GT}$$

(21) It is interesting to note that for an acceptor molecule with low symmetry a large number of states $\Psi_{S_i}{}^0$ will be coupled with Ψ_{S_0} *via* H_{PT}. For such cases the increase in k_{PT} relative to k_{GT} arising from the external (or internal) heavy-atom effect would be lessened according to the present arguments.

(22) S. P. McGlynn, T. Azumi, and M. Kinoshita, "Molecular Spectroscopy of the Triplet State," Prentice-Hall, Englewood Cliffs, N. J., Chapter 8, Section 6.

(23) G. G. Giachino and D. R. Kearns, *J. Chem. Phys.*, **52**, 2964 (1970).

(24) S. Siegel and H. S. Judeikas, *ibid.*, **42**, 3060 (1965).

(25) K. Eisenthal and M. A. El-Sayed, *ibid.*, **42**, 794 (1965).

Chemiemission from the Cesium–Oxygen Surface Reaction

by N. Moucharafieh and J. Olmsted III*[1]

Department of Chemistry, American University of Beirut, Beirut, Lebanon   *(Received November 23, 1970)*

Publication costs assisted by the American University of Beirut

Chemiemission occurring when oxygen impinges upon a suitably-prepared cesium metal surface under high vacuum has been studied at pressures from 0.8 to 8.0 × 10⁻⁸ Torr and −63.5°. The results show a more complicated variation with pressure, extent of surface coverage, and manner of surface preparation than that reported in studies carried out under less rigorous conditions. For surfaces prepared such that some oxide is probably present, the emission first increases with time, then decreases in a nonexponential fashion; photoemission, on the other hand, shows simple exponential decay. The maximum chemiemission current from such surfaces depends approximately on the square of the oxygen pressure and the maximum yield is of the order of 10^{-2} per oxygen–surface collision. A kinetic scheme is proposed involving two chemiemissive processes, one of which requires the presence of a surface intermediate; under appropriate conditions, this scheme can account for the main features of the chemiemissive behavior.

Introduction

The phenomenon of electron emission occurring upon the exposure of fresh metal surfaces to reactive gases has been known for some time. In the earliest experiments, vacuum techniques were insufficiently advanced to distinguish between processes involving chemical reaction with a gas and those which could occur independently of such a reaction; the term "exoelectron emission" was thus applied to both types of processes. (For reviews of earlier as well as some recent work, see ref 2 and 3.)

Beginning with the work of Lohff,[4] who determined that oxygen was essential for the emission of electrons from mechanically worked zinc surfaces, the chemiemissive nature of the electron emission process from originally clean metallic surfaces has been increasingly realized, and metal–oxygen reactions have been found to lead to chemiemission in several systems, including Al,[5,6] Ni[7], Mg,[8] and Ag.[9]

Although these recent studies have shed some light on the process of chemiemission, the assembled data remain too scanty to evaluate existing ideas concerning the mechanism of such emission. In particular, conflicting proposals have been put forward concerning the source of the energy required for chemiemission,[10,11] and even the nature of the elementary chemical processes that occur remains uncertain.[12] Furthermore, it is not clear whether or not theories of growth of oxide layers[13,14] are applicable to chemiemissive processes. More data are clearly needed, both as to the types of systems that can display chemiemission and as to the kinetic behavior shown by such systems.

The present work represents an attempt to obtain such data in a detailed study of the chemiemission phenomenon for a particular reactive system, in an ultraclean environment and under a variety of conditions. The cesium–oxygen system, which has not been studied previously, was chosen, in order to examine to what

extent the phenomenon, previously observed in oxidation of members of group II, III, and the transition metals, is similar for an alkali metal.

Experimentation

All chemiemission studies were carried out in an ultrahigh vacuum system consisting of a custom-fabricated Pyrex manifold connected to a Granville-Phillips series 225 ultrahigh vacuum pumping station through a Granville-Phillips 2-in. ultrahigh vacuum valve. The system pressure was determined by a Varian Associates Model UHV-12 Bayard-Alpert ionization gauge, pretreated by running in pure oxygen at 10⁻⁶ Torr for 48 hr to obtain reliable oxygen pressure measurement.[15] The ion gauge power supply was a Varian Associates Ionization Gauge Control Unit, Model 971-0023, the output of which was fed into one channel of a Moseley Autograph Model 7100B two pen recorder. The emitted electron current was collected on a gold foil and

(1) On leave of absence during 1970–1971 at Department of Chemistry, University of California, Los Angeles, Calif.

(2) A. Bohun, *J. Phys. (Paris)*, **26**, 149 (1965).

(3) F. R. Brotzen, *Phys. Status Solidi*, **22**, 9 (1967).

(4) J. Lohff, *Z. Phys.*, **146**, 436 (1956).

(5) J. Wustenhagen, *Z. Naturforsch. A*, **14**, 634 (1959).

(6) J. A. Ramsey, *Surface Sci.*, **8**, 313 (1967).

(7) T. A. Delchar, *J. Appl. Phys.*, **38**, 2403 (1967).

(8) T. F. Gesell, E. T. Arakawa, and T. A. Callcott, *Surface Sci.*, **20**, 174 (1970).

(9) N. Sato and M. Seo, *Nature*, **216**, 361 (1967).

(10) O. Haxel, F. G. Houtermans, and K. Seeger, *Z. Phys.*, **130**, 109 (1951).

(11) W. B. Lewis and W. E. Burcham, *Proc. Cambridge Phil. Soc.*, **32**, 50 (1936).

(12) J. Lohff, *Naturwissenschaften*, **44**, 228 (1957).

(13) R. Cockelbergs, A. Frennet, G. Lienard, and P. Resibois, *J. Chem. Phys.*, **39**, 585 (1963).

(14) R. Hooke and T. P. Brody, *ibid.*, **42**, 4310 (1965).

(15) R. E. Schlier, *J. Appl. Phys.*, **29**, 1162 (1958).
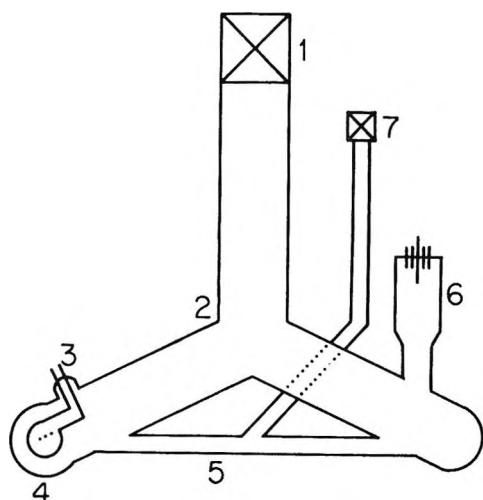
Figure 1. Pyrex vacuum system (schematic): (1) main valve; (2) Y-shaped manifold; (3) electrical leads; (4) reaction site; (5) oxygen inlet tubulation; (6) ion gauge; (7) variable leak.

measured by a Keithley Instruments Model 600A electrometer, the output of which was fed into the second channel of the recorder. To ensure high electron collection efficiency, the cesium surface was biased 35 V negative relative to the collector.

Two different Pyrex manifold designs were employed, one of which is shown schematically in Figure 1. In this design, which was used in the majority of the experiments, the ion gauge was mounted at a distance from the reaction site in order to avoid stray electrometer currents arising from electrons from the ion gauge filament or photoemission from the cesium surface induced by the spectral emission of the filament. The ion gauge and the reaction site were arranged symmetrically with respect to the pumps and oxygen inlet system, in order to obtain, as nearly as possible, equal pressures at these two points.

A second manifold design was used for some runs in order to determine whether or not gettering by the Cs surface and/or the ion gauge filament was significantly affecting the results. In this design, the ion gauge was mounted as closely as possible to the reaction site. Experiments done on this manifold yielded identical results as those done on the other, indicating that pressure imbalance between arms of the Y-shaped manifold was insignificant.

The reaction site itself was the same for both manifolds and was constructed as shown schematically in Figure 2. The cesium surface was deposited on a gold substrate which was in thermal contact with an integrally-mounted dewar flask containing a constant-temperature bath. A cesium evaporation tube, heatable by heating tape wrapped around its outer surface, was welded to the base of the outer wall of the dewar flask. The cesium metal was held in a break-seal ampoule which was opened under ultrahigh vacuum by
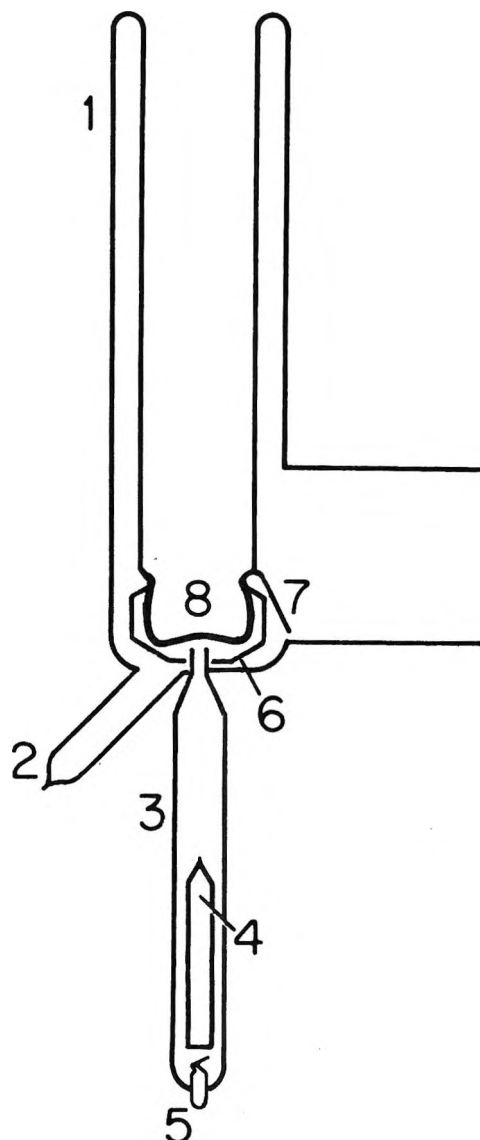
Figure 2. Cesium-oxygen reaction site (schematic): (1) dewar flask; (2) side arm for cleaning; (3) cesium evaporation tube; (4) glass-encased iron slug; (5) cesium ampoule; (6) gold electron collector; (7) gold baffle; (8) deposition site.

means of a Pyrex-encased iron slug. The electron collector was a slightly roughened gold foil mounted concentrically with the nozzle of the cesium evaporator.

Oxygen could be admitted to the system from Pyrex ampoules by means of a Granville-Phillips series 203 variable leak, manipulation of which permitted the selection of oxygen pressures ranging from 10^{-9} Torr upwards. Locally bottled oxygen of $99+\%$ purity was used without further purification, and the cesium was 99.9% purity metal from K and K or Merck, vacuum distilled at 10^{-6} Torr into the break-seal ampoules.

The Pyrex manifold and valves were baked for 4 hr at $350°$ prior to opening the cesium ampoule, and after such bakeout base pressures of 1×10^{-9} Torr or better were observed. Following bakeout, cesium films were deposited on the gold substrate at pressures not exceed-

ing 3×10^{-9} Torr. The entire manifold was wrapped in black cloth and the reaction site electrically and optically shielded, thereby reducing the background signal level to less than 10^{-10} A even in the presence of a fresh, active cesium film. All evaporations and subsequent measurements were carried out under controlled surface temperature conditions, utilizing organic solvent liquid–solid "slush" baths to achieve constant surface temperature. Cesium deposition was monitored in two ways: by observing the temperature of the evaporation tube with a copper–constantan thermocouple, and by observing the growth of photoemission from the cesium surface as deposition proceeded. Following deposition of an adequate film, further cesium evaporation was prevented by cooling the evaporation tube to a temperature lower than $-40°$.

Results

Analysis of Emission Curves. The results of a typical constant pressure, constant temperature run are illustrated in Figure 3, which shows the variation with time of the electron emission for a cesium film reacting with oxygen at a pressure of 3.7×10^{-8} Torr. All films studied showed similar behavior, namely delay of the onset of emission, followed by a relatively rapid rise in emission to a peak value, after which the emission decayed approximately exponentially. The details of this behavior have been found to depend heavily on the manner of preparation of the cesium surface as well as on the pressure of oxygen gas. The dependence on surface temperature has also been qualitatively studied.

The electron emission curve can be analyzed and characterized in several fashions. We have chosen to examine the maximum electron current I_{max}, the total emission $Q = \int I dt$, and the decay lifetime τ, since these three quantities, all relatively easy to obtain, yield important information about the nature of the emissive process.

From the maximum emission current, knowing the oxygen pressure p and the area of the cesium surface A, it is possible to determine the maximum differential yield

$$I_{max} = uA Y_{DM}e = (spA Y_{DM}e)/(\sqrt{2\pi mkT}) \quad (1)$$

where $u = sp/\sqrt{2\pi mkT}$ is the rate of adsorption of molecules per square centimeter of exposed surface area,[16] s is the sticking probability (fraction of collisions which results in adsorption), Y_{DM} is the maximum differential yield (fraction of adsorptions which results in emission), and the other symbols bear their conventional meanings. For oxygen gas at room temperature, the pressure expressed in Torr, and a surface area of 5 cm², one obtains

$$sY_{DM} = I_{max}/287p \quad (2)$$

From the total emission Q, knowing the number of cesium atoms per unit surface area and the surface area
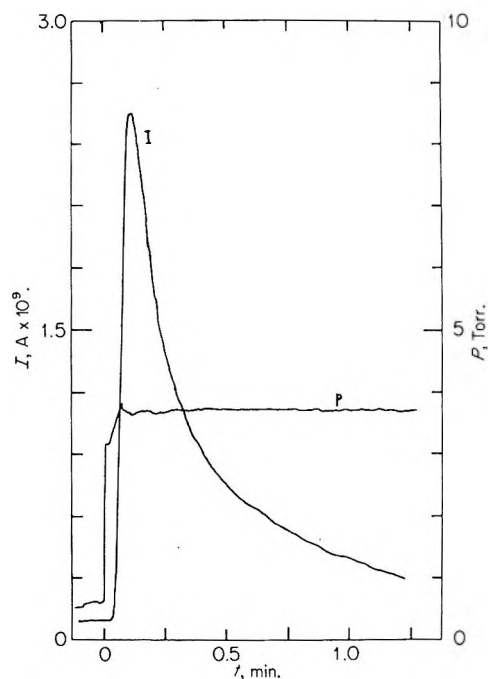
Figure 3. Variation of emission current with time, under constant pressure of oxygen, for a thick cesium film, previously reacted with oxygen and then annealed at base system pressure for 6 min.

A, it is possible to determine the integral yield Y_I (fraction of surface cesium atoms which react and emit an electron)

$$Y_I = \int I dt/neA \quad (3)$$

where n is the number of cesium atoms per square cm of surface (3.52×10^{14} atoms for body-centered cubic structure and a cesium atomic radius of 2.67 Å).

In the Cs–O_2 system at temperatures used in this study, the oxygen is sufficiently tightly bound chemically that desorption should be negligible. Incorporation of oxide into the lattice is shown below to be a significant process, but at the O_2 pressures used in these experiments it is slow relative to the rate of oxide formation at the surface. Thus, the rate of change of the fractional surface coverage depends only on the accommodation of oxygen on previously uncovered sites

$$d\theta/dt = u/n(1 - \theta) \quad (4)$$

The sticking probability s, and through it u, may be dependent on θ in a way which is in general unknown. The simplest assumption is that s does not depend on θ; then eq 4 integrates to

$$\ln (1 - \theta) = (u/n)t = (spt)/(n\sqrt{2\pi mkT}) \quad (5)$$

In the event that emissive reaction occurs with equal probability at all uncovered sites, the emission current

(16) D. O. Hayward and B. M. W. Trapnell, "Chemisorption," Butterworths, London, 1964, p 87.

is proportional to the fractional exposed surface $(1 - \theta)$

$$\ln (I/I_0) = [sp(t_0 - t)]/[n\sqrt{2\pi mkT}] \qquad (6)$$

or, for pressure in Torr and τ defined as the half-life, in minutes

$$s = (2.14 \times 10^9)/p\tau \qquad (7)$$

Equation 6 predicts that a semilog plot of emission current vs. time should be linear. The experimental chemiemission curves, on the contrary, display three distinct regions of behavior: initially, rapidly rising chemiemission; then, roughly exponential decay over somewhat more than a decade; finally, exponential decay with about three times greater half-life extending over about another decade. The assumptions leading to eq 6 thus are apparently inappropriate to describe chemiemission.

The rate of coverage of the surface, and through this the assumption of constant sticking probability, can also be monitored by observing the photoemission from the surface during oxidation. This has been done by cycling a light source on and off during a chemiemission run, thereby obtaining successively the chemiemission and the sum of chemi- and photoemission. The results are shown in Figure 4.

The striking feature of the photoemission curve is its linear behavior throughout the time period during which chemiemission is observed, which implies that the assumptions leading to eq 6 are valid for photoemission. Furthermore, the half-life of photoemission coincides within experimental error with the longer half-life observed near the end of the chemiemission process. More complex explanations than those involving constant sticking probability and emission solely from uncovered sites are of course possible; but it is unlikely that linearity over nearly two decades would result from such explanations, especially as the photoemissivity of the oxidized surface is observed to be negligible (1% or less of the initial photocurrent).

The data shown in Figure 4, which represents a run carried out at oxygen pressure of 3.8×10^{-8} Torr, yield a half-life for photoemission from which a sticking probability $s = 0.067$ is obtained. For runs in which only the chemiemission could be observed conveniently, sticking probabilities were obtained from the slopes of the final, longer-lifetime exponential portion of the chemiemission curves. This procedure is justified by the observation that, in all runs for which both chemi- and photoemission were monitored, that final portion of the chemiemission decay had a slope equal to that for photoemission decay.

Effects of Surface Preparation. Several different classes of cesium surfaces could be distinguished in these experiments: (1) thin films deposited on a gold substrate; (2) thick films deposited on a gold or cesium
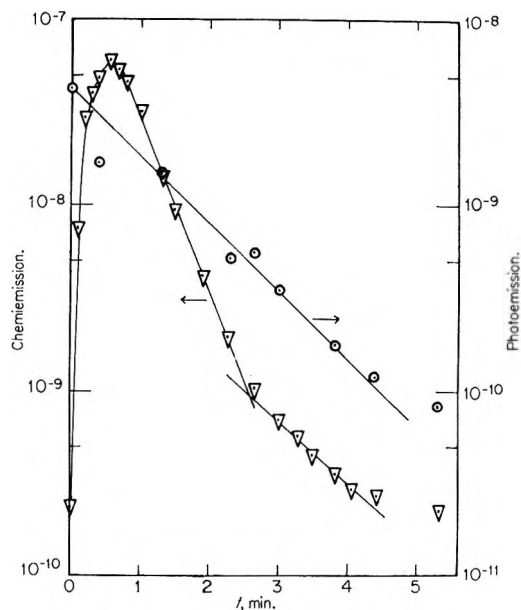
Figure 4. Variation of photoemission (○) and chemiemission (▽) with time for an annealed thick cesium film reacted with oxygen at a constant pressure of 3.8×10^{-8} Torr.

oxide substrate; (3) thin films deposited on a cesium oxide substrate; and (4) films developed by annealing oxide-coated thick films.

These films were prepared as follows. Thin films were obtained by evaporative deposition of cesium with concurrent monitoring of the photoemissivity of the surface, only until that photoemissivity reached a constant value. This generally required heating the evaporation oven to about 125° for a period of approximately 7 min. These films could be deposited either onto a clean gold substrate or on top of a previously deposited and oxidized cesium surface. Thick films were obtained by similar evaporative deposition extending over a 60-min period. Preparation by annealing involved allowing an oxide-coated thick film to stand at base pressure (10^{-9} Torr) and constant temperature ($-63.5°$) for periods of from 2 to 120 min. Each of these methods of preparation gave films having high photosensitivity.

Interpretation of the observations for thin films deposited on gold substrates is rendered difficult by the fact that gold and cesium react to form a semiconductor compound.[17] However, the fact that photoemissivity of the thin films reached a plateau value after a given deposition time is indicative that, whatever the composition of the surface layer prior to that time, it subsequently attained uniformity. Since cesium was being continuously deposited, one concludes that the uniform composition was a pure cesium layer (probably deposited over a previously formed CsAu semiconductor layer). At the point when photoemission reached a

(17) The Au–Cs reaction is reviewed in A. H. Sommer, "Photoemission Materials," Wiley, New York, N. Y., 1968, p 182.

steady-state value, deposition was discontinued. The result should have been accumulation of only a thin (several layers at most) uniform composition cesium film; this is corroborated by the observation that, in contrast to thick films, annealing of oxidized thin films did not lead to regenerated activity. The conclusion that thin films were constituted of pure cesium at their surface is further supported by the observation that such films displayed emissive behavior that was of the same type as that observed for very thick, unannealed cesium layers (see below).

The emissive behavior of these surfaces was of two strikingly different types. One, of low yields and poorly characterized chemiemission coupled with slow decay of photosensitivity, was observed for thin films deposited on a gold substrate and for all thick evaporated films. This low-yield behavior for thick films was observed whether the film was exposed to oxygen immediately after deposition or was allowed to anneal at base pressure for up to 1 hr prior to exposure to oxygen. This type of behavior gave very low differential yields ($sY_{DM} \sim 10^{-6}$) and emission decay which was so slow, irregular, and irreproducible that Y_I and s could not be determined.

The other type of behavior, giving relatively high differential yields and smooth, reproducible emission decay, was observed for thin evaporated films laid down onto previously oxidized surfaces and for films developed by annealing oxidized thick cesium films. It was further observed that a thick cesium film could be regenerated as many as 20 or 30 times; that is, following each exposure to oxygen and observation of chemiemission accompanied by loss of photosensitivity, pumpout of the oxygen and annealing for several minutes resulted in regeneration of photosensitivity and chemiemissive capability. Moreover, the degree of photosensitivity developed and the amount of chemiemission subsequently observed depended on the length of time of annealing at base pressure. In particular, the photoemission increase showed first-order behavior with a half-life for regeneration of activity equal to 30.7 min for substrate at a temperature of $-63.5°$ (Figure 5).

Effects of Extraneous Variables. In addition to the mode of surface treatment, which is observed to exert a profound effect on the chemiemissive behavior of the cesium surface, several other factors might affect the observations. These include effects due to pressure differentials in the system, due to chemically-active species generated by the ion gauge filament, and due to the action of photons at the surface. As mentioned in the experimental section, the manifold was designed to minimize as much as possible these effects, by placing the ion gauge at a distance from the reaction site but symmetrically mounted with respect to the pump. In addition, several experiments were carried out to verify the absence of such effects.

To check the possibility of effects due to pressure
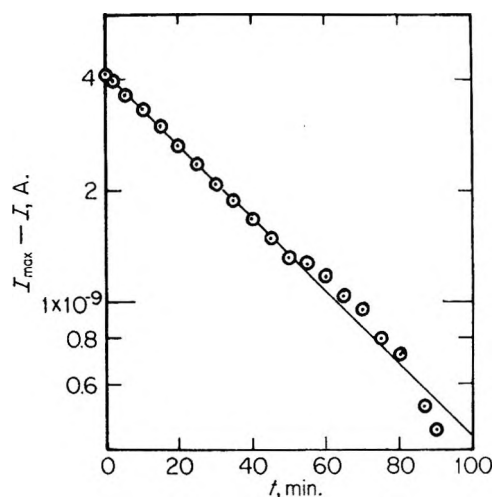
Figure 5. Plot of log ($I_{max} - I$) *vs.* time for an annealing cesium oxide coated film exposed to a constant light flux.

differentials, a second manifold was constructed wherein the ion gauge was mounted so as to view directly the reaction region and a series of experiments conducted using it. These experiments gave identical results to those using the Y-shaped manifold, both for the low-yield behavior of thick films and for the characteristic decay behavior of thin and annealed films.

The absence of active species generated by the ion gauge filament is also indicated by the results cited above, since active species if present should reach the cesium surface much more frequently in the second manifold, thereby causing different observations for the second setup than for the first. Such was not the case. Unfortunately, the need to monitor oxygen pressure as it was being admitted to the manifold prevented direct verification of the absence of gauge-induced effects, since the ion gauge had to be kept on at least during the initial introduction of oxygen. However, it was possible to turn off the gauge once a steady-state oxygen pressure was reached. Such an experiment has been done for an annealed film, turning off the gauge before the maximum emission had developed. The observed chemiemission behavior for such a run was identical to that seen in runs with the ion gauge on.

This latter result was obtained in total darkness, except for stray photons from the ion gauge during the short period when it was on. It thus also indicates that photons are not a part of the mechanism of the chemiemissive process. Further support for this conclusion is provided by the experiments wherein a light source was cycled on and off. As previously indicated, in those experiments the chemiemission showed exactly the same behavior as it did in the absence of cycled light. The total emission, in other words, was readily analyzed as the sum of purely chemiemissive and purely photoemissive components.

Analysis of Chemiemission Curves. The results of analysis of several thin films deposited and reacted at

$-63.5°$ at various pressures of oxygen are shown in Table I. All three of the parameters appear to be

Table I: Characteristics of Thin Deposited Films (Oxide Substrate)

p, Torr	Y_{DM}	Y_I	s
0.80×10^{-8}	2.2×10^{-2}	2.0×10^{-3}	0.05
0.90×10^{-8}		3.2×10^{-3}	
0.95×10^{-8}	2.5×10^{-2}	5.7×10^{-3}	0.11
0.97×10^{-8}	1.9×10^{-2}		0.16
1.8×10^{-8}	3.9×10^{-2}	3.9×10^{-3}	0.10
2.3×10^{-8}	0.66×10^{-2}	1.5×10^{-3}	0.12
3.7×10^{-8}	12×10^{-2}		0.05
5.7×10^{-8}	1.9×10^{-2}	3.4×10^{-3}	0.06
6.0×10^{-8}	0.59×10^{-2}	1.7×10^{-3}	0.01
6.6×10^{-8}	1.2×10^{-2}	2.7×10^{-3}	0.04

roughly independent of pressure over this range. However, there is considerable scatter in the individual points, owing probably to the impossibility of preparing identical surface structure and composition upon successive cesium depositions onto the cesium oxide substrate.

A larger number of studies was carried out on films activated by annealing at $-63.5°$. Yields obtained for such films were corrected to give values for full surface development by calculating the fraction of full development obtained during annealing, assuming 30.7-min development half-life. The results for such films are collected in Table II.

Table II: Characteristics of Annealed Films

p, Torr	$t_{annealing}$, min	Y_{DM}	Y_I	s
1.5×10^{-8}	14.5	0.9×10^{-2}	5.2×10^{-5}	0.08
2.2×10^{-8}	6.0	1.2×10^{-2}		0.06
3.7×10^{-8}	5.9	3.4×10^{-2}	3.4×10^{-3}	0.05
3.7×10^{-8}	93.5	5.2×10^{-2}	1.3×10^{-3}	0.12
5.5×10^{-8}	6.0	4.0×10^{-2}	3.5×10^{-3}	0.06
5.6×10^{-8}	7.0	3.8×10^{-2}	3.4×10^{-3}	0.05
5.7×10^{-8}	114.0	1.9×10^{-2}	7.0×10^{-3}	0.07
5.8×10^{-8}	7.0	4.6×10^{-2}	5.7×10^{-3}	0.04
5.8×10^{-8}	7.2	8.5×10^{-2}	5.6×10^{-3}	0.02
5.9×10^{-8}	10.0	4.5×10^{-2}	5.1×10^{-3}	0.06
6.0×10^{-8}	2.0	7.6×10^{-2}	5.7×10^{-3}	0.02
6.5×10^{-8}	10.0	3.2×10^{-2}	2.4×10^{-3}	0.13
6.6×10^{-8}	21.0	5.0×10^{-2}	6.1×10^{-3}	0.06
8.4×10^{-8}	7.0	3.9×10^{-2}	2.3×10^{-3}	0.10

As in the case of thin deposited films, there is considerable scatter of the data. This scatter is attributable again to the irreproducibility of films developed by successive annealing of previously reacted substrate. It is also due in part to the difficulty in regulating the initial pressure of oxygen upon first opening the variable
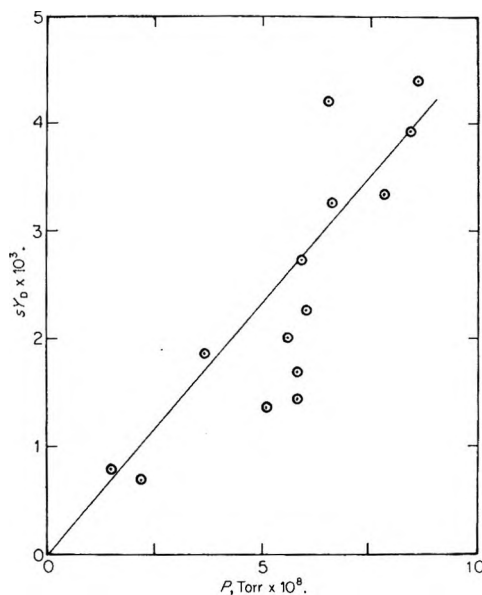
Figure 6. Variation of the experimental quantity sY_{DM} with oxygen pressure for a series of annealed cesium films.

leak, which may particularly affect the maximum current observed, since this generally appears within 30 sec of the introduction of oxygen into the system.

Unlike the case of thin deposited films, there appears to be an increase in the maximum differential yield as one goes to higher pressures. This trend is more strongly indicated if one examines the experimentally observed quantity, sY_{DM}, which is directly proportional to I_{max}/p. A plot of sY_{DM} vs. pressure is shown in Figure 6; although there is substantial scatter of the data, a linear increase of sY_{DM} with pressure seems to be indicated.

For the integral yield, on the contrary, no trend is apparent; in fact, the integral yield appears to be independent of the pressure. The mean value for the integral yield from annealed films is $Y_I = 4.9 \pm 1.2 \times 10^{-3}$, which agrees within the limits of experimental error with the mean value from thin deposited films, which is $Y_I = 3.0 \pm 0.9 \times 10^{-3}$.

Although the bulk of the measurements reported here were made at a temperature of $-63.5°$, some investigation of the effect of surface temperature on the chemiemissive phenomenon was carried out. The annealing of oxide-covered films was found to be substantially hindered as the temperature was reduced, with very little regeneration observed at $-95°$ and none observed at $-183°$. On the other hand, the chemiemission process itself was not significantly affected by the surface temperature, as was shown by the observation that a film annealed at $-63.5°$ and then cooled to $-183°$ before admission of oxygen showed chemiemissive behavior very similar to that observed at higher temperatures. Several runs were carried out at $0°$; these also gave comparable results. It should be noted that with our experimental setup the surface

temperature is controlled independently of the oxygen gas temperature; the latter was room temperature (25°) in all cases.

Discussion

One would like to describe the chemiemission reaction in terms of a simple solid-gas one-step reaction

$$O_2 + Cs \text{ (surface)} \longrightarrow CsO_2 \text{ (surface)}^+ + e^- \quad (8)$$
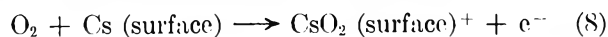
with the emitted electron being derived from the conduction band of the metal, and the energy required to overcome the work function being supplied either by the exothermic chemisorption process[10] or by the oxidation itself.[18] The time and pressure dependence of chemiemission observed in this work do not permit such a simple explanation.

An alternative tunneling mechanism as developed by Bohun, et al.,[19] might explain the observed results with the postulation of a barrier height decrease caused by the presence of some chemisorbed oxygen on the surface. Cesium oxide is widely used to lower the work function of semiconductor photoemitters,[20] but whether it can act in a similar fashion on the surface of cesium itself is not known. It does not appear to do so when covering the entire surface, since such work function lowering would be expected to cause an increase in the photoelectric yield upon irradiation with white light, contrary to our observations (Figure 4) of a steady decrease of photoemission with time upon admission of oxygen to the cesium surface. Some more complex mechanism thus must be sought.

Whatever the mechanism of chemiemission, it must explain the following observations. (1) Cesium films incorporating little or no oxygen (thick deposited films or first films deposited on gold substrate) develop chemiemission extremely slowly and give low differential yields. (2) Chemiemission grows rapidly when oxygen is first admitted onto a film which incorporates oxygen (thick deposited films or diffusion-annealed films). (3) The maximum emission current appears to be second-order dependent on the pressure. (4) Chemiemission half-lives for less than ~90% surface coverage are much shorter than photoemission half-lives. (5) The decay of photoemission is structureless and logarithmic.

The regeneration of chemiemissive activity upon annealing thick oxide-coated films is a phenomenon that has also been observed by other workers. Delchar[7] found that nickel surfaces, exposed to pulsed doses of oxygen, gave chemiemission with a twin-peaked behavior as a function of time. He attributed the second peak to freshly exposed nickel created when oxygen was incorporated into the metal lattice. For the cesium-oxygen system, Koller,[21] in studying the photoemission from cesium-cesium oxide surfaces, observed behavior which he explained in terms of diffusion of cesium and oxygen species.

The first-order regeneration of photosensitivity and temperature dependence of the regeneration (its absence at 77°K) observed in this study indicate that, as in the above-mentioned studies, the effect seen here is due to diffusion of cesium metal from the unreacted substrate through the oxide layer (or, alternatively, migration of the oxide down into the bulk substrate). This interpretation is consistent with the other properties of annealing observed in this work: the absence of regeneration of thin films (no bulk cesium present) and the absence of well-characterized emission from an annealed surface that had not had previous exposure to oxygen (no oxide present to be incorporated into the lattice).

From the purely first-order decay of the photoemission, together with the lack of any discernible trend in sticking probability, we conclude that the process of active site destruction is simple (we indicate a species present at the surface by SU)

$$O_2 + Cs(SU) \xrightarrow{k_2} O_2 \cdot Cs(SU) \quad (9)$$
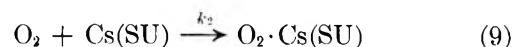
and that oxygen coverage of a site eliminates it as a photoactive site. From the rapid growth of chemiemission upon first admission of oxygen we conclude that the presence of oxygen sorbed on the surface is necessary for chemiemission to occur with a high yield

$$Cs(SU) + O_2 + O_2 \cdot Cs(SU) \xrightarrow{k_3} 2CsO_2 + Y_3 e^- \quad (10)$$
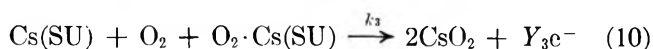
This two-step mechanism will lead to a second-order dependence of I on p.

It is reasonable to assume that the intermediate sorbed oxygen eventually will be converted to the oxide, again with a possibility of chemiemission

$$O_2 \cdot Cs(SU) \xrightarrow{k_4} CsO_2 + Y_4 e^- \quad (11)$$
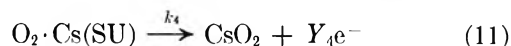
We may express $[Cs(SU)]$ in the form $(1 - \theta)Cs_0$, where θ is the fractional coverage and Cs_0 the initial surface concentration of cesium atoms. Applying the steady-state approximation for the intermediate

$$(d[O_2 \cdot Cs(SU)])/dt =$$
$$0 = k_2 p Cs_0 (1 - \theta) - k_4 [O_2 \cdot Cs(SU)] -$$
$$k_3 p Cs_0 (1 - \theta)[O_2 \cdot Cs(SU)] \quad (12)$$

which may be rearranged to give

$$[O_2 \cdot Cs(SU)] = [k_2 p Cs_0 (1 - \theta)]/$$
$$[k_4 + k_3 p Cs_0 (1 - \theta)] \quad (13)$$

The rate expression for electron production is

$$de^-/dt = I = a Y_3 k_3 p Cs_0 (1 - \theta) \times$$
$$[O_2 \cdot Cs(SU)] + a Y_4 k_4 [O_2 \cdot Cs(SU)] \quad (14)$$

(18) R. Seidl and F. Raubinek, Czech. J. Phys., 3, 309 (1953).

(19) A. Bohun, J. Sak, and M. Pšeničková, ibid., B, 15, 667 (1965).

(20) For a recent review, see R. L. Bell and W. E. Spicer, Proc. IEEE, 58, 1788 (1970).

(21) L. R. Koller, Phys. Rev., 36, 1643 (1930).

Upon substitution of eq 13, this gives

$$I = [aY_3k_2k_3p^2Cs_0^2(1 - \theta)^2 +$$

$$aY_4k_2k_4pCs_0(1 - \theta)]/[k_4 + k_3pCs_0(1 - \theta)] \quad (15)$$

where a is the film area, p the oxygen pressure, and Y_3 and Y_4 are fractional yields for electron production.

It can be seen that, under conditions where $k_4 > k_3pCs_0$ but $Y_3k_3pCs_0(1 - \theta) > Y_4k_4$, the current will appear to be proportional to the square of the pressure. The first condition is reasonable in light of the photoemission behavior. For the above kinetic scheme, we derive for the rate of decay of photosignal

$$(\text{d photons})/dt = d(1 - \theta)/dt =$$

$$-k_2p(1 - \theta)(1 + [k_3Cs_cp(1 - \theta)]/$$

$$[k_4 + k_3Cs_0p(1 - \theta)]) \quad (16)$$

which predicts the observed first-order decay only if $k_4 > k_3pCs_0$. The second condition can hold simultaneously with the first only if $Y_3 \gg Y_4$. Some idea of the relative magnitudes of Y_3 and Y_4 may be obtained from comparison of the maximum differential yield Y_{DM}, which should be largely determined by Y_3, and the integral yield Y_I, which represents an average of the contributions of Y_3 and Y_4. Tables I and II show that Y_{DM} is about 10 times Y_I at low pressures and 5–10 times Y_I at higher pressures, from which we estimate that $Y_3 \geq 100Y_4$. The substantially lower yields reported by earlier workers under conditions where fractional surface coverage was large also lend support to this estimate.[22,23]

The short early half-lives for chemiemission are also explicable using this mechanism, since for early times the decay will be dominated by the $(1 - \theta)^2$ term, while at later times the $(1 - \theta)$ term will be dominant. Other features of the chemiemission behavior are less easily rationalized by these kinetics, however. The apparent independence of pressure of the observed integral yield, for example, does not follow from the kinetic scheme. This independence is not firmly established, and more careful determinations may reveal a variation consistent with our proposed mechanism.

The slow development and low differential yields from very thick cesium films also do not fit readily into the scheme. Two alternative reasons for this behavior may be proposed: (1) the sticking probability for O_2 on such films is substantially lower than on films incorporating some oxide (i.e., k_2 is smaller for purer films); or (2) the rate of conversion of the intermediate into cesium superoxide is substantially greater for uncontaminated films [i.e., $Y_4k_4 > Y_3k_3pCs_0(1 - \theta)$]. Detailed observation of the decay of photosensitivity of such a film should help resolve this question; such a study has not yet been carried out, but qualitative observations indicate a slower decrease of photosensitivity for such films and thus support the first possibility.

If the proposed kinetic scheme is correct, one is still faced with the problem of establishing the details of the mechanism: the identity of the O_2–Cs (surface) intermediate and the source of energy for the two electron emission processes. One possibility, in light of the general observation that oxygen is chemisorbed on low work function metal surfaces as the O_2^- ion,[24] is O_2^-, chemisorbed on the surface, as the intermediate. The enhancement of chemiemission by this intermediate might then be due to a high probability of ionization of this ion upon chemisorption of another oxygen molecule at an adjacent site, and such ionization could be viewed as a tunneling process similar to that developed by Bohun, et al.,[19] or as a process involving the heat of chemisorption as proposed by Haxel, et al.[10]

Another possibility is suggested by the unique role of Cs_2O in acting as a sensitizer of the infrared photoemission from III–V-type semiconductor compounds[20] and from the Ag–O–Cs photocathode.[25] In these systems, the cesium oxide acts as a semiconductor which lowers the photoelectric threshold and enhances the photoelectric yield, presumably by creating a high efficiency electron tunneling path out of the major constituent of the cathode (Ag or the III–V compound) into the oxide. The oxide also perturbs the band structure of the semiconductor substrate; the net result in either case is creation of a low work function path for electron emission into vacuum. In our system, comprising only cesium and cesium oxides, such photoelectric effect enhancement seems to be minimal, judging from our experimental photoemission results. However, cesium oxide could be enhancing the chemiemissive process by providing a low work function path for emission of chemiexcited electrons. Chemiemission could be much more sensitive than photoemission to such local surface sites of low work function, inasmuch as the chemisorption process is confined to the surface, whereas photon absorption extends to a considerable depth below the surface. It should be emphasized that if Cs_2O is the intermediate, acting to reduce the local work function, it must eventually be destroyed with concomitant work function increase (perhaps by conversion to cesium superoxide in the presence of excess oxygen) to explain the disappearance of photoemissive activity upon full oxidation of the surface.

In our kinetic scheme, we have assumed that the first-order chemiemission is generated by the bulk oxidation process, that is, by the exothermicity of incorporation of the oxide ion into the cesium lattice. In this we follow Lohff and Raether.[23] One can also imagine the first-order chemiemission as driven by the heat of chemisorption, in which case the following

(22) W. Geiger, *Z. Phys.*, **140**, 608 (1955).

(23) J. Lohff and H. Raether, *ibid.*, **142**, 310 (1955).

(24) J. N. de Boer, "Electron Emission and Adsorption Phenomena," Cambridge University Press, London, 1935, p 142.

(25) Reference 18, Chapter 10.

kinetic scheme obtains

$$O_2 + Cs(SU) \xrightarrow{k_2'} O_2 \cdot Cs(SU) + Y_2 e^- \quad (17)$$

$$O_2 + Cs(SU) + O_2 \cdot Cs(SU) \xrightarrow{k_3} 2CsO_2 + Y_3 e^- \quad (18)$$

$$O_2 \cdot Cs(SU) \xrightarrow{k_4'} CsO_2 \quad (19)$$
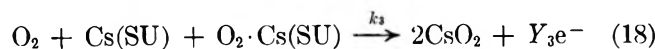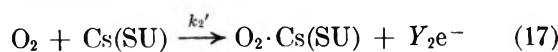
The steady-state condition is identical to that derived before, but for I one obtains the expression

$$I = aY_2 k_2' p Cs_0 (1 - \theta) +$$
$$[aY_3 k_3 k_2' p^2 Cs_0^2 (1 - \theta)^2]/$$
$$[k_4' + k_3 p Cs_0 (1 - \theta)] \quad (20)$$

The major difference, experimentally, between these mechanisms is that, whereas the former predicts that the initial emission when oxygen is admitted to the system will be zero (since initial intermediate concentration is zero), the latter predicts a nonzero initial emission to which would be added the second-order emission

as the concentration of intermediate increased. The first mechanism appears to be much more likely, inasmuch as careful attempts to observe initial emission upon first admission of oxygen to the system have met with negative results. Because the initial emission may be low, however, and because initial pressure control is difficult to attain, the second mechanism cannot be completely ruled out.

An Electron Paramagnetic Resonance Study of Hydrogen Atoms

Trapped in γ-Irradiated Calcium Phosphates

by Y. P. Virmani, John D. Zimbrick,* and E. J. Zeller

Departments of Chemistry, Radiation Biophysics, Geology, and Physics, University of Kansas, Lawrence, Kansas 66044
(Received August 6, 1970)

Publication costs borne completely by The Journal of Physical Chemistry

Epr studies were carried out on trapped H atoms in ⁶⁰Co γ-irradiated calcium phosphate powder at room temperature. The radiation yield of H atoms was relatively small [$G(H_T) \simeq 0.002$] and inversely related to the extent of hydration of the phosphate. The H atoms decayed slowly at room temperature with an initial half-time of 4 days. The epr characteristics of the H-atom doublet were very similar to those found for the same species in acidic ices except that the epr line width in phosphate was only 0.35 G compared with approximately 3.4 gauss in H_2SO_4 glassy ice at 77°K. Paramagnetic relaxation measurements *vs.* radiation dose were made on the H-atom epr lines. These data taken together with the thermal decay and dose saturation data indicated that the H atoms are produced initially in a nonuniform spatial distribution which gradually changes with dose and irradiation time to a spatially more uniform distribution.

I. Introduction

The γ radiolysis of certain calcium phosphate polycrystalline powders has been reported to yield trapped hydrogen atoms (H_T) which are comparatively stable at room temperature.[1,2] Only the g factors and splitting of the H_T have been given and these appear to be very close to the corresponding values for H_T in various rare gas matrices[3] and frozen acidic ices.[4] In the present work we have studied the radiation yields, epr

line widths, dose saturation, and paramagnetic relaxation characteristics of the H_T in several different prep-

(1) P. W. Atkins, N. Keen, M. C. R. Symons, and H. W. Wardale, *J. Chem. Soc.*, 5594 (1963).
(2) S. Ogawa and R. W. Fessenden, *J. Chem. Phys.*, 41, 1516 (1964).
(3) S. N. Foner, E. L. Cochran, V. A. Bowers, and C. K. Jen, *ibid.*, 32, 963 (1960).
(4) R. Livingston, H. Zeldes, and E. H. Taylor, *Discuss. Faraday Soc.*, 19, 166 (1955).
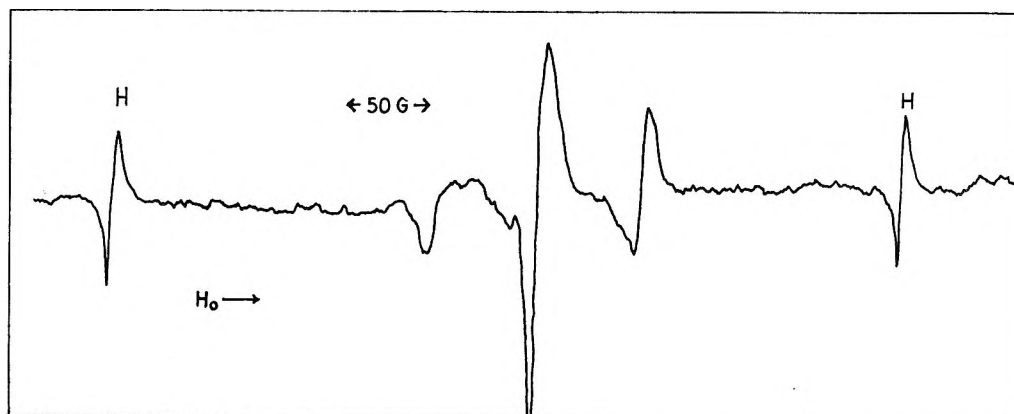
Figure 1. Epr spectrum of irradiated Matheson brand calcium phosphate at room temperature: ^{60}Co γ dose $= 1.84 \times 10^5$ rads; microwave power $= 4 \times 10^{-2}$ W; $H_m = 1.2$ G; $\nu_m = 100$ kHz.

arations of tribasic calcium phosphate $[Ca_{10}(PO_4)_6(OH)_2]$.

II. Experimental Section

Reagent grade tribasic calcium phosphate $[Ca_{10}(PO_4)_6(OH)_2]$ as polycrystalline powder was obtained from the following suppliers: Matheson, Fisher, Baker, and Mallinckrodt. These were used without further purification. The water of hydration was quoted as being the same from each supplier; however, we measured the concentration of water in each of the four brands by differential thermal analysis techniques. The results indicated that the phosphate supplied by Fisher, Baker, and Mallinckrodt had the same water content, within experimental error, but that the Matheson sample was lower than the others by about 20% (see Table III).

Samples were irradiated in Pyrex vials at ambient temperature in an Atomic Energy of Canada Model 200 ^{60}Co γ cell at a dose-rate of 10^5 rads/hr as calibrated by ferrous sulfate dosimetry.

Epr analysis was carried out on a Varian V-4502 spectrometer system, equipped with audio and 100-kHz modulation, and operated in the low power bridge configuration. The slow passage power saturation measurements were done with a modulation frequency of 200 Hz. Fast passage measurements all utilized a modulation frequency of 100 kHz. The modulation amplitude, H_m, in all experiments was set at a value of 0.15 gauss because of the unusually narrow line widths of the H_T doublet (ca. 0.35 gauss).

The microwave magnetic field, H_1, in the Varian TE_{102} single cavity was calculated from measurements of the microwave power entering the cavity by a formula recently developed by Bales and Kevan[5] and adjusted to our experimental conditions. Microwave power measurements were made with a Hewlett-Packard X-487B thermistor connected to a Microline 31A1 power meter and attached to the low-power sample cavity arm through a Hewlett-Packard precision attenuator.

G values for H_T production in the phosphate samples

(no. of H_T produced per 100 eV radiation energy absorbed) were obtained by comparison of the area of the doubly integrated H_T high-field line with that obtained from glassy 8.7 M H_2SO_4 ice at 77°K irradiated and analyzed in the same fashion and taking $G(H_T)$ in the acid ice as 1.66.[6]

III. Results and Discussion

A. *Epr Spectral Characteristics of Irradiated Calcium Phosphate.* The epr spectrum of Matheson calcium phosphate irradiated and analyzed at room temperature (^{60}Co γ dose $= 1.84 \times 10^5$ rads) appears in Figure 1. The doublet lines marked H split by 502 G are due to the H_T and closely resemble those attributed to H_T in irradiated acidic ices.[4] The width between points of maximum slope of the two lines, however, is only 0.35 G as contrasted with 3.4 G for H_T in 8.7 M H_2SO_4 and 4.3 G for H_T in 10.9 M H_3PO_4.[7] The average H_T line widths in the other three brands of phosphate are 0.38 G, which is slightly broader than the Matheson H_T value. The effects of radiation dose on the H_T line shape parameter and line width are given in Table I. The line shape parameter of any epr line determined by the derivative curve slope method[8] is 2.2 for an ideal Gaussian line and 4.0 for an ideal Lorentzian line. The value of this parameter for the H_T lines in the phosphate is 3.1 at 0.2 Mrads and increases to 3.7 at 7.3 Mrads, indicating that the lines at low doses are intermediate between Gaussian and Lorentzian and gradually approach the ideal Lorentzian shape at high doses. The line width does not vary significantly with radiation dose. However, as shown in Table II, the line width increases significantly with microwave magnetic field, H_1. The H_T lines saturate readily with increasing H_1; a representative slow passage progressive saturation curve is shown in Figure 2.

(5) B. L. Bales and L. Kevan, *J. Chem. Phys.*, **52**, 4644 (1970).

(6) R. Livingston and A. Weinberger, *ibid.*, **33**, 499 (1960).

(7) J. Zimbrick and L. Kevan, *ibid.*, **47**, 5000 (1967).

(8) R. A. Levy, *Phys. Rev.*, **102**, 31 (1956).
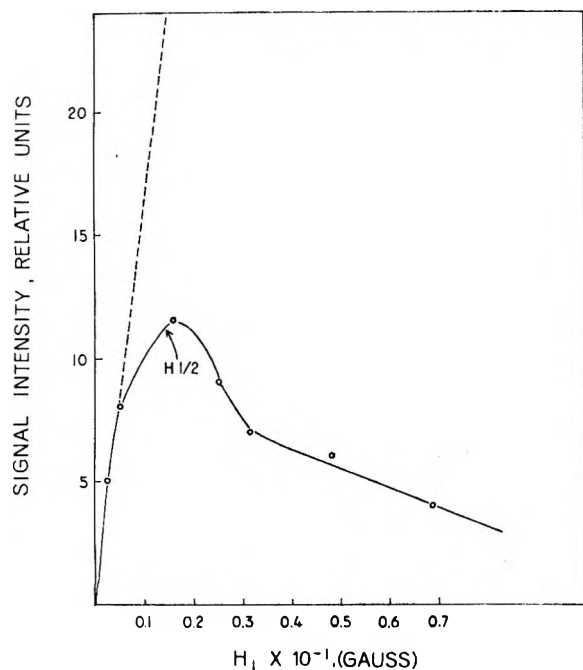
Figure 2. Slow passage power saturation of the H_T epr high-field line at room temperature: ^{60}Co γ-dose = 1.9 Mrads; H_m = 0.15 G; ν_m = 200 Hz.

Table I

^{60}Co γ dose, Mrads	Line shape parameter	ΔH_{ms}, G
0.2	3.1	0.35
0.4	3.4	0.35
0.6	3.6	0.35
1.2	3.5	0.35
2.4	3.5	0.35
4.4	3.8	0.35
7.3	3.7	0.35

Table II

ΔH_{ms}, G	H_1, G
0.35	5.24×10^{-3}
0.36	1.70×10^{-2}
0.51	7.41×10^{-2}
0.65	1.15×10^{-1}

After the onset of saturation the H_T signal intensity decreases sharply which is characteristic of epr lines broadened by significant homogeneous contributions. The line shape parameter and the broadening of the H_T lines with increasing H_1 also suggest that these lines are broadened homogeneously.

All of the above spectral characteristics of H_T in phosphate with the exception of the line widths agree closely with the corresponding characteristics of H_T in acidic

ices.[7] It would be expected that the width of the H_T lines in phosphate would be narrower than the H_T line widths in acidic ices because of at least two differences between these systems: (1) The yield of H_T in phosphate is much lower [$G(H_T)$ = 0.0032 in Matheson phosphate and 1.66 in 8.7 M H_2SO_4 glassy ice[6]] than in the concentrated acidic ice. Thus, even allowing for possible differences in spatial distribution of the H_T in the two systems, the average dipolar spin interaction between H_T is weaker and will make a smaller contribution to the observed line width in phosphate than in acidic ice. (2) The contribution to the observed line width due to unresolved hyperfine interaction between the H_T spins and surrounding protons is very probably smaller in the phosphate system than in the acidic ice system since there are much fewer protons present in phosphate than in the aqueous acidic ices. Some contribution from this type of interaction to the observed H_T line width must exist in the phosphate since the width is slightly greater in the Baker, Fisher, and Mallinckrodt brands which have about 20% more H_2O than in the Matheson brand.

The above data indicate that despite the basic differences between the powdered polycrystalline matrix of the phosphate and the glassy aqueous ice matrix, the H_T epr characteristics in the two matrices are very similar. This finding is consistent with two possible hypotheses: (1) the local environment surrounding H_T in phosphate is similar to that surrounding H_T in acidic ice; or (2) in these systems, the spectral characteristics presented above are insensitive to differences in the local environments of H_T. More studies are needed to obtain conclusive support for either of these hypotheses.

B. Radiation-Induced Yields of H_T. Using a ^{60}Co γ dose of 2 × 10^5 rads the initial yields of H_T in the four brands of calcium phosphate were determined as described in the Experimental Section; the G values are given in Table III. This table also shows the water content for each of the four brands of phosphate. The $G(H_T)$ in the phosphates is much lower than the G values found in other systems such as acidic[6] and oxyanion ices; in fact, the $G(H_T)$ in 8.7 M H_2SO_4 glassy ice (1.66) is 519 times as great as that found in Matheson phosphate (0.0032).

Table III

Supplier	$G(H_T)^a$	Water content, mg H_2O/g of solid[b]
Baker	0.0020	23.5
Fisher	0.0020	22.2
Mallinckrodt	0.0020	22.0
Matheson	0.0032	18.8

^{a} Experimental error, ±15%. ^{b} Experimental error, ±5%.
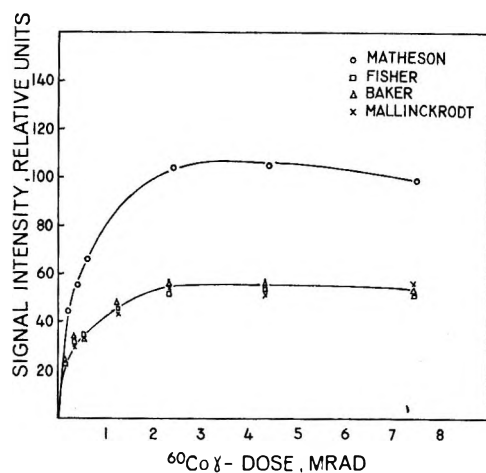
Figure 3. Relative number of H_T (represented by relative epr signal intensity) as a function of ^{60}Co γ-dose in various brands of calcium phosphate at room temperature. $H_m = 0.15$ G; $\nu_m = 100$ kHz.

Figure 4. Decay of H_T (represented by relative epr signal intensity) with storage time after irradiation at room temperature in various brands of calcium phosphate: $H_m = 0.15$ G; $\nu_m = 100$ kHz.

The $G(H_T)$ in Matheson phosphate is approximately 60% greater than that in the other three brands and contains nearly 20% less water than the others. These data indicate that an inverse correlation exists between the H_T yield and the amount of crystal hydration. The mechanism of formation of the H_T in phosphate is not known at the present time, but the presence of increasing amounts of water while necessary as a source of H· may also result in increased mobility of the H· and thus a decrease in $G(H_T)$.

C. *Radiation Dose Saturation and Decay of H_T at Room Temperature.* The number of H_T (as represented by the intensity of the high-field line of the H_T doublet) was measured as a function of ^{60}Co radiation dose in the four brands of phosphate; these data are presented graphically in Figure 3. The Matheson phosphate contains about 60% more H_T at each dose level than the other 3 brands; this result is expected because of its higher $G(H_T)$ discussed in the preceding section. However, all four brands begin to exhibit dose saturation at approximately 1.5–2.0 Mrads and the curves are very similar in shape.

Samples which had been irradiated with a ^{60}Co dose of 1.3 Mrads were analyzed for H_T signal intensity as a function of storage time after irradiation at room temperature. Figure 4 shows a graphical presentation of these data. The H_T decay relatively rapidly immediately after cessation of irradiation but the rate of decay decreases continuously with increasing time. The initial H_T half-life is about 4 days for all brands of phosphate. Atkins, *et al.*,[1] also stated that they observed slow decay of the H_T signal after irradiation in their phosphate samples. Since the H_T are not stable at room temperature there is some disappearance of this species during irradiation. Consequently, the dose at which the number of H_T begins to saturate will be dose rate dependent at low dose rates where irradiation
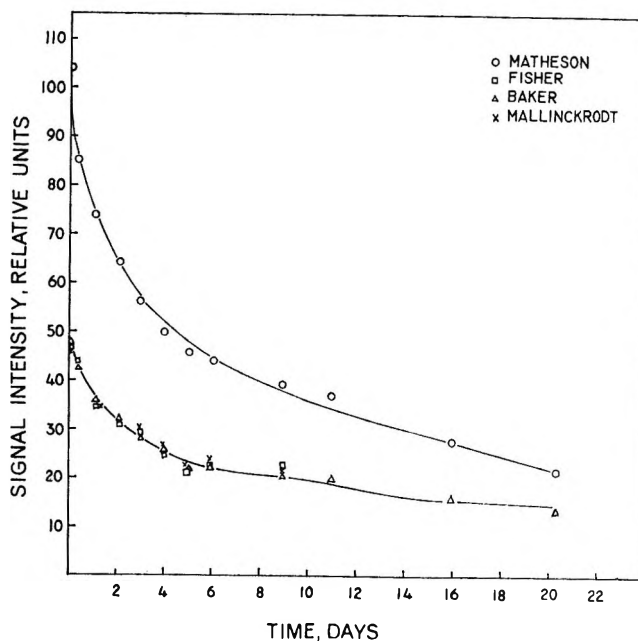
times that are appreciable fractions of the initial H_T half-times must be employed.

D. *Paramagnetic Relaxation Characteristics of the H_T Epr Doublet.* The high-field line of the H_T epr doublet was treated as a homogeneously broadened line, based on the spectral characteristics presented in part III, section A (line shape parameter, line broadening at high H_1, slope of slow passage saturation curve in Figure 2). From saturation curves the microwave power at which half-saturation occurs, $H_{1/2}$, was obtained. The characteristic relaxation time, $(T_1 T_2)^{1/2}$, was calculated from the measured $H_{1/2}$ values by Portis' theoretical treatment for ideal homogeneous line broadening.[7,9] T_1 is the spin–lattice relaxation time and T_2 is the spin-spin relaxation time. The Portis treatment should be applied only to $H_{1/2}$ measured under slow passage conditions; however, the relatively low H_T signal intensity made slow passage measurements very difficult because of spectrometer sensitivity limitations. Consequently, we obtained only one slow-passage saturation curve (that shown in Figure 2 using 200 Hz) and the rest of the saturation measurements were made using fast-passage conditions (100 kHz). A typical 100-kHz saturation curve is shown in Figure 5. A comparison of this figure with Figure 2 shows that the shapes of the slow- and fast-passage saturation curves are different. At the same dose level, the 200-Hz value of $H_{1/2}$ is 75% of the 100-kHz value, which compares well with the values of 77–89% obtained recently by Hase and Kevan,[10] for

(9) J. Zimbrick and L. Kevan, *J. Chem. Phys.*, **47**, 2364 (1967).

(10) H. Hase and L. Kevan, *ibid.*, **52**, 3183 (1970).
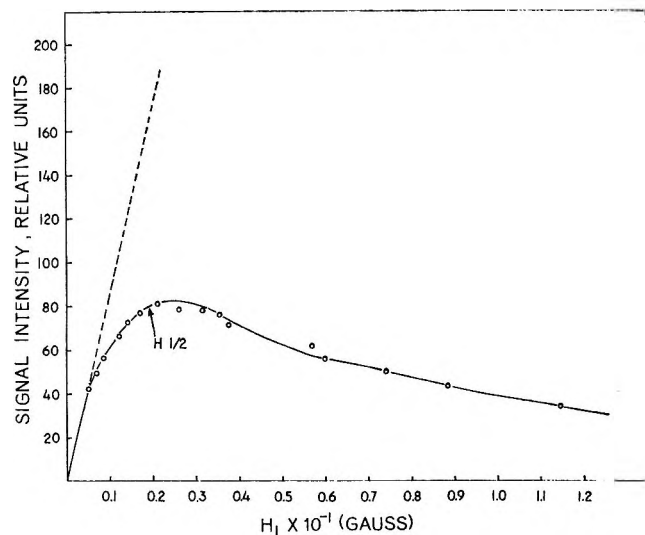
Figure 5. Fast passage power saturation of the H_T epr high-field line at room temperature: ^{60}Co γ dose = 2.4 Mrads; $H_m = 0.15$ G; $\nu_m = 100$ kHz.

Figure 6. Relaxation time $vs.$ ^{60}Co γ dose for the H_T epr high-field line in Matheson calcium phosphate at room temperature.

trapped electrons in $_1{}^3$H-irradiated alkaline ices but not with our value of 500% obtained recently for trapped electron centers in proton-irradiated diamonds.[11] Thus the statement by Hase and Kevan[10] that the "correction factor" for $H_{1/2}$ may have to be determined empirically for each spin system and set of experimental conditions appears to be applicable thus far.

If an epr line is not an ideal case of either homogeneous or inhomogeneous broadening, then the Portis treatment is not directly applicable to its power saturation curves. Such cases of intermediate line broadening have been treated by Castner;[12] his treatment, again assuming slow-passage conditions, considers inhomogeneously broadened lines to be made up of homogeneously broadened "spin packets" the widths of which are certain finite fractions of the overall observed line width. Castner's treatment was applied to our slow passage saturation curve shown in Figure 2. We obtain a value of 1.0 for the "a" parameter which indicates that the H_T doublet lines behave like ideally homogeneously broadened lines, insofar as power saturation characteristics are concerned. This result justifies the direct application of the Portis treatment to the power saturation curves obtained from the H_T epr lines.

We have measured the relaxation time product, $(T_1T_2)^{1/2}$, as a function of ^{60}Co radiation dose for the H_T epr lines. These data were obtained by application of the Portis treatment to our fast passage power saturation curves and are plotted in Figure 6. Similar measurements have been interpreted previously as being relevant to the spatial distribution of the trapped species and its change with radiation dose.[5,7,9,10] This interpretation depends only on relative values of $(T_1 \cdot T_2)^{1/2}$ within the same spin system rather than on absolute values, so that the application of Portis' treatment to our fast passage curves does not affect the
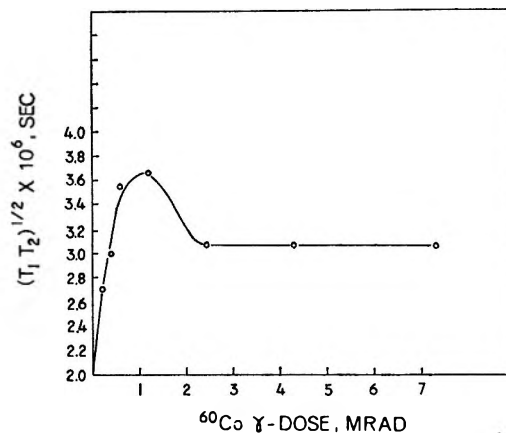
validity of the results. If $(T_1T_2)^{1/2}$ decreases with dose in a dose region in which the total number of spins is increasing, this has been shown to be due to a decrease in T_2, the spin–spin relaxation time,[13] caused by an increase in local concentration of spins. Such data are interpreted as indicating a spatially uniform trapped species.[7,9,10,13] In contrast, if $(T_1T_2)^{1/2}$ remains constant in a dose region of increasing total spins, then the local spin concentration is not changing and a nonuniform spatial distribution is indicated.[9] Figure 6 shows that $(T_1T_2)^{1/2}$ (and thus T_2) actually increases in the dose region 1–1.2 Mrads, then decreases sharply up to 2.4 Mrads, after which no further changes occur up to 7.3 Mrads, the highest dose studied. A comparison of the dose saturation data in Figure 3 with the $(T_1T_2)^{1/2}$ data indicates that the increases in $(T_1T_2)^{1/2}$ occur in the same dose region in which the total number of H_T is increasing with dose. Since epr line intensity is proportional to the total number of unpaired spins in a sample, whereas T_2 is dependent on the local concentration of spins (average distance between spins), our data suggest that the average distance between spins is increasing (local concentration of spins is $decreasing$) at the same time that the total number of spins in the sample is increasing. This behavior can be explained with the help of the data and discussion presented in part III, section C, which indicated that the H_T are not stable at room temperature and thus have some degree of mobility in the matrix. Figure 4 shows that significant decay of the H_T epr signal has occurred within a few hours after cessation of irradiation. This means that during irradiation the production of H_T is accompanied by a certain amount of H_T decay; the longer the irradiation time the more decay and the more opportunity for H · movement from its initial trapping site. Taken together these

(11) Y. P. Virmani, J. D. Zimbrick, and E. J. Zeller, unpublished work.

(12) T. G. Castner, $Phys. Rev.$, 115, 1506 (1959).

(13) H. Hase and L. Kevan, $J. Amer. Chem. Soc.$, 90, 6875 (1968).

data support the hypothesis that the H_T are produced initially with a nonuniform spatial distribution reflecting the nonuniform deposition of radiation energy but as they move slowly from their initial trapping sites the distribution gradually becomes more spatially uniform. The dose region from 0 to 1.2 Mrads in which $(T_1T_2)^{1/2}$ increases reflects the change from spatial nonuniformity to spatial uniformity. At doses between 1.2 and 2.5 Mrads (12–25 hr of irradiation) the total number of H_T is still increasing but by these times the spatial distribution is uniform so that $(T_1T_2)^{1/2}$ decreases sharply. At doses above 2.5 Mrads, there is no further increase in the number of H_T (Figure 3), their spatial distribution remains uniform, and no more change in $(T_1T_2)^{1/2}$ occurs. If this hypothesis is valid, it indicates that relaxation time data not only reflect steady-state spatial distribu-

tions but may also give useful insights into changes in these distributions with certain variables such as radiation dose and time.

A Comparison of the Reactivities of Dry and Mobile Electrons

by Harald B. Steen,* Olav Kaalhus,[1] and Magne Kongshaug[1]

Norsk Hydro's Institute for Cancer Research, Montebello, Oslo 3, Norway (*Received December 23, 1970*)

Publication costs assisted by the Norsk Hydro's Institute for Cancer Research

The scavenging efficiencies of various electron scavengers with regard to mobile electrons (e_m^-) have been determined from the yield of the X-ray-induced trapped electrons (e_t^-) in an ethylene glycol–water glass at 77°K, by measuring the rate of increase of the optical density of the glass at 585 nm during X-irradiation. The scavenger concentrations needed to halve $G(e_t^-)$ were found to be 0.047 M for H_2O_2, 0.035 M for $NaNO_3$, 0.020 M for CCl_3COOH, 0.26 M for $ClCH_2COOH$, and 0.41 M for HCl. $G(e_t^-)$ was not noticeably affected by the presence of 1 M NaCl, indicating that ionic strength was not important. The apparent reaction kinetics were not homogeneous. One reason for this seems to be the scavenging of the precursor of e_m^-, *i.e.*, the dry electrons (e^-). Comparing the scavenging efficiencies of e_m^- with those previously measured for e^- under similar conditions, we conclude that the reactivities of these entities are generally different.

Introduction

One of the basic assumptions in the new model for the radiolysis of aqueous solutions recently put forward by Hamill[2] is that electrons may react with solutes prior to hydration, that is, while they presumably are still moving with thermal—or higher—energies as unsolvated particles. According to this model these "dry electrons" (e^-) should generally react with molecules which are efficient scavengers of hydrated electrons (e_{aq}^-) with the important exception of hydrogen ions ($H_3O_{aq}^+$) towards which they should be essentially unreactive. This hypothesis has now been experimentally supported by Wolff, *et al.*,[3] who were able to perform pulse radiolysis of aqueous solutions with a time resolution of about 20 psec. They found that various electron scavengers reacted noticeably with the pre-

cursor of e_{aq}^-, *i.e.*, presumably with e^-, when present in concentrations above 0.1 M. In agreement with Hamill's hypothesis $H_3O_{aq}^+$ was found to be essentially unreactive. Additional experimental support has been reported by Steen,[4] who measured the yield of X-ray-induced phosphorescence of indole in ethylene glycol–water glass at 77°K as a function of the concentration of various electron scavengers, the reasoning being that approximately 90% of this phosphorescence appears to be due to geminate recombination between indole cat-

(1) Fellow of the Norwegian Cancer Society.

(2) (a) W. H. Hamill, *J. Chem. Phys.*, **49**, 2446 (1968); (b) W. H. Hamill, *J. Phys. Chem.*, **73**, 1341 (1969).

(3) R. K. Wolff, M. J. Bronskill, and J. W. Hunt, *J. Chem. Phys.*, **53**, 4211 (1970).

(4) H. B. Steen, *J. Phys. Chem.*, **74**, 4059 (1970).

ions and e^-.[5] The scavenging efficiencies of the various scavengers with regard to e^- obtained in this way are in good agreement with those found by Wolff, *et al.*, when compared on a relative scale.

The question arises whether these "dry electrons" are the same, *i.e.*, with respect to reactivity, as the "mobile electrons" (e_m^-) previously observed in various glassy solutions by several authors.[6-8] Hamill[2b] suggests that this is indeed the case. Kevan[7] concludes that, with the exception of hydrogen ions which have a very low reactivity with e_m^-, the reactivities of e_m^- with various electron scavengers are approximately proportional to those known for e_{aq}^- in water at room temperature. On the other hand, the scavenging efficiencies for e^- obtained by Wolff, *et al.*,[3] and by Steen[4] are definitely not proportional to those of e_{aq}^-. However, it cannot be ruled out that this apparent difference between e_m^- and e^- is due to the fact that the scavenging efficiencies have been measured in different solvents and under quite different conditions.

In the present work, therefore, we have determined the scavenging efficiencies with regard to e_m^- for various electron scavengers in the same solvent and under the same conditions as those previously employed[4] in the measurement of the scavenging efficiencies for e^-. The scavenging efficiencies for e_m^- have been determined by measuring the yield of X-ray-induced trapped electrons (e_t^-), observed by their optical absorption, as a function of the scavenger concentration. Thus, what we have observed is the competition between, on one hand, the reaction of e_m^- with the scavenger, and, on the other hand, the trapping of e_m^- and all other processes by which e_m^- can disappear, *e.g.*, recombination and reaction with the solvent. Assuming, in accordance with the results of the present work, that the rates of these latter reactions are not significantly affected by the scavenger, we conclude that the reactivities of e_m^- with various solutes are not proportional to those of e^-. It must be emphasized, however, that e^- and e_m^- are by no means well-defined entities. Rather, they should be considered as representing average properties associated with different parts of the electron degradation spectrum.

Experimental Section

Apparatus. The apparatus, by which the optical density of the samples can be measured during X irradiation, is shown in Figure 1. Six sample holders, 1 mm deep and 8 mm in diameter, are clamped onto a circular Cu disk 41 mm in diameter. The sample holders are made either of 0.05-mm Al foil, the glossy side turned up, or of "Perspex" gilded by vacuum deposition. The Cu disk is thermally connected to a reservoir of liquid N_2 by a Cu tube and is thermally isolated from the warm parts of the apparatus by two concentric German silver tubes which reach into the coolant. A heating element is located immediately below the Cu disk, and
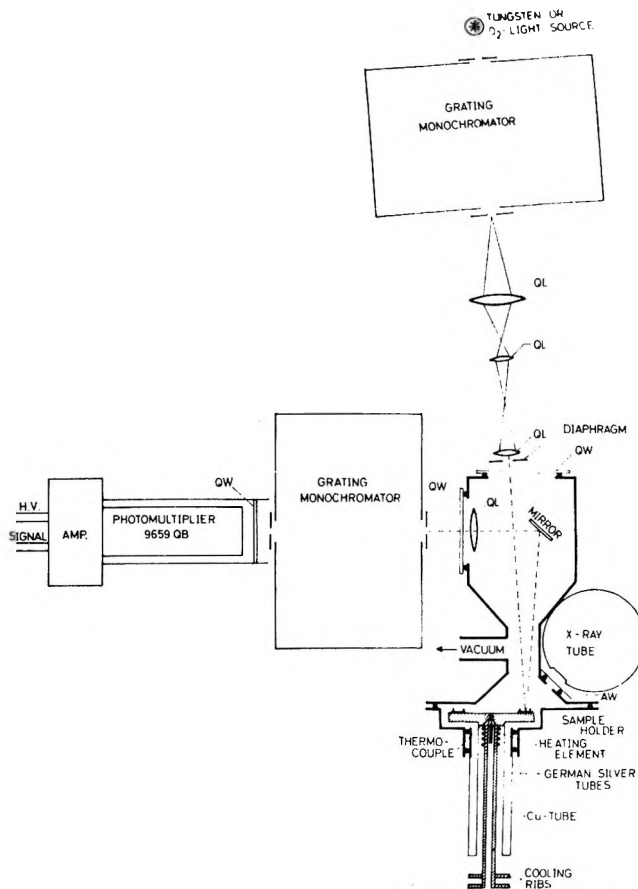
Figure 1. The apparatus used to study the optical absorption of glassy samples during irradiation with X-rays.

the temperature of the disk, which is monitored by a thermocouple, can be kept constant to within $\pm 0.5°$ anywhere between 77 and 300°K by feeding the thermocouple signal to a regulated power supply. The Cu disk is situated in a vacuum tight housing which has two ports with quartz windows (QW) for the analyzing light beam, one port (not shown) for visual inspection of the samples, and one port with a 0.1-mm Al window (AW) for the X-ray beam. The Cu disk can be rotated while under full vacuum and low temperature to irradiate and analyze one sample at a time.

A narrow monochromatic beam of analyzing light is provided by a tungsten lamp fitted to a grating monochromator (Jarrell-Ash 0.25-m Ebert type) and a set of quartz lenses (QL). The light beam, about 1 mm wide, is reflected from the bottom of the sample holder and is focused onto the entrance slit of a second monochromator (same type) which has an EMI 9659 QB photomultiplier tube at the exit. The slits of the first monochromator are set to transmit a fairly large part, *i.e.*,

(5) H. B. Steen, *Radiat. Res.*, **41**, 268 (1970).

(6) K. Eiben and D. Schulte-Frohlinde, *Z. Phys. Chem. (Frankfurt am Main)*, **45**, 20 (1965).

(7) L. Kevan in "Radiation Chemistry of Aqueous Systems," G. Stein, Ed., Interscience, Wiley, New York, N. Y., 1968, pp 21–71.

(8) H. Hase and L. Kevan, *J. Phys. Chem.*, **74**, 3358 (1970).

10 nm, of the spectrum, while the second one, which is operated at the same wavelength, is used with narrow slits corresponding to a resolution of about 1 nm. Hence, when the two monochromators scan the spectrum synchronously, slight variations in scanning speed will not affect the intensity measured at the exit of the second monochromator.

Absorption spectra of irradiated samples are obtained by comparing the transmission spectra obtained before and after irradiation.

By replacing the plane mirror shown in Figure 1 by a larger concave one, X-ray-induced fluorescence and phosphorescence can be studied.[9]

The X-ray source is a Siemens Kristalloflex 2 with a AGW 61 X-ray tube which is operated at 50 kV.

Materials. NaNO₃, H₂O₂, CCl₃COOH, ClCH₂-COOH, and HCl were all p.a. reagents from Merck. The solvent was a mixture, 1:1 by volume, of ethylene glycol, which was "chromatoquality" from Matheson Coleman and Bell, and water which was triply distilled. All reagents were used without further purification.

Experimental Procedure. The sample holders were filled with 50 μl of sample solution which was degassed by controlled evacuation of the housing during cooling to 77°K. At this temperature the samples appeared as completely transparent glasses with no cracks or bubbles. During experiment the housing was kept at a pressure of about 3×10^{-6} Torr.

The samples were irradiated, one at a time, with a constant dose rate of about 80 krads/min and the transmission of the samples at 585 nm (which is at the absorption peak of trapped electrons under the present conditions) was recorded during irradiation. The results were corrected for the light reflected from the upper surface of the sample ($\sim$5%). It was checked that the analyzing light beam caused no bleaching of the X-ray-induced absorption.

Results and Discussion

For all the samples the optical density increased linearly with the exposure time for the first 2-3 min of the irradiation. No alteration of the shape of the absorption spectrum between 400 and 800 nm could be observed with these doses. However, for larger doses the absorption spectra of the samples containing significant concentrations of scavenger became somewhat distorted and the optical density at 585 nm no longer increased linearly with dose. Because of this the yields given below are those measured at "zero dose."

The deviation from a linear relationship between optical density and dose generally increased with increasing concentration of scavenger. Furthermore, it appeared to be more pronounced for those scavengers which reduce the yield of e_t^- most efficiently. The dose effects will be described in more detail in a subsequent paper.

In the present system the trapping sites, the solute
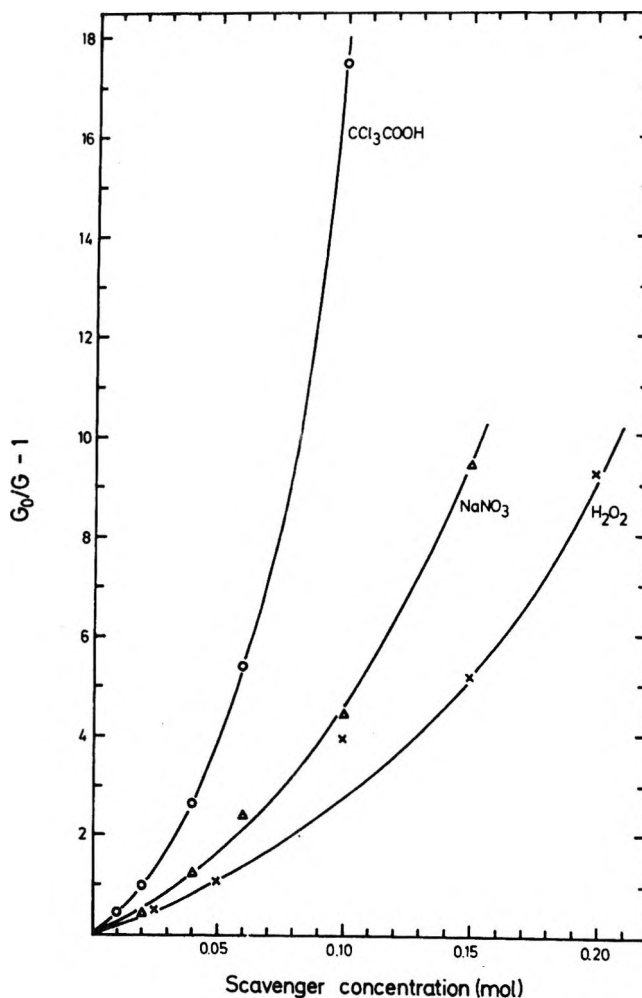
Figure 2. The yield of e_t^-, $G(e_t^-)$, in ethylene glycol–water glass with CCl₃COOH, NaNO₃, and H₂O₂, as measured by the rate of increase of the optical density at 585 nm during X-irradiation, plotted according to eq 1.

molecules, and the positive holes are supposedly fixed in the medium. If it is assumed that the probabilities that e_m^- will react with either of these species are proportional to their respective concentrations, the yield of e_t^-, $G(e_t^-)$, is given by eq 1

$$G_0(e_t^-)/G(e_t^-) = 1 + k_S[S]/(k_R + k_T[T]) \quad (1)$$

where $G_0(e_t^-)$ is the yield of e_t^- with no scavenger present. k_S and k_T may be considered as the rate constants for the reaction of e_m^- with the solute, S, and the trapping sites, T, respectively, and k_R is the probability per second that e_m^- will disappear by any other process, *e.g.*, recombination or reaction with solute. Hence, if [T] as well as k_T and k_R are independent of [S], eq 1 is formally identical with that describing homogeneous reaction kinetics.

In Figures 2 and 3 $G(e_t^-)$, as measured by the optical density at 585 nm, has been plotted according to eq 1 for the various scavengers studied. It should be noted

(9) H. B. Steen, *Photochem. Photobiol.*, **6**, 805 (1967).
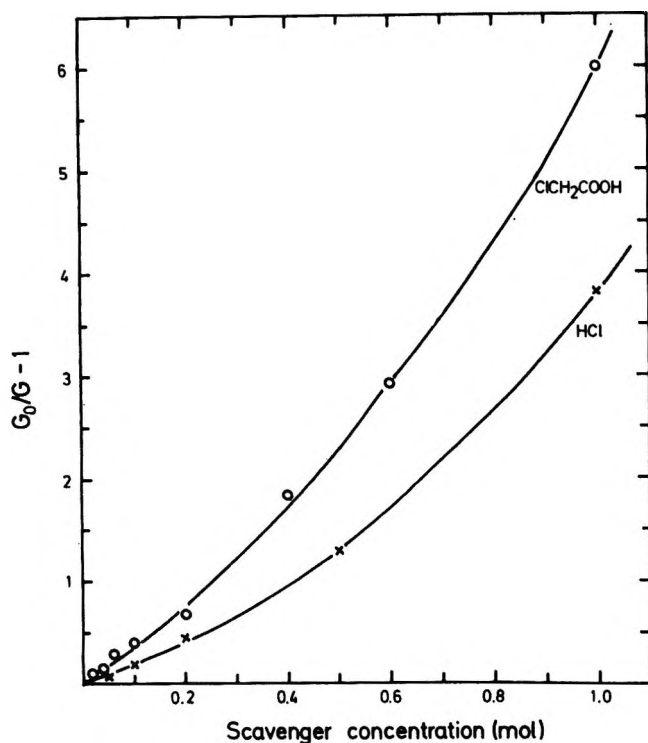
Figure 3. The yield of e_t^-, $G(e_t^-)$, in ethylene glycol–water glass with $ClCH_2COOH$ and HCl, as measured by the rate of increase of the optical density at 585 nm during X-irradiation, plotted according to eq 1.

that the pK of $ClCH_2COOH$ and CCl_3COOH, as measured in the present solvent at room temperature, implies that, with the concentrations used here, the former acid is essentially undissociated while the latter one is practically fully dissociated. Hence, assuming the pK to be roughly the same at 77°K, the results given for CCl_3COOH are those of the corresponding anion. These results have not been corrected for the small effect ($\sim 2\%$) due to H^+. The scavenging effect of HCl can be attributed entirely to H^+ since the effect of $NaCl$ (1 M) was found to be negligible.

It appears from Figures 2 and 3 that in no case are the reaction kinetics described by eq 1 obeyed. Hence, at least one of the assumptions on which eq 1 is based does not hold true. Curves similar to those in Figures 2 and 3 were obtained by Hase and Kevan,[8] who measured, by means of esr spectroscopy, the yield of e_t^- in γ- and uv-irradiated alkaline glasses containing acrylamide as a scavenger. These workers suggest that the deviation from so-called homogeneous kinetics observed at high scavenger concentrations is due to a reduction of the concentration of available trapping sites caused by the presence of the scavenger molecules, i.e., they suggest that [T] decreases when [S] increases. However, even if we make the rather extreme assumption that, to a first approximation, the concentration of trapping sites, [T], is related to the scavenger concentration, [S], by

$$[T] = [T_0] \exp(-\text{constant} \cdot [S]) \qquad (2)$$

we find that this explanation alone is not sufficient to account for the observed deviation from eq 1. On the other hand, from our previous experiments[4] we know that at least one other reaction will contribute to the curvature of the curves in Figures 2 and 3, namely the scavenging of e^- which is, supposedly, the precursor of e_m^-. A preliminary analysis of the present results indicates that if it is assumed that both the scavenging of e^- and the scavenging of trapping sites as described by eq 2 are effective, the apparent deviation from eq 1 observed in the present work can be qualitatively accounted for. However, more data are needed to decide whether this conclusion can be adequately supported on a quantitative basis.

The concentrations of the various scavengers needed to halve the yield of e_t^-, $[S]_{1/2}$, are given in Table I. Since the lifetime of e_m^- as well as its reaction kinetics under the present conditions are not known, absolute reaction rates cannot be determined. The scavenging efficiencies, defined as $K = [S]_{1/2}^{-1}$, are also shown in Table I. As noted above, the results depicted in Figures 2 and 3 include also the effect of e^- scavenging. Hence, the scavenging efficiencies obtained from these curves do not apply directly to the reaction of e_m^- with scavenger unless the effect of e^- scavenging is corrected for. This effect can be calculated provided the scavenging efficiencies for e^- are known. Thus, the scavenging efficiency relating only to e_m^-, K_m, can be found from eq 3

$$K_m = \frac{K_{e+m}(K_{e+m} - K_e)}{K_{e+m} + K_e} \qquad (3)$$

where K_{e+m} is the scavenging efficiency obtained from Figures 2 and 3 and K_e is that of the scavenging of e^-. Equation 3 is derived assuming that e^- and e_m^- both react with the solute according to eq 1. Although this does not seem to be true for e_m^-, it is a good approximation if applied only to that part of the curves in Figures 2 and 3 for which $G_0/G \leq 2$ as is the case here. The values of K_e obtained previously are reproduced in Table I. The values of K_m calculated by eq 1 from these data and those of the present experiments are given in the same table. It can be seen that, except for the case of $ClCH_2COOH$, the correction for the scavenging of e^- is small. However, it must be noted that the values of K_e given in Table I apply only to that fraction of e^- which, in the absence of any scavenger, recombines spontaneously. The scavenging efficiencies of that fraction of e^- which escapes recombination and which is the precursor of e_m^- are not necessarily the same mainly because the mean lifetime as well as the average energy of the two parts of the e^- population may be different. On the other hand, the results obtained for $ClCH_2COOH$ demonstrate that the true corrections for the scavenging of e^- can hardly be very much larger than those calculated here. Thus, the corrected scavenging efficiencies, i.e., K_m, have been

Table I[a]

Scavenger	$[S]_{1/2}$, M, $e_m^- + e^-$	K, M⁻¹ $e_m^- + e$	K, M⁻¹ e_m^-	K, M⁻¹ e^{-b}	K, rel units $e_m^- + e^-$	K, rel units e_m^-	K, rel units e^{-b}	K, rel units e_{aq}^{-c}
H_2O_2	0.047	21	18	1.7	1.0	1.0	1.0	1.0
$ClCH_2COOH$	0.26	3.8	1.6	1.5	0.18	0.09	0.9	0.5
CCl_3COOH	0.020	50	38	6.5	2.4	2.1	3.8	0.7
$NaNO_3$	0.035	29	19	5.5	1.3	1.1	3.2	0.9
HCl	0.41	2.4	2.4	<0.17	0.11	0.13	<0.1	1.9

[a] $[S]_{1/2}$ are the scavenger concentrations needed to halve the yield of the various species, while $K = [S]_{1/2}^{-1}$ is given as a measure of relative reactivity. $e_m^- + e^-$ indicates the values obtained experimentally in the present work, and e_m^- indicates these values corrected for the scavenging of e^- as measured previously. The numbers in the last four columns have been normalized to give identical values for H_2O_2. [b] Reference 4. [c] M. Anbar and P. Neta, *Int. J. Appl. Radiat. Isotopes*, **18**, 493 (1967).

given primarily to show the relative magnitude of the effect of the scavenging of e^- for the various scavengers.

Kevan[7] concludes that, with the exception of H^+, the reactivities of e_m^- with various electron scavengers in ices containing large concentrations of $H_2PO_4^-$ or HSO_4^- at 77°K are quite similar to those known for e_{aq}^- in aqueous solutions at room temperature.[10] According to the data in Table I, this is not fully borne out by the present results. However, the differences found between relative reactivities of e_m^- and e_{aq}^- are hardly conclusive since the reactivities of e_{solv}^- in the present solvent may be significantly different from those in water.

Mostly based on the observation of electron reactions in strongly acidic glasses, it is commonly assumed that e_m^- is essentially unreactive with H^+. Thus, Brown and Dainton[11] observed that a variety of metal ions in concentrations of about 0.01 M react very efficiently with electrons in 5.4 M H_2SO_4 at 77°K. These authors propose that the lack of effect of the H^+ from H_2SO_4 is due to a polymerization of this acid at low temperatures. Several workers[7,12,13] have measured the yield of trapped H atoms (H_t) in ices containing 5 M of H_2SO_4, H_3PO_4, or $HClO_4$. Kevan[7] concludes that these H atoms are formed not by the reaction between e_m^- and H^+, but by the reaction between e_m^- and the acid anions.

In view of this it is interesting to note that, although the presently measured scavenging efficiency of H^+ towards e_m^- is low in comparison with that of other efficient electron scavengers, such as CCl_3COO^- and NO_3^-, it is still noticeable, i.e., it is approximately one order of magnitude smaller than that of NO_3^-. Thus, assuming $G(e_t^-) = 2^{14}$ in the absence of scavenger, the present results (Figure 3) imply that $G(e_t^-) = 0.4$ with 1 M H^+ and probably considerably below 0.1 with 5 M H^+, if such a concentration of H^+ is at all possible under these conditions. Hence, this result does not seem to be in accordance with Kevan's conclusion that the reaction between e_m^- and H^+ in 5 M acid at 77°K is negligible. However, it cannot be ruled out that this

discrepancy is due to the fact that different solvents have been employed.

Comparing the scavenging efficiencies for e_m^- obtained in this work with those previously found for e^- under the same conditions, it clearly appears that they are not the same. Thus, for all the scavengers the scavenging efficiency for e_m^- is considerably larger than that found for e^-. Taking into account that the mobility of e^- is probably larger than that of e_m^- and assuming that the fastest reactions observed here are approximately diffusion controlled, this result indicates that the lifetime of e_m^- is at least one order of magnitude larger than that of e^-. However, these differences in lifetime and mobility cannot fully explain the different reactivities of e_m^- and e^-. Thus, when compared on a relative scale they are still significantly different as demonstrated in Table I. It should be noted also that the correction of the scavenging efficiencies for e_m^- for the scavenging of e^- tends to enhance this difference.

The use of strongly alkaline and acidic glasses has shown that the ionic strength may alter the structure of the medium and thereby affect various radiolytic processes such as the trapping of H atoms and electrons. It is important, therefore, to keep in mind that the reaction of e^- and e_m^- with the various scavengers occurs in competition with the formation of e_m^- and e_t^-, respectively, as well as with other processes such as recombination and reactions with the solvent. Consequently, K_e and K_m are proportional to the rate constants for the reactions of e^- and e_m^- with the scavengers only provided the rates of the competing processes are not influenced by the presence of the scavengers. It must be stressed, therefore, that a comparison be-

(10) M. Anbar and P. Neta, *Int. J. Appl. Radiat. Isotopes*, **18**, 493 (1967).

(11) D. M. Brown and F. S. Dainton, *Trans. Faraday Soc.*, **62**, 1139 (1966).

(12) T. Henriksen, *Radiat. Res.*, **23**, 63 (1964).

(13) B. G. Ersov and A. K. Pikaev, *Dokl. Phys. Chem.*, **169**, 481 (1966).

(14) T. Higashimura, M. Noda, T. Warashina, and H. Yoshida, *J. Chem. Phys.*, **53**, 1152 (1970).

tween the scavenging efficiencies for $c_m{}^-$ and those for other entities, such as e^- and $c_{aq}{}^-$, has relevance for the corresponding rate constants only to the extent that this condition is fulfilled. In view of this, K_m was determined for $NaNO_3$ and CCl_3COOH also in the presence of 1 M NaCl. The results thus obtained were similar (within 10%) to those given in Table I, indicating that the ionic strength is not important in the present experiments. Hence, it seems reasonable to consider the values of K_m and K_c given in Table I as relative values of the rate constants for the reactions of $e_m{}^-$ and e^- with the various scavengers.

We conclude that $e_m{}^-$ and e^- behave as different entities with regard to reactivity. Nevertheless, the physical difference between them is not known, although it is likely to be associated with the energy of the

electron and with its interaction with the medium. Since e^- is supposedly the precursor of $e_m{}^-$, which in turn precedes $c_t{}^-$, it seems probable that the energy decreases and that the degree of interaction with the medium increases in the same order. Thus, it is conceivable that there is no sharp distinction between these states of the electron, but rather that the transitions between them are continuous. This implies that the energies of e^- and $e_m{}^-$ are confined only within certain limits rather than having discrete values. Consequently, the reactivities measured for these entities should be considered as averages over the corresponding degradation spectra. At the present time our knowledge about these matters is not sufficient to estimate with any accuracy the ranges of energy associated with e^- and $e_m{}^-$.

Vibrational Spectra and Structure of Biacetyl

by J. R. Durig,* S. E. Hannum, and S. C. Brown

Department of Chemistry, University of South Carolina, Columbia, South Carolina 29208   (*Received January 7, 1971*)

The infrared spectra of biacetyl $[CH_3CO]_2$ and biacetyl-d_6 $[CD_3CO]_2$ have been recorded over the range 33 to 4000 cm^{-1} for the samples in the gaseous, liquid, and polycrystalline states. The Raman spectra of the liquid and polycrystalline solids have also been observed, and quantitative depolarization ratios have been measured. The vibrational spectra of the crystalline materials have been interpreted on the basis of C_{2h} molecular symmetry and the values observed for the fundamentals are compared with those previously reported for the fluid states. A comparison of the infrared and Raman bands in the crystal shows that the mutual-exclusion principle is operative. It is concluded from this alternate forbiddance that the molecule has a centrosymmetric structure in the crystal and that each molecule occupies a $C_i(\bar{1})$ site. The factor group of the crystal is believed to be either $C_{2h}(2/m)$ or $C_{2h}(mmm)$ with two or four molecules per primitive unit cell. No evidence could be found for the existence of the cis isomer in the fluid states. Possible reasons for its absence are discussed. The infrared active methyl torsion was observed at 217 and 157 cm^{-1} for the "light" and "heavy" molecules in the solid state, respectively, and the barriers to internal rotation were calculated to be 3.1 kcal/mol. Barriers of 2.7 and 2.8 kcal/mol were calculated from rather broad bands in the spectra of gaseous $[CH_3CO]_2$ and $[CD_3CO]_2$, respectively. The barrier values are compared to those obtained for other acetyl compounds.

Introduction

We have recently recorded the vibrational spectra of several molecules of chemical formula $[COX]_2$, where X = F, Cl, Br, and H, and determined their molecular symmetries in the solid and fluid states.[1-4] For the halogen containing molecules, the spectra for the fluid states showed the presence of two geometric isomers and the data have been shown to be consistent for that expected for the cis and trans isomers. In these studies it has been shown that structural conclusions can be correctly made only if the infrared and Raman spectra

are obtained for these compounds in at least two different physical states with one of them being the solid. Closely related to these studies is our investigation of the infrared and Raman spectra of 2,3-butanedione which is commonly called biacetyl.

(1) J. R. Durig and S. E. Hannum, *J. Chem. Phys.*, **52**, 6089 (1970).

(2) J. R. Durig, S. E. Hannum, and F. G. Baglin, *ibid.*, **54**, 2367 (1971).

(3) J. R. Durig, S. C. Brown, and S. E. Hannum, *ibid.*, in press.

(4) J. R. Durig and S. E. Hannum, *J. Cryst. Mol. Struct.*, **1**, 131 (1971).

There have been several previous vibrational studies[5-8] of biacetyl with the more recent one by Noack and Jones[7] being the most complete. However, there are some inconsistencies in the work of Noack and Jones which cannot be readily explained. For example, they have assigned the Raman lines at 240 and 538 cm^{-1} to out-of-plane bending modes of b_g symmetry, whereas there should be only *one* mode of such symmetry unless one gives the methyl torsional mode such a description. However 240 cm^{-1} is too high a frequency for the methyl torsional mode for this type of molecule. Noack and Jones[7] as well as Harris and Witkowski[8] have assigned the strong Raman line at 685 cm^{-1} as the skeletal bending mode of a_g symmetry but such an assignment leaves no reasonable explanation for the Raman line at 614 cm^{-1} which had previously been assigned to this mode by Sidman and McClure.[6] In essence the assignment of the 685-cm^{-1} Raman line to the skeletal bending mode results in too many Raman lines in the skeletal bending region to be assigned to the fundamentals of the biacetyl molecule for only the trans form. Also the C–CH$_3$ symmetrical stretching mode was not assigned by Noack and Jones; yet it should be one of the most intense Raman lines. Sidman and McClure assigned the 1004-cm^{-1} Raman line to the C–CH$_3$ stretching mode but Noack and Jones have suggested that this band is the central C–C stretching vibration. Thus, there are still several uncertainties in the vibrational assignment for biacetyl and it was hoped that an investigation of the infrared and Raman spectra of solid biacetyl would clear up these discrepancies. No vibrational studies have previously been reported for the solid.

It was hoped that a vibrational study of the solid would provide the necessary data to determine the symmetry in the solid as well as the crystal site occupied by the molecules. In addition, factor group splitting could be investigated and it was hoped that the frequencies for the methyl torsional modes might be determined. The frequency for the skeletal C–C torsional mode was also of particular interest since it had been previously reported to be at 35 cm^{-1} from a study of the electronic spectrum of the solid[9] although Fateley, et al.,[10] have reported a frequency of 48 cm^{-1} for this normal mode in the vapor state. Noack and Jones had suggested a trans, C_{2h}, structure for the molecule in the liquid although they pointed out that such a structure was contrary to the dipole moment reported by Bloom and Sutton[11] for this molecule in both the gas and liquid states. Therefore, a reinvestigation of both the liquid and gas was carried out to obtain data for comparison with the solid phase studies.

Experimental Section

The 2,3-butanedione sample was obtained from the Aldrich Chemical Co. It was degassed and stored over drying agent. The 2,3-butanedione-d_6 sample was made by deuterium exchange. Biacetyl (15 ml) was refluxed for 48 hr with 35 ml of D$_2$O made approximately 0.5 N with D$_2$SO$_4$. The biacetyl was distilled out of the solution and dried. After four such exchanges the nmr spectra showed no indication of hydrogen atoms.

Vapor phase and solid phase infrared spectra between 4000 and 200 cm^{-1} were recorded on a Perkin-Elmer Model 621 spectrophotometer and between 500 and 33 cm^{-1} on a Beckman IR-11 spectrophotometer. Both instruments were purged with dry air and calibrated with standard gases.[12,13] For studies of the vapor phases, 20-cm cells with cesium iodide windows were used in the mid-infrared, whereas a Beckman 10-m variable path cell with polyethylene windows was used for recording the far-infrared spectra. The spectra of the solids were obtained by condensing the vapor onto a cesium iodide or silicon window cooled with boiling nitrogen. The infrared spectrum of the liquid was obtained as a capillary film between cesium iodide plates. The infrared spectra of biacetyl and biacetyl-d_6 in the solid and gaseous phases are presented in Figure 1.

The Raman spectra were recorded on a Cary Model 81 spectrophotometer equipped with a Spectra Physics Model 125 helium–neon laser. The instrument was calibrated with emission lines from a neon lamp over the spectral range 0–4000 cm^{-1}. The Raman spectra of the solids were obtained by use of a low-temperature cell similar to that described by Carlson.[14] Quantitative depolarization measurements were made on a Spex Ramalog using 6471-Å Kr excitation from a mixed-gas laser. The Raman spectra of the liquids were obtained by means of small samples sealed in glass capillaries. The Raman spectra of biacetyl and biacetyl-d_6 in the solid and liquid phases are presented in Figure 2. The frequencies for the bands observed in the infrared and Raman spectra of biacetyl are listed in Table I and those of biacetyl-d_6 in Table II. The observed frequencies are believed to be accurate to ±1 cm^{-1} for all sharp bands.

Results and Discussion

No X-ray data are available for solid biacetyl. However, it is expected that the molecule will have the

(5) T. Miyazawa, *J. Chem. Soc. Jap.*, **74**, 743 (1953).

(6) J. W. Sidman and D. S. McClure, *J. Amer. Chem. Soc.*, **77**, 6471 (1955).

(7) K. Noack and R. N. Jones, *Z. Elektrochem.*, **64**, 707 (1960).

(8) R. K. Harris and R. E. Witkowski, *Spectrochim. Acta*, **20**, 1654 (1964).

(9) J. W. Sidman and D. S. McClure, *J. Amer. Chem. Soc.*, **77**, 6461 (1955).

(10) W. G. Fateley, R. K. Harris, F. A. Miller, and R. E. Witkowski, *Spectrochim. Acta*, **21**, 231 (1965).

(11) G. I. M. Bloom and L. E. Sutton, *J. Chem. Soc.*, 727 (1941).

(12) IUPAC, "Tables of Wavenumbers for the Calibration of Infrared Spectrometers," Butterworth, Washington, D. C., 1961.

(13) R. T. Hall and J. M. Dowling, *J. Chem. Phys.*, **47**, 2454 (1967).

(14) G. L. Carlson, *Spectrochim. Acta, Part A*, **24**, 1519 (1968).
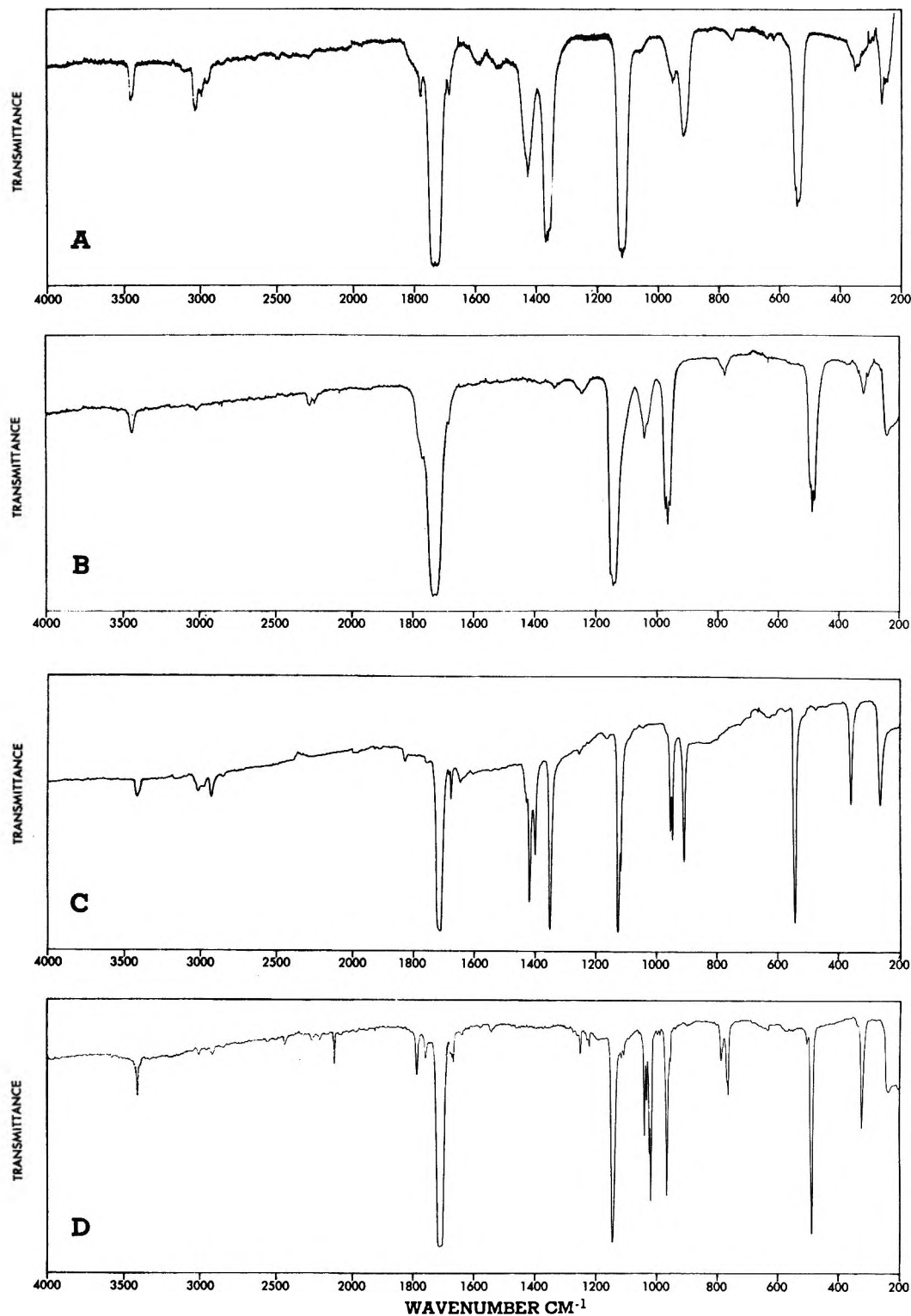
Figure 1.   Infrared spectra of biacetyl: A, gaseous biacetyl; B, gaseous biacetyl-d_6; C, solid biacetyl; D, solid biacetyl-d_6.

trans configuration in the solid. Studies of similar molecules[1-4] have shown that a center of symmetry is maintained at the site in the unit cell; thus, the rule of mutual exclusion is expected to hold in the solid and one should be able to easily determine the configuration from the spectral data.   Several of the infrared bands appear to be split by either the static or the correlation

field. However, the magnitude of this splitting is in general small compared with the separation of the fundamental vibrations so there is little difficulty in determining the frequency limits of each band.   The bands in the solid phase are quite sharp and it is possible to separate fundamentals that are badly overlapped in the gas and liquid phases.   Thus, it is possible to make
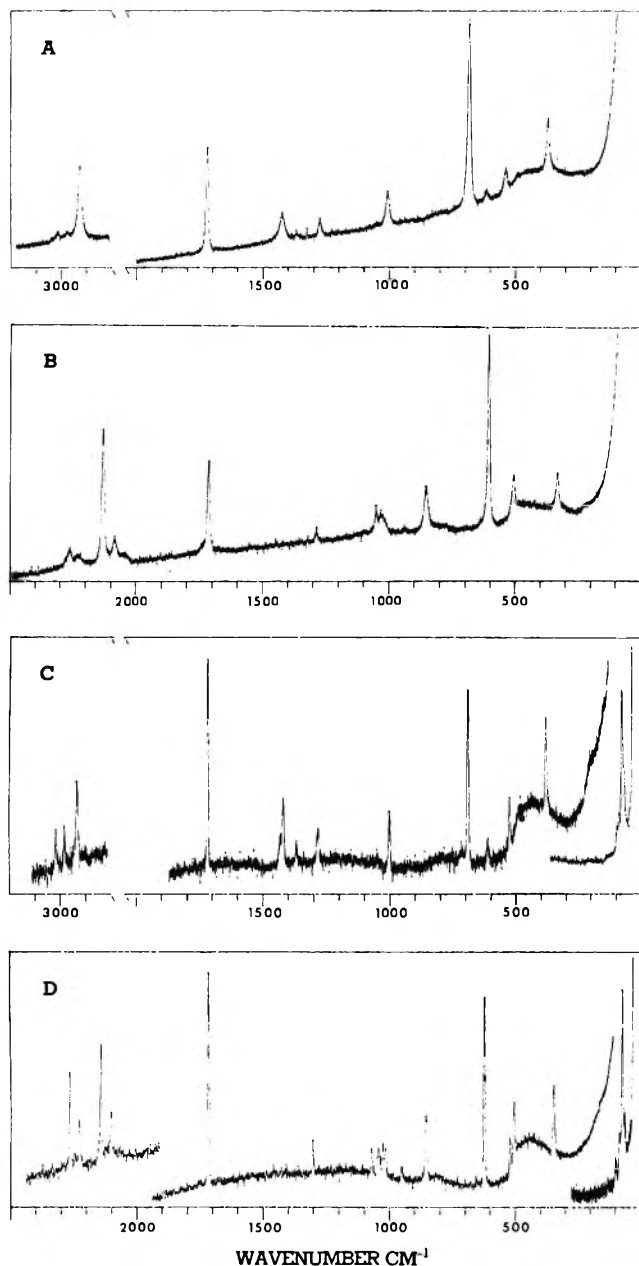
Figure 2. Raman spectra of biacetyl: A, liquid biacetyl; B, liquid biacetyl-d_6; C, solid biacetyl; D, solid biacetyl-d_6.

assignments for most of the fundamental vibrations of biacetyl and biacetyl-d_6 in the solid phase.

The results of the studies of the solid-state spectra coupled with improved data for the other phases make a more detailed analysis possible and require the reassignment of some of the bands. Since some of the bands are better delineated in the solid only the solid-state spectra will be discussed in detail with references to the spectra of the other phases being made only as they relate to the assignment of the normal modes.

The highest frequency vibrations of biacetyl arise from the C–H stretching motions of the two methyl groups. The two symmetric and four antisymmetric C–H stretching modes are divided among the symmetry

species of the C_{2h} point group with the two symmetric stretching motions being of a_g and b_u symmetry and the antisymmetric stretching modes having a_g, b_g, a_u and b_u symmetry. The Raman active C–H stretching modes are found at 3018, 2983, and 2922 cm^{-1} in solid biacetyl. In the liquid the band corresponding to the 2922-cm^{-1} band is strongly polarized, whereas the bands corresponding to the 2983- and 3018-cm^{-1} bands appear depolarized and polarized, respectively. The 2922-cm^{-1} band is assigned to the symmetric stretching motion, whereas the 2983- and 3018-cm^{-1} bands are assigned to the antisymmetric stretching motions of b_g and a_g symmetry, respectively. In the spectra of biacetyl-d_6 these bands are shifted to 2142, 2228, and 2267 cm^{-1}, respectively. The infrared active modes occur at 3012, 2975, and 2925 cm^{-1} in solid biacetyl and are assigned to the antisymmetric C–H stretching motions of b_u and a_u symmetry and to the symmetric stretching motion of b_u symmetry, respectively. In the spectrum of biacetyl-d_6 these modes are shifted, respectively, to 2267, 2216, and 2120 cm^{-1}.

It is difficult to give realistic descriptions to the motions causing the bands in the 1500–650-cm^{-1} region where the bands arising from the motions of the methyl group and those arising from the high-frequency skeletal motions are expected to occur. Miyazawa[15] has suggested that the C–CH$_3$ stretching modes of biacetyl might be expected to mix with the appropriate CH$_3$ rocking modes. As will be shown later these bands all shift upon deuteration in such a manner that it is not possible to consider them as isolated normal modes of the methyl group or the heavy skeleton; thus the descriptions given for these modes can only be considered as very poor approximations of the true normal modes.

Eight bands appear in the Raman spectra of solid biacetyl in the region 1500–650-cm^{-1}. The pair of bands at 1435 and 1421 cm^{-1} is assigned to the antisymmetric methyl deformations. These bands appear as one broad band in the liquid so it was not possible to obtain depolarization data for them. However, in the solid the 1421-cm^{-1} band is a medium sharp band, whereas the 1435-cm^{-1} band appears as a weak broad band. Since modes of a_g symmetry are generally sharp the 1421-cm^{-1} band is assigned to the antisymmetric deformation of species a_g and the 1435-cm^{-1} line is taken to be the b_g deformation. The symmetric methyl deformation is assigned to the band at 1367 cm^{-1} which is polarized in the liquid. The Raman active methyl rocking modes are assigned to the bands at 1288 and 1280 cm^{-1}. There is no indication in the solid or liquid as to the symmetry of these bands. The central carbon–carbon stretching mode occurs at 1001 cm^{-1}. This mode occurs at 1078 cm^{-1} in glyoxal,[4] 1093 cm^{-1} in oxalyl chloride,[1] and 1052 cm^{-1} in oxalyl bromide.[2]

The symmetric C–CH$_3$ stretching mode is expected to

(15) Reference 5 as quoted in ref 6.

Table I: Vibrational Data on Biacetyl[a]

Infrared, cm^{-1}			Raman, cm^{-1}		Assignment
Gas	Liquid	Solid	Liquid[b]	Solid	
3437 w	3417 m	3415 m			$1706 + 1719 = 3425$
3021 w	3010 w	3012 w			Antisymmetric C–H stretch (b_u)
			3016 vw (0.68)	3018 w	Antisymmetric C–H stretch (a_g)
2978 w	2999 w	2975 w			Antisymmetric C–H stretch (a_u)
			2978 sh	2983 w	Antisymmetric C–H stretch (b_g)
2944 w	2935 w	2925 w			Symmetric C–H stretch (b_u)
			2928 s (0.09)	2922 m	Symmetric C–H stretch (a_g)
	1807 w (sh)	1819 w			$1131 + 693 = 1824$
1775 w (sh)	1770 w (sh)	1751 w			
1734 R s	1715 vs	1706 vs			Antisymmetric C=O stretch (b_u)
1719 P					
			1720 vs (p)	1719 vs	Symmetric C=O stretch (a_g)
		1683 vw			$261 + 1421 = 1682$
			1680 vw		$693 + 1001 = 1694$
1680 w (sh)	1678 w (sh)	1676 w			
		1645 w			$360 + 1288 = 1648$
		1604 vw			$912 + 693 = 1605$
			1431 sh	1435 w	Antisymmetric CH$_3$ deformation (b_g)
			1424 m (0.57)	1421 m	Antisymmetric CH$_3$ deformation (a_g)
		1432 w (sh)			$912 + 526 = 1438$; $1367 + 66 = 1433$
		1428 w (sh)			
1424 m	1419 s	1418 s			Antisymmetric CH$_3$ deformation (a_u or b_u)
		1400 m			Antisymmetric CH$_3$ deformation (a_u or b_u)
			1364 w (0.67)	1367 w	Symmetric CH$_3$ deformation (a_g)
1365 R	1381 w (sh)				
1358 Q s	1352 s	1350 s			Symmetric CH$_3$ deformation (b_u)
1352 P	1315 w (sh)				
			1275 w (0.62)	1288 w (sh)	Symmetric CH$_3$ rock (a_g or b_g)
				1280 w	Symmetric CH$_3$ rock (a_g or b_g)
	1260 vw	1256 vw			$261 + 1001 = 1262$
		1238 vw			
	1200 vw (sh)	1226 vw			$544 + 693 = 1237$
	1171 vw (sh)	1167 vw			$544 + 614 = 1158$
1122 R					
1114 Q s	1114 s	1131 s			Antisymmetric C–CH$_3$ stretch (b_u)
1107 P		1119 sh			
	1082 vw (sh)				
	1063 vw (sh)	1045 vw			$360 + 693 = 1053$
			1050 vw	1052 vw	$2 \times 526 = 1052$
			1005 m (0.05)	1001 m	C–C stretch (a_g)
955 R		956			
949 Q w	946 m	950 m			Antisymmetric CH$_3$ rock (b_u)
945 P					
910 m	913 m	912 m			Antisymmetric CH$_3$ rock (a_u)
			685 vs (p)	693 vs	Symmetric C–CH$_3$ stretch (a_g)
			608 w (dp)	614 vw	Antisymmetric COCH$_3$ out-of-plane bend (b_g)
543 R					
538 Q s	537 s	544 s			Antisymmetric COCH$_3$ bend (b_u)
531 P					
			537 m (0.51)	526 m	Symmetric COCH$_3$ bend (a_g)
348 R w	345 w	360 m			Symmetric COCH$_3$ out-of-plane bend (a_u)
327 P					
			369 s (0.37)	380 m	Symmetric COCH$_3$ rock (a_g)
262 R					
252 Q w	264 w	261 m			Antisymmetric COCH$_3$ rock (b_u)
246 P					
			246 vw (br)		
~200 vw		217 vw			CH$_3$ torsion (a_u)
		136 w			Translational mode
		104 w			Translational mode

Table I (*Continued*)

Infrared, cm⁻¹			Raman, cm⁻¹		
Gas	Liquid	Solid	Liquid[b]	Solid	Assignment
				97 w	Librational mode
				87 m	Librational mode
				85 sh	Librational mode
				74 s	Librational mode
				67 sh	Librational mode
57		66 vw			Acetyl torsion (a_u)
47					

[a] Abbreviations: s, strong; m, medium; w, weak; v, very; sh, shoulder; p, polarized; dp, depolarized. [b] Numbers in parentheses are depolarization values.

give rise to an intense band at a somewhat lower frequency than the central C–C stretching mode. This mode corresponds to the C–X stretch of the oxalyl halides which occurs at 620 cm⁻¹ in oxalyl chloride[1] and 582 cm⁻¹ in oxalyl bromide.[2] This mode is assigned to the intense, highly polarized band at 693 cm⁻¹. As stated earlier, the assignment of this band to a bending mode would place too many bands in the bending region of the Raman spectrum. None of these bands disappeared with solidification so they cannot be attributed to another isomer. Also the intensity of the 693-cm⁻¹ band suggests that it should be assigned to the carbon–carbon stretching motion rather than to a skeletal bending mode.

The Raman spectrum of solid biacetyl-d_6 has the corresponding bands at 1301, 1062, 1035, 1018, 1009, 847, and 619 cm⁻¹ with the 1301, 1062, 847, and 619 cm⁻¹ lines being polarized in the liquid. The 847 and 619 cm⁻¹ bands are readily assigned to the central C–C and C–CD₃ stretching motions. This yields shift factors ν_H/ν_D of 1.18 and 1.12, which should be compared with the expected values of 1.05 and 1.10 for the C–C and C–CH₃ stretching modes, respectively. These larger shifts are due to the coupling of these motions with some of the methyl motions of a_g symmetry giving them shift factors greater than expected. Since the 1301- and 1062-cm⁻¹ bands are polarized they must arise from motions of a_g symmetry and are thus assigned to the two highest frequency bending modes, the antisymmetric and symmetric methyl deformations of symmetry a_g. The antisymmetric deformation of b_g symmetry is assigned to the 1035-cm⁻¹ band. The rocking motions for the "d_6" compound are assigned to the bands at 1018 and 1009 cm⁻¹.

The infrared active modes occurring in the 1500–650-cm⁻¹ region are also badly mixed. The bands at 1418 and 1400 cm⁻¹ in biacetyl are assigned to the antisymmetric deformations and the 1350-cm⁻¹ band is assigned to the symmetric deformation. In the infrared spectrum of solid biacetyl-d_6 these bands appear at 1143 cm⁻¹ and as doublets at 1041, 1034 and 1026, 1021 cm⁻¹. A comparison of the intensities of the bands in

the spectra of solid biacetyl with those of solid biacetyl-d_6 suggests that the 1143-cm⁻¹ band should be assigned to the symmetric deformation and the 1041, 1034 and 1026, 1021 cm⁻¹ bands to the antisymmetric deformations split by crystal field effects. The spectra of the samples in the gaseous state give even stronger evidence for this assignment. Bands of C-type structure are predicted for modes of a_u symmetry, whereas the b_u vibrations should show A,B, or A–B hybrid structure. The corresponding gas phase bands of both the 1350-cm⁻¹ (Figure 1A) and the 1143-cm⁻¹ (Figure 1B) bands have A-type contours, whereas the gas phase bands corresponding to the antisymmetric deformations in each case have no definite contours.

Some previous investigators have assigned the infrared bands at 953 and 912 cm⁻¹ in biacetyl as a Fermi resonance doublet. The 953-cm⁻¹ band is split in the crystal and appears as a doublet at 956 and 950 cm⁻¹. However, the spectrum of the gas phase shows that these two bands have different band contours, an indication that they arise from motions of different symmetry. The infrared spectrum of solid biacetyl-d_6 reveals bands at 790 and 769 cm⁻¹ indicating that both the 953-cm⁻¹ and the 912-cm⁻¹ bands shift upon deuteration. Thus, both bands must be due to fundamental vibrations. Since only the rocking modes and the antisymmetric C–CH₃ stretching modes are expected in this frequency region these two bands are assigned to the rocking modes. The 953-cm⁻¹ (790-cm⁻¹ for "d_6") band is assigned to the b_u rocking mode, whereas the 912-cm⁻¹ (769-cm⁻¹ for "d_6") band is assigned to the a_u rocking mode. The band contours of the 953- and 790-cm⁻¹ bands are the same as those for other bands assigned to modes of b_u symmetry. The C–CH₃ antisymmetric stretching mode is then assigned to the 1131-cm⁻¹ band, with the corresponding vibration in the d_6 compound occurring at 969 cm⁻¹. The extremely large shift of this band with deuteration clearly shows that this mode involves considerable methyl rocking motion and the description of this mode as a C–CH₃ antisymmetric stretching mode is a very poor approximation of the actual normal mode.

Table II: Vibrational Data on Biacetyl-d_6[a]

Infrared, cm^{-1}		Raman, cm^{-1}		Assignment
Gas	Solid	Liquid[b]	Solid	
3427 w	3407 m			1706 + 1716 = 3422
3006 w	3011 w			790 + 2228 = 3018
	3005 w			1301 + 1706 = 3007
	2557 vw			1706 + 847 = 2553; 2216 + 340 = 2556
	2443 w			2120 + 340 = 2460; 324 + 2142 = 2466; 237 + 2228 = 2465
	2329 vw			1716 + 619 = 2335
		2263 w (0.55)	2267 s	Antisymmetric C–D stretch (a_g)
2272 w	2267 w			Antisymmetric C–D stretch (b_u)
		2229 sh	2228 w	Antisymmetric C–D stretch (b_g)
2235 w	2216 w			Antisymmetric C–D stretch (a_u)
	2166 vw			1143 + 1018 = 2161; 1143 + 1035 = 2178
		2135 s (<0.01)	2142 s	Symmetric C–D stretch (a_g)
	2120 m			Symmetric C–D stretch (b_u)
	2085 vw			1024 + 1062 = 2086
	2080 vw			1038 + 1035 = 2073
		2042 vw (<0.01)	2065 vw	2 × 1035 = 2070
	2024 vw			969 + 1062 = 2031
	1991 vw			969 + 1035 = 2004
	1780 m			1301 + 488 = 1789
1766 sh	1761 m			1143 + 619 = 1762
		1716 vs (0.29)	1716 vs	Symmetric C=O stretch (a_g)
1729 R vs 1718 P	1706 vs			Antisymmetric C=O stretch (b_u)
	1680			
1679 sh	1679 m			
	1669 m			
	1643 w			1143 + 500 = 1643
	1583 vw			969 + 619 = 1588
	1547 w			488 + 1062 = 1550
1334 w	1400 w			790 + 619 = 1409
	1322 vw			324 + 1009 = 1333
		1282 w (0.15)	1301 w	Antisymmetric CD$_3$ deformation (a_g)
	1276 w			237 + 1038 = 1275
	1264 w			237 + 1030 = 1267
	1252 m			237 + 1018 = 1255
1241 w				
	1231 w			
	1223 m			158 + 1062 = 1220
1145 R				
1139 Q s	1143 vs			Symmetric CD$_3$ deformation (b_u)
1132 R				
	1118 m			340 + 790 = 1130
	1110 m			488 + 619 = 1107; 340 + 769 = 1109
		1053 w (0.10)	1062 w	Symmetric CD$_3$ deformation (a_g)
1038	1041 m 1034			Antisymmetric CD$_3$ deformation (a_u or b_u)
		1028 w (dp)	1038 w 1030 w	Antisymmetric CD$_3$ deformation (b_g)
1028 m	1026 s 1021			Antisymmetric CD$_3$ deformation (a_u or b_u)
		1018 sh	1018 w	Symmetric CD$_3$ rock (a_g or b_g)
			1009 w	Symmetric CD$_3$ rock (a_g or b_g)
	1000 w			488 + 515 = 1003
	992 w			488 + 500 = 988
967 R				
960 Q s	969 s			Antisymmetric C–CD$_3$ stretch (b_u)
953 P				
	952 sh			
		935 vw	944 vw	340 + 619 = 959
		845 m (0.08)	847 m	C–C stretch (a_g)
782 sh	790			Antisymmetric CD$_3$ rock (b_u)

Table II (*Continued*)

Infrared, cm⁻¹		Raman, cm⁻¹		
Gas	Solid	Liquid[b]	Solid	Assignment
772 m	770 768			Antisymmetric CD_3 rock (a_u)
		607 vs (p)	619 vs	Symmetric $C-CD_3$ stretch (a_g)
		517 s (0.65)	515 m	Antisymmetric $COCD_3$ out-of-plane bend (b_g)
			500 m	Symmetric $COCD_3$ bend (a_g)
489 483 s 476	506 w 488 s			Antisymmetric $COCD_3$ bend (b_u)
		335 s (0.36)	340 s	Symmetric $COCD_3$ rock (a_g)
314 s	324 s			Symmetric $COCD_3$ out-of-plane bend (a_u)
225 m	237 m			Antisymmetric $COCD_3$ rock (b_u)
150 vw	158 vw			CD_3 torsion (a_u)
	115 w			Translational mode
			94 w	Librational mode
	93 m			Translational mode
			80 sh	Librational mode
			72 s	Librational mode
			60 sh	Librational mode
56 47	61 vw			Acetyl torsion (a_u)

[a] Abbreviations: s, strong; m, medium; w, weak; v, very; sh, shoulder; p, polarized; dp, depolarized. [b] Numbers in parentheses under column headed liquid are depolarization values.

The skeletal bending and rocking motions lie below 650 cm⁻¹ and in the Raman spectrum of solid biacetyl there are three bands found at 614, 526, and 380 cm⁻¹. The band in the liquid corresponding to the 614-cm⁻¹ band is depolarized and is assigned to the $COCH_3$ antisymmetric out-of-plane bending mode. The 526-cm⁻¹ band is assigned to the $COCH_3$ symmetric bending motion and the 380-cm⁻¹ band is assigned to the $COCH_3$ symmetric rocking mode. These bands are shifted upon deuteration to 515, 500, and 340 cm⁻¹, respectively. The infrared active bands occur at 544, 360, and 261 cm⁻¹. The gas phase bands corresponding to the 544- and 261-cm⁻¹ bands have A-type band contours and are thus due to modes of b_u symmetry. They are assigned to the $COCH_3$ antisymmetric bending and rocking modes, respectively. The 360-cm⁻¹ band is assigned to the $COCH_3$ symmetric out-of-plane bend of a_u symmetry. The corresponding bands in biacetyl-d_6 occur at 488, 237, and 324 cm⁻¹, respectively.

There are three torsional modes to be assigned: an infrared active methyl torsion, a Raman active methyl torsion, and an infrared active acetyl torsion. The infrared active methyl torsion is assigned to a weak band at 217 cm⁻¹ which is shifted to 158 cm⁻¹ in the spectrum of biacetyl-d_6 (see Figures 3 and 4). This yields a shift factor of 1.37. Although this is less than the theoretical 1.41, it is as close as could be expected. The Raman active methyl torsion was not observed. Although a very weak broad band was observed in the Raman spectrum of liquid biacetyl at approximately 246 cm⁻¹, such a frequency seems too high for this nor-
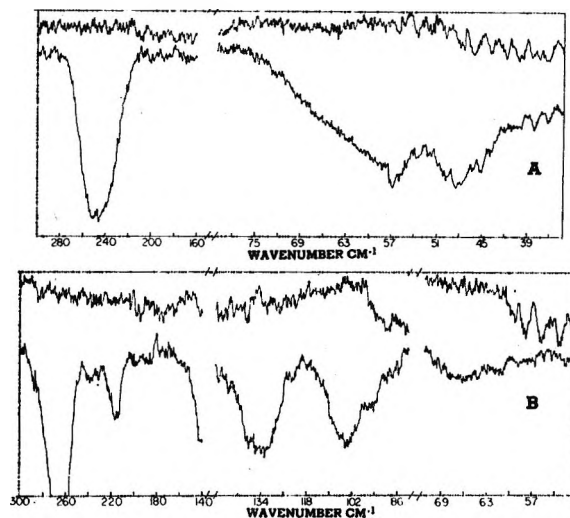
Figure 3. Far-infrared spectra of biacetyl: A, vapor phase; B, solid phase.

mal mode. Also it was not possible to locate any band with a proper shift factor for a torsional motion in the Raman spectrum of biacetyl-d_6. The acetyl torsion has been reported[10] to have a frequency of 48 cm⁻¹ in the gas phase. We observed this mode as a band centered at 52 cm⁻¹, which is shifted to a slightly higher frequency in the solid and occurs at 66 cm⁻¹. In the infrared spectrum of solid biacetyl-d_6 this mode occurs at 61 cm⁻¹. The shift factor corresponds very closely to the theoretical value and removes any doubt of the
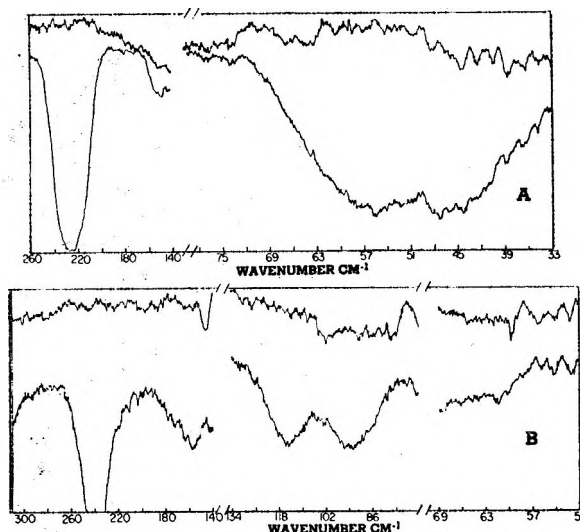
Figure 4. Far-infrared spectra of biacetyl-d_6: A, vapor phase; B, solid phase.

assignment. The previous assignment[9] of 35 cm^{-1} for the torsional frequency in the solid from a study of the electronic spectrum is apparently in error.

The infrared active methyl torsions have been observed in the vapor phase samples of biacetyl and biacetyl-d_6 at ~200 and 150 cm^{-1}, respectively. The three-fold barrier to rotation has been calculated for each case, using the method based on the Mathieu equation as illustrated by Fateley and Miller[16] with eigenvalues from Herschbach's[17] tables. Reduced moment of inertia constants of 5.426 and 2.785 cm^{-1} yield barriers of 2.65 and 2.79 kcal/mol for CH$_3$ and CD$_3$, respectively. These are higher than barriers found for other acetyl compounds in the vapor phase: acetaldehyde,[18] 1.16 kcal/mol; acetyl bromide,[19] 1.30 kcal/mol; and acetyl chloride,[20] 1.30 kcal/mol. The breadth and weakness of the torsional band in gaseous biacetyl casts some doubt on its exact position. However, for both solids the methyl torsion is sharp and well defined. Barriers calculated from the solid frequencies are 3.07 and 3.05 kcal/mol for biacetyl and biacetyl-d_6, again using the simple cosine function and neglecting intermolecular forces. The small shift in the torsion seems to justify this treatment. The barriers for solid acetyl bromide[21] and chloride[21] are 1.97 and 1.81 kcal/mol. Therefore, there is clear evidence that the barrier to methyl rotation in biacetyl is considerably higher than the barriers found for other acetyl compounds studied to date. It is not at all clear why the barrier values should differ by so much but the relatively short distance between the hydrogen and the "other" carbonyl may explain part of the effect.

Although assignment of the fundamental vibrations has been made using frequencies for the solid phase, there is no significant difference between the spectra of the three phases. Comparison of curves A and C (for

gaseous and solid biacetyl, respectively) in Figure 1 demonstrates a one-to-one correspondence of bands for the two phases. Only a sharpening of lines and splitting due to crystal field effects can be seen for the solid. A similar correspondence is seen in the Raman spectra. The fact that no band present in the gas or liqid phase disappears or shifts significantly points to the presence of only one isomeric form in all phases, the trans form. This is in contrast to our findings for (COCl)$_2$,[1] (CO-Br)$_2$,[2] and (COF)$_2$,[3] all of which exhibit two isomeric forms in the fluid states and one in the solid. Glyoxal,[4] (COH)$_2$, on the other hand, is similar to biacetyl. It thus appears that the halogens provide some stabilizing influence for the cis isomer that cannot be realized when they are replaced by hydrogen atoms or methyl groups. A nonbonded interaction probably exists between the halogens on adjacent carbons that becomes insignificant or does not exist for the H and CH$_3$ cases.

A consideration of the infrared and Raman frequencies of solid biacetyl reveals that there are no coincidences between the Raman and infrared spectra in the region of the skeletal vibrations. Although there are three near coincidences in the CH stretching and deformation regions (2933 and 2925, 1432 and 1435, and 1418 and 1421 cm^{-1}) these are considered to be accidental degeneracies which occur since the in-phase and out-of-phase methyl modes are less sensitive to skeletal structure. Also, all of the combination bands observed in the infrared spectrum could be assigned as arising from the combination of one ungerade and one gerade fundamental. In the Raman spectrum the few bands not assigned to fundamental modes could be readily assigned to overtones or combinations of Raman fundamentals. On this basis the biacetyl molecule must be in the trans form and occupying sites of at least C_i symmetry in the crystal. With C_i sites, packing considerations imply that the most probable space group would be one of the C_{2h} or D_{2h} space groups.[22]

A consideration of the factor group splitting provides a basis for the differentiation between the C_{2h} and D_{2h} space groups. The C_i-C_{2h} site-factor group combination predicts a splitting of each infrared and each Raman vibration into two components. However, the C_i-D_{2h} combination predicts the splitting of each infrared vibration into three components and each Raman vibration into four components. In the infrared spec-

(16) W. G. Fateley and F. A. Miller, Spectrochim. Acta, 19, 611 (1963).

(17) D. R. Herschbach, J. Chem. Phys., 27, 975 (1957).

(18) R. F. Curl, Jr., V. M. Rao, K. V. L. N. Sastry, and J. A. Hodgeson, ibid., 39, 3335 (1963).

(19) L. C. Krishner, ibid., 33, 1237 (1960).

(20) K. M. Sinnot, ibid., 34, 851 (1961); Bull. Amer. Phys. Soc., 1, 198 (1956).

(21) J. R. Durig, C. M. Player, Jr., and J. Bragin, J. Chem. Phys., 54, 460 (1971).

(22) F. D. Verderame, F. Castellucci, and S. Califano, ibid., 52, 719 (1970).

Table III: Fundamental Frequencies of Solid Biacetyl and Biacetyl-d_6

Vibration	Symmetry species and approximate description of the normal modes	Biacetyl Raman, Δ cm⁻¹	Biacetyl Infrared, cm⁻¹	Biacetyl-d_6 Raman, Δ cm⁻¹	Biacetyl-d_6 Infrared, cm⁻¹
		a_g			
1	C–H antisymmetric stretch	3018		2267	
2	C–H symmetric stretch	2922		2142	
3	C=O symmetric stretch	1719		1716	
4	CH₃ antisymmetric deformation	1421		1301	
5	CH₃ symmetric deformation	1367		1062	
6	CH₃ symmetric rock	1288 or 1280		1018 or 1009	
7	C–C stretch	1001		847	
8	C–CH₃ symmetric stretch	693		619	
9	COCH₃ symmetric bend	526		500	
10	COCH₃ symmetric rock	380		340	
		a_u			
11	C–H antisymmetric stretch		2975		2216
12	CH₃ antisymmetric deformation		1418 or 1400		1038 or 1024
13	CH₃ antisymmetric rock		912		769
14	COCH₃ symmetric out-of-plane bend		360		324
15	CH₃ torsion		217		158
16	Acetyl torsion		66		61
		b_g			
17	C–H antisymmetric stretch	2983		2228	
18	CH₃ antisymmetric deformation	1435		1035	
19	CH₃ symmetric rock	1288 or 1280		1018 or 1009	
20	COCH₃ antisymmetric out-of-plane bend	614		515	
21	CH₃ torsion				
		b_u			
22	C–H antisymmetric stretch		3012		2267
23	C–H symmetric stretch		2925		2120
24	C=O antisymmetric stretch		1706		1706
25	CH₃ antisymmetric deformation		1418 or 1400		1038 or 1024
26	CH₃ symmetric deformation		1350		1143
27	C–CH₃ antisymmetric stretch		1131		969
28	CH₃ antisymmetric rock		953		790
29	COCH₃ antisymmetric bend		544		488
30	COCH₃ antisymmetric rock		261		237

trum of solid biacetyl-d_6 (see Figure 1D) several of the bands showed pronounced splitting. In each case the bands are split into two components which would imply a C_{2h} space group.

Two lattice vibrations appear in the infrared spectrum of biacetyl at 136 and 104 cm⁻¹ and at 115 and 93 cm⁻¹ in the spectrum of biacetyl-d_6. These bands must be due to optic translational modes since these modes are active only in the infrared for molecules on C_i sites. Five Raman active librational modes appear in the Raman spectrum of biacetyl. These bands occur as two pairs at 74, 67 and 87, 85 cm⁻¹ and a weak band at 97 cm⁻¹. The appearance of the optical translational modes in the infrared and the doubling of the optical librational modes in the Raman implies that there are at least two molecules per unit cell. The splitting of the lattice modes is not expected to be large so the observed bands may be the result of more components than were

actually resolved. Thus the crystal structure is most likely C_{2h} with two or possibly four molecules per unit cell; however, D_{2h} can not conclusively be ruled out as the space group.

Bloom and Sutton[11] have reported that biacetyl vapor has a dipole moment of approximately 1 D at room temperature, which increases with increasing temperature. They proposed two possible explanations; one was that there were cis and trans isomers and the observed dipole moment arose from the cis isomer. The other suggestion was that the dipole moment was the result of bond moments of the trans form not cancelling during the vibration from the nonpolar equilibrium position. They decided that it was not possible to differentiate between these two explanations by means of dipole measurements. However, it seems unlikely that such a large dipole moment could arise as the result of the sum of small instantaneous dipoles.

The present investigation has eliminated the possibility of the presence of a cis isomer in the solid phase, and there is no indication of a second isomer in the liquid or vapor phase. Bloom and Sutton encountered some difficulty in purification of their sample and at least two of their runs produced erratic results. They suggested that the work should be rechecked using a sample purified by a different technique but were not able to continue the project because of the war. In light of the spectroscopic evidence and the element of doubt in the dipole moment measurements, the conclusion that biacetyl exists in only the trans configuration in all phases seems justified.

Conclusions

Vibrational assignments have satisfactorily been made for solid biacetyl according to C_{2h} symmetry.

Spectra of the liquid and vapor phases show no indication of a second isomeric form, and it is concluded that the nonbonded forces between halogens which stabilize the cis isomer of the oxalyl halides are not present between the methyls of biacetyl. The mutual exclusion between infrared and Raman spectra of crystalline biacetyl necessitates a centrosymmetric structure and the space group is probably C_{2h} or D_{2h}. The splitting of the Raman-active librational modes and the appearance of translational bands in the far-infrared spectrum indicate that there are at least two and possibly four molecules per unit cell. The barrier to methyl rotation has been calculated to be 2.65 kcal/mol, considerably higher than those found for other acetyl compounds.

Vibrational Spectra and Structure of Organophosphorus Compounds.

X.[1] Methyl Torsional Frequencies and Barriers to Internal

Rotation of Some CH₃PXY₂ Compounds[2,3]

by J. R. Durig* and J. M. Casper[4]

Department of Chemistry, University of South Carolina, Columbia, South Carolina 29208   (*Received December 18, 1970*)

Publication costs assisted by the National Institute of Arthritis and Metabolic Diseases

The far-infrared spectra of CH_3PCl_2, CH_3POCl_2, CH_3POFCl, CH_3POF_2, and CH_3PSCl_2 in the solid and gaseous states have been recorded from 33 to 350 cm⁻¹. Methyl torsional modes were observed in the solid state for all compounds except CH_3POFCl. The Raman spectra of CH_3PCl_2, CH_3POF_2, and CH_3PSCl_2 in the solid state were recorded and torsional frequencies were observed for CH_3PCl_2 and CH_3PSCl_2. The wave numbers for these internal rotations were 228, 264, 240, and 221 cm⁻¹ for the CH_3PCl_2, CH_3POCl_2, CH_3POF_2, and CH_3PSCl_2 molecules, respectively. The threefold barriers calculated from these assignments are 3.4, 4.4, 3.6, and 3.2 kcal/mol, respectively. These barrier values are compared with those previously reported for other organophosphorus compounds. Lattice modes were observed in the wave number range 65-120 cm⁻¹ in the far-infrared spectra for all compounds.

Introduction

Barriers to internal rotation are of interest to scientists because of the effect they have on molecular properties. The heat capacity, entropy, and equilibrium constant contain contributions from hindered internal rotation. Many theories have been advanced to explain the nature of the interactions causing a barrier to internal rotation and attempts have been made to predict these barriers from *ab initio* calculations.[5-11] In some cases these attempts have been hindered by in-

sufficient and inaccurate experimental results. Theoretical calculations of barrier heights and the various

(1) For Part IX, see J. R. Durig and J. W. Clark, *J. Cryst. Mol. Struct.*, 1, 43, (1971).

(2) Presented at the Twenty-fourth Symposium on Molecular Spectra and Structure, The Ohio State University, 1969, Paper D7.

(3) Taken from the thesis of J. M. Casper submitted to the Department of Chemistry, University of South Carolina, in partial fulfillment of the Ph.D. Degree, June 1971.

(4) Predoctoral National Science Foundation Fellow.

(5) W. H. Fink and L. C. Allen, *J. Chem. Phys.*, 46, 2261 (1967).

theories on the nature of the origin of specific barriers may be aided by a larger number of more accurately determined barriers to guide the efforts. In addition, values for barrier heights of molecules with varied skeletal structures are needed to provide more definitive guidelines.

It has been proposed by some proponents of neutron inelastic scattering techniques[12] that barriers to internal rotation in the solid phase cannot be obtained from infrared and Raman data even when selection rules do not forbid the observation of the torsional mode. A recent series of papers[13-18] which reported the barrier heights obtained by infrared and Raman techniques for about 40 molecules has shown this proposition is incorrect. In fact, since in the crystalline state the activity of the torsional mode is determined by the site symmetry, it is also possible to determine the barrier height for some molecules when the mode is forbidden for the isolated molecule. This was the case for the CH_3CCl_3[16] and $(CH_3)_4^{14}C$ molecules where the torsional frequencies were observed in the far-infrared spectra of the solids at $-190°$. Considering the cost and experimental difficulty, the determination of barrier heights by neutron inelastic scattering has value only for the molecules that cannot be studied by infrared, Raman, or microwave methods, or if the frequency of the torsional mode to be measured is not sufficiently separated from the frequencies of the other vibrational modes in the molecule. In favorable cases an error of 10% can be expected in barrier heights determined by the neutron inelastic scattering technique. The utilization of the far-infrared or Raman techniques allows the direct observation of the methyl torsional modes with an experimental accuracy of 1 or 2 cm^{-1} for a large number of molecules with minimal experimental difficulty or expense.

The majority of methyl torsional modes that have been observed have involved the C–C bond as an axis. The only organophosphorus molecules for which the barrier heights have been determined are CH_3PH_2, $(CH_3)_2PH$, and $(CH_3)_3P$. The torsional barrier is 1.96 kcal/mol for gaseous CH_3PH_2,[19] 2.22 kcal/mol for gaseous[20] and solid[21] $(CH_3)_2PH$, 2.6 kcal/mol for gaseous $(CH_3)_3P$,[22] and 3.58 kcal/mol for solid $(CH_3)_3P$.[17] Since the values of many more barriers to rotation about the P–C bond are necessary before the nature of the substituent effects can be reasonably predicted, it was decided to record the far-infrared spectra of the series CH_3PCl_2, CH_3POCl_2, CH_3POClF, CH_3POF_2, and CH_3PSCl_2 for the purpose of determining the frequencies of the torsional oscillations. Raman spectra of the corresponding compounds in the solid state were also recorded when feasible.

Complete vibrational assignments have been presented for these molecules in the gaseous and liquid states[23-25] but the torsional modes were not observed. Since the modes are too weak to be observed in the infrared in the gas phase and the presence of chlorine

makes a microwave study extremely difficult, it was decided to examine the infrared spectra of the crystalline phase of these molecules at $-190°$. The bands which are due to the torsional mode can be distinguished from the bending modes since it is expected that the torsional modes will have only a small change in the molecular polarizability and should be quite weak or not observed in the Raman spectra. In addition, the torsional mode can be distinguished from the intermolecular modes because its frequency should not show a large temperature dependence.

The usefulness of solid phase data can be seen from the torsional data on $(CH_3)_2S$ and $(CH_3)_2SO$. The molecule, $(CH_3)_2S$, has a barrier height to methyl rotation of 2.1 kcal/mol in the gaseous phase[26,27] and 3.22 kcal/mol in the solid state.[28] For $(CH_3)_2SO$ the corresponding barrier height is 2.8 kcal/mol in the gaseous phase[29] and 4.38 kcal/mol in the solid state.[15] Although the value of the barrier is higher for each molecule in the solid phase, the relative difference in barrier height between the compounds is nearly the same in both the solid and the gaseous phases. Since the compounds to be studied in this series are similar to each other, it is not unreasonable to expect that the trend and relative differences of barrier heights obtained in the solid phase will be a reasonable estimation of those for the isolated molecules. Therefore, the far-infrared spectra of these compounds were recorded at $-190°$ and examined for the frequency of the torsional mode.

(6) W. H. Fink and L. C. Allen, J. Chem. Phys., 46, 2276 (1967).

(7) M. Karplus and R. G. Parr, ibid., 28, 1547 (1963).

(8) J. P. Lowe and R. G. Parr, ibid., 43, 2565 (1965).

(9) J. P. Lowe and R. G. Parr, ibid., 44, 3001 (1966).

(10) K. Rudenberg, ibid., 41, 588 (1964).

(11) L. Pedersen and K. Morokuma, ibid., 46, 3941 (1967).

(12) H. Boutin and S. Yip, "Molecular Spectroscopy with Neutrons,' M.I.T. Press, Cambridge, Mass., 1968.

(13) J. R. Durig, S. M. Craven, and J. Bragin, J. Chem. Phys., 51, 5663 (1969).

(14) J. R. Durig, S. M. Craven, and J. Bragin, ibid., 52, 2046 (1970).

(15) J. R. Durig, C. M. Player, Jr., and J. Bragin, ibid., 52, 4224 (1970).

(16) J. R. Durig, S. M. Craven, K. K. Lau, and J. Bragin, ibid., 54, 479 (1971).

(17) J. R. Durig, S. M. Craven, and J. Bragin, ibid., 53, 38 (1970).

(18) J. R. Durig, C. M. Player, Jr., and J. Bragin, ibid., 54, 460 (1971).

(19) T. Kojima, E. L. Breig, and C. C. Lin, ibid., 35, 2139 (1961).

(20) R. Nelson, ibid., 39, 2382 (1963).

(21) J. E. Saunders, private communication.

(22) D. R. Lide and D. E. Mann, J. Chem. Phys., 29, 914 (1958).

(23) J. R. Durig, F. Block, and I. W. Levin, Spectrochim. Acta, 21, 1105 (1965).

(24) J. E. Griffiths, ibid., 21, 1135 (1965).

(25) J. R. Durig, B. R. Mitchell, J. S. Di Yorio, and F. Block, J. Phys. Chem., 70, 3190 (1956).

(26) L. Pierce and M. Hayashi, J. Chem. Phys., 35, 479 (1961).

(27) W. G. Fateley and F. A. Miller, Spectrochim. Acta, 18, 977 (1962).

(28) C. M. Player, Jr., private communication.

(29) W. Feder, H. Dreizler, H. D. Rudolf, and V. Typke, Z. Naturorsch. A, 24, 266 (1969).

Table I: Far-Infrared Spectra of Solid (−190°)

CH₃PCl₂ ν, cm⁻¹	Relative intensity	CH₃POCl₂ ν, cm⁻¹	Relative intensity	CH₃POFCl ν, cm⁻¹	Relative intensity	CH₃POF₂ ν, cm⁻¹	Relative intensity	CH₃PSCl₂ ν, cm⁻¹	Relative intensity	Assignment
77 (70)ᵃ	m	78	vw	86	m			68 (62)ᵃ	w	Lattice mode
89 (83)ᵃ	s	95 (88)ᵃ	m	99	s	106 (98)ᵃ	w			Lattice mode
		113 (104)ᵃ	m	120	m	122 (112)ᵃ	w			Lattice mode
202	m	202	w					198	m	PCl₂ deformation
		208								
228 (227)ᵃ	w	264 (164)ᵃ	vw			240 (239)ᵃ	vvw	221 (221)ᵃ	vw	Torsion
				242	m					P–Cl bending
243	w	234	s							PCl₂ twisting
		238								
				267	s					F–P–Cl bending
								260	s	P=S bending (PCl₂ twisting)
288	s	290	m					270	s	PCl₂ wagging
		296								
		332	s	328	w					P=O bending
		338								out-of-plane

ᵃ The frequencies listed in parentheses are from the solids at ∼ −80°.

Experimental Section

The far-infrared spectra were recorded from 33 to 350 cm⁻¹ on a Beckman Model IR-11 spectrophotometer. The instrument was purged with dry air and calibrated with water vapor using the frequencies reported by Hall and Dowling.[30] The cell used for recording the spectra has been described earlier.[31] The Raman spectrometer used for this study was a Cary Model 81 equipped with a He–Ne laser source. The spectra were recorded using a cell which has been previously described.[32] The spectrometer was calibrated with Ne emission lines.

The compounds were distilled and the purity checked by comparison of the boiling points and Raman spectra with those previously reported.[22–24] The boiling points were in exact agreement with previously reported data and the Raman spectra did not show any impurity bands. The frequencies for all observed bands are expected to be accurate to ±2 cm⁻¹ and are listed in Table I with their relative intensities and proposed assignments.

Theory

Before discussing the results, the theory employed in the potential barrier calculations will be summarized briefly. The theory of hindered internal rotation has been discussed in considerable detail elsewhere.[33,34] A cosine-type potential of the form $V(\alpha) = (^1/_2)V_3 \cdot (1 - \cos 3\alpha)$ was used with all terms higher than the threefold being considered negligible. The frequency of the torsional transition, which in the solid at −190° is assumed to be 1 ← 0, is expressed as

$$\bar{\nu} = (^1/_4)(n)^2 F \Delta b_{v_\sigma}$$

where n is related to the periodicity of the barrier (three for the molecules in this paper), F is proportional to the

inverse of the reduced moment of inertia ($F = h^2/2I_r$), and Δb_{v_σ} is the difference between the Mathieu eigenvalues. If F can be ascertained and if the frequency of the absorption due to the torsional mode is known, Δb_{v_σ} can be calculated. From the value of Δb_{v_σ}, a parameter, s, may be obtained from tables of Mathieu equation solutions. The barrier height of the torsional oscillation may then be calculated by

$$V_n = (^1/_4)(n)^2 F s$$

Since there has been no previous structural work on any of the molecules in this study, the reduced moments of inertia were calculated by transferring structural values from similar molecules. Although the assumed structures are subject to error, the difference in the moments of inertia between the skeletal part and rotor minimizes any errors which an inexact structure introduces. These structural errors should be substantially less than the experimental errors. The calculated reduced moments of inertia of the methyl groups are listed in Table II.

The barriers to internal rotation reported in this work were calculated neglecting the coupling between the inter- and intramolecular potential energies. The torsional barrier of the solid phase may not be entirely due to the magnitude of the threefold term in the torsional potential energy. However, since no splitting was observed for any of the fundamentals, except those of CH₃POCl₂, the intermolecular potential must be small compared with the intramolecular potential. This con-

(30) R. T. Hall and J. M. Dowling, J. Chem. Phys., 47, 2454 (1967).

(31) F. G. Baglin, S. F. Bush, and J. R. Durig, ibid., 47, 2104 (1967).

(32) D. J. Antion and J. R. Durig, Appl. Spectrosc., 22, 65 (1968).

(33) D. R. Hershbach, J. Chem. Phys., 31, 91 (1959).

(34) W. G. Fateley and F. A. Miller, Spectrochim. Acta, 17, 858 (1961).

Table II: Structural Data and Methyl Torsional Barriers[a]

Distance, r, Å or angle, $\not\triangleleft$, deg	CH_3PCl_2	CH_3POCl_2	CH_3POFCl	CH_3POF_2	CH_3PSCl_2
r (P–C)	1.85	1.81	1.81	1.81	1.81
r (P–Cl)	2.04	1.99	2.01		2.02
r (P–F)			1.52	1.52	
r(P=O)		1.45	1.45	1.45	
r (P=S)					1.86
$\not\triangleleft$ Cl–P–Cl	100.1	103.2			103.2
$\not\triangleleft$ F–P–F				102.5	
$\not\triangleleft$ F–P–Cl			104		
$\not\triangleleft$ Cl–P–O		112.3	112.3		
$\not\triangleleft$ Cl–P–S					112
$\not\triangleleft$ F–P–O			112.3	112.3	
F, cm^{-1}	5.46	5.52	5.55	5.61	5.50
ν, cm^{-1}	228	264		240	220
Barrier, kcal/mol	3.4	4.4		3.6	3.2

[a] The structural parameters for all molecules were assumed.
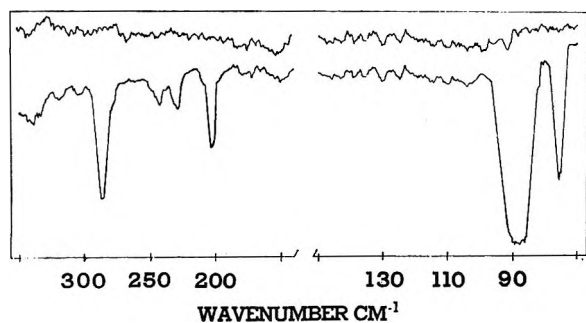
Figure 1. The far-infrared spectrum of CH_3PCl_2 taken at −190°. The upper curve is the cell background.

tention is further substantiated by the reasonably small frequency shifts observed in going from the gas phase to the solid. On this basis it is believed that the simple threefold potential should be a good approximation of the intramolecular torsional potential for these organophosphorus molecules.

Results

A. *CH_3PCl_2*. The far-infrared spectrum of CH_3-PCl_2 at −190° (Figure 1) contains six absorption bands between 33 and 350 cm^{-1}. Only the bands at 77 and 89 cm^{-1} show any appreciable frequency shift on warming from −190 to −80° and do not have counterparts in the Raman spectrum of the liquid phase. These two bands must be considered as arising from intermolecular motions, whereas the remaining four bands may be attributed to intramolecular modes. From analogy to the assignments made previously for the Raman spectrum,[24] the bands at 202, 243, and 288 cm^{-1} are assigned as arising from the PCl_2 deformational, twisting, and wagging motions, respectively. The 228-cm^{-1} band, then, is the only remaining unassigned absorption band and the methyl torsional motion is the only remaining
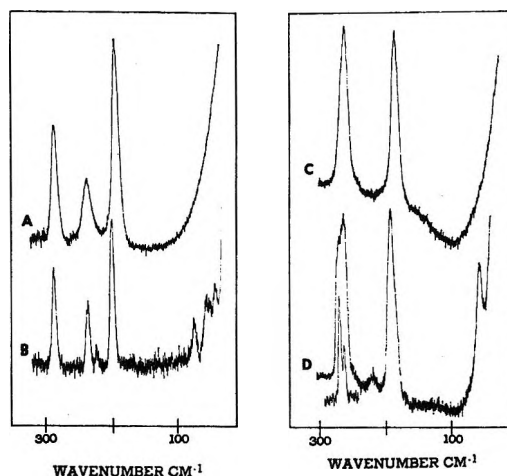
Figure 2. Low-frequency Raman spectra: A, liquid CH_3PCl_2; B, solid CH_3PCl_2 at −190°; C, liquid CH_3PSCl_2; D, solid CH_3PSCl at −190°.

intramolecular mode expected in this frequency region. Therefore, the torsional transition for CH_3PCl_2 is assigned to the 228-cm^{-1} band. An assignment to a two phonon process is not reasonable since the 228-cm^{-1} band showed no frequency shift with the variation of the sample temperature. It might also be mentioned that the 228-cm^{-1} band is sufficiently removed from the three low-frequency P–Cl_2 bending modes that it can not be considered as arising from factor group splitting.

Further evidence against the 228-cm^{-1} band resulting from factor group splitting is obtained from the Raman spectrum of the solid (Figure 2). The three PCl_2 bending modes give rise to large changes in the molecular polarizabilities associated with their motions and can be clearly identified in the Raman spectrum of the liquid. Upon solidification a weak Raman line appeared at 226 cm^{-1} and showed no frequency depen-
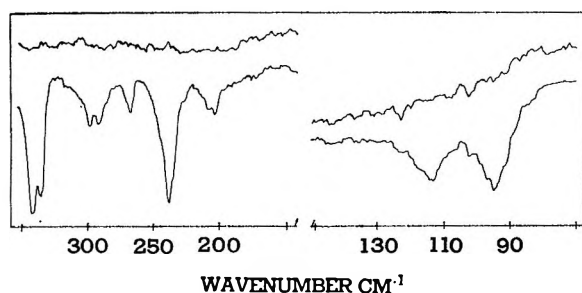
Figure 3. The far-infrared spectrum of CH_3POCl_2 taken at $-190°$. The upper curve is the cell background.

Figure 4. The far-infrared spectra of CH_3POFCl taken at $-190°$. The upper curve is the cell background.

dency on the temperature. The intensity of this Raman line is in marked contrast to those arising from the PCl_2 bending modes and therefore cannot be considered to be due to factor group splitting. Thus the 226-cm^{-1} Raman line must be assigned to the methyl torsion which appears in the solid, in part because of the decreased population of the excited torsional states.

To calculate the reduced moment of inertia, bond lengths and angles were taken from Williams, Sheridan, and Gordy's work on PCl_3[35] and Bartell and Brockway's work on $P(CH_3)_3$.[36] The H-C-H angles were assumed to be tetrahedral and the Cl-P-C angle was assumed to be equal to the Cl-P-Cl angle. These values gave an F of 5.46 cm^{-1}. Using this reduced moment and the assignment of 228 cm^{-1} for the methyl torsion, a barrier to internal rotation of 3.37 kcal/mol was calculated for CH_3PCl_2.

B. CH_3POCl_2. The far-infrared spectrum of solid CH_3POCl_2 at $-190°$ (Figure 3) is the only one of the series reported here that displays any splitting of the intramolecular modes. Four of the eight bands observed are noticeably split into doublets. These bands do not show an appreciable frequency shift with warming from -190 to $-80°$ so they may be assigned as intramolecular fundamentals. By analogy to previous work[23,24] the doublets at 202 and 208 cm^{-1}, 234 and 236 cm^{-1}, and 290 and 296 cm^{-1} may be assigned as arising from the deformational, twisting, and wagging motions of the PCl_2 moiety, respectively. The strong doublet at 332 and 338 cm^{-1} can be attributed to the P=O out-of-plane bending motion by comparison with the Raman data.[23] None of the four unsplit bands has coincident lines in the Raman spectrum of the liquid and only the band at 264 cm^{-1} does not show an appreciable frequency shift on warming from -190 to $-80°$. This band must be considered as arising from an intramolecular motion but all of the intramolecular modes, except the torsional mode, which could reasonably be expected to give rise to bands in this frequency range have been firmly assigned. Therefore the 264-cm^{-1} band is assigned as the frequency of the methyl torsional motion. The sample was lost so a Raman spectrum of the solid could not be obtained.

Bond lengths and bond angles from Cl_3PO,[35] $(CH_3)_3$-
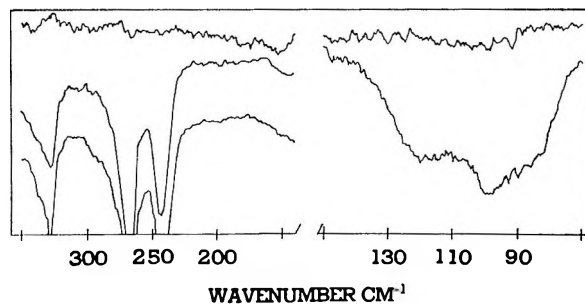
P,[36] and $(CH_3)_3PO$[37] were used to calculate the reduced moment of inertia, F. The H-C-H angle was assumed to be tetrahedral and the C-P-Cl angle was assumed to be the same as the Cl-P-Cl angle. An F of 5.52 cm^{-1} was obtained and the barrier to internal rotation of the methyl group was calculated to be 4.45 kcal/mol from the 264-cm^{-1} assignment.

C. CH_3POFCl. In the far-infrared spectrum of CH_3POFCl at $-190°$ (Figure 4) there are six bands. The bands below 150 cm^{-1} show an appreciable frequency shift with warming from -190 to $-80°$ and do not have counterparts in the Raman spectrum of the liquid phase so they are attributed to intermolecular motions. The bands above 150 cm^{-1} have essentially constant frequencies over the temperature range and have coincident lines in the Raman spectrum of the liquid which have been firmly assigned.[25] The lines at 242, 267, and 328 cm^{-1} must therefore be assigned as arising from the P-Cl bending, F-P-Cl bending, and P=O out-of-plane bending motions, respectively. No other bands were observed, even with a maximum thickness of sample. The band arising from the torsional motion is normally weak as compared to other fundamentals in the infrared spectrum and could reasonably be expected to fall in the 240-260-cm^{-1} range. It is possible, therefore, that the band from the torsional motion is hidden by one of the strong skeletal bending modes in this frequency region.

The reduced moment of inertia was calculated using the bond lengths and bond angles previously used for CH_3POCl_2 along with the F-P-Cl angles and distances from F_2ClPO and FCl_2PO.[38] The calculated F is 5.55 cm^{-1}. If the band from the torsional motion is not observed because it is hidden by the strong bands due to the phosphorus-halogen bending motions, the barrier to methyl rotation would be in the range of 3.5 to 4.5 kcal/mol.

D. CH_3POF_2. In a previous study of the Raman

(35) Q. Williams, J. Sheridan, and W. Gordy, J. Chem. Phys., 20, 164 (1952).

(36) L. S. Bartell and L. O. Brockway, ibid., 32, 512 (1960).

(37) H. K. Wong, Acta Chem. Scand., 19, 1232 (1965).

(38) L. O. Brockway and J. Y. Beach, J. Amer. Chem. Soc., 60, 1836 (1938).
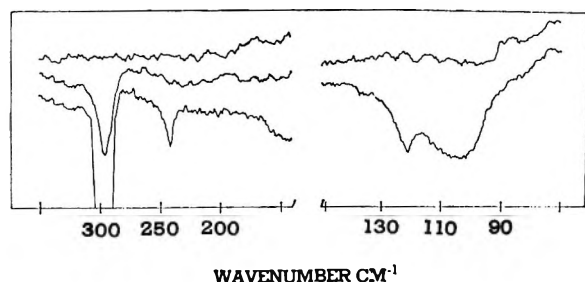
Figure 5. The far-infrared spectra of CH_3POF_2 taken at $-190°$. The upper curve is the cell background.

Figure 6. The far-infrared spectra of CH_3PSCl_2 taken at $-190°$. The upper curve is the cell background.

spectrum of liquid CH_3POF_2,[25] only one line was reported below 350 cm^{-1}. This line, at 287 cm^{-1}, was attributed to the PF_2 deformational motion. An analogous band at 294 cm^{-1} is observed in the infrared spectrum of CH_3POF_2 taken at $-190°$ (Figure 5) and it is attributed to the same motion. There are three other absorption bands observed in the far-infrared spectrum at 106, 122, and 240 cm^{-1}. The 106- and 122-cm^{-1} bands displayed a considerable frequency shift over the temperature range -190 to $-80°$ and must be attributed to intermolecular motions. However, the band at 240 cm^{-1} shows no appreciable frequency change over the temperature range, and must be considered due to an intramolecular mode. The only intramolecular mode which has not been assigned is the methyl torsional mode; therefore, 240 cm^{-1} is assumed to be the frequency of the methyl torsional motion of CH_3POF_2. The Raman spectrum of the solid had only lines which had been previously reported in the spectrum of the liquid.

Structural parameters for calculating the reduced moment of inertia of the methyl rotor were transferred from reported values for F_3PO[35] and $(CH_3)_3PO$.[37] The F–P–C angle was assumed to be the same as the F–P–F angle. The calculated F is 5.61 cm^{-1} and the barrier to rotation of the methyl group is 3.61 kcal/mol.

E. CH₃PSCl₂. It has been reported that in CH_3-$PSCl_2$ the low-frequency bending vibrations of the PS-Cl_2 group are best interpreted in terms of PX_3 bending vibrations.[25] The PX_3 bending vibrations would correspond to a PX_3 symmetric and antisymmetric deformation and a PX_3 rocking vibration, with the latter two vibrations giving rise to depolarized Raman lines. Only two Raman lines that could be attributed to PX_3 bending vibrations were observed in the spectrum of the liquid phase (265 and 187 cm^{-1}) and both were depolarized.[23] In the spectrum of the solid phase at $-190°$ the line corresponding to the 265-cm^{-1} line in the liquid was split into a doublet (259 and 268 cm^{-1}) and a very weak line was observed at 221 cm^{-1} (see Figure 2). The far-infrared spectrum of the solid at $-190°$ (Figure 6) contains four bands in the region expected for the PX_3 bending vibrations. Since these motions generally give rise to reasonably strong Raman lines, it must be concluded that the symmetric and anti-

symmetric deformational modes are giving rise to the 265-cm^{-1} Raman line in the spectrum of the liquid (259 and 268 cm^{-1} for the solid) and the 260- and 270-cm^{-1} bands in the infrared spectrum of the solid. The Raman line at 195 cm^{-1} and the infrared band at 198 cm^{-1} can then be attributed to the PX_3 rocking vibration. A study of the frequency of the unassigned infrared bands as a function of temperature over the range -190 to $-80°$ shows that the frequency of the 221-cm^{-1} band is essentially constant, whereas that of the 68-cm^{-1} band varies considerably. The frequency of the 221-cm^{-1} Raman line of the solid is also constant with varying temperature. The band at 221 cm^{-1} must be considered as arising from an intramolecular motion and since all of the modes which could reasonably be expected to give rise to bands in this frequency range have been assigned except the methyl torsional mode, the 221-cm^{-1} band is attributed to the methyl torsional motion.
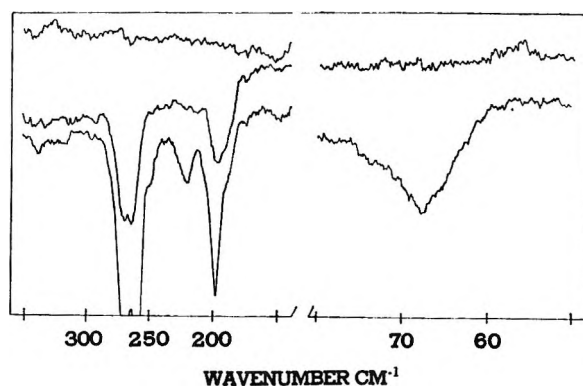
The structure used to calculate the reduced moment of inertia of the methyl group was basically that used for CH_3POCl_2 and CH_3PCl_2 with additional parameters being transferred from those reported for $(C_2H_5)_3PS$.[39] The calculated F is 5.5 cm^{-1} and the barrier to rotation of the methyl group was calculated to be 3.17 kcal/mol.

F. Lattice Modes. Lattice modes were observed in the spectra of all of the compounds. The spectra due to the intermolecular motions of CH_3POCl_2, CH_3POFCl, and CH_3POF_2 are all very similar so it is reasonable to conclude that the intermolecular forces for the solids are very nearly the same and the crystal structures are comparable. For these similar structures, the translational and librational modes can be distinguished by comparing the ratio of the frequencies with the square root of the inverse ratio of the masses (translational) and the square root of the inverse ratio of components of the moment of inertia about the principal axes (librational). On this basis the higher frequency bands, 113, 120, and 122 cm^{-1} in CH_3POCl_2, CH_3POFCl, and CH_3-

(39) M. von Meersche and A. Leonard, *Acta Crystallogr.*, 12, 1053 (1959).

Table III: Comparison of the Barriers to Internal Rotation of Some Similar Molecules

Hydrocarbons			Organophosphorus compd		
	Barrier, kcal/mol			Barrier, kcal/mol	
Molecule	Gas	Solid	Molecule	Gas	Solid
CH_3CH_3	2.928^a	3.24^b	CH_3PH_2	1.96^c	
$CH_3CH_2(CH_3)$	3.33^d	2.960^e	$CH_3PH(CH_3)$	2.22^f	2.22^g
$CH_3CH(CH_3)_2$	3.9^h	3.94^i	$CH_3P(CH_3)_2$	2.6^j	3.58^i
$CH_3C(CH_3)_3$		4.3^k			
CH_3CH_2Cl	3.71^l	4.48^m	CH_3PCl_2		3.37^o
CH_3CHCl_2	3.50^n	3.50^n			
CH_3CCl_3		5.49^n			
CH_3CH_2F	3.33^p				
CH_3CHF_2	3.18^q	3.97^r			
CH_3CF_3	3.25^s	3.29^n	CH_3POCl_2		4.45^o
			CH_3POF_2		3.61^o

[a] S. Weiss and G. E. Leroi, *J. Chem. Phys.*, **48**, 962 (1968). [b] R. R. Getty and G. E. Leroi, Symposium on Molecular Structure and Spectroscopy, The Ohio State University, 1969, Paper Q-7. [c] Reference 19. [d] E. Hirota, C. Matsumura, and Y. Morino, *Bull. Chem, Soc. Jap.*, **40**, 1124 (1967). [e] D. M. Grant, *et al.*, *J. Chem. Phys.*, **52**, 4424 (1970). [f] Reference 20. [g] Reference 21. [h] D. R. Lide, Jr., and D. E. Mann, *J. Chem. Phys.*, **29**, 914 (1958). [i] Reference 17. [j] Reference 22. [k] Reference 14. [l] W. G. Fateley and F. A. Miller, *Spectrochim. Acta*, **19**, 611 (1963). [m] Reference 18. [n] Reference 16. [o] This work. [p] G. Sage and W. Klemperer, *J. Chem. Phys.*, **39**, 371 (1963). [q] W. G. Fateley and F. A. Miller, *Spectrochim. Acta*, **17**, 857 (1961). [r] S. M. Craven, private communication. [s] C. A. Wulff, *J. Chem. Phys.*, **39**, 1227 (1963).

POF_2, respectively, appear to be due to librations about the c axis and the lower frequency bands can be attributed to translational motions. The low-frequency spectra of CH_3PCl_2 and CH_3PSCl_2 are not similar to each other or to the low-frequency spectra of the phosphonic compounds. On the basis of the frequency range of the translational and librational modes of the phosphonic compounds, it is more reasonable to assign the bands at 77 and 89 cm^{-1} in CH_3PCl_2 and 68 cm^{-1} in CH_3PSCl_2 to translational modes. Since there is no structural information available on the crystalline state of any of these compounds, all assignments of the intermolecular modes must be considered merely speculative.

The assignment of the Raman lines which appeared in the 50-cm^{-1} region of the solids is uncertain because of the frequent appearance of "ghosts" in this spectral region.

Discussion

The values of the methyl torsional barriers obtained in this study are summarized in Table II. The effect of the substitution of Cl for H can be seen by the comparison of the barriers of CH_3PH_2, 1.96 kcal/mol,[19] and CH_3PCl_2, 3.4 kcal/mol. Since the value for CH_3PH_2 is a gas phase value the barrier height difference cannot be entirely attributed to the substitution of Cl for H; however, the substitution may be tentatively said to raise the barrier height. The addition of oxygen to the framework of the molecule adds approximately 1 kcal/mol to the barrier height. This is analogous to the effect observed in solid phase DMS[28] and DMSO.[15] Replacing the Cl by F reduces the barrier as observed for CH_3POCl_2 and CH_3POF_2. Such an effect has also

been noted for the halocarbons.[40] Although the torsional frequency was not observed for CH_3POFCl, it is interesting to speculate about the height of the barrier. If the barrier height is midway between CH_3POF_2 and CH_3POCl_2, it would be 4.0 kcal/mol which would be a frequency of 248 cm^{-1}. There is some slight indication of a shoulder on the 242-cm^{-1} band in the far-infrared spectrum (Figure 4) but it could not be resolved. If the splitting of the modes observed for CH_3POCl_2 is taken as an indication of stronger intermolecular forces for this molecule over those for the other compounds and it is assumed that these forces raise the barrier height of CH_3POCl_2 slightly, the expected barrier height of CH_3POFCl would be lowered. The frequency would be accidentally degenerate with the 242-cm^{-1} band, and the torsional frequency could not be observed in the infrared spectrum of the solid. The addition of a sulfur atom to the CH_3PCl_2 molecule seems to have no appreciable effect upon the barrier height since it is lowered by only 0.2 kcal/mol.

The magnitude of the effects of the various substituents on the barrier heights may not be exactly the same as those for the isolated molecule but as pointed out with the example of DMS and DMSO, the direction of the barrier height shifts is expected to accurately reflect the isolated state and perhaps even the relative magnitude changes may be reasonably accurate. A microwave study of CH_3PF_2 and CH_3POF_2 might provide additional data on the effect on the barrier of the addition of an oxygen atom.

For the purposes of comparison we have compiled in Table III a list of experimental barriers of some similar

(40) G. Graner and A. Thomas, *J. Chem. Phys.*, **49**, 4160 (1968).

molecules. Previous trends proposed for the hydrocarbons seem to hold for the organophosphorus molecules.[40] For example, the replacement of F by a Cl increases the barrier by a few hundred calories in the hydrocarbons.[40] A similar increase is noted for the barrier in CH_3POCl_2 compared to that for CH_3POF_2. Replacement of H by Cl was also reported to raise the barrier in the hydrocarbons[40] and a similar trend is noted for the phosphorus compounds. It should also be noted that the replacement of a H by a methyl group appears to raise the barrier in both series. Several gaps appear in the phosphorus series and we plan further studies to substantiate the similarity of the trends in the two series.

Infrared Spectra of the Aluminum Family Suboxides[1]

by Daniel M. Makowiecki, Denis A. Lynch, Jr.,[2] and K. Douglas Carlson*

Department of Chemistry, Case Western Reserve University, Cleveland, Ohio 44106 (*Received October 9, 1970*)

Publication costs assisted by the National Science Foundation

Measurements and analyses of the infrared absorption spectra of the molecules Al_2O, Ga_2O, In_2O, Tl_2O, and InGaO isolated in inert gas and nitrogen matrices at liquid helium temperatures are described in this article. These experiments have been carried out in the region 2000–40 cm^{-1} for the purpose of measuring the previously unknown ν_2 bending mode and obtaining improved or new values for the ν_3 and ν_1 modes. The principal result of this investigation is that the ν_2 mode lies more than 200 cm^{-1} above energies expected on the basis of previous reasonable estimates. This result and other evidence suggest that a metal–metal bond is involved in the structure of these molecules. The following fundamental vibrational frequencies (cm^{-1}) listed in the order ν_3, ν_1, and ν_2 have been measured for an argon matrix: 991.7, 715.9, 503.0 (Al_2O); 822.6, 595.6, 416.5 (Ga_2O); 734.9, 555.1, 404.3 (In_2O); 643.6, 510.1, 381.5 (Tl_2O); 788.9, 550.5, 431.4 (InGaO).

Introduction

The suboxide molecules Al_2O, Ga_2O, In_2O, and Tl_2O have been studied over the past decade by a variety of methods. However, conclusions regarding their equilibrium geometry and molecular properties have had a controversial history. Prior to experimental evidence, it was assumed that Al_2O had a bent symmetrical C_{2v} structure,[3] and thermodynamic arguments based on bond dissociation energies were later shown to rule out asymmetrical conformations of the type C_s or $C_{\infty v}$.[4] Electric deflection experiments[5] reported in 1963, however, suggested that Al_2O possibly had a linear $D_{\infty h}$ structure. Infrared measurements based on the gaseous absorption method published in 1964[6] further indicated that Al_2O was linear while Ga_2O and In_2O were bent. In the same year, improved infrared experiments[4] based on the matrix isolation method[7] definitely established that Al_2O is bent with an apex angle near 145°.

The matrix isolation experiments also indicated that the ν_2 bending mode of Al_2O lay below 250 cm^{-1}. Such a low-lying value was subsequently found to be important to conclusions drawn from electron diffraction studies on Ga_2O and In_2O reported in 1965[8] and revised in 1968.[9] The first analysis led to bent symmetrical structures with apex angles of 130–160°, which are comparable with the value obtained from the infrared study of Al_2O. A later reassessment of the data led to the opposite conclusion that Ga_2O and In_2O are linear. This altered conclusion was based on an analysis taking into account large vibrational distortions arising from ν_2 frequencies estimated to lie considerably below 200 cm^{-1}.

(1) Supported by a grant from the National Science Foundation.

(2) NASA Graduate Trainee, 1967–1969; NSF Graduate Fellow, 1969–1971.

(3) J. Drowart, G. DeMaria, R. P. Burns, and M. G. Inghram, *J. Chem. Phys.*, **32**, 1366 (1960).

(4) M. J. Linevsky, D. White, and D. E. Mann, *ibid.*, **41**, 542 (1964).

(5) A. Buchler, J. L. Stauffer, W. Klemperer, and L. Wharton, *ibid.*, **39**, 2299 (1963).

(6) A. A. Mal'tsev and V. F. Shevel'kov, *Teplofiz. Vysokikh Temperature, Akad. Nauk SSSR*, **2**, 650 (1964).

(7) M. J. Linevsky, *J. Chem. Phys.*, **34**, 587 (1961).

(8) N. G. Rambidi and S. M. Tolmachev, *Teplofiz. Vysokikh Temperature, Akad. Nauk SSSR*, **3**, 487 (1965).

(9) N. G. Rambidi and Ym. S. Ezhov, *Zh. Strukt. Khim.*, **9**, 363 (1968).

In 1969, Hinchchliffe and Ogden[10] reported infrared measurements of the ν_3 fundamentals of matrix isolated Ga_2O, In_2O, and Tl_2O. From an analysis of the oxygen isotopic shifts on the basis of a C_{2v} structure, they obtained apex angles of 143, 135, and 131°, respectively, thus confirming the original conclusions of the electron diffraction study. Also in 1969, Shevel'kov, et al.,[11] detected both the symmetric and antisymmetric stretching frequencies in the infrared absorption spectrum of gaseous Tl_2O, which further supports a bent configuration. In addition to these fundamentals, a weak absorption in the region of 890 cm^{-1} also was observed. The investigators suggested that this may be the $\nu_3 + 2\nu_2$ combination band, which then places the ν_2 bending mode in the region of 130 cm^{-1}.

Very recently, Snelson[12] has published the results of a new infrared study on matrix isolated Al_2O. This investigation gave values for the $\nu_3(B_1)$ and $\nu_1(A_1)$ modes in good agreement with those obtained in the earlier matrix isolation experiments[4] and, in addition, indicated the absence of the ν_2 fundamental down as far as 190 cm^{-1}. Using an analogy with Li_2O, Snelson predicted the ν_2 band of Al_2O to occur near 120 cm^{-1}. On the basis of mass considerations alone, this would position the bending mode of the heavier suboxides below 100 cm^{-1}.

The purpose of this article is to summarize experiments carried out to measure these ν_2 bending frequencies for the complete series of group IIIA suboxides and to obtain improved or new values in the case of missing data for the ν_3 and ν_1 modes. During the course of this investigation, the new molecule InGaO was discovered and similarly studied.

Isolation Experiments

This investigation is based on the molecular beam sampling technique for measuring the infrared absorption spectra of molecules isolated in inert gas matrices at liquid helium temperatures.[7] The apparatus used in these experiments to produce and isolate the molecules consisted of a Knudsen-cell molecular beam source, a matrix gas source, and a cooled optically transparent condensation target. The basic features of this apparatus and its far-infrared capabilities are described in an earlier article by one of the authors.[13]

For the present experiments, the Knudsen cells were constructed with zirconia cups and lids of 1.2-cm diameter sheathed in close-fitting tantalum tubes which were sealed at both ends. The effusion orifice located in the side of the cup was approximately 1 mm in diameter. These cells and the heating devices were carefully constructed to minimize thermal gradients, to reduce radiant heating of the condensation target, and to maintain constant and precisely determined temperatures for reliable control of the amount of material deposited on the target.

The suboxide molecules were produced by vapor-

izing mixtures of the metal and solid sesquioxides contained in the Knudsen cells at temperatures between 724 and 1723°K. It is reasonably well established that zirconia cells are inert to the components of these systems and that the vapor species are predominantly the suboxide molecules with less than 10% metal atoms and no other significant species.[14,15] This was carefully confirmed, however, by an extensive mass spectrometric study carried out in collaboration with F. J. Kohl and C. A. Stearns of the NASA Lewis Research Center, Cleveland, Ohio. Table I summarizes, for example, the relative intensities and appearance potentials of the ion species measured for the vapors of the condensed $In–In_2O_3$ system at 1173°K. These data are typical of those determined for the other condensed-phase systems used to produce the various suboxide molecules. The temperature reported in this table represents approximately the mean temperature of the source in the matrix isolation study of the In_2O molecule over a range of slightly more than 50°. No significant enhancement in the relative ion intensities of the minor species was observed in the mass spectra over a temperature range of about 200°. In this mass spectrometric investigation, it was discovered that appreciable concentrations of the molecule InGaO along with smaller amounts of In_2O and Ga_2O in approximately the mole ratios 5:4:1, respectively, are produced by vaporizing In metal mixed with powdered Ga_2O_3.

Table I: Mass Spectrum of the Vapor over $In(l) + In_2O_3(s)$ at 1173°K (22-eV electrons)

Ion[a]	Relative intensity	Appearance potential	Probable parent
In_2O^+	1.0	8.3 ± 0.3	In_2O
In^+	7.5 × 10^{-1} [b]	5.79[c]	In, In_2O
In_2^+	9.2 × 10^{-2}	12.9 ± 0.5	In_2O
InO^+	1.6 × 10^{-3}	14.8 ± 0.5	In_2O
$In_2O_2^+$	3.2 × 10^{-4}	. . .[d]	In_2O_2
InO_2^+	1.4 × 10^{-6}	. . .[d]	In_2O_2 (InO_2?)

[a] No other ions containing metal atoms were detected up to $m/e = 350$; no oxygen ion species above normal background were detected. [b] The major portion (~90%) of the In$^+$ intensity was found to arise from fragmentation of In_2O. [c] Standard for calibration of the electron energy scale. [d] Intensity too low for reliable measurement.

(10) A. J. Hinchchliffe and J. S. Ogden, Chem. Commun., 18, 1053 (1969).

(11) V. F. Shevel'kov, N. A. Klyuev, and A. A. Mal'tsev, Vestn. Mosk. Univ. Khim., 24, 32 (1969).

(12) A. Snelson, J. Phys. Chem., 74, 2574 (1970).

(13) K. R. Thompson and K. D. Carlson, J. Chem. Phys., 49, 4379 (1968).

(14) R. F. Porter, P. Schissel, and M. G. Inghram, ibid., 23, 339 (1955).

(15) C. N. Cochran and L. M. Foster, J. Electrochem. Soc., 109, 144 (1962).

A knowledge of the amount of suboxide deposited and its isolation ratio were important quantities in these experiments. Since there is a serious problem with undersaturation in the vaporization process of these systems,[15] however, the true mole rates of effusion of the suboxide molecule and metal atoms were determined in a separate series of experiments. These measurements were carried out under conditions closely approximating those employed in the matrix isolation studies, and the results were used to establish the isolation ratios. These effusion experiments and the mass spectrometric analyses are to be described later in a separate publication.

The suboxide species were co-condensed with one of several purified gases for the matrix on the optically transparent condensation target, which was cooled with liquid helium. On the basis of a successful experiment employing Ne for the matrix, we estimate that the target was maintained at least as low as 10°K during the deposition in nearly all but the Al_2O experiments. The target was constructed of CsBr with outer windows of the same material for measurements in the region 4000–250 cm^{-1} or constructed from a thin sheet of polycrystalline Si[16] with windows of high density polyethylene for measurements in the region 450–40 cm^{-1}. The spectra were recorded in the range 2000–650 cm^{-1} with a Beckman IR-7 and in the range 800–40 cm^{-1} with a Beckman IR-11. These instruments were found to have a resolution and wave number accuracy within 1.0 cm^{-1} after calibration with atmospheric water and carbon dioxide.

Prior to each isolation experiment, the Knudsen cell and metal oxide sample were outgassed at temperatures in excess of that required for the deposition. Furthermore, the spectrum of the clean condensation target was recorded to confirm the absence of spurious absorptions. Then, the experimental matrix was prepared. Generally, infrared recordings were made of the initially deposited matrix, of the matrix during a slight warming up of the target to induce diffusion of the species, of the quenched matrix after diffusion, and of the target after the matrix had been allowed to vaporize. These diffusion experiments were carried out using the variable-temperature capability of the cryostat[13] to establish which bands belong to the monomer and to study other aspects of the matrix isolation. The annealed matrices in many cases led to a rather severe scattering of the infrared radiation.

Infrared Measurements

The matrix isolation experiments were carried out in a series of four sets of investigations. Generally, each set was characterized by a different experimental technique or objective, and each explored several different molecular species of interest. This approach, instead of one in which experiments for a single molecular species are carried to completion without later reexamina-
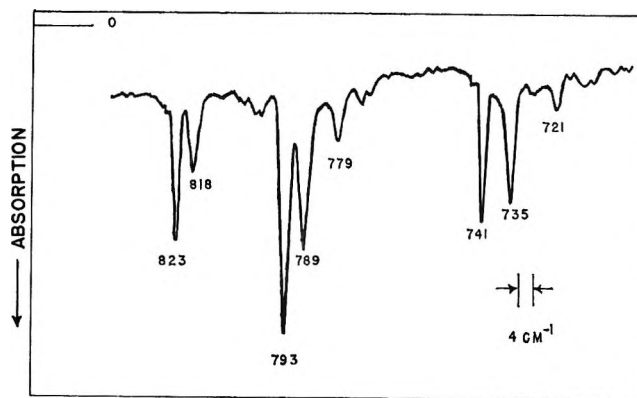
Figure 1. Infrared absorption spectrum of the molecular species of the InGaO system in Ar in the region 830–710 cm^{-1} (10-μmol total with $M/R = 620$).

tion, proved to be more efficient and very helpful in the identification of the new fundamentals and other features common to the spectra of all molecules under similar experimental conditions.

The first set employed CsBr for the condensation target and Ar for the matrix gas with M/R isolation ratios of 1030 for Tl_2O and 340–620 for the others for deposits of 5–13 μmol of the suboxide. Spectra were obtained in the region 2000–250 cm^{-1} for Ga_2O, In_2O, Tl_2O, Al_2O, and InGaO in that order without failure. The spectra of all but the mixed metal oxide displayed two prominent bands corresponding with the ν_3 and ν_1 modes reported for Al_2O in Ar by Linevsky, White, and Mann[4] and, except for a normal shift in frequencies, with the ν_3 mode of the heavier species in N_2 reported by Hinchchliffe and Ogden.[10] The spectrum of the InGaO system displayed five prominent bands, two corresponding exactly with the ν_3 and ν_1 of In_2O, one other of much smaller intensity corresponding with ν_3 for Ga_2O, and the remaining two occurring in regions expected for ν_3 and ν_1 of the mixed molecule. The relative intensities of the bands corresponded reasonably well with the known mole ratios after a matrix perturbation problem was accounted for. This helped to confirm the classification of these bands.

In addition to the two intense fundamentals, two other notable features common to all but the Al_2O spectrum were apparent. The first was that the bands classified as ν_3 were strongly split into doublets in each spectrum. This splitting is illustrated in Figure 1, which shows a tracing of the ν_3 spectra obtained in the first experiment of set 1 on the InGaO system in the region 830–710 cm^{-1}. In this figure, the doublet at 820 cm^{-1} belongs to Ga_2O, the doublet at 738 cm^{-1} belongs to In_2O, and the doublet at 791 cm^{-1} belongs to the InGaO molecule. Two satellite bands of smaller intensity are shown on the right of the doublets for InGaO and In_2O. In some respects, the doublet

(16) See footnote 12, ref 13.
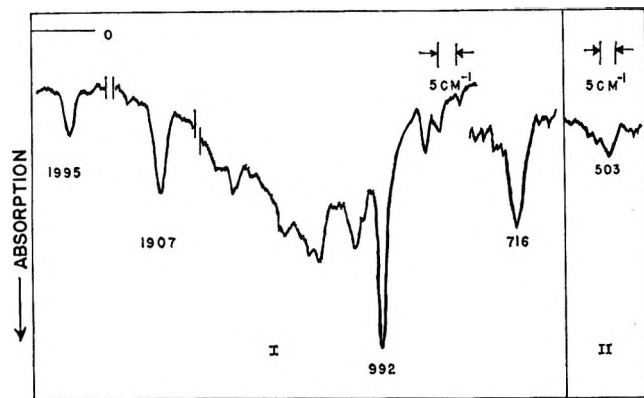
Figure 2. Infrared absorption spectrum of Al_2O in Ar in the region 2000–495 cm^{-1} (spectrum I with the IR-7 for 10 μmol at M/R = 390; spectrum II with the IR-11 for 2 μmol at M/R = 7700).

Figure 3. Infrared absorption spectrum of Ga_2O in Ar in the region 850–400 cm^{-1} (spectrum I with the IR-7 for 8.8 μmol at M/R = 750; spectrum II with the IR-11 for the same matrix).

Figure 4. Infrared absorption spectrum of In_2O in Ar in the region 980–380 cm^{-1} (spectrum I with the IR-7 for 13 μmol at M/R = 340; spectrum II with the IR-11 for the same matrix).

Figure 5. Infrared absorption spectrum of Tl_2O in Ar in the region 660–370 cm^{-1} (with the IR-11 for 5 μmol at M/R = 1030).

structures resemble metal isotopic splittings; however, such splittings would be expected only for Ga_2O which has the naturally occurring isotopes ^{69}Ga (60.4%) and ^{71}Ga (39.6%), but in this case the observed intensities are incorrect and the separations are too large. In no experiments of this or other sets were metal isotopic splittings resolved, although the structure of the ν_3 band in some of the Ga_2O experiments gave a hint of such splittings.

The second additional feature was the occurrence of a third less intense band at lower energies, which was very prominent at 381.5 cm^{-1} in the spectrum of the dilute Tl_2O and just barely observable (partly in retrospect) at 404.3 and 416.5 cm^{-1} in the more concentrated matrices of In_2O and Ga_2O, respectively. These bands are illustrated in Figures 2–5 and discussed later. A comparable band and the doublet splitting effect were not observed for Al_2O in this set. The intensities of all bands for each molecule were reduced in the diffusion experiments until they disappeared with the matrix. The diffusion process caused the bands of the ν_3 dou-

blet to sharpen, but their relative intensities and energy difference remained constant.

The second set of experiments also employed the CsBr optics for the same energy range but used both N_2 and Ar as the matrix gas with larger isolation ratios extending from 650 to 9000. In addition, the source temperatures of the suboxide beams in some experi-

ments were increased or decreased within a range of 50° to change the amount of material deposited in the matrix. Infrared measurements were carried out for In_2O, InGaO, and Tl_2O in that order, with several experiments being performed for each molecule in different dilute concentrations for different source temperatures. In the Ar experiments, no basically new features were revealed in the spectra, and all bands noted previously were obtained, including the unexplained third band in the region 381–417 cm^{-1}. However, the relative intensities of the two doublets of ν_3 were markedly different, and it was found that with increasing dilution one component of the doublet tended to disappear. In the N_2 experiments, the same spectral features were measured, except that the ν_3 band was not split. For this mode, a single sharply defined absorption was recorded at energies in close agreement with those reported by Hinchchliffe and Ogden.[10] Diffusion experiments gave results identical with those of the first set.

The CsBr optics were then replaced by the Si–polyethylene combination, and the investigations were extended down to 40 cm^{-1} in the third set of experiments. Isolation ratios varied between 350 and 6080 with Ar used as the matrix gas for deposits containing up to 45 μmol of the suboxide. Because its previous spectra had intense well-resolved bands, Tl_2O was investigated first in a series of two independent experiments. Only one band was observed in the region 450–40 cm^{-1}, and this corresponded precisely with the unexplained low-lying band at 381.5 cm^{-1} measured earlier with the CsBr optics. No hint of an absorption band in the region of 130 cm^{-1} was observed. The In_2O molecule was studied next in a series of four separate experiments. Again, only the previously measured absorption at 404.3 cm^{-1} was observed. It was then tentatively concluded that this and the comparable bands for the other molecules were the unknown ν_2 bending modes, although the difficulty with such an assignment was that this mode occurred more than 200 cm^{-1} above that predicted on the basis of reasonable arguments. The Al_2O molecule was then studied, and its infrared spectrum revealed no absorptions between 450 and 40 cm^{-1}. This is not surprising if the bands at 381–417 cm^{-1} are the ν_2 fundamentals of the heavier molecules.

Because no fundamentals below 250 cm^{-1} were detected, the CsBr optics were again installed to permit a more thorough investigation at high energies in the fourth set of experiments. In these experiments, a variety of matrix gases, isolation ratios, deposition rates, and other controllable factors were employed in attempts to increase the intensities and sharpen the bands. As a consequence, a set of much improved spectra were obtained which, in fact, clearly showed three fundamental absorption bands for all molecules including Al_2O. The low-lying ν_2 band of Al_2O was found to occur at 503 cm^{-1}, which is comparable with the similar bands of the heavier species. A tracing of the infrared spectrum of Al_2O in Ar between 2000 and 495 cm^{-1} is given in Figure 2, which shows the weak broad ν_2 band, the higher lying ν_1 and ν_3 fundamentals at 715.9 and 991.7 cm^{-1}, respectively, and two probable overtones along with some other weak structure. Similar spectra for Ga_2O, In_2O, and Tl_2O in Ar are given in Figures 3–5. Two of these figures show a more intense and better resolved ν_2 band for high dilution ratios, and all show the ν_3 doublet in Ar. Such a doublet splitting was never observed for Al_2O nor for other molecules with different matrix gases.

The results of the set IV experiments and evidence obtained earlier indicated that the method of preparing the matrix is critical in obtaining an observable ν_2 band. This band was most difficult to obtain for Al_2O, and the difficulty decreased down the series, which corresponds with a decreasing temperature required for the molecular beam source. Thus, there seems to be a deleterious effect on the matrix, probably involving a diffusion of molecules, caused by the heat radiated from the source. This suggestion is substantiated by the results of an experiment using Kr for the isolation of Al_2O. Under conditions otherwise similar to those of the Ar experiments, the ν_2 band in Kr was more intense, presumably because this heavier gas provides a more rigid matrix. The isolation ratio also was found to be important. The best procedure for preparation of the matrix was found to involve the rapid deposition of small amounts of suboxide (2–10 μmol) at fairly high dilution ratios (>1000). We believe that the difficulty of preparing a suitable matrix for the lighter molecules accounts for the apparent failure to detect, or at least identify, the ν_2 band in previous investigations.

Assignments and Analyses

The fundamental bands and other spectral features measured in this investigation are summarized in Table II for each matrix gas employed. Energies of the bands in the Ar matrix are given first for each molecule; then values obtained in experiments with other matrix gases and values taken from the available literature are reported below for comparison. The bands classified as fundamentals are listed according to their assigned vibrational mode. It is reasonable to assume from their intensities, from the results of the diffusion experiments, and from the mass spectrometric study that these bands are indeed the fundamentals of the suboxide monomer and not absorptions of impurities or other spurious bands. Absorptions which appear to be overtones and others such as satellite bands which cannot be classified are reported in the last column of the table. Presumably, some of these arise from matrix perturbations, which are rather common in such experiments.[13] An examination of the shifts in the fundamental bands with change in molecular weight of the matrix gas and a comparison of these shifts with

Table II: Infrared Bands of Matrix-Isolated Group IIIA Suboxides[a]

Molecule	Matrix	ν_3, cm^{-1}	ν_1, cm^{-1}	ν_2, cm^{-1}	Others[b]
Al₂O	Ar	991.7 (100)	715.9 (59)	503.0 (23)	$3\nu_1 = 1995.0$ (27), $2\nu_3 = 1907.4$ (55)
	Ar (lit.)[c]	994	715		$2\nu_3 = 1867$
	Kr	989.4 (100)	710 (65)	499 (42)	
Ga₂O	Ar	{822.6 (70) / 817.9 (50)}	595.6 (60)	416.5 (50)	$2\nu_1 = 1128.0$ (11), 832.1 (6), 827.1 (9), 810.8 (22), 803.5 (17)
	N₂	808.1 (72)	590.4 (100)	425.8 (39)	
	N₂ (lit.)[d]	809.4			
In₂O	Ar	{734.9 (100) / 741.3 (88)}	555.1 (76)	404.3 (16)	$2\nu_1 = 969$ (14), $2\nu_2 = 795$ (8), 728.9 (40)
	Ne	745.4 (100)	560.3 (48)	404.8 (43)	
	N₂	721.8 (100)	550.5 (52)	412.6 (29)	
	N₂ (lit.)[d]	722.4			
	Kr	728.2 (100)	551.7 (16)	403.2 (16)	
Tl₂O	Ar	{643.6 (100) / 659.8 (34)}	510.1 (100)	381.5 (57)	$2\nu_1 = 1006$ (5), 861 (3)[e] $2\nu_2 = 721$ (14), 714 (10)
	N₂	626.1 (100)	506.3 (38)	390.6 (13)	
	N₂ (lit.)[d]	625.3			
InGaO[f]	Ar	{788.9 (65) / 793.1 (100)}	550.5 (39)	431.4 (22)	779.2 (23), 720.9 (16), 570.8 (23), 542.7 (16)
	N₂	783.0 (100)	544.2 (44)		

[a] Numbers in parentheses are approximate relative absorption values. [b] These include overtones, satellite bands, and other unexplained bands obtained with Ar matrices. [c] Reference 4. [d] Reference 10. [e] This may correspond with the so-called combination band reported in ref 11. Possibly it is $\nu_1 + \nu_2$. [f] The InGaO spectra also include bands for In₂O and Ga₂O.

similar data for BeCl₂[17] suggest that the energies measured with Ar are closest to the gas phase values. The bands measured with N₂ appear to be shifted by increments larger than expected from mass considerations alone.

The assignments of the ν_3 and ν_1 modes rely in part on comparisons with the measurements based on oxygen isotopic enrichment experiments reported by others.[4,10] Where a direct comparison is available, the agreement is well within the experimental precision and accuracy. In other cases, the assignments are quite reasonable by analogy. Both components of the ν_3 doublets found only with the Ar matrix are given the same assignment, the second in order listed in the column being the component which tends to disappear with increased dilution. On this basis, the first component may be the "normal" ν_3 band, although this is questionable. It is interesting to note that this so-called "normal" band occurs at higher energies for Ga₂O but at lower energies for the other molecules.

The occurrence of this splitting and why it is observed only with the ν_3 mode in Ar matrices is perplexing. It apparent absence in Ne and the constancy of the relative intensities of the doublets after a diffusion experiment are not consistent with a molecular association phenomenon. Possibly the Ar atoms are just the right "size" to create multiple trapping sites in the matrix. The doublet splitting generally increases with increasing molecular weight, being 4.7 cm⁻¹ for Ga₂O, 6.4 cm⁻¹ for In₂O, and 16.2 cm⁻¹ for Tl₂O. This is reasonable because the heavier molecules have less

energetic vibrations, which would allow them to be more easily distorted to fit a solvent cage. However, the 4.2-cm⁻¹ splitting found for InGaO is essentially identical with that for Ga₂O rather than intermediate to that of either metal suboxide.

The assignments of the ν_2 mode may be debatable, but we can conceive of no other reasonable choice for the absorption bands in the region 503–381 cm⁻¹. These bands under satisfactory isolation conditions are quite prominent, are consistently reproducible with a variety of different experimental procedures, and appear to be related to the same species which produce the other two fundamental bands. That they are combination or overtone bands is improbable, since lower-lying fundamentals intense enough to produce such prominent absorptions should be easily detected. It is unlikely that such bands were accidently missed in every individual experiment in the several careful investigations carried out in the far-infrared region down to 40 cm⁻¹.

That these bands are a fundamental of some other molecule existing in the vapor or formed by reaction in the matrix also is improbable. According to the mass spectrometric analysis and the total effusion studies, metal atoms exist in less than 10% concentration in the vapor and other minor species exist in concentrations several orders of magnitude less over a wide temperature range. A reaction between the metal atoms and suboxide seems unlikely on the basis of the diffusion

(17) A. Snelson, *J. Phys. Chem.*, **72**, 250 (1968).

studies and thermochemical arguments. Furthermore, it is difficult to imagine that the vibrational modes of the minor oxide species have extinction coefficients many orders of magnitude greater than those of the suboxide to give such prominent absorptions. For example, the so-called ν_2 band of Tl_2O was readily apparent in these experiments with an absorption about 50% that of ν_1 for 1.6 μmol of the molecule at an isolation ratio of 8090. Comparably small amounts of the other suboxides give similar results. It seems unlikely that some major oxide molecule exists in the vapor which could not be detected mass spectrometrically because its positive ion is unstable. In any event, the relative intensities of the bands were not found to have any apparent dependence on the source temperature over a reasonably extended temperature range.

With regard to entropy arguments, the assignment of these bands as the ν_2 fundamentals leads to third-law values which are consistent with the available second-law entropies. However, nothing definitive can be concluded from such comparisons because second-law entropies of vaporization have not been established within better than 1–3 gibbs mol^{-1} and high temperature entropies of the condensed phases can only be estimated. The uncertainties in the second-law entropies of the gaseous suboxides are therefore large enough to encompass third-law values based on almost any reasonable estimate of the ν_2 fundamentals within a 300-cm^{-1} range.

The infrared spectrum obtained here for the InGaO system and the remarkably high energies measured here for the ν_2 bending modes have rather important structural implications. In the first case, the observation that there is only one detectable ν_3 band for the molecule identified as InGaO favors a structure involving a central oxygen atom. Otherwise, two closely spaced ν_3 bands should be detectable for the alternative configurations involving a terminal oxygen and two different selections of the neighboring metal atom. Since the spectrum of InGaO is quite similar to those of the pure metal suboxides, this observation gives added support to the conclusion that the other group IIIA suboxides have C_{2v} structures. The similarity is quite obvious. The ν_3 band of InGaO is intermediate to those of Ga_2O and In_2O, as expected. The ν_1 for this asymmetric molecule lies slightly lower than that of either symmetric species while the ν_2 lies slightly higher. In its general features, this shift in opposite directions is to be expected, since a change from the symmetric to asymmetric structure may be viewed in the sense of a perturbation which couples at least two modes, one certainly being the originally symmetric ν_1 stretch. Aside from this feature, all other bands for a given mode systematically decrease down the family series.

The unexpectedly high values for the ν_2 bending modes discredit the revised analysis[9] of the electron diffraction data which suggested a linear structure. The original conclusion is valid, and all other reliable measurements are in accord with a bent symmetric structure. The high ν_2 values furthermore suggest the occurrence of a metal–metal bond in these suboxides, giving a ring-type structure. There are several observations in evidence of this. First, atomization energies of all but Al_2O are in best agreement with bond energy calculations involving a metal–metal dissociation in addition to two metal–oxygen dissociations. Second, electron impact fragmentation of the M_2O species in the mass spectrometric studies give appreciable concentrations of the metal dimer ion M_2^+ but very much smaller concentrations of MO^+ except for Al_2O. Cubicciotti[18] was the first to point out the possible structural significance of this aspect in studies of Tl_2O. Third, the ν_2 bending frequencies are only slightly larger than reasonable values which have been estimated for the stretching frequencies of the homonuclear group IIIA metal diatomic molecules.[19]

Appreciable metal–metal bonding in these molecules should be reflected in the magnitude of the bending force constants derivable from a normal coordinate analysis. Unfortunately, we have insufficient data to employ the equations derived by Kohlrausch[20] for a C_{2v} ring-type structure, and equations based on simpler potential functions are notable failures, perhaps owing to abnormally large anharmonicities or matrix perturbations. The valence force description and central force model for an open structure are found to be totally inadequate. The former is reasonable for a bending frequency in the region of 250 cm^{-1} or lower, but not one appreciably higher. The possibility of a ring-type structure, however, is still reasonable, and it might consist of a π-bonding framework involving the p orbitals perpendicular to the plane of the triangle. Such a degenerate bond would involve no strain for a large apex angle at the oxygen atom and could be completely filled with the six valence electrons from the atomic p shells.

(18) D. Cubicciotti, *High Temp. Sci.*, 1, 11 (1969).

(19) W. A. Chupka, J. Berkowitz, C. F. Giese, and M. G. Inghram, *J. Phys. Chem.*, 62, 611 (1958).

(20) K. W. Kohlrausch, "Der Smekal-Raman-Effekt," J. Springer, Berlin, 1938, p 65.

Theory of Self-Diffusion in Three Model Dense Fluids

by Roger Brown

Department of Chemical Engineering

and H. Ted Davis*[1]

Departments of Chemical Engineering and Chemistry, University of Minnesota, Minneapolis, Minnesota 55455
(Received December 29, 1970)

Expressions for the self-diffusion coefficient for smooth, rough, and loaded hard spheres interacting according to the square-well potential model are obtained using Longuet-Higgins and Pople's scheme of approximating the velocity autocorrelation function by an exponentially decaying function. Adding roughness to a smooth sphere is found to decrease the self-diffusion coefficient while adding a load increases it. At low temperatures the "loaded" and "roughness" effects may be comparable, but at higher temperatures the effect of the roughness is considerably more important than the effect of the load for physically realistic values of the parameters defining the rough and loaded sphere models.

Introduction

Several authors have investigated the coefficient of self-diffusion for dense fluids interacting according to hard sphere[2,3] and square-well potentials.[4-6] While a smooth sphere with a square-well potential provides the qualitative features of a simple fluid of monatomic particles, it omits the effect of rotational degrees of freedom on diffusion. By adding a "load" to the sphere—*i.e.*, by assuming that the center of mass does not coincide with the geometric center of the spheres—one obtains the loaded sphere model which is capable of transferring rotational energy between colliding particles. Another model allowing transfer of rotational energy is the rough sphere model in which it is assumed the spheres have perfectly rough surfaces and the relative velocities of the points of contact of a pair of colliding spheres reverse. Using Boltzmann's and Enskog's kinetic equations, Dahler and coworkers[7] have studied the loaded sphere and rough sphere models extensively in the dilute gas limit and to some extent in the dense gas limit. Having no attractive interaction, these models may not give even a qualitative picture of transport in liquids. For example, it is not known whether adding an attractive potential to the rough and loaded sphere potentials will significantly alter the qualitative effects the "load" and "roughness" have on the transport properties of dense systems. The purpose of this paper is to investigate the effect an attractive potential has on the self-diffusion coefficient of these models.

Expressions for the self-diffusion coefficient for the various models are obtained using Longuet-Higgins and Pople's assumption[3] that the velocity autocorrelation function decays exponentially *via* binary collisions. It has been shown elsewhere[8] that this assumption leads to the same result for the self-diffusion coefficient as that obtained by Chapman and Enskog's first approximation to Enskog's kinetic equation.

Theory

Because the changes in the intermolecular potential occur as discontinuities, all collisions occur instantaneously. Therefore, the assumption that only binary collisions occur appears to be reasonable. One further assumption is that because of the density of the fluid, there is no correlation between successive binary collisions, *i.e.*, dynamically correlated successive collisions are neglected. At least in the case of smooth spheres there is some cancellation of the effects of consecutive collisions so that the binary collision assumption seems partially justified.

The starting equation in Longuet-Higgins and Pople's scheme is the autocorrelation function expression for the self-diffusion coefficient D

$$D = \frac{1}{3} \int_0^\infty \langle \mathbf{v}(0) \cdot \mathbf{v}(t) \rangle \mathrm{d}t \qquad (1)$$

where $\langle \ \rangle$ denotes an equilibrium ensemble average and $\mathbf{v}(t)$ is the velocity of the diffusing particle at time t. By assuming that the autocorrelation function decays exponentially they arrived at

$$D = \frac{\langle \mathbf{v}^2 \rangle}{3\zeta} \qquad (2)$$

(1) Guggenheim Fellow (1969–1970).

(2) See, for example, S. Chapman and T. G. Cowling, "The Mathematical Theory of Non-Uniform Gases," Cambridge University Press, Cambridge, 1939.

(3) H. C. Longuet-Higgins and J. A. Pople, *J. Chem. Phys.*, **25**, 884 (1956).

(4) H. C. Longuet-Higgins and J. P. Valleau, *J. Mol. Phys.*, **1**, 284 (1956).

(5) H. T. Davis, A. G. Rice, and J. Sengers, *J. Chem. Phys.*, **35**, 2210 (1961).

(6) I. McLaughlin and H. T. Davis, *ibid.*, **45**, 2020 (1966).

(7) D. W. Condiff, W. K. Lu, and J. S. Dahler, *ibid.*, **42**, 3445 (1965); J. S. Dahler and N. F. Sather, *ibid.*, **38**, 2363 (1963).

(8) R. Brown, unpublished work.

where the friction constant ζ is given by

$$\zeta = -\frac{1}{\langle \mathbf{v}^2 \rangle} \lim_{\Delta t \to 0} \left\{ \frac{\langle \mathbf{v} \cdot \Delta \mathbf{v} \rangle}{\Delta t} \right\} \qquad (3)$$

The quantity $\Delta \mathbf{v}$ is the change in velocity of a particle during a collision.

Without the square-well interaction the quantity in the braces of eq 3 is evaluated in terms of a binary collision of the spheres at contact. When the square-well interaction is added one must consider four types of binary collisions. Longuet-Higgens and Valleau[4] have discussed the four collisions in applying Longuet-Higgens and Pople's theory to hard sphere particles with a square-well attraction.

To briefly outline the possible types of collisions, let us recall that the square-well potential energy model is defined as follows

$$\phi(r_{ij}) = \infty \qquad r_{ij} \leq \sigma_1$$
$$\phi(r_{ij}) = -\epsilon \qquad \sigma_1 < r_{ij} \leq \sigma_2$$
$$\phi(r_{ij}) = 0 \qquad r_{ij} < \sigma_2$$

where r_{ij} is the distance of separation of the centers of particles i and j, and σ_1 and σ_2 are the repulsive and attractive diameters, respectively.

The four types of binary collisions for smooth, rough, and loaded spheres interacting with a square-well attractive potential are as follows. (1) Two smooth or loaded spheres initially approaching each other collide within their potential wells at a distance σ_1. The relative velocities of their centers of geometry are reversed. Two rough spheres will experience a reversal of their surface velocities at the point of contact. (2) The spheres separated by a distance greater than σ_2 approach each other and at $r_{ij} = \sigma_2$ an amount ϵ of potential energy is converted into translational energy for smooth and for rough spheres and to translational and rotational energy for two loaded spheres. (3) The spheres within the attractive radii are moving apart with more energy than is needed to escape the well. At a distance $r_{ij} = \sigma_2$ translational and rotational energy totaling ϵ of two loaded spheres will be converted into potential energy while only translational energy totaling ϵ of two smooth spheres or two rough spheres will be converted into potential energy. (4) The spheres are within each others attractive radii, initially moving apart with less energy than is needed to escape from the potential well. At a distance $r_{ij} = \sigma_2$, two loaded spheres will experience a reversal of the relative velocity of the points on their surfaces along the line between their centers, while two smooth or two rough spheres will experience a reversal of the relative velocity of their centers.

Since only self-diffusion is considered, the systems of smooth, rough, and loaded spheres are composed of identical particles. To describe completely the interaction of two smooth spheres it is necessary to describe the relative velocity and position of the centers of the spheres. Their relative position is handled by defining a unit vector $\mathbf{k}$ directed from the center of sphere 2 to the center of sphere 1. To describe the interaction of rough spheres 1 and 2 it is necessary to indicate their angular velocity vectors ω_1 and ω_2. For two loaded spheres we must also specify their orientations $\mathbf{e}_1$ and $\mathbf{e}_2$ and the distance ξ of the center of mass from its center of geometry.

To calculate the change in velocity of particle 1 upon collision with particle 2 for application in eq 3, we consider the force $\mathbf{F}_{ij}$ caused by particle 2 acting upon particle 1. Using the fact that $\mathbf{F}_{12}$ is an impulse we may integrate the laws of motion for linear and angular momentum over a time δt to obtain

$$\Delta \mathbf{v}_1 = -\frac{1}{m} \int_t^{t+\delta t} \mathbf{F}_{12} dt = -\frac{\mathbf{J}}{m}$$

$$\Delta \omega_1 = -\mathbf{I}^{-1}\xi \mathbf{e}_1 \times \mathbf{J} \quad \text{for loaded spheres}$$

$$\Delta \omega_1 = \frac{\sigma}{2I} \mathbf{k} \times \mathbf{J} \quad \text{for rough spheres}$$

where the vector $\mathbf{J}$ is the linear momentum exchange in the binary collision. The moment of inertia is a tensor $\mathbf{I}$ for loaded spheres and is a scalar I for rough spheres.

The laws of conservation of energy and momentum may be used to determine $\mathbf{J}$ as a function of the momenta and orientations of the colliding particles. The expressions for $\mathbf{J}$ are given in Table I for the various models studied. The symbol $\mathbf{v}_{21}$ in Table I denotes the relative velocity of the center of sphere 2 relative to the center of sphere 1. In the case of smooth and rough spheres

$$\mathbf{v}_{21} = \mathbf{v}_2 - \mathbf{v}_1$$

and in the case of loaded spheres

$$\mathbf{v}_{21} = \mathbf{v}_2 - \mathbf{v}_1 + \omega_2 \times \mathbf{e}_2 \xi - \omega_1 \times \mathbf{e}_1 \xi$$

The quantity $\mathbf{g}_{21}$ in Table I is by definition

$$\mathbf{g}_{21} = \mathbf{v}_{21} - \frac{\sigma}{2} (\omega_2 + \omega_1) \times \mathbf{k}$$

$\mathbf{g}_{21}$ is the relative velocity of the pair of points lying along the line of centers and on the surfaces of colliding spheres 1 and 2. The quantities μ_i appearing in Table I are defined by the expressions

$$\mu_1 = \mu_2 = \frac{2}{m}$$

$$\mu_3 = \frac{2}{m} + \mathbf{I}^{-1}:(\xi \mathbf{e}_1 \times \mathbf{k})(\xi \mathbf{e}_1 \times \mathbf{k}) +$$

$$\mathbf{I}^{-1}:(\xi \mathbf{e}_2 \times \mathbf{k})(\xi \mathbf{e}_2 \times \mathbf{k})$$

and the quantity κ is a reduced moment of inertia defined by

$$\kappa = \frac{4I}{m\sigma_1^2}$$

Table I: Momentum Exchange in the Four Binary Collisions for Smooth, Rough, and Loaded Spheres

Type of collision	Velocity limits	$\mathbf{J}$
	Smooth Spheres	
1	$\mathbf{v}_{21}\cdot\mathbf{k} > 0$	$-\dfrac{2}{\mu_1}\,\mathbf{k}\cdot\mathbf{v}_{21}\mathbf{k}$
2	$\mathbf{v}_{21}\cdot\mathbf{k} > 0$	$\dfrac{1}{\mu_1}\left\{-\mathbf{v}_{21}\cdot\mathbf{k} - \sqrt{(\mathbf{v}_{21}\cdot\mathbf{k})^2 + 2\epsilon\mu_1}\right\}\mathbf{k}$
3	$\mathbf{v}_{21}\cdot\mathbf{k} < \sqrt{2\epsilon\mu_1}$	$\dfrac{1}{\mu_1}\left\{-\mathbf{v}_{21}\cdot\mathbf{k} + \sqrt{(\mathbf{v}_{21}\cdot\mathbf{k})^2 - 2\epsilon\mu_1}\right\}\mathbf{k}$
4	$-\sqrt{2\epsilon\mu_1} < \mathbf{v}_{21}\cdot\mathbf{k} < 0$	$-\left(\dfrac{2}{\mu_1}\right)\mathbf{v}_{21}\cdot\mathbf{k}\mathbf{k}$
	Rough Spheres	
1	$\mathbf{v}_{21}\cdot\mathbf{k} > 0$	$-\dfrac{2}{\mu_2}\left(\dfrac{\kappa}{\kappa+1}\right)\left(\mathbf{g}_{21} + \left(\dfrac{1}{\kappa}\right)\mathbf{v}_{21}\cdot\mathbf{k}\mathbf{k}\right)$
2	$\mathbf{v}_{21}\cdot\mathbf{k} > 0$	$\dfrac{1}{\mu_2}\left\{-\mathbf{v}_{21}\cdot\mathbf{k} - \sqrt{(\mathbf{v}_{21}\cdot\mathbf{k})^2 + 2\epsilon\mu_2}\right\}\mathbf{k}$
3	$\mathbf{v}_{21}\cdot\mathbf{k} < \sqrt{2\epsilon\mu_2}$	$\dfrac{1}{\mu_2}\left\{-\mathbf{v}_{21}\cdot\mathbf{k} + \sqrt{(\mathbf{v}_{21}\cdot\mathbf{k})^2 - 2\epsilon\mu_2}\right\}\mathbf{k}$
4	$-\sqrt{2\epsilon\mu_2} < \mathbf{v}_{21}\cdot\mathbf{k} < 0$	$-\left(\dfrac{2}{\mu_2}\right)\mathbf{v}_{21}\cdot\mathbf{k}\mathbf{k}$
	Loaded Spheres	
1	$\mathbf{g}_{21}\cdot\mathbf{k} > 0$	$-\left(\dfrac{2}{\mu_3}\right)\mathbf{k}\cdot\mathbf{g}_{21}\mathbf{k}$
2	$\mathbf{g}_{21}\cdot\mathbf{k} > 0$	$\dfrac{1}{\mu_3}\left\{-\mathbf{g}_{21}\cdot\mathbf{k} - \sqrt{(\mathbf{g}_{21}\cdot\mathbf{k})^2 + 2\epsilon\mu_3}\right\}\mathbf{k}$
3	$\mathbf{g}_{21}\cdot\mathbf{k} < \sqrt{2\epsilon\mu_3}$	$\dfrac{1}{\mu_3}\left\{-\mathbf{g}_{21}\cdot\mathbf{k} + \sqrt{(\mathbf{g}_{21}\cdot\mathbf{k})^2 - 2\epsilon\mu_3}\right\}\mathbf{k}$
4	$-\sqrt{2\epsilon\mu_3} < \mathbf{g}_{21}\cdot\mathbf{k} < 0$	$-\left(\dfrac{2}{\mu_3}\right)\mathbf{g}_{21}\cdot\mathbf{k}\mathbf{k}$

In evaluating eq 3 we have followed the procedure outlined by Longuet-Higgins, Valleau, and Pople[2,9] in their study of smooth spheres. They assumed a Maxwell velocity distribution and defined the regions for which eq 3 is nonzero. Their assumptions are not affected by the addition of roughness or loading.

The diffusion coefficients obtained following the evaluation of eq 3 for the four types of collisions are for the square-well with smooth sphere core

$$D_1 = \frac{3}{8n\sigma_1^2}\left(\frac{kT}{\pi m}\right)^{1/2}[g(\sigma_1) + R^2 g(\sigma_2)\Xi]^{-1} \qquad (4)$$

for rough sphere core

$$D_2 = \frac{3}{8n\sigma_1^2}\left(\frac{kT}{\pi m}\right)^{1/2} \times$$
$$\left[\frac{2\kappa + 1}{\kappa + 1}\,g(\sigma_1) + R^2 g(\sigma_2)\Xi\right]^{-1} \qquad (5)$$

and for loaded sphere core

$$D_3 = \frac{3}{2U(\alpha)n\sigma_1^2}\left(\frac{kT}{\pi m}\right)^{1/2}[g(\sigma_1) + R^2 g(\sigma_2)\Xi]^{-1} \qquad (6)$$

where $R = \sigma_2/\sigma_1$, k is Boltzmann's constant, n is the number density of the fluid, $g(\sigma_1)$, $g(\sigma_2)$ are the pair distribution function values at $\sigma_1 + 0$ and $\sigma_2 + 0$

$$\Xi = e^{\epsilon/kT} - \frac{\epsilon}{2kT} - 2\int_0^\infty x^2\left(x^2 + \frac{\epsilon}{kT}\right)^{1/2}e^{-x^2}dx$$

$$U(\alpha) = \int_0^\pi \int_0^\pi [1 + \alpha(\sin^2\theta_1 + \sin^2\theta_2)]^{-1/2} \times$$
$$\sin\theta_1 \sin\theta_2\, d\theta_1 d\theta_2$$

$$\alpha = \frac{m\xi^2}{2\Gamma}$$

and Γ is the moment of inertia.

Discussion

Values of Ξ[10] and $U(\alpha)$[11] appear in Tables II and III.

Table II: Values of Ξ As a Function of ϵ/kT

ϵ/kT	Ξ
0	0.000000
0.10	0.008650
0.20	0.032386
0.30	0.070994
0.40	0.125149
0.50	0.195904
0.60	0.284573
0.70	0.392705
0.80	0.522073
0.90	0.674682
1.00	0.852779
1.10	1.058876
1.20	1.295767
1.30	1.566558
1.40	1.874694
1.50	2.223995
1.60	2.618690
1.70	3.063464
1.80	3.563500
1.90	4.124532
2.00	4.752905
2.10	5.455632
2.20	6.240471
2.30	7.116000
2.40	8.091701
2.50	9.178057

Theoretical values for $g(\sigma_1)$ and $g(\sigma_2)$ do not exist for the square-well potential so we use an approximation used with some success by Davis, Luks, and Miller in applying the square model to inert gas liquids. They approximated the contact value $g(\sigma_1)$ by

$$g(\sigma_1) = g^\circ(\sigma_1)e^{\epsilon/kT} \qquad (7)$$

(9) H. C. Longuet-Higgins and J. A. Pople, *J. Chem. Phys.*, **25**, 884 (1956).

(10) K. D. Luks, M. A. Miller, and H. T. Davis, *AIChE J.*, **12**, 1079 (1966).

(11) S. I. Sandler and J. S. Dahler, *J. Chem. Phys.*, **43**, 1750 (1965).

Table III: Values of $U(\alpha)$ As a Function of α

α	$U(\alpha)$
0.0	4.00000
0.0001	3.99973
0.001	3.99734
0.005	3.98674
0.01	3.97362
0.02	3.94781
0.03	3.92254
0.04	3.89780
0.05	3.87356
0.06	3.84980
0.625	3.84394
0.07	3.82652
0.08	3.80369
0.09	3.78130
0.167	3.62288

where $g°(\sigma_1)$ is the pair distribution function for a system of hard spheres interacting according to a purely repulsive potential. Moreover, since $g(\sigma_2)$ is never far from unity we shall set $g(\sigma_2) \equiv 1$ for the purpose of calculation. The trends to be observed will not be noticeably changed by this approximation.

If we define D^* as

$$D^* = \frac{3}{8n\sigma_1^2}\left(\frac{kT}{\pi m}\right)^{1/2}$$

we can make comparisons of the reduced diffusion coefficients D/D^* as functions of the reduced density $n\sigma^3$.

Finally, taking the Percus–Yevick theoretical value for $g°(\sigma_1)$, namely

$$g°(\sigma_1) = \frac{1 + \frac{1}{2}y}{(1 - y)^2}$$

where

$$y = \frac{\pi}{6} n\sigma_1^3$$

and taking $R = 1.85$, as is typical of inert gases, we calculate the values of D/D^* displayed in the form of generalized plots in Figures 1–4. For the purposes of comparing the effect of the addition of rotational degrees of freedom and an attractive potential applied to the diffusion of hard spheres, our assumed values of g and R should be adequate.

We are now able to examine the effect of the introduction of rotational modes and the addition of an attractive portion to the intermolecular potential of the basic hard sphere model. From Figure 4 it is evident that the square-well potential reduces the diffusion coefficient with a reduction of temperature for all the models. As temperature decreases at constant density, the translational energy of the molecules approaches the potential energy of the well. There is therefore greater cohesion between the molecules and a greater chance of
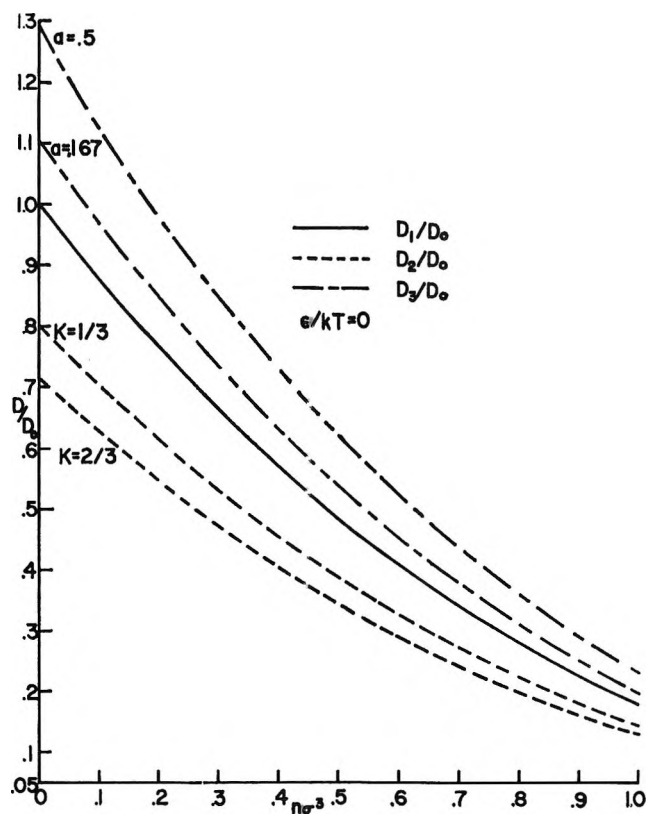
Figure 1. Reduced self-diffusion coefficients vs. reduced density for rigid, rough, and loaded spheres ($\epsilon/kT = 0$).
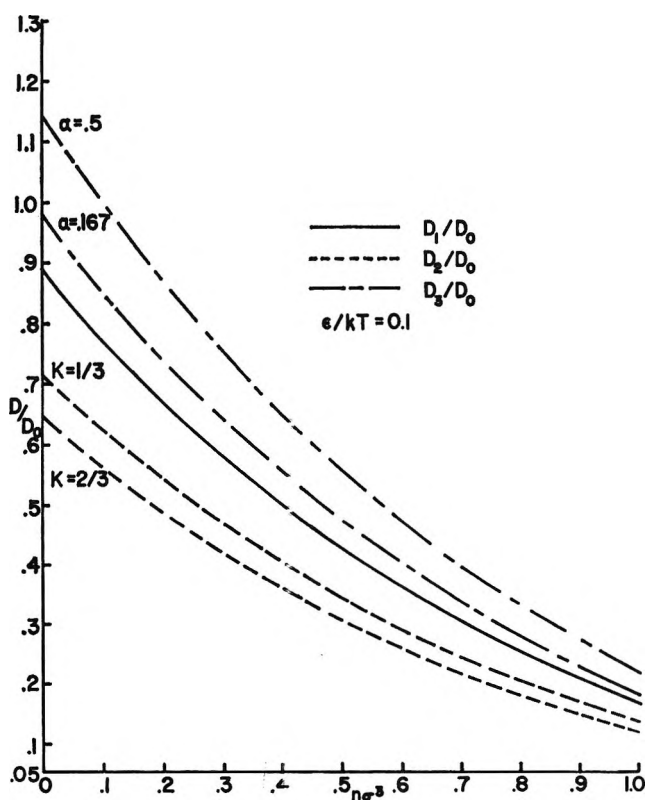
Figure 2. Reduced self-diffusion coefficients vs. reduced density for rigid, rough, and loaded hard cores with the reduced square-well attraction $\epsilon/kT = 0.1$.
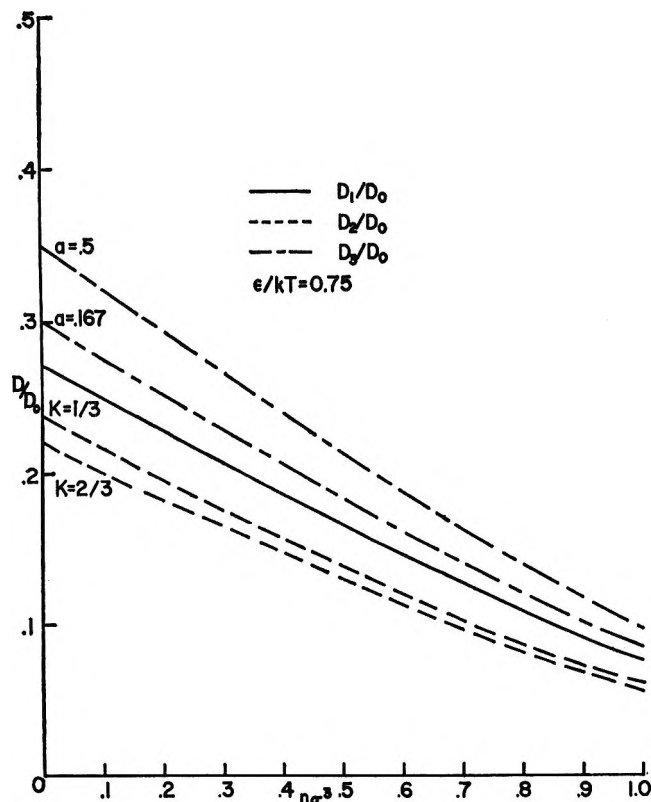
Figure 3. Reduced self-diffusion coefficients vs. reduced density for rigid, rough, and loaded hard cores with the reduced square-well attraction $\epsilon/kT = 0.75$.

Figure 4. Reduced self-diffusion coefficients vs. reduced density for rigid, rough, and loaded spheres for $\kappa = {}^2/_3$, $a = 0.5$, and several values of ϵ/kT.

back-scattering, hence the reduction of the diffusion coefficient. It is obvious from Figures 1–4 that the loaded sphere model increases the self-diffusion coefficient relative to the hard sphere model with an increase in the loading factor a, and that the rough sphere model decreases the self-diffusion coefficient with an increase in κ. Both models are similar in that they give a reduction in the diffusion coefficient with an increase in the moment of inertia.

There is apparently no simple physical explanation for the behavior of the loaded sphere model except to say that an increase in loading reduces the collision cross section and hence the chance of back-scattering.[12] The physically realistic upper limit of the loading factor a is 0.167 for HT which will raise the self-diffusion coefficient 9.5% over that of the hard sphere. Since adding a "load" to the hard sphere square-well model affects not only the type 1 hard sphere collision but also the collisions due to the square-well perturbation, we would expect the percentage change in the diffusion coefficient due to loading to be independent of temperature. This proves to be the case.

The rough sphere has the same collisional cross section as the smooth sphere, but its surface roughness increases the back-scattering effect of each collision. The physically realistic range of the reduced moment

of inertia is from 0 to ${}^2/_3$. Adding surface roughness to a smooth sphere affects only contact (type 1) collisions. Therefore we would expect that the percentage change in the diffusion coefficient due to roughness would decrease as the collisions due to the square-well (types 2–4) become more important; i.e., as temperature decreases. At $\epsilon/kT = 0$ there is a 28.6% decrease in the diffusion coefficient, while at $\epsilon/kT = 2.5$ there is only a 10.06% decrease.

On the basis of the models considered herein, we conclude that until the state of the art becomes such that calculations of liquid state diffusion coefficients are to better than 10% accuracy, inclusion of the effect of rotation does not seem worthwhile. In the high temperature region, however, the rotational contribution can be nearly 30% for rough spheres. Theories of simple dense gas transport can yield diffusion coefficients to better than 30% accuracy so that it is worthwhile to consider rotation at high temperatures.

(12) J. R. M. Miles and J. S. Dahler, *J. Chem. Phys.*, **52**, 1292 (1970).

Competitive Adsorption of Phenol and Sodium

Dinonylnaphthalenesulfonate on Nickel Oxide Powder

by Paul Kennedy,* Marco Petronio, and Henry Gisser

Pitman-Dunn Research Laboratories, Frankford Arsenal, Philadelphia, Pennsylvania 19137   (*Received November 23, 1970*)

Publication costs assisted by the Frankford Arsenal, U. S. Army

The adsorption of phenol at the nickel oxide–cyclohexane interface and the displacement of adsorbed phenol by sodium dinonylnaphthalenesulfonate were studied. The presence of physisorbed water on nickel oxide increased phenol adsorption. From adsorption isotherm plateaus, it was found that the cross-sectional area for phenol was 33.4 Å^2 on "dry" nickel oxide and 24.3 Å^2 on "wet" nickel oxide, corresponding approximately to tilted and vertical configurations in the adsorbed state. Adsorption on "wet" nickel oxide was not Langmuirian, but did follow the Frumkin isotherm, and it was found to be partly reversible, roughly corresponding to the excess adsorption promoted by physisorbed water. On "dry" nickel oxide, the adsorption was of the Langmuir-type. Competitive adsorption studies of phenol and sodium dinonylnaphthalenesulfonate on "dry" nickel oxide have indicated that competitive adsorption at high surface coverages deviated from Langmuir behavior. An approximate competitive adsorption equation, based on the Flory–Huggins isotherm, was developed to correct for the effect of adsorbate size on competitive adsorption. Competitive adsorption data fit this modified equation.

Introduction

High molecular weight alkylarylsulfonates, such as the salts of dinonylnaphthalenesulfonic acid, are effective corrosion inhibiting compounds for hydraulic and lubricating fluids. Although the actual mechanism is not well understood,[1] corrosion inhibition is related to close-packed monolayer formation which retards diffusion of corrodants to the surface and oxidation products from the surface. We have recently found[2] that the adsorption of salts of dinonylnaphthalenesulfonic acid on metal oxide powders follows a Langmuir model, and that close-packed monomolecular films (which may act as barriers) were formed at low concentrations. In technologically important lubricating systems, however, there is a multiplicity of polar additives that compete for adsorption, and this indicates that the composition of the mixed monolayer is a parameter of importance. In a study of competitive adsorption, Smith, Gordon, and Nelson[3] found that calcium dinonylnaphthalenesulfonate is displaced from the gold–white oil interface by a polyalcohol and poly(dodecylmethacrylate), and report that this adsorption is Langmuirian.

The purpose of this investigation was to study competitive adsorption and mixed film formation in technologically important situations (*e.g.*, mixed additive systems) on nickel oxide. Specifically, the competitive adsorption of phenol and sodium dinonylnaphthalenesulfonate in cyclohexane on nickel oxide powder was studied. The uv spectrum of phenol is sufficiently different from sodium dinonylnaphthalenesulfonate to facilitate mixture analysis. (Although phenol is not an effective antioxidant, this study was undertaken as preliminary to more extensive work on hindered phenols.) In this work, the adsorption characteristic of phenol was also determined in order to compare adsorption data for phenol with previously obtained adsorption data for sodium dinonylnaphthalenesulfonate, and thus develop a better insight into the competitive adsorption mechanism. Attention was also given to the effect of physisorbed water on phenol adsorption.

Experimental Section

Materials. The nickel oxide powder (Vitro Laboratories) used was prepared by a metal vaporization technique. The surface area as determined by BET measurements, using N_2 adsorption, was 36 m^2/g. "Instra-analyzed" grade cyclohexane (J. T. Baker) was used without further purification. Mallinckrodt reagent grade phenol (with H_3PO_2 preservative) was recrystallized three times from distilled water and after initial distillation of the aqueous azeotrope, a middle cut of the fraction distilling at 180° was taken. The absence of impurities was confirmed by vpc analysis. Sodium dinonylnaphthalenesulfonate was prepared from a purified sample of dinonylnaphthalenesulfonic acid (R. T. Vanderbilt) by a method previously described.[2] Analysis indicated that the purified salt contained $4.73 \pm 0.02\%$ sodium (calcd 4.76).

Adsorption Measurements. Adsorption data for phenol were obtained over the concentration range of

(1) R. R. Annand, R. M. Hurd, and N. Hackerman, *J. Electrochem. Soc.*, **112**, 138 (1965).

(2) P. Kennedy, M. Petronio, and H. Gisser, *J. Phys. Chem.*, **74**, 102 (1970).

(3) M. L. Smith, B. E. Gordon, and R. C. Nelson, *ibid.*, **69**, 3833 (1965).

0.02 to 1.0%. Volumes (10 ml) of the phenol–cyclo-hexane solution in small glass vials (fitted with Teflon liners) were equilibrated with 500 mg of nickel oxide (18 m²) for 5 days. (Initial adsorption of both phenol and sulfonate is very rapid. However, completion of the sulfonate required 2 hr as contrasted to several days for phenol.) This large surface area–volume ratio minimized the effect of any trace adsorption. The supernatant liquids, after separation as ascertained by the absence of the Tyndal effect, were analyzed spec-troscopically at 278 mμ, using a Beckman DK-2 re-cording spectrophotometer with matching 1-cm cells. Surface coverage was calculated from equilibrium data. Techniques used in the studies of the rate of adsorption, desorption by dilution, and effect of tem-perature were previously described.[2]

Competitive adsorption measurements require an accurate method of mixture analysis. The phenol–sulfonate system was found to be suitable for mixture analysis since phenol has a spike-like adsorption maxi-mum at 278 mμ with essentially no overlapping adsorp-tion at 284 mμ, which is an adsorption maximum for the sulfonate. In most experiments, phenol solution was added to the metal oxide and, after equilibration, sul-fonate solution was added. Data from reverse addition and simultaneous addition were similar. Sulfonate addition always resulted in the expected desorption of phenol and the amount of phenol desorbed increased with increasing sulfonate concentration in general accord with Langmuir theory. Experimentally, it is helpful to keep the initial concentration of one com-ponent constant so that the amount of desorption asso-ciated with an increase in the concentration of the other component could be accurately measured. The competitive adsorption experiments were run at less than full surface coverage in the range of fractional surface coverage values from 0.65 to 0.98.

Results and Discussion

The adsorption of phenol at the nickel oxide–cyclo-hexane interface was found to be complex and influenced by the amount of physisorbed water on the nickel oxide substrate. Phenol adsorption was measured on nickel oxide powder at varying states of dryness. These iso-therms are shown in Figure 1. Nickel oxide powder in equilibrium with atmospheric moisture (14 μmol of H_2O/m^2) was used in determining isotherm III. This amount of water corresponds approximately to mono-layer coverage and considerably complicates the inter-pretation of adsorption data since this amount of water is considerably in excess of the amount of water (0.015% by weight) necessary to saturate the phenol–cyclohex-ane solution. (This problem is not encountered in the sulfonate–cyclohexane system because the water is readily solubilized by sulfonate micelles.) The nickel oxide was partially dried at 110° for 1 hr (resulting in 3.0 μmol/m²) for determination of isotherm II and
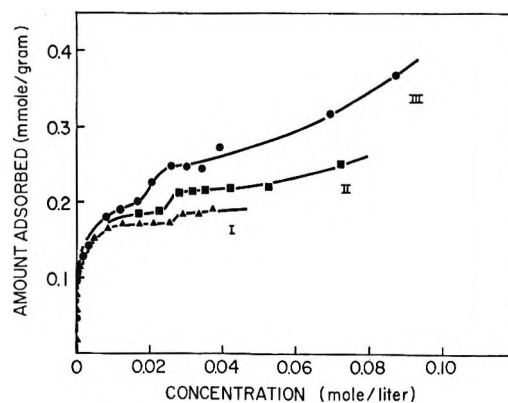
Figure 1. Phenol adsorption on nickel oxide powder. The three isotherms represent various amounts of physisorbed water on the surface: extensively dried powder (isotherm I), moderately dried powder (isotherm II), most of the surface covered by physisorbed water (isotherm III).

more vigorously dried at 120° under N_2 to constant weight (resulting in less than 1.0 μmol/m²) for deter-mination of isotherm I. Yao[4] reported a BET V_m value of 10.05 μmol/m² for physisorbed water on nickel oxide. Using this value, the surface coverage for the residual physisorbed water on the nickel oxide powders used in isotherms II and I were approximately 0.3 and less than 0.1, respectively.

Adsorption on Dry Nickel Oxide. Phenol adsorption on "dry" nickel oxide (isotherm I) is shown in Figure 1. Neglecting for the moment the presence of the small secondary plateau, isotherm I resembles a Lang-muirian adsorption, and, indeed, follows the Lang-muir relationship

$$\theta = KC(1 - \theta) \qquad (1)$$

where θ is the fraction of the surface covered, $(1 - \theta)$ is the fraction uncovered, C is the equilibrium concen-tration, and K is the adsorption coefficient or equilibrium constant. Equation 1 can be expressed as follows, and the data are shown in Figure 2.

$$C/(x/m) = 1/aK + C/a \qquad (2)$$

where x is the weight in grams of adsorbate on m grams of nickel oxide and a is the maximum value of x/m. Although it is realized that the system under study is much too complex to be explained in terms of the simple assumptions involved in the derivation of this relation-ship, Figure 2 does show that the ratio of the amount in solution to the amount on the surface does vary linearly with concentration. Adsorption constants were 33.4 Å²/molecule (as compared with 33.9 Å²/molecule as calculated from the first plateau of isotherm I, Figure 1) and 1.40 × 10³ l./mol. They represent the adsorp-tion at full and half surface coverage. In our opinion, phenol adsorption is due in part to attraction arising from the hydroxyl group. Thus, the orientation of

(4) Y.-F. Y. Yao, *J. Phys. Chem.*, **69**, 3930 (1965).
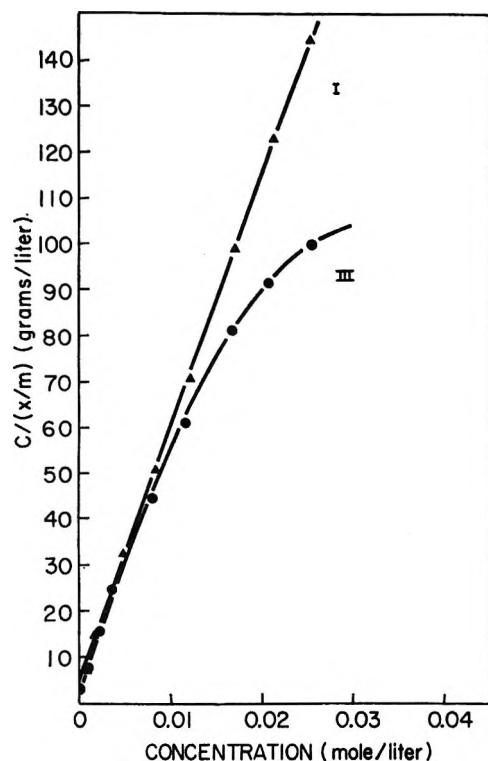
Figure 2. Langmuir plots of phenol adsorption: "dry" nickel oxide (isotherm I), "wet" nickel oxide (isotherm III).

phenol is probably tilted with the hydroxyl group pointed towards the surface. Theoretical cross-sectional areas for phenol (based on van der Waals radii) have been reported[5] as 21.7 and 41.0 Å^2 in the vertical and flat configurations, respectively. Our cross-sectional area compares closely with the value of 30.6 Å^2 as reported by Bykov and Presnyakova[5] where a similar orientation has been proposed.

For the adsorption of one component on more than one kind of elementary space, the adsorption isotherm developed by Langmuir[6] indicates that if the energies of adsorption on different sites are markedly different, adsorption will occur in definite steps as the concentration increases. Alternately, stepped isotherms on inorganic oxides have been attributed to reorientation of the molecules on the surface to become vertically oriented, thus increasing their lateral interaction.[7] The amount of physisorbed water introduced into the system via the metal oxide powder is in excess of the amount that can be solubilized by cyclohexane and suggests that at least some of the water remains on the metal oxide surface and that it participates in the adsorption process. Figure 1 indicates that phenol adsorption increases with increasing amount of physisorbed water on the surface. This observation is reasonable if it is assumed that the physisorbed water is evenly distributed over the surface and that the tilted configuration is the favored configuration for adsorption, but in the vicinity of a water molecule, phenol is forced to adsorb in a more tilted configuration. Hair

and Hertl[8] have shown that adsorbed water acts as a specific adsorption site for other molecules (e.g., benzene, ammonia).

Adsorption on Partially Dry Nickel Oxide. Isotherm II suggests a multilayer adsorption. Phenol adsorption on partially dry nickel oxide corresponds to a partially flat adsorption (32.0 Å^2) with exposure of the polar group for further hydrogen bonding. This decrease in the cross-sectional area for phenol suggests that as the concentration of physisorbed water at the interface increases, phenol assumes a more vertical orientation. Using molecular models, it can be shown that adsorption in the immediate vicinity of a bulky water molecule results in considerable steric hindrance.

Adsorption on Wet Nickel Oxide. The Langmuir plot (Figure 2) of the wet nickel oxide (isotherm III) is of interest because as θ increases, the adsorption coefficient decreases. As a first approximation, a linear variation of adsorption energy was assumed, since, in chemisorptive processes, a linear variation of the free energy of adsorption with coverage is frequently observed. A convenient relationship proposed by Biegler and Woods[9] (i.e., the basic assumption of the Frumkin isotherm) is

$$\Delta G^\circ_\theta = \Delta G^\circ_{\theta=0} + f_0 R T \theta \tag{3}$$

where ΔG°_θ is the standard free energy of adsorption at a surface coverage θ and f_0 is a constant related to an adsorption parameter such as a neighbor–neighbor interaction or a two-dimensional second virial coefficient.[10] $\Delta G^\circ_{\theta=0}$ represents the free energy of adsorption on the bare surface. Since the equilibrium constant in eq 1 is equal to $\exp(-\Delta G^\circ_\theta/RT)$, substitution of (3) into (1) gives the form of the Frumkin isotherm.

$$\frac{\theta}{1 - \theta} \exp(f_0\theta) = KC \tag{4}$$

Or in the more convenient logarithmic form, we have

$$\log C \frac{(1 - \theta)}{\theta} = f_0\theta \log e - \log K \tag{5}$$

The Frumkin plot of phenol adsorption on wet nickel oxide is shown in Figure 3 and suggests that the assumption of a variation in adsorption energy with respect to θ is reasonable. The adsorption coefficient was 3.25×10^3 l./mol compared with 1.40×10^3 l./mol on dry nickel oxide. This difference probably reflects the difference in configuration of phenol on the "dry" and "wet" surfaces. The linear variation of ΔG°_θ can

(5) V. T. Bykov and O. E. Presnyakova, *Kinet. Katal.*, **3**, 784 (1962).

(6) I. Langmuir, *J. Amer. Chem. Soc.*, **40**, 1361 (1918).

(7) S. A. Selim, R. Sh. Mikhail, and R. I. Razouk, *J. Phys. Chem.*, **74**, 2944 (1970).

(8) M. L. Hair and W. Hertl, *ibid.*, **73**, 4269 (1969).

(9) T. Biegler and R. Woods, *ibid.*, **73**, 3502 (1969).

(10) J. Lawrence and P. Parson, *ibid.*, **73**, 3577 (1969).
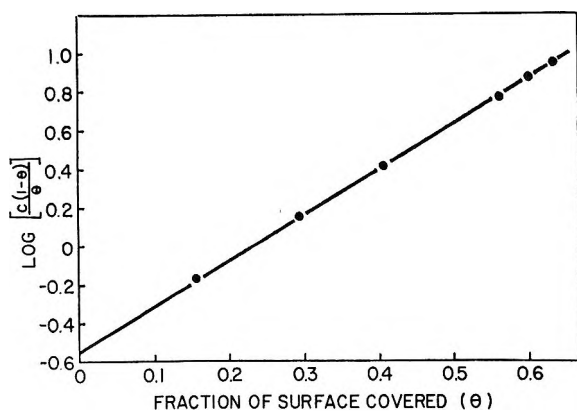
Figure 3. Frumkin plot of phenol adsorption on "wet" nickel oxide.

Figure 4. Desorption of phenol from nickel oxide powder. Each dilution represents a 75% reduction of the equilibrium concentration.

be made somewhat consistent with our model if it is assumed that $\Delta G^{\circ}{}_{\theta}$ is orientation dependent and that initial adsorption is flat, and subsequent adsorption results in progressively greater tilt. Comparison of the Langmuir and Frumkin adsorption coefficients is of questionable value. The Langmuir adsorption coefficient is an average value obtained at moderate surface coverages, and it is tacitly assumed that the adsorption coefficient on the bare surface is the same as on a moderately covered surface. The Frumkin adsorption coefficient applies only to initial adsorption and should theoretically be equal to the Langmuir coefficient; however, it can reasonably be assumed that initial adsorption on high-energy sites not reflected in the Langmuir equation is responsible for the difference in the two coefficients. The effect of adsorbed water and orientation on the value of the adsorption coefficient must be considered. The parameter f_0, which reflects the effect of physisorbed water on phenol adsorption, was 2.30. The positive slope indicates decreasing free energy with respect to coverage and is consistent with the above model.

Desorption Studies. The effect of an increased equilibrium temperature on promoting phenol desorption from dry nickel oxide was studied by determining the phenol isotherms at 22.5 and 34.6°. (Several hours was allowed for attainment of equilibrium at the higher temperature.) No significant difference was found, indicating that if there is any desorption at the elevated temperature, it takes place at a very low rate. Figure 1 suggests that a certain fraction of the phenol adsorbed on "wet" nickel oxide should be rapidly desorbable. Phenol desorption from "wet" nickel oxide was studied, using a dilution technique. The amount of phenol desorbed from the monolayer by each dilution is shown in Figure 4. Approximately $^1/_2$ of the monolayer was found to be desorbable by successive dilution of the equilibrium solution in contact with the monolayer. Approximately 13 mg of phenol per gram of nickel oxide was apparently irreversibly adsorbed. The plateau associated with adsorption on "dry" nickel
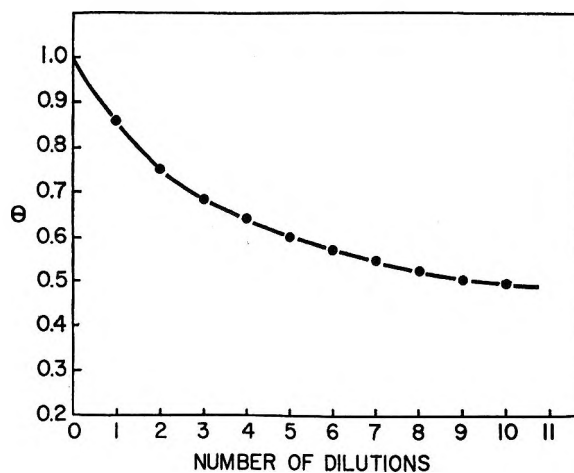
oxide (Figure 1) corresponds to approximately 17 mg per gram of nickel oxide. These studies suggest that the increased adsorption promoted by physisorbed water is a significantly weaker adsorption and is the reversible portion. A rough estimate of the equilibrium concentration at $^1/_2$ desorption indicates an adsorption coefficient of at least an order of magnitude less than the corresponding coefficients obtained from phenol adsorption measurements.

Competitive Adsorption. Langmuir adsorption theory can be applied to the special case of competitive adsorption in a system containing n components.[3] The rates of adsorption and desorption respectively of the ith component are given by

$$r_{a,i} = k_i C_i (1 - \sum \theta_i)$$
$$r_{d,i} = k_{-i} \theta_i$$

(6)

Equating rates and letting the ratio of the specific rate constants equal the adsorption coefficient, an adsorption equation similar to eq 1 is obtained

$$K_i C_i = \frac{\theta_i}{(1 - \sum \theta_i)}$$

(7)

For the ith and jth component in competitive adsorption eq 7 leads to

$$\frac{\theta_i}{K_i C_i} = \frac{\theta_j}{K_j C_j}$$

(8)

Competitive adsorption data for phenol and sodium dinonylnaphthalenesulfonate are shown in Figure 5, the broken line representing ideal behavior as predicted by eq 8. (The broken line in Figure 5 was drawn from the origin to the point of lowest surface coverage value obtainable with spectroscopic methods with the assumption that phenol-sulfonate interactions were negligible at this value.) The experimental points were obtained by keeping the initial concentration of phenol
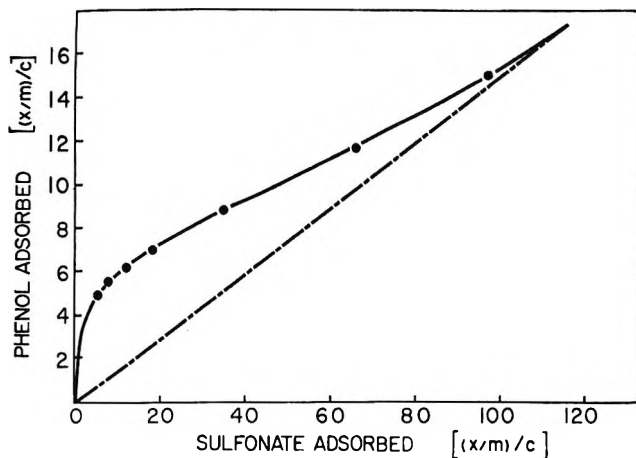
Figure 5. Competitive adsorption of phenol and sodium dinonylnaphthalenesulfonate. Dashed line represents behavior predicted by unmodified Langmuir theory.

Figure 6. Langmuir isotherms derived from competitive adsorption data: —●—●—, phenol; —■—■—, sodium dinonylnaphthalenesulfonate.

constant at 1.13×10^{-3} mol/l. The point farthest from the origin represents a mixed monolayer consisting of 0.70 sulfonate, 0.09 phenol, and 0.21 cyclohexane. As the initial concentration of sulfonate was increased, while keeping the initial concentration of phenol constant, the amount of phenol on the surface steadily decreased. The experimental deviation from ideality becomes clear when we consider the actual experimental system. If the adsorption of a minute quantity of phenol and sulfonate on a finite surface is considered, eq 8 would be valid since reduction of surface area available for adsorption is responsible for competitive effects. With increasing surface coverage, molecular interactions (attributed to the size effect) increase and result in a deviation from ideal behavior. The slope of the broken line in Figure 5 predicts that sulfonate adsorption is 6.5 to 13 times as strong as phenol adsorption. This is a reasonable estimate and can be compared with a value of 9.6 (on a weight basis) obtained from the ratio of the Langmuir coefficients which is obtained in turn from independent adsorption measurements.

Competitive adsorption was also studied at less than full monolayer coverage, and it was found that holding the initial concentration of one component constant was approximately equivalent to holding that surface coverage value constant. The per cent change in surface coverage was experimentally small. Because of this, Langmuir isotherms for phenol and sodium dinonylnaphthalenesulfonate could be derived from competitive adsorption data. These isotherms are shown in Figure 6. Data followed eq 2 except that a is now a reduced maximum adsorption equal to $a_t(1 - \Sigma\theta)$ when the initial concentration of one component is varied and the fraction of the surface covered by second component is considered constant. For example, in Figure 6, the maximum adsorption value is 6.14 mg/g for phenol compared with 16.84 mg/g for phenol from
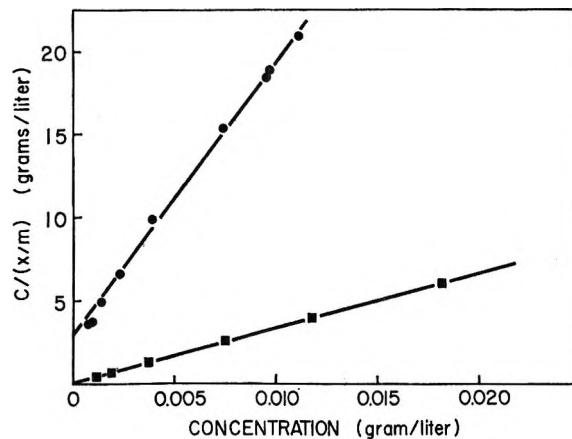
Figure 2. This reflects the reduction in surface area due to adsorption of 23.4 mg/g of sodium dinonylnaphthalenesulfonate. Using the above relationship, it is possible to calculate a value for the maximum adsorption of sulfonate close to the experimental value of 35.8 mg/g. Data shown in Figure 6 apparently contradict the data shown in Figure 5. Figure 6 indicates phenol and sodium dinonylnaphthalenesulfonate adsorption follow the Langmuir equation, but apparently do not follow eq 8 at high surface coverage values. This indicates that the basic assumptions made in the derivation of eq 8 need to be reconsidered, especially the assumption that at equilibrium a phenol molecule sees exactly the same number of sites as a sulfonate molecule. This would be true if the adsorbates are of the same molecular dimensions. However, it is known that the cross-sectional area of sodium dinonylnaphthalenesulfonate is considerably greater than phenol. (Sulfonate in the extended position[2] would occupy an area of ca. 100 Å^2 compared with 21.7–41.0 Å^2 for phenol depending on orientation.)[3] This size factor is not taken into consideration in eq 8. The sulfonate molecule is three times as large as the phenol molecule based on the experimentally found cross-sectional area of 33.4 Å^2. The failure of the competitive adsorption eq 8 to account for size differences can best be illustrated by considering the displacement of a phenol molecule from its close-packed monolayer by a sulfonate molecule. The probability that the vacant site (resulting from the desorption of one phenol molecule) will be occupied by a sulfonate molecule is zero and not some real value as predicted by the competitive adsorption eq 8. Three adjacent phenol molecules must desorb in order to have a site that is available to accommodate the sulfonate molecule.

The Flory–Huggins[10] isotherm takes into account the variation in size of the adsorbing species and has the form of

$$\frac{\theta}{r(1 - \theta)^r} = KC \qquad (9)$$

where r is the molecular size ratio of adsorbate to adsorbed solvent. Since phenol and cyclohexane have approximately the same cross-sectional area ($r = 1$), eq 1 is adequate in describing the adsorption of phenol and indicates that the quantity θ_p/C_p varies linearly with $(1 - \theta_p)$. For sulfonate adsorption eq 9 predicts that the quantity $(\theta_s/C_s)^{1/s}$ varies linearly with $(1 - \theta_s)$. This suggests that a competitive adsorption equation can be found by expressing both (θ_s/C_s) and (θ_p/C_p) as functions of the fraction of the surface area available for adsorption $(1 - \Sigma\theta)$. Equation 7 is approximately valid for phenol but not for sulfonate since its rate of adsorption is apparently not linearly dependent on the surface area available for adsorption. If experimental conditions are such that θ_s is considerably greater than θ_p, then $(1 - \theta_s)$ is approximately equal to $(1 - \Sigma\theta)$ and under these conditions an approximate competitive adsorption equation is

$$\left[\frac{\theta_p}{K_pC_p}\right]^3 = \frac{\theta_s}{3K_sC_s} \qquad (10)$$

This equation, useful only under restricted conditions, does reflect the "decreasing" adsorption of sulfonate at
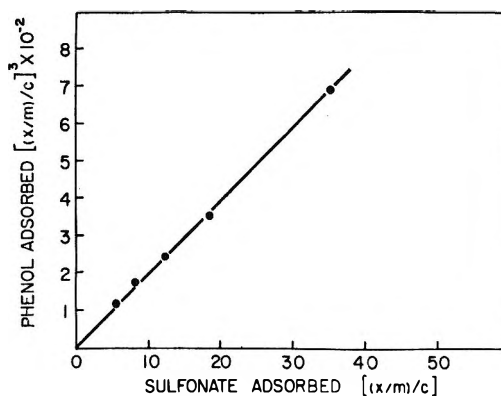
Figure 7. Competitive adsorption of phenol and sodium dinonylnaphthalenesulfonate using a modified competitive adsorption equation taking into account the relative difference in size of the two adsorbates.

high surface coverage values, which is the suspected cause of the nonideal competitive adsorption behavior. A plot of competitive adsorption data according to eq 10 is shown in Figure 7. The data are also shown in Figure 5 when plotted according to eq 8. This indicates that the cross-sectional area of the adsorbates is a parameter of importance in competitive adsorption studies.

On the Rates of Exchange between Free and Bound Counterions in

Polyelectrolyte Solutions.   I.   Electroosmotic Flows during

Determinations Made by an Electrical Transference Method

by Melvin H. Gottlieb

Laboratory of Physical Biology, National Institute of Arthritis and Metabolic Diseases,
National Institutes of Health, Bethesda, Maryland   20014   (*Received December 11, 1970*)

On the basis of a nonconventional type of electrical transference measurement, earlier workers[1] have concluded that the exchange between free and bound counterions in polyelectrolyte solutions is extremely slow. In this and the following paper, with Na–polyacrylate as the prototype polyelectrolyte, it is shown that the experimental results which led the earlier workers to this conclusion were a result of electroosmotically induced solution flows through a glass frit present in their transference cell, and that therefore the conclusion of a slow exchange rate is erroneous. The present paper experimentally demonstrates that a frit of the type used by the earlier workers is electroosmotically active in Na–polyacrylate solutions. It is also shown that flows of solution simultaneously take place in the anodic and the cathodic directions across the frit under the conditions of the transference experiments in question.

Introduction

Even in the absence of complex formation, polyelectrolyte salts behave as though a large fraction of the counterions are bound to the polyions.[2] Some 20 years ago, Wall and coworkers concluded, on the basis of indirect experimental evidence, that the exchange between free and bound counterions in Na–polyacrylate[1] and in Na–polyphosphate[3] solutions is very slow, with half-times in the range 2–20 min. This conclusion has been widely accepted.[2,4-8]

A slow rate of the exchange between the free and bound counterions is both intuitively unexpected and incompatible with present concepts of polyelectrolyte solutions. On theoretical grounds, Lifson and Jackson[9] show that the slow rate of the exchange cannot be accounted for by the entrapment of the cations in the electrostatic field surrounding the polyions. These authors also point out that even if there were ion-pair formation between the counterions and the ionized groups of the polyions, the exchange would be expected to be completed within the order of μseconds. Thus, either the slow rate of the exchange is a result of some completely unrecognized aspect of the chemistry of polyelectrolyte solutions, or Wall and coworkers incorrectly interpreted the results of their experiments.

Wall and coworkers reached their conclusion from a "nonconventional" type of electrical transference measurement which differed from conventional Hittorf transference measurements in two respects: (a) while conventional transference measurements are only concerned with *net* ionic movements, the "nonconventional" transference experiments of Wall and coworkers

concerned the *anodic and cathodic components* of the net counterion movements, and (b) their transference cell, shown schematically in Figure 1, utilized a glass frit to separate the anode and cathode compartments. This present paper will show that, as a result of electroosmosis, flows of solution simultaneously take place in the anodic and the cathodic directions across the frit under the experimental conditions of Wall, *et al.* The following paper[10] will show that these flows are large enough to account for results similar to those obtained by these workers. The third paper of the group[11] will experimentally demonstrate that the exchange is indeed much faster than concluded by Wall, *et al.* [We do not

(1) F. T. Wall and P. F. Grieger, *J. Chem. Phys.*, **20**, 1200 (1952); F. T. Wall, P. F. Grieger, J. R. Huizenga, and R. H. Doremus, *ibid.*, **20**, 1207 (1952).

(2) H. Morawetz, "Macromolecules in Solution," Interscience, New York, N. Y., 1965.

(3) F. T. Wall and R. H. Doremus, *J. Amer. Chem. Soc.*, **76**, 868 (1954).

(4) S. J. Gill and G. V. Ferry, *J. Phys. Chem.*, **66**, 995 (1962); G. V. Ferry and S. J. Gill, *ibid.*, **66**, 999 (1962); L. Noll and S. J. Gill, *ibid.*, **67**, 498 (1963).

(5) M. Spiro in "Techniques of Organic Chemistry," A. Weissberger, Ed., Vol. 1, Interscience, New York, N.Y., 1960, part 4, p 3096.

(6) M. L. Miller, "The Structure of Polymers," Reinhold Publishing Corp., New York, N. Y., 1966.

(7) (a) P. Meares in "Diffusion in Polymers," J. Crank and G. S. Park, Ed., 1968; (b) U. P. Strauss in "Characterization of Macromolecular Structure," National Academy of Science Publication, Washington, D. C., 1968.

(8) "Encyclopedia of Polymer Science and Technology," Vol. 1, Wiley, New York, N. Y., 1969, p 220.

(9) S. Lifson and J. L. Jackson, *J. Chem. Phys.*, **36**, 2410 (1962).

(10) M. H. Gottlieb, *J. Phys. Chem.*, **75**, 1985 (1971).

(11) M. H. Gottlieb, *ibid.*, **75**, 1990 (1971).
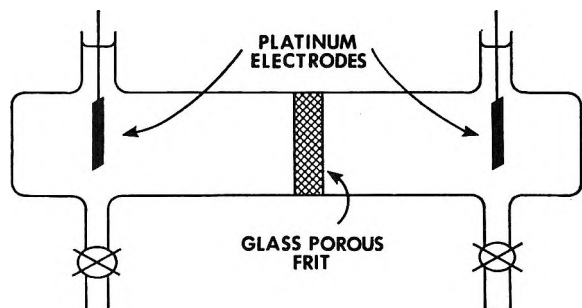
Figure 1. Schematic drawing of transference cell used by Wall and coworkers.[12]

criticize the conventional-type transference experiments (*i.e.*, concerned only with *net* ionic movements) on polyelectrolyte solutions made earlier in Wall's laboratory,[12,13] even though they too were made using a porous frit transference cell. We have confirmed the conventional-type transference results of Wall and Hill,[13] using a transference cell which had no porous frit (M. H. Gottlieb, unpublished results), and Brady and Salley[14] had earlier successfully used a similar porous frit cell for conventional-type transference determinations with simple electrolytes. The validity of the conventional-type transference measurements is readily understandable, since as will be shown later in the paper, the simultaneous flows in the anodic and cathodic directions across the frit are essentially equal to one another, and therefore do not produce *net* transfer of electrolyte.]

Flows to Be Expected in the Transference Cell of Wall and Coworkers

Despite the fact that glass frits are known to be electroosmotically active over a wide range of conditions, no *net* solution transfer across the frit was observed by Wall, *et al.*[12] Referring to Figure 1, the probable explanation for this is that net electroosmotic flow, occurring at the start of an experiment, produced a difference of solution levels between the cell compartments which, although seemingly too small to be casually noted, was sufficient to prevent further net solution movement across the frit. As discussed below, the absence of net flow across the frit as a whole does not mean the absence of flows through individual pores of the frit.

Consider first a single, cylindrical pore. Electroosmotic flow opposed by pressure is usually treated for conditions in which the opposing pressure is less than, or just equal to, that required to halt the flow.[15] The net flow through the pore is the sum of a *primary* electroosmotic flow (*i.e.*, that which would occur against zero pressure), w_p, given by the Helmholtz equation

$$w_p = \frac{D\zeta r^2 E}{4\eta l} \qquad (1)$$

and of a *backflow*, w_b, proportional to the opposing pressure, P, and given by Poiseuille's law

$$w_b = \frac{\pi P r^4}{8\eta l} \qquad (2)$$

Here D is the dielectric constant of the solution, ζ the potential difference across the movable part of the electrical double layer at the pore wall, r the pore radius, E the potential difference across the length, l, of the pore, and η is the solution viscosity (assumed Newtonian). From eq 1 and 2, P_E, the pressure at which the net flow through a pore ceases, is given by

$$P_E = \frac{2D\zeta E}{\pi r^2} \qquad (3)$$

Accordingly if the opposing pressure, P, is smaller than P_E, there is a net flow through the pore in the direction of the primary electroosmotic flow. Conversely an opposing pressure greater than P_E results in a net flow in the direction of the backflow. Most importantly, according to eq 3, the value of P_E depends strongly on the pore radius.

Consider now electroosmotic flow opposed by pressure across a porous frit. While a frit has a very complex pore structure, for present purposes we need only recognize that the pores have a range of (effective) radii, and divide them into three classes: the first consisting of narrow pores, with radii such that the P_E values are greater than the opposing pressure; the second with pores of a radius such that the P_E value is just equal to the opposing pressure; and the third with wide pore radii and P_E values less than the opposing pressure. From the previous discussion, net flow in the direction of the primary electroosmotic flow takes place through the narrow pores, no net flow occurs through those pores whose P_E value is equal to the opposing pressure, and a net backflow takes place through the wider pores.

Thus when electroosmotic flow across a heteroporous frit is opposed by pressure, the net flows through the various pores of the frit may differ in both magnitude and direction. Accordingly, when the pressure is great enough to prevent net flows across the frit as a whole, as is postulated in the present instance, the absence of net flow across the frit is a result of the counterbalancing of net flows in one direction through some of the pores, by net flows in the other direction through other pores.

Experimental Demonstration of the Flows

The polyelectrolyte most extensively studied by Wall, *et al.*, Na–polyacrylate, was chosen as the prototype polyelectrolyte for our experiments. First, to

(12) J. R. Huizenga, P. F. Grieger, and F. T. Wall, *J. Amer. Chem. Soc.*, **72**, 2636 (1950).

(13) F. T. Wall and W. B. Hill, *ibid.*, **82**, 5599 (1960).

(14) A. P. Brady and D. J. Salley, *ibid.*, **70**, 914 (1948).

(15) More detailed treatments of electroosmotic flow and other electrokinetic phenomena are available in standard textbooks, *e.g.*, S. Glasstone, "Textbook of Physical Chemistry," Van Nostrand, New York, N. Y., 1940.

directly demonstrate that a frit of the type used by these workers is indeed electroosmotically active in Na–poly-acrylate solutions, it will be shown that a net flow takes place across the frit when current is passed in a cell in which (unlike the cell of Wall and coworkers) the solution movement does not produce a hydrostatic pressure difference between the two compartments. This flow will be referred to as the *primary electroosmotic flow* across the frit.

To demonstrate and measure the simultaneous flows in the anodic and cathodic directions across the frit in a cell of the type used by Wall *et al.*, (Figure 1), a non-electrolyte was added to the Na–polyacrylate solution to serve as a tracer for the flow in each direction; q^0, the quantity of nonelectrolyte moving across the frit in a given direction, is related to the solution flow in that direction, v_s, by

$$q^0 = v_s c^0 \qquad (4)$$

where c^0 is the concentration of nonelectrolyte in the pore solution, which can be assumed to be the same as in the bulk solution.

The determinations of both the rates of primary electroosmotic flow across the frit, and of the flows which simultaneously take place in the anodic and cathodic directions under the conditions of the transference measurements of Wall, *et al.*, were accompanied by parallel measurements with solutions of a simple electrolyte, Na_2SO_4.

Experimental Section

Materials. Polyacrylic acid was obtained through the courtesy of B. F. Goodrich Co., Cleveland, Ohio (Goodrite K-702), and was extensively dialyzed against distilled water. Standard elemental analysis showed C 49.74%, H 5.57% (theoretical for $C_3H_4O_2$: C 50.00%, H 5.59%); the neutralization equivalent was 72.2 (theoretical 72.06). The viscosity of a 4.4% solution, using an Ostwald viscometer, was 4.26 cP, corresponding to a degree of polymerization of about 10,000.[16]

Radiotracers for the nonelectrolytes used, urea and glucose, were obtained as ^{14}C labeled material, from Nuclear-Chicago Corp., DesPlaines, Ill.

Porous Frits. The porous frits used were similar to those described by Wall and coworkers, *i.e.*, about 3 mm thick and of the "coarse" porosity grade supplied by Corning Glass Works, Corning, N. Y. The maximum pore diameter in such frits is 50 μ.[17]

Measurements. All measurements were made at room temperature, 23 ± 2°.

Primary Electroosmotic Flow. The cell used, illustrated in Figure 2, principally differs from that used by the previous workers (Figure 1) in having a horizontal side arm, 2 mm i.d. Movement of solution across the frit thus only displaced the meniscus in this side arm and did not change the solution level. The other compartment had a large diameter opening (2.5 cm), and only a
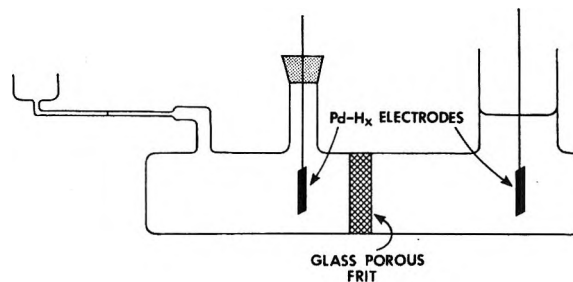
Figure 2. Schematic drawing of cell used to measure primary electroosmotic flows.

negligible (0.1 mm) change in its solution level occurred with the quantity of solution transferred in a determination 0.052 ml (see below). The dimensions of the cell were similar to those of the cell used by the earlier workers, diameter 2.5 cm, length 10 cm.

To avoid gas evolution, palladium–hydrogen (Pd–H_x) electrodes[18] were used instead of platinum electrodes.

"Sticking" of the meniscus in the horizontal side arm was tested for by noting the sensitivity of the position of the meniscus to small changes in the volume of solution in the cell. No difficulties were encountered with the Na–polyacrylate solutions; those encountered with the Na_2SO_4 solution were eliminated by addition of a small quantity of nonionic surface active agent to the region of the meniscus.

Currents were in the range 2–20 mA, the actual values chosen so that the meniscus in the horizontal tubing moved a distance of 2.0 cm (corresponding to a solution volume movement of 0.052 ml) in 10–20 sec. The rate of movement of the meniscus was determined for several reversals of current; rates in the two directions agreed to within 5%. With a given solution, the rates of electroosmosis were proportional to the current.

The resistances of the solutions were measured by the ac bridge method.

Simultaneous Solution Flows in the Anodic and Cathodic Directions in a Cell Similar to That of Wall and Coworkers (Figure 1). The dimensions of the cell were similar to that described by these workers, diameter 2.5 cm, length 10 cm; platinum electrodes were used.

The movements of nonelectrolyte across the frit, used to measure the flows, were determined radioisotopically. The nonelectrolyte was present at the same concentration, 0.01 M, in both cell compartments, being radioactively labeled in one of them. In one determination the electrode in the labeled compartment was made the anode, and the movement of nonelectrolyte across the frit in the cathodic direction was computed from the radioactivity of the cathode compartment

(16) A. Katchalsky and H. Eisenberg, *J. Polymer Sci.*, **6**, 145 (1951).

(17) Corning Glass Works Catalog LG-3, p 216.

(18) R. Neihof and S. Schuldiner, *Nature*, **185**, 526 (1960).

after the passage of current. The movement of non-electrolyte across the frit in the anodic direction was analogously determined in a second experiment (using fresh solutions), in which the electrode in the labeled compartment was made the cathode.

The detailed experimental procedures followed those of Wall, et al., in their determinations of radiotracer Na$^+$ ion movements in the transference experiments in question.[1] In particular, the solutions were not stirred, and the cells were filled so that the solution in the pores of the frit at the start of the experiment was radioactively labeled. Also following the procedure of the previous workers, all determinations were corrected for by the radiotracer movements found in control experiments in which no current was passed; in all cases this correction amounted to less than 10%. The error in the determinations of the radioactivity contents of the solutions is estimated as ±2%.

Measurements were made with two nonelectrolytes, urea and glucose, to permit effects of binding between the nonelectrolyte and ions to be recognized. The current was the same as that used by Wall, et al., 4.0 mA, and was passed for the longest time period of their measurements, 2.0 hr.

Results and Discussion

The *primary electroosmotic flow*, i.e., the net flow observed in the cell shown in Figure 2, was towards the cathode in all cases. Data for a series of Na–polyacrylate solutions in which the total polyacrylic acid concentration was 0.038 N are given in Table IA; data for 0.025 N Na$_2$SO$_4$ solutions of two pH values are given in Table IB. Assuming that the specific resistance of the solution in the pores is the same as that of the bulk solution, the quantity listed in the fifth column, W/ρ, is proportional to the primary electroosmotic flow per unit voltage difference across the frit.

Table I: Rates of Primary Electroosmotic Flow

Percentage neutralization	pH	ρ, specific resistance of solution, ohm-cm $\times$ 10^{-3}	W, primary electro-osmotic flow across frit, cm^3 amp^{-1} sec^{-1}	W/ρ, cm^2 sec^{-1} V^{-1} $\times$ 10^3
A. Na–PAA Solutions, Total Polyacrylic Acid Concentration 0.038 N				
20	5.08	2.28	0.93	0.41
40	5.94	1.44	0.65	0.45
80	7.89	1.05	0.45	0.43
98	8.75	1.00	0.45	0.45
B. Na$_2$SO$_4$ Solutions, 0.025 N				
	5.53	0.413	0.043	0.11
	9.01	0.376	0.040	0.11

The most significant aspect of the data of Table I

is that appreciable primary electroosmotic flows occurred with all Na–polyacrylate solutions studied. It can thereby be concluded that the porous frit of the cell used by Wall and coworkers was electroosmotically active under the conditions of their transference measurements, and that the absence of net flow was a consequence of a backflow of solution.

Table I also shows that the rates of primary electroosmotic flow in the Na–polyacrylate solutions are much greater than those in the Na$_2$SO$_4$ solutions, both on a unit current basis, column 4, and on the basis of the more significant quantity (cf. eq 1) of flow per unit voltage difference across the frit, W/ρ (column 5). This is probably the result of adsorption of polyacrylate ions onto the pore walls, which thereby increases the ζ potential.

We next turn to the *flows of solution which simultaneously take place in the anodic and the cathodic directions across the frit in the cell similar to that used in the transference determinations of Wall and coworkers*, i.e., that shown in Figure 1. In Table II data are shown for 0.045 N Na–polyacrylate solutions of three degrees of neutralization, and for a 0.025 N Na$_2$SO$_4$ solution.

Table II: Simultaneous Flows in Anodic and Cathodic Directions in the Cell Similar to That Shown in Figure 1. i = 4.0 mA, t = 2.0 hr

Solution Electrolyte	Non-electrolyte, 0.010 M	Solution flow To cathode, v_A, ml	To anode, v_B, ml
0.045 N PAA, 29% neutralized	Glucose	1.23	1.57
0.045 N PAA, 29% neutralized	Urea	1.63	1.87
0.045 N PAA, 45% neutralized	Glucose	1.22	1.60
0.045 N PAA, 45% neutralized	Urea	1.09	1.05
0.045 N PAA, 79% neutralized	Glucose	1.14	1.20
0.045 N PAA, 79% neutralized	Urea	1.23	0.90
0.025 N Na$_2$SO$_4$	Glucose	0.07	0.15
0.025 N Na$_2$SO$_4$	Urea	0.08	0.00

Despite the considerable scatter among quantities which ideally should be equal for a given solution (i.e., flows in the anodic and the cathodic directions, and flows as measured with glucose and with urea) the data of Table II show that with Na–polyacrylate solutions appreciable flows occur across the frit in both the anodic and the cathodic directions. The average of all the flows is 1.3 ± 0.3 ml, which for a current of 4.0 mA, for a 2.0-hr period, corresponds to a flow rate of 0.045 ml A^{-1} sec^{-1}. This is about 5–10% of the primary electroosmotic flows in similar solutions shown in Table I. Thus, the hydrostatic pressure difference produced in this cell reduced the solution flow in the cathodic direction by 90–95%.

The flows in the Na$_2$SO$_4$ solutions shown in Table II are an order of magnitude smaller than those in the Na–

polyacrylate solutions. This undoubtedly reflects the fact that at a given current the primary electroosmotic flows in Na_2SO_4 solutions are also an order of magnitude smaller than in Na–polyacrylate solutions (Table I).

On the Rates of Exchange between Free and Bound Counterions in

Polyelectrolyte Solutions. II. An Explanation for the Anomalous

Results Obtained by the Electrical Transference Method

by Melvin H. Gottlieb

Laboratory of Physical Biology, National Institute of Arthritis and Metabolic Diseases,
National Institutes of Health, Bethesda, Maryland 20014 (*Received December 11, 1970*)

This paper provides an explanation for the results obtained by earlier workers[1] in attempts to measure the rate of exchange between free and bound counterions in polyelectrolyte solutions by a nonconventional type of electrical transference measurement. It is shown that the flows which were experimentally found[2] to take place during transference measurements of the type in question are large enough to account for ionic movements which the earlier workers interpreted as indicating a very slow exchange rate.

Introduction

After reviewing the "nonconventional" transference experiments in question,[1] this present paper provides an explanation, based on the flows demonstrated in the preceding paper,[2] for the ionic movements which seemingly indicated a slow exchange between free and bound counterions. It is then shown that the experimentally measured flows are of the right order of magnitude to account for observed ionic movements.

The "Nonconventional Transference Experiments" of Wall and Coworkers. Before discussing the "nonconventional transference experiments" we must first consider the conventional-type transference measurement on Na^+–polyacrylate solutions made in Wall's laboratory,[3] in which the *net* ionic movements across the frit of a cell similar to that used in the "nonconventional" transference measurements (Figure 1, preceding paper[2]) were measured. The direction of the net Na^+ ion movement across the frit was found to depend on the degree of neutralization of the solution. It was towards the cathode in the case of solutions of less than about 50% neutralization, and towards the anode with solutions of higher degrees of neutralization. From the consideration that Na^+ ions bound to polyacrylate ions would move towards the anode along with the polyacrylate ions to which they were bound, Wall, *et al.*, interpreted the results of the conventional-type trans-

ference measurements in terms of the binding of Na^+ ions to polyacrylate ions. Degrees of ion binding thus computed were in good agreement with those determined by independent experimental methods. As indicated in the preceding paper,[2] we do not dispute the validity of these conventional-type transference experiments; also, we do not dispute their interpretation in terms of ion binding.

In the *"nonconventional" transference experiments* the anodic and cathodic components of the net Na^+ ion movement across the frit were determined through the use of radioactively labeled Na^+ ions. As with the conventional-type experiments, the solutions in the two cell compartments were chemically identical and unstirred. In the one of two separate, paired, measurements the component of Na^+ ion movement across the frit towards the cathode, referred to as q_A^{Na} by Wall, *et al.*, was determined by radioisotopically labeling the Na^+ ions of the anode compartment and measuring the amount of radioactive ions which moved to the cathode compartment on passage of current. In the second measurement, the component of Na^+ ion movement

(1) F. T. Wall and P. F. Grieger, *J. Chem. Phys.*, **20**, 1200 (1952); F. T. Wall, P. F. Grieger, J. R. Huizenga, and R. H. Doremus, *ibid.*, **20**, 1207 (1952).

(2) M. H. Gottlieb, *J. Phys. Chem.*, **75**, 1981 (1971).

(3) J. R. Huizenga, P. F. Grieger, and F. T. Wall, *J. Amer. Chem. Soc.*, **72**, 2636 (1950).

across the frit towards the anode, $q_B{}^{Na}$, was analogously determined by labeling the Na^+ ions of the cathode compartment and measuring the amount of radioactive ions which moved to the anode compartment on the passage of current. Movement of labeled Na^+ ions across the frit by diffusion during these experiments was negligible.

In relating the rate of exchange between free and bound counterions to the results of these "nonconventional" transference experiments, Wall, et al.,[1] make the implicit assumption that the ions move through the frit in a stationary medium. They derive an expression relating the rate of the exchange to the ratio of $q_A{}^{Na}$, and $q_B{}^{Na}$, and to the velocities and concentrations of the free and the bound Na^+ ions; as shown by Wall, et al., these latter quantities can be computed from the results of the conventional-type transference measurements. Although their general expression is too involved to be repeated here, the predictions for the two extreme cases of a very rapid exchange rate, and of a negligibly slow rate of the exchange, are simple.

In the case of a negligibly slow exchange, each Na^+ ion would behave solely as either a free ion or as a bound ion during a transference experiment. The free Na^+ ions would move towards the cathode in response to the applied electric field, and the bound Na^+ ions towards the anode. Accordingly, both the component of Na^+ ion movement across the frit in the direction of net Na^+ ion movement, and the component against the net Na^+ ion movement, would have finite, nonzero values; $q_A{}^{Na}$, the cathodic component, would be proportional to the velocity and the concentration of the free Na^+ ions and $q_B{}^{Na}$, the anodic component, would be proportional to the velocity and concentration of the bound Na^+ ions.

Consider now the a priori expected case of a very rapid exchange between free and bound Na^+ ions. Since all the Na^+ ions would exchange many times between the free and the bound states during the time in which they moved a significant distance in response to the applied electric field, all the Na^+ ions would exhibit the same electromigration velocity, the weighted average of the velocities of free and bound Na^+ ions. All Na^+ ions would therefore move across the frit in the same direction, towards the cathode if the product of the velocity and concentration of the free Na^+ ions were greater than that of the bound Na^+ ions, and towards the anode if the reverse were the case. Thus the component of Na^+ ion movement across the frit in the direction opposite to that of the net Na^+ ion movement would be zero.

Experimentally, Wall and coworkers found nonzero values for both the components in and opposite to the direction of the net Na^+ ion movement. The relative magnitudes of the two components corresponded to exchange rates with half-times of the order of minutes.

The Proposed Explanation for the Results in the "Nonconventional" Transference Measurements. It is helpful

to introduce the following terminology: *direction I* is the direction of net Na^+ ion movement across the frit, and *direction II*, the opposite direction. With this terminology, the problem of explaining the results of the "nonconventional" transference experiments is to account for the movement of labeled Na^+ ions across the frit in direction II, without invoking a slow rate of the exchange between free and bound counterions.

It was shown in the preceding paper[2] that, while there are undoubtedly some pores of the frit through which no net flows take place under the conditions of the transference experiments in question, net flows of solution simultaneously take place through some pores in the anodic direction, and through other pores in the cathodic direction. In other words, during the transference experiments flows take place through some pores in direction I, and through others in direction II. The solution flows in direction II provide the basis of our explanation of the Na^+ ion movements across the frit in this direction. In agreement with Wall, et al., we consider that, with a rapid exchange between the free and the bound Na^+ ions, the electric field applied during the transference experiments acts to move *all* Na^+ ions in the same direction, that of net Na^+ ion movement (direction I). However, being aware of the solution flows through the pores, we emphasize that this imparted velocity is *with respect to the solution in the pore*, while it is the movement of Na^+ ions *with respect to the frit* that is measured in the transference experiment. Since the velocity of the Na^+ ions in a pore *with respect to the frit* is the algebraic sum of their velocity *with respect to the pore solution* and of the velocity of the *pore solution with respect to the frit*, the Na^+ ions in those pores in which the solution flow is in direction II will move in this direction, if the flows are rapid enough to overcome the opposing influence of the applied electric field.

An important additional condition must be fulfilled for these flows to lead to an experimentally observable movement of *labeled* Na^+ ions across the frit in direction II. Wall and coworkers[1] show that *in the absence of other effects* the boundary between labeled and unlabeled solutions is located at the frit only at the very start of a determination, and moves in the direction of net Na^+ ion movement, i.e., in direction I, as current passes. If this were the case, the frit would become bounded on both sides by nonlabeled solutions in the one of the pair of transference experiments in which the component of Na^+ ion movement in direction II is measured, and accordingly, the flows through the pores in direction II would only produce the (experimentally undetectable) movement of *nonlabeled* Na^+ ions across the frit. We postulate that the flows through the frit cause convection in the solution near the interface, which destroys the boundary between labeled and unlabeled solutions in the solution proper. This would leave the frit surface in contact with labeled solution, a situation in

which the Na^+ ions carried across the frit by the flows in direction II would be labeled ones.

A Test of Our Explanation. Since there is no way to measure the velocities of solution flow through the various pores of the frit, a rigorous test of our explanation is not possible. However, as shown below, it is possible to test whether the flows found to occur in direction II across the frit as a whole during the transference measurements in question are of the right order of magnitude to account for the movements of Na^+ ions in this direction.

We derive below an expression relating the solution flow across the frit in direction II during the transference experiment, v_{II}, and the Na^+ ion movements in directions I and II, q_I and q_{II}, assuming the situation in which the flows would have the greatest effect on the Na^+ ion movements, *i.e.*, that the solution flow is rapid enough to overcome the force of the applied electric field on the Na^+ ions in *all* those pores in which the net flow is in direction II. The following simplifying assumptions are also made. (a) There is no *net* solution movement across the frit as a whole during a transference experiment. Referring to considerations discussed in the preceding paper,[2] this assumes a negligible value for the net solution movement, occurring at the start of an experiment, which produces the hydrostatic pressure difference that prevents further net flow during the experiment. (b) The frit is made up of parallel, noninterconnecting pores. (c) The pores are wide as compared with the thickness of the electrical double layer at the pore wall–solution interface. It follows from this latter assumption that the solution in the pores has virtually the same composition as the outer solution.

We need only consider those pores through which the flow of solution is in direction II. The resultant velocity of a Na^+ ion in direction II, $u_{II}{}^{Na}$, is the difference between the velocity of the solution with respect to the pore wall, $u_{II}{}^s$, and the velocity of the ion with respect to the solution, $u_E{}^{Na}$

$$u_{II}{}^{Na} = u_{II}{}^s - u_E{}^{Na} \qquad (1)$$

From the general relationship between velocity of a solute particle and the quantity of solute moving across a given area per unit time

$$u_{II}{}^{Na} = \frac{1000\bar{q}_{II}}{c^{Na}\bar{A}t} \qquad (2)$$

where $\bar{q}_{II}$ is the quantity of Na^+ ions, in equivalents, which move through the pore during the time, t; $\bar{A}$ is the cross-sectional area of the pore, and c^{Na} is the concentration of Na^+ ions in the solution in equiv. $l.^{-1}$.

From the general consideration that the solution velocity is the volume flow in a given time across a given cross-sectional area

$$u_{II}{}^s = \frac{\bar{v}_{II}}{t\bar{A}} \qquad (3)$$

where $\bar{v}_{II}$ is the quantity of solution flowing through the pore.

Since we have assumed that there is no *net* movement of solution across the frit during the transference measurements, the solution may be considered as stationary with respect to the frit. Accordingly, $u_E{}^{Na}$, the velocity of the Na^+ ions with respect to the solution, may be stated in terms of the *net* movement of Na^+ ions across the frit, *i.e.*, in terms of the difference between the Na^+ ion movements across the frit in the two directions, $q_I - q_{II}$. From the general relationship between the velocity of a solute particle and the quantity of solute moving across a given cross-sectional area, we may write

$$u_E{}^{Na} = \frac{1000(q_I - q_{II})}{tAc^{Na}} \qquad (4)$$

where A is the cross-sectional area of *all* of the pores of the frit.

Combining eq 1–4 gives for $\bar{q}_{II}$, the Na^+ ion movement through the pore under consideration

$$\bar{q}_{II} = \frac{c^{Na}\bar{v}_{II}}{1000} - \frac{\bar{A}}{A}(q_I - q_{II}) \qquad (5)$$

Adding expressions similar to eq 5 for all of the pores in which solution flow is in direction II and large enough to overcome the force of the electric field on the Na^+ ions gives

$$\sum\bar{q}_{II} = \frac{c^{Na}\sum\bar{v}_{II}}{1000} - \frac{\sum\bar{A}}{A}(q_I - q_{II}) \qquad (6)$$

where Σ refers to the summation of the various quantities for all these pores.

From our assumption that the flow is rapid enough to overcome the force of the applied electric field on the Na^+ ions in *all* the pores with flow in direction II, it follows that $\Sigma\bar{v}_{II}$ is equal to v_{II}, the total solution flow across the frit in direction II. Since $\Sigma\bar{q}_{II}$ is equal to q_{II}, the total Na^+ ion movement across the frit in direction II, eq 6 gives

$$q_{II} = \frac{c^{Na}v_{II}}{1000} - \frac{\sum\bar{A}}{A}(q_I - q_{II}) \qquad (7)$$

With algebraic rearrangement, and the use of the symbol α to designate $\Sigma\bar{A}/A$

$$q_{II} = \frac{v_{II}c^{Na}}{1000(1 - \alpha)} - q_I\frac{\alpha}{(1 - \alpha)} \qquad (8)$$

Obviously there is no means of independently measuring α, the ratio of the sum of the cross-sectional areas of those pores in which the solution flows are in direction II, to the sum of the cross-sectional area of all of the pores of the frit. However, the consideration that this parameter must necessarily have a value between 0 and 1 provides a means of determining whether measured v_{II} values are of the right order of magnitude to account for the movements of Na^+ ions in direction II.

Solving eq 8 for α gives

$$\alpha = \frac{\dfrac{v_{II}c^{Na}}{1000} - q_{II}}{q_I - q_{II}} \tag{9}$$

Since the denominator of the right-hand side of eq 9 is necessarily positive, the following statements may be made.

(a) A value of α significantly less than zero computed from the various experimental quantities would indicate that v_{II}, the experimentally found solution flow, is not large enough to account for the experimentally found movement of Na$^+$ ions in direction II. Accordingly the possibility of a slow exchange between free and bound counterions would have to be considered.

(b) A computed value of α significantly greater than 1 indicates that the Na$^+$ ion movement in direction II is smaller than would be expected from the solution flow. This would raise doubts about the essential validity of our model.

Computed values of α within the range 0–1 support, but, of course, do not rigorously prove, our explanation of the results of the "nonconventional" transference experiments.

To test our explanation, "nonconventional" transference experiments of the type in question were made using the same porous frit transference cell, and with solutions of the same Na–polyacrylate content, as were used in the measurements of solution flows during such experiments reported on in the preceding paper.[2] As in the preceding paper parallel experiments were made with a Na$_2$SO$_4$ solution.

Experimental Section

Materials. The radiotracer used for Na$^+$ was ^{22}Na, obtained as NaCl from Iso-Serve Corp., Cambridge, Mass. Chloride ions were not removed from the labeled solutions since the highest resulting concentration of these ions in the solutions was only about 10^{-6} N. The other materials used were as described in the previous paper.[2]

Measurements. The detailed procedure for the nonconventional transference determinations, as well as the transference cell used, were as described by Wall and coworkers.[1] Also following the procedure of these earlier workers, the amounts of radioactive Na$^+$ which moved across the frit in control experiments, in which no current was passed, were subtracted from the amounts which moved in the transference experiments proper.

As in the measurements of the magnitudes of the solution flows in each direction across the frit reported in the preceding paper,[2] measurements were made at the current used by Wall and coworkers, 4.0 mA, passed for the longest of the time periods used by them, 2.0 hr.

Results and Discussion

Table I shows the results obtained in the "noncon-

"ventional" transference determinations in Na–polyacrylate solutions and in a Na$_2$SO$_4$ solution.

Table I: Results of "Nonconventional Transference Experiments." $i = 4.0$ mA, $t = 2.0$ hr

| | Sodium movement found | |
	Anode to cathode, $q_A{}^{Na}$, mol $\times 10^5$	Cathode to anode, $q_B{}^{Na}$, mol $\times 10^5$
0.045 N PAA, 29% neutralized	5.2	0.36
0.045 N PAA, 45% neutralized	3.4	1.8
0.045 N PAA, 79% neutralized	3.0	12.7
0.025 N Na$_2$SO$_4$	10.1	0.0

The data of Table I for the Na–polyacrylate solutions are in qualitative agreement with the results of Wall and coworkers since they show, with all three solutions, nonzero values for both $q_A{}^{Na}$ and $q_B{}^{Na}$, that is, in all cases for q_{II} as well as for q_I. It can be shown that if the approach of these workers were correct, the data of Table I would indicate half-times of from 2 to 8 min for the exchange between free and bound Na$^+$ ions. Despite this qualitative agreement, the actual values of $q_A{}^{Na}$ and $q_B{}^{Na}$ of Table I are not in good quantitative agreement with those of Wall, *et al.*, the values of the previous workers for similar solutions[1] being up to several times greater. These differences are probably due to differences between the porosities of the porous frits used.

Table I also shows that there was no Na$^+$ ion movement in direction II (*i.e.*, towards the anode) in the Na$_2$SO$_4$ solution. This is as expected, since, as reported in the preceding paper,[2] little, if any, solution flows took place with Na$_2$SO$_4$ solutions under the conditions of the transference determinations.

We turn now to the "test" of our explanation of the results of the "nonconventional" transference experiments. In Table II the quantities used to compute α, the fraction of the total pore area of the frit through which flow takes place in direction II, from eq 9, and the values of α thus computed are listed. The v_{II} values listed in the fourth column are the average of the urea and glucose values in direction II from Table II of the preceding paper.[2]

The computed values of α shown in the last column of Table II are all well within the physically possible range of 0 to 1 and therefore support our explanation of the results of the nonconventional transference experiments. In view of the assumptions made in the derivation of eq 9, and of the poor precision of the solution flow measurements reported in the preceding paper, we do not believe the numerical values obtained for α warrant further discussion. Nevertheless, we will point out that the fact that similar values of α (*i.e.*, 0.41 and 0.50) were computed for the 29% and 45% neutralized solutions, and that these values are signifi-

Table II: Quantities Used in Computation of α, and Computed Values of α.
Polyacrylic acid concentration $= 0.045\ N$, $i = 4.0$ mA, $t = 2.0$ hr

Percentage neutralization of polyacrylic acid	Concentration of Na$^+$ ions, c^{Na}, equiv. l.$^{-1}$	Direction II	Solution flow, v_{II}, ml	$\dfrac{c^{Na}v_{II}}{1000}$, equiv $\times$ 10^5	Component of Na$^+$ ion movement In direction I, q_I, equiv $\times$ 10^5	In direction II, q_{II}, equiv $\times$ 10^5	α
29	1.40×10^{-2}	Towards anode	1.7	2.4	5.2 $(q_A{}^{Na})$	0.36 $(q_B{}^{Na})$	0.41
45	2.02×10^{-2}	Towards anode	1.3	2.6	3.4 $(q_A{}^{Na})$	1.8 $(q_B{}^{Na})$	0.50
80	3.60×10^{-2}	Towards cathode	1.2	4.3	12.7 $(q_B{}^{Na})$	3.0 $(q_A{}^{Na})$	0.13

cantly different from that obtained with the 80% neutralized solution (0.13), is as expected from considerations discussed in the preceding paper.[2] As shown in the preceding paper, the primary electroosmotic flow is in the same direction, towards the cathode, with all three solutions. Accordingly, while in the 80% neutralized solution the flows in direction II during the transference measurements are in the direction of the primary electroosmotic flow, in the cases of the 29% and 45% neutralized solutions the flows in direction II are backflows. As discussed in the preceding paper, the flows in the direction of the primary electroosmotic flow take place through the narrower pores of the frit, and the backflows through the wider pores. Accordingly, with the 80% neutralized solution α refers to the narrower pores of the frit, while with the 29% and 45% neutralized solutions, α refers to the wider pores of the frit.

Since the results of the "nonconventional" transference experiments reported on in this paper, and presumably those of the earlier workers, can be reasonably accounted for by electroosmotically caused solution flows, we conclude that the experimental results of Wall, et al., do not show that the exchange between free and bound counterions in polyelectrolyte solutions is slow.

On the Rates of Exchange between Free and Bound Counterions in Polyelectrolyte Solutions. III. A Demonstration That the Exchange Is Not as Slow as Indicated by the Electrical Transference Measurements

by Melvin H. Gottlieb

*Laboratory of Physical Biology, National Institute of Arthritis and Metabolic Diseases,
National Institutes of Health, Bethesda, Maryland 20014* (Received December 11, 1970)

This paper experimentally demonstrates that the exchange between free and bound counterions in Na–polyacrylate solutions is much faster than concluded by earlier workers[1] from the electrical transference measurements which were criticized in the preceding papers.[2] The experimental method used involved measurement of the rates of uptake of Na$^+$ ions from Na–polyacrylate solutions by a cation-exchange resin. It is shown that the half-times for the exchange between free and bound Na$^+$ ions must be less than 2 sec, i.e., at least 60 times smaller than half-times concluded by the earlier workers. Accordingly, there is no reason to assume that the exchange between free and bound counterions in polyelectrolyte solutions does not take place as rapidly as predicted from current concepts of polyelectrolyte solutions, that is, with half-times of the order of μseconds.

Introduction

In this last paper of this group it is experimentally demonstrated that the half-times for the exchange are much smaller than concluded by Wall and coworkers.[1] As in the preceding papers, Na–polyacrylate was used as the prototype polyelectrolyte, and parallel measurements were made with a simple electrolyte, Na$_2$SO$_4$.

The experimental method involved measurement of the rate of uptake of radioactively labeled Na$^+$ ions from Na–polyacrylate solutions in exchange for the unlabeled Na$^+$ ions of a cation-exchange resin, present in large excess. Since the polyacrylate ions cannot enter the resin because of their large size and high charge,[3] those labeled Na$^+$ ions which are bound to them would also be excluded from the resin. In order for a bound labeled Na$^+$ ion to be taken up by the resin, it would have to first become free by exchanging for a free nonlabeled Na$^+$ ion in the solution. Thus, the exchange between the free and the bound Na$^+$ ions must be at least as fast as the uptake of labeled Na$^+$ ions by the resin.

Experimental Section

Materials. The *polyacrylic acid* and *radioactive Na$^+$* were the same as described in the previous papers.[2]

Ion-Exchange Resins. A polystyrene–sulfonic acid–8% divinyl benzene ion-exchange resin of the AG50W-X8 series of Bio-Rad Laboratories, Richmond, Calif., was used. The resin was obtained in fractions with bead radii < 19 (<400 mesh), 19–37 (200–400 mesh), 37–75 (100–200 mesh), and 75–149 μ (50–100 mesh). The various resin fractions were shaken for several hours with each of 2 M HCl, 2 M NaOH, and 50% eth-

anol, each solution being followed by a thorough washing with distilled water. The ion-exchange capacity of the resin, measured by standard procedures,[3] was 2.02 mmol per ml of wet resin in the Na$^+$ state.

To determine if the polyacrylic acid and polyacrylate ions were essentially completely excluded from this ion exchange resin, 10 ml each of polyacrylic acid solutions, c = 0.045, 79% neutralized, c = 0.023, 49% neutralized, c = 0.011, 28% neutralized, were shaken for 5 min with 5 ml of air dried resin. Analysis of the solutions for Na$^+$ and for total solids indicated no change within the experimental error of the analyses, ±0.5%.

Procedures. All experiments were done at room temperature, 23 ± 1°. The procedure essentially consisted of rapidly adding a slurry of the ion-exchange resin to a well stirred ^{22}Na-labeled solution, and determining the radioactivity concentration of the solution phase as a function of time. As large a quantity of resin as was consistent with good stirring was used, in order to drive the uptake of radioactive Na$^+$ ions from the solution as far to completion as possible. In a typical experiment the slurry consisted of 50 cm^3 wet volume of ion-exchange resin and 7 cm^3 of water. The volume of the ^{22}Na-labeled solutions was 100 cm^3, corresponding to 25–100-fold excesses of the Na$^+$ contents of the ion-exchange resin to those of the solutions.

The apparatus used is shown in Figure 1. The reac-

(1) F. T. Wall, P. F. Grieger, J. R. Huizenga, and R. H. Doremus, *J. Chem. Phys.*, **20**, 1207 (1952).

(2) M. H. Gottlieb, *J. Phys. Chem.*, **75**, 1981, 1985 (1971).

(3) F. Helfferich, "Ion-Exchange," McGraw-Hill, New York, N. Y., 1962.
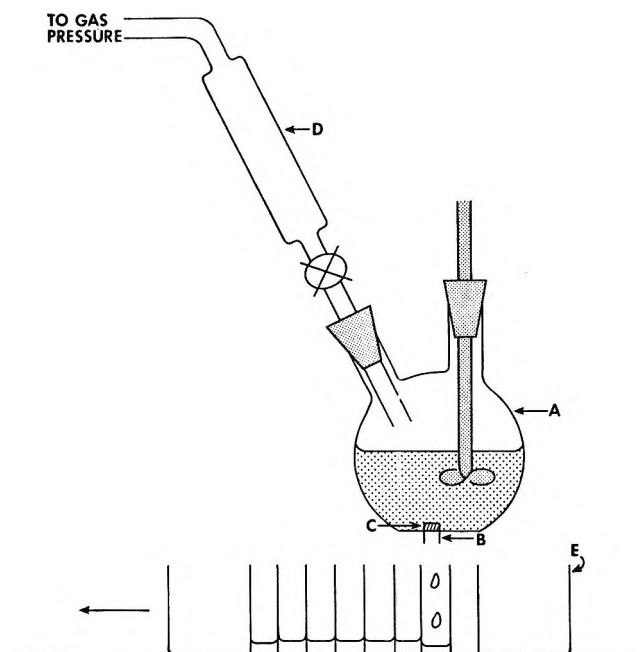
Figure 1. Apparatus used to measure rate of uptake of radioactive Na^+ ions from the solution by the ion-exchange resin.

tion vessel, A, was a two-neck 300-ml flat bottom flask, modified to include an exit tube, B, which was covered by a "coarse" Pyrex glass frit, C, whose porosity was such that resin particles could not pass through it, and solution could flow through it only under applied pressure. The addition funnel, D, which was used to hold a slurry of the ion-exchange resin prior to its addition to the reaction vessel, had an extra large (7 mm) bore stopcock. Mechanical stirring was used, the shaft of the stirrer fitting through a pressure tight stirring gland. An eight compartment sample collection box, E, was positioned below the exit tube; a constant, preset, rate of movement of the collection box was obtained using a motor controlled by a Miniarik Electric Co. (Los Angeles, Calif.) SH-14 speed control.

After the ^{22}Na-labeled solution had been placed in the reaction vessel, and stirring started, the resin slurry was poured into the addition vessel. The addition funnel was then placed under about 5 psi of nitrogen pressure, and the motor driving the sample collection box started. Just before the first sample collection compartment reached the exit tube, the stopcock of the addition vessel was opened, resulting in the almost instantaneous addition of the resin slurry to the reaction vessel, and the initiation of flow of solution through the exit tube. (There was a time lag of about 0.5 sec between the opening of the stopcock and the start of the flow through the exit tube.) After all eight compartments of the collection box had passed under the exit tube, the flow was discontinued by venting the gas pressure. Typically about 0.5 cm^3 of solution was collected in each compartment, so that the change in the

solution volume during the course of a run was not more than about 4%.

Preliminary experiments, with the 75–150-μ bead radii resin, indicated the same rate of uptake of radioactive Na^+ ions for rotation rates of the stirrer of approximately 1800 rpm and of approximately 3600 rpm; the higher rate was used in all experiments.

Results and Discussion

With the resin fraction in which the bead radii were 75–150 μ, the uptakes of labeled Na^+ ions from both Na_2SO_4 and Na–polyacrylate solutions occurred slowly enough for the time courses to be followed. The uptake of ions by the resin fractions with bead radii 75 μ and smaller was essentially completed by the time the first solution sample was collected; in these cases only an upper limit for the half-times for the uptake could be obtained.

Accordingly, the 75–150-μ resin fraction will be discussed first. In all cases, with both the Na–polyacrylate solutions and the Na_2SO_4 solutions, the uptake of radioactive Na^+ ions followed the time course expected for the rate determining step being the diffusion of Na^+ ions across unstirred layers of solution surrounding the resin particles[4]

$$\log \left[(1 + \beta)\frac{A}{A^0} - \beta \right] = -\frac{0.30}{\tau^d}(1 - \beta)t \qquad (1)$$

[Equation 1 is equivalent to that derived by Boyd, Adamson, and Myers[4] except for the presence of the term β, which these authors implicitly assume equal to zero. The expression derived by Boyd, et al., is strictly valid for the uptake of a relatively small fraction of the labeled ions from the solution, while we are interested in following the uptake of almost all of the labeled ions. The derivation of eq 1 follows that of Boyd, et al., through their eq 5a. At this point they make the approximation that all of the labeled ions originally present in the solution are taken up by the resin at infinite time, i.e., when equilibrium is reached. In the derivation of eq 1 of the present paper, we took into account the finite quantity of labeled ions remaining in the solution, in equilibrium with those in the resin.

With the small values of β is the present work, differences between plotting data according to eq 1 using the actual value of β and plotting data with the approximation that $\beta = 0$ only appear after about 80% of the labeled ions have been taken up by the resin.]

Here A^0 is the concentration of radioactive Na^+ ions in the solution before the start of the experiment; A is the concentration of these ions at any time, t, after the start of the experiment; β is the ratio of the total quantity of Na^+ ions in the solution to the total quantity of Na^+ ions in the ion-exchange resin. The time constant

(4) G. E. Boyd, E. W. Adamson, and L. S. Myers, J. Amer. Chem. Soc., 69, 2836 (1947).
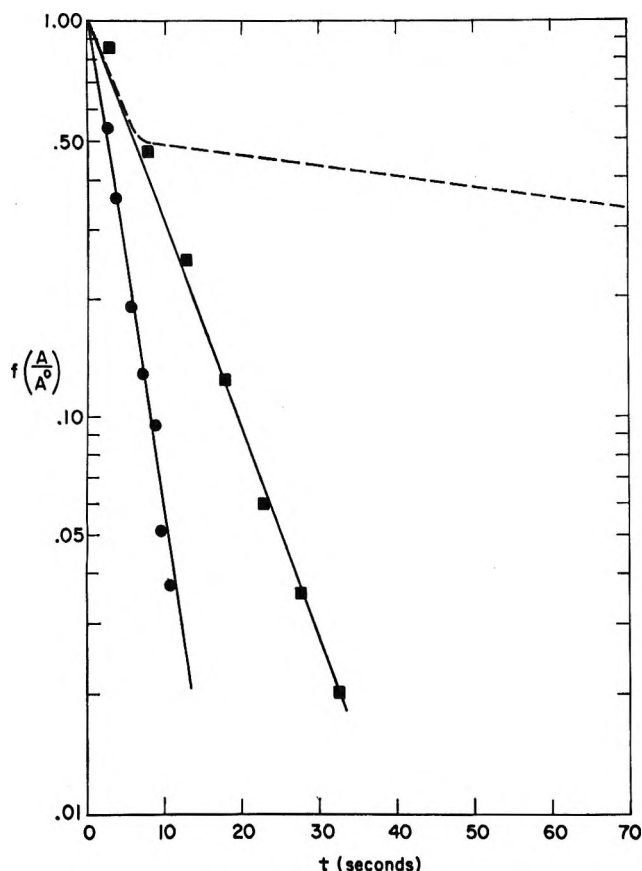
Figure 2.   Uptake of radioactive Na$^+$ ions by resin with
75–149 μ bead radii, as a function of time; $f\ (A/A^0) =$
$(1 + \beta)A/A^0 - \beta$; ●, 0.050 N Na$_2$SO$_4$; ■, Na–polyacrylate, c
= 0.045 N, 81% neutralized. The dashed curve indicates the
uptake from the Na–polyacrylate solution expected on the basis
of the smallest of the values for the half-time for the exchange
between free and bound Na$^+$ ions concluded by Wall and co-
workers, 2 min, assuming that 50% of the Na$^+$ ions are bound
to polyacrylate ions.

τ^d is related to the experimental parameters of the sys-
tem by

$$\tau^d = \frac{0.23 b \delta V}{D \bar{V}} \qquad (2)$$

where b is the radius of the resin beads, δ the thickness of
the unstirred solution layer, V the volume of the solu-
tion $\bar{V}$, the volume of the resin, and D the diffusion
coefficient of the Na$^+$ ions in the solution. Under the
experimental conditions of the present work, in which
β is in the range 0.02–0.05, τ^d is essentially equal to
the half-time for the uptake of Na$^+$ ions by the resin.

Typical plots of the function log $[(1 + \beta)(A/A^0) -$
$\beta]$ as a function of time for a Na$_2$SO$_4$ solution and for a
Na–polyacrylate solution are shown in Figure 2. Also
shown in this figure is the time course for the uptake
from the Na–polyacrylate solution which would be
expected on the basis of the smallest of the half-times
for the exchange between free and bound Na$^+$ ions con-
cluded by Wall and coworkers, 2 min; for the purposes

of this plot it was assumed that 50% of the Na$^+$ ions
are bound to polyacrylate ions.

The results obtained with the various Na$_2$SO$_4$ and
Na–polyacrylate solutions are summarized in Table I.

Table I: Uptake of Labeled Na$^+$ by
Resin with Bead Radii 75–150 μ

c, equiv. l.$^{-1}$	Percentage neutralization	Fraction of Na$^+$ ions in solution taken up during experiment	Half-time for uptake, τ, sec
	a. Na$_2$SO$_4$ Solutions		
0.010		0.92	2.8
0.050		0.95	2.4
	b. Na–Polyacrylate Solutions		
0.011	28%	0.97	4.5
0.011	49%	0.96	4.0
0.011	80%	0.91	4.0
0.022	28%	0.96	4.0
0.022	49%	0.95	3.5
0.022	80%	0.96	4.7
0.045	28%	0.96	3.9
0.045	49%	0.92	4.4
0.045	80%	0.94	5.5

The finding that the half-time for the uptake of radio-
active Na$^+$ ions from Na–polyacrylate solutions is sig-
nificantly greater than that from Na$_2$SO$_4$ solutions is as
expected from the binding of Na$^+$ to polyacrylate ions,
since, when only a fraction, f, of the Na$^+$ ions are free to
diffuse, expressions similar to eq 1 and 2 would still
apply, the only difference being that τ^d would be multi-
plied by the factor $1/f$. Values of f in the range 0.5 to
0.75 are computed from a comparison of half-times for
the uptake from the Na–polyacrylate solutions with
those for the uptake from Na$_2$SO$_4$ solution, with the
assumption that the parameters making up τ^d are the
same for both types of solutions. Other experimental
methods give f values in the range 0.3 to 0.6[5] for similar
solutions.

With the resins of bead radii 75 μ and smaller, in which
most of the radioactive Na$^+$ ions were taken up by the
time the first sample of solution could be collected, the
time of collection of the first sample clearly constitutes
an upper limit for the half-time for the uptake, and will
be denoted as $\tau_{\max}$. The runs with these resin fractions
of smaller bead radii are summarized in Table II.

The data of Table II show that the half-times for the
exchange between free and bound Na$^+$ ions in Na–
polyacrylate solutions must be less than 2 sec, *i.e.*, at
least 60 times less than the smallest value indicated by
the approach of Wall and coworkers.[1] [Two other
experimental approaches also failed to give evidence for

(5) S. A. Rice and M. Nagasawa, "Polyelectrolyte Solutions,"
Academic Press, New York, N. Y., 1961.

Table II: Uptake of Na^+ Ions by Resin Fractions
with Bead Radii 75 μ and Smaller

Solution concentration, equiv l.$^{-1}$	Percentage neutralization	Bead radii range, μ	Fractions of labeled Na$^+$ ions taken up by resin	Time of collection of first sample, τ_{max}, sec
a. Na$_2$SO$_4$ Solutions				
0.010		19–37	0.96	1.6
0.010		<19	0.95	1.6
b. Na–Polyacrylate Solutions				
0.045	47%	37–75	0.96	1.6
0.045	81%	37–75	0.77	1.9
0.045	47%	19–37	0.93	1.6
0.045	75%	<19	0.96	1.6

a rate of exchange as slow as that concluded by Wall and coworkers. In one, a Na^+ specific glass electrode monitored the appearance of free Na^+ ions on the rapid addition of KCl to Na–polyacrylate solutions. The converse experiments, in which NaCl was added to K–polyacrylate solutions were also performed, using K^+ specific electrodes. The appearance of free ions was completed within a 1-min resolving time imposed by the poorly understood[6a] erratic response of the electrodes to the addition of a second species of cation into the solution. (However, other workers have recently followed the exchange between Na^+ ions and divalent cations from clays down to about 3 sec using a similar method.[6b])

Also, ^{23}Na nuclear magnetic resonance measurements

were made (the cooperation of Dr. E. D. Becker in making these measurements is gratefully acknowledged) on Na–polyacrylate solutions similar to those considered in this paper. Here a slow rate of the exchange would be indicated by two peaks, provided that the free and the bound Na^+ ions had different "chemical shifts."[7] A single somewhat broad peak, similar to that characteristic of simple sodium salts,[8] was obtained in all instances. Although exchanges occurring with half-times greater than about 0.03 sec could have been recognized, the interpretation of these measurements is not definitive since it is not known whether the free and the bound Na^+ ions do in fact have different "chemical shifts."]

While valid measurements of the rates of exchange would undoubtedly provide important information on the nature of ion binding to polyelectrolytes, such measurements must await the development of a means to apply to this problem the now widely used methods for studying fast reactions. In the absence of evidence to the contrary, there is no reason to assume that the exchange does not take place as rapidly as predicted from current concepts of polyelectrolyte solutions, that is, with half-times of the order of μseconds.

(6) (a) G. A. Reichnitz in "Glass Electrodes for Hydrogen and Other Cations," G. Eisenman, Ed., Marcel Dekker, New York, N. Y., 1967, p 335; (b) R. L. Malcolm and V. C. Kennedy, Soil Sci. Soc. Amer., Proc., 33, 247 (1969).

(7) J. A. Pople, W. G. Schneider, and H. J. Bernstein, "High Resolution Nuclear Magnetic Resonance," McGraw-Hill, New York, N. Y., 1959, Chapter 10.

(8) O. Jardetzky and J. E. Wertz, J. Amer. Chem. Soc., 82, 318 (1960).

Catalysis of the Exchange of the Ethanol Hydroxyl Proton by Some Divalent Metallic Ions

by Ann H. Hunt and Marcus E. Hobbs*

Department of Chemistry, Duke University, Durham, North Carolina 27706   (*Received January 18, 1971*)

The catalysis of the exchange of the ethanol hydroxyl proton by several diamagnetic and paramagnetic divalent metallic ions was studied using the line broadening of nuclear magnetic resonance (nmr) signals to determine quantitatively the catalytic rate constants at approximately 39°. The order of catalytic effectiveness of the ions was found to be (Fe) > Cu > Zn > Co > Ni ~ Mn > Mg > Ca. The placement of Fe^{2+} in the sequence is somewhat uncertain because of possible contamination by Fe^{3+}. It appears, from the results obtained, that filled or partially filled d orbitals are of critical importance to the catalytic effectiveness, as Mg^{2+} with the smallest ion radius of the ions studied is only moderately effective, whereas Zn^{2+} is quite effective. Differences in the Arrhenius activation parameters for the exchange in pure, acid-catalyzed, and Cu^{2+}-catalyzed reactions suggest a different rate controlling step in the pure ethanol case from the controlling reaction in the catalyzed cases. In the paramagnetic ion solutions there is evidence of moderate unpaired electron spin density on all of the ethanol protons; however, the chemical shift is to lower resonance frequencies rather than to higher frequencies such as is often observed.

Introduction

The broadening of lines and details of line shapes in nuclear magnetic resonance (nmr) spectra have been used extensively[1,2] to study various exchange and rate phenomena and the factors which influence these phenomena. Arnold,[3] who first studied the exchange of the ethanol hydroxyl proton by nmr techniques, found that small concentrations of HCl or NaOH (10^{-6} to 10^{-5} M) in absolute ethanol caused line shape changes such that the exchange times for the hydroxyl proton could be calculated. Increase in acid or base concentration caused collapse of the hydroxyl proton triplet into a single narrow line characteristic of the fast exchange limit on the nmr time scale. Since other ions might reasonably be expected to catalyze the hydroxyl proton exchange the present investigation was undertaken to determine the relative effectiveness of several divalent metallic cations which are often found in complex compounds of chemical and biochemical interest. In an attempt to achieve some understanding of the factors which may be of significance in determining the relative catalytic effectiveness, salts of diamagnetic and paramagnetic cations were used. The salts were dissolved in absolute ethanol to make solutions covering a wide range of concentrations. In this manner the concentration range of each salt that was best suited for quantitative evaluation of the catalysis rate constant at ~39° was established. Observation of chemical shifts of the ethanol protons in the presence of paramagnetic ions allowed determination of approximate unpaired electron spin densities on the several protons, and a limited temperature range study allowed evaluation of Arrhenius activation parameters for the hydroxyl proton exchange in pure ethanol, in ethanol with acid present, and in ethanol with CuCl₂ present.

Experimental Section

Reagent grade anhydrous dichlorides of Mg, Mn, Fe, Co, and Ni were obtained from Alfa Inorganics, Inc. and were used without further treatment. Corresponding Cu and Ca salts were obtained from Fisher Scientific Co. and a reagent grade sample of Baker and Adamson anhydrous ZnCl₂ was used. The three sulfates used were anhydrous MgSO₄ and NiSO₄·6H₂O obtained from Fisher Scientific Co. and a J. T. Baker Co. sample of anhydrous CuSO₄. Anhydrous ethanol was prepared by fractional distillation from magnesium according to Fieser,[4] taking exceptional precautions to exclude air, CO₂, and moisture.

Solutions of the salts in absolute ethanol were prepared under a N₂ atmosphere in a glove bag. Dilutions of stock solutions were handled in the same way. Volumetric analyses of the chloride solutions were made with AgNO₃–dichlorofluorescein except for FeCl₂, in which case the AgCl gravimetric method was used. The nickel and copper sulfate solutions were analyzed by using N-dimethylglyoxime and α-benzoin oxime, respectively. Nuclear magnetic resonance measure-

(1) A. Carrington and A. D. McLachlan, "Introduction to Magnetic Resonance," Harper and Row, New York, N. Y., 1967, Chapter 12.
(2) (a) C. S. Johnson, *Advan. Magn. Resonance*, 1, 33 (1965); (b) J. A. Pople, W. G. Schneider, and H. J. Bernstein, "High Resolution Nuclear Magnetic Resonance," McGraw-Hill Book Co., New York, N. Y., 1959, Chapters 13, 15, 17, 18.
(3) J. T. Arnold, *Phys. Rev.*, 102, 136 (1956).
(4) L. F. Fieser, "Experiments in Organic Chemistry," McGraw-Hill, New York, N. Y., 1957, p 285.

ments were made with a Varian Model A-60 spectrometer calibrated frequently with a standardized sample of TMS–chloroform and the methyl–methylene group coupling in ethanol of 7.1 Hz.

Results and Discussion

Five of the cations studied, namely Mn^{2+}, Fe^{2+}, Co^{2+}, Ni^{2+}, and Cu^{2+}, were paramagnetic and the large fluctuating magnetic fields generated by the unpaired electrons caused all ethanol proton signals to exhibit a significant broadening because of a shortened spin–lattice relaxation time. One of the primary questions of the present investigation was, does this paramagnetic broadening preclude or significantly interfere with the observation of exchange broadening of the hydroxyl proton signal? Information bearing on this question is recorded in Table I for several ethanolic solutions of

Figure 1. Dependence of ethanol hydroxyl proton line width at ~39° on concentration of some metal chlorides in absolute ethanol.

Table I: Hydroxyl Proton Line Width,[a] $\nu_{1/2}$, and CH_2 Proton Signal for Ethanol Solutions of $CuCl_2$ (38°)

$CuCl_2$, mol l.$^{-1}$	$\Delta\nu_{1/2}$, Hz	CH_2 signal
1.19×10^{-2}	7.55	Broad quartet
4.75×10^{-3}	3.24	Broadened quartet
2.38×10^{-3}	1.90	
1.19×10^{-3}	0.84	Sharp quartet
1.19×10^{-4}	0.81	
4.76×10^{-5}	1.48	
2.86×10^{-5}	1.84	
1.43×10^{-5}	3.08	Broadened quartet
1.19×10^{-5}	3.81	
1.19×10^{-5}	4.18	Broad quartet
9.56×10^{-6}	4.18	
7.14×10^{-6}	4.82	
7.14×10^{-6}	4.87	
4.76×10^{-6}	5.07	
4.76×10^{-6}	4.13	
3.88×10^{-6}	3.68	Broad octet
2.86×10^{-6}	3.03	
1.90×10^{-6}	2.44	
1.19×10^{-6}	2.06	

[a] The line width as used here and elsewhere in this paper is the width, in Hz, of the central peak of hydroxyl proton triplet, or of the central signal in case of a coalesced or partially coalesced signal, measured at the half-height of this signal.

$CuCl_2$ at 38°. Four concentration regions in the data should be noted. At about 10^{-2} M the line width of the hydroxyl proton signal clearly indicates broadening caused by the fields of the unpaired electron of the copper ion. At 10^{-3} to 10^{-4} M there is little or no paramagnetic broadening of the hydroxyl proton signal since $\Delta\nu_{1/2} \simeq 0.8$ Hz is about the minimum width obtainable with the instrumentation used; in the 10^{-3} to 10^{-4} M concentration range the proton exchange, on the nmr time scale, is in the fast exchange limit. At about 6×10^{-6} M maximum broadening attributable to proton exchange is in evidence and the CH_2 proton signal be-

gins to show structure characteristic of hydroxyl proton spin–spin coupling. Finally at about 4×10^{-6} M and lower concentrations there is still some exchange broadening of the hydroxyl proton signal but the rate of exchange is too slow to prevent appearance of the CH_2 group signal octet structure characteristic of superposition of the hydroxyl proton coupling on the quartet structure arising from the $CH_3–CH_2$ coupling. At all $CuCl_2$ concentrations below 10^{-3} M the methyl group signal is a sharp triplet.

The separation of the paramagnetic and the exchange broadened regions of concentration occurred for all of the paramagnetic ions with the exception of the Mn^{2+} solutions. In the Mn^{2+} case there was considerable overlap of the two regions and the details of the exchange broadening were not directly observable; however, a difference measurement was performed which allowed determination of adequate detail of the exchange broadened region. Specifically $C_2H_5OH–MnCl_2$ solutions were examined with added HCl present so that the fast exchange limit for the hydroxyl proton prevailed at all $MnCl_2$ concentrations investigated. A comparison of the hydroxyl proton line width for the acid-catalyzed solutions and solutions with no acid present allowed one to make a good estimate of the concentration of Mn^{2+} at which maximum exchange broadening occurred.

Figures 1 and 2 show the line width of the ethanol hydroxyl proton as a function of the concentration of the metallic dichlorides investigated and indicate quite clearly the concentration regions of strong paramagnetic broadening as well as the regions for maximum exchange broadening. The two lines shown for Fe^{2+} in Figure 2 indicate problems of reproducibility of the data for this case in the 10^{-6} to 10^{-5} M region; it is presumed that varying amounts of Fe^{3+} in the several stock solution samples which were diluted with absolute ethanol are responsible for the poor reproducibility. The
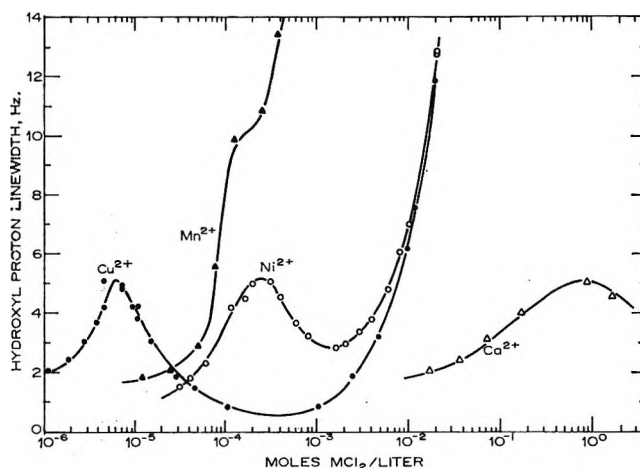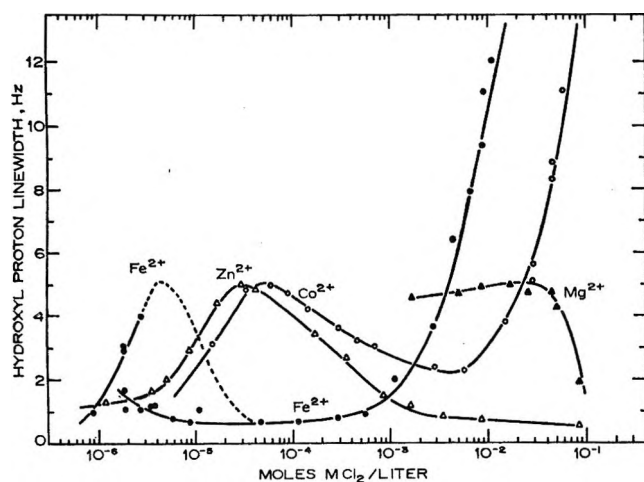
Figure 2. Dependence of ethanol hydroxyl proton line width at $\sim 39°$ on concentration of some metal chlorides in absolute ethanol.

Table II. In light of the small value of k_0, the agree-

Table II: Rate Constants for the Hydroxyl Proton Exchange Reaction in Ethanol Solutions of Some Divalent Metal Chlorides Near 39°

Ion	$[M^{2+}]_x$, mol l.$^{-1}$	k_x, l. mol^{-1} sec^{-1}	k_1, l. mol^{-1} sec^{-1}
Ca^{2+}	7.0×10^{-1}	$3.5 \times 10^{1\ a}$	
Mg^{2+}	2.5×10^{-2}	9.8×10^{2}	
Mn^{2+}	3.0×10^{-4}	8.1×10^{4}	
Ni^{2+}	2.5×10^{-4}	9.8×10^{4}	10.5×10^{4}
Co^{2+}	4.0×10^{-5}	6.1×10^{5}	7.1×10^{5}
Zn^{2+}	2.5×10^{-5}	9.8×10^{5}	8.6×10^{5}
Cu^{2+}	6.0×10^{-6}	4.1×10^{6}	3.9×10^{6}
Fe^{2+}	$3\ \times 10^{-6\ b}$	$<8.1 \times 10^{6}$	

^{a} Temperature was 36°. ^{b} This is the lower limit of the appropriate concentration value and is somewhat uncertain.

smooth curves of Figures 1 and 2 are each the average result of measurements on several separate samples of each of the salt–ethanol mixtures. The reproducibility generally achieved is illustrated by the data in Table I for CuCl$_2$.

The graphs of Figures 1 and 2 furnish a comparison of the catalytic effectiveness of the several cations but a more quantitative comparison is obtained from the rate constants for the catalysis by the various cations. From the hydroxyl proton line shape at maximum broadening and by use of appropriate tables[5] the mean time, τ_x, between proton exchanges was found to be 0.041 sec when the condition of maximum exchange broadening prevailed. The reciprocal of τ_x represents a rate in sec^{-1} and this rate can be related to the concentration of the cation, $[M^{2+}]_x$, at which maximum exchange broadening occurred by the expression

$$\frac{1}{\tau_x} = k_x[M^{2+}]_x \tag{1}$$

By using the value of τ_x and appropriate values of $[M^{2+}]_x$ for the various cations, relative values of the rate constant, k_x, can be calculated. An alternative method is to determine the τ values appropriate[5] to the hydroxyl proton line shape at several concentrations of a particular cation and by means of eq 2 determine the value of k_1 for the several cations.

$$\frac{1}{\tau} = k_0 + k_1[M^{2+}] \tag{2}$$

Values of τ appropriate to various concentrations of Zn^{2+}, Cu^{2+}, Ni^{2+}, and Co^{2+} were determined and by appropriate graphs k_1 was evaluated for each cation. It was found that k_0, the rate constant for absolute ethanol, was essentially the same for each of the salts with a value of 2.0 ± 0.2 sec^{-1} at 39°. Values of $[M^{2+}]_x$, k_x, and k_1 at 39° obtained as indicated above are given in

ment between k_1 and k_x is to be expected as the range of concentrations used in evaluating k_1 is, of necessity, near and overlaps the value of $[M^{2+}]_x$ for which k_x was evaluated.

There do not appear to be other reported values of rate constants for the systems included in Table II. However, Grunwald, et al.,[6] have reported a rate constant of 3.5×10^9 l. mol^{-1} sec^{-1} at 24.8° for the reaction

$$CH_3OH^* + CH_3OH_2^* \longrightarrow CH_3OH + CH_3OH^*H^+$$
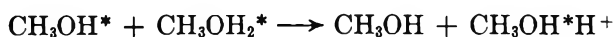
From corrections found by these authors for work previously reported by Luz, et al.,[7] for the above case and for ethanol one may infer that the value of k for the equivalent ethanol reaction is about 4×10^7 l. mol^{-1} sec^{-1}. In a further search for comparative values one may estimate on the basis of some of Arnold's[3] data that the acid catalysis rate constant is approximately 7×10^6 l. mol^{-1} sec^{-1}. By using an average of the above two values it appears that catalysis of the exchange by acid is superior to catalysis by any of the divalent cations studied in this investigation, although Fe^{2+} and Cu^{2+} compare favorably.

A detailed mechanism which will explain the relative catalytic effectiveness of the several cations is not at all apparent; however, two general observations can be made. The first is that filled or partially filled d orbitals seem essential to large catalytic effects, and the second is that there is no fully consistent relation of the ionic radii and the relative catalytic effectiveness of the several cations.

(5) "Tables of Exchanged Broadened NMR Multiplets," The Weizmann Institute of Science, Rehovoth, Israel, 1958.

(6) E. Grunwald, C. F. Jumper, and S. Meiboom, J. Amer. Chem. Soc., **84**, 4664 (1962).

(7) Z. Luz, D. Gill, and S. Meiboom, J. Chem. Phys., **30**, 1540 (1959).

Table III: Some Physicochemical Characteristics of the Systems Studied and Related Data

Ion	Fe^{2+}	Cu^{2+}	Zn^{2+}	Co^{2+}	Ni^{2+}	Mn^{2+}	Mg^{2+}	Ca^{2+}
d orbitals	d^6	d^9	d^{10}	d^7	d^8	d^5		
Crystal radius,[a] Å	0.75	~0.72	0.74	0.72	0.69	0.80	0.65	0.99
Log k_x[b]	(6.91)	6.61	5.99	5.79	4.99	4.91	2.99	1.55
Log (k_{xi}/k_{xCu})	(0.30)	0	−0.62	−0.83	−1.62	−1.70	−3.62	−5.07
Log $K_{M(OH)}$+ [c]	6.1	6.66	5.26	4.23	4.85	4.52	2.36	1.34

[a] From ref 8. [b] Rate constants are for 39°. [c] From ref 9, obtained by averaging the listed values of log K_1. See text.

For purposes of further discussion and reference, Table III shows a collection of data including the free ion d orbital configuration, the ionic radii,[8] the logarithm of the rate constant k_x and of the ratio of the catalysis rate constant k_{xi} for a particular cation i to the value of k_{xCu}, for the Cu^{2+} ion, and finally the logarithm of average value of the stability constants[9] for the monohydroxy complex of the several cations. The logarithm of the ratio log (k_{xi}/k_{xCu}) will be used for comparison of activation free energies according to the relation

$$\log (k_{xi}/k_{xCu}) = -\frac{(\Delta G^{\ddagger}_i - \Delta G^{\ddagger}_{Cu})}{2.3RT} \qquad (3)$$

where constant temperature and constant transmission coefficient are assumed. The logarithm of the stability constant of the monohydroxy complex of the cations will be used to determine if the ethanol proton exchange catalysis can be related to the form of the Brønsted catalysis law[10] as given by

$$k_M = C K_M^{\alpha} \qquad (4)$$

Here k_M is the catalytic rate constant for metal ion M, C and α are constants characteristic of the reaction, solvent, temperature, etc., and K_M is normally the stability constant of the metal ion complex with the ligand under study, but in the present case these stability constants are not known so the stability constants of the monohydroxy complex in aqueous solution will be used instead.

In the data of Table III it is apparent from the rate constant that Mn^{2+}, with partly filled d orbitals, is about two orders of magnitude more effective as a catalyst for the proton exchange reaction than is Mg^{2+}, a much smaller ion but with no available d orbitals. The case of Zn^{2+} with a d^{10} configuration is more striking as it is about a 1000 times as effective as a catalyst as Mg^{2+} and the Zn^{2+} radius is about 0.1 Å larger than the Mg^{2+} radius. On the basis of central ion radius alone one might expect the catalytic effectiveness to be reversed from that observed for both of the above cases.

The considerable difference in catalytic effectiveness found for the ions can be accounted for by only a moderate activation free energy difference. For example,

in the case of the extremes, namely Fe^{2+} and Ca^{2+}, the data of Table III used in eq 3 indicate an activation free energy difference of only 7.8 kcal mol^{-1}. A combination of small differences in the entropy of activation and of differences in separation of the hydroxyl proton and the central ion causing changes in the coulombic interaction could readily give rise to the required 7.8-kcal activation free energy difference.

In connection with the above it is of interest that the three ions Ca^{2+}, Mn^{2+}, and Zn^{2+}, all of the same period and none of which is subject to crystal field stabilization effects in weak ligand fields, do appear to have the differences in rate constants at least approximately related to the differences in ionic radii. The form of the difference in coulombic interaction for two ions, say 1 and 2, is given by

$$E_2 - E_1 = C\left[\frac{1}{a_2 + r_2} - \frac{1}{a_1 + r_1}\right] \qquad (5)$$

Here a_1 and a_2 are essentially equal distances as they represent the approximately constant distance from the ethanol hydroxyl proton to the nonbonded radius of the metal cation, r_1 and r_2 are the respective ionic radii, and C is a collective constant which includes the effective coulombic charges and the dielectric constant effective for the interactions involved. Since a^2 is significantly larger than $r_1 r_2$ and since only rough approximations are under consideration one may, by using eq 3 and 5, write

$$\Delta G^{\ddagger}_2 - \Delta G^{\ddagger}_1 = -2.3 \, RT \log k_2/k_1 = C'(r_1 - r_2)$$

or more conveniently

$$C''(r_1 - r_2) = -\log k_2/k_1 \qquad (6)$$

If Mn^{2+} is selected as reference ion 1 and the Ca^{2+} as ion 2, one calculates a value of $C'' = -17.7$ cm^{-1}; if Zn^{2+} is ion 2 the calculated value of C'' is -18.0 cm^{-1}. In light of the threefold difference in the $(r_1 - r_2)$ term for the two cases the agreement in C'' is surprisingly

(8) L. Pauling, "The Nature of the Chemical Bond," 3rd ed, Cornell University Press, Ithaca, N. Y., 1960, p 518.

(9) L. G. Sillén and A. E. Martell, "Stability Constants of Metal Ion Complexes," The Chemical Society, London, Special Publication No. 17, 1964.

(10) (a) J. F. Bunnett, *Tech. Org. Chem.*, 8, 230 (1961); (b) S. A. Bernhard, *ibid.*, 8, 604 (1961).
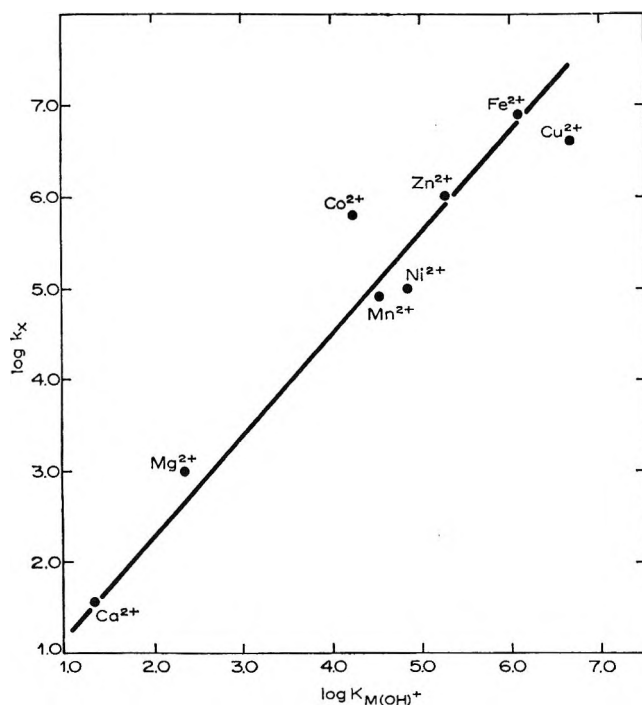
Figure 3. Comparison of catalytic rate constant, k_x, for ethanol hydroxyl proton exchange at $\sim 39°$ with stability constant, $K_{M(OH)}{}^+$, of monohydroxy metal ion complex at $-25°$.

good, and likely somewhat fortuitously so. In view of the general physicochemical effects found to be associated[11] with crystal fields the regularity in behavior of the specific cases of Ca^{2+}, Mn^{2+}, and Zn^{2+} systems may reasonably have been anticipated.

In Figure 3 the form of the Brønsted catalysis law is seen to apply to rate constants obtained in the present investigation when these are related to the stability constants of the monohydroxy complex ions of the respective cations given in Table III. As noted in Table III, an average value of log K_1 for the $M(OH)^+$ complex obtained from literature listings[9] is used since no single author seems to have reported all of the needed data. In obtaining the averages it was necessary to use data at several temperatures near 25° and to use data obtained at several ionic strengths. The lack of consistency in the values used to obtain the average value of log K_1 certainly somewhat compromises the significance of the apparent linearity shown in Figure 3. However, the range of data in Figure 3 covers approximately five decades and the average deviation for the log K_1 values used to establish the log $K_{M(OH)}{}^+$ of Figure 3 was near ± 0.2; therefore, the compromise is thought to be insignificant in the present context.

In view of the approximate linearity found in Figure 3 it is reasonable to infer that the factors which determine the catalytic rate constants are closely related to the factors which determine the stability constants of the monohydroxy complexes. This suggests that possible and certainly expected steps in the catalysis reaction

involve complexing and subsequent exchange reactions such as I and II below.

$$M^{2+} + EtOH \rightleftharpoons M(EtOH)^{2+} \qquad (I)$$

$$M(EtOH)^{2+} + EtOH \longrightarrow M(EtO)^+ + EtOH_2{}^+ \quad (II)$$
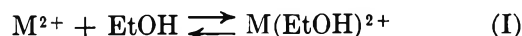
If step II is determinative in the rate of the catalysis reaction the stability of $M(EtO)^+$ will be closely related to the availability of the highly reactive species $EtOH_2{}^+$ and one could infer that the stability constants of the monohydroxy complex should compare well with the observed catalysis rate constants. Information available[12] for ethanol exchange with Mg^{2+} at 25° and for water exchange with all of the cations studied suggests that ligand exchange with the bulk medium is fast, therefore step I, and equivalent steps for exchanges of more fully complexed reactants, should become established very rapidly and would thus not become limiting in the sequence of reactions required for the catalysis.

The very large differences in the exchange rate constants for pure ethanol and for the exchange catalyzed by acid and by $CuCl_2$ made it of interest to investigate, in a limited degree, the effect of temperature on the rate constants and thus a determination of the comparative activation parameters for the three cases. The activation parameters evaluated from eq 7 are given in Table IV. The values of τ required in eq 7 were

$$\log \frac{1}{\tau} = -E_a/2.3RT + \log A \qquad (7)$$

Table IV: Activation Parameters for Ethanol Hydroxyl Proton Exchange

Substance	E_a, kcal/mol	log A
Pure ethanol	12.0	9.45
Ethanol–HCl	21.3	15.55
Ethanol–CuCl₂	9.1	13.4

determined from line shapes and the Weizmann Institute Tables.[5] It is of interest that Schneider and Reeves[13] report that in pure ethanol the methylene proton signal coalesces to a broad quartet at about 80°, whereas in the present investigation coalescence was observed at 93°. It is felt that the use of higher purity ethanol accounts for the higher coalescence temperature.

The values of the activation parameters, and the approximate activation entropy, $\Delta S^{\ddagger}$, estimated from

(11) B. N. Figgis, "Introduction to Ligand Fields," Interscience, New York, N. Y., 1966, Chapters 4 and 5.

(12) (a) T. D. Alger, J. Amer. Chem. Soc., 91, 2220 (1969); (b) A. McAuley and J. Hill, Quart. Rev., Chem. Soc., 23, 18 (1969); (c) M. Eigen and R. G. Wilkins, Advan. Chem. Ser., No. 49, 55 (1965).

(13) W. G. Schneider and L. W. Reeves, Ann. N. Y. Acad. Sci., 70, 858 (1958).

the data of Table IV, suggest that a different mechanism may be controlling in the pure ethanol from that controlling in the catalyzed cases. The approximate values of the activation entropy in calories mole^{-1} °K^{-1} are -15.4 for pure ethanol; $+12.7$ for the acid-catalyzed case; and $+2.8$ for the $CuCl_2$ case. The above data suggest that the controlling step in the reaction may be bimolecular formation of the active intermediate in pure ethanol, and possibly the unimolecular decomposition of the active intermediate in the catalyzed cases.

Two factors that could compromise the validity of the rate constants reported in this study are the influence of small amounts of water on the concentrations of the cations at which maximum exchange broadening was observed and the possible specific influence of the anions present. Both of these matters were investigated in a limited way with the following results. For an added water concentration of $1.0 \times 10^{-4} M$ in pure ethanol at 39° the $CuCl_2$ concentration necessary for maximum exchange broadening was reduced from $6 \times 10^{-6} M$, characteristic of essentially water free ethanol, to 2×10^{-6} with the water present. In light of the general reproducibility from sample to sample of the salt concentrations required for maximum exchange broadening, it is felt that the rate constants are for essentially water-free systems.

The possible specific influence of the anion on the value of the rate constant was determined using sulfates of magnesium, nickel, and copper rather than the chlorides. The differential effect of sulfates and chlorides was measured by observing the hydroxyl proton line shape in the exchange region for several sulfate salt concentrations and comparing them with concentrations of chloride salt required to give the same line shape. It was found that there were no consistent differences between the two anion systems, as any difference observed fell within the limits of reproducibility of the data.

For cases in the present investigation for which the longitudinal and transverse relaxation times, T_1 and T_2, respectively, are equal and are equally affected by paramagnetic broadening the effective moment, μ_{eff}, of the paramagnetic ion can be calculated[14] using the expression

$$1/T_1 = 4\pi^2\gamma^2\eta N_p\mu_{eff}^2/kT \qquad (8)$$

In eq 8 γ is the nuclear magnetogyric ratio, η is the viscosity of the medium, and N_p is the number of paramagnetic ions per cubic centimeter. The value of T_1 can be determined from the broadened line shape for cases in which the spin–lattice relaxation time equals the transverse relaxation time, T_2. By using a value[15] of η for ethanol at 40° of 0.016447 P, and the broadened hydroxyl proton signal in the range of paramagnetic salt concentrations for which paramagnetic broadening was clearly dominant, the values of μ_{eff} recorded in Table V were calculated. Comparison with values of

Table V: Comparison of Magnetic Moments, in Bohr Magnetons, for Some Paramagnetic Cations Obtained from Nuclear Relaxation Effects and from Susceptibility Measurements

Ion	μ_{eff} (Ethanol)	$\mu_{eff}{}^a$ (H_2O)	$\mu_{eff}{}^b$ (Suscept)
Cu^{2+}	2.0^c	2.0	2.0
Ni^{2+}	2.1	2.1	3.1
Co^{2+}	1.1	1.0	5.0
Fe^{2+}	2.7		5.3

^{a} Reference 16. ^{b} Reference 17. ^{c} All values in Table V refer to μ_{eff} for Cu^{2+} as 2.0 BM.

μ_{eff} obtained for water solution by Morgan et al.,[16] shows agreement between the ethanol and water solution values; however, for Ni^{2+}, Co^{2+}, and Fe^{2+} the susceptibility values[17] of μ_{eff} are larger than the μ_{eff} values calculated from the relaxation effect. It is probable that this discrepancy arises from a short electron spin-lattice relaxation time which causes the fields of the unpaired spins to be somewhat inefficient[18] in relaxing the protons in water and ethanol. The case of Mn^{2+} is excluded from Table V because the proton line shapes in the solutions of $MnCl_2$ were determined by the transverse relaxation time T_2, which was considerably shorter[19] than T_1 in such solutions.

The chemical shifts produced at the several ethanol protons by the paramagnetic ions can be used to estimate the unpaired electron spin density[20] at the respective protons and thus obtain some idea of the extent of possible delocalization of the electrons of the ions or of the ligand. The chemical shifts must be measured relative to some diamagnetic reference standard; in the present case TMS was used as the standard in pure ethanol to obtain reference proton shifts and then used as an internal standard in the ethanol–paramagnetic salt solutions to determine the chemical shift attributable to isotropic hyperfine interaction. Signal broadening in Mn^{2+} solutions obscured signal maxima in all but very dilute solutions ($\sim<10^{-3} M$) so chemical shift data for ethanol in $MnCl_2$ were not recorded.

The experimental chemical shifts were obtained over concentration ranges of the salts from about $2 \times 10^{-3} M$ to $2 \times 10^{-2} M$, or in case broadening was not serious, to about $6 \times 10^{-2} M$ at 39°. In all cases the chemical

(14) Reference 2b, p 207.

(15) "International Critical Tables," Vol. V, E. W. Washburn, Ed., McGraw-Hill, New York, N. Y., 1929, p 10.

(16) L. O. Morgan, A. W. Noble, R. L. Hill, and J. Murphy, *J. Chem. Phys.*, **25**, 206 (1956).

(17) R. L. Conger and P. W. Selwood, *ibid.*, **20**, 383 (1952).

(18) Reference 2b, p 210.

(19) N. Bloembergen and L. O. Morgan, *J. Chem. Phys.*, **34**, 842 (1961).

(20) (a) C. P. Slichter, "Principles of Magnetic Resonance," Harper and Row, New York, N. Y., 1963, p 89 ff; (b) reference 2a, p 221 ff.

Table VI: Chemical Shifts[a] in Hertz and Relative Unpaired Electron Spin Densities
for Ethanol Protons in Several Paramagnetic Salt Solutions (39°)

| | Groups | | | | | |
| | OH | | CH₂ | | CH₃ | |
Salts	$\frac{d\delta}{dX_m} \times 10^{-3}$	$\rho_r \times 10^3$	$\frac{d\delta}{dX_m} \times 10^{-3}$	$\rho_r \times 10^3$	$\frac{d\delta}{dX_m} \times 10^{-3}$	$\rho_r \times 10^3$
$CuCl_2$	+2.02	−0.94	−5.85	+2.7	−1.66	+0.78
$NiCl_2$	−2.42	+0.42	−8.96	+1.6	−4.36	+0.76
$CoCl_2$	−12.5	+1.2	−8.74	+0.82	−1.01	+0.09
$FeCl_2$	−10.9	+0.63	−15.3	+0.89	−3.24	+0.19
$CaCl_2$	−0.16		−0.04		−0.02	

[a] Negative chemical shifts are to lower field and correspond to an excess of α electron spin at the indicated proton; *viz.*, the electron moment opposes the static field ($\equiv$60 MHz) at the nucleus.

shifts were best represented as straight lines with zero intercepts when the chemical shift was graphed against ion concentration. With the exception of the hydroxyl proton in $CuCl_2$ solutions all shifts were to lower resonant frequencies. There is a problem of converting the chemical shifts observed in the rather dilute solutions to some basis that will make reasonable a comparison of calculated unpaired spin densities for the solution system with similar calculations for radicals and other pure substances. One alternative, and the one followed here, is to use the observed chemical shifts in the dilute solutions to obtain a somewhat fictitious "partial molal chemical shift" by extrapolation of the low concentration values to unit mole fraction of the paramagnetic ion. Since the graph of the hyperfine interaction chemical shift, δ_i, for equivalent protons of ethanol *vs.* the mole fraction of the paramagnetic ion, X_m, is found to be a straight line, the slope $d\delta/dX_m$ furnished the required "partial molal chemical shift". At the dilutions involved ($\sim 10^{-2}$ M) the mole fractions of the solutions were calculated from molarities by using the density[21] of pure ethanol at 39°. This approximation introduced an error of less than 1% in the slope.

The values of the "partial molal chemical shift" in Hertz are recorded in Table VI along with relative values of the electron unpaired spin density, ρ_r, calculated as follows.

The additional magnetic field, ΔH, experienced[22] by a nucleus because of unpaired electron spin density is given by

$$\Delta H = \frac{-A_n h(S)(S+1)}{3kT}\left[\frac{g_e\beta_e}{g_n\beta_n}\right]H \qquad (9)$$

Here A_n is the Fermi hyperfine splitting for nucleus n in Hertz, h is Planck's constant, S is the total electronic spin of the paramagnetic ion, g_e and g_n are the electronic and nuclear g factors, respectively, β_e and β_n are the Bohr and nuclear magneton, and H is the large static magnetic field. The Fermi formula for A_n in Hertz is

$$A_n = \frac{8\pi}{3h}g_e\beta_e g_n\beta_n|\psi(0)|^2 \qquad (10)$$

where β_e and β_n are in ergs/G and $|\psi(0)|^2$, the squared amplitude of the electronic wave function at the nucleus, is in electrons/cubic centimeter. By inserting appropriate values in eq 9 and 10, after replacing $\Delta H/H$ by $\delta_{Hz}/6.0 \times 10^7$ where δ_{Hz} equals $(d\delta/dX_m)$, one obtains

$$|\psi(0)|^2 = \frac{-7.48 \times 10^{17}\delta_{Hz}}{(S)(S+1)} \qquad (11)$$

It is apparent from eq 11 that a positive value of δ_{Hz}, namely a shift to a higher nuclear resonance frequency, yields a negative spin density, or, in terms of α and β electronic spins, a condition at the nucleus which causes the nucleus "to see" an excess of β electronic spin, a spin which adds the field of the electronic magnetic moment to the external static field. The relative unpaired spin density was calculated by comparing the spin density evaluated from eq 11 to the value of the spin density for the free hydrogen atom, namely

$$\rho_r = [\psi(0)]^2/2.15 \times 10^{24} \qquad (12)$$

The data for $CaCl_2$ are included in Table VI for comparison and to indicate some measure of the uncertainty in the meaning of the chemical shift data in terms of unpaired electron spin densities. It is clear that all paramagnetic cases greatly exceeded the shift effects found for $CaCl_2$; however, it is also clear that the total unpaired spin density in the ethanol molecule is small, being of the order of 7×10^{-3} for the maximum case of $CuCl_2$ and about 3×10^{-3} for $FeCl_2$.

The only alcohols that appear to have been studied[23] as to paramagnetic contact shifts, other than at low temperatures where ligand exchange is very slow,[24]

(21) "American Institute of Physics Handbook," Vol. 2, 2nd ed, McGraw-Hill, New York, N. Y., 1963, p 151.

(22) (a) D. R. Eaton and W. D. Phillips, *Advan. Magn. Resonance*, 1, 605 (1965); (b) R. M. Golding, "Physical Chemistry," Vol. IV, H. Eyring, D. Henderson, and W. Jost, Ed., Academic Press, New York, N. Y., 1960, p 459 ff.

(23) W. D. Phillips, C. E. Looney, and C. K. Ikeda, *J. Chem. Phys.*, 27, 1435 (1957).

(24) (a) Z. Luz and S. Meiboom, *ibid.*, 40, 1058, 1066 (1964); (b) Z. Luz, *ibid.*, 41, 1748, 1756 (1964).

are 1-propanol and 1-hexanol using $CoCl_2$ at concentrations ranging from about 0.1 M to about 2.7 M. By taking into account that the reported work on propanol was at 30 MHz, it is found that the chemical shift for the protons on the α carbon of propanol agrees rather well, as to absolute value, with the observed chemical shift of the methylene protons of ethanol in the present study; however, the shifts for the propanol and the ethanol are recorded as having opposite field shift directions. It is not clear from information at hand concerning the propanol and hexanol studies whether they were made at constant frequency–variable field, or at constant field–variable frequency. If it was the former the disagreement as to direction of chemical shift is only apparent, for a $+\Delta H$ value in this case would represent an excess α electronic spin for the proton under observation. There is no agreement for the propanol and hexanol as to absolute magnitude or direction for the β carbon protons, or for the hydroxyl group proton, or for the γ, δ, etc., carbon proton chemical shifts and the shifts observed for the hydroxyl and methyl group protons of ethanol.

There have been many contributions to the understanding of observed hyperfine interactions and most of these have been reviewed by Eaton and Phillips.[22a] It appears, however, that none of these will fully explain the results reported in Table VI and possibly the simplest view would be that there is polarization of the σ electronic system of the ethanol by the unpaired electron(s) of the paramagnetic ions. Judging from the magnitude of this effect as recently reported by Pople and Beveridge[25] for a methyl group proton in a plane perpendicular to the 2pπ orbital of the methylene carbon in the ethyl radical, the polarization effect will well accommodate the spin densities reported in Table VI. The attenuation in relative spin density in going from the methylene to the methyl group seems consistent with the spin polarization being transmitted through the bonding system of the ethanol. It is interesting to note that the relative spin densities calculated by eq 9–12 show a decrease of the total spin density on the ethanol protons as the number of unpaired electrons on the cations increases. It is also of interest to note that the calculated spin densities should give rise to hyperfine coupling constants of 0.5–1.5 G, a range of couplings near those found for some transition metals with the protons of metallocenes[26] and chelates.[27]

(25) J. A. Pople and D. L. Beveridge, "Approximate Molecular Orbital Theory," McGraw-Hill, New York, N. Y., 1970, p 144.

(26) H. M. McConnell and C. H. Holm, *J. Chem. Phys.*, 27, 314 (1957); 27, 749 (1957).

(27) (a) D. R. Eaton, A. D. Josey, W. D. Phillips, and R. E. Benson, *Discuss. Faraday Soc.*, 34, 77 (1962); (b) R. S. Milner and L. Pratt, *ibid.*, 34, 88 (1962); (c) D. R. Eaton, *J. Amer. Chem. Soc.*, 87, 3097 (1965).

Kinetics of the Catalysis by Reversed Micelles of

Cetyltrimethylammonium Bromide in Hexanol

by S. Friberg* and S. I. Ahmad

The Swedish Institute for Surface Chemistry, S-114 28 Stockholm, Sweden   *(Received January 25, 1971)*

Publication costs assisted by the Swedish Board for Technical Development

The influence of reversed micelles on the hydrolysis rate of p-nitrophenyl laurate has been investigated. The rate constant for hydrolysis was determined in hexanol solutions of water and cetyltrimethylammonium bromide of different compositions. The rate constant showed a pronounced increase when reversed micelles were formed in the system, giving evidence of a catalytic effect of reversed micelles.

Catalysis in micelles by cationic species has been treated in several articles following the pioneering work of Duynstee and Grunwald in 1959.[1] Cordes and Dunlap[2] have recently published an extensive review of the field. They point to two factors as being responsible for enhanced reaction rates: first, electrostatic and second, hydrophobic interactions of reactants, transition complex, and reaction products with the micellar phase. The existence of a charged transition state when a neutral molecule is hydrolyzed by hydroxide

(1) E. F. J. Duynstee and E. Grunwald, *J. Amer. Chem. Soc.*, 81, 4540 (1959).

(2) E. H. Cordes and R. B. Dunlap, *Accounts Chem. Res.*, 2, 329 (1969).

ions shows the importance of electrostatic interactions.[3,4] Structural effects in reactant species are reflected in accentuated hydrophobic bonding which gives rise to a higher concentrations in the micelles.[5]

The majority of these investigations has been carried out in aqueous solutions where the poorly soluble reactant is solubilized at the surface of normal micelles, while the second reactant, commonly the hydroxide ion, is soluble in the aqueous part. Exceptions are recent investigations on the kinetics of catalysis at the heptane–water interface[6] and on catalysis in nonhydroxylic solvents.[7] However, in none of these investigations is the possible influence of reversed micelles treated.

Electrostatic interactions have a dominant effect on reactions in aqueous micellar solutions. However, since reversed micelles present in nonaqueous solutions of surfactants have received increased attention in recent years[8-12] we considered it worthwhile to investigate the possible catalytic activity of reversed micelles. In view of the numerous treatments of hydrolysis of p-nitrophenyl esters catalyzed by cationic surfactants we chose p-nitrophenyl laurate and hexadecyltrimethylammonium bromide for the present investigation.

Experimental Section

Materials. Analytical reagents p-nitrophenyl laurate (Schuchardt, München), 1-hexanol (Fluka), and cetyltrimethylammonium bromide (Merck), CTAB, were used. Doubly distilled water, buffered to pH 11.5 by means of a 0.01 M sodium phosphate buffer, was used.

Reaction Rates. Kinetic measurements were performed by determination, at various times, of the amount of p-nitrophenolate ion from the extinction at 400 mμ by means of a Zeiss PMQ II spectrophotometer. Initial concentration of p-nitrophenyl laurate ester was 2.4 $\times$ 10^{-5} M. First-order rate constants were determined from the half-life, measured from the actual and final concentration of the phenolate ion.

The determinations were made on seven series of solutions, each with a constant ratio of hexanol:surface active substance and with varying amounts of water.

Results

The reaction rates, expressed as rate constants for a first-order reaction in the ester, were determined for the seven series according to Figure 1. The first three series with alcohol contents above 70% were chosen in the narrow region where the solubility of water is increased only slightly over that in pure hexanol. Increasing amounts of water were present in the next three series reaching a maximum of 55% in series No. 6. Series No. 7 was chosen with a higher content of CTAB and smaller amounts of water.

The results are shown in Figure 2, with Figure 3 giving a "three dimensional" picture of the variation. The first three series gave low rate constant values between 0 and 0.03 min^{-1} which were not markedly depen-
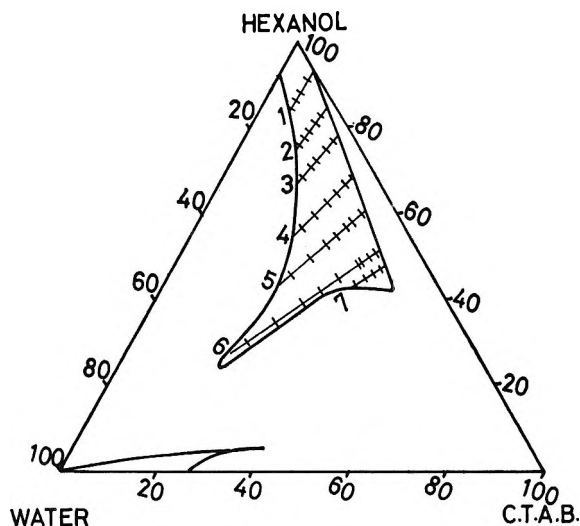
Figure 1. The hexanol solution area in the system water–CTAB–hexanol and the compositions used in the investigation. The numbers refer to the different series.

dent on the water content. At higher content of the surface active substance *ab* series 4, an increase of rate constants occurred when the water content was increased, and the rate constant reached values of between 0.1 and 0.4. This increase in rate constant took place rapidly over a narrow range of concentration.

Discussion

The results show a well-defined trend; the reaction rate constant increases rapidly over narrow concentration regions. This increase is observed when the alcohol content is reduced to below 70% (w/w) and when the water content is increased a few per cent above the minimum level where micellar solutions exist.

In order to explain this, the association conditions of the solutions in the region studied must be considered. The system water–hexanol–CTAB has been investigated by Lawrence,[13] who found the liquid alcohol phase. Recently Lindblom,[11] in a study of the counterion binding using nuclear magnetic relaxation of ^{81}Br, found a pronounced decrease of relative line width, $\Delta B/\Delta B_0$, as the alcohol concentration was reduced below about 70 wt %. Below this value the line width was con-

(3) J. L. Kurz, *J. Phys. Chem.*, **66**, 2239 (1962).

(4) R. B. Dunlap and E. H. Cordes, *ibid.*, **73**, 361 (1969).

(5) C. A. Benton, L. Robinson, and L. Sepulveda, *J. Org. Chem.*, **35**, 108 (1970).

(6) F. M. Menger, *J. Amer. Chem. Soc.*, **92**, 5965 (1970).

(7) R. L. Snell, W.-K. Kwok, and Y. Kim, *ibid.*, **89**, 6728 (1967).

(8) S. Friberg, L. Mandell, and P. Ekwall, *Acta Chem. Scand.*, **20**, 2632 (1966).

(9) G. Gillberg, H. Lehtinen, and S. Friberg, *J. Colloid Interface Sci.*, **33**, 40 (1970).

(10) G. Söderlund and S. Friberg, *Z. Phys. Chem.*, **70**, 39 (1970).

(11) G. Lindblom, B. Lindman, and L. Mandell, *J. Colloid Interface Sci.*, **34**, 262 (1970).

(12) P. Ekwall, L. Mandell, and P. Solyom, *ibid.*, **35**, 266 (1971).

(13) A. J. Hyde, D. M. Langbridge, and A. S. C. Lawrence, *Discuss. Faraday Soc.*, **18**, 239 (1954).
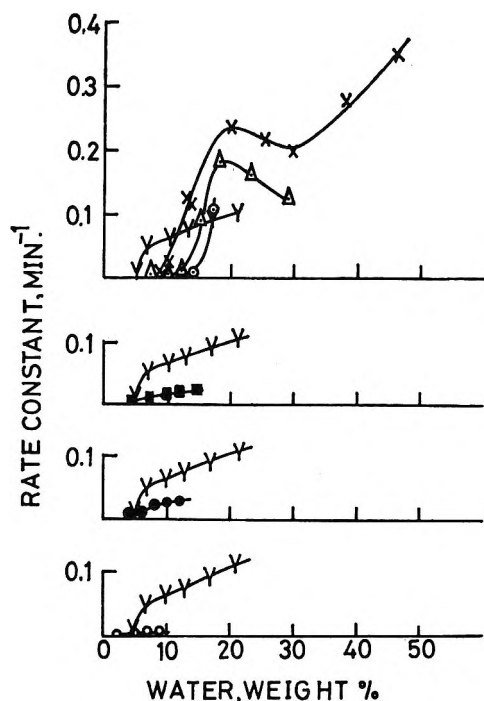
Figure 2. The rate constants as function of the water content in the different series: (sign, series), O, 1; ●, 2; ■, 3; Y, 4; △, 5; ×, 6; ⊙, 7.
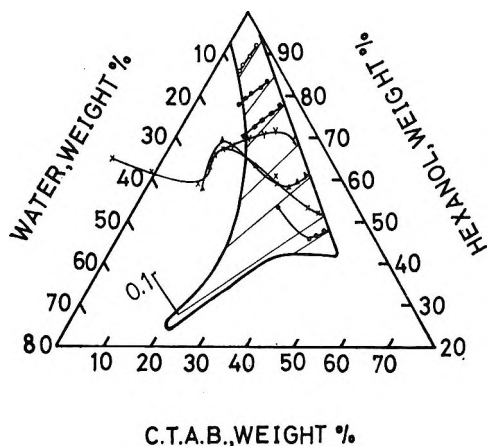
Figure 3. Overall view of the rate constants as function of the composition of the solution.

stant. After comparison with the X-ray and viscosity data of Ekwall,[12] Lindblom concluded that the three substances formed micelles at alcohol concentrations below 70%. At higher alcohol concentrations, the formation of ion pair complexes, solvated by water and hexanol, was suggested.

At the ratio 1:3.5 of CTAB to hexanol, the solutions have a maximum water solubilizing capacity. When the water content is decreased in this solution, an increase in the line width, $\Delta B/B_0$, at 20–30% water was found.[11] It was concluded that the bromide ions are more firmly bound to the micellar surface in the region with water concentrations below this value. According to Ekwall[12] both the viscosity of and the Bragg
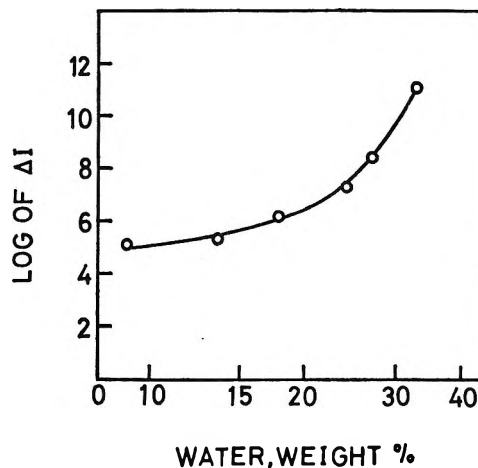
Figure 4. Change in intensity of light scattering with concentration of water.

spacing from the solutions increase considerably when the water content is in excess of 30% (w/w). As the water content is decreased from this value, the viscosity decreases linearly while the Bragg spacing increases. Our light scattering determinations (Figure 4), expressed as a plot of log ΔI against log concentration according to Malik,[14] show approximately two straight lines with an intersection at a water content of 25%. The increased Bragg spacing at low water content is not necessarily due to the formation of micelles. However, on comparison of the results from several different investigations, micellization appears highly probable at water contents above 30% (w/w).

The present results therefore strongly indicate a correlation between the formation of reversed micelles and a sudden increase of the reaction rate. For all water concentrations studied, on reduction of the concentration of hexanol, an increase of reaction rate begins at the concentration where micelles begin to form. It appears evident that hydrolysis is catalyzed to a greater extent when the water is associated into micelles, as compared when it serves as solvation for ion pairs at high alcohol concentrations. In this latter case the solvated water will probably not show the same hydroxide ion activity and the effect of the buffer in alcohol solutions cannot be directly compared with its effect in aqueous solutions. The primary cause of the increased catalytic influence when micelles are present could consequently be but is not necessarily found in these phenomena.

The rate constant referred to a first-order reaction is of the same magnitude as from investigations on normal micelles containing CTAB[15] showing a maximum value of $K_{obsd} \approx 0.26$ min^{-1}. This shows that this method of solubilizing the hydrolyzing agent gives a

(14) W. U. Malik, A. K. Jain, and O. P. Jhamb, Int. J. Appl. Radiat. Isotop., 21, 564 (1970).

(15) L. R. Ramsted and E. H. Cordes, J. Amer. Chem. Soc., 90, 4404 (1968).

similar efficiency to that obtained when the reactant is solubilized.

The calculation of a rate constant that referred to a first-order reaction is justified since the buffered aqueous solution gives a constant pH value, so that the hydroxide ion is present in large excess over the reactant even in the most water-poor solutions. The total amount of water is, however, not constant in the different solutions. Dividing by the concentration of water and by the maximum value of the rate constant gives the relative "approximate second-order rate constant" according to Figure 5. This presentation of the results shows the effect of the different activity of water in the different solutions. The sudden increase of the rate constant at micellization can formally be referred to a change of the hydroxyl ion activity. Furthermore, in all the series where a sudden increase of the reaction constant is found, a maximum value of the rate constant is observed immediately after the sudden increase. The decrease of the value of the rate constant after this maximum may be explained by assuming an increased micellar size with higher water content. Since the hydrolysis reaction must occur in a surface layer at the micelle, an increased micelle diameter will give less catalytic efficiency due to a decreased micellar surface area per volume of water. Both the results of Ekwall[12] and our light scattering data can be interpreted as originating from increased micellar size with increased water content. This would explain the decrease of the second-order rate constant with increased water content.
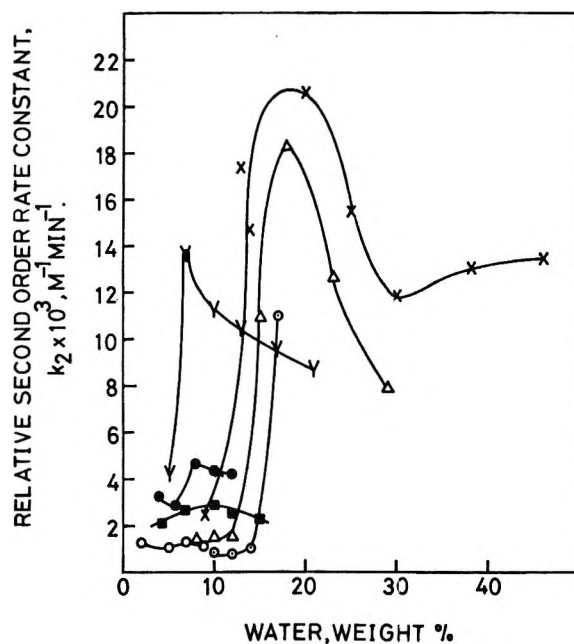
Figure 5. Relative second-order rate constants: (sign, series), O, 1; ●, 2; ■, 3; Y, 4; △, 5; X, 6; ⊙, 7.

The investigations will be continued with the reactions in surfactants under different association conditions.

Thermodynamics of Solutions with Liquid Crystal Solvents.   III.

Molecular Interpretation of Solubility in Nematogenic Solvents

Laurence C. Chow[1] and Daniel E. Martire*

Department of Chemistry, Georgetown University, Washington, D. C. 20007   (Received October 22, 1970)

Publication costs borne completely by The Journal of Physical Chemistry

Gas-liquid chromatography was used to obtain infinite dilution activity coefficients and partial molar enthalpies and entropies of solution for 42 nonmesomorphic solutes in both the nematic and isotropic liquid regions of *p*-azoxyanisole and 4,4'-dihexoxyazoxybenzene. A molecular interpretation of solubility in nematogenic solvents is proposed.

Introduction

Since the nematic mesophase differs from the isotropic liquid only in the parallel alignment of the molecular long axes, it is, from a theoretical standpoint, the least structurally complex liquid crystal phase. Recently, for example, statistical mechanical treatments[2-4] have successfully accounted for the existence, stability, and degree of order of nematic mesophases. Furthermore, the nematic phase has proven to be the most amenable to experimental investigation. During the past decade numerous physical studies (*e.g.*, electromagnetic,[5,6] optical,[7] thermal,[8] nmr,[9,10] esr,[11] ir,[12] uv,[13] etc.) have been conducted with varying degrees of success. However, no definitive thermodynamic solution studies have been performed with liquid crystal solvents until gas-liquid chromatographic (glc) investigations were undertaken in this laboratory.[14,15] Glc is a particularly advantageous method for studying the solvent properties of, structure of, and solute behavior in liquid crystals. Since the solute molecules are at infinite dilution, the long range order of the liquid crystal phase is neither disrupted nor destroyed by solute addition. Furthermore, a variety of solutes can be studied conveniently and rapidly (in contrast to static thermodynamic methods)[16,17] and with high accuracy.

In a previous study[15] on nematogenic substances, it was established that surface effects (in a thermodynamic sense) were negligible at both the gas-liquid crystal and the liquid crystal-solid support interfaces in the glc experiment, provided that the coating thickness was greater than about 1000 Å. This recent finding permits one to proceed with thermodynamic glc studies on nematogenic solvents with confidence that the results will provide information about *bulk* liquid crystal behavior.

Experimental Section

Liquid Phases (Solvents). Two nematogenic compounds, 4,4'-dimethoxyazoxybenzene or *p*-azoxyanisole (PAA) and 4,4'-dihexoxyazoxybenzene (DHAB)

were studied.

$$\text{PAA (solid} \xrightarrow{117.5^\circ} \text{nematic} \underset{\longleftarrow}{\overset{134.2^\circ}{\rightleftharpoons}} \text{isotropic)}$$

was 99.6% pure.

$$\text{DHAB (solid} \xrightarrow{81.0^\circ} \text{nematic} \underset{\longleftarrow}{\overset{128.2^\circ}{\rightleftharpoons}} \text{isotropic)}$$
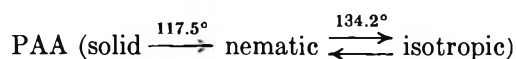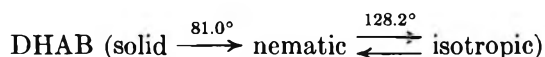
was 99.7% pure. The chemical source, purification procedure, purity determinations, and transition temperature determinations are described elsewhere.[15]

Solutes. Nonmesomorphic organic solutes (42) were chosen for this study. This group of compounds (listed in Table I) exhibits a reasonable range of molecular size, shape, rigidity, polarity, and polarizability. For each of the solutes the physical properties (saturated vapor

(1) Submitted by L. C. Chow to the Department of Chemistry, Georgetown University in partial fulfillment of the requirements for the Ph.D. degree.

(2) M. A. Cotter and D. E. Martire, *Mol. Cryst. Liquid Cryst.*, **7**, 295 (1969).

(3) M. A. Cotter and D. E. Martire, *J. Chem. Phys.*, **52**, 1902, 1909 (1970); **53**, 4500 (1970).

(4) A. Wulf and A. G. deRocco in "Liquid Crystals and Ordered Fluids," T. F. Johnson and R. S. Porter, Ed., Plenum Press, New York, N. Y., 1970, p 227.

(5) R. Williams, *J. Chem. Phys.*, **39**, 384 (1963).

(6) R. P. Twitchell and E. F. Carr, *ibid.*, **46**, 2765 (1967).

(7) G. H. Heilmeier, L. A. Zanoni, and L. A. Barton, *Appl. Phys. Lett.*, **13**, 46 (1968).

(8) E. M. Barrall, II, R. S. Porter, and J. F. Johnson, *J. Phys. Chem.*, **68**, 2810 (1964).

(9) A. Saupe, *Angew. Chem., Int. Ed. Engl.*, **7**, 97 (1968).

(10) J. D. Rowell, W. D. Phillips, L. R. Melby, and M. Panar, *J. Chem. Phys.*, **43**, 3442 (1965).

(11) D. G. Chen, P. G. James, and G. R. Luckhurst, *Mol. Cryst. Liquid Cryst.*, **8**, 71 (1969).

(12) W. Maier and K. Markau, *Z. Phys. Chem.*, **28**, 190 (1961).

(13) A. Saupe and W. Maier, *Z. Naturforsch. A*, **16**, 816 (1961).

(14) D. E. Martire, P. A. Blasco, P. F. Carone, L. C. Chow, and H. Vicini, *J. Phys. Chem.*, **72**, 3489 (1968).

(15) L. C. Chow and D. E. Martire, *ibid.*, **73**, 1127 (1969).

(16) M. L. McGlashan and A. G. Williamson, *Trans. Faraday Soc.*, **57**, 588 (1961).

(17) A. J. Ashworth and D. H. Everett, *ibid.*, **56**, 1609 (1960).

pressures and second virial coefficients) needed for determining the infinite dilution solution activity co-efficients are available or can be accurately estimated. Since solute purity is not an important consideration in this study, the solutes, obtained from five different chemical suppliers (see Table I), were used without further purification.

Table I: Solute Components

Solute no.	Compd	Solute no.	Compd
1	n-Heptane[a]	22	n-1-Decene[a]
2	n-Octane[a]	23	n-1-Undecene[c]
3	n-Nonane[a]	24	1-Chloropentane[b]
4	2-Methyloctane[c]	25	1-Chlorohexane[b]
5	2,2-Dimethylheptane[c]	26	1-Chloroheptane[b]
6	3,3-Dimethylheptane[c]	27	1-Chlorooctane[b]
7	4,4-Dimethylheptane[c]	28	1-Bromohexane[b]
8	2,6-Dimethylheptane[c]	29	1-Iodohexane[b]
9	3-Ethylheptane[c]	30	o-Xylene[b]
10	3,3-Diethylpentane[c]	31	m-Xylene[b]
11	n-Decane[a]	32	p-Xylene[b]
12	n-Undecane[b]	33	o-Dichlorobenzene[b]
13	n-1-Heptene[a]	34	m-Dichlorobenzene[e]
14	n-1-Octene[a]	35	p-Dichlorobenzene[d]
15	n-cis-2-Octene[c]	36	o-Chlorotoluene[e]
16	n-trans-2-Octene[c]	37	m-Chlorotoluene[b]
17	n-cis-3-Oetene[c]	38	p-Chlorotoluene[b]
18	n-trans-3-Octene[c]	39	n-Butylbenzene[b]
19	n-cis-4-Octene[c]	40	Isobutylbenzene[b]
20	n-trans-4-Octene[c]	41	sec-Butylbenzene[b]
21	n-1-Nonene[a]	42	tert-Butylbenzene[c]

[a] Humprey Chemical Co. [b] Baker Chemical Co. [c] Chemical Samples Co. [d] Fisher Scientific Co. [e] Eastman Organic Chemicals.

Preparation of Columns. Since the results of the preceding paper[15] indicated that a highly inert solid support which provides a moderate surface area would be most suitable for this work, the only type of support used here was Johns-Manville 60–80 mesh, acid washed and DMCS-treated Chromosorb W. The solid support was coated with the liquid crystal as previously described.[15] The exact weight per cent of liquid crystal in the packing (dried coated support) was found by taking the average of at least three gravimetric determinations, with about 1 g of packing, done both before and after combustion of the liquid crystal.[18] The coated support was packed into 0.25-in. o.d. copper tubing, which was then coiled to fit the chromatograph oven. The columns were conditioned with a gentle flow of helium (the carrier gas) at about 150° for about 24 hr. Details of the column compositions are given in Table II.

Apparatus and Procedure. The glc apparatus and experimental procedure used in obtaining our solute specific retention volumes $(V_g°)$ have been described previously.[15]

Table II: Composition of Columns

Liquid Crystal	PAA	DHAB
Molecular weight	256.4	395.6
Liquid crystal weight %	18.24	10.00
Liquid crystal surface area[a]	0.6	0.7
Approx film thickness, Å[b]	2600	1200
Total weight, g, of packing	9.8333	6.7473
Total weight, g, of liquid crystal	1.794	0.675

[a] In meters²/gram packing; values interpolated from Figure 2 of ref 19. [b] Estimated by using a mean liquid crystal density of 1.15 g/ml (see ref 15).

Results

Specific Retention Volumes. $V_g°$ data were obtained at five to seven reasonably spaced temperatures in both the nematic and isotropic liquid phases of PAA and DHAB. The probable error in the measurement of $V_g°$ is estimated to be 1.0%.[20] As expected, with helium as the carrier gas and at the low mean column pressures used here, the $V_g°$ values showed no dependence on the gas flow rate.[21-23] The only system for which published $V_g°$ values are available for comparison is o-xylene–PAA.[24] However, because of insufficient information, we are unable to assess the probable error in their measurement; nevertheless, the agreement is reasonable (see Figure 1).

Solute Activity Coefficients. Solute activity coefficients at infinite dilution (γ_p^∞) were determined from the expression[25]

$$\gamma_p^\infty = \frac{1.704 \times 10^7}{M_1 P_2° V_g°} \quad (1)$$

where M_1 is the solvent (liquid crystal) molecular weight, and $P_2°$ is the vapor pressure of the pure saturated solute vapor in Torr. For all but three of the solutes the vapor pressures were calculated from the Antoine equation using the constants from Dreisbach's compilation.[26] For the chlorotoluenes (solutes 36, 37, and 38) the vapor pressures were determined by computer interpolation of published vapor pressure data.[27]

(18) D. E. Martire and P. Riedl, *J. Phys. Chem.*, **72**, 3478 (1968).

(19) R. L. Pecsok, A. de Yllana, and A. Abdul-Karim, *Anal. Chem.*, **36**, 452 (1964).

(20) L. C. Chow, Doctoral Dissertation, Georgetown University, 1970, pp 41, 59 and 60.

(21) D. H. Desty, A. Goldup, G. R. Luckhurst. and W. T. Swanton, "Gas Chromatography," M. van Swaay, Ed., Butterworths, London, 1962, p 67.

(22) D. E. Martire and L. Z. Pollara, *Advan. Chromatogr.*, **1**, 335 (1965).

(23) A. J. B. Cruickshank, M. L. Windsor, and C. L. Young, *Proc. Roy. Soc., Ser. A*, **295**, 259 (1966).

(24) H. Kelker and A. Verhelst, *J. Chromatogr. Sci.*, **7**, 79 (1969).

(25) D. E. Martire, "Gas Chromatography," L. Fowler, Ed., Academic Press, New York, N. Y., 1963, p 33.

(26) R. R. Dreisbach, *Advan. Chem. Ser.*, **No. 15**, (1955); *ibid.*, **No. 22** (1959); *ibid.*, **No. 29** (1961).

(27) D. R. Stull, *Ind. Eng. Chem.*, **39**, 517 (1947).
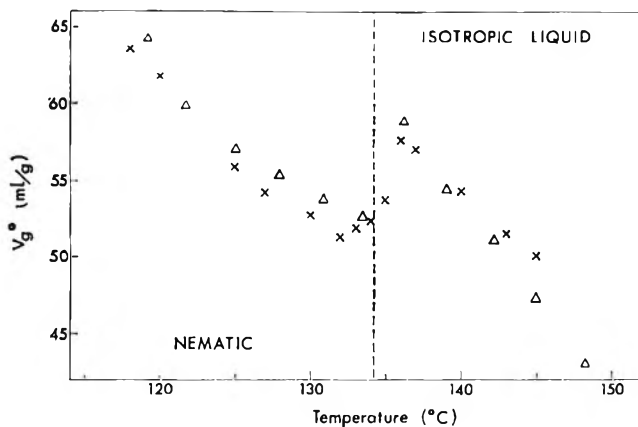
Figure 1. The specific retention volumes $(V_g{}^\circ)$ of o-xylene in PAA. Comparison with results from ref 24: $\triangle$, this study; $\times$, ref 24. (Transition temperature indicated by dashed vertical line.)

Solute activity coefficients fully corrected for the non-ideality of the vapor phase $(\gamma_f{}^\infty)$ were obtained from the expression[22]

$$\ln \gamma_f{}^\infty = \ln \gamma_p{}^\infty - \frac{P_2{}^\circ B_{22}}{RT} \qquad (2)$$

where B_{22} is the second virial coefficient of the pure solute vapor at T.

The virial coefficients were computed from the modified corresponding states equation of McGlashan and Potter.[28-30]

$$\frac{B_{22}}{V_c} = 0.430 - 0.886\left(\frac{T_c}{T}\right) - 0.694\left(\frac{T_c}{T}\right)^2 -$$
$$0.0375(n - 1)\left(\frac{T_c}{T}\right)^{4.5} \qquad (3)$$

where V_c and T_c are the solute critical volume and critical temperature, respectively, and n is the effective carbon number of the solute. Critical constants have been reported[26,31,32] for 34 of our solutes. For the other eight (solutes 24–29, 37, and 38) they were estimated from the normal boiling points[26] (T_B) and parachors[33] (P) through Herzog's[33] empirical expressions

$$T_c = T_B[a - b \log (P)] \qquad (4)$$

$$V_c = 2.92(P)^{1.2}/T_c{}^{0.3} \qquad (5)$$

where T_B is in Kelvin, and the values of the constants a and b are given in ref 33. The third parameter in eq 3, the effective carbon number n, was taken as the actual number of carbon atoms in the molecule for the pure hydrocarbons.[28-30] In determining n for the halogenated hydrocarbons, unit values of 1.0, 1.5, and 2.0 were assigned (based on size considerations) for each chlorine, bromine, and iodine atom, respectively, in the molecule. It is estimated that the maximum uncertainty (when estimated rather than measured critical constants are used) in determination of B_{22} from eq 3 is about 10%.

Taking into account all possible sources of error,[20] it is estimated that the probable error in the measurement of the corrected infinite dilution activity coefficient $(\gamma_f{}^\infty)$ is about 1.5%.

Partial Molar Excess Enthalpies and Entropies. From solution thermodynamics, we have

$$\ln \gamma_f{}^\infty = \frac{\bar{G}_2{}^e}{RT} = \frac{\bar{H}_2{}^e}{RT} - \frac{\bar{S}_2{}^e}{R} \qquad (6)$$

where $\bar{G}_2{}^e$, $\bar{H}_2{}^e$, and $\bar{S}_2{}^e$ are, respectively, the infinite dilution solute partial molar excess free energy, enthalpy, and entropy. From the $\gamma_f{}^\infty$ results, $\bar{H}_2{}^e$ and $\bar{S}_2{}^e$ were determined for each solute in both the nematic and isotropic liquid phases of PAA and DHAB from linear least-squares plots of $\ln \gamma_f{}^\infty$ against reciprocal temperature (see Figures 2–7 for several representative plots). The values are listed in Tables III and IV along with the corresponding standard errors. Smoothed $\gamma_f{}^\infty$ values and the best least-squares linear plots can be generated from eq 6 and the tabulated excess properties.

Partial Molar Enthalpies and Entropies of Solution. For comparing the solution behavior of a series of solute molecules, the enthalpies $(\Delta\bar{H}_2{}^{soln})$ and entropies $(\Delta\bar{S}_2{}^{soln})$ of solution, rather than the excess enthalpies and entropies, are the more meaningful quantities because of the absence of solute–solute interactions in the former terms.[14] The reference state for $\Delta\bar{H}_2{}^{soln}$ and $\Delta\bar{S}_2{}^{soln}$ is an ideal gaseous mixture (solute plus inert carrier gas) where the solute is at infinite dilution. Thus, for example, $\Delta\bar{H}_2{}^{soln}$ refers to the heat absorbed or given off when an infinite dilution transfer of solute takes place from the ideal gaseous mixture to the actual solution. $\Delta\bar{H}_2{}^{soln}$ and $\Delta\bar{S}_2{}^{soln}$ are obtainable from the partial molar excess quantities, since

$$\Delta\bar{H}_2{}^{soln} = \bar{H}_2{}^e - \Delta H_2{}^{vap} \qquad (7)$$

and

$$\Delta\bar{S}_2{}^{soln} = \bar{S}_2{}^e - \frac{\Delta H_2{}^{vap}}{T} \qquad (8)$$

where $\Delta H_2{}^{vap}$ is the pure solute molar enthalpy of vaporization. Alternatively, $\Delta\bar{H}_2{}^{soln}$ is obtainable from the slope of a $\ln V_g{}^\circ$ vs. reciprocal temperature plot, and, since

$$\bar{G}_2{}^e = \Delta\bar{G}_2{}^{soln} = \Delta\bar{H}_2{}^{soln} - T\Delta\bar{S}_2{}^{soln} \qquad (9)$$

$\Delta\bar{S}_2{}^{soln}$ is readily determinable as well. The values of $\Delta\bar{H}_2{}^{soln}$ and $\Delta\bar{S}_2{}^{soln}$ are listed in Tables V and VI.

(28) M. L. McGlashan and D. J. B. Potter, *Proc. Roy. Soc., Ser. A*, **267**, 478 (1962).

(29) M. L. McGlashan and C. J. Wormald, *Trans. Faraday Soc.*, **60**, 646 (1964).

(30) E. A. Guggenheim and C. J. Wormald, *J. Chem. Phys.*, **42**, 3775 (1965).

(31) K. E. Kobe and R. E. Lynn, Jr., *Chem. Rev.*, **52**, 117 (1953).

(32) A. P. Kudchadker, G. H. Alani, and B. J. Zwolinski, *ibid.*, **68**, 659 (1968).

(33) O. S. Quayle, *ibid.*, **53**, 439 (1953).
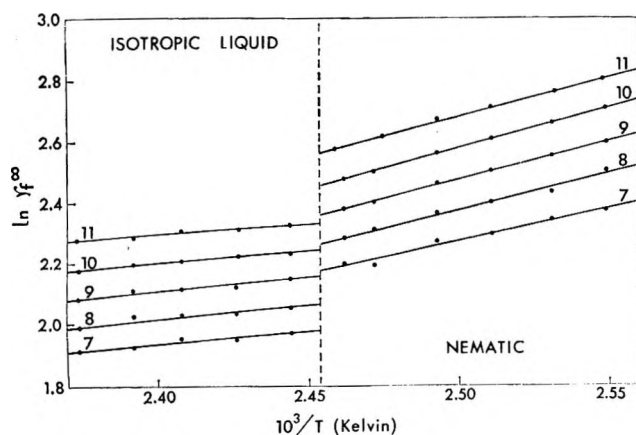
Figure 2. *n*-Alkanes in PAA. Logarithm of infinite dilution solute activity coefficient (ln γ_f^∞) *vs.* reciprocal temperature in Kelvin ($10^3/T$). Plots for several representative families of solutes. (Transition temperature is indicated by dashed vertical line. The number above the experimental plot corresponds to the number of carbon atoms in the solute.)
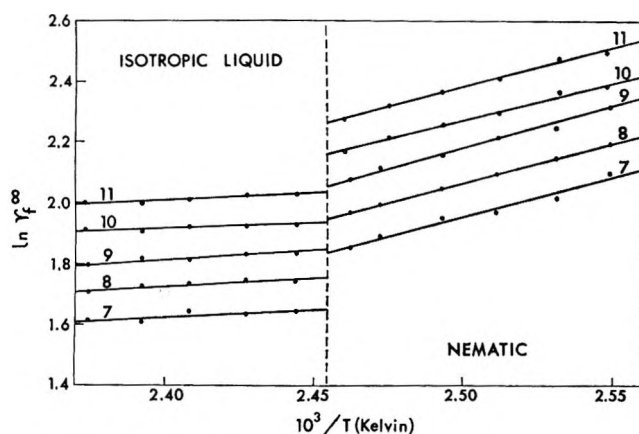
Figure 3. *n*-1-Alkenes in PAA. (See Figure 2.)
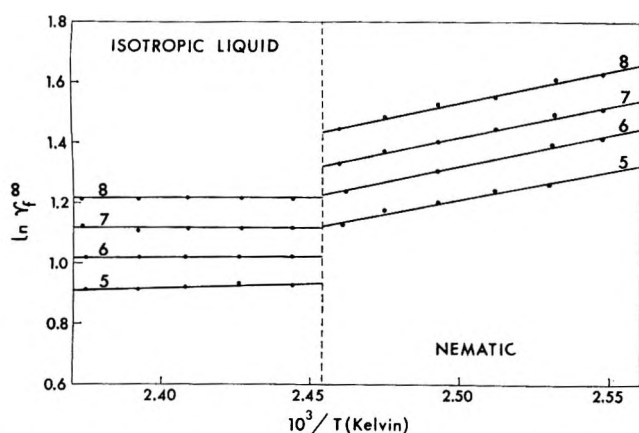
Figure 4. *n*-1-Chloroalkanes in PAA. (See Figure 2.)

Interpretation of Results

Proposed Solution Effects. The following approximate expression can be readily derived from basic statistical mechanics[34]
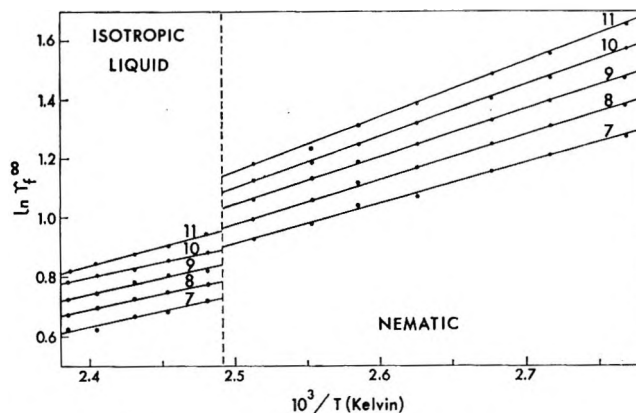
Figure 5. *n*-Alkanes in DHAB. (See Figure 2.)
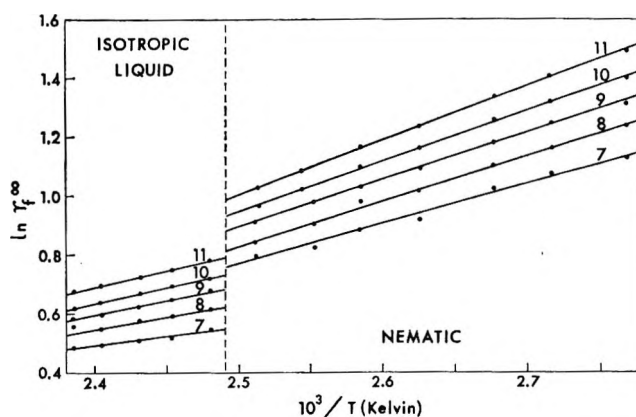
Figure 6. *n*-1-Alkenes in DHAB. (See Figure 2.)
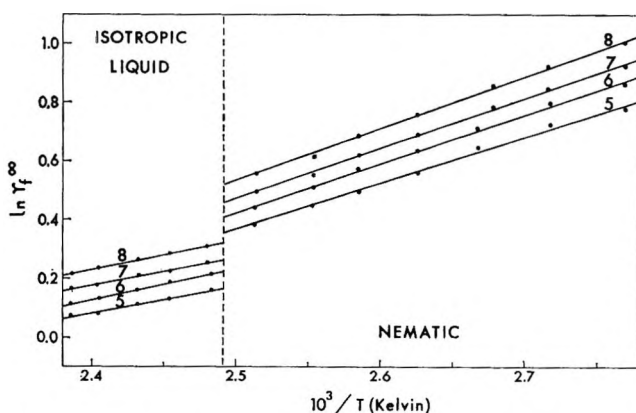
Figure 7. *n*-1-Chloroalkanes in DHAB. (See Figure 2.)

$$\Delta \bar{A}_2{}^{\text{soln}} = RT \ln\left(\frac{\bar{Z}_g}{\bar{Z}_s}\right)_{\text{trans.}} \left(\frac{\bar{Q}_g}{\bar{Q}_s}\right)_{\text{rot.}} \left(\frac{\bar{Q}_g}{\bar{Q}_s}\right)_{\text{vibr}} \quad (10)$$

where $\Delta \bar{A}_2{}^{\text{soln}}$ is the infinite dilution solute partial molar Helmholtz free energy of solution (transfer from the gaseous phase, subscript g, to the solution phase, subscript s), $\bar{Z}_{\text{trans.}}$ is the solute configurational molecular partition function (*i.e.*, the potential energy contribution to the translational partition function), and $\bar{Q}_{\text{rot.}}$

(34) See L. C. Chow, Doctoral Dissertation, Georgetown University, 1970, pp 97–102, for the derivation of eq 10.

Table III: Partial Molar Excess Properties[a] of Solutes in PAA

Solute no.	Nematic		Isotropic	
	$\bar{H}_2{}^e$	$\bar{S}_2{}^e$	$\bar{H}_2{}^e$	$\bar{S}_2{}^e$
1	4.10 ± 0.27	5.73 ± 0.62	1.61 ± 0.26	0.01 ± 0.55
2	4.60 ± 0.25	6.79 ± 0.56	1.65 ± 0.32	-0.06 ± 0.68
3	4.98 ± 0.06	7.53 ± 0.13	1.72 ± 0.26	-0.05 ± 0.56
4	5.60 ± 0.14	9.13 ± 0.32	1.92 ± 0.44	0.55 ± 0.95
5	6.54 ± 0.37	11.06 ± 0.84	1.70 ± 0.33	-0.34 ± 0.70
6	6.82 ± 0.19	11.93 ± 0.42	1.76 ± 0.42	0.02 ± 0.87
7	6.91 ± 0.23	12.13 ± 0.52	1.79 ± 0.30	0.08 ± 0.64
8	6.59 ± 0.19	11.19 ± 0.43	1.29 ± 0.44	-1.35 ± 0.96
9	7.03 ± 0.17	12.49 ± 0.38	1.79 ± 0.20	0.13 ± 0.43
10	7.59 ± 0.09	14.28 ± 0.21	1.64 ± 0.05	0.21 ± 0.11
11	5.23 ± 0.01	8.10 ± 0.03	1.68 ± 0.13	-0.33 ± 0.29
12	5.12 ± 0.07	7.48 ± 0.16	1.24 ± 0.19	-1.59 ± 0.41
13	5.04 ± 0.38	8.71 ± 0.87	0.94 ± 0.34	-0.97 ± 0.74
14	5.14 ± 0.13	8.71 ± 0.29	1.11 ± 0.22	-0.77 ± 0.47
15	5.85 ± 0.43	10.43 ± 0.99	0.72 ± 0.15	-1.76 ± 0.31
16	5.48 ± 0.42	9.50 ± 0.96	0.87 ± 0.15	-1.44 ± 0.32
17	4.87 ± 0.29	7.90 ± 0.67	0.85 ± 0.26	-1.54 ± 0.57
18	4.84 ± 0.31	7.73 ± 0.72	1.05 ± 0.16	-1.15 ± 0.35
19	5.74 ± 0.20	9.99 ± 0.46	0.69 ± 0.09	-1.97 ± 0.20
20	4.67 ± 0.47	7.33 ± 1.08	0.74 ± 0.12	-1.90 ± 0.25
21	5.20 ± 0.30	8.67 ± 0.69	1.07 ± 0.20	-1.03 ± 0.42
22	4.86 ± 0.18	7.64 ± 0.41	0.62 ± 0.19	-2.32 ± 0.42
23	5.11 ± 0.14	8.05 ± 0.32	1.08 ± 0.18	-1.40 ± 0.39
24	3.73 ± 0.29	6.91 ± 0.65	0.69 ± 0.13	-0.19 ± 0.28
25	4.15 ± 0.17	7.74 ± 0.36	0.13 ± 0.04	-1.73 ± 0.09
26	4.18 ± 0.12	7.62 ± 0.27	-0.07 ± 0.17	-2.40 ± 0.37
27	4.17 ± 0.16	7.38 ± 0.38	0.01 ± 0.12	-2.39 ± 0.26
28	4.34 ± 0.01	8.27 ± 0.02	0.38 ± 0.08	-1.03 ± 0.18
29	4.46 ± 0.05	8.47 ± 0.12	0.02 ± 0.16	-1.99 ± 0.33
30	4.19 ± 0.04	8.60 ± 0.09	0.32 ± 0.21	-0.51 ± 0.45
31	4.20 ± 0.07	8.52 ± 0.17	0.17 ± 0.33	-0.99 ± 0.70
32	3.52 ± 0.04	6.80 ± 0.09	0.36 ± 0.09	-0.62 ± 0.19
33	4.25 ± 0.13	9.36 ± 0.28	-0.35 ± 0.17	-1.54 ± 0.36
34	4.46 ± 0.22	9.80 ± 0.50	-0.58 ± 0.20	-2.20 ± 0.41
35	3.70 ± 0.10	8.14 ± 0.23	-0.72 ± 0.13	-2.43 ± 0.27
36	4.35 ± 0.06	9.17 ± 0.14	0.06 ± 0.58	-0.98 ± 1.26
37	4.13 ± 0.11	8.69 ± 0.25	0.20 ± 0.60	-0.58 ± 1.28
38	3.32 ± 0.16	6.79 ± 0.37	0.22 ± 0.69	-0.49 ± 1.49
39	4.78 ± 0.08	9.28 ± 0.18	0.20 ± 0.07	-1.52 ± 0.14
40	5.93 ± 0.21	12.65 ± 0.45	0.20 ± 0.11	-1.62 ± 0.23
41	5.59 ± 0.29	11.17 ± 0.64	0.24 ± 0.09	-1.48 ± 0.19
42	5.93 ± 0.16	12.00 ± 0.35	0.16 ± 0.19	-1.70 ± 0.39

[a] Enthalpies are in kcal/mol and entropies are in cal/mol-deg.

and $\bar{Q}_{\text{vibr}}$ are, respectively, the solute rotational and vibrational molecular partition functions. In the derivation of eq 10 it is assumed that: (a) the translational, rotational, and vibrational modes act independently; (b) in the gaseous phase (treated as ideal) the solute molecular energy states are unaffected by the environment; thus $(\bar{Z}_g)_{\text{trans.}}$ is unity, and $(\bar{Q}_g)_{\text{rot.}}$ and $(\bar{Q}_g)_{\text{vibr}}$ depend only on the solute molecular structure; and (c) in the liquid state (isotropic and anisotropic) much of the solute molecular motion may be restrained or lost due to solvent environmental effects, leading to changes in the configurational, rotational, and vibrational partition functions upon solution. Further, it is assumed that while the solute possibly affects the local structure of the solvent, the long range structure and the molecular energy states (on the average) of the solvent are unaltered due to the infinite dilution condition of the solute. This last assumption is consistent with existing esr evidence[11] obtained with low concentration paramagnetic probes.

Since the partial molar volume of the solute in solution ($\bar{V}^s$) is negligibly small compared with the same quantity in the gas phase ($\bar{V}^g$), and since the solution process takes place under constant pressure conditions, we have from eq 9 and 10

$$RT \ln \gamma_f{}^\infty = \Delta \bar{G}_2{}^{\text{soln}} =$$

$$\Delta \bar{A}_2{}^{\text{soln}} + P(\bar{V}_2{}^s - \bar{V}_2{}^g) = \Delta \bar{A}_2{}^{\text{soln}} - RT \quad (11)$$

Table IV: Partial Molar Excess Properties[a] of Solutes in DHAB

Solute no.	Nematic $\bar{H}_2^e$	Nematic $\bar{S}_2^e$	Isotropic $\bar{H}_2^e$	Isotropic $\bar{S}_2^e$
1	2.71 ± 0.08	4.97 ± 0.23	2.12 ± 0.21	3.84 ± 0.60
2	2.99 ± 0.06	5.52 ± 0.18	2.12 ± 0.06	3.71 ± 0.16
3	3.15 ± 0.04	5.78 ± 0.11	2.08 ± 0.15	3.53 ± 0.42
4	3.26 ± 0.05	6.19 ± 0.16	2.25 ± 0.11	4.06 ± 0.29
5	3.31 ± 0.06	5.94 ± 0.19	2.49 ± 0.05	4.32 ± 0.15
6	3.41 ± 0.06	6.33 ± 0.18	2.46 ± 0.06	4.42 ± 0.16
7	3.48 ± 0.11	6.48 ± 0.31	2.44 ± 0.11	4.36 ± 0.27
8	3.32 ± 0.08	5.97 ± 0.22	3.03 ± 0.06	5.56 ± 0.16
9	3.38 ± 0.08	6.31 ± 0.24	2.61 ± 0.14	4.82 ± 0.38
10	3.54 ± 0.10	6.98 ± 0.29	2.71 ± 0.07	5.38 ± 0.21
11	3.44 ± 0.08	6.40 ± 0.08	2.00 ± 0.06	3.22 ± 0.17
12	3.69 ± 0.17	6.93 ± 0.05	2.57 ± 0.14	4.51 ± 0.39
13	2.79 ± 0.10	5.47 ± 0.29	1.18 ± 0.13	1.86 ± 0.35
14	3.07 ± 0.10	6.04 ± 0.28	1.16 ± 0.27	1.66 ± 0.76
15	2.91 ± 0.06	5.62 ± 0.16	1.11 ± 0.17	1.56 ± 0.48
16	2.72 ± 0.05	5.10 ± 0.14	2.00 ± 0.19	3.65 ± 0.53
17	2.93 ± 0.16	5.61 ± 0.46	1.52 ± 0.17	2.46 ± 0.48
18	2.75 ± 0.07	5.04 ± 0.19	1.25 ± 0.21	1.71 ± 0.58
19	2.88 ± 0.08	5.43 ± 0.22	1.98 ± 0.15	3.57 ± 0.42
20	2.64 ± 0.06	4.78 ± 0.18	1.67 ± 0.10	2.75 ± 0.29
21	3.19 ± 0.05	6.20 ± 0.14	2.00 ± 0.09	3.62 ± 0.26
22	3.38 ± 0.05	6.57 ± 0.14	2.12 ± 0.06	3.85 ± 0.16
23	3.64 ± 0.04	7.09 ± 0.13	2.21 ± 0.04	3.92 ± 0.11
24	3.16 ± 0.08	7.17 ± 0.22	1.88 ± 0.12	4.34 ± 0.34
25	3.31 ± 0.07	7.44 ± 0.21	2.06 ± 0.06	4.69 ± 0.18
26	3.40 ± 0.05	7.55 ± 0.14	1.95 ± 0.10	4.33 ± 0.27
27	3.51 ± 0.05	7.72 ± 0.14	2.05 ± 0.03	4.46 ± 0.08
28	3.45 ± 0.06	7.82 ± 0.12	2.16 ± 0.05	4.99 ± 0.15
29	3.66 ± 0.04	8.29 ± 0.10	1.98 ± 0.10	4.51 ± 0.29
30	3.18 ± 0.02	7.66 ± 0.05	1.75 ± 0.05	4.45 ± 0.13
31	3.09 ± 0.02	7.36 ± 0.06	1.93 ± 0.06	4.82 ± 0.16
32	2.95 ± 0.02	7.00 ± 0.07	1.83 ± 0.04	4.51 ± 0.11
33	3.74 ± 0.05	9.36 ± 0.14	1.92 ± 0.07	5.19 ± 0.20
34	3.60 ± 0.06	8.97 ± 0.17	1.94 ± 0.10	5.18 ± 0.29
35	3.44 ± 0.06	8.66 ± 0.16	1.77 ± 0.04	4.81 ± 0.11
36	3.26 ± 0.11	7.91 ± 0.26	2.17 ± 0.07	5.55 ± 0.15
37	3.56 ± 0.10	8.76 ± 0.25	1.22 ± 0.05	3.29 ± 0.11
38	2.94 ± 0.10	7.21 ± 0.24	1.90 ± 0.01	4.94 ± 0.02
39	3.65 ± 0.12	8.26 ± 0.33	1.97 ± 0.07	4.49 ± 0.20
40	3.62 ± 0.10	8.13 ± 0.28	2.13 ± 0.12	4.83 ± 0.33
41	3.83 ± 0.12	8.60 ± 0.35	2.11 ± 0.10	4.77 ± 0.28
42	3.62 ± 0.07	8.07 ± 0.19	2.19 ± 0.09	4.93 ± 0.25

[a] Enthalpies are in kcal/mol and entropies are in cal/mol-deg.

and

$$\gamma_f^\infty = \left(\frac{1}{\bar{Z}_s}\right)_{\text{trans.}} \left(\frac{\bar{Q}_g}{\bar{Q}_s}\right)_{\text{rot.}} \left(\frac{\bar{Q}_g}{\bar{Q}_s}\right)_{\text{vibr}} e^{-1} \qquad (12)$$

Although eq 12 is not rigorously exact, it provides an adequate basis for a self-consistent interpretation of our γ_f^∞ results in terms of the statistically averaged solute molecular behavior in the ideal gaseous state and in the real solution. According to eq 12, the magnitude of γ_f^∞ should be influenced by three effects[35]— a potential energy effect, a rotational effect, and a vibrational effect—which, for our systems, are describable as follows.

(1) Potential Energy Effect. Upon solution in an anisotropic or isotropic solvent, solute–solvent interactions take place. The stronger the potential energy of interaction, the greater the potential energy (or configurational) partition function $(\bar{Z}_s)_{\text{trans.}}$, and the lower the value of γ_f^∞. Thus, solubility is favored by strong solute–solvent interaction.

(2) Rotational Effect. The rotational partition function for a given free rotational mode is proportional to the square root of the moment of inertia corresponding to that mode. If, upon solution, certain rotational motion is restricted or lost, the ratio $(\bar{Q}_g/\bar{Q}_s)_{\text{rot.}}$ becomes

(35) Strictly, the three effects are interrelated and coupled. However, it is often convenient to consider them separately in the comparisons which follow.

Table V: Partial Molar Enthalpies and Entropies of Solution in PAA[a]

Solute no.	Nematic $\Delta \bar{H}_2^{soln}$	Nematic $\Delta \bar{S}_2^{soln}$	Isotropic $\Delta \bar{H}_2^{soln}$	Isotropic $\Delta \bar{S}_2^{soln}$
1	−3.02	−12.10	−5.28	−16.65
2	−3.61	−13.79	−6.23	−19.37
3	−4.30	−15.71	−7.27	−21.82
4	−3.45	−13.52	−6.89	−20.78
5	−1.88	−10.05	−6.49	−20.15
6	−1.85	−9.79	−6.69	−20.44
7	−1.68	−9.38	−6.59	−20.20
8	−2.05	−10.45	−7.12	−21.71
9	−2.03	−10.18	−7.04	−21.24
10	−1.27	−7.92	−7.05	−20.81
11	−5.12	−17.96	−8.43	−24.79
12	−6.37	−21.30	−9.94	−28.64
13	−1.95	−8.80	−5.83	−17.37
14	−2.95	−11.53	−6.74	−19.76
15	−2.21	−9.75	−7.12	−20.73
16	−2.55	−10.61	−6.95	−20.34
17	−3.07	−11.99	−6.87	−20.23
18	−3.12	−12.20	−6.69	−19.88
19	−2.18	−9.86	−7.02	−20.62
20	−3.24	−12.51	−6.96	−20.54
21	−3.96	−14.27	−7.83	−22.59
22	−5.37	−18.00	−9.34	−26.43
23	−6.20	−20.28	−9.94	−28.07
24	−3.81	−11.96	−6.63	−17.88
25	−4.46	−13.81	−8.24	−21.97
26	−5.49	−16.58	−9.49	−25.12
27	−6.55	−19.47	−10.45	−27.70
28	−5.04	−15.20	−8.74	−23.12
29	−5.65	−16.85	−9.84	−25.85
30	−4.87	−14.10	−8.54	−21.96
31	−4.69	−13.74	−8.53	−22.03
32	−5.27	−15.23	−8.24	−21.43
33	−6.12	−16.61	−10.47	−26.03
34	−5.57	−15.32	−10.38	−25.90
35	−6.40	−17.15	−10.59	−26.29
36	−5.50	−15.49	−9.90	−25.08
37	−5.81	−16.22	−9.65	−24.42
38	−6.46	−17.72	−9.71	−24.49
39	−5.83	−17.29	−10.17	−26.61
40	−4.03	−12.32	−9.52	−25.14
41	−4.47	−14.02	−9.58	−25.25
42	−3.99	−12.86	−9.54	−25.15

[a] Enthalpies are in kcal/mol and entropies are in cal/mol-deg.

Table VI: Partial Molar Enthalpies and Entropies of Solution in DHAB[a]

Solute no.	Nematic $\Delta \bar{H}_2^{Soln}$	Nematic $\Delta \bar{S}_2^{soln}$	Isotropic $\Delta \bar{H}_2^{soln}$	Isotropic $\Delta \bar{S}_2^{soln}$
1	−4.79	−14.68	−4.76	−12.82
2	−5.57	−17.04	−5.86	−15.60
3	−6.53	−19.74	−6.91	−18.24
4	−6.11	−18.52	−6.57	−17.27
5	−5.46	−17.18	−5.70	−15.49
6	−5.59	−17.36	−5.99	−16.04
7	−5.40	−16.99	−5.94	−15.93
8	−5.65	−17.68	−5.38	−14.71
9	−5.98	−18.38	−6.23	−16.56
10	−5.65	−17.06	−5.98	−15.64
11	−7.39	−22.15	−8.11	−21.24
12	−8.25	−24.56	−8.61	−22.54
13	−4.51	−13.78	−5.59	−14.53
14	−5.34	−16.14	−6.69	−17.33
15	−5.46	−16.45	−6.73	−17.44
16	−5.62	−16.89	−5.82	−15.25
17	−5.31	−16.12	−6.21	−16.23
18	−5.52	−16.75	−6.51	−17.02
19	−5.35	−16.27	−5.73	−15.08
20	−5.58	−16.91	−6.03	−15.89
21	−6.33	−18.96	−6.91	−17.94
22	−7.24	−21.43	−7.84	−20.28
23	−8.09	−23.83	−8.82	−22.75
24	−4.70	−13.53	−5.43	−13.35
25	−5.63	−16.14	−6.30	−15.55
26	−6.62	−18.87	−7.46	−18.44
27	−7.58	−21.54	−8.41	−20.85
28	−6.27	−17.81	−6.97	−17.10
29	−6.81	−19.30	−7.88	−19.36
30	−6.17	−16.98	−7.11	−17.00
31	−6.08	−16.81	−6.76	−16.22
32	−6.13	−16.94	−6.77	−16.30
33	−6.99	−18.93	−8.20	−19.30
34	−6.77	−18.31	−7.86	−18.51
35	−7.00	−18.89	−8.09	−19.05
36	−6.61	−18.13	−6.79	−18.55
37	−6.43	−17.46	−8.67	−19.54
38	−6.84	−18.58	−8.03	−19.08
39	−7.30	−20.60	−8.40	−20.61
40	−6.69	−19.08	−7.58	−18.68
41	−6.56	−18.79	−7.71	−19.01
42	−6.63	−18.98	−7.51	−18.53

[a] Enthalpies are in kcal/mol and entropies are in cal/mol-deg.

greater than unity. The greater the loss of rotational motion, the greater the value of $(\bar{Q}_g/\bar{Q}_s)_{rot.}$, and the greater the value of γ_f^∞. Hence, solubility is *not* favored by a loss of rotational motion.

(3) Vibrational Effect. There are energy barriers of up to a few kcal, for internal rotation in flexible (nonrigid) molecules such as *n*-alkanes, but many conformations are possible in the gaseous phase (although the zigzag conformation is most probable). However, if these molecules become confined to a solvent system where certain conformations become highly improbable (*e.g.*, due to space restrictions), then a conformational energy loss would occur. Since this loss of motion

would appear in the vibrational modes, it would lead to a value of $(\bar{Q}_g/\bar{Q}_s)_{vibr}$ greater than unity. Again, this situation does *not* favor solubility, and acts to increase the value of γ_f^∞.

Following the argument used to establish eq 12, one can write the expression

$$\Delta \bar{H}_2^{soln} = \Delta \bar{E}_2^{soln} - RT =$$

$$\Delta E_{pot.} + \Delta E_{r.v.} - RT \quad (13)$$

where $\Delta E_{pot.}$ is the solute internal energy loss due to interaction with the solvent and $\Delta E_{r.v.}$ is the combined solute rotational and vibrational internal energy losses.
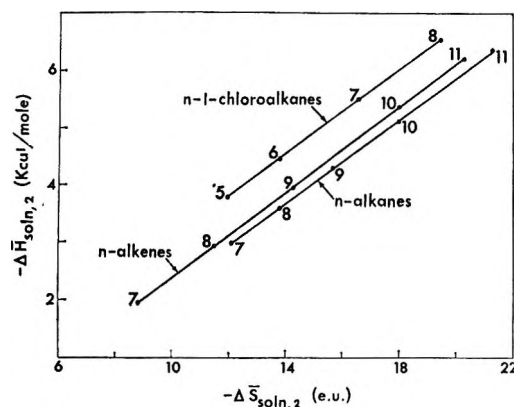
Figure 8. Partial molar enthalpy of solution $(\Delta \bar{H}_2{}^{soln})$ vs. partial molar entropy of solution $(\Delta \bar{S}{}^{soln})$. Plots for three homologous series in nematic PAA. (The numbers adjacent to the experimental points indicate the number of carbon atoms in the solute molecule.)

Table VII: Slopes and Intercepts of the Linear Correlation[a] between $\Delta \bar{H}_2{}^{soln}$ and $\Delta \bar{S}_2{}^{soln}$ for Three Homologous Series in PAA and DHAB

Solute series	Nematic phase		Isotropic phase	
	a	b	a	b
PAA				
n-Alkanes	-1.40	0.364	-1.20	0.389
n-1-Alkenes	-1.32	0.371	-0.871	0.386
n-1-Chloroalkanes	-0.585	0.366	-0.340	0.390
DHAB				
n-Alkanes	-0.404	0.352	-0.315	0.396
n-1-Alkenes	-0.418	0.357	-0.114	0.392
n-1-Chloroalkanes	-0.191	0.361	0.127	0.397

[a] Where $\Delta \bar{H}_2{}^{soln} = a + b\Delta \bar{S}_2{}^{soln}$; all correlation coefficients for the linear plots were in excess of 0.99.

Consistent with the observed exothermic behavior of the solution process, both of these quantities are negative.

Discussion

The corresponding free energy terms of the two additive contributory factors to $\Delta \bar{H}_2{}^{soln}$ act in opposite directions in influencing the magnitude of $\gamma_f{}^\infty$. Hence, when examining a variety of solutes, no direct correlation between the $\Delta \bar{H}_2{}^{soln}$ and the $\gamma_f{}^\infty$ (or $\Delta \bar{S}_2{}^{soln}$) values is to be expected, and indeed none is observed. However, when considering a homologous series of solutes, one finds that there is a linear relationship between $\Delta \bar{H}_2{}^{soln}$ and $\Delta \bar{S}_2{}^{soln}$ in both phases of PAA and DHAB. Illustrated in Figure 8 are the linear plots for the n-alkanes, n-alkenes, and 1-chloroalkanes in nematic PAA. Similar linear correlations for a series of solutes in a given solvent have been found during the past 30 years, and their physical significance has been discussed.[36] Our systems fall within one of Bell's general categories in which the solute molecules are small relative to the solvent, and the same type of intermolecular forces operate for the solute series. It appears that such correlations are better the more alike the solute molecules are; this accounts for the separate correlations for each homologous series. The slopes and intercepts for the straight line relationship between $\Delta \bar{H}_2{}^{soln}$ and $\Delta \bar{S}_2{}^{soln}$ for the three series in both phases of PAA and DHAB are listed in Table VII.

Before proceeding to a detailed solute-to-solute comparison, two observations can be made concerning the relative values of $\Delta \bar{H}_2{}^{soln}$ and $\gamma_f{}^\infty$ in PAA and DHAB.[37]

(1) The $\gamma_f{}^\infty$ values in DHAB are much smaller than those in the corresponding phase of PAA. According to eq 12, this could be due to either or both of the following reasons: (a) DHAB interacts more strongly with the solute; (b) the solutes undergo smaller losses of rotational and vibrational motion with DHAB.

(2) The $\Delta \bar{H}_2{}^{soln}$ values with nematic PAA are much

smaller (less negative) than those with isotropic PAA, whereas for DHAB the nematic values are only slightly smaller than the isotropic values. This seems to suggest that there is a greater difference in solvent behavior between the nematic and isotropic liquid phases for PAA.[37]

Utilizing eq 12 and 13, and based on inference from our thermodynamic results (Tables III through VI) alone, a molecular interpretation of solubility in nematogenic solvents follows. In this discussion some subscripts and superscripts will be deleted; $\Delta \bar{H}_2{}^{soln}$ becomes ΔH, and $\gamma_f{}^\infty$ becomes γ. Furthermore, when referring to $\Delta \bar{H}_2{}^{soln}$ values, larger or greater should be taken to mean more negative, and smaller or less to mean less negative. The 42 solutes will be considered in ten separate groups.

A. Normal Alkanes (Solutes 1–3, 11, and 12). In the nematic phase of PAA the ΔH and γ values of the n-alkanes increase with increasing chain length. This may be explained in various ways, but a solution mechanism will be proposed that will be shown to be consistent with the thermodynamic results for the other solute groups as well. Upon solution in the anisotropic nematic environment, it seems reasonable that the rotational motion of the alkane should become restricted in the two directions perpendicular to its molecular long axis (in the same way that the solvent rotational motion is hindered, *i.e.*, space restriction). Furthermore, it is assumed that the zigzag conformation becomes more exclusively preferred in order for the solute to provide the maximum profile for interaction with the more or less parallel and rod-like liquid crystal. We assume that the foregoing situation leads to the lowest free energy state for the dissolved n-alkane solute, *i.e.*, that a situation where freer rotations and many confor-

(36) (a) R. P. Bell, *Trans. Faraday Soc.*, **33**, 496 (1937); (b) O. K. Rice, *J. Chem. Phys.*, **15**, 875 (1947).

(37) In a later paper (L. C. Chow and D. E. Martire, *Mol. Cryst. Liquid Cryst.*, in press) PAA and DHAB will be compared in more detail.

mations are allowed would lead to weaker solute–solvent interactions (due to an increase in the mean intermolecular distance and a reduction of solute contact surface area) and a higher free energy state. Thus, according to this solution mechanism, the molecule with the largest molecular polarizability should have the strongest interaction with the solvent, and the greatest $\Delta E_{pot.}$ value. Further, the most elongated and most flexible molecule (in terms of number of possible conformations in the gaseous phase) stands to lose the most rotational and vibrational energy upon solution. Since $\Delta E_{pot.}$ and $\Delta E_{r.v.}$ would then be expected to increase with increasing chain length, the observed trend in ΔH is understood. The trend of increasing γ with increasing chain length indicates (according to eq 12) that the vibrational and rotational effects (which act to increase γ) predominate over the potential energy effect (which acts to decrease γ) for these solutes.

Turning to the isotropic phase of PAA one finds the same trend of increasing ΔH and γ with increasing chain length. However, the ΔH values in isotropic PAA are larger than those in nematic PAA. Since $\Delta E_{r.v.}$ should be smaller in isotropic PAA, this indicates that $\Delta E_{pot.}$ should be larger in the isotropic state. For a "normal" solvent, the solute–solvent interaction effect decreases with increasing temperature owing to increased thermal motion of the molecules and increased intermolecular separation. However, with nematogenic solvents, nonmesomorphic solutes are energetically more compatible with the higher temperature isotropic state. Thus, as the solvent molecules attain a more isotropic distribution, solute geometry and orientation become less critical, i.e., the solute need not sacrifice as much rotational and vibrational motion to gain a strong potential energy of interaction. Note that the γ values for the n-alkanes in isotropic PAA are considerably less than those in nematic PAA. This is consistent with the suggestion of an increased potential energy effect and a reduced rotational–vibrational effect.

The situation for the n-alkanes in DHAB is very similar to that in PAA. The two readily observable differences between the two solvents were mentioned earlier.

B. n-1-Alkenes (Solutes 13, 14, and 21–23). The n-1-alkenes closely follow the behavior of the n-alkanes in both the nematic and isotropic phases of the solvents. In the nematic phase, the alkenes appear to have smaller ΔH and lower γ values than those of the corresponding alkanes. Possible reasons for the smaller ΔH values are: (a) the alkenes are less flexible than the alkanes and hence lose smaller amounts of vibrational energy upon going into solution, resulting in smaller $\Delta E_{r.v.}$ values; (b) the double bond makes one end of the molecule rigid and declined from the molecular long axis in the zigzag conformation of the methylene groups; this may hinder the attainment of parallel alignment with the ordered solvent and thus lead to re-

duced solute–solvent interaction strength, resulting in smaller $\Delta E_{pot.}$ values. The lower γ values for the alkenes suggest that the more favorable vibrational effect for solution outweighs the less favorable potential energy effect (assuming that the rotational effects are comparable for alkanes and alkenes).

In the isotropic liquid of the two solvents, the alkenes have larger ΔH values than the corresponding alkanes. Since the $\Delta E_{r.v.}$ values should be approximately equal in this state, the indication is that the enhanced polarity and polarizability of the alkene leads to a larger $\Delta E_{pot.}$ with an isotropic distribution. A greater potential energy effect would also explain the observed lower γ values for the alkenes in this phase.

C. 1-Chloro-n-alkanes (Solutes 24–27). This group of solutes also behaves similarly to the n-alkanes. However, substitution of a chlorine atom for a methyl group appears to lead to stronger solute–solvent interaction. For example, if we consider the ΔH values of 1-chloroheptane and n-octane in the nematic state, and assume that the two molecules have similar values of $\Delta E_{r.v.}$, then $\Delta E_{pot.}$ for 1-chloroheptane is about 2 kcal/mol greater in nematic PAA and about 1 kcal/mol greater in nematic DHAB. Similar comparisons can be made for the isotropic liquid phase, leading to the same conclusion of enhanced interaction. The larger potential energy effect would also explain the much lower γ values for the 1-chloroalkanes in both phases of the solvents.

D. 1-Halo-n-hexanes (Solutes 25, 28, and 29). In the nematic phase of PAA and DHAB we have the following trend in ΔH: iodohexane > bromohexane > chlorohexane. This is to be expected since iodohexane should have both the largest $\Delta E_{pot.}$ and the largest $\Delta E_{r.v.}$ for the following reasons: (a) since iodohexane has the largest molecular polarizability, it should have the strongest interaction with the solvent; (b) since iodohexane is the largest molecule, it stands to lose the most rotational energy upon solution. Considering the influence of the solution effects on the γ values, iodohexane should have the least favorable rotational effect, whereas chlorohexane should have the least favorable potential energy effect. Since chlorohexane always has smaller γ values than iodohexane, this indicates that the rotational effect dominates in establishing the trend. Interestingly one finds that bromohexane has the smallest γ values of all in the nematic state.[38]

In the isotropic phase, the trend in the ΔH values remains the same (although the absolute values increase due to increased $\Delta E_{pot.}$). Furthermore, there is no clear trend in the γ values which are all quite close (although the γ values decrease relative to the nematic values because of the increased potential energy effect).

(38) Dipolar interaction between the haloalkanes and the solvent may be occurring as well. However, its contribution must be small (or equivalent) for all haloalkanes, since it does not affect the trends in ΔH and γ.

According to eq 12, this would indicate that the rotational effect is still operative (though not as pronounced) in the isotropic liquid; this is consistent with existing evidence[39] of some residual solvent alignment in the isotropic phase.

E. Isomeric Nonanes (Solutes 3–10). The nonanes form an interesting group in that their shapes vary widely, from that of a straight chain (*n*-nonane) to that of a quasisphere (3,3-diethylpentane). The ΔH values for this group in nematic PAA increase with decreasing branching (*i.e.*, increasing "linearity" or length-to-breadth ratio). According to the proposed solution mechanism this trend is reasonable since: (a) a more linear molecule can achieve a more favorable spatial orientation and a shorter intermolecular distance (between the long molecular axes) relative to the ordered solvent, leading to a stronger solute–solvent interaction and a greater $\Delta E_{pot.}$ value; (b) a more linear alkane is also more flexible and has a larger principal moment of inertia (in the long axis direction), thus would lose more vibrational and rotational energy upon solution, leading to a greater $\Delta E_{r.v.}$ value. It then follows that, when considering the γ values, a more linear molecule should have a more favorable potential energy effect (acting to reduce γ), but a less favorable rotational–vibrational effect (acting to increase γ). As a result, no clear trend in the γ values is observed among the isomeric nonanes. In nematic PAA the values have the following relative magnitudes: $10 < 4 < 3 < 9 < 6 \leq 5 \leq 7 < 8$. Thus, the most spherical (least "rod-like") solute has the lowest free energy of solution. This is an indication that, although 3,3-diethylpentane has the least favorable potential energy of interaction with the solvent, this is more than compensated for by its having the least rotational and vibrational motion loss upon solution, *i.e.*, being "spherical," it cannot interact as effectively with the rod-like solvent, but it can rotate more freely and can maintain more of its gas phase conformations upon solution.

In nematic DHAB, the same trends are followed for ΔH and γ, but the spread in the ΔH values is smaller than in nematic PAA. Finally, in the isotropic liquid of the two solvents, the ΔH values are very close and, as expected, do not follow the trend of the linearity of the molecules; the γ's again show no dependence on molecular shape. However, in both solvents *n*-nonane has the greatest ΔH and 3,3-diethylpentane has the smallest γ—additional evidence of residual alignment in the isotropic liquid.

F. Isomeric cis- and trans-Octenes (Solutes 15–20). In the nematic phase of the two solvents, the *trans*-octenes have greater ΔH values than their cis counterparts. Possible reasons for this are: (a) since the trans isomers are more rod-like, they interact more strongly with the liquid crystals, producing greater $\Delta E_{pot.}$ values; (b) the trans isomers, being more rod-like, stand to lose more rotational energy upon solution in the

anisotropic environment, leading to greater $\Delta E_{r.v.}$ values. The nematic γ values show interesting behavior. In the lower temperature range of the nematic phase the trans isomers have smaller γ values than the corresponding cis isomers, but at higher temperatures the trans values are larger. This indicates that the more favorable potential energy effect for the *trans*-octenes dominates at lower temperatures, but is overcome by the less favorable rotational effect at higher temperatures.

In the isotropic liquid phase the *cis*-octenes generally have greater ΔH values than those of the corresponding trans isomers. Under the best of circumstances the two types of isomers would lose equal amounts of rotational energy upon solution. Clearly then, the cis compounds must have greater $\Delta E_{pot.}$ values. This is most likely due to the fact that the cis isomers are slightly polar, thus can interact more strongly with the solvent, since molecular shape is no longer as important a criterion for interaction as it is with the nematic state. This also explains the lower γ values for the *cis*-octenes.

G. Xylenes (Solutes 30–32). In nematic PAA, the ΔH values follow the trend *p*-xylene > *o*-xylene > *m*-xylene. Since these isomers are fairly rigid, little vibrational energy loss is to be expected upon solution. Therefore, $\Delta E_{r.v.}$ should follow the probable order of rotational energy loss, *i.e.*, the order of solute molecular length-to-breadth ratio: *p*-xylene > *m*-xylene > *o*-xylene. From the trends in ΔH and $\Delta E_{r.v.}$, *m*-xylene should have the smallest $\Delta E_{pot.}$. Now, *o*-xylene (and, to a lesser extent, *m*-xylene) is capable of some dipolar interaction with the solvent. However, *p*-xylene should be in a spatially more favorable position for dispersion interaction with the solvent. Thus, since it is not certain which of the two isomers has the greater $\Delta E_{pot.}$, it will be assumed that they are comparable. With this assumption, the trend in the γ's can be readily explained by the usual arguments based on eq 12.

In nematic DHAB, the behavior of the xylenes is essentially identical to that in nematic PAA, except that the ΔH values now have the trend *p*-xylene $\approx$ *o*-xylene > *m*-xylene. This change in the trend may be due to the fact that, since DHAB is somewhat more flexible than PAA, the shape of the solute has less of an effect on solute–solvent interactions,[40] and, hence, the polar *o*-xylene may have a slightly greater $\Delta E_{pot.}$ than *p*-xylene.

In the isotropic liquid phase of the solvents ΔH

(39) C. C. Gravatt and G. W. Brady, *Mol. Cryst. Liquid Cryst.*, **7**, 355 (1969).

(40) The flexibility of DHAB relative to PAA may account for the following observations: (a) with an *n*-alkane and an *n*-1-alkene of the same carbon number, the difference in the ΔH values is greater in nematic PAA than in nematic DHAB; (b) with the isomeric nonanes, the spread in the ΔH values is greater in nematic PAA than in nematic DHAB.

follows the trend of solute polarity, and γ follows the ΔH value (i.e., the larger the ΔH, the smaller the γ). The potential energy effect obviously governs these trends.

H. Dichlorobenzenes (Solutes 33–35). The dichlorobenzenes have solution properties more or less similar to the xylenes. The nematic phase trends in ΔH and γ can be interpreted in a manner similar to the xylene systems. However, in the isotropic phase the γ values for *p*-dichlorobenzene are somewhat lower than expected on the basis of the usual arguments.

Comparing the ΔH values of the dichlorobenzenes to those of the xylenes and assuming equal $\Delta E_{r.v.}$ values for similar-type isomers, we find that $\Delta E_{pot.}$ is about 1.1 kcal/mol greater for the dichlorobenzenes in nematic PAA, and about 0.8 kcal/mol greater in nematic DHAB. On the basis of ΔH comparisons between the *n*-alkanes and chloroalkanes, one might have expected that the substitution of two CH_3 groups by two Cl groups would enhance $\Delta E_{pot.}$ by about 3.6 kcal in nematic PAA and about 2.0 kcal in nematic DHAB. A possible explanation for the observed lower enhancement is that the polarizability of the aromatic ring is reduced when electron-withdrawing Cl groups are substituted for electron-donating CH_3 groups.

I. Chlorotoluenes (36–38). Since the vapor pressures for this group are less accurately known than those for the rest of the solutes, there is a slightly greater uncertainty in the γ and ΔH values. Thus, the solution properties for the chlorotoluenes can be interpreted with less confidence.

In the nematic phase of the solvents the ΔH trend is approximately: *p*-chlorotoluene > *m*-chlorotoluene ≈ *o*-chlorotoluene. This is reasonable since the para isomer is both structurally (most rod-like) and electronically (most polar) favored for interaction. In addition to having the largest $\Delta E_{pot.}$, it should also have the largest $\Delta E_{r.v.}$. The γ values for *p*-chlorotoluene are smaller than those for the ortho or meta isomers, indicating that the potential energy effect is dominant. In the isotropic phase there are no discernible trends, except that the activity coefficient of the para isomer, as expected, is generally the lowest.

J. Isomeric Butylbenzenes (Solutes 39–42). In both phases of the solvents *n*-butylbenzene always has the greatest ΔH and the smallest γ, while the other three compounds have ΔH and γ values that are essentially equal to each other. Since *n*-butylbenzene is more rod-like and flexible than the other three isomers (which

have comparable lengths and rigidities), it should have the largest $\Delta E_{r.v.}$. The fact that it also has the lowest γ values is an indication that *n*-butylbenzene has a very favorable potential energy effect and the largest $\Delta E_{pot.}$. It can, in fact, be demonstrated with molecular models that the three branched butyl groups hinder the solute aromatic ring from close approach to the solvent. These steric effects are more pronounced in the nematic phase of the more rigid PAA, as a comparison of the ΔH values will confirm.

Conclusion

From the thermodynamic information obtained here by glc measurements, we have inferred the molecular behavior of a variety of solutes in two nematogenic solvents. We have shown that the three proposed solution effects lead to a self-consistent interpretation of the solute activity coefficients and enthalpies (and, indirectly, the entropies) of solution. However, the proposed solution mechanism cannot be substantiated until definitive spectroscopic (e.g., infrared, microwave, and Raman) studies are made on similar systems. These studies are needed to help establish the extent of any rotational and vibrational changes that take place in the solute upon solution.[41] Furthermore, with our present knowledge of liquid crystals, and in the absence of any applicable statistical mechanical solution theories and additional thermodynamic data, a quantitative treatment of the solution behavior of nonmesomorphic solutes in nematogenic solvents is hardly possible at this time.

The present study should prove helpful to those interested in analytical glc separation of isomers using liquid crystals.[42] The prevailing "rule of thumb" that the more rod-like isomer should be the more soluble in a liquid crystal is both naive and misleading. It is clear that the size, shape, flexibility, polarity, and polarizability of the molecules must all be taken into account before attempting to judge relative solubilities.

(41) For example, a solute that appears to have a large loss of rotational and vibrational motion is *n*-decane when dissolved in nematic PAA. It has approximately the same ΔH as the rigid *p*-xylene, but has a γ *five* times as large.

(42) See, e.g., W. L. Zielinski, Jr., D. H. Freeman, D. E. Martire, and L. C. Chow, *Anal. Chem.*, **42**, 176 (1970).

High-Precision Viscosity of Supercooled Water and Analysis of the

Extended Range Temperature Coefficient

by Lawrence D. Eicher and Bruno J. Zwolinski*

Thermodynamics Research Center, Department of Chemistry, Texas A&M University, College Station, Texas 77843
(Received October 19, 1970)

An improved photocell meniscus detection system as used for measurement of efflux times with Cannon-Ubbelohde suspended-meniscus viscometers is described. Using this system, we have obtained high-precision viscosity measurements from 40 to $-8.28°$ for water. Excellent agreement is found with selected literature data in the higher temperature range. A reduced three-parameter equation is presented which is believed to represent the entire range (-10 to 150°) with accuracy comparable with that of the primary standard and should have wide applicability to liquids other than water. The extended temperature range data analysis suggests that no viscous anomalies exist and that the practice of fitting Arrhenius and Vogel-type equations to higher and lower temperature ranges, respectively, may not be justified.

Introduction

The transport properties of water in its normal liquid state at ambient pressures have been the subject of many experimental and theoretical investigations. Recently, Korosi and Fabuss[1] have extended the range of high-precision viscosity data well above the normal boiling point, but data of similar precision through the melting point and into the supercool range have been difficult to obtain.[2,3]

We have been successful in obtaining high-precision viscosity data for liquid water at temperatures as low as $-8.28°$, thus extending the range of accurately known viscosity data from well above to well below the ice point. An analysis of the high-precision data over the extended temperature on the basis of the Vogel equation[4-7] is unsatisfactory, even if the Vogel equation is used only in the lower temperature range and an Arrhenius equation is used in the higher range. A new three-parameter semiempirical equation for relative viscosities is proposed which appears to reproduce both our data and also the standard NBS viscosity data for liquid water, including the supercooled region well within the precision and accuracy of the data (0.02 to 0.2%).[8]

Experimental Method

A Cannon-Ubbelohde suspended-meniscus viscometer was used for all measurements. A photocell detector component (Figure 1) which was purchased from the Hewlett-Packard Co. was attached to the viscometer with the upper and lower detectors positioned approximately at the fiducial marks. This unit, rigidly attached by its horizontal clamping screws (the shafts between photocells are not rigidly held) was further protected from the corrosive action of the bath fluid by coating it with Apiezon wax. This method of

photocell meniscus detection has advantages over other methods in which the detectors are not attached to the viscometer in that the entire unit may be removed from the bath, for cleaning and sample transfer, without changing the position of the detectors relative to the viscometer. The triggering signal, which is approximately 10 mV from the photocells, was amplified to a dc pulse of about 4 V. This signal was used to trigger a general purpose electronic counter (Atec Inc. Model 6C36) which provided digital display of efflux times in milliseconds. The photocell light source circuitry was modified so that the intensity of the light at each detector could be adjusted. In this manner, the triggering signal from each detector could be controlled, its characteristic magnitude being kept constant for different degrees of light absorption by the test fluid. The amplified triggering signal was periodically monitored using an oscilloscope and adjusted for each run to a constant pretrigger signal voltage. Preliminary testing indicated that for efflux times in excess of 250 sec there was a measurable heating effect (introducing a small error in efflux time measurements) from the light sources if they remained on for the duration of the run. Therefore, provision was made to turn the light sources off

(1) A. Korosi and B. M. Fabuss, *Anal. Chem.*, **40**, 157 (1968).

(2) J. Hallett, *Proc. Phys. Soc.*, **82**, 1046 (1963).

(3) G. White and R. Twining, *Amer. Chem. J.*, **50**, 380 (1913).

(4) L. Korson, W. Dorst-Hansen, and F. J. Millero, *J. Phys. Chem.*, **73**, 34 (1969).

(5) A. Bondi, "Physical Properties of Molecular Crystals, Liquids, and Glasses," Wiley, New York, N. Y., 1968.

(6) A. J. Barlow, J. Lamb, and A. J. Matheson, *Proc. Roy. Soc. Ser. A*, **A292**, 322 (1966).

(7) A. J. Matheson, M. R. Carpenter, and D. B. Davies, *J. Chem. Phys.*, **46**, 2451 (1967).

(8) R. S. Marvin and D. L. Hogenboom, "Viscosity of Liquids," in "American Institute of Physics Handbook," 3rd ed, McGraw-Hill, New York, N. Y., in press.
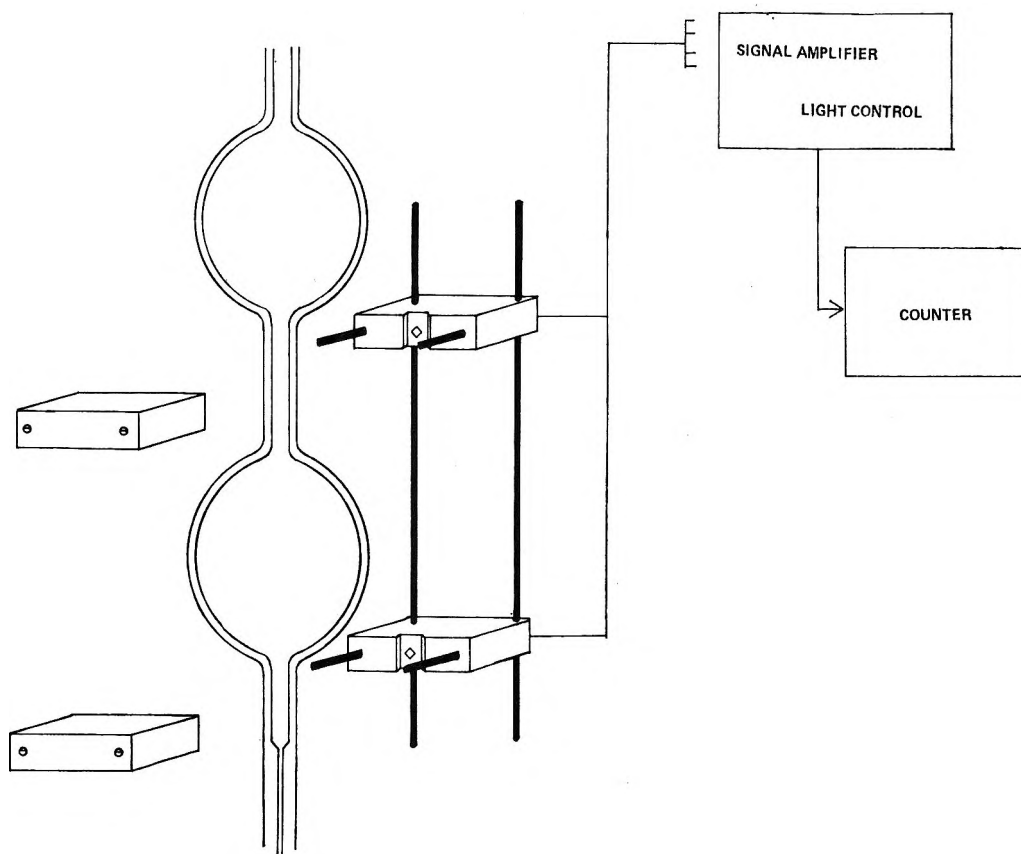
Figure 1. Schematic representation of photocell meniscus-detector unit.

after the initial triggering signal and back on just previous to the final signal at a rate which did not cause the counter to stop but quickly enough so that the total "light-on" time did not exceed 50 sec. A variation of ±10 sec in this "light-on" time was not detectable in our efflux time measurements.

The Pyrex viscometer was modified as shown schematically in Figure 2. The gas manifold at the top of Figure 2 is connected as indicated by continuous Pyrex tubing to the viscometer arms a, b, and c. It is attached to an adjustable frame (for ease of alignment) which is, in turn, mounted to the side of the outer bath. The entire unit to connection E is removed from the bath to a vacuum sample transfer system from which the sample vapor entering at D is condensed in the reservoir of the viscometer. Positioning of the viscometer is accomplished by a dual plumb line alignment with a capillary (not shown in Figure 2) which is glass-welded to the main body of the viscometer, extending well above the top of the bath. This capillary and the viscometer capillary are aligned prior to immersion of the unit in the bath.

The gas control valves A, B, and C allow the viscometer to be charged by creating a pressure differential across arms a and b with side arm c closed, and thereafter to equilibrate the pressure in all arms with ambient pressure at F.

The thermostat system consists of an insulated glass

outer bath with heating and cooling coils and a Plexiglas inner bath which houses the viscometer and a platinum resistance thermometer. The bath is filled with a commercially available antifreeze (ethylene glycol base), and the inner and outer baths are stirred independently. The temperature was monitored with a platinum-in-glass resistance thermometer in conjunction with a G-2 Mueller bridge and a nanovolt null detector. The platinum thermometer R_0 calibration was made using a triple-point-of-water cell.

The water used in the experiment was first distilled in a commercial still and then passed through a column of ion-exchange resin. This deionized water was made approximately 0.01 M in potassium permanganate and sodium hydroxide and distilled in an all-glass, grease-free still. The distillate was collected directly in a polyethylene bottle and sealed under nitrogen. Individual samples of this water were transferred in vacuo to the viscometer without ebullition. Following the completion of the sample transfer, the entire unit was filled with nitrogen gas which had been passed through Ascarite (to remove CO_2 traces). This same supply of nitrogen was used to pressurize the viscometer for charging. Conductivity measurements prior to the last sample transfer gave values of 1×10^{-6} ohm^{-1} cm^{-1}.

Experimental Results and Calculations

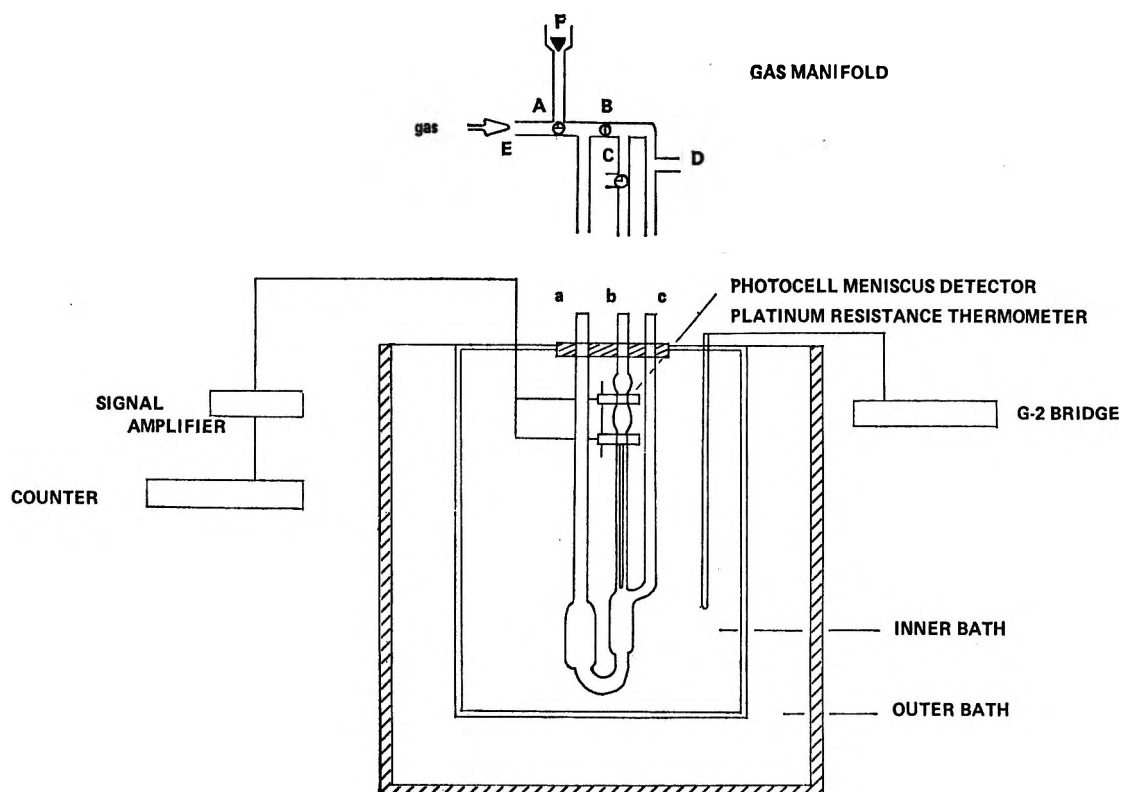Kinematic viscosities were determined at precise 5°

Figure 2. Composite schematic of viscometer system.

intervals from 40 to 0° and at conveniently separated temperatures in the supercooled region. Kinematic viscosities "η/ρ" were converted to absolute viscosities using the selected values for density of water published in the TRC Data Project Tables.[9]

The inner bath was controlled to ±0.002° with drift rates less than $0.004°/2\tau_t$ (τ_t is the efflux time at temperature t) for both determinations used in the calibration calculations. Similar control was obtained for the other determinations falling off slightly to about ±0.01° for the lower sub-ice point runs. Oscilloscope observations indicated that at $\tau_t \approx 550$ sec (corresponding to a temperature near zero), a single triggering event was of 1.3-msec duration, indicating that an ≈3.0-msec minimum uncertainty band could be expected for these or longer flow rates. The entire sample transfer technique and the determination of τ_{20} was repeated until three successive determinations gave equal values of τ_{20} within the precision limits reported below. A fourth τ_{20} determination made at the conclusion of the experiment also reproduced the τ_{20} observation. Each determination of τ_t was accomplished by fitting a linear equation in t to a set of observations $\{\tau_t,t\}$ in the range t' $-0.010 \leq t \leq t' + 0.010$, where t' is the reported temperature. The precision limits assigned to τ_t were calculated to represent a 99% confidence band for the two calibration points and a 95% confidence band for all others.[10]

Table I is an example of a typical data log given for the determination of τ_{25}. Conversion of (τ_t,t) data to

Table I: Data Log for Determination of $\tau_{25.000}$

Water Sample No. 4

Run	t, °C	τ, sec
1	25.007	275.882
2	25.006	275.890
3	25.003	275.907
4	24.999	275.939

Linear Least-Square Equation[a]

$(\tau - 275.900) = a + b(t - 25.000)$

[a] Parameters: $a = 0.0308$; $b = -7.01$; $\tau_{25.000}$ (predicted) = 275.931 ± 0.006 sec.

kinematic viscosities requires application of standard corrections as outlined in NBS Monograph 55.[11] Using eq 1,[12] we find that

$$\nu_t = C[1 + \xi(t - t_c)]M_t\tau_t - \frac{E[1 + \xi(t - t_c)]^{5/2}}{\tau_t^2} \quad (1)$$

where ν_t is the kinematic viscosity at temperature t and efflux time τ_t. The C, E, ξ, and t_c symbols represent

(9) "Selected Values of Properties of Chemical Compounds," Thermodynamics Research Center Data Project, Texas A&M University, College Station, Texas (loose-leaf data sheets, extant, 1970).

(10) G. W. Snedecor, "Statistical Methods," Iowa State College Press, Ames, Iowa, 1946.

(11) R. C. Hardy, Nat. Bur. Stand. (U. S.) Monogr., No. 55, (1962).

(12) M. R. Cannon, R. E. Manning, and J. D. Bell, Anal. Chem., 32, 355 (1960).

Table II: Experimental Results Summary

Viscometer constants $C = 0.00323885 \pm 0.00000015$ $E_{max} = 70.12$
$E_{min} = 66.65$

Celsius temperature	Efflux time, sec	Correction, cSt $E[(1 + \xi(t - t_c)]^{5/2}/\tau_t^2$	ν, cSt	ρ, g cm^{-3}	η, cP	(η/η_{20}) for $\eta_{20} = 1.0020$, cP
-8.280	759.35	0.00012	2.45876	0.998502	2.4551	2.4502 ± 0.0006
-6.647	709.88	0.00014	2.2986	0.998878	2.2960	2.2914 ± 0.0005
-4.534	653.242	0.00016	2.11519	0.999329	2.1137	2.1096 ± 0.0001
-1.108	575.504	0.00021	1.8634	0.999752	1.8630	1.8593 ± 0.0001
0.000	553.490	0.00022	1.79216	0.9998396	1.7919	1.7883 ± 0.0001
5.000	469.158	0.00031	1.51904	0.9999641	1.5190	1.5160 ± 0.0001
10.000	403.740	0.00042	1.3071	0.9997000	1.3067	1.3041 ± 0.0001
15.000	351.902	0.00055	1.1392	0.9991005	1.1381	1.1358 ± 0.0002
20.000	310.148		1.0038^a	0.9982058	1.0020	1.0000
25.000	275.931	0.00090	0.89283	0.9970474	0.89020	0.88842 ± 0.00004
30.000	247.548	0.00111	0.80072	0.9956540	0.79723	0.79564 ± 0.00003
35.000	223.753	0.00136	0.72342	0.9940313	0.71911	0.71767 ± 0.00001
40.000	203.582		0.65782^a	0.9922189	0.65270	0.65140

^{a} Values used in calibration (see ref 1).

the viscometer constant, the kinetic energy correction constant, the mean linear coefficient of thermal expansion for the viscometer glass ($\xi = 3.25 \times 10^{-6}$ deg^{-1}), and one of two calibration temperatures ($t_c = 20.000°$), respectively. When Cannon-Ubbelohde suspended-meniscus viscometers, in which no appreciable correction for variation in surface tension is needed, are used to make measurements on the same liquid used in calibration, M_t reduces to a correction for gas column density at t. In our calculation of this factor, we assumed that Dalton's law of mixtures was adequate for the water-saturated nitrogen mixture. Values of M_t range from 0.99987 at −8.28° to 0.99761 at 40°.

Following the recommendations of Cannon, *et al.*,[12] we view E as proportional to $V^{1/2}l^{-1/2}(Cr)^{-1/2}$ at t_c and determine it experimentally (V, l, and r are the viscometer dimensions, *i.e.*, volume, capillary length, and radius). The constants C and E were calculated from the calibration data at 20° ($\nu_{20} = 1.0038$ cSt)[9,13] and 40° ($\nu_{40} = 0.6578$ cSt)[8,9] after application of the M_t and expansion corrections to the observed times. The precisions assigned to the values of C and E were calculated from those obtained experimentally for τ_{20} and τ_{40}. That is, the extreme values of τ_{20} and τ_{40} obtained from the 99% confidence band were used to calculate the four possible C-E pairs. The value reported for C is the mean of the largest and smallest values thus obtained, and its precision band extends to include both. The values of E reported in Table II correspond to the extreme values of C. In the calculation of the precisions assigned to the reported values of viscosity, these maximum deviations for C and E were used in combination with the extreme values for τ_t obtained from the 95% confidence band, thus giving a $\nu_{t\text{-max}}$ and a $\nu_{t\text{-min}}$. The reported kinematic viscosity

in Table II is the mean of $\nu_{t\text{-max}}$ and $\nu_{t\text{-min}}$. Finally, precision bands were assigned to the reported viscosities assuming that the accuracy of the density data is such that no additional uncertainty is obtained in the conversion: η/ρ to η.

The results of fitting the experimental viscosity data to the following three-parameter equation are reported in Table III. In eq 2*, T' is the Kelvin temperature

Table III: A Comparison of Observed Viscosities with Those Calculated from Eq 2* with $n = -2.349$; $B = 156.3418$; $T_0 = 195.809$ K

t, °C	η_{obsd}, cP	η_{calcd}, cP	Per cent deviation	Relative experimental uncertainty, %
-8.28	2.4551	2.45469	0.017	0.05
-6.647	2.2960	2.29623	-0.010	0.08
-4.534	2.1137	2.11390	-0.009	0.01
-1.108	1.8630	1.86313	-0.007	0.01
0.000	1.79187	1.79199	-0.007	0.01
5.000	1.5190	1.51887	0.008	0.01
10.000	1.3067	1.30659	0.011	0.02
15.000	1.1381	1.13812	-0.002	0.04
20.000	1.0020	1.00200	0.000	a
25.000	0.89020	0.89030	-0.011	0.01
30.000	0.79723	0.79738	-0.019	0.01
35.000	0.71911	0.71916	-0.007	0.01
40.000	0.65270	0.65260	0.015	a

^{a} Values used in calibration.

$$\frac{\eta}{\eta'} = \left(\frac{T}{T'}\right)^n \exp[B(T' - T)/(T' - T_0)(T - T_0)] \quad (2^*)$$

(13) J. F. Swindells, J. R. Coe, Jr., and T. B. Godfrey, *J. Res. Nat. Bur. Stand.*, **48**, 1 (1952), RP2279.

Table IV: A Tabulation of Consistency Corrected Experimental Viscosities (cP) from This and Other Investigations (Standard Values: Viscosity Standard, η_{20} = 1.0020 cP; Density Data, TRC Data Project Values)

t, °C	This work	White and Twining[a]	Hallet[b]	t, °C	This work	Korson, et al.[c]	Hardy and Cottington[d]	Korosi and Fabuss[e]	Geddes[f]	Bingham[g]	Coe and Godfrey[h]
−12.0			2.90	0.000	*1.7919*						
−11.0			2.78	5.000	*1.5190*		*1.5184*				
−10.0			2.66	10.000	*1.3067*	1.3069					
−9.3		2.546		15.000	*1.1381*	1.1382					
−9.0			2.55	20.000	*1.0020*	*1.0020*	*1.0020*	*1.0020*	1.0020	1.0020	1.0020
−8.48		2.456		25.000	*0.8902*	0.8903			0.8903	0.8911	0.8903
−8.28	*2.4551[i]*			30.000	*0.7972*	0.7975			0.7963	0.7983	0.7976
−8.0			2.45	35.000	*0.7191*	0.7195					
−7.23		2.339		40.000	*0.6527*	0.6532	*0.6531*	*0.6527*	0.6532	0.6540	0.6531
−7.0			2.35	45.000		0.5963					
−6.65	*2.2960*			50.000		0.5471				0.5468	
−6.20		2.248		55.00		0.5042					
−6.0			2.25	60.00		0.4666	*0.4665*	*0.4665*	0.4669	0.4674	
−5.0			2.16	65.00		0.4334					
−4.70		2.119		70.00		0.4039					
−4.534	*2.1137*			75.00				*0.3784*			
−4.0			2.08	80.00			*0.3584*		0.3560		
−3.0			2.01	85.00							
−2.10		1.928		90.00			*0.3148*				
−2.0			1.93	95.00			*0.2976*				
−1.180	*1.8360*			100.00			*0.2822*	*0.2820*			
−1.0			1.86	110.00			*0.2549*				
0.000	*1.7919*	1.796	1.79	120.00			*0.2321*				
				125.00			*0.2220*	*0.2219*			
				135.0				*0.2040*			
				145.0				*0.1884*			
				150.0				*0.1815*			

[a] See ref 3. [b] See ref 2. [c] See ref 4. [d] See ref 16. [e] See ref 1. [f] See ref 17. [g] See ref 18. [h] See ref 19. [i] All values in italics are those selected for the determination of the parameters in eq 2* for the extended temperature range (see text).

(293.15) at $\eta' = \eta_{20}$ = 1.002 cP,[14] T is the Kelvin temperature, and n, B, and T_0 are empirically adjusted parameters. The equation parameters were adjusted by a least-squares technique.[15] Further discussion of this equation is deferred to the next section.

Analysis of the Extended Range Data

Table IV is a compilation of experimentally determined water viscosities taken from the literature.[1-4,16-19] The data have been corrected for consistency in the following manner. If the author(s) used a value other than 1.002 cP—for example, η^a_{20} for η_{20}[13] in calibration, the reported values, η_r, were corrected as $\eta_r(1.002/\eta^a_{20})$. In cases where kinematic viscosities were measured, the reported absolute viscosities were corrected to be consistent with the Thermodynamics Research Center (TRC) Data Project[9] densities, if the reported densities of the author, ρ^a_r, differed from the TRC Data Project values, ρ_{TRC}, as $\eta_r(\rho_{TRC}/\rho^a_r)$. In this compilation and in our experimental work, the International Practical Temperature Scale of 1948 was used.

The excellent agreement between the results of this work and that of Hardy and Cottington[16] of the National Bureau of Standards and of Korosi and Fabuss[1]

in the regions of data overlap is, we believe, especially significant in that the range of self-consistent, high-precision viscosity data is extended from well above the normal boiling point to well below the normal freezing point.

In comparing data obtained by different methods, we have selected certain data sets to which we have assigned uncertainties that were used to compute weighting factors in the data analysis. An uncertainty, $U = 0.2\%$, the estimated accuracy of the primary standard,[8] was assigned to those measurements whose relative precision was estimated to be equal to or better than this figure. In other cases, we have assigned uncertainties as estimated by the authors.

Figure 3 represents the data compiled in Table IV

(14) Throughout this paper the following units are used, and their conversion to SI units is as follows: cP (centipoise) = 10^{-3} N sec/m²; cSt (centistoke) = 10^{-6} m²/sec; ρ (g/cm³) = 10^3 kg/m³.

(15) P. R. Bevington, "Data Reduction and Error Analysis for the Physical Sciences," McGraw-Hill, New York, N. Y., 1969.

(16) R. Hardy and R. Cottington, *J. Res. Nat. Bur. Stand.*, **42**, 573 (1949), RP1994.

(17) J. A. Geddes, *J. Amer. Chem. Soc.*, **55**, 4832 (1933).

(18) E. Bingham and R. Jackson, *Bur. Stand. (U. S.) Bull.*, **14**, 59 (1916).

(19) J. R. Coe, Jr. and T. B. Godfrey, *J. Appl. Phys.*, **15**, 625 (1944).
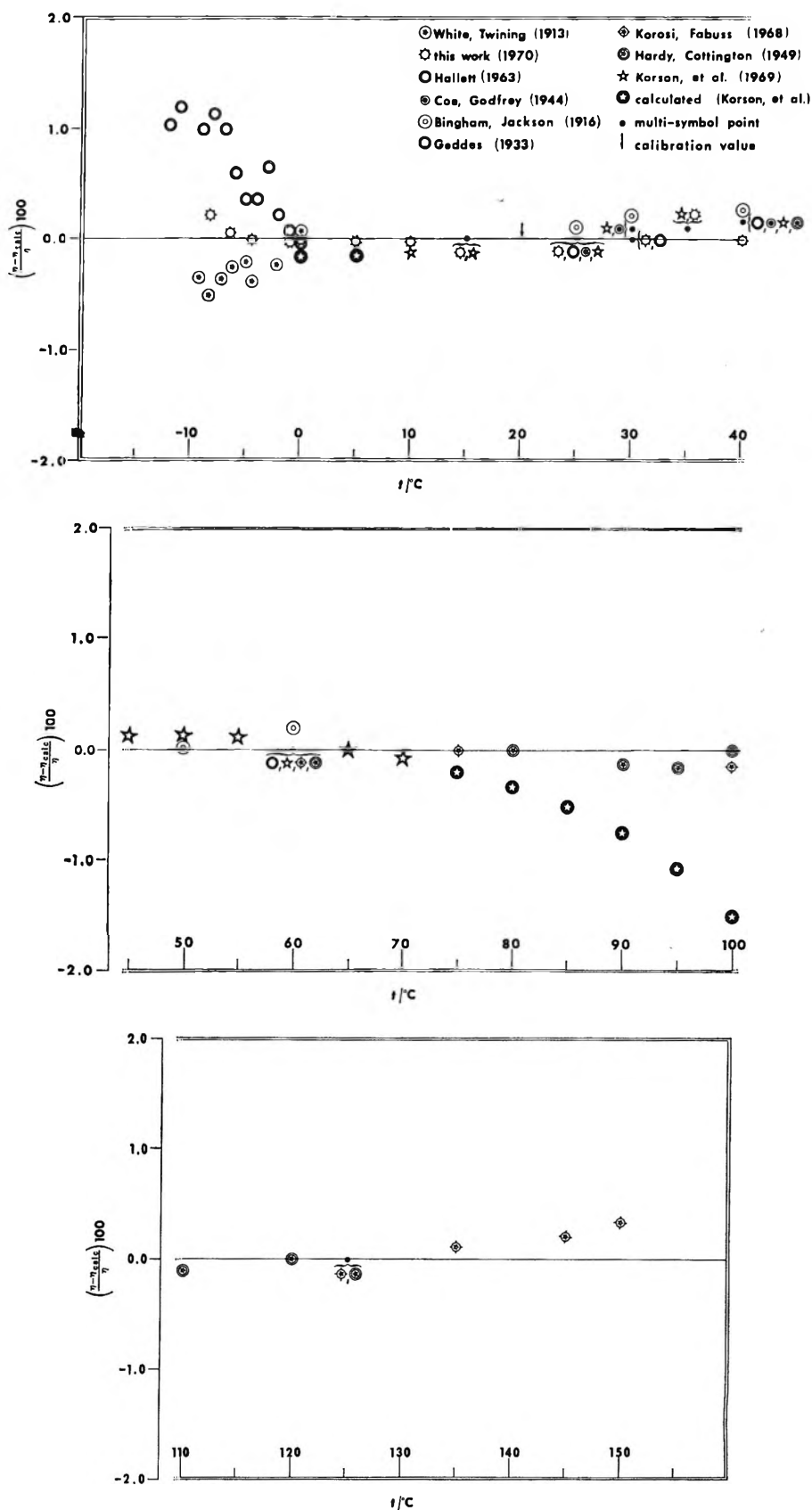
Figure 3.   A graphical representation of per cent deviation *vs.* Celcius temperature for literature and experimental viscosities. The zero line represents 0.00% deviation from viscosities calculated from eq 2* with $n = -1.43395$, $B = 245.661$, $T_0 = 181.630$.

plotted as per cent deviation from viscosities calculated from eq 2* in which the three parameters were adjusted

by the same least-squares method to fit three selected data sets as follows.

(i) This work	$U = 0.2\%$
(ii) Hardy and Cottington[16] (1949)	$U = 0.2\%$
(iii) Korosi and Fabuss[1] (1968)	$U = 0.2\%$ ($t \leq 70°$)
	$= 0.4\%$ ($t > 70°$)

The 29 individual data points were weighted as the square of the reciprocal of their assigned uncertainties. It is apparent from Figure 3 that the agreement between the calculated and fitting data is exceptionally good, with the average absolute per cent deviation being 0.11%. All the data points in Figure 3 represent measured values with the exception of those indicated as calculated by Korson, et al.[4] We regard the divergence of these calculated values to result from the method used to obtain the correction terms in eq 1. It should be noted, however, that these authors claim accurate prediction by their empirical methods only for the range $10° \leq t \leq 70°$. It is seen also from Figure 3 that the data of this work fall almost directly between those measured by other investigators.[2,3] These results lead us to assume that eq 2* predicts the viscosity of liquid water over the entire extended range within accuracy limits comparable to that of the primary standard (0.2%). The constants for eq 2* for the extended range are $n = -1.43395$, $B = 245.661$, $T_0 = 181.630$ K.

A General Empirical Function for the Shear Viscosity–Temperature Coefficient of Liquids

Equation 2* used in the previous sections is a reduced form of a new empirical relation (see eq 2 below) relative to a viscosity at a selected standard temperature. The new four-parameter equation defined below for the shear viscosities of liquids was formulated after a thorough analysis of the various viscosity equations found in the literature for the temperature coefficient of Newtonian liquids.

$$\gamma = A T^n \exp[B/(T - T_0)] \qquad (2)$$

In eq 2, A, B, n, and T_0 are four adjustable parameters; γ is the viscosity or kinematic viscosity and T is the Kelvin temperature. With proper choice of the four parameters, five different relations for the temperature dependence of viscosity of Newtonian liquids found in the literature readily follow from eq 2.

$$\gamma = A \exp[B/T] \qquad (2a)$$

$$\gamma = A \exp[B/(T - T_0)] \qquad (2b)$$

$$\gamma = A T^{1/2} \exp[B/(T - T_0)] \qquad (2c)$$

$$\gamma = A T^{1/2} \exp[B/T] \qquad (2d)$$

$$\gamma = A T^n \exp[B/T] \qquad (2e)$$

All of these special cases represent empirical and semiempirical equations which have been proposed and tested as viscosity formulas for the temperature coefficient of one or more Newtonian liquids.[20] In par-

ticular, eq 2 embraces the basic concepts of Arrhenius–Eyring rate theory[21,22] as also the free-volume, glass transition concepts of the Vogel,[23] Doolittle,[24] and Cohen–Turnbull[25] relations. Without concerning ourselves with the theoretical significance of the newly proposed viscosity–temperature relation, this equation very nicely satisfies the need of a reliable empirical equation for fitting shear viscosity data for simple liquids over an extended range. The fact that it reproduces the high-precision data on an abnormal liquid such as water speaks well for its applicability as an interpolation equation for correlating viscosities of van der Waals liquids, including those with specific interactions. Extrapolations of viscosity data beyond measured temperature ranges require additional consideration.

Multirange Application of the Vogel and Arrhenius Equations

Others[22] have shown that the Vogel equation (eq 2b) does not reproduce the viscosity data for water even over the limited 5–100° range. In smoothing viscosity data over wide temperature ranges, proposals[7] have been made to use the Vogel equation (eq 2b) and the usual form of the Arrhenius equation (eq 2a) for the lower and higher temperature ranges, respectively.

Apparently, Vogel in 1921 was the first to use eq 2b to represent the viscosity temperature coefficients of lubricating oils. More recently, the Vogel type of analytical function has been invoked in various theories to relate the additive constant "T_0" in the exponential to glass transition temperatures of supercooled liquids.[6,7] To cope with the problem of smoothing extended viscosity temperature data, Matheson, et al., have applied an empirical scheme plotting log η vs. T^{-3} to locate "kink" temperature regions which serve to define two temperature ranges. Gilra[26] has also applied this concept to the data of Hallett[2] for supercooled water. The necessity of defining two temperature regions for shear viscosities remains an issue.

To test this proposal, we have developed an analytical scheme which is designed to define the different temperature ranges for which the Vogel and Arrhenius equations should be used, if there is reasonable evidence for their existence. The validity of this approach as compared with log η vs. T^{-3} plots lies in the fact that the analysis is in terms of the Vogel parameters themselves. The mathematical justification rests on the principle that three data points determine three parameters;

(20) S. G. Brush, *Chem. Rev.*, **62**, 513 (1962).

(21) S. Glasstone, K. J. Laidler, and H. Eyring, "The Theory of Rate Processes," McGraw-Hill, New York, N. Y., 1941.

(22) A. A. Miller, *J. Chem. Phys.*, **38**, 1568 (1963).

(23) H. Vogel, *Phys. Z.*, **22**, 645 (1921).

(24) A. K. Doolittle, *J. Appl. Phys.*, **29**, 901 (1951).

(25) M. H. Cohen and D. Turnbull, *J. Chem. Phys.*, **31**, 1164 (1959).

(26) N. K. Gilra, *Can. J. Phys.*, **46**, 2123 (1968).

Table V: A Tabulation of Per Cent Deviations, Weighted Variance, and Root-Mean-Square Deviation for Observed and Calculated Water Viscosities of Five Empirical Equations

	Ref	$t,$ °C	$d_i\%^a$ eq 2b	$d_i\%$ eq 2e	$d_i\%$ eq 2a–2b	$d_i\%$ eq 4	$d_i\%$ eq 2*
1	b	−8.28	1.0	4.1	−1.3	0.3	0.2
2	b	−6.647	0.7	3.2	−0.9	0.1	0.1
3	b	−4.534	0.3	2.2	−0.5	−0.0	−0.0
4	b	−1.108	−0.1	1.0	−0.0	−0.2	−0.1
5	b	0.000	−0.2	0.8	0.1	−0.2	−0.1
6	b	5.000	−0.4	−0.1	0.5	−0.2	−0.2
7	16	5.000	−0.4	−0.2	0.5	−0.2	−0.2
8	b	10.000	−0.4	−0.4	0.6	−0.2	−0.1
9	b	15.000	−0.2	−0.4	0.4	−0.1	−0.1
10	13	20.000	−0.0	−0.0	0.0	0.0	−0.0
11	b	25.000	0.2	0.5	−0.6	0.1	0.0
12	b	30.000	0.5	0.0	−1.4	0.1	0.1
13	b	35.000	0.7	1.7	−2.4	0.2	0.1
14	16	40.000	1.0	0.2	−3.5	0.2	0.2
15	1	40.000	0.9	2.3	−3.4	0.2	0.1
16	1	60.00	1.4	4.2	−7.3	0.1	0.0
17	1	75.00	1.4	4.7	−8.1	0.0	0.0
18	16	80.00	1.2	4.6	−8.2	−0.0	−0.1
19	16	90.00	0.9	4.0	−8.0	−0.1	−0.1
20	16	95.00	0.8	0.4	−7.8	−0.2	−0.2
21	16	100.00	0.6	3.1	−7.4	−0.1	−0.1
22	1	100.00	0.6	3.0	−7.5	−0.2	−0.2
23	16	110.00	0.1	1.7	−6.6	−0.2	−0.1
24	16	120.00	−0.3	−0.1	−5.6	−0.1	−0.0
25	16	125.00	−0.6	−1.2	−5.1	−0.0	0.0
26	1	125.00	−0.7	−1.3	−5.1	−0.0	−0.0
27	1	135.00	−1.2	−3.8	−3.9	0.1	0.1
28	1	145.00	−1.9	6.9	−2.7	0.3	0.2
29	1	150.00	−2.2	8.6	−2.0	0.5	0.4

Weighted Variance[c]

			0.00324	0.0117	0.0182	0.000761	0.000541

Rms Deviation[d]

			0.00671	0.0270	0.0177	0.00206	0.00157

Values of Adjustable Parameters Obtained by Least Squares

	A	B	C	n	T_0	T^{*}
Eq 26		491.299			152.968	
Eq 7		5426.90		11.0644		
Eq 2b–2a		258.394			188.233	317.587
Eq 6	2.92964	2.66987×10^{-2}	98.6542			
Eq 2*		245.661		−1.43395	181.630	

^{a} $d_i\% = 100\ d_i/n_i$; $d_i = n_i^{\text{calcd}} - n_i^{\text{obsd}}$. ^{b} This work. ^{c} Weighted variance $= \sum_i w_i d_i^2$. ^{d} Rms deviation $= (1/N\Sigma d_i^2)^{1/2}$.

---

thus, $n - 2$ consecutive triples in a set of n data points determine $n - 2$ sets of parameters. The variation with temperature of one "T_0" of these parameters is compared with what would reasonably be expected if application of the Vogel equation to only the lower temperature range viscosity data could be used to obtain glass transition temperatures for the supercooled liquid.

Equation 3 is a solution for T_0 of the Vogel equation for the ith, jth, and kth data points.

$$T_0 = T_j - \frac{Y_i - Y_k}{Z_{ij} - Z_{kj}} \qquad (3)$$

where

$$Y_i = \ln \eta_i \qquad Y_k = \ln \eta_k$$

$$Z_{kj} = \frac{\ln \eta_k - \ln \eta_j}{T_j - T_k} \qquad Z_{ij} = \frac{\ln \eta_i - \ln \eta_j}{T_j - T_i}$$

Our application of this test to the 27 consecutive triples of the data sets used to fit eq 2* over the extended range did not define one, two, or more distinct temperature ranges. Our analysis showed a trend toward higher values of T_0 in the lower temperature range with very erratic behavior at higher temperatures, $t > 50°$. A further test of the two-range fit is shown in Table V,

in which a nonlinear least-squares fit of the selected data to a Vogel equation in the low range ($t \leq 44.437°C$) and an Arrhenius equation at higher temperatures are compared with least-squares fits for several other equations. In fitting the two-range case (eq 2a and 2b), the condition of continuity (equal values and equal slopes) at the boundary temperature T^*, plus that of forcing a fit at $\eta' = \eta_{20}$, reduces the number of independent parameters to three, including T^*; i.e., the least-squares criteria are used to determine the boundary temperature and also the two remaining independent parameters.

A comparison of the fits for eq 2b and 2a, eq 2* and 4, which has been recommended at various times for

$$\ln \frac{\eta'}{\eta} = \frac{A(t - 20) + B(t - 20)^2}{C + t} \qquad (4)$$

water viscosity,[1,11] is instructive in that all three have three independent adjustable parameters. It is apparent that in the two-range Vogel–Arrhenius case the deviations are both systematic and in excess of experimental uncertainty. We therefore conclude that this procedure is apparently not justified empirically and that values of T_0 so calculated are of questionable significance.

Equation 2e, representative of forms suggested by application of Absolute Rate Theory to viscous flow, is also included in Table V. It was, as were all the equations tested, forced to fit at $\eta' = \eta_{20}$, thus reducing the number of adjustable parameters by one.

Summary and Discussion

In the foregoing sections, we find that the extension of high-precision viscosity data for water to the supercooled state does not support the view of distinct temperature regions in which glass-like transitions at lower temperatures influence the temperature coefficient of viscous flow.[22,26] We further find that a reasonably simple reduced three-parameter empirical equation fits the entire extended range, suggesting that there are no thermal anomalies or "kinks"[24-26] in the viscosity temperature curve for pure water in the normal or in the metastable liquid state extending through its normal melting point. The success of eq 2* for the case of pure water suggests its usefulness for other liquids.

Appendix

The statistical method, used to obtain the parameter values for the various data fitting equations discussed in the text, is the method of nonlinear least squares.[15] In the general case, the k free parameters p_k of the nonlinear function are varied iterationally, each iteration providing a set of p_k values calculated to reduce the weighted squared deviation sum, χ^2. Each parameter increment Δp_k is calculated as $h\delta_k$, where h is normally one and δ_k is obtained from the normal equations of the first-order Taylor expansion of the fitting function about the parameters p_k. Convergence is reached when the condition $\Delta p_k/p_k \leq E$ is satisfied for each free parameter, where E is an externally supplied test value that for this work was set at 10^{-6}. The program, a modified version of one developed by Vogt and Buhl,[27] was written in FORTRAN IV and was run on an IBM 360/65 computer.

(27) D. Vogt and A. R. Buhl, "A Generalized Non-Linear Least Squares Data-Fitting Program," NDL-TM-55, U. S. Army Nuclear Defense Lab, Edgewood Arsenal, Md., Clearinghouse, 1969.

The Organic Solid State.   IV.   The Effect of Environment on Electron

Transfer in Biferrocene[Fe(II)Fe(III)] Picrate[1]

by D. O. Cowan,[2] R. L. Collins,[3] and F. Kaufman[4]

Department of Chemistry, The Johns Hopkins University, Baltimore, Maryland 21218 and
The Department of Physics, The University of Texas, Austin, Texas 78712   (Received October 26, 1970)

Publiction costs assisted by the Petroleum Research Fund

The synthesis and physical properties of a new ferrocene salt, biferrocene[Fe(III)Fe(III)] fluoroborate are described.   The results of electronic and nuclear magnetic resonance spectroscopy are used to assign the mixed valence absorption in biferrocene[Fe(II)Fe(III)] picrate to an electron-transfer transition.   The Mössbauer data are consistent with a thermal rate of electron hopping in the solid of $<10^7$ sec^{-1}.   The reasons for the reduction in rate, relative to solution, are discussed.

Though there are a large number of inorganic compounds that contain metal ions of the same element in two formally different oxidation states, there are very few organometallic compounds of this type known. We have recently reported[5] the synthesis and physical properties of biferrocene[Fe(II)Fe(III)] picrate, a mixed valence salt of ferrocene, which was predicted to show considerable intramolecular interaction on the basis of its electronic and infrared spectra and on its electrical conductivity.   Three mechanisms for the mixed valence transition were postulated and we wish here to present additional experimental data that bear directly on this question.   The results of electronic, nuclear magnetic resonance, and Mössbauer spectroscopy are reported for the biferrocene[Fe(II)Fe(III)] picrate, as well as for a newly synthesized salt of biferrocene, biferrocene[Fe(III)Fe(III)] fluoroborate.

Experimental Section

Apparatus and Techniques.   Electronic spectra were obtained on a Cary 14 recording spectrophotometer. All solutions (Spectrograde) were degassed with prepurified nitrogen and used immediately after they were prepared.   Potassium bromide pellets for optical studies were prepared from a 1.5-mg sample in 150 mg of Spectrograde KBr.   A Spex Industries press (3600 psi) was used on a Perkin Elmer evacuable die (sample diameter, 1.5 mm).   Infrared spectra were measured on a Perkin-Elmer 521 instrument and all samples were run as mulls on CsBr plates.   Nuclear magnetic resonance experiments were performed on Varian HA 100 and HR 100 spectrometers.   Mössbauer spectroscopy was performed on an apparatus that has been previously[6] described.   The quadrupole splitting parameter (Q.S.) and isomer shift (I.S.) values in units of mm/sec have an estimated error of not more than 0.03 mm/sec. Elemental analyses were performed by Galbraith Laboratories, Knoxville, Tenn.

Preparation of Compounds.   Biferrocene[Fe(II)Fe-(III)] Dipicrate.   Biferrocene, 0.3 g (8 × 10^{-4} mol) dissolved in 45 ml of benzene, was added to 50 ml of benzene which contained 0.55 g (2 × 10^{-3} mol) of picric acid and 0.073 g (6.75 × 10^{-4} mol) of benzoquinone.   The solution, heated for several minutes at 65°, turned black and was allowed to stand at room temperature for 48 hr.   The filtered solution yielded 0.33 g (60%) of black microcrystals, which were washed with ≃500 ml of cold benzene.

Anal.   Calcd for $C_{32}H_{22}N_6O_{14}Fe_2$: [$C_{20}H_{18}Fe_2$$^+$($C_6H_2$-$N_3O_7$)$_2$$^-$] C, 46.53; H, 2.66; Fe, 13.52.   Found: C, 46.49; H, 2.84; Fe, 14.68 (ash).

The Mössbauer spectrum of the dipicrate salt was identical with that of the monopicrate, except for the presence of 10% ferrous iron, which may explain the discrepancy in the iron analysis.

Biferrocene[Fe(II)Fe(III)]   Picrate.   The monopicrate salt of biferrocene was prepared by recrystallization of the dipicrate salt, described above.   To 40 ml of methanol was added 0.1 g of dipicrate salt.   Distilled water, 25 ml, was added to the filtered solution, which was cooled in the freezer for 24 to 48 hr.   The black platelets of biferrocene[Fe(II)Fe(III)] picrate, 0.049 g, showed mp 190°, dec.   Far-ir see Table I; uv max (CH$_3$-CN) 220 nm (ϵ 6.64 × 10^4), 295 (1.45 × 10^4), 375 (2.21 × 10^4), 550 (1800), 1900 (551).

Anal.   Calcd   for $C_{26}H_{20}N_3O_7Fe$:   [$C_{20}H_{18}Fe_2$$^+$($C_6$-

(1) F. Kaufman and D. O. Cowan, *J. Amer. Chem. Soc.*, **92**, 6198 (1970).

(2) Author to whom inquiries should be addressed at The Johns Hopkins University; A. P. Sloan Fellow.

(3) The University of Texas.

(4) Taken from the Ph.D. Thesis of F. Kaufman and submitted to The Johns Hopkins University; National Institutes of Health Predoctoral Fellow.

(5) (a) D. O. Cowan and F. Kaufman, *J. Amer. Chem. Soc.*, **92**, 219 (1970);   (b) F. Kaufman and D. O. Cowan, *ibid.*, **92**, 6198 (1970).

(6) R. L. Collins and R. Pettit, *J. Inorg. Nucl. Chem.*, **29**, 503 (1967).

D. O. Cowan, R. L. Collins, and F. Kaufman

$H_2N_3O_7)^-]$ C, 52.20; H, 3.37; Fe, 18.67. Found: C, 52.01; H, 3.18; Fe, 18.44. ir 3085 (CH stretch), 1414 (CC stretch); 1109, 1102 (ring breadth), 1002 (CH bend) 818, 812 (CH bend).

Biferrocene[Fe(III)Fe(III)] 2BF₄. To a cold, rapidly stirred solution of 120 ml of benzene which contained 0.6 g (1.6 × 10⁻³ mol) of biferrocene and 0.037 g (3.4 × 10⁻³ mol) of benzoquinone was added 2 ml (0.016 mol) of BF_3–Et_2O (Eastman, White Label). The solution, which instantly turned black, was stirred for several minutes then allowed to stand cold for 3 hr. A blue solid was collected from the solution and washed with 500 ml of cold benzene. In a typical purification run, 30 mg of crude product was dissolved in the minimum amount of nitromethane (≅ 1 ml) to yield a syrupy, greenish solution. After filtration from any residue, an equal volume of diethyl ether was quickly added to precipitate the product. The cloudy solution was kept in the refrigerator for 36 hr, then filtered to give 12 mg (37%) of the biferrocene[Fe(III)Fe(III)] 2BF₄ salt. The deep blue solid was rinsed with ether until the wash was colorless, then dried for several days in a desiccator under high vacuum, dec >226°: ir (solid) 408 cm⁻¹ (antisymmetric ligand–metal stretch); uv max (solid in Nujol mull) 760 nm; Mössbauer data (see text). Magnetic susceptibility and electron spin resonance studies[7] of this compound confirm our valence and structural assignment. (For solution properties, see text.)

Anal. Calcd for $[C_{20}H_{18}Fe_2^{+2}(BF_4)_2^{2-}]$: C, 44.17; H, 3.31. Found: C, 43.93; H, 3.41.

2,3-Dichloro-5,6-dicyanoquinone (DDQ) Salt of Biferrocene. The method of Brandon, Osiecki, and Ottenberg was used:[8] In 20 ml of benzene was dissolved 0.02 g of biferrocenyl (2 × 10⁻⁴ mol) and 0.002 g of DDQ (1 × 10⁻⁴ mol). The black solution was stirred for 1 hr, allowed to stand for several days, then filtered from 30 mg (19%) brown solid: mp 240° dec.

Anal. Calcd for $[(C_{20}H_{18}Fe_2)^{2+}(C_8O_2Cl_2N_2)_2^{2-}]$: C, 52.40; H, 2.19: Found: C, 52.38; H, 2.50; (see text for discussion of solution properties).

Results and Discussion

The Nature of the Mixed Valence Transition in Biferrocene[Fe(II)Fe(III)] Picrate. The spectral properties of biferrocene[Fe(III)Fe(III)] 2BF₄ have been studied in fluid media and in the solid state. Acetonitrile solutions of this compound show absorption bands (ultraviolet to near-infrared) that are identical with those observed for the biferrocene(2,3) cations. The near-infrared region is dominated by an absorption band, λ_{max} 1850 (ϵ 445) that had been tentatively assigned[5] to an electron-transfer transition between the +2 and +3 Fe atoms in the mixed valence salt of biferrocene. Far-infrared spectra of films (made by evaporation of solutions that contained the (3,3) compound) showed absorption bands that were characteris-

tic of biferrocenyl and the (2,3) cation. The spectral results on films and the seeming insensitivity of the $^2E_{2g} \rightarrow {}^2E_{1u}$ transition of the (3,3) ferrocenium ions to substitution prompted us to study the spectrum of this compound in the solid state.

Mössbauer (see below) and far-infrared spectral studies were consistent with an Fe(III)Fe(III) assignment: a Nujol mull of the finely powdered solid gave a single strong absorption at 408 cm⁻¹ (see Table I).

Table I: Far-Infrared Band Positions

	Ring–metal[a] stretch, cm⁻¹	Ring-tilt, cm⁻¹[a]
Biferrocene[Fe(II)Fe(III)] picrate	448	495
Biferrocene[Fe(III)Fe(III)] fluoroborate	408	
Ferrocene[b]	478	492
Biferrocene	478	489
Ferrocenium picrate	405	
Ferrocenium fluoroborate	425	

[a] Antisymmetric vibrations. [b] M. Rosenblum, "Chemistry of the Iron Group Metallocenes," Wiley, New York, N. Y., 1965.

Since this is in the range expected (425–403)[9] cm⁻¹ for ferrocenium salts and occurs at a lower frequency than the absorption of ferrocenium fluoroborate (425 cm⁻¹)[9], the far-infrared assignment was considered to be ambiguous. These mulls were studied in the spectral region, 500–2000 nm[10] and, *in contrast* to the solution results, no absorptions were seen at wavelengths greater than 950 mμ. An absorption at 760 nm was observed and we have assigned it to the $^2E_{2g} \rightarrow {}^2E_{1u}$ transition of the substituted $Fe(Cp)_2^+$ ion.

Solutions of the 2DDQ salt of biferrocene dication show the same behavior as the fluoroborate and it would therefore appear that the properties of biferrocene cations are independent of the nature of the anion.[11] The (3,3) species are well defined in the solid state and show *no* mixed valence transition near 2000 nm. We conclude that these dications are unstable in solution and are rapidly reduced to the (2,3) species, which always exhibit an absorption in the near-infrared region. In contrast to the (3,3), the *monocation* shows no evidence of valence changes as a function of state; the

(7) D. O. Cowan, G. A. Candela, and F. Kaufman, *J. Amer. Chem. Soc.*, in press.

(8) R. L. Brandon, J. H. Osiecki, H. Ottenberg, *J. Org. Chem.*, 31, 1214 (1966).

(9) (a) Unpublished results of F. Kaufman; (b) T. Pavlik and J. Klikorka, *Coll. Czech. Chem. Commun.*, 30, 664 (1965).

(10) At wavelengths less than 500 nm the scattering was too severe to allow the detection of any sample absorption.

(11) For polarized absorption studies on crystals of ferrocenium picrate, Kuroda [*J. Molec. Spectrosc.*, 30, 355 (1969)] has suggested that overlap between the component anion and cations is small.

The Journal of Physical Chemistry, Vol. 75, No. 13, 1971

long wavelength transition *is* observed in a thin film or as a powdered solid dispersed in a KBr matrix. The mixed valence transition is dependent on there being one molecule of ferrocene and its ion, held closely enough to interact. Highly concentrated solutions, containing both of these species, display no extra spectral bands. The separation of the two ferrocene moieties in biferrocenyl mercury[12] is large enough to preclude the possibility of extensive interaction.[13]

We had previously proposed[5b] three mechanisms to account for the mixed valence transition in the biferrocene(2,3) cation. Since we showed that the difference in ligand field environments between $Fe(Cp)_2$ and $Fe(Cp)_2^+$ was negligible, the prime factor that determines the physical properties should be the extent of orbital interaction. In the *absence* of overlap between adjacent metal orbitals, the new spectral transition could be explained by an intramolecular metal–ligand charge transfer. On the other hand, a *small* amount of overlap between the $^2E_{2g}[a_{1g}^2e_{2g}^3]$ and $^1A_{1g}[a_{1g}^2e_{2g}^4]$ states of the $Fe(Cp)_2^+$ and $Fe(Cp)_2$ portions of the molecule would lead to an optical electron transfer (hopping) process between the two iron atoms. *Extensive* orbital interactions would undoubtedly lead to metal–metal bonding *via* the e_{2g} orbitals.

It is well known that the intensities of mixed valence transitions depend directly on the extent of electron delocalization between the two interacting atoms.[14,15] From the relatively low molar absorptivity (ϵ 550), we can estimate[14] that the optical electron spends less than 0.1% of its time tunneling through the intramolecular barrier that exists between the two equivalent sites. This means that meaningful integral oxidation numbers can be assigned to the iron atoms in the biferrocene-(2,3) cation since the electrons are virtually localized at each iron atom. That the metal valences are indeed distinct is supported by the Mössbauer data (see below) and the esr and magnetic susceptibility values for the (2,3) and (3,3) biferrocene salts.[7] The lack of any absorption in the near-infrared spectrum of the (3,3) is also consistent with this interpretation.

The assignment of the mixed valence transition to a metal–ligand charge-transfer transition would imply that resonance interactions in the biferrocenyl system are so extensive as to stabilize dramatically an antibonding ligand orbital. Though there is evidence in the electronic spectrum of biferrocene for increased ring conjugation, the wavelength shifts and heightened extinction coefficients are not large enough to account for the very low spectral energy of the mixed valence transition. Though hypsochromic shifts in the visible band of some substituted ferrocenium ions are found to be as large[16] as 2700 cm^{-1}, relative to the parent ion, we have detected no new absorptions in the long wavelength region of the spectrum in sulfuric acid solutions of benzoyl–ferrocene.[17] In addition, highly concentrated solutions of biferrocene in benzene exhibit no electronic

transitions at wavelengths greater than 500 nm (limit of detection, ϵ <3).

In the absence of extensive interaction between the metal atoms or the ligands in the biferrocenyl system, the interpretation of the mixed valence transition must depend on weak intramolecular interactions between the $Fe(Cp)_2$ and $Fe(Cp)_2^+$ halves of the (2,3) cation. The electron-transfer band[5] hypothesis for the mixed valence transition agrees with this picture because it requires that the orbitals involved interact only through higher vibrational states. The width of the mixed valence band and its low energy have been shown[5] to be consistent with an optical electron-transfer process. The calculated thermal transfer rate agrees well with what is predicted from experiment. The absence of any transitions in the spectrum of the biferrocene(3,3) dication seems to indicate that one "hole" $^2E_{2g}[(a_{1g})^2(e_{2g})^3]$ and one "electron" $^1A_{1g}[(a_{1g})^2(e_{2g})^4]$ in the e_{2g} state is necessary for the appearance of the absorption. An electron-transfer transition between the $Fe(Cp)_2^+$ species in the (3,3) is considered unlikely because this would involve the formation of a +4 oxidation state for iron. The inability to detect a long wavelength band in biferrocene is also good evidence for needing one hole and one electron per molecule for transfer to take place. Taube[18] has also assigned the long wavelength absorption band in a ruthenium(2,3) mixed valence compound to an electron-transfer transition because of the lack of any new absorptions in the parent (2,2) and (3,3) species.

Thermally Activated Electron Transfer in Solutions of the Biferrocene(2,3) Cation. It is well known that in solution ferrocene and ferrocenium ion undergo very rapid electron transfer. Measurements by isotopic exchange[19] and nmr line broadening[20] have established that the transfer rate is not significantly less than would be predicted for a diffusion controlled process. The $Fe(C_5H_4)_2^+$, $Fe(C_5H_5)_2$ couple, in contrast to many inorganic systems, is uniquely suited for fast exchange.[21] The reorganizational energies required for the chemical change of oxidation state are small. An exchange process between these two bulky species, with a net charge

(12) M. Rausch, M. Vogel, and H. Rosenberg, *J. Org. Chem.*, **22**, 901 (1957).

(13) Unpublished results of F. Kaufman. Solutions of the oxidized mercury compound (benzoquinone–picric acid) only show a "ferrocenium" transition at 630 nm when subjected to spectral analysis.

(14) M. B. Robin and P. Day, *Advan. Inorg. Chem. Radiochem.*, **10**, 247 (1967).

(15) N. S. Hush, *Progr. Inorg. Chem.*, **8**, 391 (1967).

(16) Private communication from R. Prinz.

(17) This compound was chosen because the width (4800 cm^{-1}), λ_{max} (570 nm) and molar absorptivity (ϵ 2000) of its ferrocenium ion transition are very similar to the spectral data for biferrocene.

(18) C. Creutz and H. Taube, *J. Amer. Chem. Soc.*, **91**, 3988 (1969).
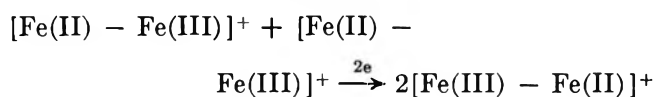
(19) D. R. Stanks, *Discuss. Faraday Soc.*, **29**, 73 (1960).

(20) N. W. Dietrich and A. C. Wahl, *J. Chem. Phys.*, **38**, 159 (1963).

(21) D. O. Cowan, G. Pasternak, and F. Kaufman, *Proc. Natl. Acad. Sci. U. S.*, **66**, 837 (1970).

of $+1$, can be expected to show very little coulombic interactions and small activation energies for reorganization of solvent molecules.

In solution the average encounter diameter between ferrocene and ferrocenium ion has been estimated to be 7.6 Å.[19] The iron–iron distance in biferrocene[Fe-(II)Fe(III)] picrate has been calculated from models to be from 3.8 (cis coplanar) to 5.1 Å (trans coplanar). Regardless of the configuration of the (2,3) compound in solution, therefore, the exchanging species in the mixed valent compound are expected to be at least 33% closer to each other than in the free ion case where van der Waals interactions determine the average encounter distance. The shorter metal–metal distance in the biferrocene skeleton and the smaller reorganizational energy of solvent during the transfer process, relative to the parent species, means that solutions of biferrocene[Fe(II)Fe(III)] picrate should exhibit very rapid, thermally activated intramolecular electron transfer. Intermolecular exchange processes are expected to be slow because they involve a two-electron transfer between the exchanging species.

$$[Fe(II) - Fe(III)]^+ + [Fe(II) -$$

$$Fe(III)]^+ \xrightarrow{2e} 2[Fe(III) - Fe(II)]^+$$

A one-electron transfer process should be energetically unfavored because it involves the formation of the highly unstable (3,3) cation.

$$[Fe(II) - Fe(III)]^+ + [Fe(II) - Fe(III)]^+ \xrightarrow{1e}$$

$$[Fe(II) - Fe(II)] + [Fe(III) - Fe(III)]^{2+}$$
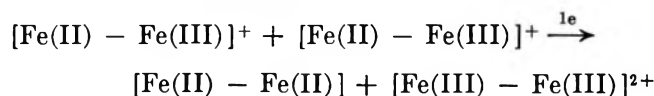
The electron transfer between $Fe(Cp)_2$ and $Fe(Cp)_2^+$ can be studied by nuclear magnetic resonance spectroscopy. The oxidized species shows a contact shifted resonance at -30.0 ppm[22] (1700 Hz line width), whereas the nominally diamagnetic, neutral ferrocene molecule shows no separate absorption in equimolar solutions containing the cation. The signal of the ferrocene species cannot be seen because of the rapid rate at which its valence changes due to the electron exchange process. Inequivalent protons in substituted ferrocenium species are also effected by the paramagnetism of the unpaired 3d iron electron. Depending on the distance from the paramagnetic site, substituents have been shown to absorb at resonances of as large as 18.5 ppm, contact shifted from the spectral position in the diamagnetic derivative.

We have studied the nuclear magnetic resonance spectra of solutions of biferrocene[Fe(II)Fe(III)] picrate and have not observed a separate signal (range ± 20 ppm) due to the ring protons of the ferrocene portion of the molecule. In the absence of rapid intramolecular exchange, it is expected that the cyclopentadienyl protons farthest removed from the paramagnetic site would be observable because it is known[23] that the

iron atom in ferrocene effectively insulates one ring from the other. We have observed in the nmr (HR 100 with C.A.T.) spectrum a very broad signal which we have assigned to all of the cyclopentadienyl protons in the biferrocene(2,3) system. As in the case of solutions containing equimolar quantities of $Fe(Cp)_2$ and $Fe-(Cp)_2^+$, our results are consistent with a very rapid electron transfer process.[24]

Mössbauer Results on Biferrocene Compounds. Mössbauer spectroscopy has been applied to a large number of ferrocene derivatives (see Table II) and the results have been very helpful in the assignment of electronic structure. The characteristic differences in the quadrupole splitting parameter for ferrocene (2.4 mm/sec) and ferrocenium ion (<0.1 mm/sec) are particularly useful in defining the 3d configuration of the iron atom. The quadrupole splitting observed (2.4 mm/sec) for the ferrocene–TCNE complex was used to define that compound as a charge-transfer complex,[6] and not as an ionic salt as had been previously suggested.

We have measured the Mössbauer parameters for the salts of biferrocene and the results are tabulated in Table II. In both compounds, there are absorptions

Table II: Mössbauer Data

Compd	T, °K	Q.S., mm/sec	I.S., mm/sec
Biferrocene[Fe(II)Fe(III)] picrate[a]			
Ferrocenyl iron(II)	77	2.141	+0.510
	298	2.053	+0.419
Ferrocenium iron(III)	77	0.288	+0.518
	298	0.302	+0.421
Biferrocene[Fe(III)Fe(III)] fluoroborate[a]	77	0.163	+0.497
	298	0.170	+0.422
Biferrocene[b,c]	78	2.36	+0.67
Ferrocenium picrate[c,d]	78	0	+0.67
Ferrocenium fluoroborate[c,e]	298	0.76	+0.54
$(C_{10}H_{13}Fe)_2$–CH$^+$BH$_4^-$[f,g]	100	2.11	+0.78

[a] Isomer shifts (I.S.) relative to iron foil. [b] I.S. relative to a Co^{57} (chromium) source. [c] G. K. Wertheim, R. H. Herber, *J. Chem. Phys.*, **38**, 2106 (1963). [d] I.S. relative to 321 S.S. [e] I.S. relative to Sundvik 2R2. [f] I.S. relative to S.N.P. [g] R. H. Herber in "Characteristization of Organometallic Compounds," M. Tsutsui, Ed., Wiley, New York, N. Y., 1968.

with quadrupole splittings in the range found for other ferrocenium ions. This observation indicates that we are dealing with materials that have Fe(III) ions present and are, therefore, not charge-transfer complexes.

(22) H. P. Fritz, H. J. Keller, and K. E. Schwarzhans, *J. Organo-metal. Chem.*, **6**, 652 (1966).

(23) M. Rosenblum, "Chemistry of the Iron Group Metallocenes," Wiley, New York, N. Y., 1965.

(24) The lack of nuclear hyperfine structure is consistent with the magnetic spin states proposed for these compounds in our magnetic susceptibility and electron spin resonance studies.[7]
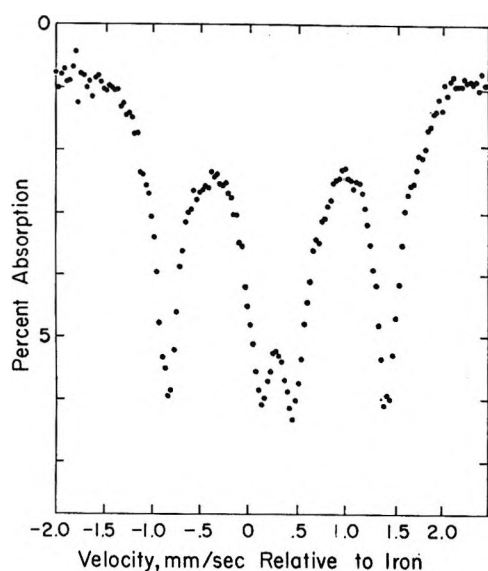
Figure 1. Mössbauer spectrum of biferrocene[Fe(II)Fe(III)] picrate at 77°K.

Figure 2. Mössbauer spectrum of biferrocene[Fe(II)Fe(III)] picrate at 298°K.

The Mössbauer results on the (3,3) compound are consistent with the elemental analysis, which indicated a 1:1 molar ratio of ferrocenium:BF$_4$. In contrast to the Mössbauer data on the dipicrate salt of biferrocene, there are no signs of ferrocenyl iron(II) in the spectrum of the (3,3) compound. This means that within the limits of detection of the instrument, the material consists entirely of Fc(III)Fc(III) units. These results agree well with the absorptions seen in the far-infrared spectrum of the (3,3) (see earlier discussion). Interestingly, the large quadrupole splitting seen in the Fc$^+$-BF$_4^-$ derivative has been substantially reduced in the dimer compound. Presumably, these results are due to the lower 3d electron density that exists at the iron atoms of the (3,3) salt.

The Mössbauer spectrum of biferrocene Fe(II)Fe-(III) picrate at 78°K is shown in Figure 1. The spectrum is essentially a composite of absorptions due to a Fe(Cp)$_2$ and a Fe(Cp)$_2^+$ unit and is in sharp contrast to the data obtained for the other bridged ferrocene derivative studied by this technique, [(C$_{10}$H$_9$)$_2$Fe]$_2$CH$^+$-BF$_4^-$.[25] The latter compound was thought[26] to have contributing resonance forms with unpaired electron density residing on the metal atom, but the diamagnetism[26] of the sample and the large quadrupole splitting in the Mössbauer spectrum indicate negligible interaction between the iron atom and the carbonium carbon. *The composite spectrum of the (2,3), on the other hand, establishes this compound as a true mixed valence ferrocene derivative.* The quantitative features of the spectrum confirm the earlier discussion on the extent of interaction between the metal atoms: integral oxidation numbers can be assigned to the metal since there is no evidence of strong metal–metal interactions. The larger quadrupole splitting of the mixed valence picrate, compared with (Cp)$_2$Fe$^+$ picrate$^-$, can be interpreted by
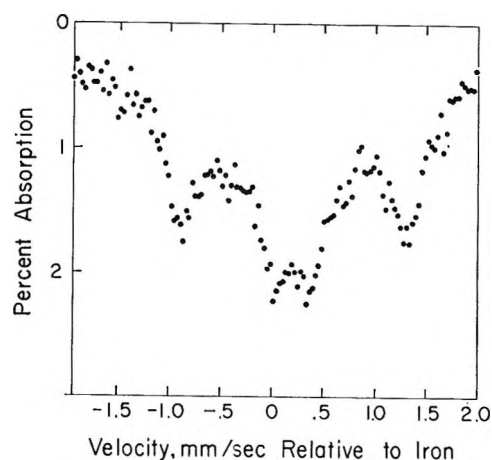
assuming that the weak intramolecular interactions result in increased electron density at the ferrocenium center due to the electron donor effect of the ferrocene substituent.

Comparison of these results with the data on the far-infrared spectrum of biferrocene(2,3) picrate (Table I) indicates that the latter technique must be used in conjunction with several complimentary modes of analysis. From the infrared results alone, one predicts that the valence states of the two metal atoms in the (2,3) cation are identical. The disagreement with the Mössbauer technique indicates that the ligand–metal stretching transitions in the (2,3) cation cannot be analyzed on the assumption that the two halves of the molecule are vibrationally distinct. Presumably a complete normal mode analysis of the biferrocene system would yield the observed interdependence of these stretching transitions in the mixed valence compound.

The Mössbauer spectrum of the (2,3) picrate at 298°K (see Figure 2) is quantitatively similar to that seen at liquid nitrogen temperature but important differences can be seen. The central narrow (ferrocenium) doublet has increased in intensity relative to the broad (ferrocene) absorption. In addition, a new set of absorptions have begun to appear in the region between the two original doublets. These changes may indicate that an exchange reaction is occurring. In the absence of electron exchange, the Mössbauer spectrum of an Fe(II)Fe(III) system is expected to look like the superposition of the signals due to each species taken individually. Electron exchange interactions, however, are expected to affect profoundly the shape and intensity of the absorption curves. Systems that are exchanging at a rate faster than $\sim 10^8$ sec^{-1} can only show a single average absorption since the mean lifetime of the Mössbauer active nuclear excited state is 1.4×10^{-7} sec.

(25) R. H. Herber, *Inorg. Chem.*, **8**, 174 (1969).

(26) C. Jutz, *Tetrahedron Lett.*, 1 (1959).

Exchange rates that lie near this value have a complicated but definite effect on the line shape and resolution.

The "hybrid" character of the Mössbauer line shape in the room temperature spectrum of biferrocene Fe-(II)Fe(III) picrate probably indicates the existence of an intramolecular exchange process taking place at a rate less than 10^7 sec^{-1}. At liquid nitrogen temperature, the Boltzmann factor would be sharply reduced, and the resulting rate would be too small to effect the Mössbauer spectrum appreciably. However, this explanation must be regarded as tentative since other factors in addition to nuclear state lifetimes can also effect the line shapes. If there is a reduction in the electron-transfer rate from 10^{10} sec^{-1} in fluid media to $<10^7$ sec^{-1} in the solid state, this reduction may be due to the inability of the picrate anion to readily readjust its position in the crystal after electron transfer.

Perhaps the best precedent for this view is found in the area of inorganic compounds where the mixed iron cyanides[14] have been studied for over 250 years. Prussian blue, $KFe^{III}[Fe^{II}(CN)_6]$, has been shown to have discrete iron valences on the basis of a wide variety of experiments, including Mössbauer, conductivity, and electronic spectroscopy. The "trapped" valences occupy one of the two unequivalent octahedral sites in the crystal: either the carbon ends of the cyanides, or the nitrogen ends. This mixed valent inorganic solid is an intrinsic semiconductor with a resistivity at room temperature ($\rho = 10^7$ ohm-cm) that is very similar ($\rho = 5 \times 10^7$ ohm-cm) to that of the mixed valence organometallic compound biferrocene(2,3) picrate.

The Interactions of Positrons with Defects in Sodium Chloride Crystals[1]

by Charles S. Tumosa, J. Blair Nicholas, and Hans J. Ache*

Department of Chemistry, Virginia Polytechnic Institute and State University, Blacksburg, Virginia 24061
(Received December 14, 1970)

The positron lifetime spectra of nearly perfect NaCl crystals were decomposed into two components with the lifetimes $\tau_A = 4.0 \times 10^{-10}$ sec and $\tau_B \simeq 1.0 \times 10^{-9}$ sec and corresponding intensities of $I_A \simeq 96$ and $I_B \simeq 4\%$. Upon proton-, γ-, or X-irradiation or doping with Al metal a significant decrease in the lifetimes and a marked increase in the intensity of the long-lived component was observed, approaching "saturation values" of $\tau_A \simeq 2.8 \times 10^{-10}$ sec, $\tau_B \simeq 5.6 \times 10^{-10}$ sec and $I_B \simeq 40\%$ with increasing radiation doses. The results were explained in terms of a simple model which involves the trapping of positrons in cation vacancies. On the basis of this model a maximum rate of 7.6×10^8 sec^{-1} was found for the capture of positrons in these vacancies, which corresponds to a defect fraction of about 2.6×10^{-7}. A mechanism is proposed to account for the observed saturation values in the positron lifetime spectra.

Introduction

The positron annihilation process in alkali halides and in sodium chloride has been the subject of several investigations. Earlier work by Bisi, Fiorentini, and Zappa[2a,b] has shown that the observed lifetime spectra can be decomposed into at least two components, which eliminates a unique fate for all positrons.

Positronium formation and subsequent annihilation is the more prevalent reason for the appearance of two components in the lifetime spectra of most molecular substances, molecular crystals, liquids, or gases. Ferrell,[3] however, had concluded from thermodynamic arguments that the formation of positronium in perfect or nearly perfect alkali halide crystals is forbidden and his conclusion was supported by both angular correlation[4] and three quantum decay yield measurements.[5] Thus positronium formation has to be ruled out in these

(1) Work supported by the U. S. Atomic Energy Commission. Acknowledgment is also made to the Petroleum Research Fund for partial support.

(2) (a) A. Bisi, A. Fiorentini, and L. Zappa, *Phys. Rev.*, **131**, 1023 (1963); (b) A. Bisi, A. Fiorentini, and L. Zappa, *ibid.*, **134**, A328 (1964).

(3) R. A. Ferrell, *Rev. Mod. Phys.*, **28**, 308 (1956).

(4) A. T. Stewart and N. K. Pope, *Phys. Rev.*, **120**, 2033 (1960).

(5) A. Bisi, L. Bussolati, S. Cova, and L. Zappa, *ibid.*, **141**, 348 (1966).

crystals and decay modes involving positron bound states other than positronium have to be invoked to account for the complex positron lifetime in the alkali halide crystals.

Three major types of bound states have been suggested: (1) a positron anion state (e⁺-anion), (2) a polaron state of the positron, and (3) a positron attached to crystal defects.

The first model has been studied by a number of authors, particularly Bussolati, et al.,[6] who presented evidence for the possibility of such a system. This model, however, fails to explain the results obtained by Williams and Ache[7] upon introduction of radiation defects. The positron lifetime of 0.5 nsec calculated for the positron–polaron state which has been discussed by Gol'danski and Prokop'ev[8-10] is close to the observed lifetimes but cannot provide an adequate explanation for the variations in the lifetimes between the different alkali halides.

Recent studies in solid and liquid metals as well as in insulators suggest that positrons can be trapped in crystal defects where they can annihilate in a region of low electron density.[11-18] This is also borne out particularly in studies by Brandt and coworkers,[16-19] who investigated positron lifetimes in doped and plastically deformed alkali halide crystals and by Bertolaccini and Dupasquier,[20] who explained the above findings and phase dependences of positron lifetimes in such crystals in terms of a trapping model.

In a previous paper, Williams and Ache[7] have studied the radiation damage dependence of positron lifetimes in proton- or γ-irradiated sodium halide crystals. In the present investigation positron lifetimes and their relative intensities were measured in NaCl crystals which have been subjected to proton-, γ-, and X-ray irradiation or which have been doped with aluminum.

The observed positron lifetime spectra were decomposed into two components and the data obtained in this way show generally the same trend as previously reported. The better resolution of the timing system used in the present work and a more detailed study of the lifetimes as a function of the various experimental parameters revealed, in addition to the previously observed intensity variations, significant changes in the lifetimes depending on the history of the crystals.

In the following it is shown that the data can be adequately explained by using an approach similar to that of Brandt's vacancy annihilation center model. It was possible to calculate the positron capture rates and to assess the effective vacancy defect concentration. Furthermore, an attempt was made to interpret the observed flattening off or "saturation" effect of the lifetimes and intensities at relative low-vacancy concentrations.

Experimental Section

A. Sample Preparation. The procedure by which

the NaCl samples were prepared has been described previously in greater details.[7] All samples were single crystals of sodium chloride obtained from Harshaw Co. They were irradiated with the 30-MeV proton beam of the 60-in. BNL cyclotron. The ^{22}Na formed in the reaction ^{23}Na(p,pn)^{22}Na was practically homogeneously distributed in the crystal and provided the source of the positrons. The crystal size was about $4 \times 4 \times 20$ mm with ^{22}Na activities between 20 and 50 μCi. The proton doses were between $\sim 4.4 \times 10^{16}$ and 1.8×10^{17} protons. The radiation energy absorbed during the proton irradiation can be estimated from the proton dose to be approximately 10^2 to 10^3 eV per atom.

The proton dose rate varied considerably during the radiation of the various samples and thus the temperature of the samples.

B. Thermal Annealing. Crystal defects introduced during the initial proton bombardment were subsequently reduced by thermal annealing of the crystal, as shown in Table I. The disappearance of the point defects was monitored by spectrophotometric measurements using a Cary 14 spectrometer.

C. γ Irradiation. The annealed samples were subjected to ^{60}Co γ irradiation in the γ irradiation facilities of BNL. Dose rate was approximately 1.25×10^4 rads sec^{-1}. The irradiated samples were subsequently annealed as described above.

D. X-Ray Irradiations. The NaCl crystals were irradiated with 35-kV X-rays. The X-ray tube current was 30 mA and a Cu target was used. During the irradiation the NaCl samples were constantly rotated.

E. Uv Irradiations. Uv irradiations were carried out with a Pen-ray type quartz lamp (2537 Å), Model SCT 1, Fisher Scientific, 10 W.

F. Doping of the NaCl Crystals. A thin layer of Al

(6) L. Bussolati, A. Dupasquier, and L. Zappa, *Nuovo Cimento,* 52, 529 (1967).

(7) T. L. Williams and H. J. Ache, *J. Chem. Phys.,* 51, 3536 (1969).

(8) V. I. Gol'danskii and E. P. Prokop'ev, *Fiz. Tverd, Tela,* 6, 3301 (1968).

(9) E. P. Prokop'ev, *ibid.,* 8, 464 (1966).

(10) V. I. Gol'danskii and E. P. Prokop'ev, *ibid.,* 8, 515 (1965).

(11) (a) I. K. Mackenzie, T. L. Khoo, A. B. McDonald, and B. T. A. McKee, *Phys. Rev. Lett.,* 19, 946 (1967). (b) W. Brandt, H. F. Waung, and P. Levy, in Proceedings of the International Symposium in Polar Centers in Alkali Halides, Rome, 1968, unpublished work.

(12) B. Bergersen and M. T. Scott, *Solid State Commun.,* 7, 1208 (1969).

(13) D. C. Connors and R. N. West, *Phys. Lett. A,* 30, 24 (1969).

(14) C. H. Hodges, *Phys. Rev. Lett.,* 25, 284 (1970).

(15) P. Hautojarvi, A. Tamminen, and P. Fauho, *ibid.,* 24, 459 (1970).

(16) W. Brandt and H. F. Waung, *Phys. Lett. A,* 27, 700 (1968).

(17) W. Brandt, G. Coussot and R. Paulin, *ibid.,* in press.

(18) W. Brandt in Positron Annihilation, Proceedings of a Conference at Wayne State University, A. T. Stewart and L. O. Roellig, Ed., Academic Press, New York, 1967, p 155 ff.

(19) W. Brandt and H. F. Waung, in press.

(20) M. Bertolaccini and A. Dupasquier, *Phys. Rev. B,* 1, 2896 (1970).

Table I: Positron Lifetimes and Intensities Observed after Thermal Annealing of Proton- and γ-Irradiated NaCl Samples

Treatment	$\lambda_A \times 10^9$, sec^{-1}	$\lambda_B \times 10^9$, sec^{-1}	I_B, %
Proton irradiation (30 MeV) 1.4 × 10^{16}	3.12 ± 0.25	1.48 ± 0.12	27.0 × 2.0
Thermal annealing 4 hr at 400°	2.83 ± 0.22	1.46 ± 0.12	18.8 ± 1.0
γ-Irradiation ^{60}Co 500 Mrads	3.28 ± 0.25	1.35 ± 0.11	31.7 ± 2.0
Thermal annealing			
2 hr at 115°	3.17 ± 0.23	1.37 ± 0.11	28.6 ± 1.8
2 hr at 160°	2.94 ± 0.23	1.30 ± 0.11	21.1 ± 1.7
2 hr at 205°	2.86 ± 0.23	1.29 ± 0.12	15.0 ± 1.0
2 hr at 250°	2.65 ± 0.22	1.14 ± 0.11	9.8 ± 1.0
4 hr at 400°	2.40 ± 0.22	0.87 ± 0.10	4.8 ± 1.0

metal was deposited on NaCl single crystals, containing ^{22}Na, and heated for several hours (*in vacuo*) at 400°. After this treatment the crystals showed a strong absorption in the uv region. Analysis of typical samples indicated aluminum concentrations in the ppm range.

G. Lifetime Measurements. The lifetime measurements followed the standard procedure using delayed coincidence techniques as previously described.[21] By applying constant fraction timing descrimination, an optimum resolving time, as characterized by the full-width half-maximum of the prompt spectrum of a ^{60}Co source, of 0.35 nsec was achieved. The data obtained in the delayed coincidence spectrum were fitted by the method of least squares to determine the annihilation lifetimes. The calculations were performed on an IBM 360/50-65 computer, using computational methods developed by Cumming[22] or Tao.[23] The intensities were calculated by normalizing the areas under each of the components to that of the entire distribution. The intensity is then given by the ratio of the area of each component to that of the total area under the distribution curve. The errors stated in the tables are conservative estimates; errors computed from the scatter of the results are usually much smaller.

Results and Discussion

The present investigation consisted mainly of four parts. The first step was the preparation of NaCl crystals which could be used as standards in the following studies. As described in details in the experimental part, samples were prepared by proton irradiation of NaCl single crystals. This method introduced the ^{22}Na activity rather homogeneously into the crystal. Hence, measurements were more representative of the bulk properties than surface effects as would be the case in samples where the ^{22}Na source has been sandwiched between two single NaCl crystals or in polycrystalline samples. However, the high-intensity proton bombardment caused simultaneously the appearance of

several different types of defects and carefully controlled thermal annealing was necessary to reduce the number of defects. The disappearance of the radiation-induced defects, which was followed by spectrometric measurements of the absorption in the uv region (V-band absorption) and in the visible region (F-band absorption), was accompanied by an increase in the two lifetimes and a reduction of the intensity of the second long-lived component, as listed in Table I.

Standards prepared in this way showed no absorption in the uv, visible, or ir range and were used to study the influence of defects introduced by various types of radiation and radiation doses, etc., on the positron annihilation process in NaCl crystals. It seemed reasonable to assume that these crystals contained only a minimum of defect concentration.

In Figures 1 and 2 the observed positron lifetimes and corresponding intensities are plotted to be directly proportional to exposure time, which can be assumed to be directly proportional to the absorbed radiation dose. From these it can be seen that the lifetimes of both components decreased with the absorbed dose from initially $\tau_A = 0.355$ nsec and $\tau_B = 0.701$ nsec to a "saturation" value of about $\tau_A \simeq 0.29$ nsec and $\tau_B \simeq 0.58$ nsec after 10 hr of irradiation. This change in the lifetimes was accompanied by an increase in the intensity of the long-lived component from initially $I_B = 18\%$ to approximately $I_B = 40\%$. Prolonged irradiation of up to 66 hr of exposure did not cause any additional variations in the observed lifetimes or intensities.

Similar results were obtained when the NaCl crystals were exposed to moderate γ-ray doses ranging from 565 rads to 10 Mrads. (Table II). Both lifetimes decreased as a function of the absorbed dose to $\tau_A = 0.29$ nsec and $\tau_B = 0.57$ nsec, again accompanied by an increase of I_B, the intensity of the long-lived component, to about 35%. In contrast to the results observed with X-ray irradiation or moderate γ doses, higher γ doses of 100-500 Mrads reversed the trend in the lifetime changes of the second long-lived component seen in the former cases and τ_B assumed larger values of about 0.74 nsec without any noticeable changes in the corresponding intensity I_B or in the lifetime of the short-lived component τ_A which remained fairly constant at $I_B \simeq 31\%$ or $\tau_A = 0.29$ nsec. In the fourth part NaCl samples were doped with aluminum. This was accomplished by depositing a layer of aluminum on the crystal and heating it (*in vacuo*) for several hours at 400°. Again there was the familiar phenomenon of a rapid increase in I_B from initially 9.8% to about 39% and decrease in τ_A and τ_B from $\tau_A = 0.29$ nsec and $\tau_B = 0.57$ nsec.

Although these samples were treated in quite differ-

(21) T. L. Williams and H. J. Ache, *J. Chem. Phys.*, **50**, 4493 (1969).

(22) J. B. Cumming, BNL Report 6470.

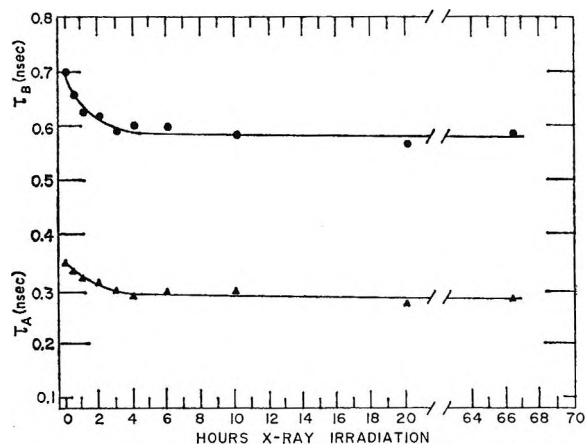(23) S. J. Tao, *IEEE Trans. Nucl. Sci.*, 175 (1968).

Figure 1. Positron lifetimes in X-ray-irradiated NaCl crystals as a function of irradiation time; 35-kV X-rays, 30-mA X-ray tube current.
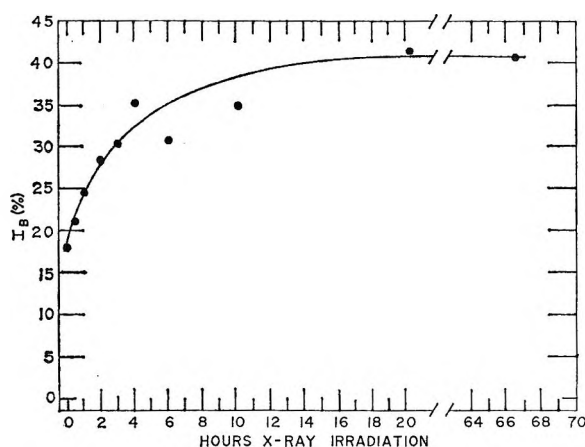

Figure 2. Intensities of the long-lived component observed in the lifetime spectra of X-irradiated NaCl crystals as a function of irradiation time. (Same experimental conditions as in Figure 1.)

Table II: Positron Lifetimes and Intensities in NaCl Crystals Following γ Irradiation

γ-Ray dose	$\lambda_A \times 10^9$, sec^{-1}	$\lambda_B \times 10^9$, sec^{-1}	I_B, %
None	2.97 ± 0.22	1.54 ± 0.13	16.6 ± 1.5
565 rads[a]	3.47 ± 0.25	1.73 ± 0.15	31.0 ± 2.5
100 Krads[b]	3.58 ± 0.30	1.81 ± 0.16	33.7 ± 2.6
233 Krads	3.31 ± 0.24	1.77 ± 0.15	31.3 ± 2.5
1 Mrads	3.24 ± 0.22	1.67 ± 0.13	30.0 ± 2.0
10 Mrads	3.46 ± 0.25	1.67 ± 0.13	31.2 ± 2.0
100 Mrads	3.28 ± 0.22	1.35 ± 0.10	31.7 ± 1.5

[a] Dose rate, 300 rads/hr. [b] Dose rate, 1 Mrads/hr.

ent ways, they all seem to show one common feature: the change of the lifetimes to shorter values and an increase in the intensity of the long-lived component reaching the same limiting values following the treatments specified above. This suggests that the same types of defects or mechanisms are responsible for the positron annihilation process in each individual case.

X-Rays and γ rays are known to produce a great variety of defects such as F, V, and other centers and equilibria between these different individual species and more complex centers seem to exist.

In the present study, however, samples which were exposed to X-rays or to low to moderate γ doses and which initially showed the presence of V and F centers, as indicated by the strong absorption in the corresponding uv or visible region, displayed practically the same lifetimes and intensities before and after optical bleaching of the F centers. From that one would conclude that the positron annihilation is mainly deter-

mined by the presence of species which are related to those that show V-band absorption. Further and perhaps even more conclusive support for the above contention can be derived from the fact that in the case of the aluminum doping of the NaCl crystals, where preferentially cation vacancies are being formed accompanied by intense absorption in the uv region (V band), the same trends and limiting values for lifetimes and intensities were obtained.

Since V-band absorption is a strong indication of the presence of vacancies, especially cation vacancies, we would like to follow Brandt's model[18] which assumes interactions between positive ion vacancies and positrons. A positive vacancy is negatively charged and should attract positrons while repulsing electrons. Because of the reduced likelihood of interacting with an electron at such a site, the lifetime of any positron reaching such a site should be extended. If one considers only one type of defect the physical situation can then be described as follows. Positrons after having slowed down annihilate in the perfect crystal at a rate λ_0 or are captured by the positive cation vacancies at a rate K, which is proportional to the defect density. The trapped positron can then either annihilate at a rate λ_1 or escape from these vacancies at a rate γ. With the condition that no positrons are initially trapped this model can be described by the following kinetic equations. By assuming first-order kinetics the change per unit of time of the number of positrons (N_n) populating the two postulated states is given by the following set of equations

$$\frac{dN}{dt} = -(\lambda_0 + K)N + \lambda N_1 \qquad (1)$$

$$\frac{dN_1}{dt} = -(\lambda_1 + \gamma)N_1 + KN \qquad (2)$$

where N = number of free positrons, N_1 = number of positrons trapped in positive ion vacancies, λ_0 = annihilation rate of positrons in perfect crystal, λ_1 = annihilation rate of positrons trapped in positive ion vacancies, K = capture rate of positrons in positive ion

vacancies, and γ = escape rate of positrons from positive ion vacancies. From the solution of the differential equations two observable annihilation rates are obtained

$$\lambda_{A,B} = \frac{1}{2}\{\lambda_0 + \lambda_1 + K + \gamma \pm$$
$$\sqrt{(\lambda_0 + K - \lambda_1 - \gamma)^2 + 4\gamma K}\} \quad (3)$$

In the following, two special cases will be discussed. In the first one the assumption is made that positrons are trapped in vacancies for times long compared with λ_1, i.e., escape of trapped positrons can be neglected: $\gamma \rightarrow 0$. With this simplification two observable annihilation rates result from eq 3

$$\lambda_A = \lambda_0 + K \quad (4)$$

and

$$\lambda_B = \lambda_1 \quad (5)$$

The fact, however, that in the present study both lifetimes assume shorter values with increasing radiation defects in the crystals shows that this simple model without invoking some modifications cannot adequately describe the phenomena observed in these systems. The second case takes into account the possible escape of positrons from the vacancies. With the assumption that at relatively low defect concentration K and γ are small compared with λ_1 or λ_0, eq 3 can be reduced to

$$\lambda_A = \lambda_0 + K \quad (6)$$
$$\lambda_B = \lambda_1 + \gamma \quad (7)$$

In deriving eq 1 and 2 the capture rate K has been assumed to be a linear function of the number of vacancies (n_v) available for positron trapping (see also eq 12) and λ_A should increase accordingly with the vacancy concentration.

The escape rate, γ, will also depend on the number of crystal defects, if one understands the positron escape as an interaction of the cation vacancy, in which the positron is trapped with another defect species, most likely a hole or a cation. As a result of this interaction a new cation vacancy defect bound state, which might be energetically more favorable than the bound state of positron and cation, can be formed. The e^+-cation-vacancy bond is broken and the positron reenters the pool of free positrons.

The lifetime spectrum (two-quantum decay rate) can be described by the following expression

$$R_{2\gamma} = I_A\lambda_Ae^{-\lambda_At} + I_B\lambda_Be^{-\lambda_Bt} \quad (8)$$

where the intensities are given by

$$I_A = \frac{\lambda_0 - \lambda_B}{\lambda_A - \lambda_B} \quad (9)$$

and

$$I_B = \frac{\lambda_A - \lambda_0}{\lambda_A - \lambda_B} \quad (10)$$

or

$$K = I_B(\lambda_A - \lambda_B) \quad (11)$$

From eq 11, K, the capture rate at which positrons are trapped by the vacancies at a given defect concentration can be determined directly from the experiment.
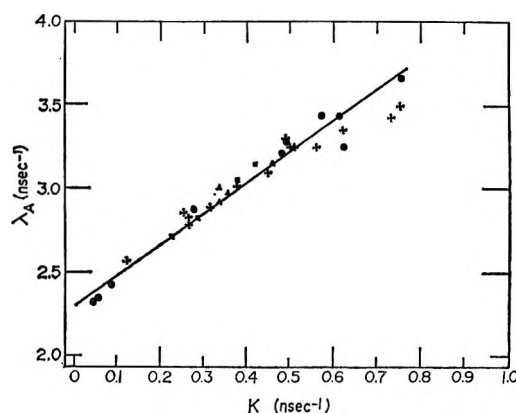

Figure 3. Observed annihilation rate λ_A plotted as a function of the capture rate K; +, X-ray-irradiated NaCl crystals; ●, γ-irradiated or Al-doped NaCl crystals; ○, thermally annealed NaCl crystals; ▲, thermally annealed samples at low temperature ($-196°$ to $25°$); ■, polycrystalline NaCl samples at higher temperatures (taken from ref 20).

The annihilation rate, λ_0, of positrons in a perfect crystal can be obtained from the extrapolation of λ_A to zero defect concentration, $K \rightarrow 0$; this has been done in Figure 3 where λ_A has been plotted as a function of K, which was computed from eq 11. This figure includes data derived from a number of samples in which defects have been introduced by various methods, such as X-ray irradiation, γ-ray irradiation (low and moderate doses), doping with aluminum, or just having an equilibrium defect concentration at a given temperature as shown by the data of Wang and Ache,[24] who measured positron lifetimes and intensities in NaCl crystals at low temperatures, and Bertolaccini and Dupasquier,[20] who did similar measurements at higher temperatures. They all fall on a straight line with an intercept of $\lambda_A = \lambda_0 = 2.34$ nsec^{-1} at $K = 0$ or $\tau_0 = 0.43$ nsec. λ_1 and γ cannot be derived in this way without additional assumptions, the number of the unknowns being greater than the number of available independent equations. However, an estimate can be made by assuming that the obtained experimental values for λ_B at a corresponding intensity I_B close to zero are representative of the rate λ_1. From Table III one obtains $\lambda_B = 0.91 \times 10^9$ sec^{-1} and $\lambda_1 = 1.7 \times 10^9$ sec^{-1}, from which a limiting value for $\gamma \simeq 0.8 \times 10^8$ sec^{-1} can be derived. These results imply that capture as well as escape rate are of the same order of magnitude

(24) C. M. Wang and H. J. Ache, unpublished results.

$K = 0 - 7.6 \times 10^8 \text{ sec}^{-1}$; $\quad \gamma = 0 - 8 \times 10^8 \text{ sec}^{-1}$

Although the overall changes in $\lambda_A - \lambda_B$ and I_B as a function of the defect density can be accounted for by this simple trapping model, one other phenomenon observed in the present study requires additional explanations: the limiting values which λ_A, λ_B, and I_B approach with increasing radiation dose or doping. From

Table III: Typical Lifetimes, Annihilation Rates, and Intensities Observed in Irradiated, Doped, and Annealed NaCl Crystals

Sample	Treatment	$\lambda_A \times 10^9$, sec^{-1}	$\lambda_B \times 10^9$, sec^{-1}	I_B, %
	Thermal Annealing			
I	4 hr at 400°	2.87 ± 0.28	1.43 ± 0.14	17.9 ± 1.5
III	4 hr at 400°	2.40 ± 0.25	1.01 ± 0.11	3.8 ± 1.0
VII	4 hr at 400°	2.38 ± 0.25	0.92 ± 0.11	3.0 ± 1.0
	Doping with Al Metal			
V	18 hr at 345°	3.13 ± 0.26	1.71 ± 0.12	28.3 ± 2.0
	36 hr at 345°	3.68 ± 0.24	1.80 ± 0.14	39.6 ± 3.2
	72 hr at 345°	3.39 ± 0.25	1.75 ± 0.25	33.0 ± 2.5

eq 6, 7, and 11, it follows immediately that the common cause for that phenomenon must be the fact that K (and γ) assumed saturation values. The capture rate K might be assessed by the following approach[19] which is based on a model of weak interaction between positrons and lattice in which case the following expression is derived for K

$$K = n_v V_+ \sigma_v \rho \qquad (12)$$

ρ = reciprocal unit cell volume; n_v = defect concentration; v_+ = velocity of free positrons; σ_v = positron capture cross section of the vacancies $\simeq 4 \times 10^{-14}$ cm²). At room temperature $v_t \sigma_v$ assumes a value of about 5×10^{-7} cm³ sec^{-1}.

From eq 12 a maximal vacancy fraction of about 2.6 $\times 10^{-7}$ is derived, which appears to be too small to represent the total number of positive ion vacancies expected to be present under the given experimental conditions. It might therefore be more adequate to consider them as the fraction of vacancies capable of trapping the positrons most likely free cation vacancies.

The observed "flattening off or saturation effect" of the positron lifetimes and intensities might then be understood by considering the thermodynamical equilibria between the free vacancies and other crystal defects such as dislocations, etc., which can act as sources and as traps for vacancies and which may preserve certain equilibrium concentrations.[25]

It seems that after a certain concentration of vacancies which can act as positron traps is reached, they may enter a more complex relationship with other defect species produced by the same process, i.e., radiolysis or doping. The overall result is that a limited number of effective positron traps is reached. This leads to the observed "saturation" values for λ_A, λ_B, and I_B.

One other observation deserves attention; the increase in the lifetime of the long-lived component at high γ or proton doses. To explain this trend it seems reasonable to assume that under these experimental conditions the damage done to the crystal is extensive enough to change the mechanism of the positron annihilation process responsible for the presence of the long-lived component. Optical spectra reveal that in this case F-centers outnumber the (effective) vacancy centers by several orders of magnitude. Consequently F-centers or aggregates of such defects could be quite large in such crystals, and spatial and perhaps energetic long-lived positronium-like positron–electron-bound state or vacancy A' center. This is supported by angular correlation measurements in additively colored KCl which have revealed the presence of a narrow component,[17,26] as it would be expected from the annihilation of positrons in vacancy A' centers.[27]

Summarizing, it can be said that the positron annihilation process can be adequately described by a model in which positrons are being trapped by positive ion vacancies from which they may annihilate as such or escape as free positrons.

It is hoped that the present study can contribute to our understanding of the interactions between positrons and crystal defects in order to develop positron annihilation techniques as a chemical probe for the identification and measurement of radiation-induced defects.

(25) A. B. Lidiard and K. Tharmalingano, *Discuss. Faraday Soc.*, 28, 64 (1959).

(26) D. Herlach and F. Heinrich, *Phys. Lett.*, 31A, 47 (1970).

(27) A. Dupasquier, *Lett. Nuovo Cimento*, 4, 13 (1970).

Oxidation Kinetics of 2-Mercaptoethylamine Hydrochloride by

Ferricyanide Ion in Acid Medium

by R. C. Kapoor,* R. K. Chohan, and B. P. Sinha

Department of Chemistry, University of Jodhpur, Jodhpur, Rajasthan, India   (*Received November 2, 1970*)

Publication costs borne completely by The Journal of Physical Chemistry

The kinetics of oxidation of 2-mercaptoethylamine hydrochloride by ferricyanide ion in aqueous hydrochloric acid medium are described. The two react in 1:1 molar ratio as the substrate is shown to be oxidized to its corresponding disulfide. The order is unity both in oxidant and the thiol hydrochloride. Ferrocyanide acts as an autocatalyst. The rate decreases on increasing initial concentration of ferricyanide and hydrogen ion concentration and is accelerated on increasing dielectric constant and temperature. Addition of disulfide or neutral electrolytes produces no effect. A reaction scheme is postulated to account for the observations.

Introduction

The kinetics of oxidation of compounds containing a sulfhydryl group has, of late, received considerable attention. In a number of such cases the oxidation scheme has been worked out by McAuley, *et al.*,[1-4] using a variety of oxidants. In a similar publication[5,6] from this laboratory, the oxidation kinetics of thioglycolic and thiomalic acids by ferricyanide ion in acid and alkaline media, respectively, were described. In furtherance of the work, mechanistic studies on the oxidation of 2-mercaptoethylamine hydrochloride (hereafter referred to as thiol hydrochloride) were carried out using the same oxidant. Similar studies on this compound have been reported using oxidants[7,8] other than ferricyanide ion.

Experimental Section

The solution of 2-mercaptoethylamine hydrochloride (assay 98% supplied by Evans Chemetics Inc., New York, N. Y.) was prepared by an approximate weighing of the sample and it was subsequently diluted in air-free doubly distilled water. It was stored in nitrogen atmosphere. Known volumes were withdrawn with the help of a calibrated hypodermic syringe and standardized with a standard solution of iodine. E. Merck analytical reagent grade potassium ferricyanide was used. The solutions were prepared freshly as needed. The disulfide, *i.e.*, 2-2'-diaminoethyl disulfide dihydrochloride, was obtained by oxidizing the thiol hydrochloride with dimethyl sulfoxide[9] and also by air in an alkaline medium.[10] The solution of 3,3'-dimethylnaphthidine disulfonic acid (B.D.H., L.R.) used as an indicator was prepared in dilute ammonia. All other reagents used throughout the investigations were analytical grade.

Absorbance spectra were obtained with the aid of a Hilger UVispeck spectrophotometer Model H700-8 fitted with a thermostatic arrangement. The polaro-

grams were taken with a Toshniwal manual polarograph.

Constituents of the reaction mixture, except for the thiol hydrochloride solution, were taken in a Jena flask coated black on the outside to preclude any photochemical effect. The solution of thiol hydrochloride was taken in a separate vessel. Both were kept immersed in a thermostat regulated at the desired temperature and were flushed with purified nitrogen. When the reactants had attained the temperature of the bath, the requisite quantity of thiol hydrochloride solution was withdrawn with the help of a syringe and injected into the reaction vessel. Aliquots were withdrawn at different intervals of time and added to a quenching mixture containing 10 ml of 4 N H_2SO_4 and 2 ml of 50% ferrous ammonium sulfate solution. Since the reaction practically stops[11] at this high acid concentration, the kinetics could be followed conveniently by estimating ferrocyanide volumetrically. This was done by titrating against a standard solution of zinc sulfate using 3,3'-dimethylnaphthidine disulfonic acid as an indicator. From the volume of zinc sulfate solution consumed, the concentration of ferrocyanide was calculated from the following relationship.

(1) J. Hill and A. McAuley, *J. Chem. Soc., A*, 156 (1968).

(2) W. F. Pickering and A. McAuley, *ibid.*, 1173 (1968).

(3) J. Hill and A. McAuley, *ibid.*, 2405 (1968).

(4) U. D. Gomwalk and A. McAuley, *ibid.*, 2948 (1968).

(5) R. C. Kapoor, O. P. Kachhwaha, and B. P. Sinha, *J. Phys. Chem.*, **73**, 1627 (1969).

(6) O. P. Kachhwaha, B. P. Sinha, and R. C. Kapoor, *Indian J. Chem.*, **8**, 806 (1970).

(7) W. O. Foye, A. M. Hebb, and J. Michels, *J. Pharm. Sci.*, **56**, 292 (1967).

(8) R. E. Basford and F. M. Heunnekens, *J. Amer. Chem. Soc.*, **77**, 3873 (1955).

(9) W. W. Epstein and F. W. Sweat, *Chem. Rev.*, **67**, 247 (1967).

(10) M. Asthana, R. C. Kapoor, and H. L. Nigam, *Electrochim. Acta*, **11**, 1587 (1966).

(11) A. I. Vogel, "Quantitative Inorganic Analysis," Longmans Green and Co., New York, N. Y., 1962, p 402.

$$3Zn^{2+} + 2K_4[Fe(CN)_6] \longrightarrow K_2Zn_3[Fe(CN)_6]_2 + 6K^+$$
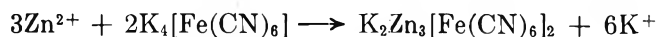
The value of ferrocyanide so obtained when subtracted from the initial concentration of ferricyanide taken gives the concentration of the latter left at that instant of time.

Stoichiometry. The stoichiometry of the reaction could be confirmed by polarographic as well as other analytical methods. The former method also led to the characterization of the final product. The thiol hydrochloride gives an anodic wave while its disulfide gives a cathodic reduction wave.[12] First, a polarogram of thiol hydrochloride solution of known concentration was taken (Figure 1a) and then of a reaction mixture described in the figure which had been allowed sufficient time under nitrogen atmosphere. The polarogram thus obtained (Figure 1b) practically coincided with the former. Similarly, a polarogram of the known concentration of disulfide was compared with that of the reaction mixture (Figure 1c and d). The two waves nearly coincided. The polarographic circuit used was as described by Lingane and Kolthoff.[13] The capillary

Figure 2. Absorption spectra of (a) 2-mercaptoethylamine hydrochloride (1×10^{-2} M), (b) 2,2-diaminoethyl disulfide dihydrochloride (5×10^{-3} M) to be compared with, (c) the disulfide produced in the reaction mixture.

characteristics were $m = 2.070$ mg/sec and $t = 3.78$ sec with an open circuit at a mercury column of 40 cm. These results point to a stoichiometry of 1:1 and also show that the final product of oxidation is the corresponding disulfide.

Thiol hydrochloride was found to have a λ_{max} at 228 nm while its disulfide had one at 245 nm (Figure 2a and b). Spectra of a reaction mixture kept for a sufficient length of time gave a figure similar to 2b with almost the same value of λ_{max}, thus showing that the final product is the disulfide. From an evaluation of concentrations from optical density measurements it was again found that the stoichiometry was 1:1. Thus the overall reaction is

$$2RSH + 2Fe(CN)_6{}^{3-} \longrightarrow$$
$$RSSR + 2Fe(CN)_6{}^{4-} + 2H^+$$
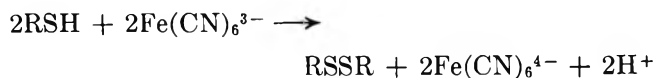
where R denotes the remaining part of the molecule.

Results

The dissociation constant of (–SH) group in 2-mer-

(12) W. Stricks, J. K. Frischmann, and R. G. Mueller, *J. Electrochem. Soc.*, 109, 518 (1962).

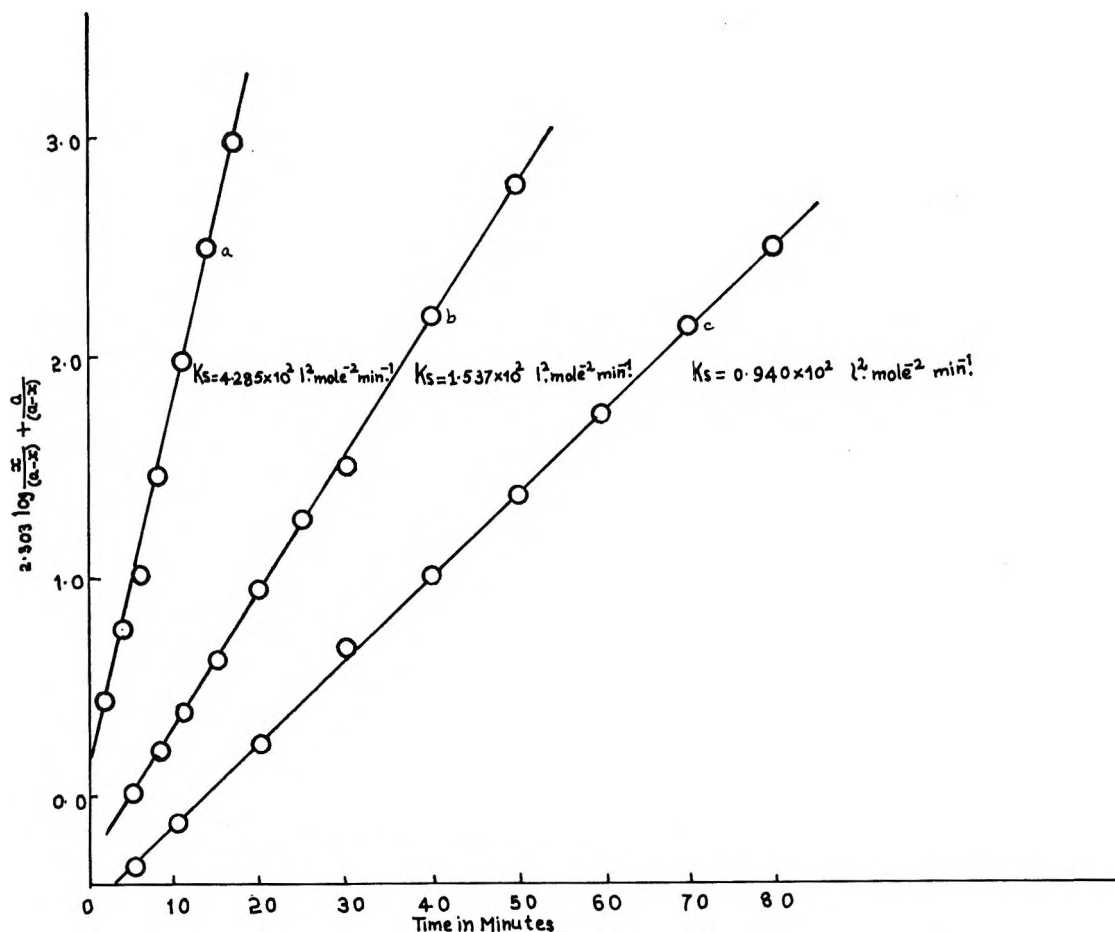(13) J. J. Lingane and I. M. Kolthoff, *J. Amer. Chem. Soc.*, 61, 825 (1939).

Figure 3. Third-order plot for three different runs (temperature 35°; [K$_3$Fe(CN)$_6$], 2 × 10^{-2} M, [thiol hydrochloride], 2 × 10^{-2} M);
(a) [HCl], 1.0 × 10^{-2} M, [KCl], 15.0 × 10^{-2} M; (b) [HCl], 5.0 × 10^{-2} M, [KCl], 11.0 × 10^{-2} M; (c) [HCl], 10.0 × 10^{-2} M,
[KCl], 6.0 × 10^{-2} M.

captoethylamine hydrochloride as determined potentiometrically was found to be 1.995 × 10^{-11} at 35°.

The reaction was found to be a case of autocatalysis due to ferrocyanide. The velocity coefficients were calculated with the help of the formula obtained on solving the differential equation

$$\mathrm{d}x/\mathrm{d}t = k(a - x)^2 x$$

where a denotes the initial concentrations of ferricyanide and thiol hydrochloride and x stands both for the concentrations of ferricyanide and thiol hydrochloride consumed and also that of the autocatalyst ferrocyanide generated in the system at that instant of time. The equation on being subjected to definite integration within limits t_1, t_2, and x_1, x_2 gave the solution

$$k = \frac{1}{(t_2 - t_1)} \left[\frac{2.303}{a^2} \log \frac{x_2(a - x_1)}{x(a - x_2)} + \frac{1}{a} \left\{ \frac{1}{a - x_2} - \frac{1}{a - x_1} \right\} \right]$$

The applicability of the above formula is demonstrated in a typical run described in Table I. Further, in the event of applicability of this equation, a plot of

$$2.303 \left\{ \log \frac{x}{(a - x)} + \frac{a}{(a - x)} \right\}$$

vs. time should given a straight line with slope equal to ka.[2] This was found as expected (Figure 3). The two procedures give very nearly the same value of rate constant. The order of the reaction was also confirmed from application of the vant Hoff differential method. Initial rates $(-\mathrm{d}C/\mathrm{d}t)$ corresponding to different initial concentrations C were determined and plotted in the manner as shown in the Figure 4. A straight line with a slope nearly equal to 2 was obtained. This demonstrates that initially, when the concentration of ferrocyanide is almost negligible, the total order between the reactants is 2. That the order in ferrocyanide is unity as presumed earlier could be shown by measuring $(-\mathrm{d}C/\mathrm{d}t)$ corresponding to different values of C in a single run. Now when log $(-\mathrm{d}C/\mathrm{d}t)/[\mathrm{Fe(CN)}_6{}^{4-}]$ was plotted against log C (Figure 5), a straight line was obtained which has also a slope of nearly 2. The order in ferricyanide was determined by isolating ferricyanide and keeping its concentration fairly low in order to minimize the effect of ferrocyanide. A plot of log $(a - x)$ against time yielded a straight line for about

Table I

$[K_3Fe(CN)_6] = 2.0 \times 10^{-2}\,M$ $[HCl] = 1.0 \times 10^{-2}\,M$
$[HS(CH_2)_2NH_2 \cdot HCl] = 2.0 \times 10^{-2}\,M$ Temp, 35°
$[KCl] = 15.0 \times 10^{-2}\,M$ $I = 0.3\,M$ $t_1 = 2$ min

Time, min	Volume of 0.005 M ZnSO$_4$ reqd., ml	Volume of 0.02 M ferro-cyanide products x, ml	Volume of 0.02 M ferri-cyanide left $(a - x)$, ml	$k_{obsd} \times 10^3$,^{a} min^{-1}
2	8.4	1.4	3.6	
4	9.9	1.65	3.35	6.80
6	11.5	1.92	3.08	7.00
8	12.9	2.15	2.85	6.85
11	15.0	2.5	2.50	6.91
14	16.8	2.8	2.20	6.89
17	18.3	3.05	1.95	6.84

Av $= 6.88 \times 10^{-3}$ min^{-1}

^{a} Standard rate constant $k_s = 6.88 \times 10^{-3} \times (5/2 \times 10^{-2})^2$, where numerator in parentheses denotes the volume of reaction mixture withdrawn for estimation and denominator the concentration as required by factor $(v/s)^2$ for conversion of a pseudo-first-order rate constant to a third-order rate constant. Hence, $k_s = 4.30 \times 10^2\,l.^2\,mol^{-2}\,min^{-1}$; k_s (graphically) $= 4.28 \times 10^2\,l.^2\,mol^{-2}\,min^{-2}$ (all rate constants recorded subsequently are standard rate constant unless otherwise stated).

Figure 5. Relationship between log $(-dC/dt)/[Fe(CN)_6{}^{4-}]$ and log C for a single run (temperature, 35°; $[K_3Fe(CN)_6]$, 2.0 $\times 10^{-2}\,M$; [thiol hydrochloride], 2.0 $\times 10^{-2}\,M$; [HCl], 1.0 $\times 10^{-2}\,M$; [KCl], 15.0 $\times 10^{-2}\,M$; $I = 0.3$).
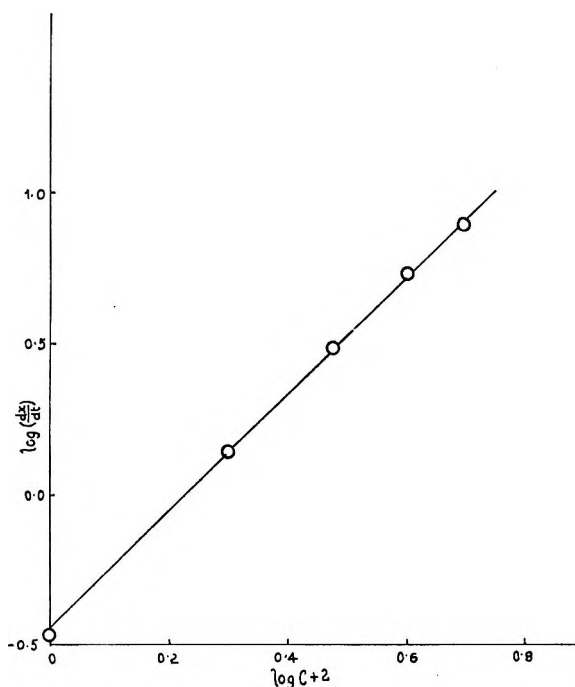
Figure 4. Relationship between initial rate and corresponding different initial concentrations of reactants (temperature, 35°; [HCl], 1.0 $\times 10^{-2}\,M$; $I = 0.4$).

Table II

$[K_3Fe(CN)_6] = 1.0 \times 10^{-2}\,M$ Temp, 35°
$[H^+] = 1.0\,M$ $I = 1.40\,M$

[HS(CH$_2$)$_2$NH$_2$HCl] $\times 10^2\,M$, C	Pseudo-first-order constant, $k_1 \times 10^2$ min^{-1}	$10k_1/C$
8.0	8.13	10.16
10.0	10.07	10.07
12.0	12.05	10.04
14.0	14.05	10.03
17.0	17.19	10.11

30% of the reaction. Thus the order in oxidant is unity. The order in thiol hydrochloride is also unity as could be concluded by the near constant values of k_1/C recorded in Table II.

The rate was also found to depend on the initial concentration of ferricyanide. The increase in the con-
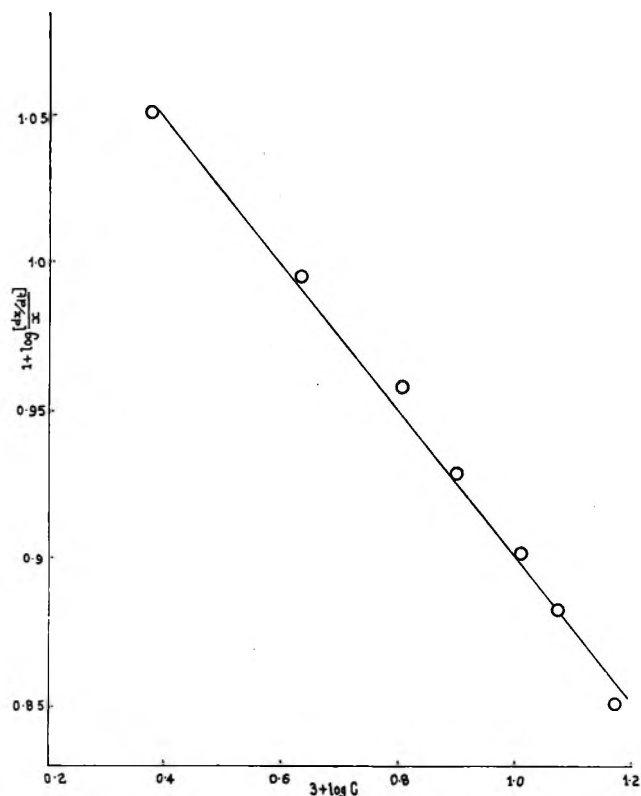
centration led to the retardation in rate as shown in Table III. There was, however, no effect of variation of initial concentration of thiol hydrochloride when all other parameters were maintained constant.

The effect of hydrogen ion was studied by following runs at different concentrations of hydrochloric acid. The ionic strength was maintained constant with potassium chloride. The results are recorded in Table IV. The rate was not found to be any simple function of hydrogen ion concentration.

The effect of ferrocyanide was also investigated by adding externally different concentrations of the compound. The rate constants were calculated by making use of the solution of differential equation, $dx/dt =$
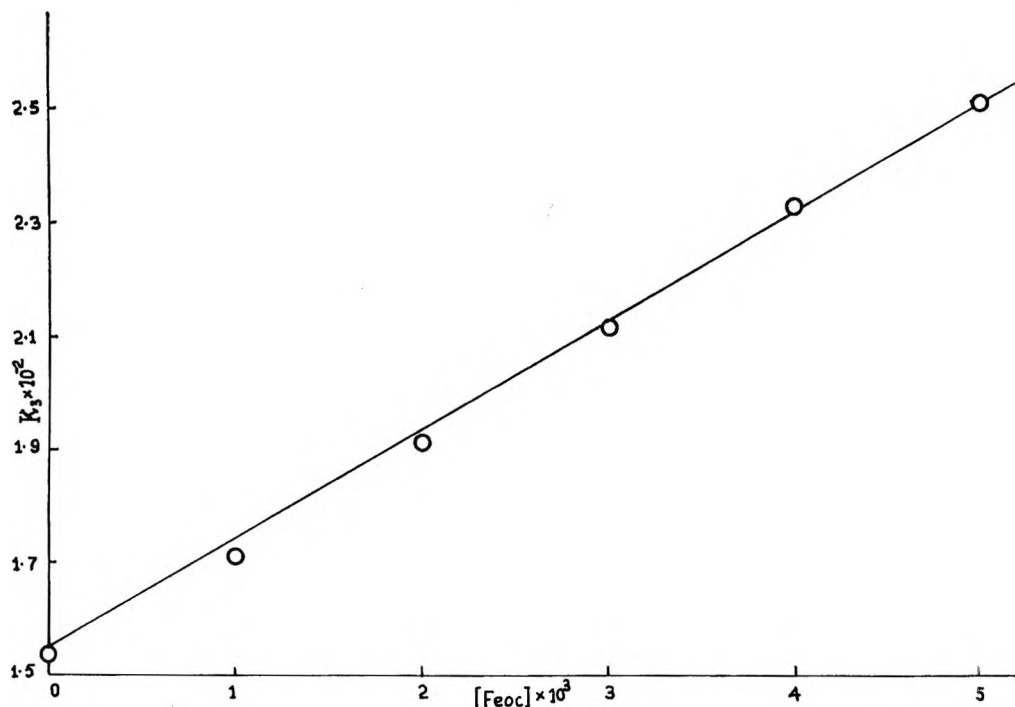
Figure 6. Dependence of the rate on ferrocyanide concentration (temperature, 35°; [$K_3Fe(CN)_6$], $2.0 \times 10^{-2} M$; [thiol hydrochloride], $2.0 \times 10^{-2} M$; [HCl], $5.0 \times 10^{-2} M$; $I = 0.3$).

Table III

[HS(CH$_2$)$_2$NH$_2 \cdot$HCl] $= 10.0 \times 10^{-2} M$ Temp, 35°
[HCl] $= 1.0 M$ $I = 1.2 M$

[$K_3Fe(CN)_6$] $\times 10^3 M$	Pseudo-first-order rate constant, $k_1 \times 10^2$, min^{-1}
10.0	10.07
8.0	11.05
6.0	12.74
5.0	13.90
4.0	15.74

Table IV

[$K_3Fe(CN)_6$] $= 2.0 \times 10^{-2} M$ Temp, 35°
[HS(CH$_2$)$_2$NH$_2 \cdot$HCl] $= 2.0 \times 10^{-2} M$ $I = 0.3 M$

[H$^+$] $\times 10^2$ mol l.$^{-1}$	Third-order rate constant, $k_3 \times 10^{-2}$, l.^{2} mol^{-2} min^{-1}
5.0	1.537
4.0	1.955
2.5	2.205
2.0	2.754
1.5	3.28
1.0	4.28

$k(a - x)^2(b + x)$ where b denotes the concentration of externally added ferrocyanide. The integration was carried out with the usual limits and the rate constants were evaluated graphically. The rate is found to in-

crease linearly with ferrocyanide concentration as shown in Figure 6.

Experiments were also carried out in the presence of potassium cyanide. The addition reduces the value of k_3 but it becomes practically independent of cyanide concentration above $6.0 \times 10^{-3} M$. These are recorded in Table V.

Table V

[$K_3Fe(CN)_6$] $= 2.0 \times 10^{-2} M$ Temp, 35°
[HS(CH$_2$)$_2$NH$_2 \cdot$HCl] $= 2.0 \times 10^{-2} M$ $I = 0.3 M$
[HCl] $= 5.0 \times 10^{-2} M$

[KCN] $\times 10^3 M$	Third-order rate constant, $k_3 \times 10^{-2}$, l.^{2} mol^{-1} min^{-1}
0.0	1.537
5.0	1.430
6.0	1.313
8.0	1.306
10.0	1.299
20.0	1.290

This observation is somewhat similar to that made by Kolthoff, et al.,[14] in their studies on the oxidation of n-octyl mercaptan by ferricyanide ion. The effect of variation of dielectric constant was also investigated. Doubly distilled ethanol was used for the purpose. A

(14) I. M. Kolthoff, P. J. Meehan, M. S. Tsao, and Q. W. Choi, J. Phys. Chem., 66, 1233 (1962).
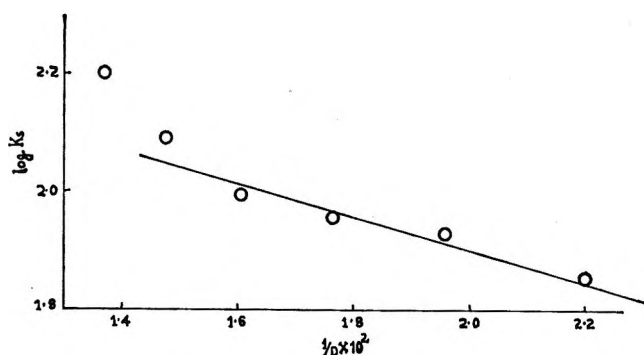
Figure 7. Dependence of the rate on dielectric constant (temperature, 35°; [$K_3Fe(CN)_6$], 2.0×10^{-2} M; [thiol hydrochloride], 2.0×10^{-2} M; [HCl], 5.0×10^{-2} M; [KCl], 11.0×10^{-2} M; $I = 0.3$).

plot of log k_3 against $1/D$ gave a straight line as shown in Figure 7.

A number of runs were studied at different temperatures at different dielectric constant. The Arrhenius plot was found to be a straight line. Thermodynamic parameters, heat of activation, entropy, and free energy of activation, were also evaluated with the aid of usual expressions. These are recorded in Table VI.

Table VI

D	ΔH^*, kcal mol^{-1}	ΔS^*, eu	ΔG^*, kcal mol^{-1}
73.12	24.24	18.0	18.86
62.41	22.0	12.9	18.14

Increase in the concentration of the either disulfide or neutral electrolytes produced no significant effect on the rate of oxidation.

Discussion

2-Mercaptoethylamine hydrochloride would largely exist in an aqueous solution in ionized form with its cationic part as [HS − (CH$_2$)$_2$ − NH$_3^+$]. Since in the present case the thiol group provides the reaction site, the cationic part referred above will, for the sake of convenience, be represented hereafter as $^+$RSH, where $^+$R represents the remaining part of the ionic species. The reaction mechanism probably consists of the following steps

$$Fe(CN)_6^{3-} + {}^+RSH \xrightarrow{k_1} HFe(CN)_6^{3-} + {}^+RS \cdot \quad (1)$$

$$HFe(CN)_6^{3-} + {}^+RSH \underset{k_{-2}}{\overset{k_2}{\rightleftharpoons}}$$

$$\{HFe(CN)_5SR^+\}^{3-} + HCN \quad (2)$$

$$\{HFe(CN)_5SR^+\}^{3-} + Fe(CN)_6^{3-} + HCN \xrightarrow{k_3}$$

$$2HFe(CN)_6^{3-} + {}^+RS \cdot \quad (3)$$

$${}^+RS \cdot + \cdot SR^+ \xrightarrow{fast} {}^+RSSR^+ \quad (4)$$
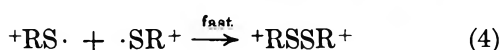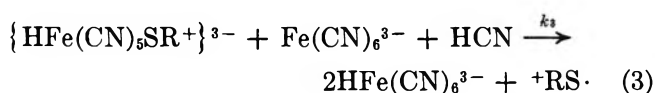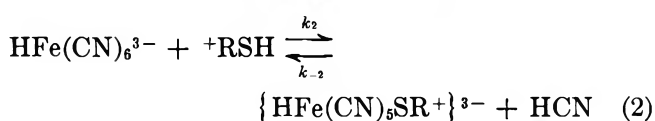
Thus

$$\frac{-d[Fe(CN)_6^{3-}]}{dt} = k_1[Fe(CN)_6^{3-}][{}^+RSH] +$$

$$k_3[\{HFe(CN)_5SR^+\}^{3-}][Fe(CN)_6^{3-}][HCN] \quad (5)$$

The stationary state concentration of $\{HFe(CN)_5$-$SR^+\}^{3-}$ as given by steps 2 and 3 is

$$[\{HFe(CN)_5SR^+\}^{3-}] =$$

$$\frac{k_2[HFe(CN)_6^{3-}][{}^+RSH]}{[HCN]\{k_{-2} + k_3[Fe(CN)_6^{3-}]\}} \quad (6)$$

Substitution in eq 5

$$-\frac{d[Fe(CN)_6^{3-}]}{dt} = k_1[Fe(CN)^{3-}][{}^+RSH] +$$

$$\frac{k_2k_3[Fe(CN)^{3-}][{}^+RSH][HFe(CN)_6^{3-}]}{k_{-2} + k_3[Fe(CN)_6^{3-}]} \quad (7)$$

It would be seen that the final rate equation derived is composed of two parts; the first one, viz., k_1[Fe(CN)$_6^{3-}$][$^+$RSH] represents the uncatalyzed part of the reaction, while the second part, i.e.

$$\frac{k_2k_3[Fe(CN)_6^{3-}][{}^+RSH][HFe(CN)_6^{3-}]}{k_{-2} + k_3[Fe(CN)_6^{3-}]}$$

describes the catalyzed part due to ferrocyanide which has been shown earlier to act as an autocatalyst. If as a crude approximation the first part is neglected, the rate equation reduces to

$$\frac{-d[Fe(CN)_6^{3-}]}{dt} =$$

$$\frac{k_2k_3[Fe(CN)_6^{3-}][{}^+RSH][HFe(CN)_6^{3-}]}{k_{-2} + k_3[Fe(CN)_6^{3-}]} \quad (8)$$

The above rate equation explains practically most of the observations including the effect of ferricyanide.

As regards the effect of hydrogen ion it was observed that the rate falls off on increasing its concentration, though no simple mathematical dependence was observed. It may be remarked here that in oxidation kinetics of thiols the role of hydrogen ion has generally been observed to be rather complex.[15] In the present case the complications are bound to be accentuated further due to the formation of different species of ferrocyanic acid. While ferricyanic acid is a strong acid, ferrocyanic acid is strong only in the dissociation of its first two hydrogens. The values of K_3 and K_4 as determined by Nekrasov and Zotov[16] are, respectively, 1×10^{-3} and 5×10^{-5} (obtained at 16–18° and corrected to $I = 0$). It can be shown that below pH 4, only a negligible fraction of iron(II) is present as ferrocyanide ion.

(15) M. Kharasch, "Organic Sulfur Compounds," Vol. 1, Pergamon Press, London, 1961, p 99.

(16) B. V. Nekrasov and G. V. Zotov, Zh. Prikl. Khim., 14, 264 (1941).

In the pH region 1–2, the major constituents[17] are $HFe(CN)_6{}^{3-}$ and $H_2Fe(CN)_6{}^{2-}$. An increase in hydrogen ion concentration will obviously shift the equilibria toward more proton rich species of $HFe(CN)_6{}^{3-}$. This will naturally lead to a retardation in rate according to the rate law derived. Consequently, unless an exact distribution of ferrocyanide between its protonated species is known with certain accuracy at the hydrogen ion concentration employed, it would not be possible to make substitution for $[HFe(CN)_6{}^{3-}]$ in the rate expression. Under the circumstances, obviously, it is difficult to expect any definite index of inverse relationship.

An additional feature of this reaction is that it is found to be accompanied by a moderately large and positive value of ΔS^*, whereas electron-transfer reactions are generally characterized by a negative value of entropy of activation. This departure can be attributed to the particular type of reaction scheme which also includes the step leading to the substitution of a cyanide ligand in a practically inert ferrocyanide complex. A substitution of this type is bound to lead to loosening of the structure causing greater randomness in the resultant species and the resultant large positive entropy changes. The net magnitude of ΔS^* may, therefore, show the observed behavior. It may be re-marked here that the substitution of a cyanide ligand in a ferrocyanide complex has been assumed in a number of cases.[18-21] Though speculative, in present reaction the autocatalytic behavior of ferrocyanide and the effect of external addition of potassium ferrocyanide lend support to such a situation.

In the formulation of the above reaction mechanism the formation of free radical has been shown. In majority of cases studied so far it has been presumed that the oxidation of thiols proceeds *via* free radical formation. This assumption is largely based on capability of such systems to initiate the polymerization of vinyl cyanide.

(17) M. A. Rawoof and J. R. Sutter, *J. Phys. Chem.*, **71**, 2767 (1967).

(18) E. J. Meehan, I. M. Kolthoff, and H. Kakiuchi, *ibid.*, **66**, 1238 (1962).

(19) K. K. Girdhar and D. V. S. Jain, *J. Inorg. Nucl. Chem.*, **27**, 2653 (1965).

(20) R. S. Murray, *Chem. Commun.*, **14**, 824 (1968).

(21) S. Roman and R. G. Wilkins, *Inorg. Chem.*, **8**, 156 (1969).

Electron Spin Resonance Studies of Cation Radicals Produced

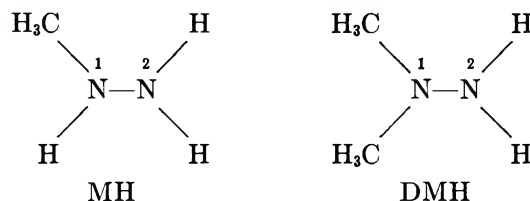# during Oxidation of Methylhydrazines

by Thomas V. Atkinson and Allen J. Bard*

Department of Chemistry, The University of Texas at Austin, Austin, Texas 78712   (Received September 4, 1970)

The radical cations of methylhydrazine (MH) and 1,1-dimethylhydrazine (DMH) were generated by reaction with cerium(IV) in sulfuric acid solutions in a fast-flow mixing chamber. The electron spin resonance (esr) spectra of these were recorded and experimental nitrogen and proton coupling constants were determined by simulation of the spectra. Under some conditions, oxidation of DMH led to the radical cation of tetramethyl-2-tetrazene. A brief discussion of molecular orbital calculations for these molecules and implications of this study to reaction mechanisms for the oxidation of the hydrazines is also given.

Extensive studies have been made on the mechanisms of the chemical and electrochemical oxidation of hydrazine and methyl-substituted hydrazines.[1-8] The mechanisms of the oxidations and the number of electrons transferred in the initial step, one or two, are very dependent upon the nature of the substituents on the hydrazine, the reaction conditions, and the oxidant. Adams and Thomas[9] and Falle[10] observed the cation radical of hydrazine, $N_2H_4^+$, formed by reaction of hydrazine and cerium(IV) in a 1 M H_2SO_4 medium in a rapid-flow system, by esr spectroscopy. This work provided unambiguous evidence for the existence of short-lived radical cation intermediates in the oxidation of hydrazine, itself. Observation of $N_2H_4^+$ by esr in the solid state has also been reported.[11,12] This study was undertaken to investigate whether radical cations of methylhydrazines could be formed under similar conditions and to provide information about the nature and stability of these radical ions. Flow-system studies of both methylhydrazine (MH) and 1,1-dimethylhydrazine (DMH) were carried out.

cation of the radical. Upon stopping the flow, this small signal disappeared and no further signal appeared. There is one complication in the application of stopped-flow systems to the study of hydrazines. Upon oxidation of the hydrazines nitrogen gas is vigorously evolved. Ordinarily the rapid-flow rate causes the bubbles to form outside of the esr cavity. However, when the flow is stopped, the bubbles form in the cavity pushing out the solution. This causes a decrease in signal because of the decrease in sample volume and especially detuning of the spectrometer because of the change of dielectric constant. However, there probably are no subsequent radicals formed upon decomposition of the initial radical species in concentrations high enough to be observed. A more intense spectrum was obtained upon decreasing the H_2SO_4 concentration. The spectrum in Figure 1a was obtained with 0.2 M solution of MH and a 0.2 M solution of cerium(IV) which was also 0.5 M in H_2SO_4. A better spectrum (Figure 1b) resulted from using a 0.44 M MH solution, and a 0.18 M cerium(IV) solution in 0.5 M H_2SO_4 with

$$\begin{array}{cc} \text{MH} & \text{DMH} \end{array}$$

Results

Methylhydrazine. When MH was oxidized by flowing together a 0.1 M solution of ceric ammonium sulfate and a 0.2 M solution of MH, both 1 M in sulfuric acid, in a rapid-flow mixing chamber directly below the esr cell (essentially the same conditions and methods of Adams and Thomas),[9] only a very weak esr signal was observed. The spectrum consisted of several broad lines and had a total span greater than 100 G; the poor signal level and resolution prevented further identifi-

(1) H. Wheland, "Die Hydrazine," Verlag F. Enke, Ed., Stuttgart, 1913.

(2) L. F. Audrieth and B. A. Ogg, "The Chemistry of Hydrazine," Wiley, New York, N. Y., 1951.

(3) C. G. Overberger, J. P. Anselme, and J. G. Lombardino, "Organic Compounds with Nitrogen-Nitrogen Bonds," Ronald Press, New York, N. Y., 1966.

(4) S. Karp and L. Meites, *J. Amer. Chem. Soc.*, **84**, 906 (1962).

(5) A. J. Bard, *Anal. Chem.*, **35**, 1602 (1963).

(6) S. Szpak, P. Storehart, and T. Kazan, *Electrochim. Acta*, **10**, 563 (1965).

(7) D. M. King and A. J. Bard, *J. Amer. Chem. Soc.*, **87**, 419 (1965).

(8) M. Michlmayr and D. T. Sawyer, *J. Electroanal. Chem.*, **23**, 375 (1969).

(9) J. Q. Adams and J. R. Thomas, *J. Chem. Phys.*, **39**, 1904 (1963).

(10) H. R. Falle, *Can. J. Chem.*, **46**, 1703 (1968).

(11) J. A. Brivati, J. M. Gross, M. C. R. Symons, and D. J. A. Tinling, *J. Chem. Soc.*, 1965, 6504.

(12) J. K. S. Wan, J. R. Morton, and H. J. Bernstein, *Can. J. Chem.*, **44**, 1957 (1966).
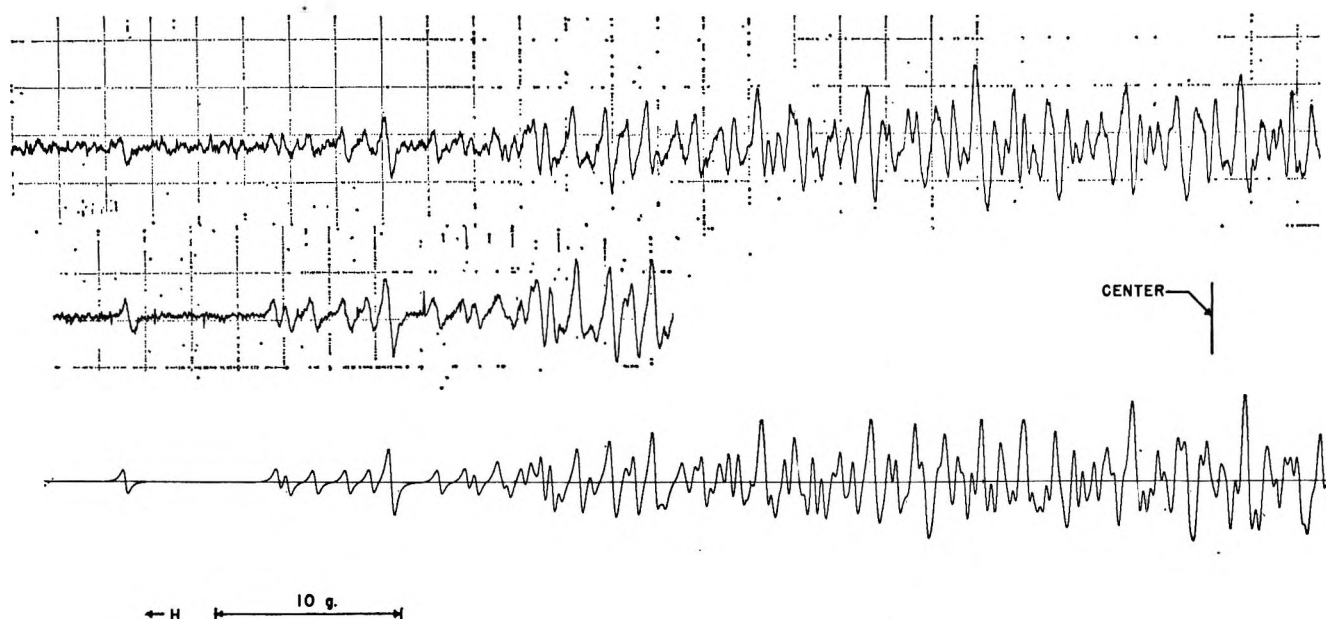
←H ├──── 10 g. ────┤

Figure 1.   Esr spectra of methylhydrazine cation radical.   (a) Top: experimental spectrum; the sweeping field is increasing from right to left.   (b) Middle: experimental spectrum showing outer portion more clearly.   (c) Bottom: calculated spectrum using constants given in Table I.

the flow rate of the MH solution somewhat larger than that of the cerium(IV) solution.

The spectrum can be interpreted as the cation radical, MH$^+$.   The best simulation of the spectrum, based on the coupling constants in Table I, is shown in Figure 1c.   The deviations between the simulation and the experimental spectrum arise from some nonlinearity of the magnetic field sweep and the fact that the spectrum arises from a large set of coupling constants of low multiplicity of about the same magnitude.   This produces a spectrum with a central portion having a large number of lines of similar intensity, where any small changes in the coupling constants cause major changes in the appearance of the spectrum.   The assigned coupling constants are those which give the best fit to the outer portion of the spectrum.

1,1-Dimethylhydrazine.   When an aqueous solution of 0.23 M DMH was oxidized in a flow system by an aqueous solution of 0.15 M ceric ammonium sulfate–0.2 M H$_2$SO$_4$ solution, a new fairly strong signal was observed.   A typical spectrum is seen in Figure 2a.   More intense signals were obtained when the DMH flow rate was greater than that of the cerium(IV) solution.   Adams and Thomas[9] and Falle[10] also employed hydrazine to ceric ion ratios of 2:1 in the generation of hydrazine cation radical, however, at H$_2$SO$_4$ concentrations at least five times as high.   Upon halting the flow of reactants, the above signal disappeared and no further signals were observed.

This spectrum can be interpreted as the DMH cation radical.   A comparison of a computer-simulated spectrum, based on the coupling constants and line width in Table I, and an experimental spectrum is given in Figure 2.

Different results are obtained at higher H$_2$SO$_4$ concentrations.   No signal was observed during flow when 0.1 M cerium(IV) and 0.2 M DMH in 1 M H$_2$SO$_4$ were employed.   Upon stopping the flow, a fairly stable signal appeared within 1 min.   This signal was very similar to that reported by Tolles, *et al.*,[13] for tetramethyl-2-tetrazene (TMT) cation radical produced in acetone by electrochemical oxidation or by reaction with tetranitromethane.   The coupling constants found here in

CH$_3$ CH$_3$
   \   /
    \ 1   2   3   4 /
     N—N=N—N
    /   \
CH$_3$ CH$_3$

TMT
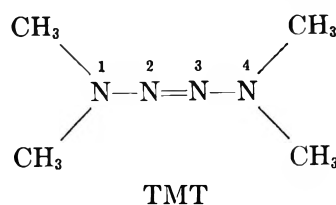
the aqueous solution (Table I) are slightly different than those found in acetone.   This results in a spectrum in aqueous solution with fewer lines; the observed line width in aqueous solution is narrower, however.   To give further evidence that the observed spectrum was that of TMT$^+$, an authentic sample of TMT in 1 M H$_2$SO$_4$ was prepared and electrolytically oxidized at a platinum electrode inside the esr cell.   A spectrum identical with that obtained in the flow experiments resulted.

The nature of the reaction leading to the TMT cation radical was investigated in a semiquantitative study of the effects of the concentrations of DMH, cerium(IV), and acid on the resulting spectra.   The solutions were mixed outside the spectrometer and after a known

(13) W. M. Tolles, D. W. Moore, and W. E. Thun, *J. Amer. Chem. Soc.*, **88**, 3476 (1966).

Table I: Esr Data for the Hydrazine and Tetrazene Cation Radicals

Position	No. of equiv nucleii	Nucleus	Experimental coupling constant, a, G	Calcd residues,[a] G — Hückel	MacLachlan	a_H/a_N	a_{Me}/a_N
			Hydrazine Cation [Ce(IV) H₂O][b]				
1	2	N	11.5	−0.66	−0.63		
1	4	H	11.0	−0.97	−0.51	0.96	
			Methylhydrazine Cation [Ce(IV) H₂O][c]				
1	3	H(Me)	15.0	−0.17	14.40		1.09
1	1	N	13.8				
1	1	H	12.5	0.21	−0.65	0.90	
2	1	N	10.7	0.68	−0.05		
2	1	H	9.1 ⎱	−1.62[d]	2.02	⎰0.85	
2	1	H	8.9 ⎰			⎱0.80	
Line width			0.3				
			1,1-Dimethylhydrazine Cation [Ce(IV) H₂O][c]				
1	1	N	16.05	−0.02	0.89		
1	6	H(Me)	14.39	−0.22	8.91		0.90
2	1	N	9.69	0.66	−0.62		
2	2	H	6.91	−2.83	3.71	0.71	
Line width			0.26				
			Tetramethylhydrazine Cation (electrochemical oxid/MeCN)[e] **(tetramethyl-2-tetrazine, MeI H₂O)[f]**				
1	2	N	13.41[e] 13.5[f]	0.52	0.43		
1	12	H(Me)	12.69 12.7	0.58	3.59		0.94
			Tetramethyl-2-tetrazene Cation [DMH, Ce(IV)/H₂O][c] **(tetranitromethane, TMT/acetone, −30°)[g]**				
1	6	H(Me)	11.52[c] 11.72[g] ⎱	1.91[d]	1.55		1.05
1	6	H(Me)	10.40 10.45 ⎰				0.95
1	2	N	10.96 10.93	0.77	0.04		
2	2	N	1.20 1.07	−0.88	0.15		
Line width			0.26 0.39				

[a] The residues contain the results of the correlation of calculated spin density with experimental coupling constants. Residue = $a_{experimental} - a_{calculated}$. The regression analysis yields the spin polarization parameters which are listed below with the standard deviation of the parameter given in parenthesis. Huckel, $S^N = 36.70 (1.87)$, $Q_{NH}^N = -6.19 (0.72)$, $Q_{NC}^N = -3.28 (0.80)$, $Q_{NE}^N = -13.98 (0.92)$, $Q_{NN'}^N (= -Q_{N'N}^N) = 8.97 (2.57)$, $Q_{CN}^N = 10.25 (2.00)$, $Q_{NH}^H = 23.93 (0.92)$, $Q_Y = 347.98 (7.54)$, ($a_{NMe}^H = Q_{Y\rho Y}$ and NMe = N-X-Y); MacLachlan, $S^N = 38.63 (1.77)$, $Q_{NH}^N = -7.19 (0.69)$, $Q_{CN}^N = -6.16 (0.66)$, $Q_{NE}^N = -13.98 (0.92)$, $Q_{NN'}^N = 7.76 (1.83)$, $Q_{CN}^N = 13.11 (1.71)$, $Q_{NH}^H = 23.02 (0.97)$, $Q_Y = 397.17 (67.18)$, ($\lambda = 1.2$ used in MacLachlan calculations). [b] From ref 9, 10. [c] This work. [d] The average of the experimental couplings for these positions were used in the correlation. [e] From S. F. Nelson, *J. Amer. Chem. Soc.*, **88**, 1930 (1966). [f] From W. H. Bruning, C. J. Michejda, and D. Romans, *Chem. Commun.*, 11 (1967); *J. Amer. Chem. Soc.*, **91**, 3859 (1969). [g] From ref 13.

time placed in the spectrometer; their spectra were then recorded as a function of time. The time required for the signal to reach maximum intensity depended strongly on the acid strength, concentration of the reactants, and even the speed of mixing. In all of the external mixing experiments, the maximum intensity was reached in the 1–2 min necessary to mix the solutions and place an aliquot in the spectrometer. The most intense signal was found to result from a molar ratio of cerium(IV) to DMH of 1.0:2.0. The intensity also varied with the acid strength with molar ratios of cerium(IV) to DMH to acid in the range of 1.0:2.0: 8.0 to 1.0:2.0:16.0 giving essentially equivalent and optimum results; the signal intensity decreased when the ratio of reactants departed in either direction from this range. The absolute concentrations were also

important. The optimum concentration of cerium(IV) was 0.080 M with those of the other reactants being in the proper ratio. The speed of mixing also affected the results. A quick complete mixing of the reactants gave the best results. Dropwise addition of the oxidant to the other components resulted in almost no signal.

Potassium bromate was also used as an oxidant. The most pronounced difference between it and cerium(IV) was the time necessary for the appearance of the TMT⁺ radical. In contrast to the cerium(IV) case, in which less than 2 min was required for the radical to appear, as long as 15 min was required when bromate was used. This induction period was a function of the acid concentration. With solutions 0.20 M in DMH and 0.10 M in KBrO₃, 2 min was required for a solution 0.6 M in acid and 13 min for a solution 0.3 M in acid.
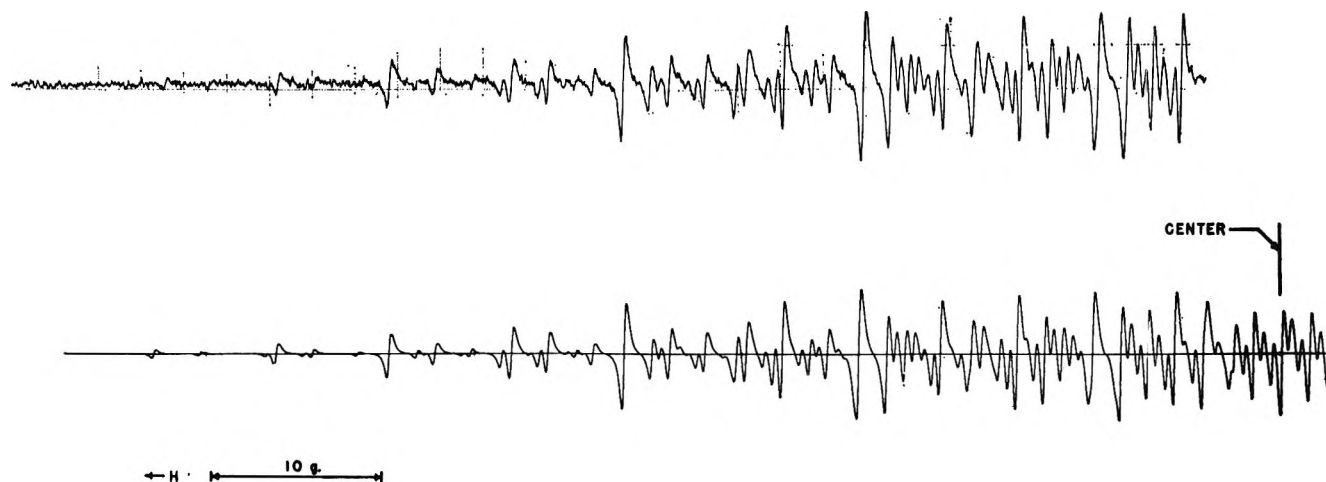
Figure 2. Esr spectrum of dimethylhydrazine cation radical. (a) Top: experimental spectrum; the sweeping field is increasing from right to left. (b) Bottom: experimental spectrum showing outer portion more clearly.

Discussion

Coupling Constants and Molecular Orbital Calculations. Radicals containing nitrogens with substituent protons or methyl groups are frequently compared with respect to the ratio of the proton coupling constant, a_H, to that of the nitrogen to which it is attached, a_N, $R_H = a_H/a_N$ or the ratio of the methyl proton coupling constant, a_{Me}, to a_N, $R_{Me} = a_{Me}/a_N$.[14-16] These ratios range from 0.6 to 2.0 and are frequently close to 1 for molecules such as those reported here, although these ratios can be very sensitive to steric effects, as found, for example, in the cation radical of tetrakis(dimethyl-amino)ethylene.[14] The ratios in the cation radicals of MH and DMH are shown in Table I and are in the expected range of values; a tabulation of R_H and R_{Me} for 25 related compounds is given elsewhere.[17] The ratio R_H (0.71) for DMH cation radical is somewhat lower than that expected from similar compounds.

Hückel molecular orbital (HMO) calculations were attempted for these molecules as a confirmation of the spectral assignments and to find a set of parameters useful in treating molecules of this type. The hydrazine cation radicals were assumed to be planar with the nitrogens sp^2 hybridized.[9,12] Both nitrogens of 2,2-diphenyl-1-picrylhydrazyl (DPPH) have been shown to be trigonal in the crystalline state, although steric effects prevent coplanarity of the entire molecule.[18] The following procedure was adopted for the HMO calculations and the calculation of the coupling constants. A set of reasonable HMO parameters was adopted; these are given in Table II with references to their sources. The parameters were used to perform HMO and McLachlan calculations for 27 radical ions, including those of hydrazines, amines, anilines, p-phenylenediamines, and N-methylated azines.[17] The resultant spin densities were then correlated against the experimental coupling constants using the appropriate spin polarization equations by means of multiple re-

gression[19] analysis using the spin-polarization parameters $(Q_{NH}^N, Q_{NC}^N,$ etc.) as adjustable coefficients. The spin-polarization parameters giving the best least-squares fit are given in the footnotes to Table I. These polarization parameters show varying degrees of agreements with those suggested in other studies.[15,19,20]

The value of Q_Y which relates the nitrogen–methyl proton splitting a_{Me}^H to the spin density on the pseudo-p orbitals formed from the methyl proton s orbitals, ρ_Y, by the relationship $a_{NMe} = Q_Y\rho_Y$ has been found to be

Table II: HMO Parameters for Spin Density Calculations

h_A	A	k_{AB}	AB	Radicals	Ref
1.3	N	0.95	CN	NH_2R, R=N, C	a
1.2	N	0.85	CN	NHMeR, NMe_2R, NR_2Me, R=N, C, Me	a
0.75	N	0.95	CN	NR_2E, R=N, C, H	b
		1.0	NN	All	c
−0.10	X	0.70	NX	N-Me = N-X-Y	a
−0.50	Y	2.50	XY	N-Me = N-X-Y	a
2.01	N	1.62	NO	Nitro groups	d
1.5	O	1.04	CN	Nitro groups	d

a P. D. Sullivan and J. R. Bolton, *J. Mag. Res.*, 1, 356 (1969). b A. Carrington and J. dos Santos-Viega, *Mol. Phys.*, 5, 21 (1962). c E. W. Stone and A. H. Maki, *J. Chem. Phys.*, 39, 1635 (1963). d P. T. Cottrell and P. H. Rieger, *Mol. Phys.*, 12, 149 (1967).

(14) K. Kuwata and D. H. Geske, *J. Amer. Chem. Soc.*, 86, 2101 (1964).

(15) B. L. Barton and G. K. Fraenkel, *J. Chem. Phys.*, 41, 1455 (1964).

(16) P. Smith and W. M. Fox, *Can. J. Chem.*, 47, 2227 (1969).

(17) T. V. Atkinson, Ph.D. Dissertation, The University of Texas at Austin, Austin, Texas, 1970.

(18) D. E. Williams, *J. Amer. Chem. Soc.*, 88, 5665 (1966).

(19) J. Q. Adams, S. W. Nicksic, and J. R. Thomas, *J. Chem. Phys.*, 45, 654 (1966).

(20) C. L. Talcott and R. J. Myers, *Mol. Phys.*, 12, 549 (1967).

348 (using HMO calculations) or 397 (using the Mc-Lachlan calculation). Normally a value of about 169 would be expected.[15] The exceptionally high value obtained in this case may be due to the use of the molecular orbital parameters for the methyl group shown in Table I, which were originally intended for the toluene anion rather than for an N-methyl group. In addition, the neglect of the spin density on the methyl carbon may also add some contribution to this exceptionally high term. An alternative expression for the methyl group may be given by $a_{NMe} = Q_{NMe}^H \rho_N$, where ρ_N is the spin density in the nitrogen π orbital. In this case, Q_{NMe}^H has been found to be 25.5 ± 0.5 for McLachlan calculations and 33.8 ± 1.2 for HMO calculations, which compare favorably with similar parameters obtained for the carbon–methyl group.

The value for Q_{NH}^H used in the expression for the nitrogen-proton splittings are -23.9 ± 0.9 for McLachlan calculations and -23.0 ± 1.0 for HMO calculations. This is significantly lower than that obtained by Barton and Fraenkel, of -34, who based this parameter on a different analysis.[15] They point out, however, that small changes in the molecular orbital parameters will have a significant effect on Q_{NH}^H. In general, Q factors obtained in this work and those obtained in other studies compare satisfactorily within the framework of HMO-type calculations.

Calculated coupling constants for the radicals of interest here based on these parameters are given in Table I. While the values calculated from HMO theory show fair agreement with the experimental values, they cannot be used with confidence to either support or refute the assignments suggested.

Implications to Reaction Mechanisms. The chemical and electrochemical oxidations of alkyl-substituted hydrazines[7,21] have generally only produced evidence for a primary two-electron step. For example, the oxidation of DMH with alkali halates and halogens[20] in acidic solutions was shown to produce the moderately stable 1,1-dimethyldiazenium ion
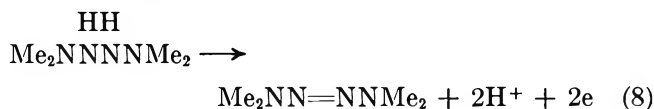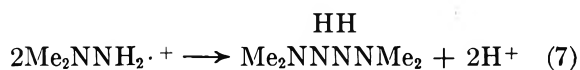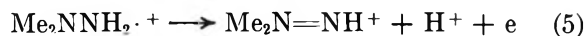
$$Me_2NNH_3^+ \longrightarrow Me_2N=NH^+ + 2H^+ + 2e \quad (1)$$
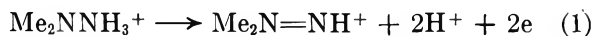
In alkaline solutions, this ion deprotonated and coupled to form TMT

$$Me_2N=NH^+ + OH^- \longrightarrow Me_2N=N + H_2O \quad (2)$$

$$2Me_2N=N \longrightarrow Me_2NN=NNMe_2 \quad (3)$$
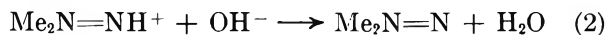
The electrochemical oxidation of DMH in 1 M H_2SO_4 at a platinum electrode also gave unequivocal evidence of an initial two-electron step, followed by a slow decomposition of the diazenium ion and further oxidation. The results here demonstrate that, at least when a one-electron oxidizing agent such as cerium(IV) is employed, the radical cation may be an intermediate in the formation of the diazenium ion and further oxidation products. Moreover, since the DMH cation

radical spectrum can be assigned based on the structure $(CH_3)N-NH_2 \cdot {}^+$, the radical cation formed, even in acid solutions, is not protonated. This indicates that the basicity of DMH cation radical is much smaller than that of the parent DMH. Similarly, the cation radical of TMT is unprotonated in acidic solutions, although the pK_b of the parent TMT is 7.80.[21a] The existence of the cation radical of TMT following oxidation of DMH with a one-electron oxidant suggests alternate paths of TMT from radical intermediates may be possible. The following reactions then can be added to pathways already proposed.

$$Me_2NNH_3^+ \longrightarrow Me_2NNH_2 \cdot {}^+ + H^+ + e \quad (4)$$

$$Me_2NNH_2 \cdot {}^+ \longrightarrow Me_2N=NH^+ + H^+ + e \quad (5)$$

$$2Me_2NNH_2 \cdot {}^+ \longrightarrow Me_2NNH_3^+ + Me_2N=NH^+ \quad (6)$$

$$\qquad\qquad\qquad\qquad HH$$
$$2Me_2NNH_2 \cdot {}^+ \longrightarrow Me_2NNNNMe_2 + 2H^+ \quad (7)$$

$$HH$$
$$Me_2NNNNMe_2 \longrightarrow$$
$$\qquad\qquad Me_2NN=NNMe_2 + 2H^+ + 2e \quad (8)$$

$$Me_2NN=NNMe_2 \longrightarrow Me_2NN=NNMe_2^+ + e \quad (9)$$

Analogous expressions have been proposed for the oxidation of hydrazine.[1-3] The absence of any evidence of radical cation formation during electrochemical oxidation of the hydrazines in similar solutions, even for experiment durations of about 10 msec, suggests that the electrode acts as a polyelectronic oxidant so that cation radicals formed in the vicinity of the electrode are immediately oxidized further (eq 5). In the flow experiment the ratio of hydrazine to oxidant is such that cation radicals can be formed in the absence of any excess oxidizing agent.

Experimental Section

MH and DMH were obtained from Aldrich Chemical Co. and Matheson Coleman and Bell Chemical Co. Ceric ammonium sulfate was obtained from G. F. Smith Chemical Co. All were employed without further purification. TMT was prepared by the method of McBride and Kruse.[21a]

A Varian Associates V-4502 Spectrometer employing 100-kc field modulation was employed. The field sweep was calibrated by using Fremy's salt; the high- and low-field coupling constants were taken as 13.160 $\pm$ 0.008 and 13.101 $\pm$ 0.004. Flow experiments were performed using the V-4549 liquid flow mixing chamber system, comprising a four-jet mixing chamber with a 0.05-ml volume and a flat quartz cell. Solution flow rates of 1 to 10 ml/sec were employed.

(21) (a) W. R. McBride and H. W. Kruse, *J. Amer. Chem. Soc.,* **79**, 572 (1957); (b) W. R. McBride and E. M. Bens, *ibid.,* **81**, 5546 (1959); (c) W. R. McBride and W. E. Thun, *Inorg. Chem.,* **5,** 1846 (1966).

The spectra were simulated using the program Breit[17] which simulates spectra having second-order shifts[22] of the line positions. This program is based on the first-order simulation program of Stone and Maki[23] but is extended to include second-order shifts for nuclei of any spin.

(22) (a) R. W. Fessenden, *J. Chem. Phys.*, **37**, 747 (1965); (b) G. K. Fraenkel, *J. Phys. Chem.*, **71**, 139 (1967).

(23) E. W. Stone and A. H. Maki, *J. Chem. Phys.*, **38**, 1999 (1963)

Electron Paramagnetic Resonance Spectroscopic Study of Radical

Cations from Hydrazine, Methylhydrazine, and Dimethylhydrazines[1]

by P. Smith,* R. D. Stevens, and R. A. Kaba

Paul M. Gross Chemical Laboratory, Department of Chemistry, Duke University, Durham, North Carolina 27706
(Received September 28, 1970)

The substrates hydrazine, methylhydrazine, 1,1-dimethylhydrazine, and 1,2-dimethylhydrazine have been investigated in turn within an aqueous continuous-flow system at $25 \pm 2°$ using the titanous chloride–hydrogen peroxide radical-generating method. For each hydrazine the electron paramagnetic resonance spectrum of the corresponding monopositive radical ion was the only one observed, viz. $[NH_2NH_2] \cdot {}^+$, $[CH_3NHNH_2] \cdot {}^+$, $[(CH_3)_2NNH_2] \cdot {}^+$, $[cis\text{-}CH_3NHNHCH_3] \cdot {}^+$, and $[trans\text{-}CH_3NHNHCH_3] \cdot {}^+$. The hydrogen and nitrogen nuclear hyperfine coupling constants of these radical cations have been determined and discussed in terms of the $\sigma\text{-}\pi$ interaction theories of Karplus and Fraenkel and McConnell. Values for several empirically calculated spin-polarization parameters are presented.

Introduction

The reaction between titanous chloride and hydrogen peroxide in dilute aqueous sulfuric acid has been shown to furnish the basis of a useful continuous-flow method for the generation of transient free radicals from reactive substrates for the purpose of electron paramagnetic resonance (epr) spectroscopic observations.[2]

The mechanisms of the reactions which occur with the use of this radical-generating system have attracted recent attention.[3-12] These studies indicate that the basic initial reaction may be adequately represented by the equation

$$Ti(III) + H_2O_2 \longrightarrow Ti(IV) + OH^- + \cdot OH \quad (1)$$
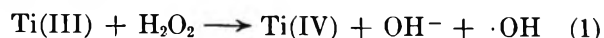
and this is followed by secondary processes such as

$$\cdot OH + SH \longrightarrow H_2O + S\cdot \quad (2)$$

or

$$\cdot OH + SH \longrightarrow \cdot SHOH \quad (3)$$
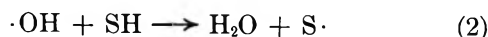
where SH denotes the reactive substrate.

Norman, *et al.*,[13] have shown that with the use of hydrazine as substrate this radical-generating system produces an epr spectrum of nine equally spaced lines with relative intensities close to 1:6:17:30:36:30:

(1) This work was supported by National Science Foundation Grants GP 7534 and GP 17579.

(2) W. T. Dixon and R. O. C. Norman, *J. Chem. Soc.*, 3119 (1963).

(3) K. Takakura and B. Rånby, *J. Phys. Chem.*, **72**, 164 (1968).

(4) H. Fischer, *Ber. Bunsenges. Phys. Chem.*, **71**, 685 (1967).

(5) R. E. Florin, F. Sicilio, and L. A. Wall, *J. Phys. Chem.*, **72**, 3154 (1968).

(6) Y. S. Chiang, J. Craddock, D. Michewich, and J. Turkevich, *ibid.*, **70**, 3509 (1966).

(7) R. O. C. Norman, *Proc. Roy. Soc.*, *Ser. A*, **302**, 315 (1968).

(8) M. S. Bains, J. C. Arthur, Jr., and O. Hinojosa, *J. Phys. Chem.*, **72**, 2250 (1968).

(9) R. O. C. Norman and P. R. West, *J. Chem. Soc. B*, 389 (1969).

(10) R. E. James and F. Sicilio, *J. Phys. Chem.*, **74**, 1166, 2294 (1970).

(11) Y. Shimizu, T. Shiga, and K. Kuwata, *ibid.*, **74**, 2929 (1970).

(12) G. Czapski, H. Lavanon, and A. Samuni, *Isr. J. Chem.*, **7**, 375 (1969).

(13) W. T. Dixon, R. O. C. Norman, and A. L. Buley, *J. Chem. Soc.*, 3625 (1964).

17:6:1. Adams and Thomas[14] have reported a similar but better resolved spectrum when hydrazine is treated with ceric ion in dilute aqueous sulfuric acid within a continuous-flow system and have assigned this spectrum to the hydrazine radical cation, $[NH_2NH_2] \cdot {}^+$, with a_N and $a_H^{NH_2}$ equal to 11.5 and 11.0 G, respectively. Consequently, Norman, et al.,[13] attributed their spectrum to the same radical cation with a_N and $a_H^{NH_2}$ being both equal to 11.5 G. They postulated this radical cation[13] to be formed by the hydroxyl radical either abstracting a hydrogen atom from the conjugate acid of hydrazine or removing an electron from hydrazine itself. More recently, the epr spectrum of the $[NH_2NH_2] \cdot {}^+$ radical cation produced by the ceric-ion oxidation method has been restudied over the temperature range 15–55°, the results at 25° being in excellent agreement with those of the first workers using the same method.[15]

Several investigations using the titanous chloride–hydrogen peroxide radical-generating system have been reported already from this laboratory.[16-22] The present study concerns the extension of our investigations to a number of methyl-substituted hydrazines, all of which were found to give radical cations analogous to that formed from hydrazine but not previously studied by epr spectroscopy. Although the epr spectra of these methyl-substituted hydrazine radical cations were complex, they were all successfully characterized. In addition, for comparison purposes, hydrazine was re-examined and found to give a spectrum similar to but better resolved than that of the earlier workers[13] with the use of this same substrate and radical-generating method. This improved resolution allowed the values of a_N and $a_N^{NH_2}$ for the $[NH_2NH_2] \cdot {}^+$ radical cation to be determined as equal to 11.5 and 11.1 G, respectively.

These hydrazine radical cations are very similar to the well known Wurster's Blue-type radical cations.[23,24] These latter radicals have complex epr spectra few of which have been completely characterized, e.g., the p-phenylenediamine radical cation[25,26]

$$\left[H_2N - \bigcirc - NH_2 \right]^{\cdot +}$$

1
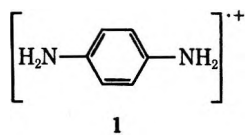
and the N,N,N',N'-tetramethyl-p-phenylenediamine radical cation[27-29]

$$\left[(CH_3)_2N - \bigcirc - N(CH_3)_2 \right]^{\cdot +}$$

2
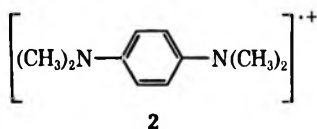
Our characterization of the epr spectra of methyl-substituted hydrazine radical cations provides a unique opportunity of studying unsymmetrical analogs of

Wurster's Blue-type radical cations without the complication of interactions from aromatic protons.

Experimental Section

The experimental arrangement and procedures were essentially as described before.[19] However, owing to the basic nature of the hydrazines it was found useful to modify the two-stream continuous-flow system of all our previously reported[16-22] investigations by adding a third stream. As was the case for the other two streams, this third stream originated in a 2-l. separatory funnel and its flow rate was controlled with the use of a Teflon-stemmed glass needle valve and monitored with a calibrated flow meter (Roger Gilmont Instruments, Inc., Model F 1300). The third stream was an aqueous solution of substrate together with CP sodium hydroxide when necessary. As before,[19] one of the other two streams was reserved for an aqueous solution of titanous chloride and the other, for one of hydrogen peroxide; and the epr cell was constructed of Suprasil to the Borg mix-and-flow design.[30] The third stream joined the flow system by way of a Y-piece located in the hydrogen peroxide stream about 10 cm upstream from the confluence of the titanous chloride and hydrogen peroxide streams. As before,[19] after passing through the epr cell, the reaction mixture was collected in a 10-l. bottle maintained at a constant pressure, 25.0 ± 0.1 cm, with the use of the house vacuum and a manostat (Labglass Inc., Model LG 8762). This use of a third stream prevented unnecessary decomposition of the hydrogen peroxide and oxidation of the hydrazine prior to their entry into the mixing chamber.

Fresh samples of the following were examined as

(14) J. Q. Adams and J. R. Thomas, J. Chem. Phys., **39**, 1904 (1963).

(15) H. R. Falle, Can. J. Chem., **46**, 1703 (1968).

(16) P. Smith and P. B. Wood, ibid., **45**, 649 (1967).

(17) P. Smith, J. T. Pearson, P. B. Wood, and T. C. Smith, J. Chem. Phys., **43**, 1535 (1965).

(18) J. T. Pearson, P. Smith, and T. C. Smith, Can. J. Chem., **42**, 2022 (1964).

(19) P. Smith and P. B. Wood, ibid., **44**, 3085 (1966).

(20) P. Smith, J. T. Pearson, and R. V. Tsina, ibid., **44**, 753 (1966).

(21) P. Smith and W. M. Fox, ibid., **47**, 2227 (1969).

(22) P. Smith, W. M. Fox, D. J. McGinty, and R. D. Stevens, ibid., **48**, 480 (1970).

(23) A. R. Forrester, J. M. Hay, and R. H. Thomson, "Organic Chemistry of Stable Free Radicals," Academic Press, New York, N. Y., 1968, Chapter 6.

(24) G. Vincow, "Radical Ions," E. T. Kaiser and L. Kevan, Ed., Interscience, New York, N. Y., 1968, Chapter 4.

(25) M. T. Melchior and A. H. Maki, J. Chem. Phys., **34**, 471 (1961).

(26) L. H. Piette, P. Ludwig, and R. N. Adams, Anal. Chem., **34**, 916 (1962).

(27) J. R. Bolton, A. Carrington, and J. dos Santos-Veiga, Mol. Phys., **5**, 615 (1962).

(28) K. H. Hausser, ibid., **7**, 195 (1963–1964).

(29) B. M. Latta and R. W. Taft, J. Amer. Chem. Soc., **89**, 5172 (1967).

(30) D. C. Borg, Nature, **201**, 1087 (1964).

substrates: hydrazine, hydrazine dihydrochloride, hydrazine sulfate, methylhydrazine, and methylhydrazine sulfate (Eastman Reagent Grade), 1,1-dimethylhydrazine (Eastman Practical Grade and Aldrich), and 1,2-dimethylhydrazine dihydrochloride (Aldrich). When an acid salt was used the hydrazine was liberated in solution immediately prior to use by the addition of the appropriate quantity of CP sodium hydroxide. Except in the case of 1,1-dimethylhydrazine it was possible to compare the results so obtained with those from the direct use of the hydrazine and to show that both forms of substrate gave identical epr spectra. Nevertheless, in view of the convenience, where possible the acid salts were used as sources in preference to the free hydrazines.

The following reaction conditions were employed: total flow rate, 2–4 ml sec^{-1}, the flow rates of the titanous chloride, hydrogen peroxide, and hydrazine solutions being maintained in the ratio 6:1:5, respectively; the reaction temperature, $25 \pm 2°$; the titanous chloride stream, 0.005 and 0.1 M in titanous chloride and sulfuric acid, respectively; the hydrogen peroxide stream, 0.15 M in hydrogen peroxide with no added sulfuric acid; the substrate stream, 0.1, 0.2, 0.1, and 0.05 M in hydrazine, methylhydrazine, 1,1-dimethylhydrazine, and 1,2-dimethylhydrazine, respectively, and when the substrate was used as an acid salt, 2 mol of sodium hydroxide was added to the substrate stream per 1 mol of substrate.

The spectra were recorded as the first derivatives and where necessary the signal-to-noise ratio at the wings of the spectrum was improved by using a standard Varian C-1024 Time Averaging Computer (TAC).
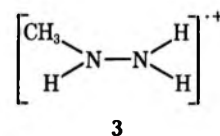
All g values were measured as before by comparison with aqueous peroxylamine disulfonate,[19] the maximum uncertainty being ±0.0002. Since the peroxylamine disulfonate proved to be unstable in the presence of the hydrazines, the solution of the peroxylamine disulfonate was utilized as follows: either[21] within an external, thin-walled Pyrex capillary held to the side of the mix-and-flow cell while this cell was being employed for the generation of the hydrazine radical cation or as a static sample within the mix-and-flow cell in conjunction with the Varian C-1024 TAC to store the spectrum obtained which was then superimposed upon that from the hydrazine radical cation. Both methods gave the same results.

Results

Hydrazine, NH_2NH_2. This compound produced the characteristic spectrum[13-15,31,32] of the hydrazine radical cation, $[NH_2NH_2] \cdot {}^+$, *viz.* a quintet (1:2:3:2:1) of quintets (1:4:6:4:1). As mentioned above, previous authors[13] using this same substrate and radical-generating system observed only a broad nine-line spectrum from this radical cation, consistent with $a_N = a_H^{NH_2} = 11.5$ G and could not achieve the resolution of Adams

and Thomas[14] who formed the $[NH_2NH_2] \cdot {}^+$ radical cation *via* the oxidation of hydrazine with ceric ion within an aqueous flow system. The spectrum observed in this present study, although not of the same quality as observed with the ceric-ion method, showed sufficient structure to allow the nitrogen and hydrogen nuclear hyperfine couplings to be measured directly. The values we obtained for a_N and $a_H^{NH_2}$ were 11.5 and 11.1 G, respectively, in reasonable agreement with the results of all earlier workers, these results relating to this species both when in aqueous solution[13-15,31] and in the solid state.[31,32]

Methylhydrazine, CH_3NHNH_2. Reaction with this compound gave rise to an absorption consisting of many equally intense broad lines. By accumulating the spectrum, the end lines were located and were found to be sufficiently intense to allow a reliable analysis. The spectrum was characterized by the interactions of three inequivalent protons (8.5, 8.9, and 12.2 G), two inequivalent nitrogen nuclei (10.4 and 13.2 G), and three equivalent protons (14.4 G). This analysis is conformable to the methylhydrazine radical cation of structure

$$\left[\begin{array}{c} CH_3 \\ \\ H \end{array} \!\!\! \diagup\!\!\!\!\searrow N\!-\!N \diagup\!\!\!\!\searrow \begin{array}{c} H \\ \\ H \end{array} \right]^{\cdot +}$$

3

in which all nuclei save the three methyl-group protons are in the same plane. This structure is analogous to that of the $[NH_2NH_2] \cdot {}^+$ radical cation which is considered[31,32] to be planar, with D_{2h} symmetry, having the unpaired electron in an antibonding orbital over the two nitrogen nuclei. The hyperfine coupling constants of the $[CH_3NHNH_2] \cdot {}^+$ radical cation were assigned from a knowledge of the total width of the spectrum and by comparison with those for the other hydrazine radical cations we have studied where they have been assigned with more certainty. However, the couplings of the protons in the –NH$_2$ group, 8.5 and 8.9 G, could not be specifically assigned cis or trans with respect to the –CH$_3$ group attached to the other nitrogen atom (see structure 3). A typical accumulated spectrum with the theoretical stick plot is shown in Figure 1.

1,1-Dimethylhydrazine, $(CH_3)_2NNH_2$. This compound reacted to produce a single species which gave a well resolved, complex spectrum made up of a triplet (1:1:1) of septets (1:6:15:20:15:6:1) of triplets (1:1:1) of triplets (1:2:1) with couplings equal to 15.8, 14.2, 9.6, and 6.9 G, respectively. This pattern is consistent with that expected for the 1,1-dimethylhydrazine radical cation which may be represented by a planar structure (4)

(31) J. A. Brivati, J. M. Gross, M. C. R. Symons, and D. J. A. Tinling, *J. Chem. Soc.*, 6504 (1965).

(32) O. Edlund, A. Lund, and Å. Nilsson, *J. Chem. Phys.*, **49**, 749 (1968).

4
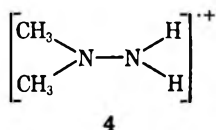
analogous to structure **3**. As before, analysis was facilitated by the use of accumulated spectra such as that shown in Figure 2 with a theoretical stick plot. Studies[21,23-29] of Wurster's Blue-type radical cations such as **1** and **2** and related nitrogen-bearing radicals have revealed that both the $a_N/a_H^{NCH_3}$ and a_N/a_N^{NH} ratios are close to unity. Since the nitrogen hybridization in these Wurster's Blue-type radical cations and that of the hydrazine radical cations of this present work are expected to be very similar, we have assigned the larger nitrogen nuclear hyperfine coupling constant, 15.8 G, to the nitrogen in the $-N(CH_3)_2$ group in structure **4** and the smaller nitrogen nuclear hyperfine coupling, 9.6 G, to that in the $-NH_2$ group.

1,2-Dimethylhydrazine, $CH_3NHNHCH_3$. This compound reacted to give rise to a spectrum composed of a quintet (1:2:3:2:1) of septets (1:6:15:20:15:6:1) of triplets (1:2:1) with hyperfine coupling constants of 13.0, 12.2, and 9.8 G, respectively. This spectrum is attributed to the 1,2-dimethylhydrazine radical cation, $[CH_3NHNHCH_3]\cdot^+$. However, a careful comparison of the theoretical stick plot with the observed spectrum revealed that although the majority of the spectrum was accounted for by this analysis there were many other lines which were not and that these extra lines were real and not due to noise. Moreover, since the 1,2-dimethylhydrazine was freshly generated *in situ* from the dihydrochloride salt, the extra lines were unlikely
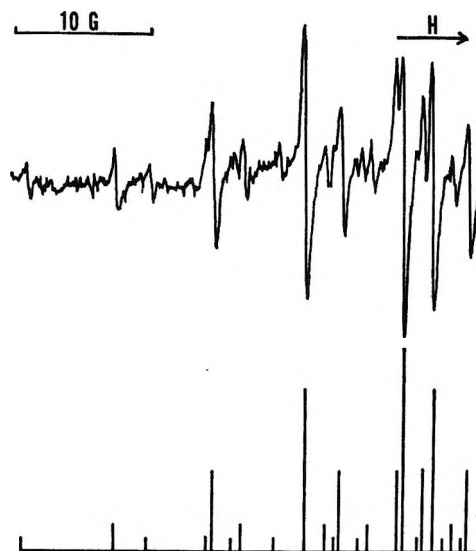

Figure 2. The accumulated first-derivative plot of the low-field end epr spectrum of the 1,1-dimethylhydrazine radical cation: temperature 25°; [TiCl$_3$] in the reducing stream, 0.005 M in 0.1 M sulfuric acid; [H$_2$O$_2$] in the oxidizing stream, 0.15 M; [(CH$_3$)$_2$NNH$_2$] in the substrate stream, 0.05 M; total flow rate 4.0 ml sec^{-1}; pH of the mixed streams, ca. 1.6. The stick plot shows the positions and the theoretical intensity distribution of the lines for the radical cation [(CH$_3$)$_2$NNH$_2$] $^+$, a septet (1:6:15:20:15:6:1) of triplets (1:1:1) of triplets (1:1:1) of triplets (1:2:1).

Figure 1. The accumulated first-derivative plot of the low-field end epr spectrum of the methylhydrazine radical cation: temperature 25°; [TiCl$_3$] in the reducing stream, 0.005 M in 0.1 M sulfuric acid; [H$_2$O$_2$] in the oxidizing stream, 0.15 M; [CH$_3$NHNH$_2$] in the substrate stream 0.2 M; total flow rate 3.5 ml sec^{-1}; pH of the mixed streams, ca. 2.1. The stick plot shows the positions and the theoretical intensity distribution of the lines for the radical cation [CH$_3$NHNH$_2$] $^+$, a quartet (1:3:3:1) of triplets (1:1:1) of triplets (1:1:1) of three doublets (1:1).

to be derived from impurities. This radical can exist in geometrically different forms

5 and **6**
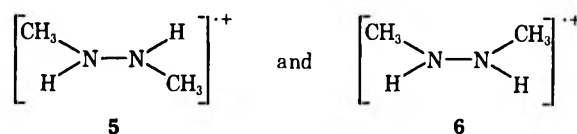
Consequently, we propose that the entire spectrum is that of a mixture of these two isomeric radicals centered on essentially the same g value. The major radical would be expected to be the more stable isomer and energy considerations would demand that this possess a trans configuration about the nitrogen–nitrogen bond as shown for structure **5**. The spectrum of [*cis*-CH$_3$NHNHCH$_3$]$\cdot^+$, **6**, would be expected to have a similar width and structure to those of [*trans*-CH$_3$NHNHCH$_3$]$\cdot^+$, **5**, and this is borne out by observation. Using the [*trans*-CH$_3$NHNHCH$_3$]$\cdot^+$ as a template, the coupling constants for the *cis* isomer were estimated as 14.7, 12.6, and 10.8 G, for a_N, $a_H^{NCH_3}$, and a_H^{NH}, respectively, and the theoretical reconstruction of the spectrum showed that all the extra lines present could be rationalized. Comparison of line heights[17] from the spectra of the two isomers indicated that about 15 mol % of the radical species were [*cis*-CH$_3$NHNHCH$_3$]$\cdot^+$.

The hyperfine coupling constants and g values for the radical cations observed from all four hydrazines are presented in Table I together with comparable data reported by previous workers.[14,15,23-29,31-34]

Table I: Hyperfine Coupling Constants and g Values for the Hydrazine Radical Cations and Related Radical Cations[a]

Radical	a_N^N	$a_N^{N'}$	a_H^{NH}	$a_H^{N'H}$	$a_H^{NCH_3}$	a_N^N/a_H^{NH}	$a_N^{N'}/a_H^{N'H}$	$a_N^N/a_H^{NCH_3}$	g value	Ref
$[NH_2N'H_2]\cdot{}^+$	11.5	11.5	11.0	11.0		1.05	1.05		2.00342	14
	11.5	11.5	11.0	11.0		1.05	1.05		2.00346	15
	11.5	11.5	11.0	11.0		1.05	1.05		2.0030	31
	11.0	11.0	10.4	10.4		1.06	1.06		2.0036	32
	11.54	11.54	11.09	11.09		1.04	1.04		2.0034	b
$[CH_3NHN'H_2]\cdot{}^+$	13.20	10.36	12.19	8.53	14.42	1.08	1.21	0.92	2.0034	b
				8.94			1.16			
$[(CH_3)_2NN'H_2]\cdot{}^+$	15.85	9.56		6.93	14.21		1.38	1.11	2.0035	b
$[trans\text{-}CH_3NHN'HCH_3]\cdot{}^+$	13.03	13.03	9.77	9.77	12.19c	1.33	1.33	1.07d	2.0032	b
$[cis\text{-}CH_3NHN'HCH_3]\cdot{}^+$	14.7	14.7	10.8	10.8	12.6c	1.36	1.36	1.17d	2.0032	b
$[p\text{-}NH_2C_6H_4N'H_2]\cdot{}^+$	5.29	5.29	5.88	5.88		0.90	0.90			25
	5.12	5.12	5.67	5.67		0.90	0.90			26
$[p\text{-}(CH_3)_2NC_6H_4N'H_2]\cdot{}^+$	7.62	4.73		5.16	7.75		0.92	0.98		29
$[p\text{-}(CH_3)_2NC_6H_4N'(CH_3)_2]\cdot{}^+$	6.99	6.99			6.76			1.03d		27
	7.02	7.02			6.74			1.04		28
	7.01	7.01			6.83			1.03		29
$[4,4'\text{-}NH_2C_{12}H_8N'H_2]\cdot{}^+$ e	3.60	3.60	3.97	3.97		0.91	0.91			33
$[4,4'\text{-}(CH_3)_2NC_{12}H_8N'(CH_3)_2]\cdot{}^+$ f	4.88	4.88			4.70			1.04		33
	4.86	4.86			4.74			1.02		29, 34

[a] Coupling constants are in Gauss and their signs are omitted. [b] Present work; the data were taken at 25 ± 2°, the solutions being within the pH range ca. 1.5–2.1; the a values and g values are judged to have a maximum uncertainty of ca. 0.05 G and ca. 0.0002, respectively, except for the case of $[cis\text{-}CH_3NHN'HCH_3]\cdot{}^+$ where the maximum uncertainty in the a values is ca. 0.1 G. [c] $a_H^{NCH_3} = a_H^{N'CH_3}$. [d] $a_N^N/a_H^{NCH_3} = a_N^{N'}/a_H^{N'CH_3}$. [e] $[4,4'\text{-diamino-diphenyl}]\cdot{}^+$. [f] $[4,4'\text{-bis(dimethylamino)-diphenyl}]\cdot{}^+$.

Discussion

There has been considerable interest in the measurement of isotropic hyperfine nitrogen-14 couplings in charged and neutral nitrogen-bearing radicals and the relation of such couplings to the π-electron spin density distribution in these species.[21,35-59] Two chief approaches have been used to describe these hyperfine coupling constants. The first, by analogy with the Karplus and Fraenkel[60] theory of carbon-13 interactions, proposes that the coupling constant, a_N, for an sp²-hybridized nitrogen atom directly bonded to three atoms, X_i, be described by

$$a_N = \left(S_N + \sum_{i=1}^{3} Q_N^{NX_i}\right)\rho_N^\pi + \sum_{i=1}^{3} Q_N^{X_iN}\rho_{X_i}^\pi \quad (4)$$

where S_N represents the direct spin polarization contribution of the π-electron spin density on the nitrogen atom, ρ_N^π, to the 1s orbital of the nitrogen atom and the Q_N terms represent the indirect spin polarization contribution of either ρ_N^π or the π-electron spin density on atom X_i, $\rho_{X_i}^\pi$, to the 2s orbital of the nitrogen atom. The second, more simple approach describes this coupling by a linear McConnell-type relationship[61] to ρ_N^π

$$a_N = Q_N^N \rho_N^\pi \quad (5)$$

Although both descriptions have been successful, when applied to homologous series of such radicals, the first appears to be the more so. The main feature of these studies has been to show that the dominant contribution to the hyperfine coupling constant of the nitrogen is due to the π-electron spin density on that nitrogen atom (which readily explains the success of the second description for some radicals) with smaller contributions from π-electron spin densities on neighboring atoms.

(33) P. Smejtek, J. Honzl, and V. Metalova, *Collect. Czech. Chem. Commun.*, **30**, 3875 (1965).

(34) J. M. Fritsch and R. N. Adams, *J. Chem. Phys.*, **43**, 1887 (1965).

(35) (a) R. L. Ward, *J. Amer. Chem. Soc.*, **83**, 3623 (1961); (b) *ibid.*, **84**, 332 (1962).

(36) A. Carrington and J. dos Santos-Veiga, *Mol. Phys.*, **5**, 21 (1962).

(37) N. M. Atherton, F. Gerson, and J. N. Murrell, *ibid.*, **5**, 509 (1962).

(38) E. W. Stone and A. H. Maki, *J. Chem. Phys.*, **39**, 1635 (1963).

(39) A. Zweig and A. K. Hoffmann, *J. Amer. Chem. Soc.*, **85**, 2736 (1963).

(40) C. A. McDowell and K. F. G. Paulus, *Mol. Phys.*, **7**, 541 (1964).

(41) B. L. Barton and G. K. Fraenkel, *J. Chem. Phys.*, **41**, 1455 (1964).

(42) E. T. Strom, G. A. Russell, and R. Konaka, *ibid.*, **42**, 2033 (1965).

(43) D. H. Geske and G. R. Padmanabhan, *J. Amer. Chem. Soc.*, **87**, 1651 (1965).

(44) J. C. M. Henning, *J. Chem. Phys.*, **44**, 2139 (1966).

(45) M. T. Jones, *J. Amer. Chem. Soc.*, **88**, 227, 5060 (1966).

(46) J. Q. Adams, S. W. Nicksic, and J. R. Thomas, *J. Chem. Phys.*, **45**, 654 (1966).

(47) P. T. Cottrell and P. H. Rieger, *Mol. Phys.*, **12**, 149 (1967).

(48) C. T. Talcott and R. J. Myers, *ibid.*, **12**, 549 (1967).

(49) T. Kubota, K. Nishikida, H. Miyazaki, K. Iwatani, and Y. Oishi, *J. Amer. Chem. Soc.*, **90**, 5080 (1968).

(50) G. A. Russell, J. McDonnell, and C. Myers, *J. Phys. Chem.*, **72**, 1386 (1968).

(51) J. R. Bolton, "Radical Ions," E. T. Kaiser and L. Kevan, Ed., Interscience, New York, N. Y., 1968, Chapter 1.

Table II: π-Electron Spin Densities for Hydrazine Radical Cations Calculated by HMO Methods and with the Use of Eq 6

Radical	$\rho_N^{\pi\,a}$	$\rho_{N'}^{\pi\,a}$	$\rho_N^{\pi\,b}$	$\rho_{N'}^{\pi\,b}$	$\rho_{CH_3}^{\pi\,b}$	$\rho_N^{\pi\,c}$	$\rho_{N'}^{\pi\,c}$
$[NH_2N'NH_2]\cdot{}^+$	0.500	0.500	0.500	0.500			
$[CH_3NHN'H_2]\cdot{}^+$	0.621	0.379	0.526	0.428	0.046	0.550	0.395^d
$[(CH_3)_2NN'H_2]\cdot{}^+$	0.724	0.276	0.546	0.367	0.044	0.587^e	0.313
$[CH_3NHN'HCH_3]\cdot{}^+$	0.500	0.500	0.462	0.462	0.038	0.441^f	0.441^f

^{a} By the HMO method[62] using an inductive model for the methyl group and assuming $\alpha_N = \alpha_C + (0.75)\beta_{CC}$[36] and $\beta_{NN} = \beta_{CC}$, and, for a methyl-substituted nitrogen atom, $\alpha_{N(CH)_{3n}} = \alpha_N - n(0.50)\beta_{CC}$,[62] where α and β represent the Coulomb and resonance integrals, respectively. ^{b} By the HMO method using a heteroatom model and assuming $\alpha_N = \alpha_C + (0.75)\beta_{CC}$,[36] $\beta_{NN} = \beta_{CC}$ $\alpha_{C(CH_3)} = \alpha_C + (2.00)\beta_{CC}$, and $\beta_{NC(CH_3)} = (0.70)\beta_{CC}$.[62] ^{c} From eq 6 and the NH-proton hyperfine coupling constants in Table I on the assumption that Q_H^{NH} equals $-22.1_8 \pm 0.2$ G, the value found for the $[NH_2NH_2]\cdot{}^+$ radical cation using eq 6 with ρ_N^{π} and a_H^{NH} equal to $^1/_2$ and $-11.0_9 \pm 0.1$ G, respectively. ^{d} With the use of the average of the two values of $a_H^{N'H_2}([CH_3NHN'H_2]\cdot{}^+)$. ^{e} On the assumption that 5.0% of the spin density is localized on each carbon atom in the $[(CH_3)_2NNH_2]\cdot{}^+$ radical cation. ^{f} With the use of the value of a_H^{NH} ($[trans\text{-}CH_3NHN'HCH_3]\cdot{}^+$), this being considered more likely than that of a_H^{NH} ($[cis\text{-}CH_3NHN'HCH_3]$) to be consonant with the assumed value of Q_H^{NH}.

The evaluation of the σ–π or Q parameters for the hydrazinium cations of this present investigation (see Table I) clearly requires a knowledge of the π-electron spin densities. We have gained this knowledge by calculations with the use of our experimentally determined proton hyperfine coupling constants listed in Table I. In these calculations we assumed that, since the hybridization of the nitrogen in all these hydrazine radical cations is expected to be roughly the same, the value of Q_H^{NH} calculated for the $[NH_2NH_2]\cdot{}^+$ radical cation via the McConnell-type relationship

$$a_H^{NH} = Q_H^{NH}\rho_N^{\pi} \qquad (6)$$

where ρ_N^{π} may be taken to equal $^1/_2$ and a_H^{NH} is known by experiment (see Table I), can be employed in conjunction with eq 6 and the appropriate proton hyperfine coupling data in Table I to give reasonable estimates of the required nitrogen π-electron spin densities for the other radical cations of the series. The results of these calculations are listed in Table II.

In addition, Table II presents the results of two sets of simple Hückel molecular orbital, HMO, calculations[36,62] of nitrogen π-electron spin densities for this same series of radical cations. There is reasonable agreement between these π-electron spin densities based on HMO calculations and those obtained with the use of the experimentally determined proton hyperfine coupling data and eq 6. The results of these HMO calculations indicate that methyl substitution on a nitrogen atom, keeping the extent of substitution of the other end of the molecule unchanged, increases the π-electron spin density on that nitrogen and decreases that on the other nitrogen. Such a conclusion is in line with the qualitative trend shown by most of the experimental results (Table I) that the size of the nuclear hyperfine coupling constant of a nitrogen atom increases with the number of methyl substituents on that nitrogen and decreases with the number of methyl substituents on the other nitrogen.

Table I also suggests that the sum of the two nitrogen

nuclear hyperfine coupling constants in a given radical increases with the total number of methyl substituents, and the size of the ratios a_N^N/a_H^{NH} and $a_N^N/a_H^{NCH_3}$ for each nitrogen nucleus increases with the total number of methyl substituents in the radical. These observations highlight the inadequacy of eq 5 to describe nitrogen nuclear hyperfine coupling constants for this series of radical cations.

Application of eq 4 to the unsubstituted nitrogen atom in the series of radical cations $[NH_2N'H_2]\cdot{}^+$, $[CH_3NHN'H_2]\cdot{}^+$, and $[(CH_3)_2NN'H_2]\cdot{}^+$, respectively, yields

$$a_N^{N'} = 11.5\text{ G} = A\rho_{N'}^{\pi} + Q_{N'}^{NN'}\rho_N^{\pi} \qquad (7)$$

$$a_N^{N'} = 10.4\text{ G} = A\rho_{N'}^{\pi} + Q_{N'}^{NN'}\rho_N^{\pi} \qquad (8)$$

and

$$a_N^{N'} = 9.6\text{ G} = A\rho_{N'}^{\pi} + Q_{N'}^{NN'}\rho_N^{\pi} \qquad (9)$$

where

$$A = S_{N'} + 2Q_{N'}^{N'H} + Q_{N'}^{N'N} \qquad (10)$$

Although each of the $S_{N'}$, $Q_{N'}^{N'H}$, $Q_{N'}^{N'N}$, and $Q_{N'}^{NN'}$ terms is assumed to have the same numerical values

(52) M. T. Jones, ref 51, Chapter 6.

(53) T. Yonezawa, T. Kawamura, and H. Kato, *J. Chem. Phys.*, **50**, 3482 (1969).

(54) H. Paul and H. Fischer, *Ber. Bunsenges. Phys. Chem.*, **73**, 972 (1969).

(55) P. D. Sullivan and J. R. Bolton, *J. Mag. Res.*, **1**, 356 (1969).

(56) E. G. Janzen and J. W. Happ, *J. Amer. Chem. Soc.*, **73**, 2335 (1969).

(57) K. D. Sales, *Advan. Free-Radical Chem.*, **3**, 139 (1969).

(58) A. R. Buick, T. J. Kemp, C. T. Neal, and T. J. Stone, *J. Chem. Soc. A*, 1609 (1969).

(59) H. Taniguchi, *J. Phys. Chem.*, **74**, 3143 (1970).

(60) M. Karplus and G. K. Fraenkel, *J. Chem. Phys.*, **35**, 1312 (1961).

(61) A. Carrington, *Quart. Rev. Chem. Soc.*, **17**, 67 (1963).

(62) A. Streitwieser, Jr., "Molecular Orbital Theory for Organic Chemists," Wiley, New York, N. Y., 1961, Chapter 5.

throughout eq 7–9, this is not true for either the ρ_N^{π} or the $\rho_{N'}^{\pi}$ term.

The sign of a_N is assumed[31,32] to be positive and since,[38] for similarly hybridized nitrogen atoms

$$Q_{N'}^{N'N} = -Q_{N'}^{NN'} \tag{11}$$

eq 7 gives $(S_{N'} + 2Q_{N'}^{N'H})$ equal to $+23.1 \pm 0.2$ G as both ρ_N^{π} and $\rho_{N'}^{\pi}$ in the $[NH_2N'H_2]\cdot^+$ radical cation may be taken to equal $^1/_2$. The quoted error in this value and others derived in this Discussion section are the maximum absolute uncertainties based on the assumption that a values have a maximum error of ± 0.1 G, $cf.$ Table I. Substituting in eq 8 this value for $(S_{N'} + 2Q_{N'}^{N'H})$ of $+23.1$ G and the ρ_N^{π} and $\rho_{N'}^{\pi}$ values for the $[CH_3NHN'H_2]\cdot^+$ radical cation found via eq 6 and listed in Table II[63] produces a value for $Q_{N'}^{NN'}$ of $+8.1 \pm 2.4$ G. Similarly, with the use of this same value of $(S_{N'} + 2Q_{N'}^{N'H})$ and those of ρ_N^{π} and $\rho_{N'}^{\pi}$ for the $[(CH_3)_2NN'H_2]\cdot^+$ radical cation calculated via eq 6 which are given in Table II,[64] eq 9 leads to an estimate for $Q_{N'}^{NN'}$ of $+8.2 \pm 1.6$ G. Consequently, throughout the remaining discussion $Q_{N'}^{NN'}$ is assumed to be $+8.2 \pm 2$ G, the average of the two values calculated with the use of eq 8 and 9.

Since eq 6 is inapplicable to the fully substituted nitrogen atom in the $[(CH_3)_2NNH_2]\cdot^+$ radical cation, ρ_N^{π} in this species was estimated in the following manner. The results of those HMO calculations where the presence of methyl groups was taken into account gives values for the π-electron spin density on a methyl group, $\rho_{CH_3}^{\pi}$, in the range 0.046–0.038 (see Table II). The nitrogen π-electron spin densities derived for the $[CH_3NHNH_2]\cdot^+$ radical cation using eq 6 indicate that the value of $\rho_{CH_3}^{\pi}$ in this radical ion is 0.055, and the similar calculations for the $[trans\text{-}CH_3NHNH\text{-}CH_3]\cdot^+$ radical cation give $\rho_{CH_3}^{\pi}$ values of 0.059 for each methyl group. Accordingly, we have estimated $\rho_N^{\pi}([(CH_3)_2NN'H_2]\cdot^+)$ by assuming the unpaired electron to be delocalized to the extent of 5% on each methyl group.

Application of eq 4 to the substituted nitrogen atom in the series of radical cations $[CH_3NHN'H_2]\cdot^+$, $[(CH_3)_2NN'H_2]\cdot^+$, and $[trans\text{-}CH_3NHN'HCH_3]\cdot^+$, respectively, gives equations analogous to eq 7–9

$$a_N^N = 13.2 \text{ G} = \mathbf{B}\rho_N^{\pi} + Q_N^{CN}\rho_C^{\pi} + Q_N^{N'N}\rho_{N'}^{\pi} \tag{12}$$

$$a_N^N = 15.8 \text{ G} = \mathbf{C}\rho_N^{\pi} + 2Q_N^{CN}\rho_C^{\pi} + Q_N^{N'N}\rho_{N'}^{\pi} \tag{13}$$

$$a_N^N = 13.0 \text{ G} = \mathbf{D}\rho_N^{\pi} + Q_N^{CN}\rho_C^{\pi} + Q_N^{N'N}\rho_{N'}^{\pi} \tag{14}$$

where

$$\mathbf{B} = S_N + Q_N^{NC} + Q_N^{NH} + Q_N^{NN'} \tag{15}$$

$$\mathbf{C} = S_N + 2Q_N^{NC} + Q_N^{NN'} \tag{16}$$

and

$$\mathbf{D} = S_N + Q_N^{NC} + Q_N^{NH} + Q_N^{NN'} \tag{17}$$

In line with the assumptions given following eq 7–10, $\mathbf{B}$ and $\mathbf{D}$ are assumed to be identical.

Since eq 12–14 are not linearly independent, an approximation must be made before attempting to determine the terms $\mathbf{B}$ and $\mathbf{C}$. A basis for a suitable approximation is as follows: first, the range of values for Q_N^{CN} in the literature,[35,37,38,41–44,47–49,53,54,58,59] $viz.$ $+14$ to -7 G, suggests that $|Q_N^{CN}|$ is not large and, generally it is agreed that Q_N^{CN} may be a small negative value; second, $\rho_{CH_3}^{\pi}$ and, hence, ρ_C^{π} is small for the radicals of concern here (see Table II). Hence we propose to neglect the product term $Q_N^{CN}\rho_C^{\pi}$ in eq 12–14.

With the use of this simplification, eq 13 now gives for $(S_N + 2Q_N^{NC})$ the value $+31.2 \pm 2$ G by substituting the value -8.2 ± 2 G obtained above[65] for $Q_N^{NN'}$ and the data for ρ_N^{π} and $\rho_{N'}^{\pi}$ derived using eq 6 and listed in Table II. Adding this value of $+31.2$ G to that of $+23.1$ G for $(S_N + 2Q_N^{NH})$ obtained above[66] from eq 7 gives an estimate of the term $(S_N + Q_N^{NC} + Q_N^{NH})$ as 27.1 ± 1 G. The quantity $(S_N + Q_N^{NC} + Q_N^{NH})$ may be directly calculated from eq 12 and 14 by neglecting $Q_N^{CN}\rho_C^{\pi}$ and substituting for $Q_N^{NN'}$ the value -8.2 G and the appropriate values of ρ_N^{π} and $\rho_{N'}^{\pi}$ found using eq 6.[67] This procedure yields values for $(S_N + Q_N^{NC} + Q_N^{NH})$ of $+26.5 \pm 1$ G and $+29.6 \pm 1$ G, respectively, in good agreement with the initial determination of $+27$ G.[68]

From the above equations it is not possible to separately evaluate the terms S_N, Q_N^{NH}, and Q_N^{NC}. Nevertheless, the results of the above, incomplete analysis may still be satisfactorily compared with the comparable data in the literature, as shown below.

(63) All such values of ρ_N^{π} and $\rho_{N'}^{\pi}$ employed may be assigned maximum error limits in accord with that of ± 0.1 G assumed for the a values. Hence, throughout this work, in calculations of the influence of the propagation of experimental errors (D. P. Shoemaker and C. W. Garland, "Experiments in Physical Chemistry," 2nd ed, McGraw-Hill, New York, N. Y., 1967, pp 30–35) on the values of the derived Karplus–Fraenkel parameters, it was necessary to allow for the fact that ρ_N^{π} and $\rho_{N'}^{\pi}$ values were not generally independent of a values.

(64) As discussed in the next paragraph, the calculated value of $\rho_N^{\pi}([(CH_3)_2NN'H_2]\cdot^+)$ depends on that of $\rho_{N'}^{\pi}([(CH_3)_2NN'H_2]\cdot^+)$ and the assumed value of the π-electron spin density on each methyl group, $\rho_{CH_3}^{\pi}$. For the purpose of the error analysis, the latter was taken to be 0.050 ± 0.020.

(65) By analogy with eq 12, we assume that $Q_N^{NN'} = -Q_N^{N'N} = -Q_{N'}^{NN'} = Q_{N'}^{N'N}$. In calculating the propagation of experimental errors arising from the use of eq 14–16, allowance was made for the fact the $Q_N^{NN'}$ value depended on a values.

(66) $(S_N + 2Q_N^{NH})$ is denoted above as $(S_{N'} + 2Q_{N'}^{N'H})$.

(67) Because ρ_N^{π} and $\rho_{N'}^{\pi}$ in eq 14 are equal, the value of $(S_N + Q_N^{NC} + Q_N^{NH})$ found with the use of eq 14 happens not to depend on that assumed for $Q_N^{NN'}$.

(68) The maximum error limits for each of the quantities derived from eq 12–14 and cited in this paragraph take no account of the possible contribution of the neglected product term $Q_N^{CN}\rho_C^{\pi}$. It may be readily shown that the observed good agreement between all three calculated values for $(S_N + Q_N^{NC} + Q_N^{NH})$ does not in itself validate the neglect of $Q_N^{CN}\rho_C^{\pi}$, since the contribution of this term largely cancels out in such a comparison. A reasonable estimate of the size of $Q_N^{CN}\rho_C^{\pi}$ is 0.0 ± 0.5 G, from which it follows that the derived values of $(S_N + Q_N^{NC} + Q_N^{NH})$ would have maximum error limits of ± 2 G rather than ± 1 G.

There is considerable variation in size for the many nitrogen-14 $\sigma-\pi$ parameters which have been calculated for nitrogen-bearing radicals. The reasons for this variation have been the subject of a number of discussions[24,46,51,57] which indicate that the observed variation may be largely an artifact of the semiempirical calculation procedures employed. These procedures commonly make use of experimentally observed proton coupling constants, causing the calculated nitrogen-14 $\sigma-\pi$ parameters to depend upon the assumed sizes of other $\sigma-\pi$ parameters or theoretically calculated π-electron spin densities, when they depend on the values chosen for the heteroatom parameters employed in the particular theory. The nitrogen-14 $\sigma-\pi$ parameters in the literature fall roughly into two groups defined by the size of Q_N^{CN} which is either about $+10$ G or about zero and probably negative. A negative value for Q_N^{CN} is preferred on theoretical grounds.[53] Moreover, in a few instances,[38,41] it has been possible to evaluate Q_N^{CN} without making assumptions about the sizes of other $\sigma-\pi$ parameters and without using theoretically calculated π-electron spin densities. Such Q_N^{CN} values are found to be about zero. One such low value of Q_N^{CN}, equal to -2 ± 2 G, together with self-consistent values for other $\sigma-\pi$ parameters, have been obtained by Stone and Maki[38] from a study of several o- and p-polyazine radical anions, e.g., those from pyridazine and pyrazine, respectively.

These parameters have been applied with reasonable success to many other radical anions, including those from azodicarbononitrile,[45] [NCN:NCN]·⁻, and trans-azobenzene,[42] [trans-C₆H₅N:NC₆H₅]·⁻, and they appear to be the most complete set relevant to the species we have studied.

Stone and Maki[38] were able to calculate $(S_N + 2Q_N^{NC})$ as being equal to 30.9 ± 2 G. This agrees well with out reported value for $(S_N + 2Q_N^{NC})$ of $+31.2 \pm 2$ G[69] based upon the use of eq 13. Our two values for $(S_N + Q_N^{NC} + Q_N^{NH})$ found with the use of eq 12 and 14 may be combined with that of $+23.1$ G for $(S_N + 2Q_N^{NH})$ to give 33.9 ± 2 G[69] and 36.1 ± 2 G,[69] respectively, for $(S_N + 2Q_N^{NC})$. These also agree with the value of Stone and Maki for $(S_N + 2Q_N^{NC})$.

Generally, previous investigations have found that a self-consistent set of nitrogen-14 $\sigma-\pi$ parameters exists for a homologous series of radicals. The results of this present study seem to accord with these general conclusions.

(69) This error limit would be ± 4 G if $Q_N^{CN}\rho_C^\pi$ is assumed to be 0.0 ± 0.5 G (see ref 68).

Molecular Conformation of 1,3,5-Trinitrohexahydro-s-triazine

(RDX) in Solution

by Alain Filhol,

Laboratoire de Cristallographie et de Physique cristalline, associé au C.N.R.S., Faculté des Sciences, 33-Talence, France

**Claude Clement, Marie-Thérèse Forel,* Jean Paviot, Madeleine Rey-Lafon,
Georges Richoux, Claire Trinquecoste,**

Laboratoires de Chimie Physique, associés au C.N.R.S., Faculté des Sciences, 33-Talence, France

and Jean Cherville

BP2, 33-Le Barp, France   (Received December 29, 1970)

This study using several different methods, *viz.*, infrared, Raman, and nmr spectroscopy, dipole moment, and depolarized Rayleigh scattering measurements, and INDO calculations, suggests that the RDX molecule has approximate C_{3v} symmetry in solution, with some distortion associated with the NO_2 groups. The ring undergoes rapid interconversion in which the cyclic nitrogens oscillate about the planar (sp^2) position.

Introduction

Although the crystal structure of 1,3,5-trinitrohexahydro-s-triazine (hexogen or RDX or cyclonite) has been determined,[1] the geometry of the molecule in solution is unknown. Some investigations have indicated that the molecular structures must be different in these two states.[2,3] It is therefore of interest to study RDX solutions in order to specify the difference in molecular conformation between the two states and to determine the effect of intermolecular forces in the crystal on the molecular geometry.

This paper presents the results obtained by infrared, Raman, and nmr spectroscopy, dipole moment, depolarized Rayleigh scattering measurements, and INDO (Intermediate Neglect of Differential Overlap) calculations for the RDX molecule in solution. However, certain of the parameters necessary for the definition of the molecular conformation are deduced from earlier structural investigations of the crystalline solid.

I. Structure

The crystal structure of RDX was determined by Harris and Reed[1] and refined by Filhol.[4] The ring is in the "chair" conformation, and the molecule occupies a site of symmetry C_1. However, the bond lengths and angles are such that one of the planes formed by a methylene group and a N–N bond opposite it is approximately a plane of symmetry. The angle δ defined in Figure 1, which determines the geometry of the nitramine groups, takes on the values 21.5, 33, and 32.4°. Thus, the hybridization of the nitrogen atoms can be regarded as intermediate between sp^2 ($\delta = 0°$) and sp^3 ($\delta = 54°44'$). In the RDX–sulfolane complex pre-

pared by Michaud, *et al.*,[5] whose structure was established by Rerat and coworkers,[3] one of the $\frac{C}{C}{>}N_1{-}N_2{<}\frac{O}{O}$ groups in nearly planar ($\delta = 7°$). In this case, then, the state of hybridization of the cyclic nitrogen is close to sp^2.

Recently, Orloff, *et al.*,[2] have calculated the uv absorption spectra of four possible conformations of RDX using the CNDO/2 method. These authors concluded that the most reasonable conformation of the molecule in solution is that of the "chair" with three planar $\frac{C}{C}{>}N_1{-}N_2{<}\frac{O}{O}$ groups (symmetry C_{3v}).

II. Experimental Methods

The solvents used in this work were of spectroscopic purity. The RDX was provided by the "Poudrerie Nationale de Sorgues." It was purified by precipitation from acetone solution by the addition of water, followed by recrystallization from acetone. Finally, optically detectable impurities were eliminated by boiling the product in acetone solution in the presence of activated charcoal. The purified sample exhibited only one peak in its high-resolution nmr spectrum.

(1) P. M. Harris and P. Reed, AFSOR. TR. 59. 165, Ohio State University, 1959.

(2) M. K. Orloff, P. A. Mullen, and F. C. Rauch, *J. Phys. Chem.*, **74**, 2189 (1970).

(3) B. Rerat, J. Berthou, A. Laurent, and C Rerat, *C. R. Acad. Sci. Ser. C*, **267**, 760 (1968).

(4) A. Filhol, Engineering Doctoral Thesis, University of Bordeaux, Talance, France, 1970.

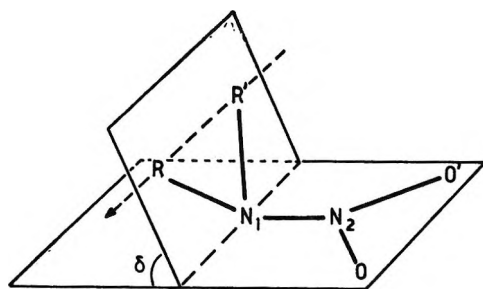(5) C. Michaud, H. Merx, G. Poulain, and S. Lepage, *C. R. Acad. Sci., Ser. C*, **276**, 652 (1968).

Figure 1. Geometry of the nitroamine group.

Figure 2. Thermogram of melting and decomposition of RDX.

The point at which fusion of RDX begins was found at 201.5 ± 1° using differential microcalorimetry CEA "CPC 600" with a heating rate of 2° min⁻¹ (Figure 2). This value might seem low, since McCrone[6] reported 205° and Orloff, et al.,[2] found a value of 204.5–205° by microscopic determination. However, McCrone did not indicate the method used, while Orloff, et al., did not specify the rate of heating.

The Raman spectra were obtained with a Coderg PH-1 instrument using the 6328.17-Å line of an He–Ne laser, while the infrared spectra were recorded on a Perkin-Elmer Model 225 spectrometer. The frequency precision is in all cases ±2 cm⁻¹. The nmr spectra were measured with a Varian Type A-60 instrument. The molecular optical anisotropy was determined by depolarized Rayleigh scattering using a "Gamma diffusomètre E.L.A."

The atomic positions for various molecular conformations were calculated using a Fortran II program on the IBM 1620 computer at the University of Bordeaux. The calculations by the INDO method were carried out with the aid of QCPE program number 144 with help of Messrs. Faurens and Foucault. Molecular optical anisotropies were calculated by means of a Fortran IV program, written by Mr. Revesche.

III. Spectroscopic Results

A. Infrared and Raman. The infrared and Raman spectra of RDX in the crystal and in solution are shown in Figure 3 from 3200 to 200 cm⁻¹. A complete vibrational assignment has been proposed by Rey-Lafon, et al.[7] The fact that the spectrum of the solution does not exhibit more bands than that of the solid suggests the existence of but one rotational isomer in solution.

A more detailed analysis of the experimental results yields, in addition, some information concerning the geometry of RDX in solution. The interpretation of the spectra of single crystals assuming C_s site symmetry allows the vibrations to be classified under species A' and A''. Observed doublets consisting of one A' and one A'' component should reduce to a single, doubly degenerate vibration in the spectrum of the solution if the molecular geometry has C_{3v} symmetry. This result is indeed observed in a number of cases. For example, a doublet near 1430 cm⁻¹, which is assigned to an in-plane methylene bending mode, δ(CH₂), in the spec-
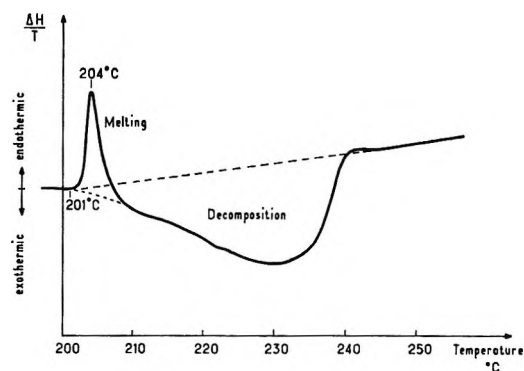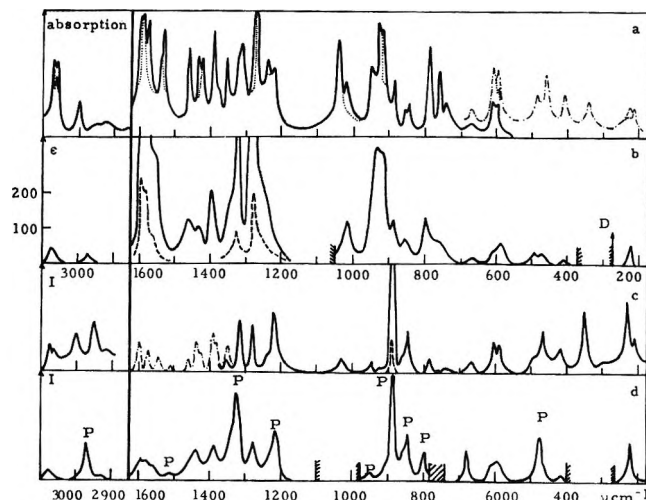

Figure 3. Vibrational spectra of RDX between 3200 and 200 cm⁻¹. a and b, infrared spectra of RDX as a powder and in acetonitrile solution (CH₃CN and CD₃CN), · · · · · · · ·, spectrum of an oriented polycrystalline film deposited on a cesium iodide window. c and d, Raman spectra of RDX as a powder and in dimethyl sulfoxide solution (DMSO and DMSO-d₆): –·–·–·–, $I \times 2$; –––––––––, $I/2$. Slit widths for the Raman spectra were chosen as follows: 2 cm⁻¹ for solution spectra; 6 cm⁻¹ between 3200 and 2800 cm⁻¹ and 4 cm⁻¹ between 1700 and 200 cm⁻¹ for spectra to the powder.

trum of the solid corresponds to a single band at 1431 cm⁻¹ in the spectrum of the solution. An analogous effect is observed for the doublet near 1030 cm⁻¹ and the corresponding band at 1020 cm⁻¹, which is due to a skeletal mode. However, a few exceptions are observed for modes associated with the NO₂ groups. The broad feature observed between 1600 and 1500 cm⁻¹ in the spectrum of the solution, which is assigned to the antisymmetric stretching vibration $\nu_a(NO_2)$, is composed of an intense absorption with two shoulders, while only a single band would be expected. Similarly, between 670 and 500 cm⁻¹ the spectrum of the solution exhibits three maxima, all of which are assigned to in-plane rocking of the three NO₂ groups, $\rho(NO_2)$. Again,

(6) W. C. McCrone, *Anal. Chem.*, **7**, 954 (1950).

(7) M. Rey-Lafon, C. Trinquecoste, R. Cavagnat, and M. T. Forel, submitted for publication in *J. Chim. Phys.*

only a single $\rho(NO_2)$ band should be observed in the molecule possesses a ternary symmetry axis.

From the above results the ring of the RDX molecule appears to have C_{3v} symmetry, the NO_2 groups being slightly distorted.

B. Nuclear Magnetic Resonance. In all solvents used the room temperature, high-resolution nmr spectra of RDX consist of a single line situated at 4.108 ppm with respect to tetramethylsilane. When the temperature is increased from $-75°$ to $+75°$ only a broadening of the line is observed. This effect is due to the interaction of the proton with the quadrupole moments of the nitrogen nuclei.

The existence of only a single line over the temperature range investigated can be accounted for either by a planar ring or by a rapid interconversion of two or more cyclic structures. This interpretation is similar to the conclusion drawn from an nmr study of derivatives of 1,3,5-hexahydro-s-triazine by Lehn, *et al.*[8] These authors also observed that the interconversion persists at progressively lower temperatures as the masses of the substituents on the cyclic nitrogens become heavier. Moreover, using epr spectroscopy down to $-30°$, Darnez and Paviot[9] observed the equivalence of the four protons in the radical.

$$
\begin{array}{ccc}
 & CH_2\!-\!NNO_2 & \\
\diagup & & \diagdown \\
\cdot N & & CH_2 \\
\diagdown & & \diagup \\
 & CH_2\!-\!NNO_2 &
\end{array}
$$
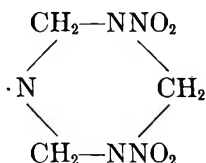
IV. Determination of Conformation

A. Assumptions and Choice of Parameters. Various structures which are compatible with the experimental results presented above have been chosen as the bases for conformational calculations. All structures considered thus possess a ring of the "chair" form and C_{3v} symmetry, with each nitramine group parallel to the line joining the two respective α carbon atoms.

Studies of nitramines show that, in general, two parameters vary with the molecular conformation, namely, the angle δ and the N–N bond length. However, these parameters are related, as shown in Figure 4.[10–12] The other geometrical parameters, which are only slightly dependent on conformation, were chosen as follows: (a) C–N = 1.45 Å, N–O = 1.21 Å, and < ONO = 126°, which are average values measured for crystalline nitramines;[4,10] (b) C–H = 1.09 Å and < HCH = 109°28′, which are assumed values; and (c) < NCN = 109°28′, as its variation as a function of δ is unknown.

B. Calculations by the Method of INDO. The method proposed by Pople[13] has been used to calculate the dipole moments and the total energies, E_t, of the conformations considered. The results are shown in Figure 5. The curve of $E_t(\delta)$ has a minimum at $\delta = 0$ and $E_t = -5313.4$ eV. The minimum is quite shallow,
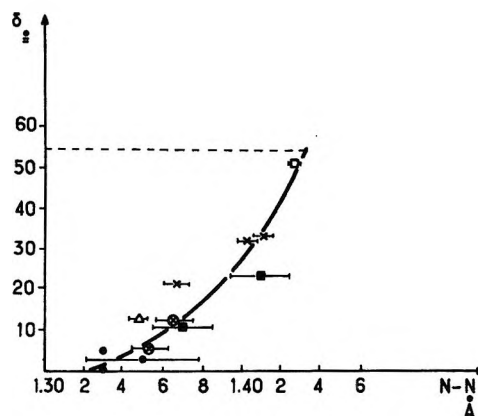

Figure 4. N–N bond length as a function of δ for various nitramines: $\otimes$, HMX α;[10] HMX β;[10] X, RDX,[1] nitramine;[10] $\triangle$, tetryl;[12] $\bullet$, nitroguanidine, dimethylnitramine, ethylene dinitramine.[12]
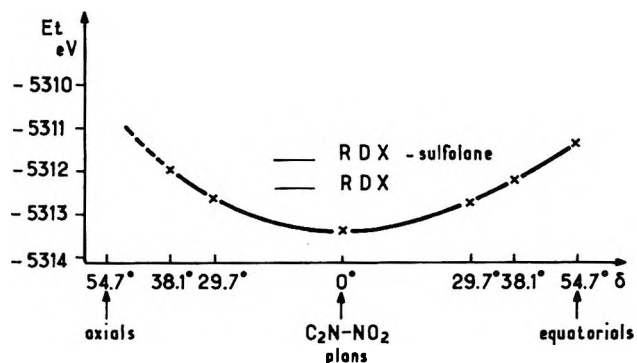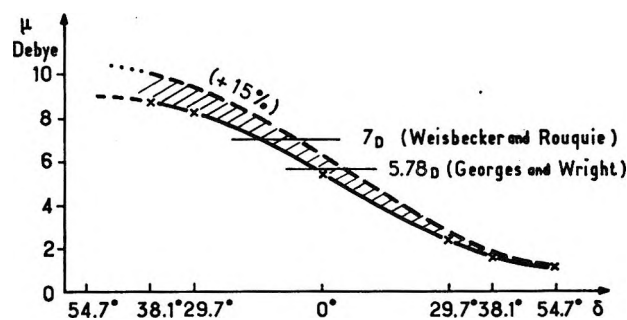
Figure 5. Total energies E_t and dipole moment μ as functions of δ calculated by the INDO method.

as a variation in δ of 10° corresponds to an increase in E_t of only about 1 kcal/mol.

(8) J. M. Lehn, F. C. Riddell, B. J. Price, and J. O. Sutherland, *J. Chem. Soc.*, 387 (1967).

(9) C. Darnez and J. Paviot, *Int. J. Radiat. Phys. Chem.*, in press.

(10) H. H. Cady, A. C. Larson, and D. T. Cromer, *Acta Crystallogr.*, 16, 617 (1967).

(11) J. K. Tyler, *J. Mol. Spectrosc.*, 11, 39 (1963).

(12) See Table I. O. Bastiansen, *Acta Crystallogr.*, 3, 46 (1950); E. G. Cox and W. Costain, *Nature*, 160, 13 (1947); F. J. Llwellyn and F. E. Whitmore, *J. Chem. Soc.*, 262, 1316 (1948); J. M. Bryden, L. A. Burkordt, E. W. Hughes, and J. Donahue, *Acta Crystallogr.*, 9, 573 (1956); H. H. Cady, *ibid.*, 23, 601 (1957).

(13) J. A. Pople, D. L. Beveridge, and P. A. Dobosh, *J. Chem. Phys.*, 47, 2026 (1967); M. S. Gordon and J. A. Pople, *ibid.*, 49, 4643 (1968).

Within the limitations of the assumptions made in IV-A the conformation corresponding to this minimum total energy is that of an idealized "chair" ring, with three planar $\mathrm{^C_C{>}N_1{-}N_2{<}^O_O}$ groups (δ = 0°) and N–N distances equal to 1.32 Å. This conformation will be designated I. Its total energy is 27 and 22 kcal/mol less than those observed for the RDX conformations in the sulfolane complex and in the crystal, respectively. It should be noted that Orloff,[2] using the method of CNDO/2, found a difference of 7 kcal/mol between the energy of I and that observed for the crystal. However, he did not specify the values of the angles and bond lengths used for I.

The dipole moment calculated for I is 5.48 D, while George and Wright[14] found 5.78 D for RDX in solution in dioxane and Weisbecker and Rouquié[15] estimated a value of 7 D in the case of polar solvents. Considering the usual results of theoretical determinations of dipole moments, the agreement of these values is satisfactory. Furthermore, the same calculations carried out on nitramine and dimethylnitramine, whose structures and dipole moments are well known, show that the method of INDO yields values which are approximately 15% too low. It can be concluded, therefore, that for these calculations conformations near I (δ = 0) are satisfactory for both the total energy and the dipole moment.

C. Molecular Optical Anisotropy. The usual method of structure determination has been employed, that is, the molecular optical anisotropy is determined by measurements of depolarized Rayleigh scattering and compared with theoretical results for various structures. The theoretical optical anisotropy for a given conformation is determined using values of the anisotropy of bonds or groups of bonds taken from analogous molecules.

1. Experimental Results. The experimental results shown in Table I show that the molecular optical anisotropy of RDX is, within experimental error, independent of the nature of the solvent in which RDX can be dissolved. Recent work has shown that in such cases it can be assumed that there is no orientational correlation between the solute and solvent molecules.[16] Hence, for sufficiently low concentrations the measured molecular optical anisotropy is that of the "free" molecule.

Table I

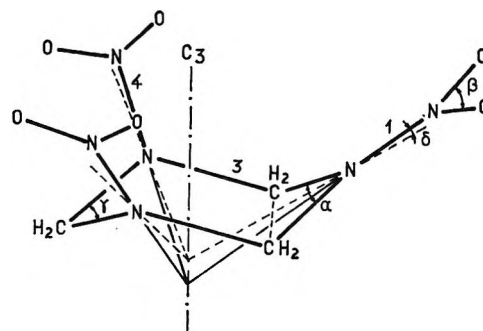| Solvent	Optical molecular anisotropy Å
Acetonitrile	30 ± 4
Acetone	36 ± 4
Cyclohexanone	35.6 ± 0.4
Dimethyl sulfoxide	34.6 ± 1.0

Figure 6. Conformation of the RDX molecule in solution: angles, α = 120°, β = 109° 28', δ = 0°; bond lengths, N–N 1.34 Å, N–O 1.21 Å, C–N 1.45 Å, C–H 1.09 Å.

2. Calculated Optical Anisotropy. The calculation is carried out following the optical-valence theory by tensor addition of optical anisotropies γ_i of the bonds or groups of bonds which make up the molecule. The geometry is that described in IV-A. The optical anisotropy parameters of the cyclic C–N bond and the N–NO$_2$ groups, as determined from studies of related molecules, were used to calculate the molecular optical anisotropy of RDX as a function of δ. The parameters employed in the present calculations were[17]

$$\gamma_{CN(ring)} = 1.11 \text{ Å}^3$$

$$\gamma_{N-NO_2(sp^2)} = 4.05 \text{ Å}^3$$

$$\gamma_{N-NO_2(sp^3)} = 3.68 \text{ Å}^3$$

It has been shown several times[18] that nonbonded electrostatic interactions must be considered in the calculation of optical anisotropy. In the case of the RDX molecule, one must take into account the nonbonded interactions of the type (1)...(3) between N–NO$_2$ bonds and CN or CH bonds and the nonbonded interactions (1)...(4) between N–NO$_2$ bonds (Figure 6). The calculated and experimental values of optical anisotropy are in good agreement when δ takes a value very near of 0°.

Conclusion

This study implies that the RDX molecule has approximate C_{3v} symmetry in solution, with some distortion associated with the NO$_2$ groups. The ring undergoes rapid interconversion in which the cyclic nitrogens

(14) M. V. George and V. F. Wright, *J. Amer. Chem. Soc.*, **80**, 1200 (1958).

(15) A. Weisbecker and A. M. Rouquie, *C. R. Acad. Sci. Ser. C*, **270**, 572 (1970).

(16) C. Such, C. Clement, and P. Bothorel, *ibid.*, **271**, 228 (1970); P. Bothorel, Preprints, 42nd National Colloid Symposium, *J. Colloid Sci.*, 529 (1968).

(17) C. Clement and P. Bothorel, *C. R. Acad. Sci. Paris*, 258 (1964), (for C–H bond); G. Richoux and C. Clement, *J. Chim. Phys.*, in press.

(18) A. Caristan, Doctoral Thesis No. A.O. 1344, University of Bordeaux (1968); A. Caristan and P. Bothorel, *J. Chem. Phys.*, **66**, 740 (1969); C. Clement, A. Caristan, and P. Maraval, *ibid.*, **67**, 542 (1970); P. Foulani and C. Clement, *Bull. Soc. Chim.*, **2**, 450 (1970).

oscillate about the planar (sp²) position with $\delta_{max} \sim$ 0°. The N-N bonds are short—approximately 1.34 Å; this conformation is very different from that determined by Harris, et al.,[1] in the solid and studied theoretically by Stals.[19] The latter author showed that the cohesion of the crystal arises from electrostatic forces and not by directional bonds. This state results principally from an equilibrium between attractive and repulsive forces acting between intra- or intermolecular nitramine groups.

It has been shown here that the effect of these forces is to bring about a change in molecular conformation and in particular to modify the state of hybridization of the cyclic nitrogens. The result of this effect is an increase in the total energy of the molecule in the crystal with respect to that of the molecule free or in solution.

(19) J. Stals, *Aust. J. Chem.*, 22, 2505, 2515 (1969).

Association Equilibria of Silver and Chloride Ions in Liquid Ammonium

Nitrate-Water Mixtures. I. The Molar Ratio Range H₂O : NH₄NO₃

0.4-1.4 at 110°

by Mordechai Peleg

Department of Inorganic and Analytical Chemistry, Hebrew University of Jerusalem, Israel (Received December 14, 1970)

Publication costs borne completely by The Journal of Physical Chemistry

The electromotive force of the cells Ag|NH₄NO₃, H₂O, AgNO₃||NH₄NO₃, H₂O, AgNO₃, NH₄Cl|Ag as a function of the concentrations of water, silver nitrate, and ammonium chloride has been measured at a temperature of 110°. Association constants of the silver ion with the chloride ion were calculated to vary between 2580 and 1760 (mol/mol of nitrate)⁻¹ for molar ratios of water to ammonium nitrate ranging between 0.4 and 1.4. The results are discussed in terms of a quasi-lattice model for highly concentrated aqueous solutions.

Introduction

Interest has lately centered on the investigation of concentrated aqueous solutions, implying by "concentrated solutions" not more than about six moles of water per mole of salt.

Angell[1] has proposed that fused hydrated salts such as calcium nitrate tetrahydrate and magnesium chloride hexahydrate might be treated as molten salts with large cations, with the water bound to the cation. The proposal of a hydrated cation has been further substantiated by studies of transport properties[2,3] and volumetric properties[4] in Ca(NO₃)₂4·H₂O and in its mixtures with KNO₃ and by spectrophotometric studies of Ni(II) in aqueous magnesium chloride solutions.[5] With less than 4-6 mol of water per mole of salt there is insufficient water to form complete hydration sheaths about the ions, interactions like those in molten salts must obtain and as stated by Braunstein[6] no description of these systems is possible without consideration of ion–ion, ion–water, and water–water interactions.

Braunstein[6,7] has further proposed a quasi-lattice mode based on that of molten salts to explain hydration and association equilibria in these highly concentrated aqueous solutions. The ammonium nitrate–water system is one of the simplest systems (from a practical point of view) for the examination of highly concentrated aqueous solutions. It is possible to cover the entire range from water to anhydrous molten salt (using several temperatures) without having recourse to high

(1) C. A. Angell, *J. Electrochem. Soc.*, 112, 1224 (1965).

(2) C. T. Moynihan, *J. Phys. Chem.*, 70, 3399 (1966).

(3) J. Braunstein, L. Orr, A. R. Alvarez-Funes, and H. Braunstein, *J. Electroanal. Chem.*, 15, 337 (1967).

(4) J. Braunstein, L. Orr, and W. Macdonald, *J. Chem. Eng. Data*, 12, 415 (1967).

(5) C. A. Angell and D. M. Gruen, *J. Amer. Chem. Soc.*, 88, 5192 (1966).

(6) J. Braunstein, "Ionic Interactions: Dilute Solutions to Molten Salts," Sergio Petrucci, Ed., Academic Press, New York, N. Y., in press.
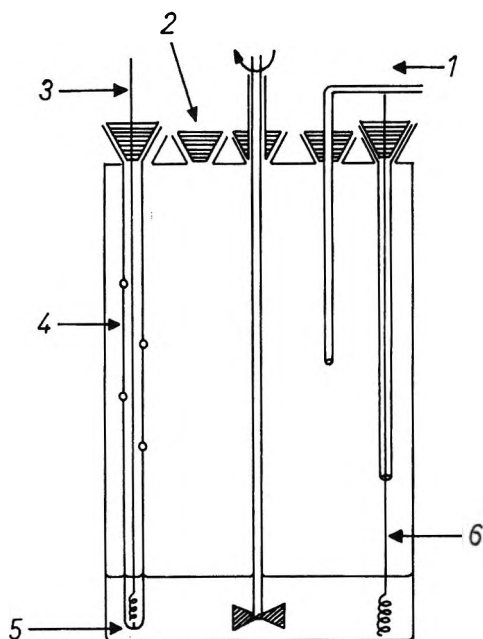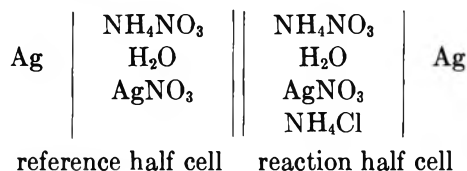
(7) J. Braunstein, *J. Phys. Chem.*, 71, 3403 (1967).

Figure 1. Electrochemical cell: 1, water vapor; 2, addition port; 3, silver wire; 4, reference electrode compartment; 5, asbestos fiber; 6, indicating electrode.

pressures or high temperatures.[8] It was decided to utilize the ammonium nitrate–water system as a medium for investigating the association equilibria of the silver ion and the chloride ion at various water–salt ratios and at different temperatures. The present paper reports the work carried out at 110°.

Experimental Section

Electromotive force measurements were made on the concentration cell

$$
\text{Ag} \left|
\begin{array}{c} NH_4NO_3 \\ H_2O \\ AgNO_3 \end{array}
\right\|
\begin{array}{c} NH_4NO_3 \\ H_2O \\ AgNO_3 \\ NH_4Cl \end{array}
\right| \text{Ag}
$$

reference half cell   reaction half cell

The apparatus was set up as shown in Figure 1. The electrochemical cell consisted of an 8-cm diameter vessel containing five inlets that provided for the introduction of the indicating silver electrode, the reference electrode, the stirrer, quantities of the complexing (chloride) ion, and the passage of water vapor over the solution.

A continuous stream of nitrogen containing water vapor at the same vapor pressure as that of the solution under examination was passed through the cell in order to reduce evaporation of the water. The data of Campbell[9] were used to calculate the vapor pressure over the solution. The indicating electrode was a 1-mm diameter high-purity silver wire wound into the form of a spiral. The reference compartment consisted of a 1-cm diameter tube with an asbestos fiber or glass frit sealed into the lower end. Small holes were pierced high up

in the tube so that the water vapor passing over the main solution would also blanket the reference solution, thus preventing change in the water content.

Procedure. A weighed amount of ammonium nitrate was added to the cell together with a known volume of water (triple distilled) and a known quantity of silver nitrate. The cell was stoppered and suspended in a well stirred oil bath thermostated at 110 ± 0.2°. After reaching thermal equilibrium, the empty reference compartment was placed in position and slowly filled over a period of about 1 hr with the ammonium nitrate–water–silver nitrate solution. The indicating silver electrode was then introduced into the cell and the reference electrode wire into the reference compartment. After about 15 min the difference of potential observed between the two compartments was less than 1 mV. The stream of water vapor passing over the solution and the rate of stirring were adjusted until the potential of the cell remained constant to within ±0.1 mV over a period of 0.5 hr. Addition of chloride ions in the solid form was done by preparing a solid solution of ammonium chloride in ammonium nitrate. Attainment of equilibrium on addition of the chloride took approximately 5 min.

On completion of a run (which took no longer than 2 hr from the first addition of chloride ion) portions of the still liquid solution were quickly transferred into glass-stoppered bottles. These samples were then analyzed for water content by heating in an open vessel at 75° to constant weight. Owing to the low values of the solubility product for silver chloride ($\sim 10^{-9}$ mol fraction) in the solvent studied,[10] low concentrations of silver and chloride ions had to be employed. The silver ion concentration was thus limited to a range between 1×10^{-5} and 4×10^{-5} mol Ag$^+$/mol ammonium nitrate (1.25×10^{-4} to 5×10^{-4} mol Ag$^+$/kg ammonium nitrate). Preliminary experiments showed that the Nernst equation was obeyed in this region with respect to the stoichiometric concentration of silver (Figure 2).

The concentration units are given as mole ratios R, where

$$ R_{Ag^+} = R_{AgNO_3} = n_{AgNO_3}/n_{NH_4NO_3} $$

$$ R_{Cl^-} = R_{NH_4Cl} = n_{NH_4Cl}/n_{NH_4NO_3} $$

$$ R_{H_2O} = n_{H_2O}/n_{NH_4NO_3} $$

where n is the number of moles of AgNO$_3$, NH$_4$NO$_3$, NH$_4$Cl, and H$_2$O.

Results

The emf of the concentration cell was measured as a function of changing concentrations of silver ion and water at 110°. The Nernst equation is obeyed by the

(8) I. L. Millican, A. F. Joseph, and T. M. Lowry, *J. Chem. Soc.*, 959 (1923).

(9) A. N. Campbell, J. B. Fishman, G. Rutherford, T. P. Schaefer, and L. Ross, *Can. J. Chem.*, **34**, 151 (1956).
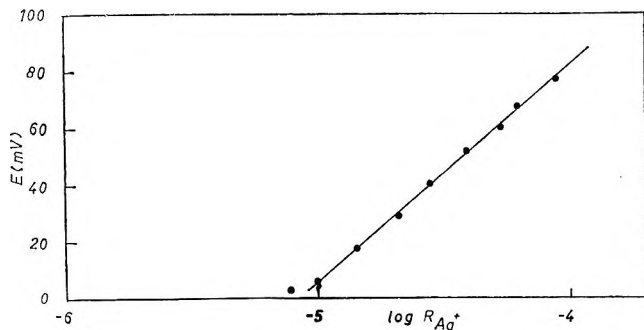
(10) M. Peleg, unpublished work.

Figure 2. Typical Nernst plot for the silver–silver ion electrode in ammonium nitrate–water solvent at 110°.
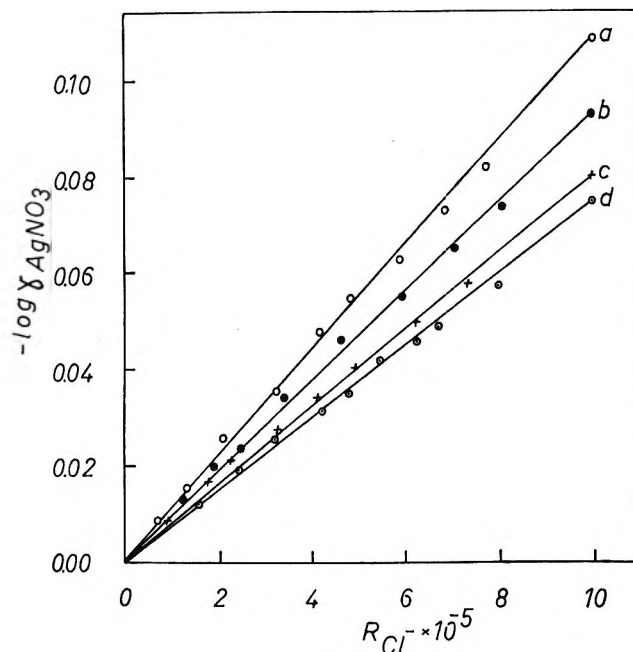

Figure 3. $R_{Ag^+} = 1.25 \times 10^{-5}$ mol/mol of ammonium nitrate: a, $R_{H_2O} = 0.42$; b, $R_{H_2O} = 0.65$; c, $R_{H_2O} = 1.00$; d, $R_{H_2O} = 1.25$.

silver nitrate in the absence of the complexing ion, and the liquid junction potential in such a cell is virtually zero since the concentration of chloride and silver in the solutions is less than 10^{-4} mol ratio and the current is carried virtually entirely by the solvent ions. Therefore, the change in cell emf on addition of chloride ions to the indicating compartment is related to the stoichiometric activity coefficient of silver nitrate by the formula

$$-\ln \gamma_{AgNO_3} = \frac{F}{RT} \Delta E \qquad (1)$$

where ΔE is the difference in cell emf between the presence and absence of chloride.[11] The potentiometric data appear as supplementary material in the microfilm edition.[12] Thermodynamic equilibrium constants for the association reaction $Ag^+ + Cl^- = AgCl$ were calculated by the graphical analysis of the activity coefficient as described by Braunstein[13]

$$K_1 = K_{AgCl} = -\lim_{\substack{R_{NH_4Cl}\to 0 \\ R_{AgNO_3}\to 0}} \left(\frac{\partial \ln \gamma_{AgNO_3}}{\partial R_{NH_4Cl}}\right)_{R_{AgNO_3}} \qquad (2)$$

or

$$K_1 = -\lim_{\substack{R_{NH_4Cl}\to 0 \\ R_{AgNO_3}\to 0}} S_0 \quad \text{where } S_0 = \lim \left(\frac{\partial \ln \gamma_{AgNO_3}}{\partial R_{NH_4Cl}}\right)_{R_{AgNO_3}}$$

It was found difficult to repeat the same solvent composition for different silver concentrations. Thus it was more convenient to obtain plots of $\ln \gamma_{AgNO_3}$ against R_{NH_4Cl} for a fixed silver concentration at several solvent compositions. The limiting slope S_0 was measured as shown in Figure 3 and the values of S_0 were then plotted against R_{H_2O} and the best fitting line was drawn through the results obtained (Figure 4). This procedure was repeated for the other silver compositions. Finally the limiting slope S_0 was plotted against R_{AgNO_3} for various water concentrations and the graph was extrapolated to zero silver concentration, the intercept giving K_1. Values of K_1 at different water concentrations are given in Table I.
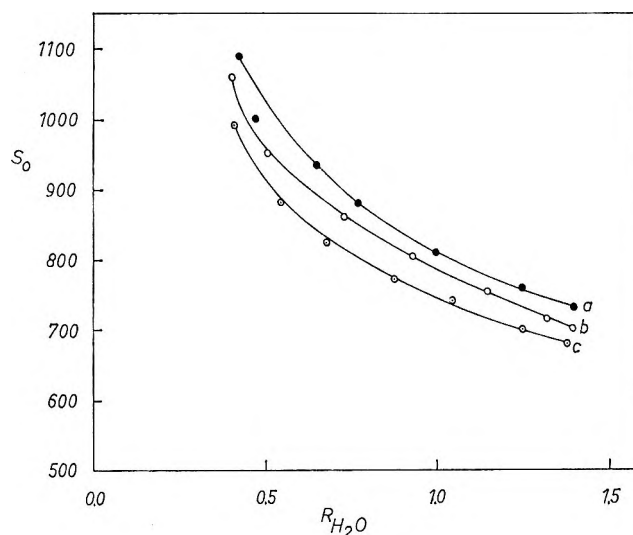
Figure 4. Limiting slope S_0 vs. R_{H_2O}: a, $R_{Ag^+} = 1.25 \times 10^{-5}$; b, R_{Ag^+} 2.50×10^{-5}; c, $R_{Ag^+} = 4 \times 10^{-5}$.

The association constants were also evaluated using the computer method as described by Inman.[14] Results similar to those obtained by the graphical method

(11) J. M. C. Hess, J. Braunstein, and H. Braunstein, *J. Inorg. Nucl. Chem.*, **26**, 811 (1964).

(12) The potentiometric data will appear immediately following this article in the microfilm edition of this volume of the journal. Single copies may be obtained from the Reprint Department, ACS Publications, 1155 Sixteenth Street, N. W., Washington, D. C. 20036. Remit $3.00 for photocopy or $2.00 for microfilm.

(13) J. Braunstein, M. Blander, and R. M. Lingren, *J. Amer. Chem. Soc.*, **84**, 1529 (1962).

(14) D. Inman, I. Regan, and B. Girling, *J. Chem. Soc.*, **59**, 348 (1964).

Table I: Association Constants of Silver Ion with Chloride Ion in Liquid Ammonium Nitrate–Water Mixtures[a]

R_{H_2O}	K_1, (mol/mol ammonium nitrate)$^{-1}$
0.4	2580
0.5	2400
0.6	2310
0.8	2090
1.0	1960
1.2	1830
1.4	1760
	Error ±75
2.0	1675[b]

[a] $T = 110°$. [b] Extrapolated from Gal's results (see ref 16 and 17).

were obtained. Due to the limited range available for changing the chloride concentration ($R_{Cl^-} = 1 \times 10^{-5} \rightarrow 1 \times 10^{-4}$ for low silver concentration, $R_{Cl^-} = 1 \times 10^{-5} \rightarrow 3 \times 10^{-4}$ for the highest silver content) it was observed that the computerized K_1 values obtained varied quite a lot. However, their average values agreed remarkably well with those obtained graphically. It was possible by examining the results from both methods to derive reasonable error limits. An attempt to evaluate high association constants (i.e., for Ag_2Cl^+, $AgCl_2^-$ etc.) using the computer technique yielded error limits greater than the evaluated association contents, so this was not pursued further.

The results show that with decreasing water content the stability of the AgCl complex increases. Hence it appears that as the water molecules are removed it is
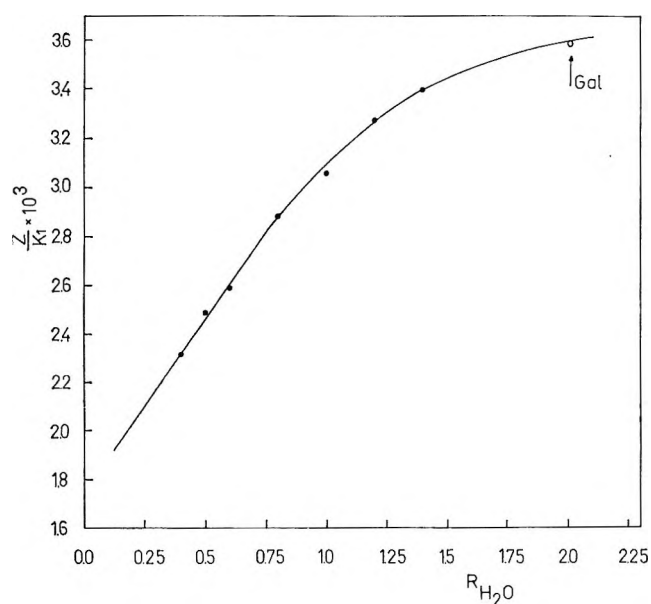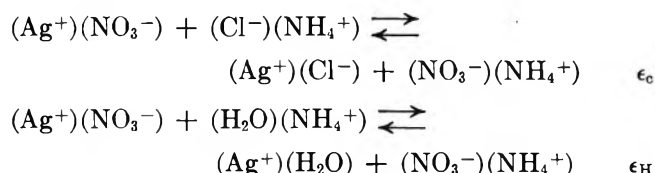
easier for the chloride ion to displace the nitrate ion from the coordination sphere of the silver ion than it is to displace the water dipole. Braunstein[6,7] has proposed a quasi-lattice model to account for the variation with water content of the association constant of the solute cation in very concentrated aqueous solutions. This is based on the quasi-lattice model for molten salts as developed by Blander, et al., and Braunstein.[15]

The basis of the quasi-lattice model is the assumption of two interpenetrating sublattices. The assumptions are made that the cations (deriving from solvent and solute) mix randomly with one another on the sites of the cation sublattice while the anions and the water dipoles occupy sites, although not randomly mixed, on the anion sublattice. Occupancy of the same sublattice by water molecules and anions is equivalent to the assumption that only the cations are hydrated. The association reactions may be interpreted as the exchange of neighbors on the quasi-lattice

$$(Ag^+)(NO_3^-) + (Cl^-)(NH_4^+) \rightleftharpoons$$
$$(Ag^+)(Cl^-) + (NO_3^-)(NH_4^+) \qquad \epsilon_c$$
$$(Ag^+)(NO_3^-) + (H_2O)(NH_4^+) \rightleftharpoons$$
$$(Ag^+)(H_2O) + (NO_3^-)(NH_4^+) \qquad \epsilon_H$$

ϵ_c is the cation–ligand interaction energy and ϵ_H is the cation–water interaction energy.

The statistical thermodynamic evaluation of the association constant based on the Planck–Boltzmann relations leads to the expression

$$1/\alpha + \frac{\beta}{\alpha} R_H = \frac{Z}{K_1 + 1 + \dfrac{Z-1}{1+R_H}} \approx \frac{Z}{K_1} \qquad (3)$$

where $\alpha = e^{-\epsilon_c/kT}$ and $\beta = e^{-\epsilon_H/kT}$; Z is the coordination number, which may have values from 4 to 6, 6 being the value generally chosen. When $R_H = 0$ the equation corresponds to the asymmetric quasi-lattice model of anhydrous molten salts.

Equation 3 has been applied to the present results as shown in Figure 5 for $Z = 6$. The only other results available for the NH_4NO_3–H_2O system are those of Gal,[16] who carried out a series of solubility measurements of silver chloride on the NH_4NO_3–$2H_2O$ composition at various temperatures. Extrapolation of his results to 110° shows agreement with the present results (Figure 5).

By extrapolation of the present results to $R_H = 0$, the pure anhydrous molten salt state, and applying the limiting form of eq 3

$$1/\alpha = Z/K_1 \qquad (4)$$

Figure 5. Plot of z/K_1 vs. R_{H_2O}: $T = 110°$; $K_1 = 1675$ (mol/mol ammonium nitrate)$^{-1}$ at $R_{H_2O} = 2.0$, extrapolated from Gal's results.[16,17]

(15) (a) M. Blander, J. Phys. Chem., **63**, 1262 (1959); (b) M. Blander and J. Braunstein, Ann. N. Y. Acad. Sci., **79**, 838 (1960); (c) M. Blander, J. Chem. Phys., **34**, 432, 697 (1961); (d) J. Braunstein, J. Phys. Chem., **71**, 402 (1967).

(16) I. J. Gal, Inorg. Chem., **7**, 1611 (1968).

a value of ϵ_0 equal to -4.9 ± 0.5 kcal/mol is obtained. This compares with a value of -4.4 kcal/mol estimated by Braunstein[17] from values for silver complex formation in molten alkali nitrate. Thus the present results agree fairly well within experimental limits with existing data.

By measuring the slope of the straight line portion of the graph (Figure 5) it is possible to evaluate ϵ_H in eq 3. The cation–water interaction energy ϵ_{Ag-H_2O} was calculated to be $+0.5 \pm 0.5$ kcal/mol, which corresponds to a nearly random distribution of water between ammonium and silver ions. This agrees with Braunstein's evaluation[17] of Gal's results.[16] Further, the heats of vaporization of water from concentrated aqueous silver nitrate solutions and from concentrated aqueous ammonium nitrate solutions differ by less than 0.1 kcal/mol,[9] suggesting a value near zero for ϵ_{Ag-H_2O}.

The fact that the present results do not agree entirely with the Braunstein equation over the entire concentration range examined may be due to the assumption that only the cations are hydrated. In the case of a concentrated aqueous solution containing lithium ions it can be assumed from the work of Peleg[18] that for low water contents almost all of the water is bound to the cation. However, for a salt such as ammonium nitrate, anion hydration could well exist as suggested by Keenan[19] from his cryoscopic measurements.

It does appear that for water contents of less than 1 mol per mol of salt a straight line is obtained as suggested by Braunstein.[6,7] It seems possible therefore that for the ammonium nitrate system the water molecules up to a water:salt ratio of 1:1 are held by the ammonium cation (the water molecules sit on the anion sublattice) while additional water molecules may hydrate the anion as well. From the work of Kebarle,[20] who studied by mass spectrometry ion–solvent molecule interactions in the gas phase, it can be inferred that the addition of a water molecule into the first hydration sheath of the alkali and ammonium ions decreases the hydration energy with respect to any additional water molecules which may enter into the hydration layer. Similarly in the present system, values up to $R_H = 1$, the cationic hydration energy is stronger than that of the anion, while after addition of one water molecule into the ammonium hydration sheath anionic hydration begins to be more competitive.

Further work on the $NH_4NO_3-H_2O$ system is now in progress, including investigation on the pure melt, and until these results are available further discussion should be delayed.

(17) J. Braunstein and H. Braunstein, *Inorg. Chem.*, **8**, 1558 (1969).

(18) M. Peleg, *J. Phys. Chem.*, **7**, 4553 (1967).

(19) A. G. Keenan, *ibid.*, **61**, 780 (1957).

(20) (a) P. Kebarle, *Advan. Chem. Ser.*, **No. 72**, 24 (1968); (b) A. M. Hogg and P. Kebarle, *J. Chem. Phys.*, **43**, 449 (1965); (c) M. Arshadi, R. Yamdagni, and P. Kebarle, *J. Phys. Chem.*, **74**, 1475 (1970).

NOTES

Hydrogen Promotion of the Palladium-Catalyzed Carbon Monoxide Oxidation

by Robert L. Goldsmith,[*1] Michael Modell,
and Raymond F. Baddour

*Massachusetts Institute of Technology, Cambridge,
Massachusetts 02139 (Received September 21, 1970)*

Several investigators have reported that hydrogen pretreatment or addition to a metal catalyst alters the activity for carbon monoxide oxidation or the infrared spectrum of adsorbed carbon monoxide. Moss and Thomas reported that prior exposure to hydrogen increased the activity of palladium foils for the batchwise oxidation of carbon monoxide.[2] Modell suggested that palladium–hydrogen alloys decrease the activation energy for the oxidation.[3] Changes in the infrared spectra of CO chemisorbed on platinum[4] and nickel[5] samples, brought about by the the addition of hydrogen, have been reported. However, these separate kinetic and spectral changes were not correlated because each employed different catalyst samples.

It has been shown that the kinetics of CO oxidation and the corresponding spectra of chemisorbed species on palladium are sensitive to catalyst history (*e.g.*, pretreatment and break-in phenomena)[6,7] and the conditions of reaction (*e.g.*, batch *vs.* steady state).[8] The present study was undertaken to determine the effect of hydrogen on kinetics and spectra which were measured simultaneously under well-defined conditions. In particular, a differential flow reactor was operated under steady-state conditions with and without hydrogen addition to the reactants. The catalyst was silica-supported palladium, the activity of which had stabilized after undergoing break-in.

Experimental Section

Carbon monoxide, oxygen, and hydrogen in a helium diluent (all CP grade) were treated to remove traces of CO_2 and H_2O, as described elsewhere.[7] The mixture was passed over a catalyst sample at atmospheric pressure. The catalyst was 10% palladium on silica (Cabosil) pressed into porous disks partially transparent to infrared radiation. The palladium existed as approximately 50-Å particles dispersed on the silica support, as determined by electron microscopy. Details of the flow reactor design and construction and catalyst preparation have been reported previously.[7]

At steady-state conditions, conversion of reactants was maintained below 10%, and as the reaction is not product inhibited, the reactor was treated kinetically as a differential reactor. The product gas mixture was analyzed by gas chromatography for CO, O_2, and CO_2, and its flow rate measured. The catalyst disk temperature was determined by measuring the resistance of a palladium wire imbedded within the disk. A minor correction to the resistivity was required for the effect of dissolved hydrogen. Accuracy in the temperature measurement was within 2°. The reactor was heated above room temperature by infrared heating lamps.

The data reported were taken for experiments at 30 to 175°, and CO and O_2 reactant pressures about 12 Torr, and hydrogen pressures of 0 and 10 Torr. Reaction rate was determined as the product of the gas flow rate times the CO_2 concentration in the reactor effluent.

The reactor had windows transparent to infrared radiation, and the beam of an infrared spectrometer (Perkin-Elmer Model 21) was passed through the catalyst disk. The frequency region in which carbonyl bonds absorb, 1800 to 2200 cm^{-1}, was scanned.

Absorption bands of vapor phase H_2O and CO were used for calibration of the spectrometer, and an accuracy of better than ± 2 cm^{-1} was obtained. In this manner, absorption spectra of chemisorbed carbon monoxide were recorded under reaction conditions.

Results

The presence of hydrogen in the reactant gas mixture had a marked promoting effect on the palladium catalytic activity. In the presence of 10 Torr hydrogen, the apparent activation energy for the carbon monoxide oxidation decreased from about 30 kcal/mol (without hydrogen) to below 8 kcal/mol at about 100°, and to below 0.4 kcal/mol at room temperature, as is indicated by the Arrhenius plots of Figure 1. The J series

(1) Abcor Inc., Cambridge, Mass. 02139.

(2) R. L. Moss and D. H. Thomas, *Trans. Faraday Soc.*, 60, 1110 (1964).

(3) M. Modell, Sc.D. Thesis, Dept. of Chem. Eng., Massachusetts Institute of Technology, 1964.

(4) R. P. Eischens, *J. Chem. Phys.*, 35, 385 (1958).

(5) R. P. Eischens in "The Surface Chemistry of Metals and Semiconductors," H. C. Gatos, Ed., Wiley, New York, N. Y., 1960.

(6) R. L. Goldsmith, Ph.D. Thesis, Dept. of Chem. Eng., Massachusetts Institute of Technology, June 1966.

(7) R. F. Baddour, M. Modell, and R. L. Goldsmith, *J. Phys. Chem.*, 74, 1789 (1970).

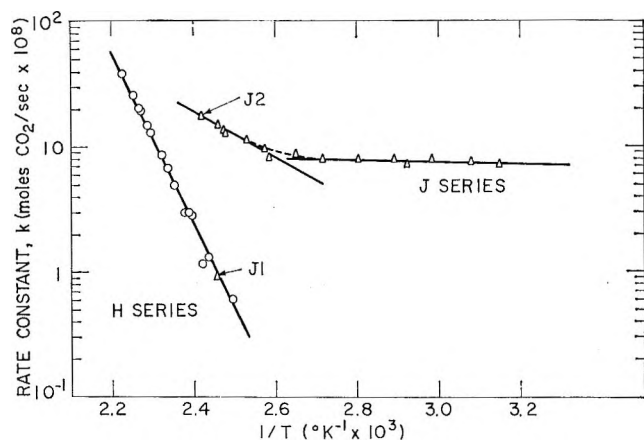(8) R. F. Baddour, M. Modell, and U. K. Heusser, *ibid.*, 72, 3621 (1968).
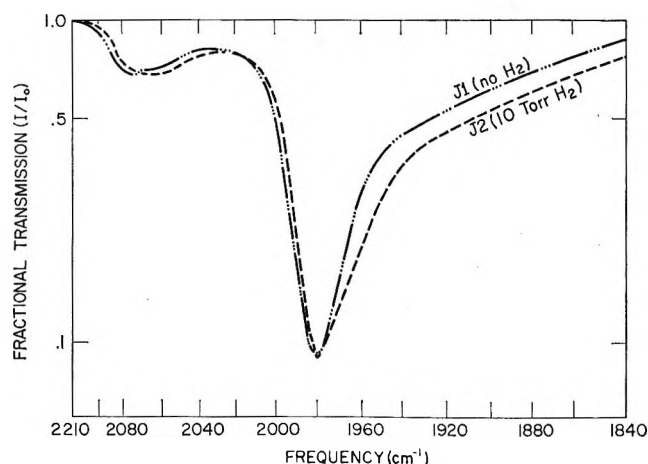
Figure 1. Effect of hydrogen on catalytic activity.

Figure 2. Effect of hydrogen on spectrum of chemisorbed CO (123°, 11.7 Torr of CO, 12 Torr of O_2).

data (catalyst sample no. 1), except point J1, were recorded in the presence of hydrogen, and the H series data (catalyst sample no. 2) and point J1 in the absence of hydrogen. These results were reversible. Following catalyst evacuation at 10^{-5} Torr and room temperature for several hours, data taken for the J series catalyst fell on the H series line. The hydrogen did not noticeably react with oxygen, since oxygen in the reactant feed mixture could be accounted for by unreacted oxygen and CO_2 in the product mixture.

The presence of hydrogen slightly changed the spectrum of adsorbed carbon monoxide, as shown in Figure 2 (points J1 and J2). Based on band interpretation proposed by Eischens, et al.,[9] the two absorption bands have been identified with "linear" and "bridged" surface CO species. In the presence of hydrogen, both bands were shifted to lower frequencies. The shift was greater for the "linear" band center (2076 to 2065 cm^{-1}) than for the "bridged" band center (1982 to 1978 cm^{-1}). Infrared absorption on the low-frequency side of the bridged band was increased.

Discussion

In addition to the promoting effect of hydrogen, promotion of the carbon monoxide oxidation has been de-

scribed for palladium-alloy systems. The activation energy for the reaction on silver-palladium[10] and gold-palladium[11] alloys suddenly decreases when the palladium content is decreased to the point where the palladium 4d band is filled. Thus alloying palladium with hydrogen, silver, or gold appears to produce the same change in its catalytic behavior for the carbon monoxide oxidation.

An explanation in terms of electrons from dissolved hydrogen filling the metallic 4d band of palladium is proposed. Mechanistically, the promoting effect is attributed to the increased ease of oxygen adsorption. Oxygen, being very electronegative, chemisorbs by partially withdrawing electrons from the metal surface. This electron extraction occurs with difficulty with palladium 4d electrons. However, s or sp hybrid electrons can be much more easily polarized by oxygen molecules at the metal surface, and oxygen chemisorption on metals is thought to involve these electrons.[12] Upon hydrogen dissolution in palladium, the 1s electrons of hydrogen fill the 4d band. Less energy is required for the subsequent promotion of 4d electrons into the 5s band and correspondingly for oxygen adsorption, which is hypothesized to be the reaction rate limiting step.

The spectral results confirm this model. Eischens[6] has concluded that any change which increases the ease of electron donation by the metal will shift both linear and bridged bands to lower frequencies, in accord with the present results.

(9) R. P. Eischens, S. A. Francis, and W. A. Pliskin, J. Phys. Chem., 60, 194 (1956).

(10) G. M. Schwab and K. Gossner, Z. Phys. Chem. (Frankfurt am Main), 16, 39 (1958).

(11) A. G. Daglish and D. D. Eley, Proc. Int. Congr. Catal., 2nd, 2, 1615 (1961).

(12) D. O. Haywood and B. M. W. Trapnell, "Chemisorption," 2nd ed, Butterworth, Washington, D. C., 1964.

Phase Transitions in Tetraalkylammonium Iodide Salts

by J. Levkov, W. Kohr, and R. A. Mackay*

Drexel University, Philadelphia, Pennsylvania 19104
(Received October 15, 1970)

A report appeared recently on the fusion properties of some ionic quaternary ammonium compounds.[1] The

Table I: Transition Temperatures, Enthalpies, and Entropies of Tetralkylammonium Iodide Salts. The ΔH Values Are in Kcal Mole⁻¹, Where the Upper Value Is from the Heating Curve and the Lower Value from the Cooling Curve. The ΔS Are in eu, Calculated from the Upper ΔH Values. Temperatures Are in °K

1 Salt R₄NI	2 Trans 1 ΔH	3 ΔS	4 T	5 Trans 2 ΔH	6 ΔS	7 T	8 Trans 3 ΔH	9 ΔS	10 T	11 Fusion ΔH	12 ΔS	13 T
Methyl												
Ethyl	5.1 ± 0.1	11.0	465									
	5.1 ± 0.3		458									
Propyl	0.7 ± 0.03	3.1	224	3.3 ± 0.3	8.0	418						
	0.2 ± 0.1		214	3.6 ± 0.1		398						
Butyl	6.7 ± 0.1	17.2	392							2.2	5.2	418
Pentyl	3.3 ± 0.4	8.2	403							9.0 ± 0.1	22.0	410
	3.9 ± 0.1		399							9.8 ± 0.2		404
Hexyl	5.8 ± 0.3	16.9	344				1.4 ± 0.02	4.1	352	4.1 ± 0.1	11.0	378
	1.6 ± 0.1		335	4.5 ± 0.1		341	1.5 ± 0.06		350	4.2 ± 0.1		374
Heptyl	2.2 ± 0.1	6.0	358	0.6 ± 0.05	1.4	392				8.7 ± 0.1	21.8	396
	0.2 ± ?		342	0.6 ± 0.06		388				9.0 ± ?		392
p-Dibromobenzene (reported)										4.63 ± 0.19		362
										4.84		
Naphthalene (reported)										4.25 ± 0.17		355
										4.56		

results were interpreted essentially on the basis of a configurational disordering of the alkyl chains of the cation. In the course of studies on the premelting transitions of tetraalkylammonium salts, we have examined the series of tetra-n-alkylammonium iodides from methyl through heptyl. In addition to the calorimetric studies, we have examined the ir spectra of the methyl, ethyl, and propyl iodides, and our data indicate that a structural change other than a conformational change of the cation occurs in the premelting transition for all of the salts.

The enthalpies of transition were measured on a Perkin-Elmer Model DSC-1b differential scanning calorimeter.[2] At least three separate samples of each salt were run, and each was recycled several times. The enthalpies and entropies of transition and fusion for the butyl-, pentyl- and heptylammonium iodides are in substantial agreement with those reported by Coker, Ambrose, and Janz,[1] but their values for the propyl salt are more than twice as large as those reported here. The ir measurements were performed on a Perkin-Elmer 621 spectrophotometer using pressed disks composed of the pure salt. Measurements were made at several temperatures both below and above the temperature corresponding to a transition.

The results of the calorimetric study are presented in Table I. The salt is listed in column 1; column 2 lists the transition enthalpies and their average deviation in units of kilocalories per mole. The upper value corresponds to heating, the lower value to cooling. The entropy change in column 3 is calculated from the upper enthalpy value. In column 4 are the temperatures, in absolute units, at which the transitions occur. Columns 5–10 list the enthalpies, entropies, and temperatures of succeeding transitions if they occur. The

values for the fusion transition appear in columns 11–13. Also included in the table are the enthalpies of fusion for p-dibromobenzene and naphthalene obtained in this work and reported in the literature.

The effect of temperature on the infrared spectra is, as expected, to increase bandwidths and decrease band heights. In the absence of any physical or chemical changes, the total integrated band intensities should remain constant. Band intensities were estimated by taking the product of the height times the width at half-height, normalized to the room temperature value. Relative absorbances obtained in this manner will decrease with increasing temperature, approximately linearly with $1/T$ since the tails of the peaks will become increasingly important. The Me₄NI salt showed no transitions over the temperature range studied. The Et₄ and Pr₄ salts possess bands at 467 and 511 cm⁻¹, respectively, corresponding to the 446-cm⁻¹ band in Me₄NI. Plots of relative absorbance vs. $1/T$ for these salts show breaks at about 459 and 409°K corresponding to observed transitions. Upon cooling, the bands reappear and the temperature dependence of the spectra is "reversible."

Transition one in Et₄NI, two in Pr₄NI, and one in Pe₄NI all have comparable ΔH (3–5 kcal/mol) and ΔS (8–11 eu/mol) values. In addition, the behavior of the ir band in the 450–500-cm⁻¹ region is the same for the two salts examined (Et and Pr). This indicates that the cause of these transitions may be essentially the same for all three salts.

At room temperature, Et₄NI has a distorted wurtzite-

(1) T. G. Coker, J. Ambrose, and G. J. Janz, J. Amer. Chem. Soc., 92, 5293 (1970).

(2) E. S. Watson, M. J. O'Neill, J. Justin, and N. Brenner, Anal. Chem., 36, 1233 (1964).

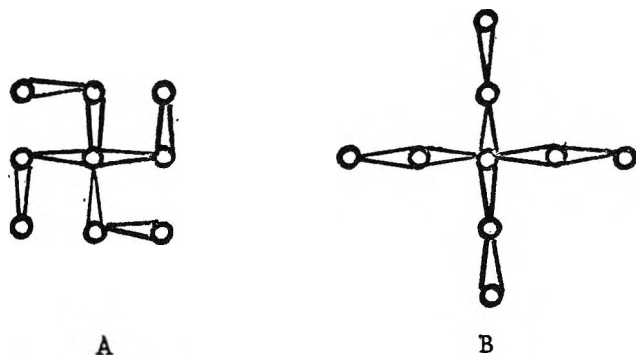Figure 1. Form A, Nordic cross formation of the Et_4N^+ ion. Form B, formation found in the Et_4NBr–succinamide lattice compound.

Figure 2. Transition enthalpies and entropies for $(C_nH_{2n+1})_4$ NI salts as a function of n (odd or even). The quantity $\Delta(\Delta H) = \Delta H$ (n-even) $- \Delta H$ (n-odd), and similarly for $\Delta(\Delta S)$.

type structure[3] where the conformation of the Et_4N^+ ion is that which in projection forms a Nordic cross (swastika). This is form A (Figure 1). Similar possibilities exist for the higher homologs. Form B has been found in the Et_4NBr–succinamide lattice compound. It is possible therefore that the above transitions correspond to a conformational change from form A to form B. Since form B is of higher symmetry (D_{2d}, neglecting the protons) than form A, the disappearance of some ir bands may be expected. Such a transition may also account for the relatively large ΔH and ΔS values observed. A strong proof that this transition is in fact due to such a conformation change could be provided by the absence of the ir band in the 450-cm^{-1} region for a compound in which the Et_4N^+ ion is known to be in form B. Unfortunately, in the Et_4NBr–succinamide compound, the tail of a strong succinamide band obscures the region of interest. An absorption band at 463 cm^{-1} is present in the spectrum of a concentrated solution of Et_4NBr in chloroform. On the basis of steric considerations the energy of form A should be somewhat less than that of form B. However, solvation by chloroform could reverse this and no conclusion can be reached on the basis of the solution spectrum. The Pr_4N^+ ion is in form B in Pr_4NBr,[4] and this compound has a band at 473 cm^{-1}. A DSC scan of Pr_4NBr revealed two transitions, at 375 and at 393°K, with relative areas of 28:1. In light of the above hypothesis, the band at 473 cm^{-1} should have been absent, as should have one, or both, of the transitions detected in the DSC measurements.

The band at 446 cm^{-1} in Me_4NI has been assigned as a $\delta(NC_4)$ mode; i.e., an F_2 ir active bending mode (ν_4) of the NC_4 tetrahedron.[5]

If the 467- and 511-cm^{-1} bands in Et and Pr salts may be similarly assigned, then a change to higher symmetry should not cause their disappearance. An X-ray determination of the structure of Pr_4NI would aid in the assignment of this transition and the interpretation of the ir data.

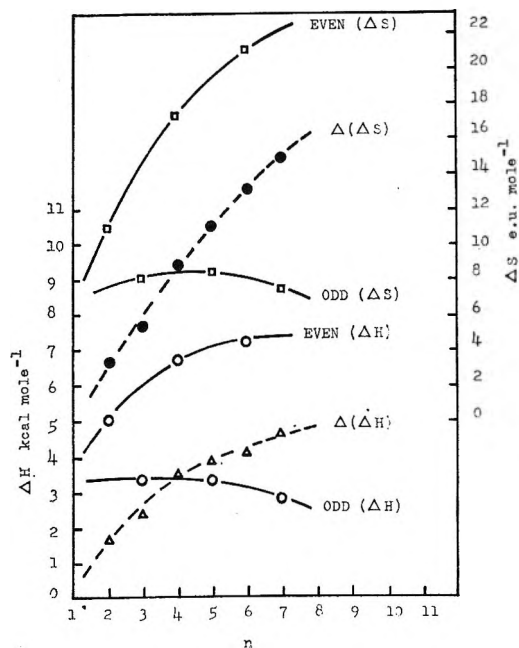Finally, if the 473-cm^{-1} band in Pr_4NBr is an over-

tone or combination involving torsional or lattice modes, the corresponding band in the iodide (511 cm^{-1}) frequency should decrease in the order Me > Et > Pr, while the reverse is found. The fact that the band is observed in solution also shows that it is associated with the R_4N^+ ion itself. The "disappearance" of this band is thus associated with an effect of the premelting transition on the R_4N^+ ion. Whether this effect is due to a change in unit cell symmetry or to a conformation change accompanied by distortion cannot be determined on the basis of the ir data.

Some insight into the problem may be gained by examining the ΔH and ΔS for the premelting transitions. Where there are two or three closely spaced transitions, as for hexyl and heptyl, $\Delta H = \Sigma \Delta H$ and similarly for ΔS. A fundamental difference between n-odd and n-even for the $(C_nH_{2n+1})_4NI$ salts is indicated in Figure 2 where ΔH and ΔS are plotted vs. n. It is seen that in each of these plots two separate curves are generated, one for n-odd (the smaller values) and the other for n-even (the larger values).

Since the ir band behavior is the same for the Et and Pr salts, it is likely that all R_4NI salts undergo a similar transition with a ΔH of about 3 kcal/mol and a ΔS of about 9 eu. In addition, the even-n salts undergo another transition which the odd-n do not. The ΔH and ΔS for this transition increases with increasing

(3) E. Wait and H. M. Powell, J. Chem. Soc., 1872 (1958).

(4) A. Zalkin, Acta Crystallogr., 10, 557 (1957).

(5) E. A. V. Ebsworth and N. Sheppard, Spectrochim. Acta, 13, 261 (1959).

chain length. The observed enthalpies and entropies of fusion are consistent with this idea, the odd-n salts having the higher ΔH and ΔS of fusion.
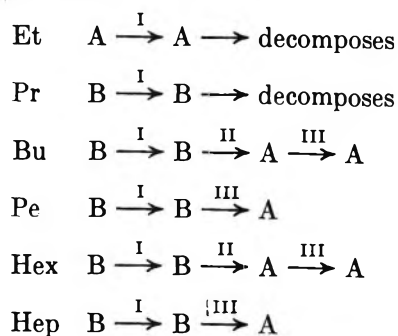
The solid-state transition just preceding melting in tetraamylammonium thiocyanate was largely accounted for by a kink-block type of rearrangement of the alkyl groups within the quarternary ammonium cation.[6] Here, however, it would seem more reasonable to ascribe the "first" transition, which we postulate as being common to all the salts, to a crystal structure change. The magnitude and relative uniformity of the ΔH and ΔS for this transition as well as the crystal structures of Et_4NI[3] and Pr_4NBr[4,5] are in accord with such an assignment. Both salts crystallize in the trigonal space group $I\bar{4}$, each ion having four nearest neighbors of the opposite charge approximately at the corners of a tetrahedron. Thus, the salts may have similar crystal structures while still having different cation conformations, and it is conceivable that a conformation change and crystal structure change could occur either separately or in conjunction. This may explain how more than one transition could give rise to only one observed DSC peak or why sometimes two or three closely spaced peaks of constant total area but variable individual area may be observed.

As the chain length increases the number of different conformations increase. The differences in energy (at least due to intramolecular interactions) between conformations would tend to decrease with increasing chain length. This would explain the increasing difference between ΔH and ΔS values for both the odd and even-n salts, and the fact that the even-n ΔH values are beginning to level off at higher n while the ΔS values are still increasing.

If these considerations are correct, then the conformation of the even-n ions in the solid just below the melting point should be essentially the same as in the melt, while this should not be true of the odd-n ions.

The Et_4N^+ ion has conformation A (卐) at room temperature, and we propose that the propyl and higher homologs, due to their greater chain lengths which would enable them to "wrap around" the iodide ion, have conformation B (X). The first transition, which may be a change in crystal structure, is designated as

I, and the second transition, postulated to be a conformation change, as II. The fusion transition is III. This scheme is shown below.[7]

$$Et \quad A \xrightarrow{\text{I}} A \longrightarrow \text{decomposes}$$

$$Pr \quad B \xrightarrow{\text{I}} B \longrightarrow \text{decomposes}$$

$$Bu \quad B \xrightarrow{\text{I}} B \xrightarrow{\text{II}} A \xrightarrow{\text{III}} A$$

$$Pe \quad B \xrightarrow{\text{I}} B \xrightarrow{\text{III}} A$$

$$Hex \quad B \xrightarrow{\text{I}} B \xrightarrow{\text{II}} A \xrightarrow{\text{III}} A$$

$$Hep \quad B \xrightarrow{\text{I}} B \xrightarrow{\text{III}} A$$

While we have not directly considered it, there may be a configuration disordering involved in transition I.[8]

The fact that no transition is observed for the Me_4NI salt is also consistent with the postulated nature of the transitions. There is, of course, no possibility of a conformational change for the Me_4N^+ ion, and on the basis of radius ratio it is conceivable that the crystal structure of Me_4NI is different from that of the higher homologs. In any event, due to the smaller cation size, it is not unreasonable to expect that any structure change could occur at a considerably higher temperature which may be above the decomposition point.

In summary, we conclude that all of the R_4NI salts may undergo a similar transition accompanied by the disappearance (or large decrease in intensity) of an ir band around 500 cm^{-1}. The even-n salts undergo an additional transition, close to the first, which is probably associated with a conformational change of the R_4N^+ ion as discussed by Coker, Ambrose and Janz.[1] This is reflected in the lower enthalpies and entropies of fusion of the even-n salts.

(6) T. G. Coker, B. Wunderlich, and G. J. Janz, *Trans. Faraday Soc.*, **65**, 3361 (1969).

(7) We wish to note that a transition designated as X → X (or B → B), etc., does not necessarily imply no change in conformation at all, since for the longer chains a change in conformation at the end of a chain will produce only a small change in (intramolecular) energy. We consider, however, that at least the "core" conformation (the first two carbons in each chain attached to the nitrogen) does not undergo any change in conformation.
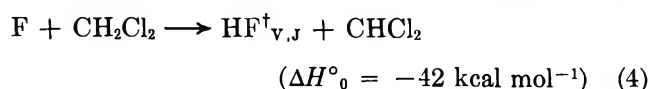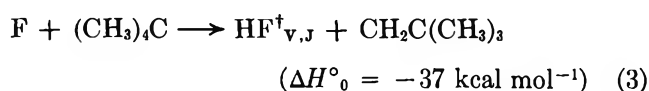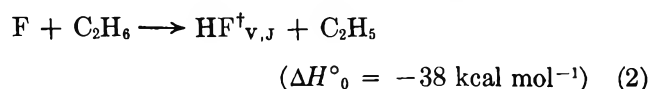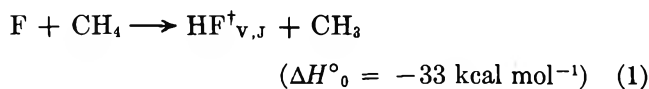
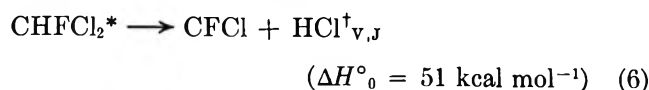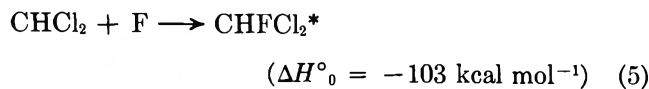(8) W. Wong and E. Westrum, Jr., *J. Phys. Chem.*, **74**, 1303 (1970).

COMMUNICATIONS TO THE EDITOR

Comparison of Energy Partitioning from Three-Centered Processes. Bimolecular Transfer and Unimolecular Elimination Reactions
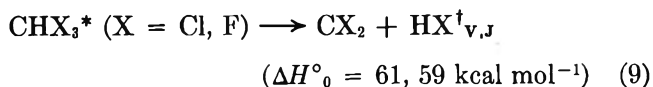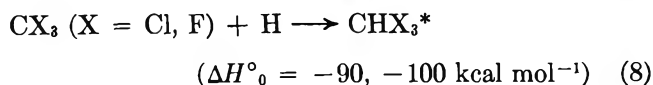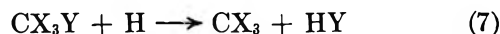
Sir: Infrared chemiluminescence from gas phase chemical reactions allows direct measurement of the energy partitioning patterns.[1-4] We wish to report on infrared chemiluminescence from HF and HCl which are products from two types of three centered reactions: (1) hydrogen abstraction by fluorine atoms from methane, ethane, neopentane, and dichloromethane; (2) unimolecular elimination from vibrationally excited halomethanes. The abstraction reactions and their thermochemistry[5,6] are given below (the small activation energy for abstraction is neglected).

$$F + CH_4 \longrightarrow HF^{\dagger}_{v,J} + CH_3$$

$$(\Delta H^{\circ}_0 = -33 \text{ kcal mol}^{-1}) \quad (1)$$

$$F + C_2H_6 \longrightarrow HF^{\dagger}_{v,J} + C_2H_5$$

$$(\Delta H^{\circ}_0 = -38 \text{ kcal mol}^{-1}) \quad (2)$$

$$F + (CH_3)_4C \longrightarrow HF^{\dagger}_{v,J} + CH_2C(CH_3)_3$$

$$(\Delta H^{\circ}_0 = -37 \text{ kcal mol}^{-1}) \quad (3)$$

$$F + CH_2Cl_2 \longrightarrow HF^{\dagger}_{v,J} + CHCl_2$$

$$(\Delta H^{\circ}_0 = -42 \text{ kcal mol}^{-1}) \quad (4)$$

Vibrationally excited $CHFCl_2^*$ was produced in the F plus CH_2Cl_2 system *via* secondary combination of $CHCl_2$ with fluorine atoms. At the pressures of our experiments, all of the chemically activated molecules eliminate HCl or HF; the former is the predominant reaction.[7]

$$CHCl_2 + F \longrightarrow CHFCl_2^*$$

$$(\Delta H^{\circ}_0 = -103 \text{ kcal mol}^{-1}) \quad (5)$$

$$CHFCl_2^* \longrightarrow CFCl + HCl^{\dagger}_{v,J}$$

$$(\Delta H^{\circ}_0 = 51 \text{ kcal mol}^{-1}) \quad (6)$$

It also was possible to observe HF and HCl emission from two entirely different three-centered unimolecular elimination reactions by utilizing the interaction of hydrogen atoms with CCl_3Br and CF_3I.

$$CX_3Y + H \longrightarrow CX_3 + HY \quad (7)$$

$$CX_3 (X = Cl, F) + H \longrightarrow CHX_3^*$$

$$(\Delta H^{\circ}_0 = -90, -100 \text{ kcal mol}^{-1}) \quad (8)$$

$$CHX_3^* (X = Cl, F) \longrightarrow CX_2 + HX^{\dagger}_{v,J}$$

$$(\Delta H^{\circ}_0 = 61, 59 \text{ kcal mol}^{-1}) \quad (9)$$

The energy available for partitioning is the difference between the C–H or C–F bond energies and the energy change for the elimination reaction. The latter are not known well[8] but the estimates given above should be reliable to within ± 5 kcal mol^{-1}. Since the thresholds[8b] for the reverse reactions ($CX_2 + HX \rightarrow CHX_3$) are probably less than 5 kcal mol^{-1}, virtually all of the energy arises from (8) or from (5) and not from release of potential energy by elimination of HX.

The reactions were studied in two vessels. One vessel was a 4.25-in. i.d. stainless steel flow reactor which was pumped by a liquid nitrogen trap, a 4-in. diffusion pump, and a mechanical pump. Observations were made through an NaCl window placed 3 cm downstream from the reagent and atom mixing zone. The second vessel, which had walls cooled to liquid N_2 temperature, had a diameter of 6 in. and was pumped with a liquid nitrogen trap, a 6-in. diffusion pump, and a mechanical pump. The vessel was fitted with internal mirrors for more efficient collection of light. Hydrogen atoms were generated by a Wood's tube discharge and fluorine atoms were formed by passing CF_4 or SF_6 through a microwave discharge. Results from both F-atom sources were the same, which provide evidence against the possibility of complicating reactions from other products from the discharge. Because of the weak intensity from the unimolecular elimination reactions, the population ratio for the $v = 2$ and $v = 3$ levels was obtained by scanning the overtone region with a wide

(1) K. G. Anlauf, P. J. Kuntz, D. H. Maylotte, P. D. Pacey, and J. C. Polanyi, *Discuss. Faraday Soc.*, **44**, 183 (1967).

(2) K. G. Anlauf, J. C. Polanyi, W. H. Wong, and K. B. Woodall, *J. Chem. Phys.*, **49**, 5189 (1968).

(3) J. C. Polanyi and D. C. Tardy, *ibid.*, **51**, 5717 (1970).

(4) R. L. Johnson, M. J. Perona, and D. W. Setser, *ibid.*, **52**, 6372 (1970).

(5) B. deB. Darwent, "Bond Dissociation Energies in Simple Molecules," U. S. Department of Commerce National Bureau of Standards, Washington, D. C., NSRDS-NBS 31, 1970.

(6) J. A. Kerr, *Chem. Rev.*, **66**, 465 (1966).

(7) H. W. Chang; unpublished RRKM calculations give 10^{-11} sec as a typical lifetime of the chemically activated halomethanes produced by reactions 5 and 7.

(8) (a) W. J. R. Tyerman, *J. Chem. Soc. A*, 2483 (1969); (b) T. Smail and F. S. Rowland, *J. Amer. Chem. Soc.*, **92**, 1866 (1970).

Table I: Vibrational Distributions of HX Products

| | | | Relative population of HF and HCl | | | | | | |
| | | | v = 1 | | v = 2 | | v = 3 | | |
Reaction	Vessel	Pressure, μ	Exptl[a]	Cor[b]	Exptl[a]	Cor[b]	Exptl[a]	Cor[b]	$\%E_v$[c]
$CH_4 + F$	1	1	0.29	0.18	0.64	0.74	0.07	0.08	64
	2	3.8	0.33	0.27	0.55	0.57	0.12	0.16	
$C_2H_6 + F$	1	0.5	0.19	0.12	0.45	0.42	0.37	0.47	68
$C(CH_3)_4 + F$	1	0.5	0.24	0.17	0.55	0.58	0.21	0.25	62
$CH_2Cl_2 + F$	1	0.5	0.30	0.26	0.32	0.26	0.38	0.48	>58
$CH_2Cl_2 + F$[d]	2	5.0	0.65		0.23		0.12		
$CHFCl_2$*	2	40.0	0.92		0.08				
CHF_3*	2	5.0	0.84		0.10		0.06		>6
$CHCl_3$	2	5.0	0.80		0.10		0.10		>5

[a]Vessel 1 and 2 denote the 6-in. cooled-wall and the 4-in. flow reactors, respectively. Experiments were done at the pressures indicated in the third column. The rotational distributions in vessel 2 were characterized by a single rotational temperature of $\sim 350°$K. The rotational distributions from vessel 1 could not be fitted to a single Boltzmann temperature, which is evidence that most of the vibrational relaxation has been arrested. [b] The steady-state populations were corrected for radiative cascade using integrated absorption data [G. A. Kuipers, *J. Mol. Spectrosc.*, **2**, 75 (1955)] which give an emission lifetime of 5 msec for $HF_{v=1}$. The observation time for our experiments was taken as ~ 0.5 msec. [c] The per cent of energy released to HF or HCl as vibrational energy; the population for $v = 0$ was obtained from extrapolation of the measured populations in $v' = 1, 2,$ and 3. For the abstraction reactions the population in $v = 0$ was taken as zero. [d] Included so the degree of relaxation of the last two entries can be estimated by comparison with the F + CH_2Cl experiments. We suspect that H_2-CF_3I or H_2-CCl_3Br mixtures (1:8) are less efficient at vibrational deactivation than $CF_4-CH_2Cl_2$ mixtures due to the large dipole moment of CH_2Cl_2.

slit. However, the intensity from the abstraction reactions was sufficient to resolve the rotational lines in the fundamental spectra. The area of each rotational line was converted into a relative population using the detector response and the transition probability for that rotational line.[9,10] The relative vibrational populations were obtained by summing the rotational populations.

The relative steady-state vibrational populations are shown in Table I. The distribution obtained from CH_4 is very close to that obtained by Parker and Pimentel[11] in their laser work. Jonathan, Meiliar-Smith, and Slater[12] have investigated reaction 1 in a fast-flow apparatus and found $N_1:N_2:N_3 = 0.21:0.64:0.15$. All three studies are in reasonably close agreement, and we conclude that most of the vibrational relaxation was arrested in our cold wall experiments with CH_4. The vibrational relaxation for ethane and neopentane also must have been arrested, perhaps even to a greater degree than for methane, because (i) the rotational distributions are non-Boltzmann, (ii) the pressure was considerably lower for the condensable reagents and SF_6 as the F-atoms source, (iii) moderate variation in pressure in the cold-wall vessel did not significantly affect the relative populations, and only small differences in relative populations were found for experiments in the two vessels. Unfortunately, CH_2Cl_2 seems to be more efficient at removing energy from $HF^\dagger$ because variation of pressure in the cold-wall vessel caused a change in population, as did changing from one vessel to another. Nevertheless, formation rates into the highest vibrational levels of HF are favored by (4) although our data provide only lower limits for the formation of $v = 2$ and 3.[13] In general, the abstraction

of hydrogen from a carbon atom seems to favor the highest accessible levels of HF and the shift toward $v = 3$ for reactions 2, 3, and 4 reflects the increase in the available energy.

The unimolecular eliminations result from secondary reactions and they only could be observed in the 4-in. flow vessel. Relaxation of the initial $HCl_v^\dagger$ distribution from the $CHFCl_2$ elimination reaction undoubtedly is very serious; however, relaxation should be less for the HCX_3* cases, which were studied at lower pressure. The degree of relaxation can be estimated by comparison (see footnote d) with the distributions from F + CH_2Cl_2 at the two pressures listed in Table I. We feel that the trend of strongly declining populations for the higher vibrational levels is a true feature of the energy partitioning for the unimolecular three-centered elimination reactions.

The most definitive and interesting result is that replacing H atoms by methyl groups did not alter the energy partitioning for F + H–CR$_3$ type reactions. We also have found the same result for F + CF_3CH_3, $Si(CH_3)_4$, and c-C_6H_{12}. Evidently the release of potential energy occurs in such a way that little energy is made accessible to the internal degrees of freedom of

(9) H. S. Heaps and G. Herzberg, *Z. Phys.*, **133**, 48 (1952).

(10) R. Herman and R. F. Wallis, *J. Chem. Phys.*, **23**, 637 (1955).

(11) (a) J. H. Parker and G. C. Pimentel, *ibid.*, **51**, 91 (1969), reported $N_2/N_1 = 2.7 \pm 0.6$; (b) more recent work by W. H. Green and M. C. Lin, private communication, gives a similar but somewhat improved ratio.

(12) N. Jonathan, C. M. Melliar-Smith, and D. H. Slater, *Mol. Phys.*, **20**, 93 (1971).

(13) M. C. Lin and W. H. Green, *J. Chem. Phys.*, **53**, 3383 (1970).

the CR$_3$ radical. A similar result was deduced from earlier studies[4] of H + SCl$_2$ and S$_2$Cl$_2$. This result from covalent reactions seems to be slightly different from molecular beam results[14] for K + RI reactions. Our data also demonstrate that any effect of a substituent, e.g., R = H, Cl, CH$_3$, and CF$_3$, upon the pattern of energy release for H-atom abstraction from carbon by fluorine atoms is small.

Our measurements are the second example of infrared chemiluminescence from products of unimolecular reactions[15] proceeding on ground electronic surfaces. Although having more energy and fewer degrees of freedom, the elimination reactions partition less energy to HX than the abstraction reactions, even if some allowance is made for relaxation in the unimolecular reaction experiments. In fact, the HX† distribution from three-centered elimination is similar to a statistical distribution. According to statistical theories of unimolecular reactions, any energy in the molecule *above the threshold* is randomly distributed[16] among the internal degrees of freedom of the chemically activated CHX$_3$* molecule and, consequently, should be distributed statistically to the degrees of freedom of the products. Since reactions 6, 8, and 9 have quite small activation energies for the reverse reactions, i.e., the release of potential energy is small, the pattern for the energy release is expected to be nearly statistical, and these data provide a qualitative confirmation for randomization of the internal energy above the threshold of the molecule in a unimolecular reaction.[16]

We also have measured the energy partitioned to HF† and HCl† by the unimolecular *four-centered* elimination reactions of chemically activated haloethanes.[17a] Our results agree with Clough, Polanyi, and Taguchi[15a] who found the HX vibrational energy to be somewhat larger than the statistical amount,[17b] although the fraction of the energy released to HF† is relatively small compared with the F + HCR$_3$ reactions of Table I.

Acknowledgment. This work was supported by the National Science Foundation under Grants G.P.-9245 and -27536X. We wish to acknowledge helpful dis-

cussions with Dr. Richard Johnson of Villanova University.

DEPARTMENT OF CHEMISTRY   H. W. CHANG
KANSAS STATE UNIVERSITY   D. W. SETSER*
MANHATTAN KANSAS 66502   M. J. PERONA

RECEIVED MARCH 29, 1971

Kinetic Energy Isotope Effects of Bromine Reactions Activated by Radiative Neutron Capture in Gaseous CH$_3$F and CD$_3$F[1]

Sir: Although there have been many studies[2-4] relating to isotope effects (differences in organic yields) of (n,γ)-activated bromine reactions in condensed state hydrocarbons, aromatics, and alkyl halides, no study reports, for a single gaseous system, organic yields for (n,γ)-activated ^{80}Br, ^{80}Br^m, and ^{82}Br^m + ^{82}Br reactions. For condensed-state systems employing high-purity reagents and correcting for ^{82}Br^m(I.T.) ^{82}Br reactions,[5,6] no bromine isotope effects were generally found.

Unlike the reactions of (n,γ)-activated ^{128}I with CH$_4$,[7] reactions of (n,γ)-activated ^{80}Br with CH$_4$[8] occur principally as a result of the recoil kinetic energy acquired by the ^{80}Br in the (n,γ)-activation process. While other activation processes such as the (γ,n) and (n,p) processes impart to the atom a very high kinetic energy ($>10^5$ eV), the (n,γ) activation process results in a distribution of energies ranging from some very low value (near zero) to a maximum of $\sim 10^2$ eV.[9] If the three activation processes ^{79}Br(n,γ)^{80}Br, ^{79}Br(n,γ)^{80}Br^m, and ^{81}Br(n,γ)^{82}Br^m + ^{82}Br impart to the respective atoms different kinetic energy spectra,[10] and if the pop-

(1) This research was supported through an Atomic Energy Commission Contract No. AT(11-1)-1617. This is AEC. Document No. COO-1617-28.

(2) For references to the earlier literature see J. E. Willard, *Annu. Rev. Nucl. Sci.*, **3**, 193 (1953); *Annu. Rev. Phys. Chem.*, **6**, 141 (1955); *Nucleonics*, **19** (10), 61 (1961); *Chem. Eff. Nucl. Transform. Proc. Symp., 1961*, **1**, 215 (1961); *Chem. Eff. Nucl. Transform 1964*, **1**, 221 (1965).

(3) J. A. Merrigan, W. K. Ellgren, Jr., and E. P. Rack, *J. Chem. Phys.*, **44**, 174 (1966).

(4) J. A. Merrigan, J. B. Nicholas, and E. P. Rack, *Radiochim. Acta*, **6**, 94 (1966).

(5) J. F. Emory, *J. Inorg. Nucl. Chem.*, **27**, 903 (1965).

(6) O. U. Anders, *Phys. Rev.*, B, **138**, (1965).

(7) E. P. Rack and A. A. Gordus, *J. Chem. Phys.*, **34**, 1855 (1961).

(8) E. P. Rack and A. A. Gordus, *J. Phys. Chem.*, **65**, 944 (1961).

(9) In ref 8, it is seen that ^{80}Br can have maximum of about 357 eV.

(10) Since the complete neutron capture γ-ray cascade spectrum is not known for bromine isotopes, it is not possible to calculate the distribution of bromine recoil energies. Because of partial cancellation of γ-recoil momenta in cascade γ-emission, bromine atoms will be formed with a distribution of energies.

(14) G. H. Kwei, J. A. Norris, and D. R. Herschbach, *J. Phys. Chem.*, **52**, 1317 (1970).

(15) (a) P. N. Clough, J. C. Polanyi, and R. T. Taguchi, *Can. J. Chem.*, **48**, 2919 (1970); (b) M. J. Berry and G. C. Pimentel, *J. Chem. Phys.*, **49**, 5190 (1968); (c) M. J. Berry and G. C. Pimentel, *ibid.*, **53**, 3453 (1970). This interesting paper describes the HCl vibrational populations resulting from flash photolysis of dichloroethylene. Both three- and four-centered processes were found; however, it was not established whether these reactions occur from electronically excited or from ground states. Nevertheless, the HCl† populations declined with increasing v.

(16) Y. N. Lin and B. S. Rabinovitch, *J. Phys. Chem.*, **74**, 1769 (1970).

(17) (a) D. W. Setser, American Chemical Society and Chemical Institute of Canada Joint Conference, Toronto, Canada, May 1970; (b) the energy available for partitioning by the CH$_3$CF$_3$ unimolecular reaction consists of both *excess energy above the threshold for reaction* and *potential energy* released after crossing the barrier in about equal amounts.

ulation of atoms with kinetic energies comparable to the reactive region E_2-E_1[11] is great enough, then we would expect bromine isotope effects for systems involving endothermic reactions. Wolfgang[11] originally suggested that the initial energy of atoms produced by (n,γ) processes may not meet the requirements of assumption Ia of the kinetic theory, which states that the initial energy E_0 of the hot atom is sufficiently high so that the atom has made a large number of collisions above energy E_2.

In this communication we report the existence of an isotope effect between (n,γ)-activated ^{80}Br, $^{80}Br^m$, and $^{82}B^m + {}^{82}Br$ in gaseous CH_3F and CD_3F. A description of our sample making techniques, irradiation procedures, and extraction techniques can be found elsewhere.[3,4,8,12-14] Two different kinds of experiments were performed: (a) those systems containing only CH_3F or CD_3F with varying concentrations of Br_2 at various system pressures; (b) those systems containing CH_3F, Br_2 source, and rare gas additives. From experiment (a) we determined possible pressure effects and limiting bromine isotope organic yields at zero mole fraction Br_2. The results of experiment (b) suggested the role of kinetic energy on bromine reactions with CH_3F and the importance, if any, of thermal reactions to the organic yield. The effects of He and Ar moderations on the (n,γ)-activated reactions of the various bromine isotopes are depicted in Figure 1.[15]

Our experimental results can be summarized as follows. (1) A pressure effect between 50 and 200 Torr total system pressure for all bromine-isotope organic yields was found. The organic yields increased with total system pressure from 50 to 200 Torr, remaining constant from 200 to 800 Torr, the highest pressure studied. Apparently above 200 Torr, energetically excited molecules are collisionally stabilized. (2) The limiting (n,γ) organic yields at zero mole fraction Br_2 in CH_3F at 800 Torr system pressure are: ^{80}Br, 8.5 ± 0.3%; $^{80}Br^m$, 10.0 ± 0.3%; $^{82}Br^m + {}^{82}Br$, 7.5 ± 0.3%. (3) The limiting (n,γ) organic yields at zero mole fraction Br_2 in CD_3F at 800 Torr system pressure are ^{80}Br, 5.8 ± 0.3%; $^{80}Br^m$, 7.5 ± 0.3%; $^{82}Br^m + {}^{42}Br$, 5.0 ± 0.3%. (4) From Figure 1, it can be seen that the limiting bromine organic yield at zero mole fraction CH_3F for both He and Ar additives is zero, indicating that the reactions occur entirely as a result of the recoil kinetic energy acquired by the bromine in its activation process.[16] Similar results were found in CD_3F systems. (5) The bromine isotope effect appeared regardless of additive, concentration of additive, or total system pressure. From the several hundred samples irradiated, the average organic yields of 50 samples picked at random from the CH_3F systems studied were; ^{80}Br, 5.27; $^{80}Br^m$, 7.66; $^{82}Br^m + {}^{82}Br$, 4.42, showing that the effect is a general one and not specific for a particular condition. (6) The limiting (I.T.) induced ^{82}Br organic yields at zero mole fraction Br_2 in CH_3F and
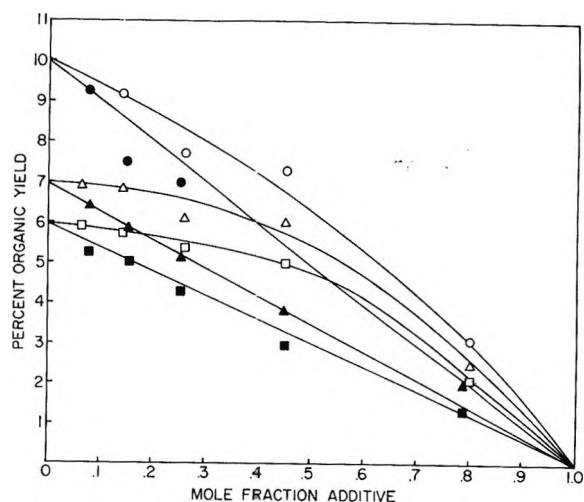

Figure 1. Effect of additives on the reaction of gaseous CH_3F with $^{80}Br^m$, ^{80}Br, and $^{82}Br + {}^{82}Br^m$ activated by radiative neutron capture: $^{80}Br^m$ with helium, O; ^{80}Br with helium, △; $^{82}Br + {}^{82}Br^m$ with helium, □; $^{80}Br^m$ with argon, ●; ^{80}Br with argon, ▲; $^{82}Br + {}^{82}Br^m$ with argon, ■.

CD_3F at 800 Torr system pressure were 7.5 ± 0.5% and 4.5 ± 0.5%, respectively. From moderation plots similar to Figure 1, the data appeared to extrapolate at zero mole fraction CH_3F or CD_3F to 1%. This indicates for $^{82}Br + CH_3F$ systems 7.5% − 1% is formed via kinetic energy processes and that 1% is formed via thermal ionic processes.

A bromine isotope effect can be due to either a difference in the population of positively charged bromine species produced by the three (n,γ) activation processes or due to different kinetic energy spectra of the (n,γ) activated bromine atoms. Since it has been previously shown[8] that reactions of bromine activated by (n,γ) occur independently of any positive charge, we suggest that the observed bromine isotope effect is due to differences in the kinetic energy spectra of the activated atoms. The organic yields increase in the

(11) Using notation consistent with R. Wolfgang, *J. Chem. Phys.*, **39**, 2983 (1963).

(12) J. A. Merrigan and E. P. Rack, *J. Phys. Chem.*, **69**, 2795 (1965).

(13) J. B. Nicholas and E. P. Rack, *J. Chem. Phys.*, **48**, 4085 (1968).

(14) Quartz bulblets (10 ml) filled with 10 mm of Br_2, CH_3F, and CD_3F, and rare gas additive with a total gas pressure of 500 Torr were irradiated for 30 sec. Pressure study samples contained only CH_3F and Br_2 with system pressures ranging from 50 to 800 Torr. Samples for (n,γ) studies were extracted immediately after irradiation (1.5 min from start of rradiation). This prevented the possibility of thermal reactions between labeled inorganic bromine with impurities resulting in an "impurity" isotope effect. The data for ^{80}Br, $^{80}Br^m$, and $^{82}Br^m + {}^{82}Br$ organic yields were acquired from the same sample. Samples for $^{82}Br^m$ isomeric transition (I.T.) studies were allowed to stand before extraction. See ref 13 for details.

(15) It should be noted that the extrapolation of the points in Figure 1 to zero mole fraction moderator is for a system containing 10 mm Br_2. These extrapolated results are, of course, lower than the organic yields reported for extrapolation to zero mole fraction Br_2.

(16) The efficiency of He, Ar, and Br_2 moderation of the Br endothermic reaction with CH_3F is as we would expect of a kinetic energy moderator.

order $^{82}Br^m$ + ^{82}Br, ^{80}Br, and $^{80}Br^m$. This would mean that the initial kinetic energies imparted to the bromine atoms are not sufficiently high that the atoms have made a number of collisions before reaching the upper limit of the reaction zone E_2.[11] If the conditions of Wolfgang's assumption 1(a)[11] are met, no isotope effect would be expected. Therefore, we conclude that the kinetic energy spectra are such that more $^{80}Br^m$, than ^{80}Br, than $^{82}Br^m$ + ^{82}Br are born with energies greater than the reaction zone E_2–E_1.

A simple test to determine if the isotope effect is really due to a difference in kinetic energy spectra of the bromine atoms is to plot the ratio of individual isotope organic yields in CH_3F to CD_3S as a function of bromine concentration. As mentioned previously, the organic yields are consistently lower in CD_3F than in CH_3F. Although we really do not know what molecular parameters—moderation effects, difference in reac-tivity integrals, or differences in bond strength—are responsible for the target molecule isotope effect, all are related directly to the bromine kinetic energy, if a sufficient population of atoms have energies near the reaction zone E_2–E_1. If more $^{80}Br^m$ atoms are born with higher kinetic energies than are ^{80}Br, than are $^{82}Br^m$ + ^{82}Br then we would expect the ratio in organic yields to decrease in the order $^{82}Br^m$ + ^{82}Br > ^{80}Br > $^{80}Br^m$. This is what we find. In a plot of organic yield ratio in CH_3F to CD_3F as a function of bromine concentration from zero to 0.1 mol fraction bromine, the ratios for the three isotopes are parallel to the mole fraction axis extrapolating for $^{82}Br^m$ + ^{82}Br, ^{80}Br, and $^{80}Br^m$ to 1.625, 1.550, and 1.388, respectively.

CHEMISTRY DEPARTMENT   R. W. HELTON
UNIVERSITY OF NEBRASKA   M. YOONG
LINCOLN, NEBRASKA   68508   E. P. RACK*

CHEMICAL REACTIONS IN ELECTRICAL DISCHARGES
ADVANCES IN CHEMISTRY SERIES NO. 80

Thirty-seven papers from a symposium sponsored by the Division of Fuel Chemistry and the Division of Physical Chemistry of the American Chemical Society, chaired by Bernard D. Blaustein.

A wide range of topics are covered in these papers by chemists, physicists, and engineers including treatments of decomposition and dissociation reactions, ion-molecule reactions, chemical syntheses, and chemical engineering aspects and physics of reactions in electrical discharges.

514 pages with index   Clothbound (1969) $15.00

Set of L.C. cards free with library orders upon request

Other books in ADVANCES IN CHEMISTRY SERIES on topics of industrial interest include:

No. 85 Stabilization of Polymers and Stabilizer Processes. Twenty-two papers survey progress and report recent work on a variety of stabilization problems—thermal stabilization, antioxidants and antiozonants for polyolefins, rubbers, and rubbers containing polymers. Other topics include microbial stabilization, ultraviolet light absorbers, and fire retardants. 332 pages
Cloth   (1968) $12.00

No. 78 Literature of Chemical Technology. Forty articles discuss the literature of many aspects of chemical technology, including chlor-alkali and electrochemistry, ceramics, rocket propulsion, photography, medicinal chemistry, leather and glue, waxes, textile, paper, soap, plastics, coatings, explosives, petroleum, dyes, aerosols, pesticides, and foods. Special attention is given to rubber with eight articles and one on carbon black. Included for each article is discussion of special literature sources and services, books, periodicals, patent classes, and bibliographies.   732 pages
Cloth   (1968) $17.50

No. 76 Oxidation of Organic Compounds—II. Thirty-one papers on gas phase oxidations, homogeneous catalysis, applied oxidation, and synthetic processes.   438 pages
Cloth   (1968) $13.50

No. 70 Homogeneous Catalysis. Industrial Applications and Implications. Concentrates on reactions in solution. Reviews the kinds of substances that can be used as homogeneous catalysts and how they function, contrasts homogeneous with heterogeneous catalysis, reviews industrial applications of homogeneous catalysis, and treats in detail many special topics.   283 pages
Cloth   (1968) $10.50

No. 69 Fuel Gasification. Waning natural gas supplies and the threat of nuclear fuels are renewing interest in converting solid fuels to high B.t.u. gas. Sixteen studies survey current research in the U.S. and elsewhere from which commercial processes seem imminent.   276 pages
Cloth   (1967) $10.50

No. 64 Regenerative EMF Cells. Seventeen papers survey current progress and research on regenerative systems for converting and storing electrical energy. Principal emphasis is on thermally regenerative systems, but chemical and photochemical systems are considered.   309 pages
Cloth   (1967) $11.00

No. 51 Selective Oxidation Processes. Surveys methods for selectively oxidizing petroleum fractions by vapor phase and liquid phase processes, such as hydroxylation of aromatics and olefins; covers use of SO_2, NO_2, and O_3 and surveys carbanion oxidation.   177 pages
Cloth   (1965) $8.00

No. 48 Plasticization and Plasticizer Processes. Seventeen papers survey recent studies on plasticizer action, properties, and production. Includes chapters on glass transition, plasticizer mobility, processes for phthalates and other plasticizers, and antiplasticizers.   200 pages
Cloth   (1965) $8.00

No. 46 Patents for Chemical inventions. What to do about your patentable idea before you call the attorney. 117 pages
Cloth   (1964) $5.50

No. 38 Saline Water Conversion—II. Fourteen papers from two symposia; includes recovery of minerals from sea water, minimizing scale formation, wiped thin-film distillation, diffusion still, solar flash evaporation, osmosis, electrodialysis (3 papers), research in Israel, hydrate process.   199 pages
Paper   (1963) $8.00

No. 34 Polymerization and Polycondensation Processes. An I&EC Division symposium with emphasis on unit processes. Twenty-one papers on addition polymerization, polycondensation reactions, commercial polymerization processes, and equipment design.   260 pages
Paper   (1962) $10.00

No. 27 Saline Water Conversion. A Water and Waste Chemistry Division symposium; includes thermodynamics of desalting, solvent extraction, freezing, centrifugal phase barrier recompression distillation, multistage flash evaporation, ion exchange, osmosis, and electrochemical demineralization.   246 pages
Paper   (1960) $9.00

No. 21 Ozone Chemistry and Technology. Sixty papers from the International Ozone Conference; includes ozone chemistry, high concentration ozone, ozone analysis and technology, formation in electrical discharge, toxicity, sterilization, and water purification.   465 pages
Cloth   (1959) $10.00

No. 19 Handling and Uses of Alkali Metals. Nineteen articles on the chemistry, manufacture, and use of the alkali metals; five are devoted solely or partly to lithium, two to potassium, the remainder to sodium.   177 pages
Paper   (1957) $7.00

No. 5 Progress in Petroleum Technology. Survey of 25 years of progress at the ACS Diamond Jubilee. Thirty-two papers on all aspects of petroleum processing and products.   392 pages
Cloth   (1951) $8.00

All books postpaid in U.S. and Canada; plus 20 cents foreign and PUAS.

Order from **SPECIAL ISSUES SALES**
AMERICAN CHEMICAL SOCIETY
1155 SIXTEENTH ST., N.W.
WASHINGTON, D.C. 20036